Transactions of the ASME®

Editor
ROBERT M. McMEEKING
Assistant to the Editor
LIZ MONTANA

APPLIED MECHANICS DIVISION
Executive Committee
(Chair) S. KYRIAKIDES
P. D. SPANOS
M. C. BOYCE
W.-K. LIU
T. N. FARRIS
Associate Editors
E. ARRUDA (2004)
J. R. BARBER (2003)
R. C. BENSON (2003)
A. A. FERRI (2003)
H. GAO (2003)
D. A. KOURIS (2005)
A. NEEDLEMAN (2004)
O. O'REILLY (2004)
M.-J. PINDERA (2003)
K. R. RAJAGOPAL (2003)
K. T. RAMESH (2003)
K. RAVI-CHANDAR (2003)
W. S. SARIC (2003)
D. A. SIGINER (2003)
T. E. TEZDUYAR (2003)
N. TRIANTAFYLLIDIS (2003)

BOARD ON COMMUNICATIONS
Chair and Vice-President
OZDEN OCHOA

OFFICERS OF THE ASME
President, S. SKEMP
Executive Director, V. R. CARTER
Treasurer, R. E. NICKELL

PUBLISHING STAFF
Managing Director, Engineering
THOMAS G. LOUGHLIN
Director, Technical Publishing
PHILIP DI VIETRO
Managing Editor, Technical Publishing
CYNTHIA B. CLARK
Manager, Journals
JOAN MERANZE
Production Coordinator
JUDITH SIERANT
Production Assistant
MARISOL ANDINO

Transactions of the ASME, Journal of Applied Mechanics (ISSN 0021-8936) is published bimonthly (Jan., Mar., May, July, Sept., Nov.) The American Society of Mechanical Engineers, Three Park Avenue, New York, NY 10016. Periodicals postage paid at New York, NY and additional mailing office. POSTMASTER: Send address changes to Transactions of the ASME, Journal of Applied Mechanics, c/o THE AMERICAN SOCIETY OF MECHANICAL ENGINEERS, 22 Law Drive, Box 2300, Fairfield, NJ 07007-2300. **CHANGES OF ADDRESS** must be received at Society headquarters seven weeks before they are to be effective. Please send old label and new address. **STATEMENT from By-Laws.** The Society shall not be responsible for statements or opinions advanced in papers or . . . printed in its publications (B7.1, Para. 3).
COPYRIGHT © 2003 by The American Society of Mechanical Engineers. For authorization to photocopy material for internal or personal use under those circumstances not falling within the fair use provisions of the Copyright Act, contact the Copyright Clearance Center (CCC), 222 Rosewood Drive, Danvers, MA 01923, tel: 978-750-8400, www.copyright.com. Request for special permission or bulk copying should be addressed to Reprints/Permission Department. **INDEXED** by Applied Mechanics Reviews and Engineering Information, Inc. Canadian Goods & Services Tax Registration #126148048.

Journal of Applied Mechanics

Published Bimonthly by The American Society of Mechanical Engineers

VOLUME 70 • NUMBER 3 • MAY 2003

TECHNICAL PAPERS

BRIEF NOTES

(Contents continued on inside back cover)

This journal is printed on acid-free paper, which exceeds the ANSI Z39.48-1992 specification for permanence of paper and library materials. ♾™
♻ 85% recycled content, including 10% post-consumer fibers.

ANNOUNCEMENTS AND SPECIAL NOTES

The ASME Journal of Applied Mechanics is abstracted and indexed in the following:

Alloys Index, Aluminum Industry Abstracts, Applied Science & Technology Index, AMR Abstracts Database, Ceramic Abstracts, Chemical Abstracts, Civil Engineering Abstracts, Compendex (The electronic equivalent of Engineering Index), Computer & Information Systems Abstracts, Corrosion Abstracts, Current Contents, EEA (Earthquake Engineering Abstracts Database), Electronics & Communications Abstracts Journal, Engineered Materials Abstracts, Engineering Index, Environmental Engineering Abstracts, Environmental Science and Pollution Management, Fluidex, Fuel & Energy Abstracts, GeoRef, Geotechnical Abstracts, INSPEC, International Aerospace Abstracts, Journal of Ferrocement, Materials Science Citation Index, Mechanical Engineering Abstracts, METADEX (The electronic equivalent of Metals Abstracts and Alloys Index), Metals Abstracts, Nonferrous Metals Alert, Polymers Ceramics Composites Alert, Referativnyi Zhurnal, Science Citation Index, SciSearch (Electronic equivalent of Science Citation Index), Shock and Vibration Digest, Solid State and Superconductivity Abstracts, Steels Alert, Zentralblatt MATH

A. J. Zak
e-mail: azak@mech.gla.ac.uk

M. P. Cartmell
e-mail: matthewc@mech.gla.ac.uk

Department of Mechanical Engineering,
University of Glasgow,
James Watt Building,
Glasgow G12 8QQ, Scotland

W. Ostachowicz
Institute of Fluid-Flow Machinery PASci,
Gdansk,
ul. Fiszera 14,
80-952, Poland
e-mail: wieslaw@imp.gda.pl

Dynamics of Multilayered Composite Plates With Shape Memory Alloy Wires

In this paper certain aspects of the dynamic behavior of a multilayered, composite plate with shape memory alloys (SMA) wires have been investigated. The influence of parameters such as the orientation and location of SMA wires, the orientation and relative volume fraction of reinforcing fibers, the thickness-to-length and length-to-width ratios, and different boundary conditions, on changes in the critical load, the natural frequencies and the modes of vibrations of the plate have all been studied and discussed in the paper. The use of two different techniques, generally known in the literature as the active property tuning and active strain energy tuning methods, has also been investigated. The results presented in this paper have been obtained by the use of the finite element method and a new finite element formulated for multilayered composite plates has been applied for this purpose. [DOI: 10.1115/1.1546263]

Introduction

The use of different composite materials has been continuously growing in recent years. Although many applications for composite materials have been identified, extensive research is still being carried out in order to expand this field. New materials and technologies have been researched, enabling more original and more advanced applications. One such new application is the integration of shape memory materials within composite materials.

Shape memory alloys (SMAs) possess the inherent ability to change their material properties, in particular their Young's modulus, [1,2], damping capacity, [3,4], as well as a great capacity for the generation of large internal forces, [5]. Integrating SMAs within composite material structures potentially allows the active control of the static and dynamic behavior of the integrated structure. Precise tuning of SMA components, [6,7], enables the control of certain static and dynamic characteristics of composite material structures, notably deflection and shape, natural frequencies and modes of vibrations, amplitudes of forced vibrations, and also their damping properties. SMA components embedded into, or bonded to, composite material structures can be utilized in two different ways. The first implementation is in the use of the active property tuning method, [6,7], which only exploits changes in the stiffness of the SMA components during their activation. In the active strain energy tuning method, [6,7], the shape memory effect is exploited differently. In this technique the activation of previously pseudo-plastically elongated SMA components integrated within appropriate composite material structures of interest, leads to the generation of high recovery stresses. (See Table 1.)

Various applications for using integrated SMA-composite components have been investigated by several researchers and have been published in the literature. For example, Rogers et al. [6] presented concepts for using SMA wires for the control of natural frequencies and modes of vibrations of simply supported plates. Both the active property tuning and active strain energy tuning methods were considered in their work. They also discussed two different techniques for bonding SMA wires to composite structures. For the active property tuning method SMA wires can be directly bonded to the host structure, while for the active strain energy tuning method they can be fully bonded, or put into sleeves and then attached to the host structure at strategic points, in order to eliminate the high shearing stresses which arise from this form of activation. Rogers et al. [6] showed that significant changes in natural frequencies and modes of vibration can be achieved for simply supported plates with integrated SMA wires, and also stated that the use of the active strain energy tuning method leads to much better results than the use of the active property tuning method. Changes in natural frequencies of fully clamped composite beams with integrated SMA wires were investigated analytically and experimentally by Baz et al. [8]. Baz et al. showed that SMA wires embedded into composite beams can be successfully used for controlling their natural frequencies. The influence of different initial strain levels, as well as temperature effects due to the activation of the SMA wires, were also considered in their study. Baz et al. [9] also investigated the use of SMA components for shape control of composite beams. They demonstrated that SMA components in the form of strips, previously trained for the two-way shape memory effect, and then embedded into composite beams, can be used for the shape control of such structures. The natural frequencies of composite beams modified in this manner were also significantly affected. Lee and Lee [10] investigated the buckling and post-buckling behavior of simply supported and fully clamped composite plates with embedded SMA wires. They found that SMA wire activation can increase the critical load of composite plates, but this effect is a function of the relative location of the SMA wires, and also the buckling direction. Pae et al. [11] used SMA wires and piezoceramic actuators for controlling the modes of vibrations of simply supported and cantilevered beams. Using compressive forces generated by the SMA wires and concentrated moments from the piezoceramic actuators they managed to control the higher vibration modes of a cantilever beam and also the second mode of vibration of a simply supported beam. Song et al. [12] used SMA wires for active position control of a honeycomb structure composite beam. They demonstrated, numerically and experimentally, that SMA wires can be used for very accurate and effective monitoring of the beam shape, in the case of a cantilever boundary condition. Ostachowicz et al. [13,14] studied the dynamic and buckling behavior of various composite plates, reinforced by SMA wires. They successfully confirmed that SMA wires can be used to influence the natural frequencies and the thermal buckling of such structures. Ostachowicz and Cartmell [15] investigated the flutter behavior of

Contributed by the Applied Mechanics Division of THE AMERICAN SOCIETY OF MECHANICAL ENGINEERS for publication in the ASME JOURNAL OF APPLIED MECHANICS. Manuscript received by the ASME Applied Mechanics Division, Nov. 20, 2001; final revision, June 10, 2002. Associate Editor: N. C. Perkins. Discussion on the paper should be addressed to the Editor, Prof. Robert M. McMeeking, Department of Mechanical and Environmental Engineering, University of California–Santa Barbara, Santa Barbara, CA 93106-5070, and will be accepted until four months after final publication of the paper itself in the ASME JOURNAL OF APPLIED MECHANICS.

 Copyright © 2003 by ASME

Table 1 Mechanical properties of composite material components and SMA wires

Material	Young's Modulus	Poisson's Ratio	Density
Epoxy resin	3.43GPa	0.35	1250.0 kg/m^3
Aluminum	70.0 GPa	0.33	2800.0 kg/m^3
Glass fibers	65.5 GPa	0.23	2250.0 kg/m^3
Kevlar fibers	130.0 GPa	0.22	1450.0 kg/m^3
Graphite fibers	275.6 GPa	0.20	1900.0 kg/m^3
Boron fibers	399.6 GPa	0.21	2580.0 kg/m^3
SMA—Martensite	26.3 GPa	0.30	6448.1 kg/m^3
SMA—Austenite	67.0 GPa	0.30	6448.1 kg/m^3

a composite plate in a supersonic airflow. In their work they showed that substantial modifications can be achieved to the dynamic behavior of the plate by means of the SMA wires, and also that flutter frequencies of the plate can be significantly increased.

Results presented in the literature indicate many possible applications for SMA components in the active control of the static and dynamic behavior of composite material structures. However, a more detailed study is required for a complete and rigorous understanding of this behavior because the results presented in the literature invariably refer to somewhat specific cases. This, therefore, is the motivation behind this paper.

Continuing with this review of appropriate literature it is interesting to note that Rogers et al. [6] only examined SMA/epoxy composite plates, for which the relative volume fraction of SMA wires was very high. The behavior of such plates is determined by the high ratio of the Young's modulus of the SMA to that of the epoxy matrix, and also by the high relative volume fraction of the SMA wires. The same assumption regarding the high relative volume fraction of SMA components was made by Baz et al. [9], who investigated glass/epoxy composite beams with embedded SMA strips. Furthermore, Baz et al. [8,9] investigated composite beams of very low thickness-to-length ratio. Although such structures are characterized by very good static and dynamic performance when the SMA components are activated, they tend to have very few engineering applications due to their low stiffness and low critical loads. Lee and Lee [10] studied the buckling and post-buckling behavior of composite plates with embedded SMA wires, for which the assumed values for activation recovery stresses were very close to their ultimate tensile strength.

From the foregoing it can be seen that the static and dynamic behavior of composite material structures with embedded SMA components strongly depends on the following factors; the Young's modulus of the SMA to the Young's modulus of the reinforcing fibers (glass, Kevlar, graphite, boron, etc.), the relative volume fraction of the SMA components, the relative volume fraction of the reinforcing fibers, structural geometry, and the location and orientation of the SMA components within their host structures, temperature, moisture, etc. It should be noted that contrary to Rogers et al. [6] and Baz et al. [9], for most advanced composite materials the ratio of the SMA Young's modulus to that of the reinforcing fibers is low—see Table 1 for reference, [16–18]. Moreover, the high relative volume fraction of the SMA components is not really desirable due to the fact that the thermal effect of resistive heating during SMA activation is very likely to result in the softening of the composite material. However, this effect can be easily avoided by an appropriate selection of the SMA transformation temperatures, which can normally be adjusted accurately. For commonly available SMAs (refer to Shape Memory Application, Inc. at http://www.sma-inc.com) the transformation temperatures can remain within a fully controllable temperature range from as low as -53°C to -5°C to as high as 59°C to 121°C, with a total hysteresis span of 26°C to 46°C in the case of binary alloys. The hysteresis span can be further reduced to 10°C by the addition of copper, or, alternatively, enhanced to 100°C by the addition of niobium, together with further alloying.

In this paper the finite element method has been used to investigate certain aspects of the dynamic behavior of a multilayered composite plate with embedded SMA wires. In order to accomplish this a new finite element is proposed for modeling multilayered, composite plates—see the Appendix for more details. It should be noted that although all the mechanical influences mentioned previously have been incorporated into the modeling, thermal and hygrothermal effects have not been taken into account in this study. It is fair to say that in some practical applications these additional effects could have a significant influence on the behavior. For the research presented in this paper thermal and hygrothermal phenomena were neglected mainly due to the fact that the necessary physical properties for this sort of analysis relating to different composite material components are not currently available in the literature, and provision of this data was well outside the scope of this particular funded study.

Composite Plate With SMA Wires

Figure 1 shows a multilayered composite plate with embedded SMA wires. This particular plate is of length 500 mm, width 500 mm, and thickness 9 mm, although these dimensions are by no means critical. It is assumed that the plate consists of 12 layers of composite material, comprising, in turn, of two SMA/epoxy layers and ten graphite/epoxy layers. The orientation of the reinforcing graphite fibers and the SMA wires for each layer is defined by the angle α. It is also assumed that the SMA/epoxy layers are placed symmetrically across the cross section of the plate, as depicted in Fig. 1, in the form of two outer layers. The thickness of each SMA/epoxy layer is 0.5 mm, and the corresponding relative volume fraction of the SMA wires is 0.57. Additionally, the SMA wires stay fully bonded within each SMA/epoxy layer of the plate. The relative volume fraction of the graphite fibres within the inner graphite/epoxy layers is 0.5, and the thickness of each graphite/epoxy layer is 0.8 mm. The ply stacking sequence of the plate is $[0°/(\pm 45°)_5/0°]$.

Initially a convergence analysis was carried out whereby the results obtained from the finite element method using the new formulated multilayered composite plate element, were verified against the exact solution, [16,19], for different mesh densities. Simply supported boundary conditions of the plate (i.e., where all the edges are simply supported) were chosen to carry out this test. The first six bending natural frequencies of the plate, as well as the critical load in the x-direction, were investigated as a function of the mesh density. It was assumed that the SMA wires should not be activated in this particular case. The results obtained are presented in Table 2.

It can be seen from the results presented in Table 2 that a very good accuracy is obtained at relatively low mesh densities for the

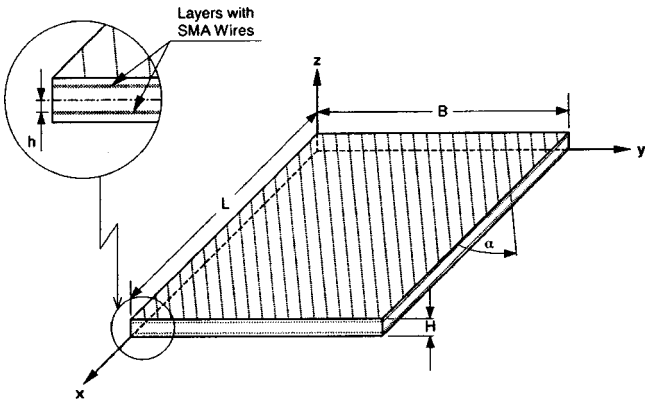

Fig. 1 A multilayered composite plate with embedded SMA wires

Table 2 An analysis of the convergence of the finite element results for a simply supported plate (SMA wires not activated)

Mesh Density	Mode I	Mode II	Mode III	Mode IV	Mode V	Mode VI	N_{crit} [1)]
2×2	179.28 Hz	417.06 Hz	422.83 Hz	741.94 Hz	763.69 Hz	938.27 Hz	−540.28 kN/m
3×3	178.60 Hz	408.23 Hz	414.31 Hz	710.36 Hz	756.11 Hz	772.93 Hz	−536.63 kN/m
4×4	178.39 Hz	407.54 Hz	413.65 Hz	706.31 Hz	750.25 Hz	767.25 Hz	−535.37 kN/m
5×5	178.29 Hz	407.21 Hz	413.32 Hz	704.53 Hz	749.98 Hz	767.03 Hz	−534.81 kN/m
6×6	178.24 Hz	407.03 Hz	413.14 Hz	703.62 Hz	749.74 Hz	766.82 Hz	−534.52 kN/m
7×7	178.22 Hz	406.92 Hz	413.04 Hz	703.10 Hz	749.58 Hz	766.67 Hz	−534.34 kN/m
8×8	178.20 Hz	406.85 Hz	412.97 Hz	702.77 Hz	749.48 Hz	766.58 Hz	−534.23 kN/m
9×9	178.18 Hz	406.80 Hz	412.92 Hz	702.55 Hz	749.41 Hz	766.52 Hz	−534.15 kN/m
10×10	178.17 Hz	406.77 Hz	412.89 Hz	702.40 Hz	749.37 Hz	766.47 Hz	−534.10 kN/m
Exact CPT [2)]	179.06 Hz	411.37 Hz	417.65 Hz	716.26 Hz	764.57 Hz	782.51 Hz	−539.09 kN/m
Exact FSDT [3)]	178.19 Hz	406.97 Hz	413.09 Hz	702.65 Hz	750.37 Hz	767.52 Hz	−533.87 kN/m

[1)] N_{crit} is the critical load of the plate calculated in the x-direction
[2)] Classical plate theory [20,21]
[3)] First-order shear deformation theory [20,21]

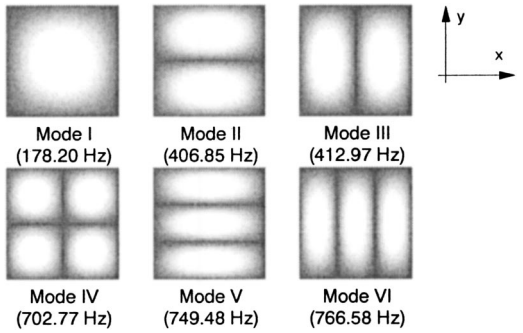

Fig. 2 Modes of vibration of a simply supported plate (SMA wires not activated)

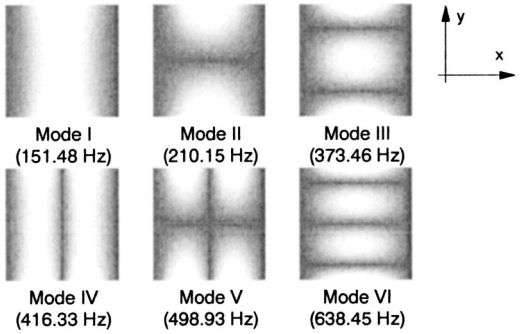

Fig. 3 Modes of vibration of a two-sided-clamped plate (SMA wires not activated)

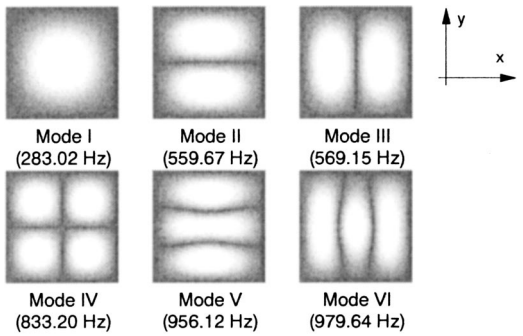

Fig. 4 Modes of vibration of a fully clamped plate (SMA wires not activated)

proposed new plate finite element. Because of this the following calculations have been undertaken for the plate divided up into 64 plate finite elements (mesh density 8×8).

In general three different types of plate boundary conditions are discussed in this paper, these being simply supported (i.e., where all the edges are simply supported), two-sided clamped (i.e., where the two edges parallel to the y-axis are clamped), and fully clamped (i.e., where all the edges are clamped). The results of the numerical calculations presented in this work are related to particular modes of plate vibration, and these are presented in Figs. 2–4 for each type of boundary condition. The performance of the active property tuning method and the active strain energy tuning method are also critically compared. In the case of the active strain energy tuning method the assumed recovery stress level for the SMA wires is equal to 172.1 MPa (after Dynalloy, Inc.—http://www.dynalloy.com). Certain mechanical properties used for the graphite/epoxy composite and the SMA wires are presented in Table 1. It should be mentioned here that the relative quantities of the natural frequencies and the critical loads (noting that only the critical load of the plate in the x-direction is investigated) presented in this paper, are defined as ratios of the values of these quantities, calculated for the plate when the SMA wires are activated (for both the active property tuning method and the active strain energy tuning method, respectively), to the corresponding values when the SMA wires are not activated.

Numerical Calculations

In the first numerical example the natural frequencies and the critical load of the plate are investigated as a function of plate dimensions. The numerical results obtained for the active property tuning method, and the active strain energy tuning method, for different values of the length-to-width ratios, L/B, of the plate are illustrated in Figs. 5–7 inclusive. It should be mentioned that during the calculations the total area of the plate stays constant, so the total mass of the plate is also constant and remains unaffected by changes in the plate dimensions. From the results presented in Figs. 5–7 it is clearly seen that for the simply supported type of boundary condition greater relative changes in the plate's natural frequencies, and the critical load, are observed towards smaller length-to-width ratios, L/B. In the case of the two-sided-clamped boundary condition the observed behavior is different. A greater general plate performance can be noted for larger values of the length-to-width ratios, L/B.

However, it should also be appreciated that for both types of boundary conditions those natural frequencies for which the nodal lines of the modes are perpendicular to the orientation angle of the SMA wires are the most significantly affected. These are mode III and mode VI for the simply supported plate, and mode I and mode IV for the two-sided-clamped plate (also see Figs. 2–3 for more details). Furthermore, for the active strain energy tuning method the changes in the natural frequencies and the observed critical load are bigger than for the active property tuning method, and the

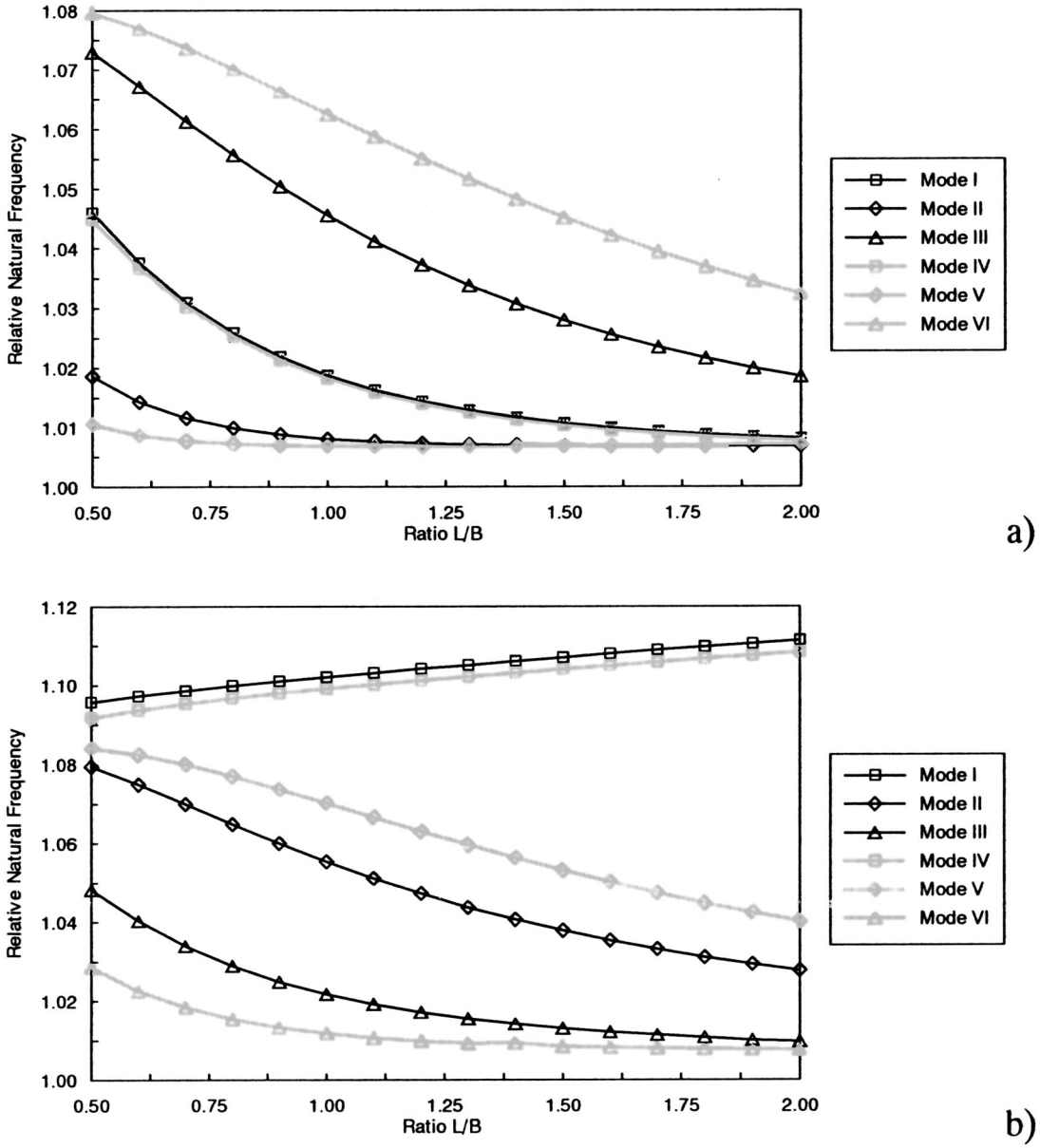

Fig. 5 Natural frequencies of a (*a*) simply supported and (*b*) two-sided-clamped, plate versus the length-to-width ratio (active property tuning method)

lower modes are the most noticeably affected ones. Additionally, for the simply supported plate certain changes in the buckling modes can be observed, as depicted in Fig. 7. In this case the buckling mode of the plate changes from mode I to mode III (see Fig. 2), when the length-to-width ratio L/B increases. It should be emphasized here that for the case when the SMA wires are not activated the transition point between the modes is point A, whereas it is point B when the SMA wires are activated. The transition of the buckling mode influences the relative critical load of the plate, and this increases rapidly over the transition region due to the change in the buckling mode. Such behavior is not observed in the case of the two-sided-clamped plate.

In the following example the influence of the relative plate thickness H/L is investigated. It is assumed that the thickness of the inner graphite/epoxy layers can vary, while the thickness of the outer SMA/epoxy layers remains constant. The results of numerical calculations for the relative changes in the natural frequencies and the critical load, as a function of the relative plate thickness H/L, are given in Figs. 8–10 inclusive. For both methods the results show a strong influence of the thickness-to-length ratio H/L on the natural frequencies and the critical load of the plate. The performance of the plate (greater relative changes in the natural frequencies and the critical load) is greater for smaller thickness-to-length ratios, and this is related to the fact that when the thickness of the inner graphite/epoxy layers decreases, the stiffness of the outer SMA/epoxy layers becomes dominant. This effect is especially strong at very small thickness-to-length ratios of the plate. Moreover, it should also be noted in this case that for the active strain energy tuning method the changes in the natural frequencies and the critical load, in general, are greater than for the active property tuning method. An additional influence in the form of boundary condition dependence is observed.

The next example concerns the influence of the volume fraction of the reinforcing graphite fibers on the plate's dynamic behavior. A general assumption of this part of the work is that the properties of the outer SMA/epoxy layers remain constant, whilst the relative volume fraction of the reinforcing graphite fibers in the inner graphite/epoxy layers have been allowed to vary.

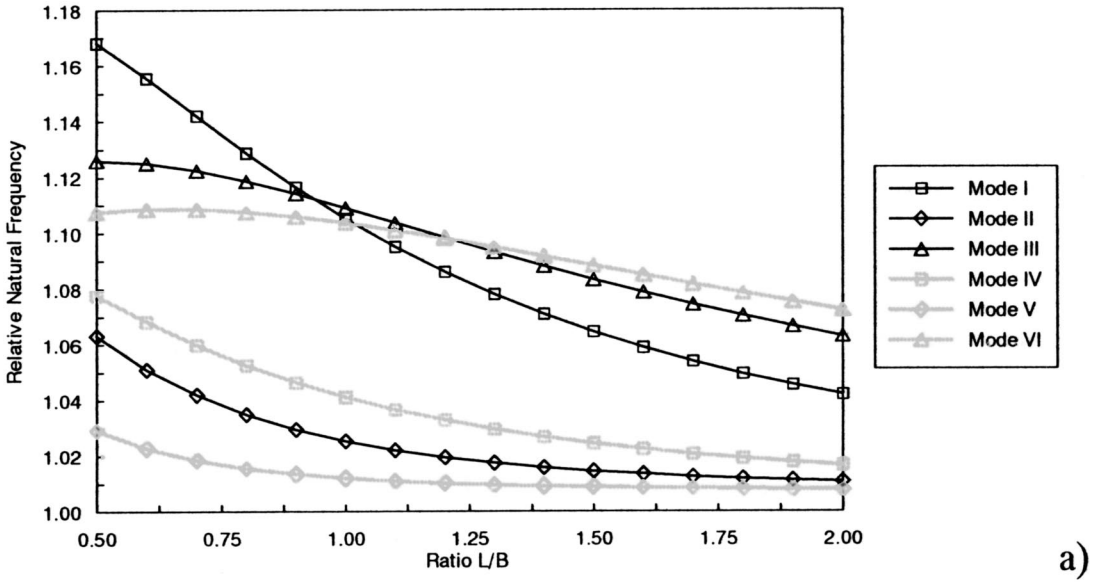

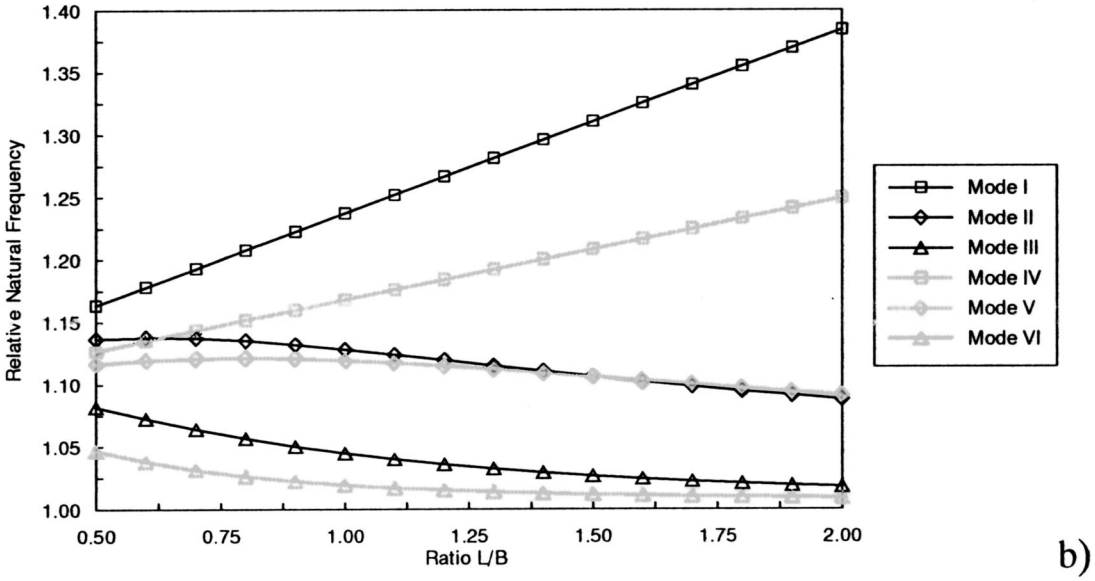

Fig. 6 Natural frequencies of a (*a*) simply supported and (*b*) two-sided-clamped, plate versus the length-to-width ratio (active strain energy tuning method)

In Figs. 11–13 results are illustrated for relative changes in the natural frequencies and the critical load of the plate. The numerical calculations show that for both the active property tuning and active strain energy tuning methods the plate performance increases when the relative volume fraction of the graphite fibers within the inner graphite/epoxy layers decreases. This effect is directly linked to the ratio of the longitudinal Young's modulus of the outer SMA/epoxy layers to the same quantity for the inner graphite/epoxy layers. In the case when the relative volume fraction of the graphite fibres is low, or equal to zero, the stiffness contribution of the outer SMA/epoxy layers of the plate becomes predominant, and the observed changes in the natural frequencies and the critical load are therefore maximal.

The influence of the orientation angle of the reinforcing graphite fibers on the natural frequencies and the critical load of the plate is investigated next. It is assumed here that the orientation angle α of the graphite fibers within the inner graphite/epoxy layers can vary, while the properties of the outer SMA/epoxy layers remain constant. In this case the constant value of 90° is assumed for the orientation angle of the graphite fibers between subsequent inner graphite/epoxy layers. The ply stacking sequence of the plate can therefore be defined as $[0°/(\alpha/(\alpha+90°))_5/0°]$. The results presented in Figs. 14–16 show the influence of the orientation angle α of the reinforcing graphite fibres on changes in the natural frequencies and the critical load for two boundary condition of the plate considered. It is obvious from the results stated in Figs. 14–16 that for the chosen ply stacking sequence the performance of the plate varies with the modes of vibration and the type of boundary conditions. Generally, the greatest performance (the greatest relative changes in the natural frequencies and the critical load) is obtained for the modes whose nodal lines are perpendicular to the orientation angle of the SMA wires within the outer SMA/epoxy layers of the plate. Consequently, the smallest performance is obtained for the modes whose nodal lines are parallel to that reference (see also Figs. 3–4 for more details).

Additionally, in the case of the active strain energy tuning method a further increase in the plate performance is obtained from the in-plane load generated by the recovery stresses during

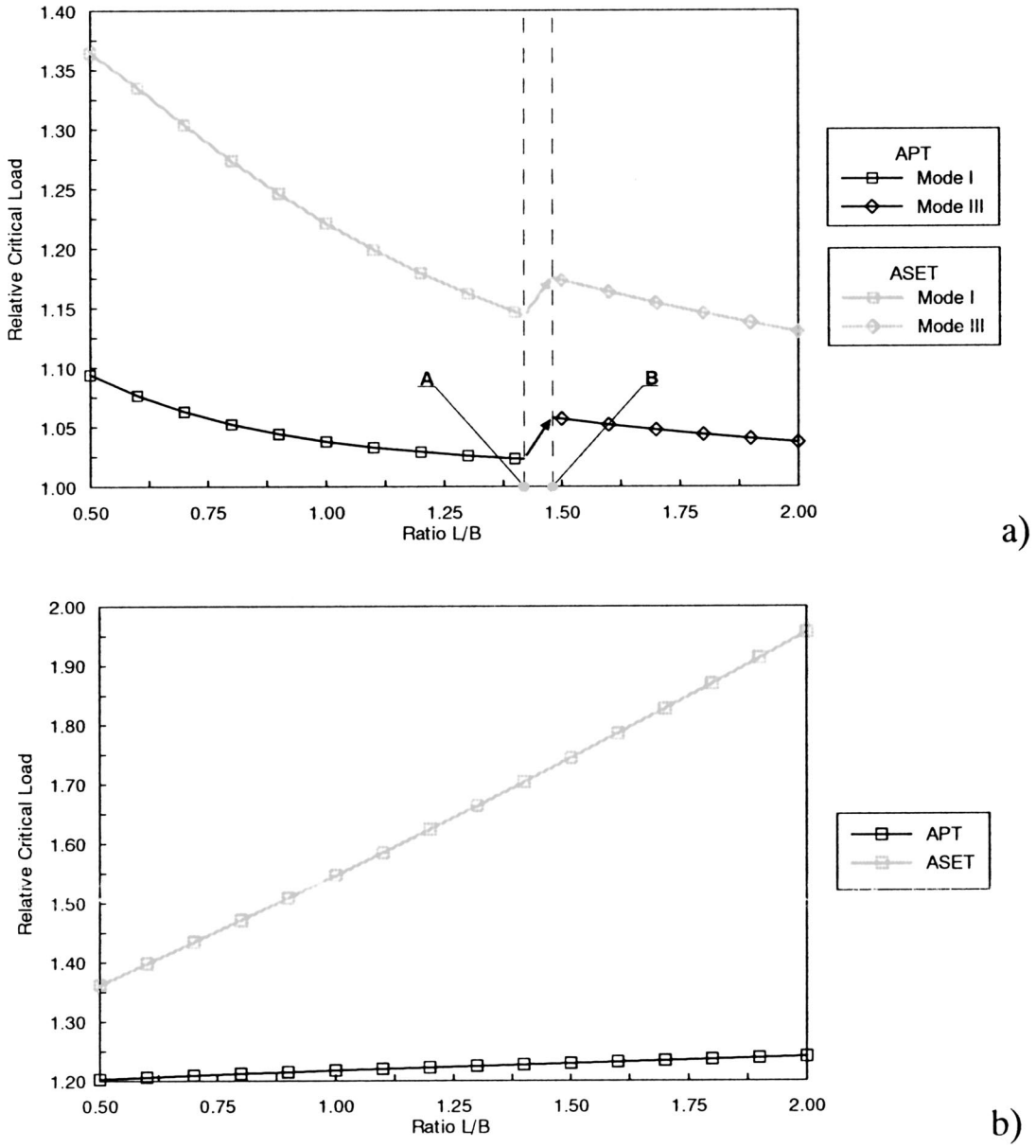

Fig. 7 The critical load of a (*a*) simply supported and (*b*) two-sided-clamped plate versus the length-to-width ratio

activation of the SMA wires. However, this additional increase of the plate performance mostly affects the first natural frequency.

Finally, a study has been made of the influence of the location of the SMA wires within the plate. In this case the mechanical properties of each SMA/epoxy and graphite/epoxy layer remain constant. However, it is assumed that the location of the SMA/epoxy layers within the plate can be changed. The relative location of the SMA/epoxy layers changes from the extreme outer layer to the central one, and this corresponds to a change in the ply stacking sequence of the plate from $[0°/(\pm 45°)_5/0°]$ to $[(\pm 45°)_2/45°/(0°)_2/-45°/(\pm 45°)_2]$, respectively. In Figs. 17–19 inclusive results are quoted for the relative changes in the natural frequencies and the critical load, as a function of the relative location of the SMA wires, h/H.

From these results it arises that the location of the SMA wires within the plate has a major influence on the plate's behavior. The greatest performance is observed when the SMA wires are fitted within the extreme layers of the plate. When the SMA wires are incorporated within the central layers of the plate changes in the natural frequencies and the critical load of the plate are minimal. This effect is related to the fact that the bending contribution of each layer of the plate increases rapidly with the distance between the layer and the neutral plane of the plate. For this reason the extreme layers of the plate give the greatest stiffness contribution. However, it should be noticed that the stiffness of the graphite/epoxy layers is usually greater than the stiffness of the SMA/epoxy layers, which leads to a slight reduction in the natural frequencies and the critical load.

Furthermore, the influence of SMA activation on changes to the modes of the plate is also investigated, and here it is also assumed that the properties of the inner graphite/epoxy layers remain constant, while the orientation angle α of the SMA wires within the outer SMA/epoxy layers is assumed to be equal to 0 deg and 90 deg, respectively. This corresponds to a ply stacking sequence of $[0°/(\pm 45°)_5/90°]$. In this case only the active property tuning method is investigated and the results presented in Fig. 20 show that the activation of the SMA wires in either the upper or lower layers of the plate has a very definite influence on the plate's

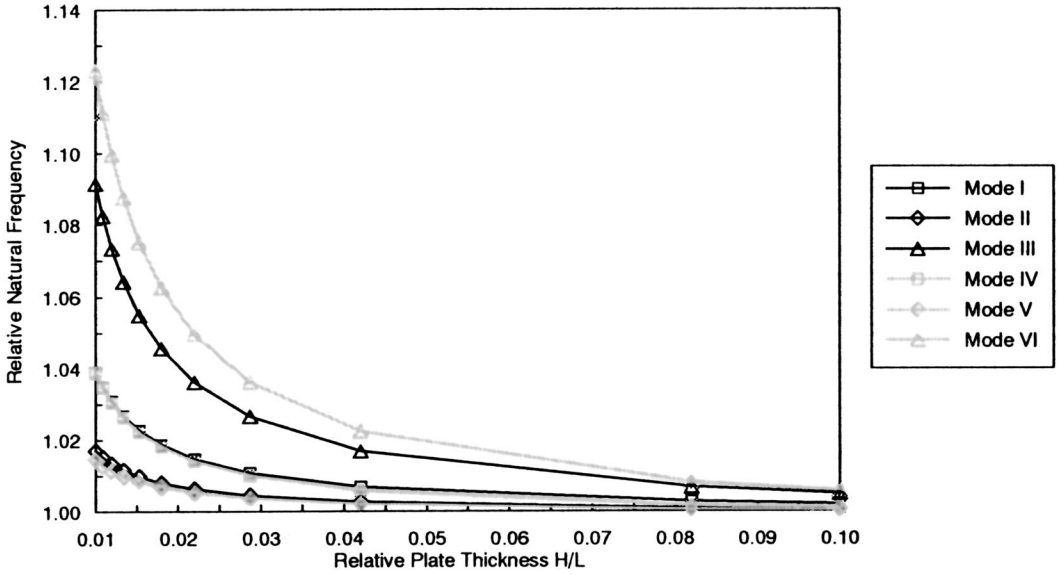

Fig. 8 Natural frequencies of a simply supported plate versus the relative plate thickness (active property tuning method)

behavior. However, in the case of the two-sided-clamped plate no influence of the activation of the SMA wires is observed, and this differs from the case of the simply supported and fully clamped type of boundary conditions. Active control of plate vibration modes can be achieved by selective activation of the SMA wires in different plate layers, and this phenomenon is evident from Fig. 20. The activation of the upper or lower SMA/epoxy layers shows a changeover between certain twin modes of vibration in the form of mode II and mode III, mode V and mode VI, mode VII and mode VIII, etc. Moreover, the observed changes in the modes of vibrations occur practically at the same natural frequency. In the case considered only two SMA/epoxy layers for vibration control of the plate are used, but more extensive control vibration modes can be realised by the use of numerous SMA/epoxy layers, differently placed within the plate.

Conclusions

The influence of different parameters on the dynamic behavior of a multilayered composite plate with embedded SMA wires have been investigated in this paper. The research carried under this program has led to the following general conclusions:

1. In general, greater dynamic performance in terms of relative changes in the natural frequencies and the critical load of the plate is observed for the active strain energy tuning method than for the active property tuning method. The performance of the plate is not only a function of vibration modes, but is also a function of the boundary conditions. The greatest changes in the natural frequencies and the critical load are observed not for the lowest modes of vibration, but generally for those modes where the nodal lines are

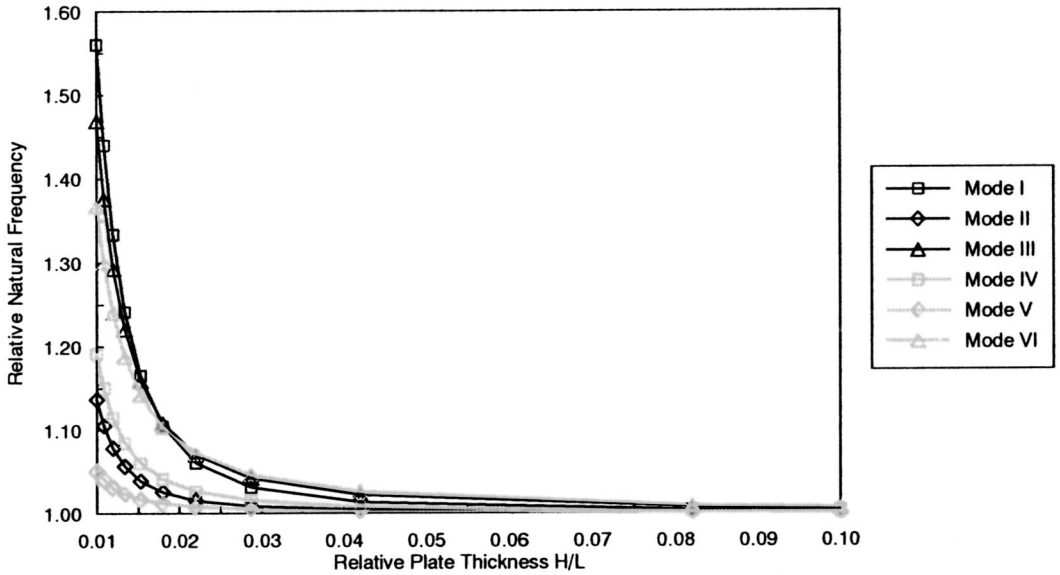

Fig. 9 Natural frequencies of a simply supported plate versus the relative plate thickness (active strain energy tuning method)

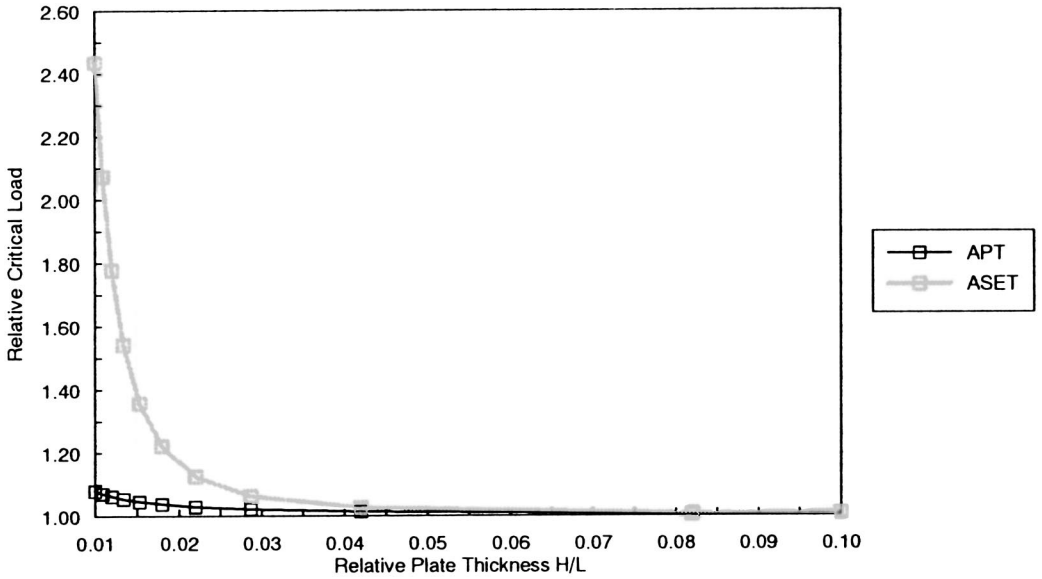

Fig. 10 The critical load of a simply supported plate versus the relative plate thickness

perpendicular to the orientation angle of the SMA wires. This behavior can be explained by the fact that changes in the plate's stiffness due to activation of the SMA wires are maximal in the direction of the SMA wires. This is so in the case of the active property tuning method and also for the active strain energy tuning method. Consequently, the most significant affected modes are those for which most of vibration energy is associated with the plate motion in the direction of the SMA wires. For the active strain energy tuning method the in-plane load resulting from activation of the SMA wires additionally influences the lowest natural frequencies of the plate, principally the fundamental natural frequency of the plate. The number of constraints imposed by different types of boundary conditions also influences the results. For more flexible types of boundary conditions a smaller number of constraints can be imposed, and then both the natural frequencies and the critical load of the plate are necessarily lower. This means that the influence of the SMA generated in-plane load in the case of active strain energy tuning is greater. As a consequence the greatest changes in the natural frequencies and the critical load are observed in the case of the two-sided-clamped type of boundary condition, whilst the lowest changes are observed in the case of the fully clamped type of boundary condition.

It is likely that in practice the use of the active strain energy tuning method will be limited. This is because additional SMA boundary conditions are required (noting that these are independent of the structural boundary conditions) in order to produce the necessary tensile recovery stresses during SMA activation. If this condition is not met then the recovery stresses produced during SMA activation will be compressive, and may greatly reduce the natural frequencies and the critical load of the structure. Moreover, high recovery stresses (and these could be tensile or compressive) produced during SMA activation may also generate high shearing stresses within the structure, thereby leading to damage.

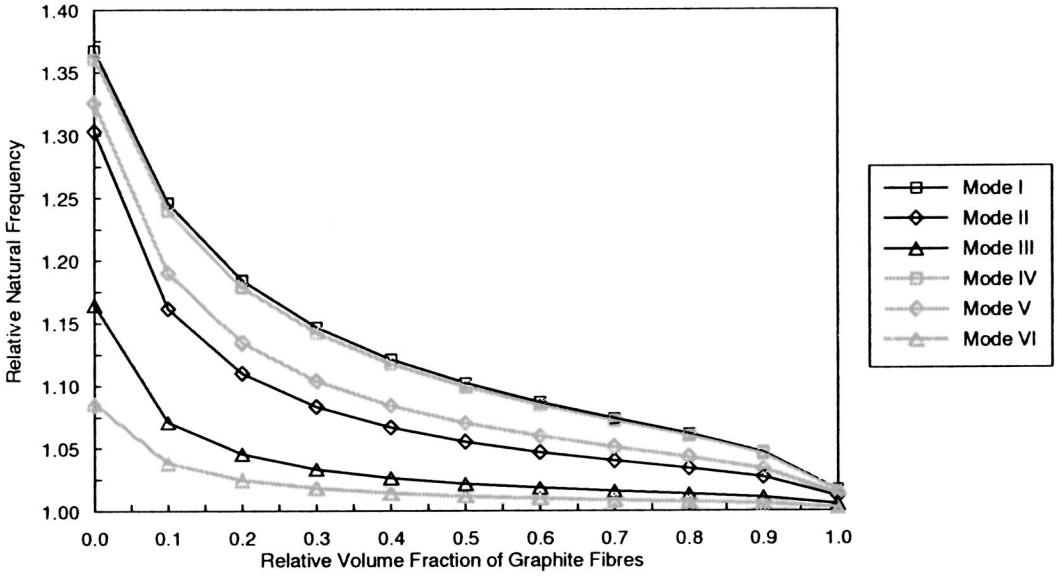

Fig. 11 Natural frequencies of a two-sided-clamped plate versus the relative volume fraction of graphite fibers (active property tuning method)

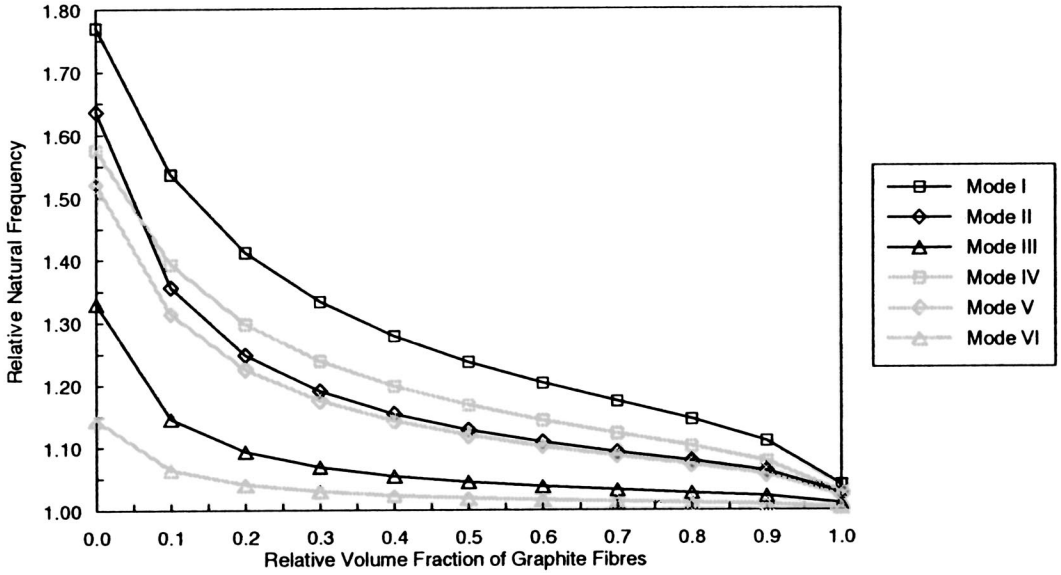

Fig. 12 Natural frequencies of a two-sided-clamped plate versus the relative volume fraction of graphite fibers (active strain energy tuning method)

In contrast with this the natural frequency and critical load changes generated by the active property tuning method will be smaller than those due to active strain energy tuning. Therefore the active property tuning method provides a potentially safer methodology for the application of SMA wires in the active control of the dynamic behavior of composite structures. It is important to note that the active strain energy tuning method can possibly be successfully used for shape control of composite structures, as long as certain define disadvantages are understood and accounted for. On that basis it is prudent to recommend that the active strain energy tuning method probably requires further investigation.

3. The dynamic performance of the multilayered composite plate is not only a function of the modes of vibration but also a function of the boundary conditions that are operative. For the multilayered composite plate the changes observed in the natural frequencies and the critical load are, additionally, a function of the orientation of the SMA wires, as well as the length-to-width ratio of the plate.

4. In the case of the multilayered composite plate, the greatest performance (in terms of the greatest relative changes in the natural frequencies and the critical load) is observed for the modes whose nodal lines are perpendicular to the orientation angle of the SMA wires. This allows selective, as well as economical, use of SMAs for active control of the dynamics of composite material structures. The SMA wires can be orientated within a structure in the most effective way, affecting only the necessary and relevant natural frequencies and modes.

The use of the active strain energy tuning method has an additional influence on the lowest natural frequencies and the corresponding modes, and thus the performance of the plate can be increased.

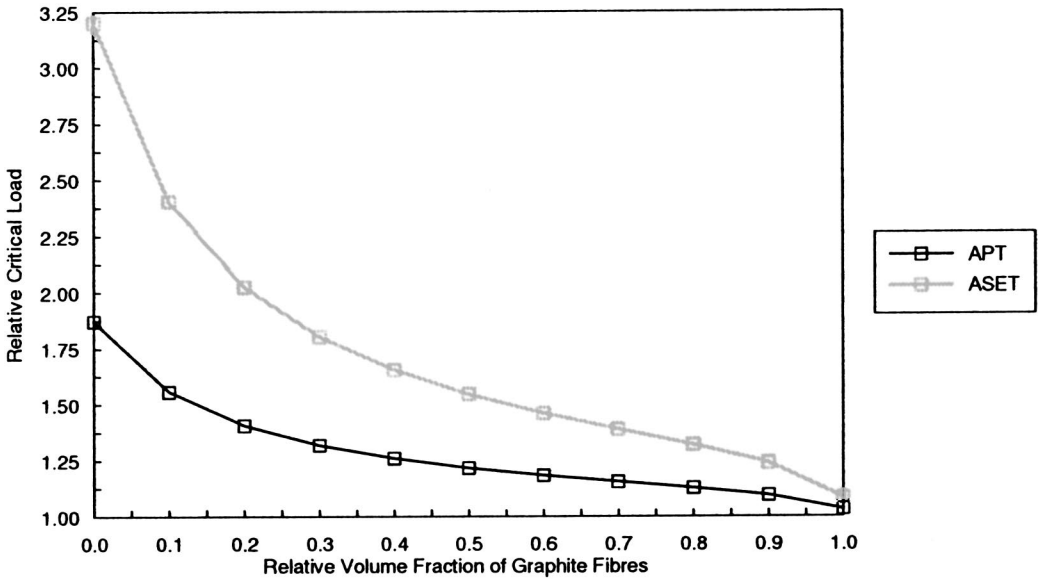

Fig. 13 The critical load of a two-sided-clamped plate versus the relative volume fraction of graphite fibers

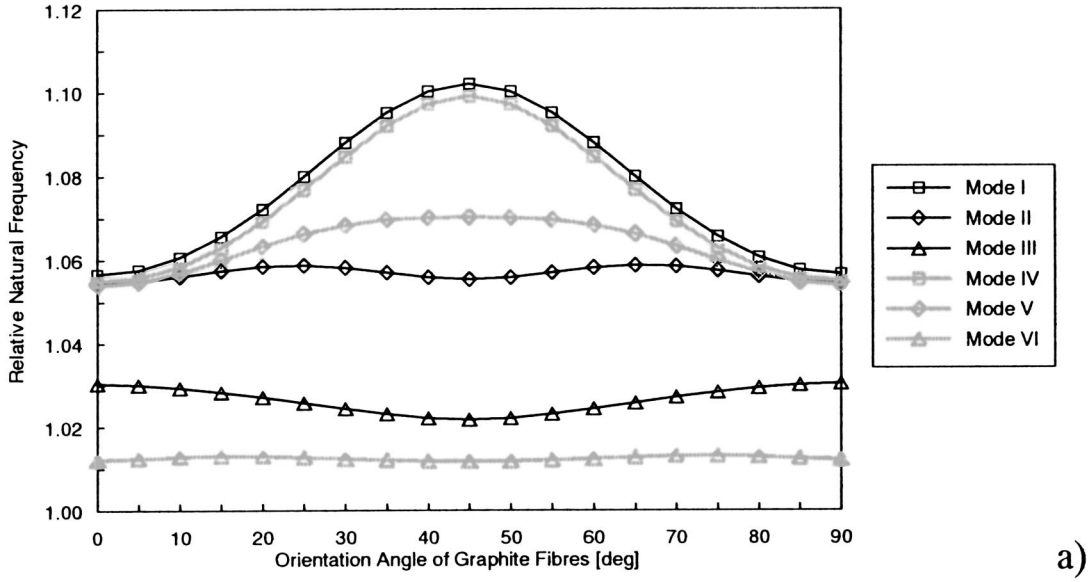

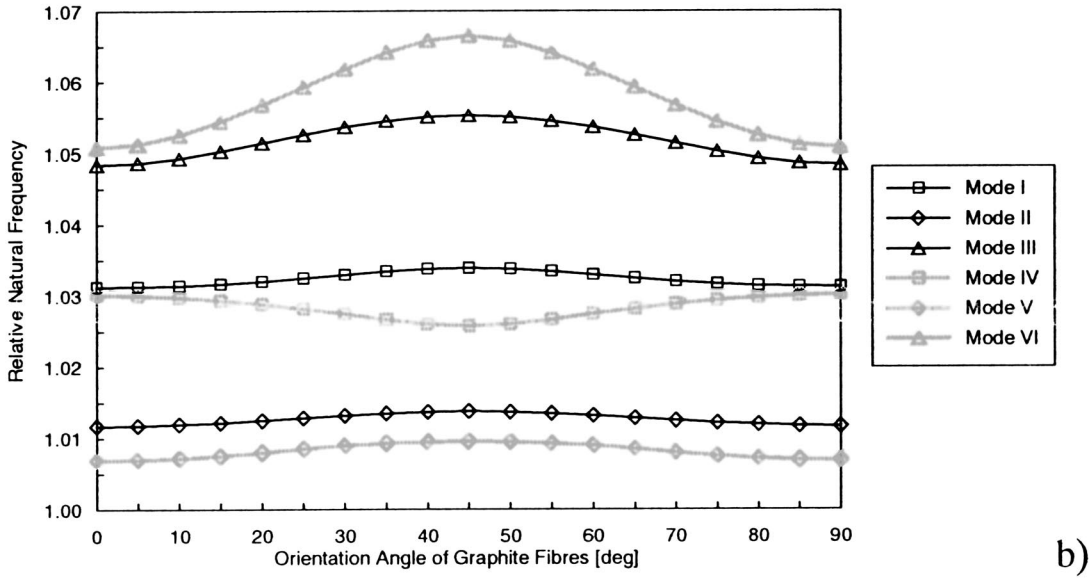

Fig. 14 Natural frequencies of a (*a*) two-sided-clamped and (*b*) fully clamped, plate versus the orientation angle of graphite fibers (active property tuning method)

5. The dynamic behavior of the multilayered composite plate also depends on the orientation of the reinforcing graphite fibers. However, it should be noted that structural components made of composite materials are commercially available in sheet form, for which the orientation angle of the reinforcing fibers is determined by the manufacturing process and it is possible to obtain different quasi-isotropic composite material sheets in the [0°/90°] layout from certain commercial outlets. For that reason the use of this particular parameter for dynamic optimization is greatly limited. Some influence can be achieved by the optimal choice of the ply stacking sequence.

6. For both the active property tuning and active strain energy tuning methods the results presented in this paper show that the thickness-to-length ratio is highly influential, as is the relative volume fraction of the reinforcing graphite fibers. However, it needs to be appreciated that in most engineering applications the thickness-to-length ratio of composite structural elements is principally determined by the lowest natural frequency, or the critical load, of the structure.

The relative volume fraction of the reinforcing fibres is also limited by commercially available structural composite components, for which the relative volume fraction of the reinforcing fibers varies from 0.4 to 0.6. These values determine many applications for which the SMA wires can be successfully used in the form proposed in this paper.

7. The location of the SMA wires has great significance for the dynamic behavior of the composite multilayered composite plate. The greatest performance is observed when SMA wires are located in the outer layers of the beam and plate; however, the natural frequencies and the critical load are slightly reduced in these cases. It is worth noting that when the SMA wires are located within the inner layers, close to the neutral plane of the plate for example, then the natural frequencies and the critical load are not much affected. This is because the SMAs add little or no contribution to the plate stiffness. Additionally, strong thermal effects can be observed due to heat transfer, resulting in composite material softening during activation of the SMAs for location

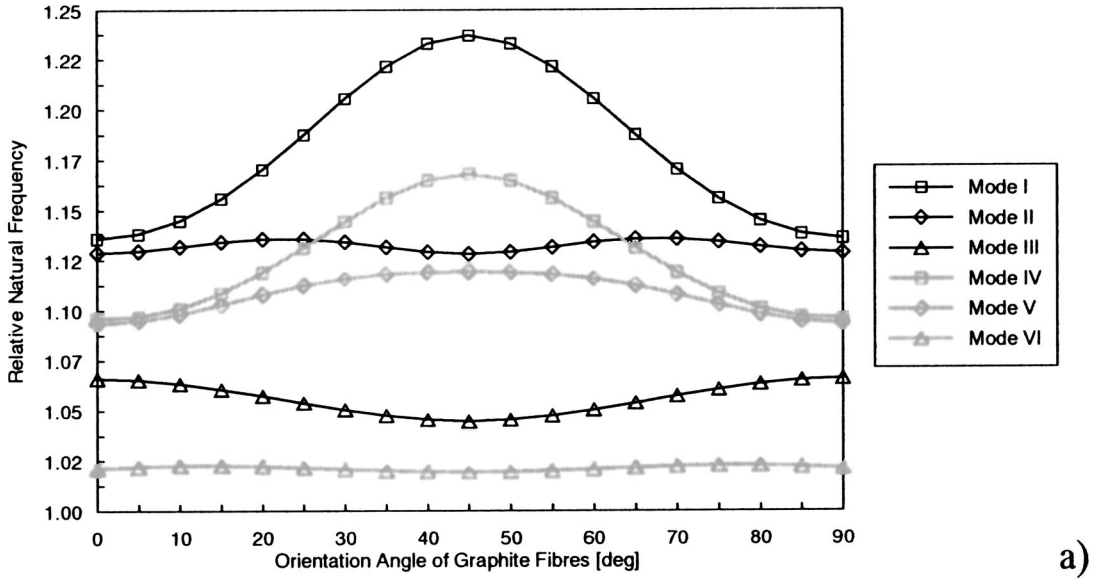

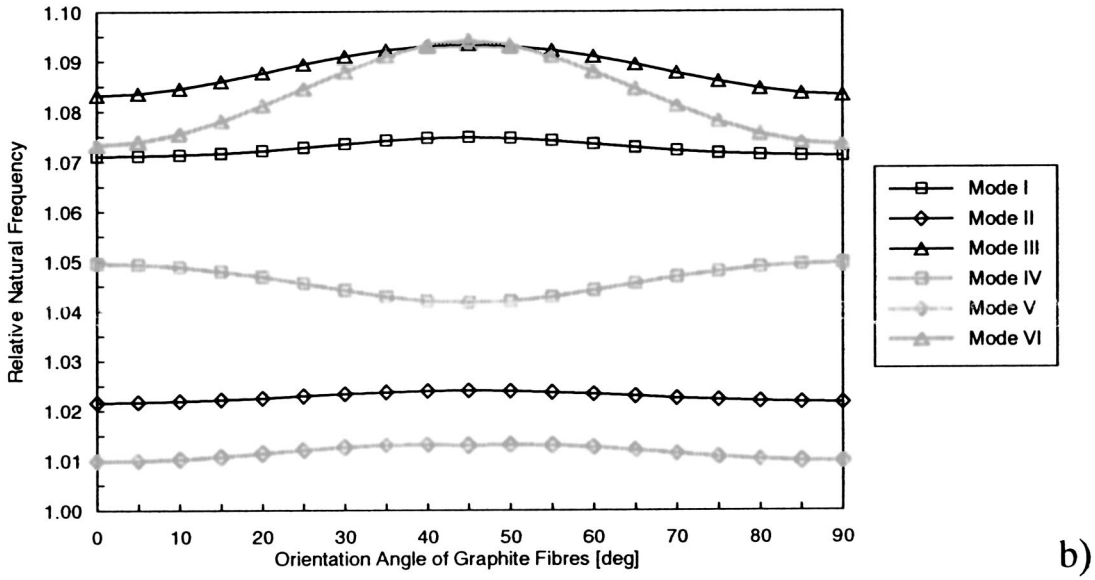

Fig. 15 Natural frequencies of a (*a*) two-sided-clamped and (*b*) fully clamped plate versus the orientation angle of graphite (active strain energy tuning method)

within the neutral plane of the plate. When the SMA wires are located within the outer layers of a structure the thermal effect are not likely to be as strong due to better cooling conditions.

8. It has successfully been shown that SMA wires can be used for active control of the modes of vibrations of the composite multilayered composite plate. The observed behavior shows that activation of the SMA wires in different layers of the plate enables interesting changeovers between certain twin modes of vibrations. Moreover, by the use of numerous layers whereby the SMA wires are placed differently within the plate more extensive modal control can be achieved. However, it should be noted that successful active modal control can only be performed for certain types of plate boundary conditions.

Acknowledgments

The authors wish to acknowledge the support provided for this research by the UK's Engineering and Physical Sciences Research Council, via grants GR/N06267 and GR/N06328. The support of Rolls-Royce plc is also gratefully acknowledged.

Appendix

In this paper a new multilayered composite plate finite element is proposed, as shown in Fig. 21. The element has eight nodes and seven degrees-of-freedom at each node. These degrees-of-freedom are defined as the longitudinal in-plane displacements u and v, the transverse displacement w, the rotations φ_x and φ_y due to the transverse displacement w, and the independent correction rotations θ_x and θ_y for the rotations φ_x and φ_y, and due to shearing effects. The length of the element is L, the width is B, and the thickness is H. In general the element consists of N layers made up of a unidirectional composite material. In the case of the analysis presented in this paper these are two SMA/epoxy layers and ten graphite/epoxy layers. Reinforcing fibers (SMA wires, graphite fibres) are arbitrarily orientated within the layers, and

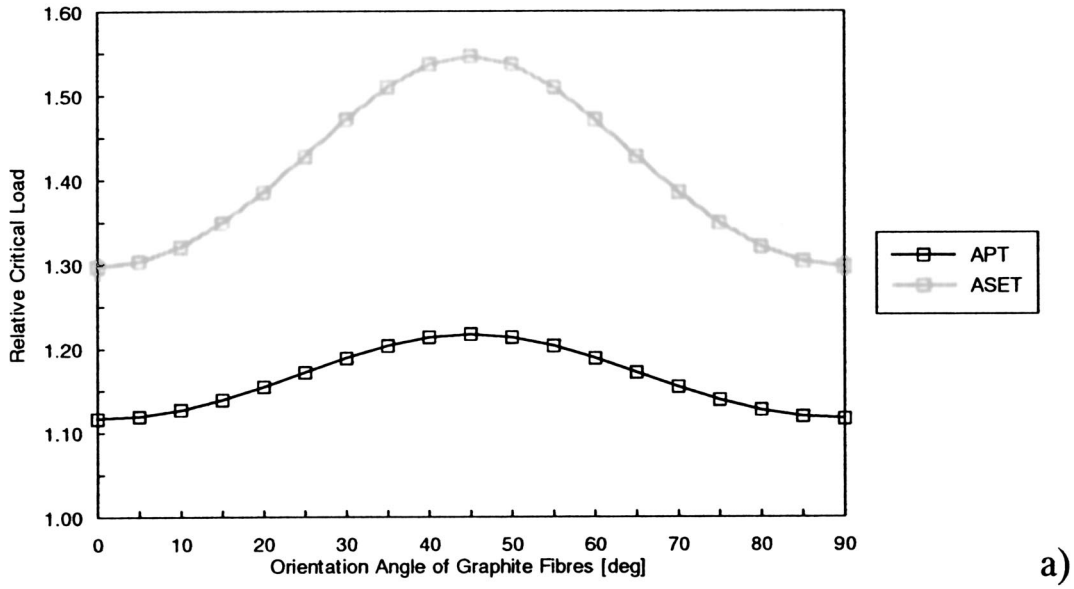

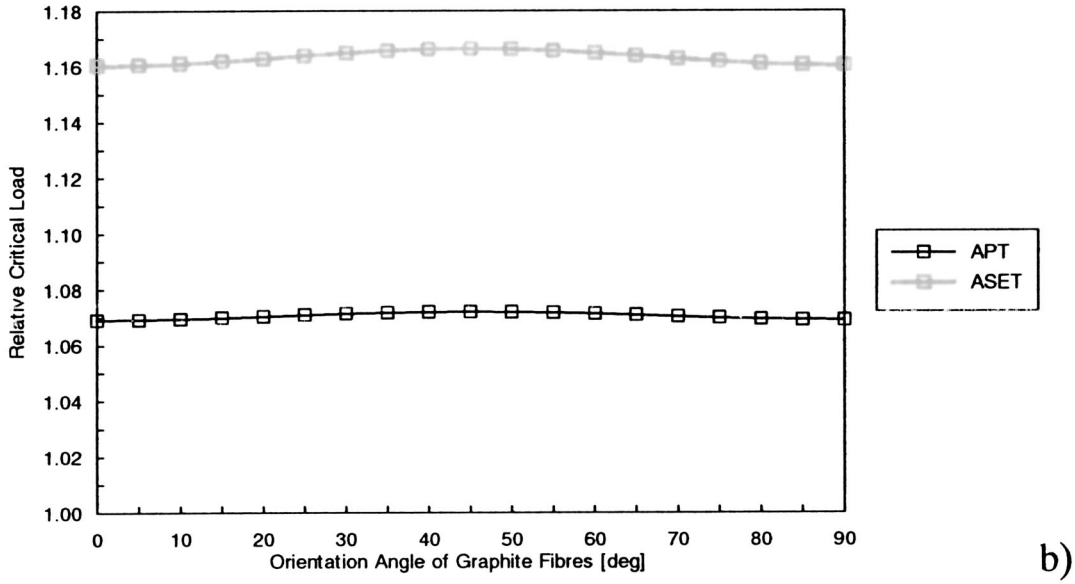

Fig. 16 The critical load of a (*a*) two-sided-clamped and (*b*) fully clamped plate versus the orientation angle of graphite fibers

their orientation angle α is measured within the x-y plane of the element

The displacement field within the element is assumed to be as follows, according to first-order shear deformation theory, [20,21]:

$$\begin{cases} u(x,y,z) = u_0(x,y) + z \cdot \varphi_x(x,y) + z \cdot \dfrac{H}{L} \cdot \theta_x(x,y) \\ v(x,y,z) = v_0(x,y) + z \cdot \varphi_y(x,y) + z \cdot \dfrac{H}{B} \cdot \theta_y(x,y) \\ w(x,y,z) = w_0(x,y) \end{cases} \tag{1}$$

where $u_0(x,y)$ and $v_0(x,y)$ are the longitudinal displacements, with $w_0(x,y)$ being the transverse displacement of the plate element defined within the neutral plane of the plate. The rotations $\varphi_x(x,y)$ and $\varphi_y(x,y)$ of the element can be expressed as the negative first partial derivatives of the transverse displacement $w_0(x,y)$, respectively. Under this assumption the displacement field within the element takes the following form:

$$\begin{cases} u(x,y,z) = u_0(x,y) - z \cdot \partial_x w_0(x,y) + z \cdot \dfrac{H}{L} \cdot \theta_x(x,y) \\ v(x,y,z) = v_0(x,y) - z \cdot \partial_y w_0(x,y) + z \cdot \dfrac{H}{B} \cdot \theta_y(x,y) \\ w(x,y,z) = w_0(x,y) \end{cases} \tag{2}$$

Utilizing known finite element techniques and using boundary conditions for the nodal displacements of the element, the shape functions of the element can be easily derived, [21,22]. It can be seen that the nodal degrees-of-freedom which are assumed for the element allow an improved approximation for the transverse displacement $w_0(x,y)$. For the longitudinal in-plane displacements $u_0(x,y)$ and $v_0(x,y)$, and the independent correction rotations $\theta_x(x,y)$ and $\theta_y(x,y)$ second-order approximation polynomials are used, as in the case of the classical plate finite element, on the

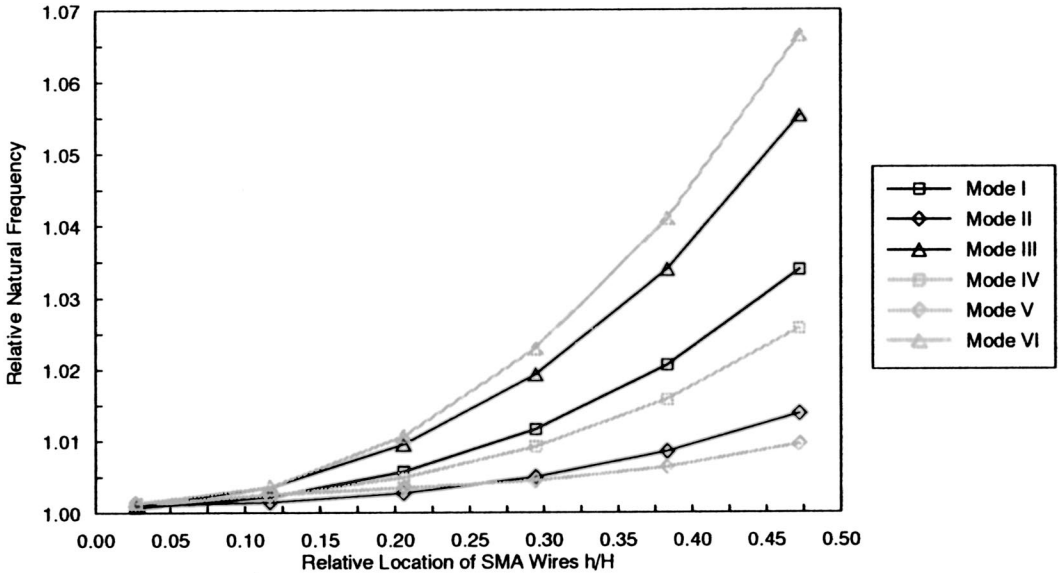

Fig. 17 Natural frequencies of a fully clamped plate versus the relative position of SMA wires (active property tuning method)

assumption of first-order deformation theory. However, for the transverse displacement $w_0(x,y)$ higher-order approximation polynomials can be used.

For small displacement theory the strains, [20], within the element can be expressed as

$$\begin{cases} \varepsilon_x = \partial_x u_0 - z \cdot \partial_{x,x} w_0 + z \cdot \dfrac{H}{L} \cdot \partial_x \theta_x \\ \varepsilon_y = \partial_y v_0 - z \cdot \partial_{y,y} w_0 + z \cdot \dfrac{H}{B} \cdot \partial_y \theta_y \\ \gamma_{xy} = \partial_y u_0 + \partial_x v_0 - 2z \cdot \partial_{x,x} w_0 + z \cdot \dfrac{H}{L} \cdot \partial_y \theta_x + z \cdot \dfrac{H}{B} \cdot \partial_x \theta_y. \\ \gamma_{xz} = \partial_z u + \partial_x w = \dfrac{H}{L} \cdot \theta_x \\ \gamma_{yz} = \partial_z v + \partial_y w = \dfrac{H}{B} \cdot \theta_y \end{cases} \tag{3}$$

It can be seen that for small thickness-to-length ratios the displacement and strains fields of the new element are consistent with Kirchhoff plate theory, while for higher thickness-to-length ratios influence from shearing strains is included. The finite element proposed here is characterized by better dynamic and static behavior than the classical plate finite element, and as a consequence of this no locking effects are observed.

Stresses within the nth layer of the element consisting of N layers of a unidirectional composite material can be expressed by Eq. (4), where matrix $\mathbf{Q}_n$ is the matrix of elastic coefficients, and has a very well-known structure, [23]. It should be noted that the elements of matrix $\mathbf{Q}_n$ depend on the relative volume fractions of composite material components, and also on the orientation of the reinforcing fibers within the layer (for details see, for example, [20,23]).

$$\mathrm{col}[\sigma_x, \sigma_y, \sigma_{xy}, \sigma_{xz}, \sigma_{yz}]_n = \mathbf{Q}_n \cdot \mathrm{col}[\varepsilon_x, \varepsilon_y, \varepsilon_{xy}, \varepsilon_{xz}, \varepsilon_{yz}]_n \tag{4}$$

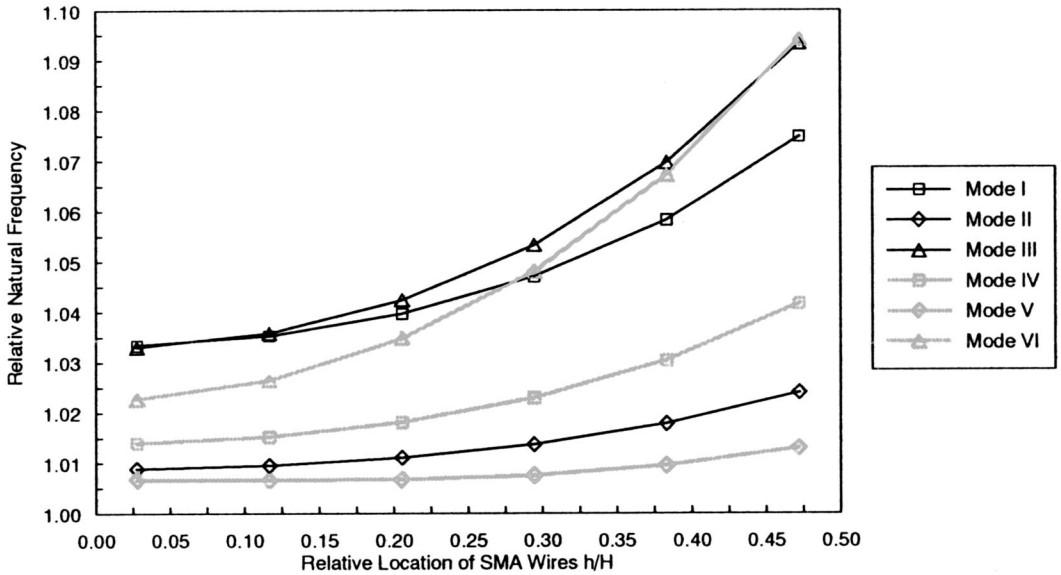

Fig. 18 Natural frequencies of a fully clamped plate versus the relative position of SMA wires (active strain energy tuning method)

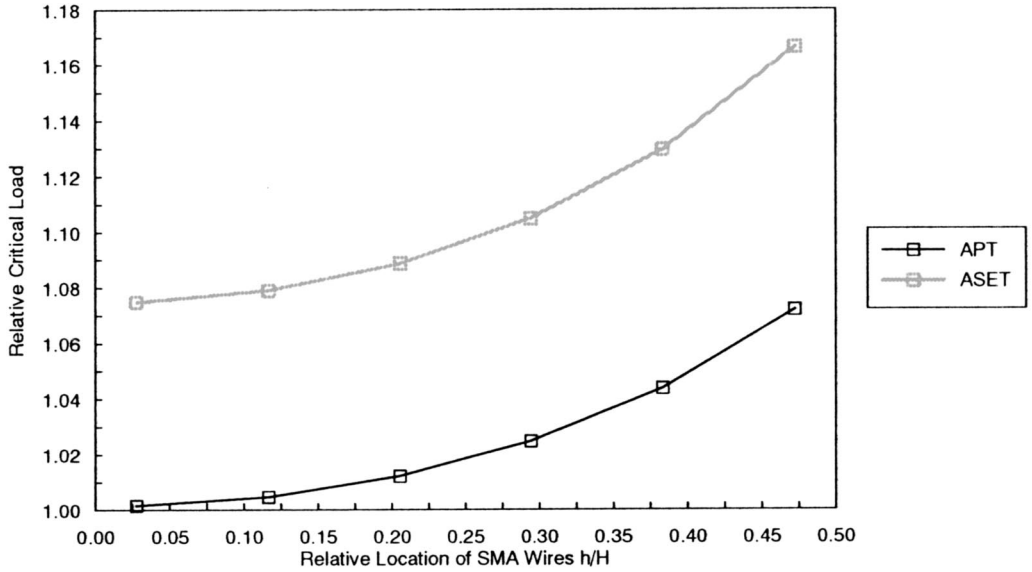

Fig. 19 The critical load of a fully clamped plate versus the relative position of SMA wires

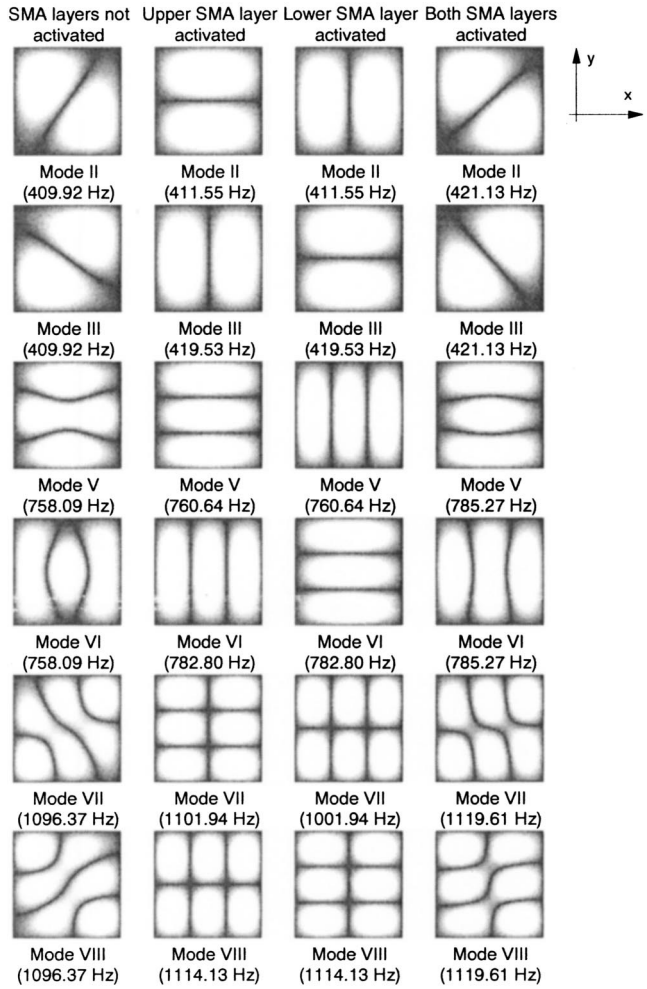

Fig. 20 The influence of SMA wire activation on the vibration modes of a simply supported plate (active property tuning method)

From this application of the well-known procedures of the finite element method, [21,22], means that the characteristic mass matrix, stiffness matrix, and also the geometrical stiffness matrix of the element can be easily obtained.

It should be noted here that in the case of the active property tuning method the results obtained (natural frequencies, the critical load, or modes of vibrations) correspond to the case when activation of the SMA wires within the SMA/epoxy layers leads only to changes in the element stiffness matrix, while the mass matrix of the element remains unaffected. The same also applies to the global stiffness and mass matrices. In the case of the active strain energy tuning method, however, besides changes in the element stiffness matrix, the in-plane load resulting from the activation of the SMA wires within the SMA/epoxy layers is also taken into account by means of the element geometrical stiffness matrix. In both cases the solution procedure used in the paper is analogous to that presented in [13,14].

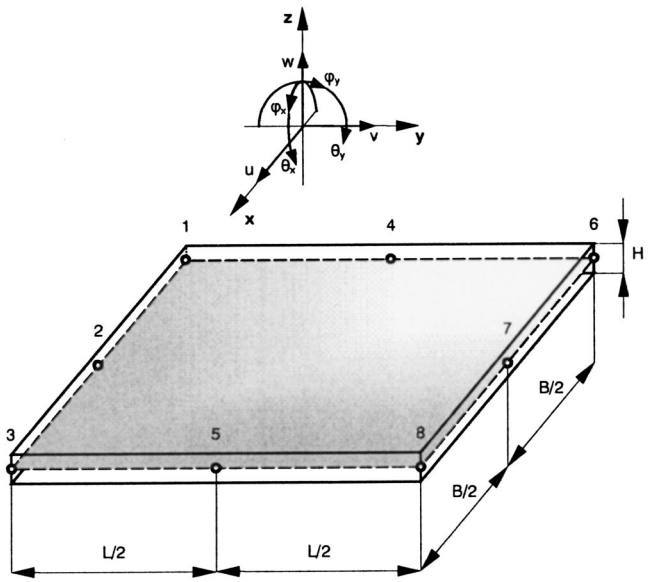

Fig. 21 The proposed new multilayered composite plate finite element

References

[1] Otsuka, K., and Wayman, C. M., 1998, *Shape Memory Materials*, Cambridge University Press, Cambridge, UK.

[2] Ford, D. S., and White, S. R., 1996, ''Thermomechanical Behavior of 55Ni45Ti Nitinol,'' Acta Mater., **44**, pp. 2295–2307.

[3] Piedboeuf, M. C., Gauvin, R., and Thomas, M., 1998, ''Damping Behavior of Shape Memory Alloys: Strain Amplitude, Frequency and Temperature Effects,'' J. Sound Vib., **214**, pp. 885–901.

[4] Gandhi, F., and Wolons, D., 1999, ''Characterization of the Pseudoelastic Damping Behavior of Shape Memory Alloy Wires Using Complex Moduls,'' J. Smart Mat. Struct., **8**, pp. 49–56.

[5] Rogers, C. A., Baker, D. K., and Jaeger, C. A., 1989, ''Introduction to Smart Materials and Structures,'' *Smart Materials, Structures, and Mathematical Issues*, Technomic, Lancaster, PA.

[6] Rogers, C. A., Liang, C., and Baker, D. K., 1989, ''Dynamic Control Concepts Using Shape Memory Alloy Reinforced Plates,'' *Smart Materials, Structures, and Mathematical Issues*, Technomic, Lancaster, PA.

[7] Fuller, C. R., Elliott, S. J., and Nelson, P. A., 1996, *Active Control of Vibration*, Academic Press Ltd., London.

[8] Baz, A., Poh, S., Ro, J., and Gilheany, J., 1995, ''Control of the Natural Frequencies of Nitinol-Reinforced Composite Beams,'' J. Sound Vib., **185**, pp. 171–185.

[9] Baz, A., Chen, T., and Ro, J., 2000, ''Shape Control of Nitionol-Reinforced Composite Beams,'' Composites, Part B, **31**, pp. 631–642.

[10] Lee, H. J., and Lee, J. J., 2000, ''A Numerical Analysis of the Buckling and Post-Buckling Behavior of Laminated Composite Shells With Embedded Shape Memory Alloy Wire Actuators,'' J. Smart Mat. Struct., **9**, pp. 780–787.

[11] Pea, S., Lee, H., Park, H., and Hwang, W., 2000, ''Realization of Higher-Mode Deformation of Beams Using Shape Memory Alloy Wires and Piezoceramics,'' J. Smart Mat. Struct., **9**, pp. 848–854.

[12] Song, G., Kelly, B., and Agrawal, B. N., 2000, ''Active Position Control of a Shape Memory Alloy Wire Actuated Composite Beam,'' J. Smart Mat. Struct., **9**, pp. 711–716.

[13] Ostachowicz, W., Krawczuk, M., and Żak, A., 1999, ''Natural Frequencies of a Multilayer Composite Plate With Shape Memory Alloy Wires,'' Int. J. Finite Elements Anal. Design, **32**, pp. 71–83.

[14] Ostachowicz, W., Krawczuk, M., and Zak, A., 2000, ''Dynamics and Buckling of a Multilayer Composite Plate With Embedded SMA Wires,'' Compos. Struct., **48**, pp. 163–167.

[15] Ostachowicz, W., and Cartmell, M. P., 1999, ''Modification to the Vibration Response of an Aero-Excited Composite Panel by Means of Embedded SMA Wires,'' *Identification in Engineering Systems*, Proceedings 2nd International Conference, Swansea, pp. 548–556.

[16] Vinson, J. R., and Sierakowski, J. R., 1986, *The Behavior of Structures Composed of Composite Materials*, Martinus Nijhoff Publishers, Dordrecht.

[17] Brinson, L. C., and Lammering, R., 1993, ''Finite Element Analysis of the Behavior of Shape Memory Alloys and Their Applications,'' Int. J. Solids Struct., **30**, pp. 3261–3280.

[18] GoodFellow Metals Ltd. Catalogue, 2001, *Metals and Materials for Research and Industry*.

[19] Whitney, J. M., 1987, *Structural Analysis of Laminated Anisotropic Plates*, Technomic, Lancaster, PA.

[20] Ochoa, O. O., and Reddy, J. N., 1992, *Finite Elements Analysis of Composite Laminates*, Kluwer Academic Publishers, Dordrecht.

[21] Reddy, J. N., 1993, *An Introduction to the Finite Element Method*, McGraw-Hill, Singapore.

[22] Rao, S. S., 1982, *The Finite Element Method in Engineering*, Pergamon Press, Oxford, UK.

[23] Vinson, J. R., and Sierakowski, R. L., 1986, *The Behavior of Structures Composted of Composite Materials*, Martinus Nijhoff, Dordrecht.

Multiscale, Multiphenomena Modeling and Simulation at the Nanoscale: On Constructing Reduced-Order Models for Nonlinear Dynamical Systems With Many Degrees-of-Freedom

E. H. Dowell
Professor,
Director of the Center for Nonlinear and Complex Systems,
Dean Emeritus, Pratt School of Engineering

D. Tang
Research Associate Professor

Department of Mechanical Engineering and Materials Science,
Duke University,
Durham, NC 27708-0300

The large number of degrees-of-freedom of finite difference, finite element, or molecular dynamics models for complex systems is often a significant barrier to both efficient computation and increased understanding of the relevant phenomena. Thus there is a benefit to constructing reduced-order models with many fewer degrees-of-freedom that retain the same accuracy as the original model. Constructing reduced-order models for linear dynamical systems relies substantially on the existence of global modes such as eigenmodes where a relatively small number of these modes may be sufficient to describe the response of the total system. For systems with very many degrees-of-freedom that arise from spatial discretization of partial differential equation models, computing the eigenmodes themselves may be the major challenge. In such cases the use of alternative modal models based upon proper orthogonal decomposition or singular value decomposition have proven very useful. In the present paper another facet of reduced-order modeling is examined, i.e., the effects of "local" nonlinearity at the nanoscale. The focus is on nanoscale devices where it will be shown that a combination of global modal and local discrete coordinates may be most effective in constructing reduced-order models from both a conceptual and computational perspective. Such reduced-order models offer the possibility of reducing computational model size and cost by several orders of magnitude.
[DOI: 10.1115/1.1558079]

Introduction

In the theoretical and computational modeling of nanoscale devices and phenomena, e.g., nanooscillators and crack propagation in solids, recent work, [1,2], has emphasized the benefits of an appropriate blend of finite element continuum models, molecular dynamics models, and quantum mechanical models. The motivation for creating such multiscale models is clear. On the one hand continuum models fail to describe the phenomena of interest in certain regions of nanoscale devices or of crack tips, for example, and must be replaced by molecular or quantum models. But on the other hand computational cost prohibits the use of molecular or quantum models over the entire computational domain of the device or phenomena. Thus continuum (finite element) models are required over most of the computational domain to keep the computation manageable and are entirely adequate to describe the physical behavior of the device in those regions. Yet molecular or quantum effects must be modeled in some smaller, yet critical regions.

There are two major questions that arise in blending two distinct conceptual and computational models, e.g., a finite element continuum model with a molecular dynamics model. One question is, how do we choose the two spatial regions, i.e., the continuum region and the molecular dynamics region? This is currently done based upon the anticipated behavior of the response, i.e., it depends on one's experience and is essentially a matter of good judgment. The second question is, how does one consistently and correctly connect the two distinct computational models at the interface between the two spatial regions? The work of [1,2] and references cited therein is largely devoted to answering this latter question. And significant progress has been made, although a certain amount of judgment and numerical experimentation is still required to answer this question using current methodologies.

In the present paper, a new approach is proposed that is both computationally effective and rigorously addresses both questions. In the present approach, the total model is initially based upon the finer scale model, e.g., molecular dynamics, but then a continuum approximation is extracted from this model for those portions of the spatial region where such an approximation is appropriate. Moreover, since the methodology permits one to choose any division of the total computational domain into a continuum region on the one hand and say a molecular dynamics region on the other, one may rapidly simulate the model response for different choices of continuum and molecular dynamics regions to determine the optimum choice of computational subdomains.

As will be seen the methodology has a certain feature which permits a check for self-consistency as to whether the continuum approximation may be used in a given portion of the computational domain. And of course the method is very computationally efficient, by virtue of creating a (substantially) reduced-order model. We expect computational advantages for the proposed method comparable to those recently achieved for computational fluid dynamics (CFD) models where the number of degrees-of-

Contributed by the Applied Mechanics Division of THE AMERICAN SOCIETY OF MECHANICAL ENGINEERS for publication in the ASME JOURNAL OF APPLIED MECHANICS. Manuscript received by the ASME Applied Mechanics Division, Dec. 9, 2001; final revision, Sept. 25, 2002. Associate Editor: A. K. Ferri. Discussion on the paper should be addressed to the Editor, Prof. Robert M. McMeeking, Department of Mechanical and Environmental Engineering University of California–Santa Barbara, Santa Barbara, CA 93106-5070, and will be accepted until four months after final publication of the paper itself in the ASME JOURNAL OF APPLIED MECHANICS.

 Copyright © 2003 by ASME

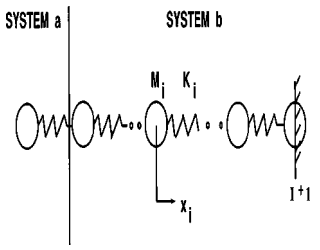

Fig. 1 A one-dimensional, discrete spring-mass system

freedom and associated computational costs have been decreased by *several orders of magnitude* for complex systems with *weak global* nonlinearities, [3], using reduced-order models. In this paper, the challenge of addressing either *weak* or *strong local nonlinearities* is addressed.

The construction of reduced-order models for nonlinear systems can be treated in the abstract, but some insight into the physical effects of the nonlinearity will often suggest, if not dictate, the most effective approach to take. When the nonlinearity is distributed globally over the spatially domain, effective techniques have been revised to construct reduced-order models, [3–12]. In this paper we consider a representative system with a *strong local* nonlinearity. It is a one-dimensional system with many discrete nonlinear spring/masses or nonlinear force laws such as those that arise in molecular dynamics. The goal is to develop a local discrete model near the termination of the spring/mass or molecular system to provide detailed information in that region while using a modal representation to describe the motion of the system sufficiently for away from the termination region. This model may be thought of as combining the most attractive features of a complementary particle/wave (eigenmode) description of the overall model. This approach is attractive for either a linear or a nonlinear model in the termination region, but is especially useful for the latter.

Application of this model to material specimens that are stretched by an atomic force microscope (AFM) is a nanoscale device of significant current interest, [13]. Also this method may be extended to two or three dimensions where such models might be used to describe crack propagation, for example [1,2]. If these extensions prove successful, and success is not guaranteed, this approach will open new research frontiers for the rational design of nanoscale devices and the analysis of nanoscale phenomena.

The readers attention is also drawn to the interesting work of Burton et al. [14] and Friswell et al. [15] who also discuss issues of reduced order modeling in related, but distinct contexts.

Reduced-Order Models for Nonlinear Systems With Strong Local Nonlinearities

We begin with a simple spring model, before turning to a nanoscale molecular dynamics model per se.

Analysis of a Wave-Particle Model for a One-Dimensional Model With Discrete Masses/Nonlinear Springs. In Fig. 1 the spring-mass system is shown. The ''springs'' may arise from microscale or macroscale forces. Now consider this system as being decomposed into two systems; one (a) is composed of particles and the other (b) is composed of waves (eigenmodes). Of course the waves or eigenmodes of system (b) may be found by starting from a particle description and then determining the eigenmodes of system (b). So there is a particle/wave duality here, but it is entirely in terms of classical mechanics for this example. The wave or eigenmode description for system (b) will be advantageous when the spatial/temporal resolution needed is global rather than local and the number of eigenmodes required is much smaller than the number of particles in system (b).

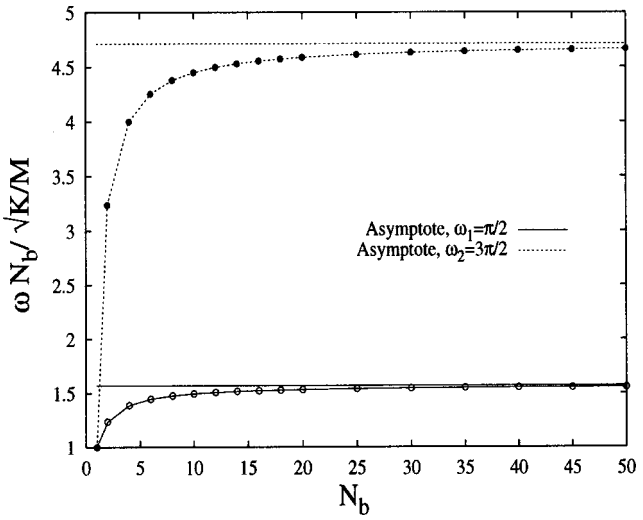

Fig. 2 Natural frequencies of first two modes for various total number of particles, N_b, in system (b). Note: Natural frequencies are scaled by multiplication by N_b so that a finite asymptote is reached as $N_b \to \infty$, corresponding to a continuum limit.

The kinetic and potential energies for the entire system (a+b) may be written as

$$T = \frac{1}{2}\sum_{i=1}^{I} M_i \dot{x}_i^2 \tag{1}$$

$$U = \frac{1}{2}\sum_{i=1}^{I} K_i (x_i - x_{i+1})^2. \tag{2}$$

Note that in Eq. (2), $x_{I+1}=0$ for the example shown in Fig. 1, i.e., the $I+1$ mass is fixed in the wall on the right-hand side and does not move.

And the virtual work may be expressed as

$$\delta W = \sum_{i=1}^{I} F_i \delta x_i . \tag{3}$$

For simplicity of exposition, in the following only free vibration is considered, i.e., $F_i \equiv 0$. Now consider system (b) by itself. For system (b) each mass and spring is assumed to be identical for simplicity and, more importantly, the spring is linear. In Fig. 2 the first two natural frequencies (eigenvalues) for this system are shown as a function of the total number of masses and springs, N_b. The limit as N_b approaches infinity may be thought of as the discrete system approaching a continuum model and the eigenvalues have been appropriately scaled to display this limit more clearly. Note that if only the lower eigenmodes for system (b) are needed, a relatively small number of N_b is sufficient to model the system even if the actual number of N_b is very large. This is the advantage of a finite element or finite difference representation of system (b) starting from a continuum model; but now the equivalent result is seen here from a different perspective, i.e., as a wave or eigenmode description of a discrete system with many degrees-of-freedom.

System (b) is now represented in terms of its (lower) eigenmodes for any value of N_b. Thus taking b_n to be the generalized coordinates associated with an eigenmode expansion of the motion, one has the following expressions for kinetic and potential energy:

$$T_b = \frac{1}{2}\sum_{n=1}^{N_b' \ll N_b} \dot{b}_n^2 M_n^b \tag{4}$$

$$U_b = \frac{1}{2}\sum_{n=1}^{N_b' \ll N_b} b_n^2(\omega_n^b)^2 M_n^b .$$

By contrast, however, system (a) is modeled with discrete local coordinates. We first consider system (a) in the linear approximation and then we will consider the nonlinear case.

System (a) is linear:

System (a) is represented as a discrete set of masses and springs. Indeed for purposes of illustration, let system (a) be a single spring-mass with kinetic and potential energies as follows:

$$T_a = \frac{1}{2} M_1^a (\dot{x}_1^a)^2$$
$$U_a = \frac{1}{2} K_1^a (x_1^a - x_2^a)^2 . \tag{5}$$

Of course, the mass of system (b) immediately adjacent to that of system (a) is the first mass of system (b). And thus there is a constraint condition that describes the connection between systems (a) and (b), viz.,

$$x_2^a = x_1^b . \tag{6}$$

If the dynamics of system (b) are now expressed in terms of its eigenmodes, then x_i^b may be written in terms of the eigenmodal coordinates for system (b) as follows:

$$x_i^b = \sum_n E_{in} b_n \tag{7}$$

where $[E]$ is a matrix whose columns are the eigenvectors of system (b). And in particular,

$$x_1^b = \sum_n E_{1n} b_n . \tag{8}$$

Defining

$$f \equiv x_2^a - \sum_n E_{1n} b_n \tag{9}$$

then the constraint equation that expresses the connection between systems (a) and (b) is simply

$$f = 0. \tag{10}$$

From Lagrange's equations using a Lagrange multiplier to enforce the constraint condition, the equations of motion for system (a+b) are

$$M_n^b[\ddot{b}_n + (\omega_n^b)^2 b_n] - \lambda E_{1n} = 0 \tag{11}$$
$$M_1^a \ddot{x}_1^a + K_1^a[x_1^a - x_2^a] = 0 \tag{12}$$
$$-K_1^a[x_1^a - x_2^a] + \lambda = 0. \tag{13}$$

The dynamical response unknowns are x_1^a, x_2^a, b_n, and λ which are determined by solving Eqs. (10)–(13).

One can put this set of equations for system (a+b) in a standard eigenvalue form by eliminating the variables λ and x_2^a using Eqs. (10) and (13) and reducing the set of equations to the determination of the unknowns, x_1^a and b_n. This new set of equations is thus

$$M_n^b[\ddot{b}_n + (\omega_n^b)^2 b_n] - E_{1n} K_1^a \left[x_1^a - \sum_m E_{1m} b_m \right] = 0 \tag{14}$$
$$M_1^a \ddot{x}_1^a + K_1^a \left[x_1^a - \sum_m E_{1m} b_m \right] = 0. \tag{15}$$

Of course, Eqs. (14) and (15) are coupled among the coordinates, x_1^a and b_n, but the number of b_n is usually dramatically reduced by a truncation of eigenmodes of system (b).

System (a) is nonlinear:

The present approach is particularly advantageous if the dynamics of system (a) are governed by nonlinear relationships, but system (b) is entirely linear, [14,15]. For example, consider a nonlinear spring connecting system (a) to system (b). Then the potential energy might be represented as

$$U = \frac{1}{2} K_{11}^a (x_1^a - x_2^a)^2 + \frac{1}{4} K_{31}^a (x_1^a - x_2^a)^4 . \tag{16}$$

Using this expression and following through on the development of the equations of motion as before, it is seen that Eqs. (10) and (11) are unchanged, but Eqs. (12) and (13) are now nonlinear in the unknowns x_1^a and x_2^a. Even so one may obtain a solution to these equations by time marching Eqs. (11) and (12) for x_1^a, b_n, using Eq. (10) to determine x_2^a at each time step in terms of b_n and Eq. (13) to determine λ at each time step in terms of x_1^a and x_2^a. For the nonlinear case, Eqs. (12) and (13) become explicity

$$M_1^a \ddot{x}_1^a + K_{11}^a (x_1^a - x_2^a) + K_{31}^a (x_1^a - x_2^a)^3 = 0 \tag{12}$$
$$-K_{11}^a (x_1^a - x_2^a) - K_{31}^a (x_1^a - x_2^a)^3 + \lambda = 0. \tag{13}$$

Although this is not pursued here, the reader may readily verify that had the (linear) eigenmodes of the combined (a+b) system been used to describe the system, the conceptual and computational difficulty with such an approach when including the effect of the nonlinearity would be substantially greater than that described above.

If the goal is to determine the free vibrations of such a system and one is content with a single harmonic, then a particularly simple and direct result can be obtained, [16,17]. Omitting details it is simply noted that it is advantageous to define a new coordinate which is the stretching of the nonlinear spring, viz

$$\Delta x \equiv x_1^a - x_2^a \tag{17}$$

and replace the two unknowns x_1^a and x_2^a with x_1^a and Δx. Also note that Eqs. $(12)_{NL}$ and $(13)_{NL}$ can be combined to produce a single linear equation in terms of Δx and λ. From Eqs. (*B*1), (B2), $(12)_{NL}$ and $(13)_{NL}$ the governing equation for the free vibrations becomes

$$-K_{11}^a \Delta x - K_{31}^a (\Delta x)^3 + \Delta x \omega^2 M_1^a \Big/ \left[1 - \omega^2 M_1^a \sum_n \frac{E_{1n}^2}{M_n^b[-\omega^2 + (\omega_n^b)^2]} \right] = 0. \tag{18}$$

The solution for the nonlinear frequencies of free vibration can be effected by plotting the right-hand side and left-hand side of Eq. (18) versus frequency, ω, for a chosen amplitude, Δx, and determining their intersection.

Note that after the solution is obtained one may check to see if the solution has significant nonlinear response in either the nonlinear spring per se or in any of the nominal linear springs. If in fact a nominally linear spring has a response that exceeds its linear response range, then that spring must be transferred to system (a) and re-analysis and re-simulation must be done.

Discussion and Generalization

A few generalizations of this example are now discussed. For example, the specific form for the potential energy can be readily replaced by any well-behaved function of the stretching of the spring. Also the one-dimensional model may be replaced with a two or three-dimensional model. In both cases results analogous to the above are readily obtained including Eq. (18) if only a single nonlinear spring is present. For multiple nonlinear springs, although the formalism goes through, the number of analogous equations becomes larger as the number of nonlinear elements increases. Yet the present approach will still be advantageous rela-

tive to either including coordinates for each spring mass in systems (a) and (b) on the one hand or using the eigenmodes of the combined system (a+b) on the other. Here we briefly discuss the formulation for the one-dimensional model using the Lennard-Jones potential, a well-known model often used in molecular dynamics, [18]. The extensions to two and three dimensions are left to future work.

Theoretical Model. The Lennard-Jones potential has the following form:

$$U = Cr_0^n\left[\frac{r_i^{m-n}}{r^m} - \frac{1}{r^n}\right] \tag{19}$$

where r is the distance between mass particles, C has the dimensions of energy, r_i is the value of r for which $U=0$, and without loss of generality one may also select $r_0 = r_i$.

It will be of interest to determine the value of $r = r_s$ for which $\partial U/\partial r = 0$ that arises in the static equilibrium or confirmation of a system of particles. Using (19), r_s may readily be determined as follows:

$$\frac{r_s}{r_i} = \left(\frac{m}{n}\right)^{1/(m-n)}. \tag{20}$$

For typical values, say $m=12$ and $n=6$,

$$\frac{r_s}{r_i} = 2^{1/6}. \tag{21}$$

Also the value of $\partial^2 U/\partial r^2$ when $r=r_s$ will be of interest. It is found to be

$$\left.\frac{\partial^2 U}{\partial r^2}\right|_{r=r_s} = Cr_i^{-2}[m(m+1)\alpha^{-m-2} - n(n+1)\alpha^{-n-2}] \tag{22}$$

where

$$\alpha \equiv \frac{r_s}{r_i} = \left(\frac{m}{n}\right)^{1/(m-n)} \tag{23}$$

and again for $m=12$ and $n=6$,

$$\left.\frac{\partial^2 U}{\partial r^2}\right|_{r=r_s} = Cr_i^{-2}[18\times 2^{-1/3}]. \tag{24}$$

Consider now the static equilibrium of a one-dimensional array of masses (recall Fig. 1) whose potential energy is now described by the Lennard-Jones potential. Furthermore a ''nearest neighbor'' approximation will be used (a commonly invoked assumption in treating the statics and dynamics of many particle systems). This assumption leads to simple results, but perhaps more importantly the results may be used in an iteration process to account for many neighbor potential energy interactions, if desired.

Now the total potential energy of the one-dimensional array of particles using the nearest neighbor assumption is

$$U_T = U(r_1) + U(r_2) + U(r_3) + \ldots. \tag{25}$$

where

$$r_1 = x_1, \quad r_2 = x_2 - x_1, \quad r_3 = x_3 - x_2 \ldots. \tag{26}$$

Here it is convenient to use a numbering system for the mass particles that starts with the mass nearest the ''wall'' or fixed point. See Fig. 1. Note this numbering system is reversed from that of the previous ''spring'' example.

The conditions of static equilibrium are of course that

$$\frac{\partial U_T}{\partial x_i} = 0 \quad \text{for } i = 1,2,3,\ldots. \tag{27}$$

and using Eqs. (25) and Eq. (26)

$$\frac{\partial U_T}{\partial x_1} = \frac{\partial U}{\partial r_1}\frac{\partial r_1}{\partial x_1} + \underbrace{\frac{\partial U}{\partial r_2}\frac{\partial r_2}{\partial x_1} + \frac{\partial U}{\partial r_3}\frac{\partial r_3}{\partial x_1} + \ldots}_{0}$$

or

$$\frac{\partial U_T}{\partial x_1} = \frac{\partial U}{\partial r_1} - \frac{\partial U}{\partial r_2}. \tag{28}$$

Similar expressions are obtained for $\partial U_T/\partial x_i$ until the last mass, x_I, is considered. For the last mass

$$\frac{\partial U_T}{\partial x_I} = \frac{\partial U_T}{\partial r_I} = 0. \tag{29}$$

But Eq. (29) implies that

$$x_I - x_{I-1} = r_s \tag{30}$$

recalling Eq. (20). But from Eq. (29) and the preceding equation for $\partial U/\partial x_{I-1}$ one infers that

$$\frac{\partial U_T}{\partial r_{I-1}} = 0 \quad \text{and} \quad x_{I-1} - x_{I-2} = r_s \tag{31}$$

and eventually that

$$\frac{\partial U_T}{\partial r_1} = 0 \quad \text{and} \quad x_1 = r_s. \tag{32}$$

Thus the static equilibrium values of x_i are

$$x_i = x_{is} \equiv ir_s \quad \text{for } i = 1,2,\ldots N \tag{33}$$

and it is seen that each ''spring'' is stretched more than the previous one in proportion to its ''distance'' from the ''wall.''

Next, turn to the dynamic equations of motion. These of course are of the form (assuming for simplicity of exposition that all masses are equal, though this assumption is not essential to the proposed method).

$$m\ddot{x}_i + \frac{\partial U_T}{\partial x_i} = 0 \quad \text{for } i = 1,2,\ldots I. \tag{34}$$

First consider small dynamic perturbations about the static equilibrium positions or confirmation. Then, for example,

$$\frac{\partial U_T}{\partial x_1} = \frac{\partial U_T}{\partial r_1} - \frac{\partial U_T}{\partial r_2}. \tag{35}$$

But using a Taylor Series and the ansatz $x_1 = x_{1s} + \hat{x}_1$, etc., one determines that

$$\frac{\partial U_T}{\partial r_1} = \underbrace{\left.\frac{\partial U_T}{\partial r_1}\right|_{x_1 = x_{1s}}}_{0} + \left.\frac{\partial^2 U_T}{\partial r_1^2}\right|_{x_1 = x_{1s}} \hat{x}_1 + HOT \tag{36}$$

and similarly

$$\frac{U_T}{r_2} = \underbrace{\left.\frac{\partial U_T}{\partial r_2}\right|_{x_1 = x_{1s}, x_2 = x_{2s}}}_{0} + \left.\frac{\partial^2 U_T}{\partial r_2^2}\right|_{x_1 = x_{1s}, x_2 = x_{2s}} (\hat{x}_2 - \hat{x}_1) + HOT. \tag{37}$$

Note, however, that

$$\left.\frac{\partial^2 U}{\partial r_1^2}\right|_{x_1 = x_{1s}} = \left.\frac{\partial^2 U}{\partial r^2}\right|_{r=r_s} = \left.\frac{\partial^2 U}{\partial r_2^2}\right|_{x_1 = x_{1s}, x_2 = x_{2s}}. \tag{38}$$

Thus

$$\frac{\partial U}{\partial x_1} = \left.\frac{\partial^2 U}{\partial r^2}\right|_{r=r_s} [2\hat{x}_1 - \hat{x}_2] \tag{39}$$

from Eqs. (35)–(38). And the first mass (furthest from the ''wall'') equation of motion becomes

$$m\ddot{\hat{x}}_1 + \left.\frac{\partial^2 U}{\partial r^2}\right|_{r=r_s} [2\hat{x}_1 - \hat{x}_2] = 0. \tag{40}$$

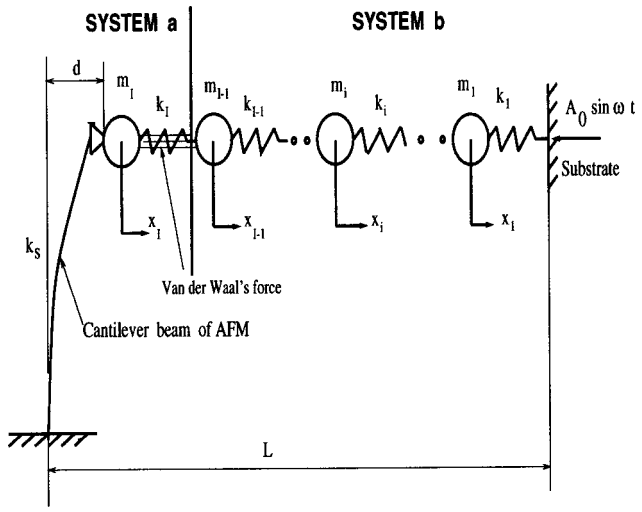

Fig. 3 Schematic diagram of macromolecular chain model with AFM measurement system

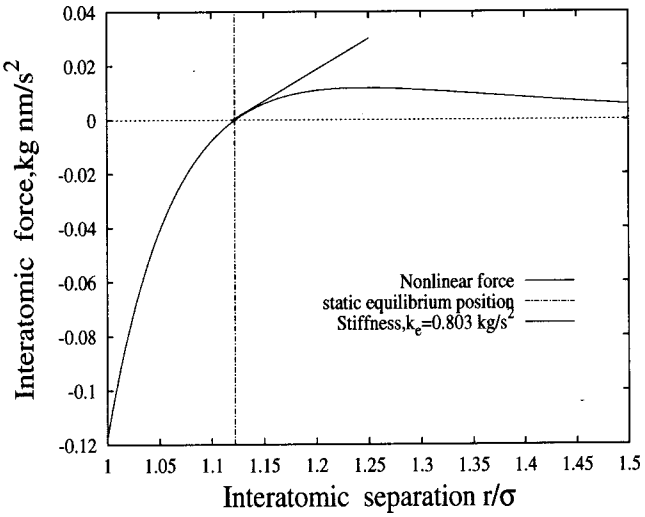

Fig. 4 Nonlinear interatomic force versus the interatomic separation, r/σ

From a similar calculation the equation of motion for the second mass is

$$m\ddot{\hat{x}}_2+\left.\frac{\partial^2 U}{\partial r^2}\right|_{r=r_s}[2\hat{x}_2-\hat{x}_1-\hat{x}_3]=0. \tag{41}$$

The equations of motion for the other masses are similar except for the mass furthest from the ''wall'' whose governing equation is

$$m\ddot{\hat{x}}_I+\left.\frac{\partial^2 U}{\partial r^2}\right|_{r=r_s}[\hat{x}_I-\hat{x}_{I-1}]=0. \tag{42}$$

Finally, now consider the last ''spring'' or potential to be nonlinear. As with the previous examples, think of the other linear ''springs'' and associated masses as being modeled by their eigenmodes. Again this is called system (b). System (a) is the last mass furthest from the wall with its associated nonlinear ''spring'' or potential.

As before one may determine the eigenmodes for system (b) using the dynamic small perturbation equations of motion, Eqs. (40)–(42). Think now of adding a nonlinear mass/spring (potential) with coordinates x^a_{I+1} and x^a_I, i.e., system (a). The kinetic and potential energies of system (a) are

$$T_a=\frac{1}{2}m(\dot{x}^a_{I+1})^2 \tag{43}$$

$$U_a=U(x^a_{I+1}-x^a_I) \tag{44}$$

and the constraint equation that connects system (a) to system (b) is

$$x^a_I=x^b_I. \tag{45}$$

As before the dynamics of x^b_i, $i=1,2,\ldots I$ are to be represented by a small number of dominant eigenmodes of system (b). Employing the Lagrange multiplier formalism, one obtains a small number of equations to represent the combined nonlinear system in terms of the (dominant) eigenmodes of system (b) and an individual particle description of system (a). These choices are both conceptually and computationally compact as well as convenient. As was true for the previous example, the equations of motion are linear in the modal coordinates of system (b) and also the Lagrange multiplier that represents the force of constraint that connects system (a) and system (b) through the enforcement of the constraint, Eq. (45). However, the coordinates of system (a), x^a_{I+1} and x^a_I or, more particularly, the difference of these two, $x^a_{I+1}-x^a_I\equiv r^a_{I+1}$, will appear in a nonlinear form. Recall Eq. (18) from the previous nonlinear ''spring'' example. The details are described in Appendix B.

Numerical Example. As is well known, the rupture force of single covalent bonds under an external load can be measured with an atomic force microscope (AFM). In the present numerical example, a polysaccharide macromolecular chain with 101 atoms is considered and the last atom is covalently attached to the AFM tip which is mounted on a cantilever beam and the first atom is attached to a substrate surface. A schematic diagram of this model is shown in Fig. 3. For details of this experimental model, see Ref. [19]. Here this experimental model is simulated using molecular dynamics and a reduced order model. We assume that the substrate surface is excited by a single harmonic motion, $A_0 \sin \omega t$ where A_0 and ω are the excitation amplitude and frequency. In Fig. 3, the AFM cantilever beam base (tip probe) can be moved to change the distance, L, between the tip and the substrate surface. Also the deflection of cantilever beam, d, will be changed with a change in L. The cantilever beam has a spring constant of $k_s=0.58\ \mathrm{kg/s^2}$ and the beam mass is m_s.

For the present example, the Lennard-Jones potential is given by

$$U(r)=4\epsilon\left[\left(\frac{\sigma}{r}\right)^{12}-\left(\frac{\sigma}{r}\right)^{6}\right]$$

with experimentally determined parameters $\sigma=0.34$ nm and $\epsilon=0.0104$ eV.

In this example, for illustrative purposes, we assume the AFM tip probe is removed from the macromolecular chain and therefore does not attach to the macromolecular chain, i.e, L is large enough that the last mass, m_I, of the chain is free. This example is used to examine the utility of the reduced-order model. The dynamic response of this system is calculated using Eqs. (35)–(45).

When the tip probe is moved close to the last mass of the macromolecular chain and it is covalently attached to the AFM tip of the cantilever beam and (the boundary condition) of the last mass, m_I, is constrained by its attachment to the cantilever beam (AFM). Results for this case will be reported separately in another paper.

• *Normal static equilibrium position*

As described before, for the present example, the normal static equilibrium position of the macromolecular chain is $x_i=ir_s$, $i=1,2,\ldots I$, and $I=101$. See Eq. (33). $r_s=0.382$ nm or $2^{1/6}\sigma$ corresponding to $\partial U/\partial r=0$.

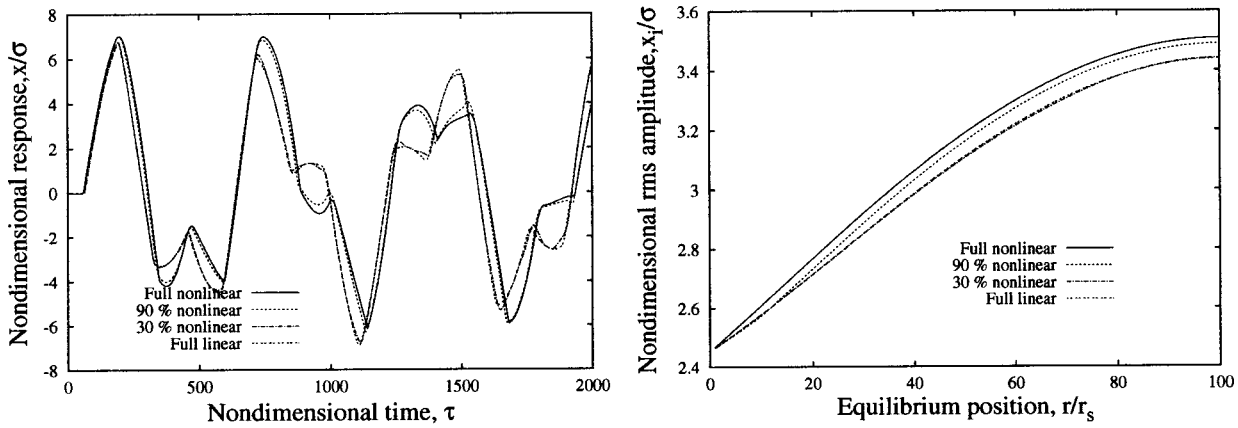

(*a*) **Time history at free end** (*b*) **RMS amplitude**

Fig. 5 Dynamic response of the macromolecular chain for $A_0/\sigma=3.5$ and $\mu=0.01$

Two alternative equations of motion, a perturbation (linearized) equation and a full nonlinear equation are derived. For a small dynamic perturbation about the static equilibrium position, the linear "spring" stiffness of the chain is $k_1=k_2=\ldots=k_I=k_e$ and the interatomic force is modeled as linear. The linearized stiffness, k_e, is determined by

$$k_e=\left.\frac{\partial^2 U}{\partial r^2}\right|_{r=r_s}=0.803 \ \text{kg/s}^2.$$

For the full nonlinear equation of motion, the interatomic force is nonlinear. The nonlinear interatomic force, f_N, is determined by

$$f_N=\frac{\partial U}{\partial r}=-\frac{4\epsilon}{\sigma}\left[12\left(\frac{\sigma}{r}\right)^{13}-6\left(\frac{\sigma}{r}\right)^{7}\right].$$

Figure 4 shows the nonlinear interatomic force versus the interatomic separation, r/σ. In this figure the linear "spring" stiffness of the chain, i.e., the slope of the curve at the static equilibrium position, r_s, is also shown. The small dynamic perturbation theory is effective over a small, but nontrivial, range of r/σ, as will be seen.

• *Small dynamic perturbations*

The macromolecular chain can be modeled as a dynamic perturbation linear system when the interatomic force is linearized about the static equilibrium position, but as a nonlinear system when the full interatomic (Van der Waal's) force is used as in Fig. 4. The equations are normalized by the length factor, σ, and a time factor, $1/\Omega$ where $\Omega^2\equiv 24\epsilon/\sigma^2 m$ and m is the atom mass of the macromolecular chain. The nondimensional time is $\tau=\Omega t$ and the nondimensional frequency is $\mu=\omega/\Omega$. A viscous damping force, f_{viscous}, is added to the chain that is assumed to be of the form $f_{\text{viscous}}=2\xi m\Omega\dot{x}$ with ξ taken to be 0.01. Here we consider the molecular chain to be immersed in a viscous fluid.

Figure 5 shows a typical dynamic response using the perturbation linear equations and also the original nonlinear equations for a nondimensional excitation frequency, $\mu=0.01$ and a base excitation amplitude of $A_0/\sigma=3.5$. Figure 5(*a*) shows the dynamic response at the free end versus the nondimensional time, τ. The solid line indicates the results from the linearized equations and the broken line is for the results from the nonlinear equations. The two results are close, but not identical.

Another (intermediate) model can be constructed in which a nonlinear force representation is used near the free end of the chain and a linear model is used near the substrate end. Results using a 90% and 30% nonlinear force model (when 90% or 30% of the force laws are nonlinear and the remainder are linear) are also plotted in Fig. 5(*a*) for comparison. Figure 5(*b*) shows the rms deflection amplitude for each atom of the macromolecular chain. The atom static equilibrium position is normalized by r_s and is measured from the substrate surface. The agreement between the full nonlinear and full linear results is on the whole good, but there are detailed differences. For the partial nonlinear model the results are between the full nonlinear and the full linear cases, as expected.

However, when A_0/σ increases, e.g., $A_0/\sigma=5$ and $\mu=0.01$, the results from linear and nonlinear models can be quite different as shown in Fig. 6 for the response time history at the free end. The perturbation theory is no longer accurate. But more significantly the nonlinear model shows a diverging oscillation indicating the chain is "breaking" for such a large amplitude excitation.

Figures 7(*a*),(*b*) show the rms deflection amplitude for each atom of the macromolecular chain for $\mu=0.05$, $A_0/\sigma=0.1$ and $\mu=0.2$, $A_0/\sigma=0.075$, respectively. There is reasonably good agreement between the linear and nonlinear models in the small interatomic separation range, i.e., for small r/r_s. The agreement between the two models generally improves for smaller A_0/σ and smaller μ.

One can define a total rms error, err, as follows:

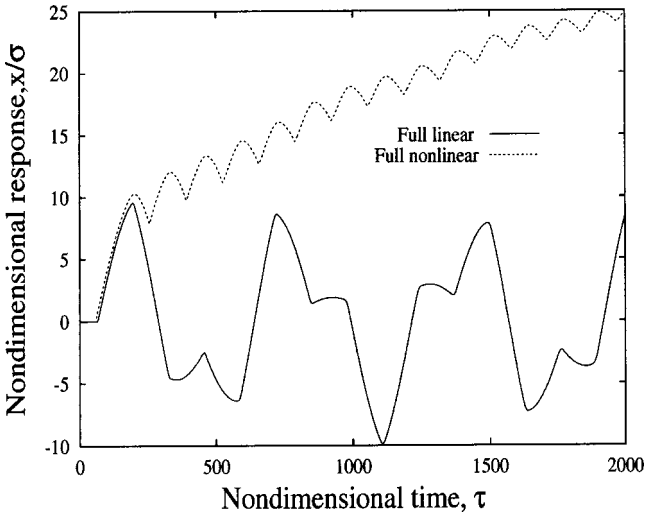

Fig. 6 Time history at free end for $A_0/\sigma=5$ and $\mu=0.01$

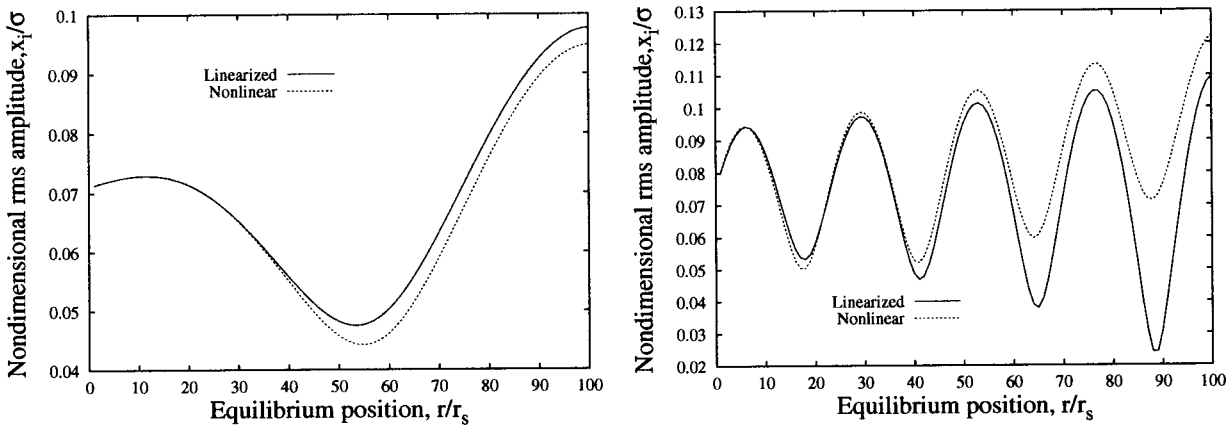

(*a*) $\mu=0.05,\ A_0/\sigma=0.1$ (*b*) $\mu=0.2,\ A_0/\sigma=0.075$

Fig. 7 RMS amplitude of the macromolecular chain

$$\text{err}=\left(\sqrt{\frac{1}{101}\sum_{i=I}^{101}\left(\frac{x_{i,\text{linear}}-x_{i,\text{nonlinear}}}{x_{i,\text{nonlinear}}}\right)^2}\right)\%$$

where $x_{i,\text{nonlinear}}$ is the rms amplitude of ith atom of the macromolecular chain from the nonlinear model, and $x_{i,\text{linear}}$ is the rms amplitude of ith atom from the perturbation linear model.

To illustrate the nature of the threshold dependence of the perturbation theory, results for the total rms error versus excitation amplitude, A_0/σ, are shown in Fig. 8 for several different excitation frequencies, $\mu=0.01$, 0.05, and 0.2. The effective range of the perturbation linear model increases as μ and A_0/σ decrease. For less than 10% error, the maximum A_0/σ is 3.65 for $\mu=0.01$; 0.75 for $\mu=0.05$ and 0.1 for $\mu=0.2$, respectively. Note the rapid change in error with A_0/σ at certain critical threshold values.

To better understand the critical threshold values, consider the nondimensional deflection response between the last two atoms, i.e., $r_I/\sigma=(x_I-x_{I-1})/\sigma$, versus τ as shown in Fig. 9(*a*) for $A_0/\sigma=3.65$ and $\mu=0.01$; Fig. 9(*b*) for $A_0/\sigma=0.75$ and $\mu=0.05$; and Fig. 9(*c*) for A_0/σ 0.1 and $\mu=0.2$. Note that the nondimensional peak response amplitude for r_I/σ is nearly the same for the three different combinations of A_0/σ and μ. This suggests that the threshold levels observed in Fig. 9 all correspond to a critical value of r_I/σ, i.e., approximately $r_I/\sigma=0.02$.

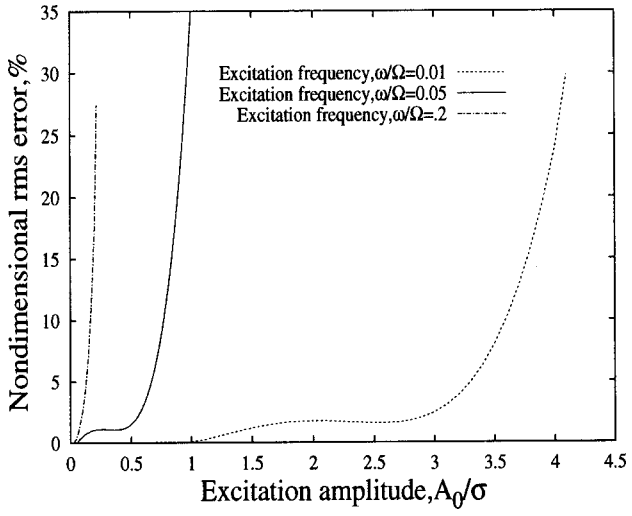

Fig. 8 Total rms error versus excitation amplitude, A_0/σ for different excitation frequency, $\mu=0.01$, 0.05, and 0.2

• *Reduced-order model with quasi-static correction*

Now consider the construction of a reduced-order model for this example. For simplicity and illustration purposes, system (b) is chosen to be linear with 100 degrees-of-freedom and system (a) is nonlinear with one degree-of-freedom, i.e., a nonlinear Van der Waal's force between x_I and x_{I-1}. For system (b), the eigensolution is calculated and the eigenvalues are shown in Fig. 10 as the nondimensional natural frequency, ω_i/Ω, versus the eigenmode number. The lowest nondimensional natural frequency, ω_1/Ω, is 0.0154.

Recalling Eqs. (40)–(42), for the system (b), the dynamic perturbation equations are rewritten in matrix form:

$$[M]\{\ddot{\hat{x}}\}+[K]\{\hat{x}\}=\{f(t)\} \tag{46}$$

where $\{f(t)\}^T=\{k_1A_0\sin\omega t,0,0,\ldots 0\}^T$. Let

$$\hat{x}=\hat{x}_{Qs}+\hat{\hat{x}} \tag{47}$$

where $\hat{x}_{Qs}$ is the quasi-static response and $\hat{\hat{x}}$ is a small dynamic response. The quasi-static response is defined to be that when the inertia terms, $\ddot{\hat{x}}$, (and also the damping terms) are neglected. From Eqs. (46) and (47), we thus have

$$\hat{x}_{Qs}=[K]^{-1}\{f(t)\} \tag{48}$$

and

$$[M]\ddot{\hat{\hat{x}}}+[K]\{\hat{\hat{x}}\}=-[M]\{\ddot{\hat{x}}_{Qs}\}. \tag{49}$$

Following the modal analysis described in the Appendix B, one obtains a reduced-order model for $\hat{\hat{x}}$ with a quasi-static correction (QSC) for $\hat{x}_{Qs}$. When using Eqs. (48) and (49), note that the initial conditions are $\hat{x}|_{t=0}=0$ and $\dot{\hat{x}}|_{t=0}=0$, and thus $\hat{\hat{x}}|_{t=0}=\hat{x}_{Qs}|_{t=0}=0$, and $\dot{\hat{\hat{x}}}|_{t=0}=-\dot{\hat{x}}_{Qs}|_{t=0}$.

Figure 11 shows a typical dynamic response using the reduced order model approach with and without quasi-static correction and, for reference, the response determined from the full original nonlinear equations for $\mu=0.01$ and $A_0/\sigma=0.1$. Also, for reference, a result from a full perturbation linear model, i.e., using all modes in system (b) and a linear perturbation model for system (a), was obtained. For the chosen values of A_0/σ and μ this result was the same as for the full nonlinear model. Figure 11(*a*) shows the dynamic response at the free end of the chain versus the nondimensional time, τ. The solid line indicates the result when all

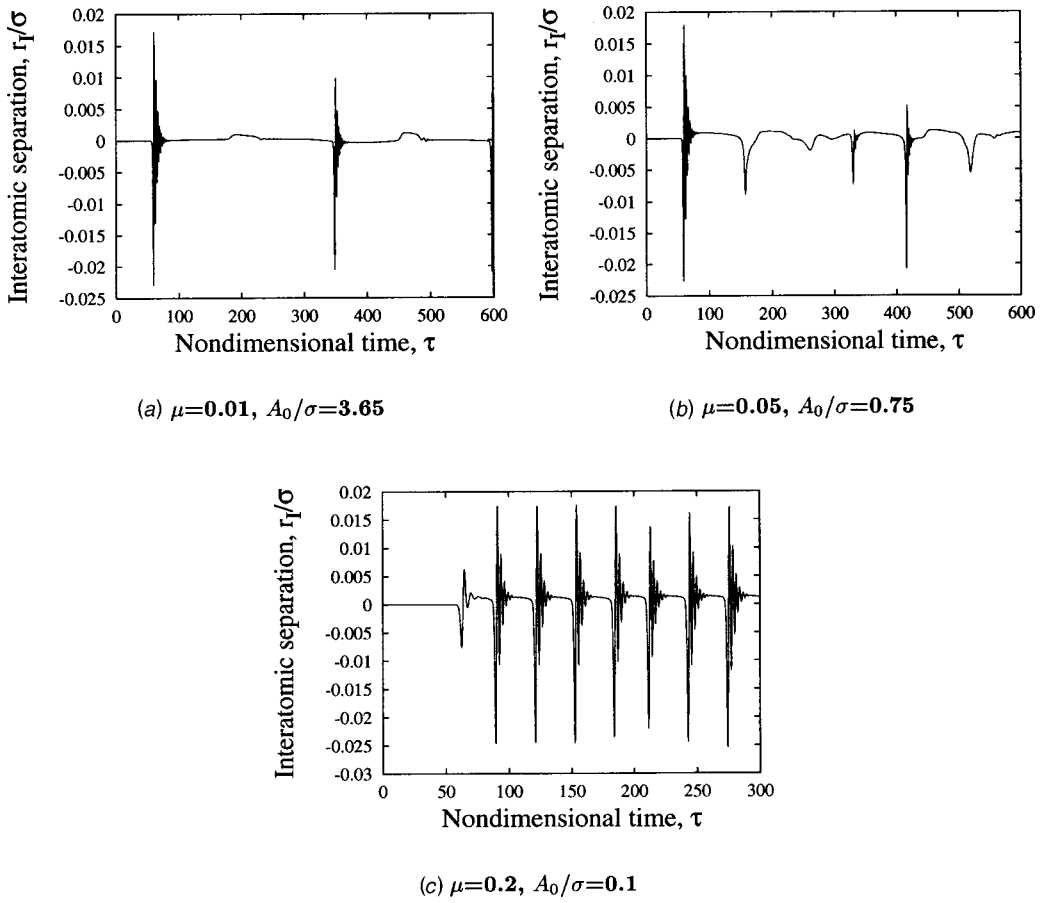

Fig. 9 Deflection response between last two atoms, $r_l/\sigma=(x_l-x_{l-1})/\sigma$, versus τ for several different A_0/σ and μ

modes (100) are included, i.e., the original full equations, and the broken line is the result using only the first two modes without QSC, and dash-dot line is the result using only the first two modes with QSC. The two results using the full modes or only two modes with the QSC are very close. However, the computation time using the reduced-order model (two modes) is only 11% that of the full model. The results for only one mode also provide a good approximation for this case. Note, moreover, that when the macromolecular chain consist of an even larger number of particles, the computational advantage of the reduced-order model will be even greater.

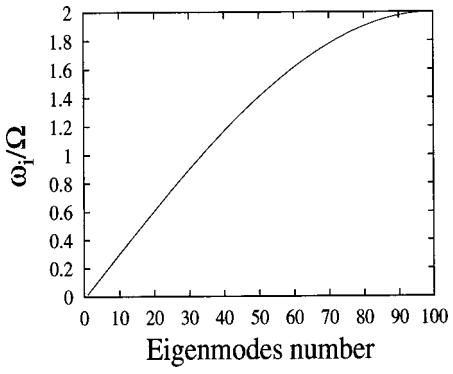

Fig. 10 Nondimensional natural frequencies of the system (a) versus the eigenmodes number

Figure 11(*b*) shows the rms deflection amplitude for each atom of the macromolecular chain for the different modes included. The agreement between the full and reduced-order model (two modes) with QSC is very good. However it is very poor near the excitation end of the chain when only using two modes and still poor using ten modes without QSC. Hence the QSC is an important part of the reduced-order model methodology.

Figure 12 shows the total rms error versus the number of included eigenmodes for $A_0/\sigma=0.1$ and $\mu=0.01$ using the full modes and reduced-order model with and without quasi-static correction. As expected, the total error decreases as number of included eigenmodes increases. As shown in Fig. 12, the quasi-static correction significantly improves the computational accuracy of the reduced-order model.

Figure 13 shows a typical dynamic response using the reduced order model approach with quasi-static correction for a nondimensional excitation frequency of $\mu=0.05$ and an amplitude of $A_0/\sigma=0.1$. Figure 13(*a*) shows the dynamic response at the free end of the chain versus the nondimensional time, τ. The solid line indicates the results when all modes (100) and the broken lines are for the results using only the first two modes, and dash-dot line is the result using the first five modes, respectively. The two results using the full modes and only five modes are very close. Figure 13(*b*) shows the rms deflection amplitude for each atom of the macromolecular chain for the different modes included. The agreement between the full and reduced-order model when using five modes is very good. However, it is poor when only using two modes.

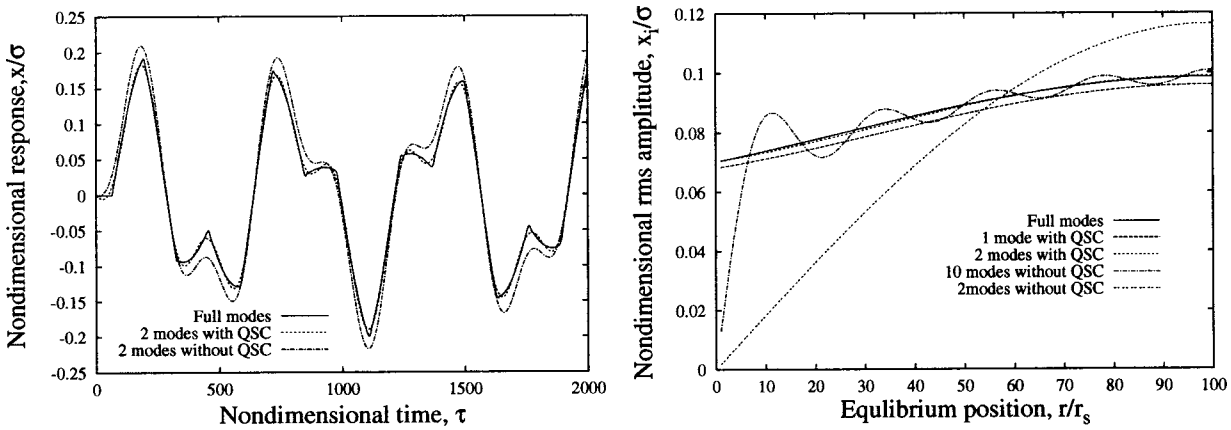

(*a*) **Time history at the free end** (*b*) **RMS amplitude**

Fig. 11 Dynamic response of the macromolecular chain using reduced-order model with and without the quasi-static correction (QSC) for $A_0/\sigma=0.1$ and $\mu=0.01$

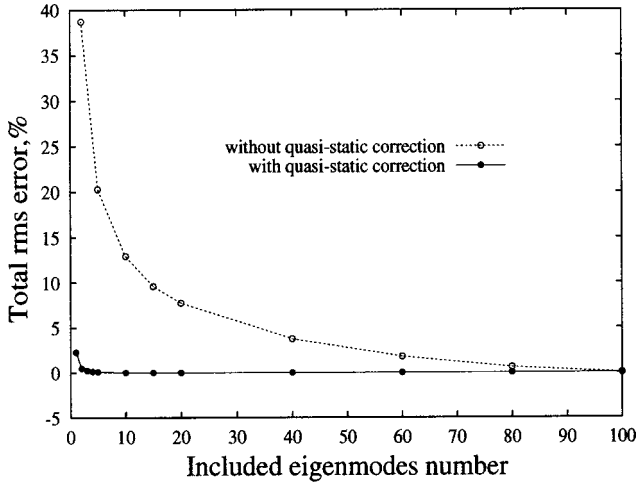

Fig. 12 Total rms error versus eigenmodes, for $A_0/\sigma=0.1$ and $\mu=0.01$, using the reduced-order model with and without quasi-static correction

Figure 14 shows the rms deflection amplitude for each atom of the macromolecular chain for $A_0/\sigma=0.075$ and $\mu=0.2$. Eight modes give good results, but five modes do not.

Summarizing the results of Figs. 11, 13, and 14 for the several excitation frequencies, $\mu=0.01$, 0.05, and 0.2, and the corresponding A_0/σ, the total rms error versus the number of included eigenmodes with quasi-static correction is shown in Fig. 15(*a*). As is expected, when μ increases, we need more eigenmodes in the reduced-order model for a certain prescribed accuracy. For the cases shown in Fig. 15(*a*) the system is responding to a relatively small excitation amplitude, thus the induced local nonlinear (Van der Waal's) force between the last two atoms is weak. Now if the excitation amplitude is increased to say $A_0/\sigma=3.65$ for $\mu=0.01$ and $A_0/\sigma=0.75$ for $\mu=0.05$, the effect of the nonlinearity is more evident. These results are shown in Fig. 15(*b*). For comparison, the results from the smaller excitation amplitude are also shown in the figure as indicated by the broken line. There is only a small difference between the two sets of results for small and large excitations. The reduced-order model with quasi-static correction still is quite accurate even in the presence of strong local nonlin-

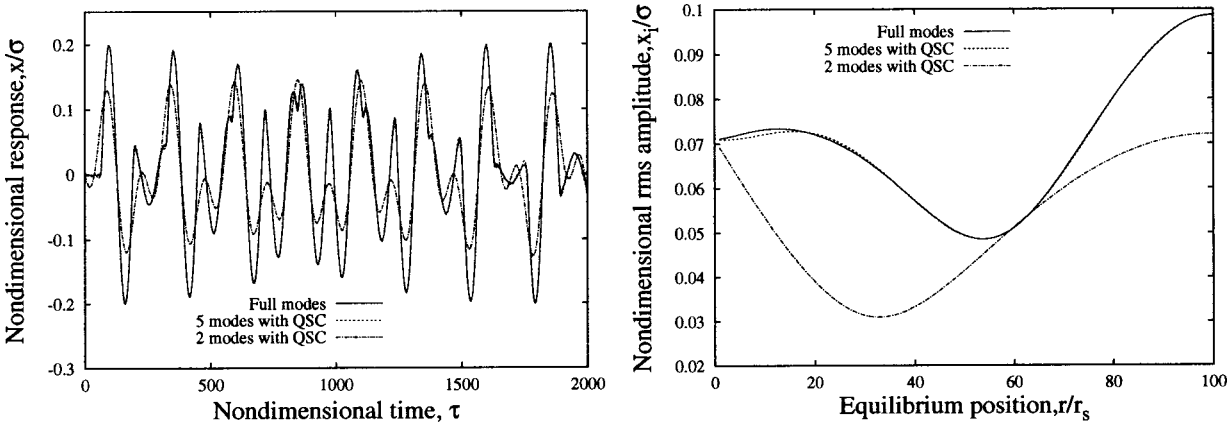

(*a*) **Time history at the free end** (*b*) **RMS amplitude**

Fig. 13 Dynamic response of the macromolecular chain using the reduced-order model with quasi-static correction (QSC) for $A_0/\sigma=0.1$ and $\mu=0.05$

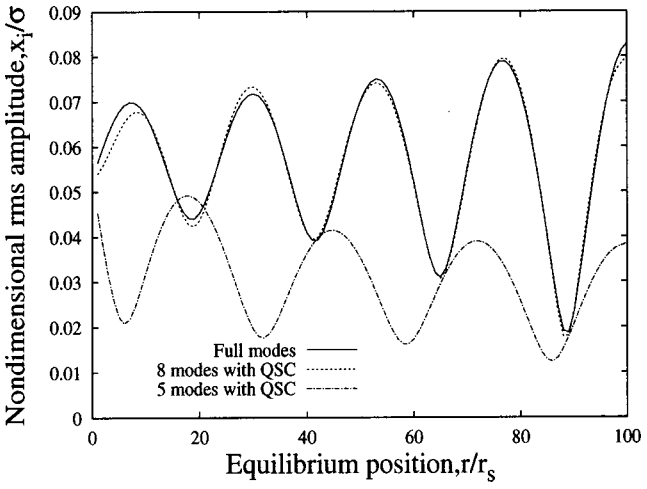

Fig. 14 RMS amplitude using the reduced-order model with quasi-static correction (QSC) for $A_0/\sigma=0.075$ and $\mu=0.2$

earities. Future work will include adding more nonlinear elements to investigate the efficacy of reduced-order modeling under these circumstances.

Concluding Remarks

By an appropriate choice of coordinates to describe the dynamics of a high-dimensional system with nonlinearities that are local or global, a substantial reduction in the conceptual and computational complexities associated with such systems can be achieved. If the nonlinearity is local, a combination of eigenmodal and discrete coordinates may be most advantageous. Applications to both the macroscale, e.g., conventional springs and masses, and the microscale, e.g., Lennard-Jones potential, are illustrated.

Future work will extend the analysis presented here to (1) two and three dimensions and (2) a physically significant one-dimensional model for an atomic force microscope (AFM) pulling on a nanoscale specimen to generate, for example, protein folding (''snap buckling'' of a protein fragment) and the study of the dynamics which determine re-folding (''hysteresis'') of the protein.

In Ref. [19] a simple low-dimensional model using a single nonlinear spring/mass to represent the protein dynamics has been considered. Using the present reduced-order method, a multimass, multiple degree-of-freedom model may be used to represent the protein, thereby significantly enhancing the physical fidelity of the model and its simulation with substantial reductions in computational cost and complexity compared to other existing methods.

Other nanoscale devices and phenomena with significant nonlinearities may be modeled in a similar way. For more sophisticated physical and mathematical models, multiple static equilibria may exist and the choice of eigenmodes and the associated static equilibrium will need to be addressed.

Appendix A

Relationship Between a Finite Difference Model for Axial Vibrations of a Beam Represented in Terms of Finite Differences and the Mass-Spring Model. For the spring-mass system shown in Fig. 2, the potential and kinetic energies for a spring-mass may be written as

$$U_s=\frac{1}{2}\sum_{i=1} K(x_{i-1}-x_i)^2 \tag{A1}$$

$$T_s=\frac{1}{2}\sum_{i=1} M\dot{x}_i^2. \tag{A2}$$

On the other hand, the potential and kinetic energies for the axial deformations of a rod may be written as

$$U_a=\frac{1}{2}\int_0^L EA\left(\frac{\partial u}{\partial x}\right)^2 dx=\frac{EA}{2}\Delta x\sum_{i=1} (u_{i-1}-u_i)^2/$$

$$\Delta x^2=\frac{EA}{2\Delta x}\sum_{i=1} (x_{i-1}-x_i)^2 \tag{A3}$$

$$T_a=\frac{1}{2}\int_0^L m\dot{u}_i^2 dx=\frac{1}{2}\Delta x m\sum_{i=1} \dot{u}_i^2=\frac{1}{2}\Delta x m\sum_{i=1} \dot{x}_i^2 \tag{A4}$$

where $u_i\equiv x_i$, and a change of notation is introduced.

Comparing (*A*3), (*A*4) to (*A*1), (*A*2), an equivalence between the spring-mass and axial rod models is obtained:

$$M=m\Delta x$$

$$K=\frac{EA}{\Delta x}.$$

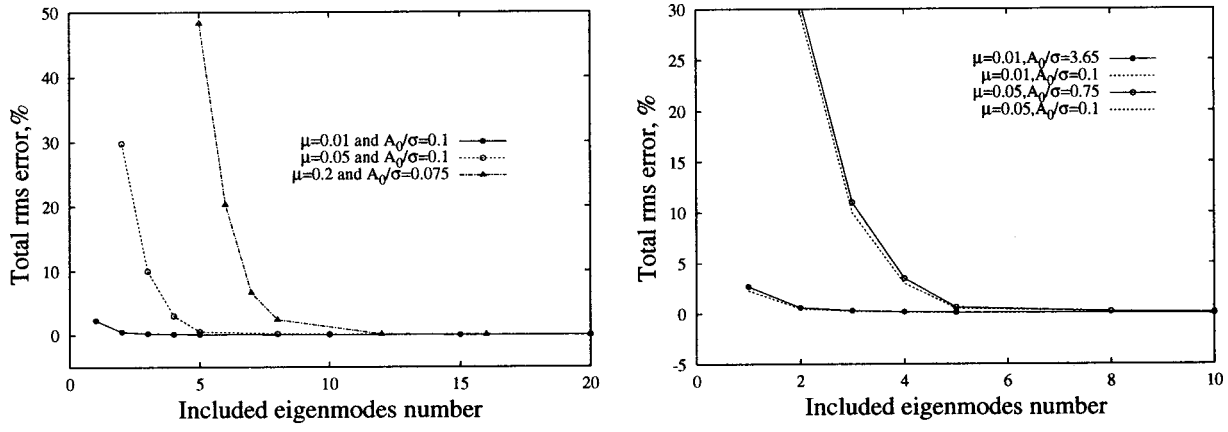

(*a*) **Weak local nonlinearities** (*b*) **Strong local nonlinearities**

Fig. 15 Total rms error versus eigenmodes for different excitation frequency, $\mu=0.01$, 0.05, and 0.2, using the reduced-order model with quasi-static correction. (*a*) For smaller excitation amplitude (weak local nonlinearities) and (*b*) for larger excitation amplitude (strong local nonlinearities).

For a continuum axial beam model, the Euler-Lagrange equation is

$$EA\frac{\partial^2 u}{\partial x^2}+m\frac{\partial^2 u}{\partial t^2}=0.$$

The general solution for the differential equation is (assuming simple harmonic motion with the goal of obtaining the natural frequencies)

$$u=A\cos\sqrt{\frac{m\omega^2}{EA}}x+B\sin\sqrt{\frac{m\omega^2}{EA}}x.$$

The boundary conditions are $u=0$ at $x=0$ and $\partial u/\partial x=0$ at $x=L$. Thus $A=0$ and $B\neq 0$, and the eigenvalue solution is

$$\cos\sqrt{\frac{m\omega^2}{EA}}L=0$$

or

$$\frac{m\omega^2L^2}{EA}=\left(\frac{\pi}{2}\right)^2,\left(\frac{3\pi}{2}\right)^2,\ldots.$$

Thus the equivalence between discrete and continuum models is

$$\frac{m\omega^2L^2}{EA}=\frac{M}{\Delta x}\frac{\omega^2}{K\Delta x}(\Delta x)^2N_b^2=\frac{M\omega^2}{K}N_b^2\Rightarrow\left(\frac{\pi}{2}\right)^2,\left(\frac{3\pi}{2}\right)^2,\ldots$$

$$\text{as } N_b\rightarrow\infty,$$

or

$$\sqrt{\frac{M}{K}}\omega N_b\rightarrow\frac{\pi}{2},\frac{3\pi}{2},\ldots\text{ as } N_b\rightarrow\infty. \tag{A5}$$

See representative numerical results in Fig. 2.

Appendix B

Equations of Motion for the Eigenmode/Particle Model Governed by the Lennard-Jones Potential. The kinetic and potential energies of system (b) expressed in terms of eigenmode coordinates are

$$T_b=\frac{1}{2}\sum_{n=1}^{N_b}M_n^b\dot{b}_n^2 \tag{B1}$$

$$U_b=\frac{1}{2}\sum_{n=1}^{N_b}M_n^b(\omega_n^b)^2b_n^2 \tag{B2}$$

where N_b are the (dominant) eigenmodes of system (b) and ω_n^b are the natural frequencies (eigenvalues).

System (a) is represented in terms of x_I^a and x_{I+1}^a or $x_{I+1}^a-x_I^a\equiv r_{I+1}^a$. Thus the potential and kinetic energies of system (a) may be written as

$$U_a=U(r_{I+1}^a) \tag{B3}$$

$$T_a=\frac{1}{2}M_{I+1}^a(\dot{x}_I^a+\dot{r}_{I+1}^a)^2 \tag{B4}$$

and the constraint equation is

$$x_I^a-x_I^b=0. \tag{B5}$$

Now

$$x_I^b=\sum_n E_{In}b_n \tag{B6}$$

where E_{In} is the appropriate transformation obtained from the eigenvectors of system (b).

Using Lagrange's equation with a Lagrange multiplier to enforce the constraint equation, one obtains

$$M_n^b[\ddot{b}_n+(\omega_n^b)^2b_n]-\lambda E_{In}=0 \tag{B7}$$

$$M_{I+1}^a(\ddot{x}_I^a+\ddot{r}_{I+1}^a)+\frac{\partial U(r_{I+1}^a)}{\partial r_{I+1}^a}=0 \tag{B8}$$

$$M_{I+1}^a(\ddot{x}_I^a+\ddot{r}_{I+1}^a)+\lambda=0 \tag{B9}$$

and the constraint equation becomes

$$x_I^a=\sum_n E_{In}b_n. \tag{B10}$$

Note that in this formulation, the only nonlinear term appears in (*B*8) through the gradient of the potential energy between the two masses furthest from the "wall." This formulation is readily generalized to several particles in system (a) and to two and three-dimensional arrays of particles. Of course, the computational complexity increases as the number of particles in system (a) increases. But in the present formulation this number will be much smaller than in more conventional approaches involving a particle representation for both system (a) and (b).

References

[1] Rudd, R. E., and Broughton, J. Q., 1999, "Atomistic Simulation of MEMS Resonators Through the Coupling of Length Scales," J. Model. Sim. Microsyst., **1**, p. 29.

[2] Rudd, R. E., and Broughton, J. Q., 2000, "Concurrent Coupling of Length Scales in Solid State Systems," Phys. Status Solidi B, **217**(1), pp. 251–281.

[3] Dowell, E. H., and Hall, K. C., 2001, "Modeling of Fluid-Structure Interaction," Annu. Rev. Fluid Mech., **33**, pp. 445–490.

[4] Bolotin, V. V., 1963, *Nonconservative Problems of the Elastic Theory of Stability*, Pergamon Press, New York.

[5] Dowell, E. H., 1975, *Aeroelasticity of Plates and Shells*, Kluwer, Dordrecht, The Netherlands.

[6] Dowell, E. H., and Ilgamov, M., 1988, *Studies in Nonlinear Aeroelasticity*, Springer-Verlag, New York.

[7] Pescheck, E., Pierre, C., and Shaw, S. W., 2001, "Accurate Reduced Order Models for a Simple Rotor Blade Model Using Nonlinear Normal Modes," Math. Comput. Modell., **33**(10–11), pp. 1085–1097 (also see references therein to the earlier literature on nonlinear normal modes).

[8] Lyon, R. H., and De Jong, R. G., 1995, *Theory and Applications of Statistical Energy Analysis*, Butterworth-Heinemann, Boston.

[9] Dowell, E. H., and Tang, D. M., 1998, "The High Frequency Response of a Plate Carrying a Concentrated Mass/Spring System," J. Sound Vib., **213**(5), pp. 843–864 (also see references therein to the earlier literature on asymptotic modal analysis).

[10] Craig, R. R, 1981, *Structural Dynamics: An Introduction to Computer Methods*, John Wiley and Sons, New York, Chap. 19 (Professor Craig is one of the pioneers in component mode analysis and this book provides a very readable introduction to the fundamental concepts).

[11] Dowell, E. H., 1972, "Free Vibrations of an Arbitrary Structure in Terms of Component Modes," ASME J. Appl. Mech., **39**, pp. 727–732.

[12] Castanier, M. P., Tan, Y. C., and Pierre, C., 2001, "Characteristic Constraint Modes for Component Mode Synthesis," AIAA J., **39**(6), pp. 1182–1187.

[13] Grandbois, M., Beyer, M., Rief, M., Clausen-Schaumann, H., and Gaub, H. E., 1999, "How Strong Is a Covalent Bond?," Science, **283**, pp. 1727–1730.

[14] Burton, T. D., Hemez, and Rhee, W., 2000, "A Combined Model Reduction/SVD Approach to Nonlinear Model Updating," *Proceedings of IMAC*, Society for Experimental Mechanics, Bethel, CT, pp. 116–123.

[15] Friswell, M. I., Penny, J. E. T., and Garvey, S. D., 1996, "The Application of the IRS and Balanced Realization Methods to Obtain Reduced Models of Structures With Local Non-Linearities," J. Sound Vib., **196**(4), pp. 453–468.

[16] Tongue, B. H., and Dowell, E. H., 1983, "Component Mode Analysis for Nonlinear, Nonconservative Systems," ASME J. Appl. Mech., **50**, pp. 204–209.

[17] Ibrahimbegovic, A., and Wilson, E. L., 1990, "A Methodology for Dynamic Analysis of Linear Structure Foundation Systems With Local Nonlinearities," Earthquake Eng. Struct. Dyn., **19**(8), pp. 1197–1208.

[18] Haile, J. M., 1992, *Molecular Dynamics Simulation*, John Wiley and Sons, New York.

[19] Shapiro, B. E., and Qian, Hong, 1997, "A Quantitative Analysis of Single Protein-Ligand Complex Separation With the Atomic Force Microscope," Biophys. Chem., **67**, pp. 211–219.

Coefficients of Restitution Based on a Fractal Surface Model

Chung-Jen Lu[1]
Associate Professor
e-mail: cjlu@ccms.ntu.edu.tw

Ming-Chang Kuo
Graduate Student

Department of Mechanical Engineering,
National Taiwan University,
No. 1 Roosevelt Road, Section 4,
Taipei 10617, Taiwan

Equations of rigid-body mechanics provide a means to predict the post-collision behavior without recourse to highly complex, detailed analysis of deformations during contact. Before the prediction can be completed, the coefficient of restitution, which relates the rebound velocity to the incident velocity, must be estimated properly. The coefficient of restitution depends on the surface topography in addition to the material properties and incident velocity. Recent investigations showed that surface topography can be characterized properly by fractal models. This paper proposes a normal contact model for a fractal surface in contact with a rigid smooth half-space. The fractal surface is constructed based on the Cantor set and composed of elastic-perfectly plastic material. Asymptotic continuous expressions for the load-displacement relations during loading and unloading are derived. Based on these results, we study the effects of surface roughness, material properties and incident velocity on the coefficient of restitution.
[DOI: 10.1115/1.1574063]

1 Introduction

The analysis of impact phenomena has important applications in different fields. For example, impacts between the slider and disk greatly influence the reliability of magnetic disk drives. Accurate analysis of the collision between two deformable bodies is difficult and time-consuming even for the large-scale computational capabilities developed recently. If the local deformations at the contact area and the transient response during collision are not of interest, the colliding bodies can be treated as rigid for predicting the post-collision behavior. In this case, a coefficient of restitution, purports to describe the energy loss during collision, must be incorporated to relate the rebound velocity to the incident velocity. When the impact is perpendicular to the nominal plane of the interface, the coefficient of restitution e is defined to be the ratio of the rebound velocity to the incident velocity. Values of $e=1$ and $e=0$ denote the idealized concepts of perfectly elastic and plastic impacts, respectively. Introduction of the coefficient of restitution greatly simplifies the procedure for determining the post-collision motion. The success of the rigid-body impact analysis depends on the correct estimation of the coefficient of restitution.

An important subject is how the coefficient of restitution is related to the basic physical material properties. Tabor [1], Goldsmith [2], and Johnson [3] considered the impact between a sphere and a stationary half-space at moderate impact velocities. Both colliding bodies were assumed to be smooth. As indicated by Johnson [3], when the impact velocity is small compared with the elastic wave velocity, the static contact force-compression law can be employed to investigate the impact behavior. Under this condition, the coefficient of restitution can be estimated based on principles of energetics. Up to the instant of maximum compression, the initial kinetic energy transforms into strain energy, elastic and plastic, of the two colliding bodies. After the point of maximum compression, there is a release of elastic stresses and the kinetic energy of rebound is equal to the work done during elastic recovery. If the compliance relationship of load and displacement for elastic-plastic contact is known, the rebound velocity and hence the coefficient of restitution can be determined. However, the compliance relationship for elastic-plastic contact is not precisely defined, so that a theory of elastic-plastic impact is necessarily approximate. By choosing suitable compliance relationships, the dependence of the coefficient of restitution on the material properties, incident velocity, and radius of the ball can be estimated, [1–3].

All engineering surfaces are rough in nature and have random height distribution, [4,5]. The compliance relationship of real bodies depends closely on the waviness and roughness of the contact surfaces, [3]. Therefore, it stands to reason that surface topography of contact bodies will have a large effect on the collision process, especially at the initial stage of compression. Several probabilistic theories have been developed to model the mechanical behavior of contacting rough surfaces, [6–11]. One of the most popular models is the Greenwood and Williamson (G&W) model, [6]. In this model, the rough surface is represented by a collection of hemispherical asperities having a constant radius of curvature. The heights of the summits are distributed normally about the mean asperity plane and it is assumed that the contacting asperities deform elastically according to Hertz theory. Chang et al. [12] modified the G&W model and proposed an elastic-plastic contact model of rough surfaces. Based on this model, Chang and Ling [13] derived the relationship between the coefficient of restitution and the surface topography. However, recent studies showed that conventional statistical parameters used to characterize the surface topography, including the summit radius in the G&W model, are not unique to a surface. These parameters depend on the resolution and scan length of the roughness-measuring instrument, [14–17]. This result suggests the use of fractal geometry, [18], for the characterization of surface roughness. Lately several fractal surface models have been proposed to describe the interaction between rough surfaces in different areas, [17,19–24]. Majumdar and Bhushan [21] used the Weierstrass-Mandelbrot function to simulate surface roughness and employed modified Hertz equations to model the elastic-plastic deformation of the surface. Borodich and Mosolov [23] constructed a fractal rigid die using the Cantor set. They derived asymptotic compliance expressions for the fractal die penetrating a rigid-perfectly plastic half-space and elastic half-space, respectively. Warren et al. [24] generalized the method of Borodich and Mosolov [23] by allowing the fractal surface to deform. A continuous asymptotic model incorporating volume conservation was developed to describe the rigid-perfectly elastic deformation of a fractal surface in contact with a smooth and rigid half-space. Although

[1]To whom correspondence should be addressed.

Contributed by the Applied Mechanics Division of THE AMERICAN SOCIETY OF MECHANICAL ENGINEERS for publication in the ASME JOURNAL OF APPLIED MECHANICS. Manuscript received by the ASME Applied Mechanics Division, October 10, 2001; final revision, September 9, 2002. Associate Editor: K. T. Ramesh. Discussion on the paper should be addressed to the Editor, Prof. Robert M. McMeeking, Department of Mechanical and Environmental Engineering University of California–Santa Barbara, Santa Barbara, CA 93106-5070, and will be accepted until four months after final publication of the paper itself in the ASME JOURNAL OF APPLIED MECHANICS.

 Copyright © 2003 by ASME

much work has been done on the normal contact behavior between rough surfaces using fractal surface model, little attention has been devoted to the significance of the fractal parameters on the coefficient of restitution.

The purpose of this paper is to investigate the effect of surface roughness on the coefficient of restitution. We consider a fractal surface composed of elastic-perfectly plastic material in contact with a smooth rigid half-space. Following Borodich and Mosolov [23] and Warren et al. [24], the fractal surface is constructed based on the Cantor set. Continuous asymptotic compliance relations during loading and unloading are derived, respectively. These relations are then used to express the coefficient of restitution in terms of surface topography and material properties, in addition to impact velocity.

2 Cantor Set Surface Model

The Cantor set surface shown in Fig. 1 is constructed by joining the segments obtained from successive stages of the Cantor set. At each stage, the middle sections of the previous segments are removed such that the total length of the remaining segments is $1/f_x$ times that of the previous segments. The recess depth at the $(n+1)$th stage is $1/f_z$ times that at the nth stage. Therefore, the horizontal length at the nth stage is

$$l_n=(1/f_x)l_{n-1}=(1/f_x)^n l_0, \tag{1}$$

while the recess depth is

$$h_n=(1/f_z)h_{n-1}=(1/f_z)^n h_0. \tag{2}$$

As shown by Borodich and Mosolov [23], the fractal dimension D can be related to the fractal parameters f_x and f_z as

$$D=1-\frac{\ln f_z}{\ln(2\,f_x)}+\frac{\ln 2}{\ln(2\,f_x)}, \tag{3}$$

where $1<f_x$ and $1<f_z<2$. The fractal dimension D along with the parameters l_0, h_0, f_x, and f_z can be determined experimentally from a surface profile of the rough surface using the method proposed by Warren et al. [24].

3 Normal Contact Model

Consider a Cantor set fractal surface of unit depth in contact with a smooth rigid half-space as shown in Fig. 2. The rough surface is modeled as a Winkler foundation [25] of thickness H^* and composed of elastic-perfectly plastic material with Young's modulus E, yield stress σ_y, and yield strain $\varepsilon_y=\sigma_y/E$. A load is applied to press the rigid half-space into the rough surface and then removed gradually. The loading and unloading process can be considered as quasi-static. Assume that each asperity behaves as an axially loaded rod and there is no interaction between the rods. Thus the total load applied to the rigid half-space is the sum of the contact load of each asperity.

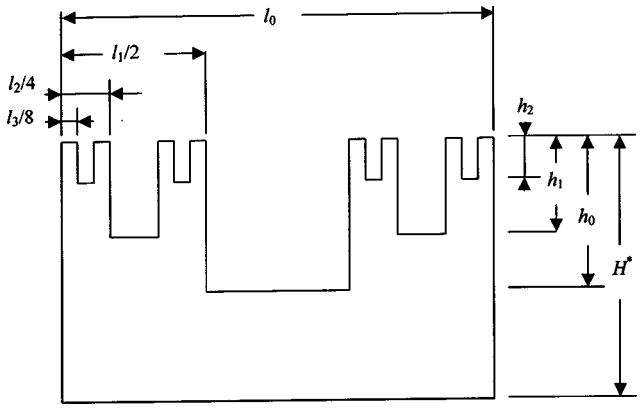

Fig. 1 Fractal surface constructed from the Cantor set

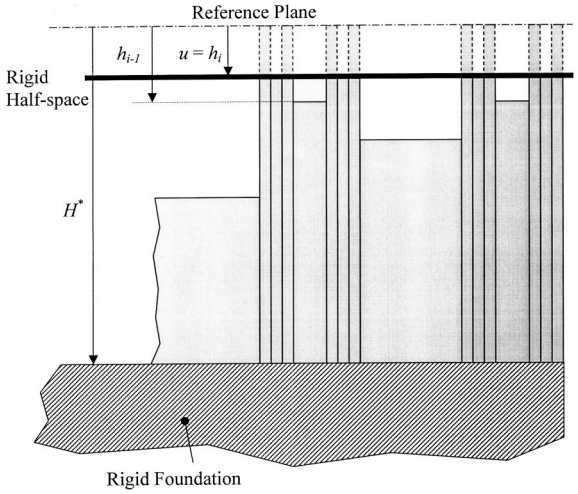

Fig. 2 A Cantor set surface in contact with a smooth rigid half-space

3.1 Load-Unload Behavior of a Single Rod. Consider the load-unload behavior of a single asperity first. The displacement of the rigid half-space is measured from a reference plane that is H^* apart from the bottom of the rod (Fig. 3). The distance between the top of the rod and the reference plane is h_i. When the rigid half-space with a displacement u is in contact with the rod, the strain of the rod is

$$\varepsilon_i=\frac{u-h_i}{H^*-h_i}. \tag{4}$$

In the elastic region, $\varepsilon_i<\varepsilon_y$, the contact load P_i is

$$P_i=E\varepsilon_i s, \tag{5}$$

where s denotes the contact area. It can be easily shown that the inception of plastic deformation occurs when the displacement of the rigid plane reaches u_y,

$$u_y=\varepsilon_y(H^*-h_i)+h_i. \tag{6}$$

For $u>u_y$, the deformation is uniformly plastic and the corresponding contact load is

$$P_i=\sigma_y s=E\varepsilon_y s. \tag{7}$$

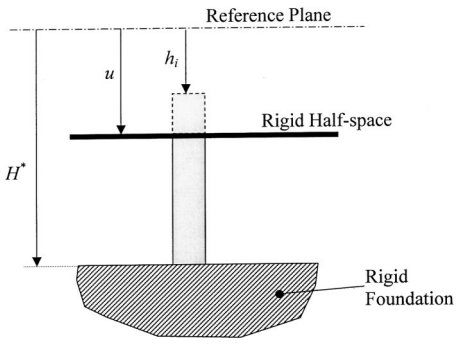

Fig. 3 A single asperity in contact with a smooth rigid half-space

Then consider the unloading behavior of the rod. Assume that the rod is unloaded from a maximum strain $\varepsilon_{\max} > \varepsilon_y$. Let σ_u and P_u indicate the stress and load during the unloading process, respectively. Then

$$P_u = \sigma_u s. \tag{8}$$

Due to the plastic deformation, there is a residual strain ε_r when the load is removed. In the unloading stage, σ_u is related to ε by

$$\sigma_u = E(\varepsilon - \varepsilon_r). \tag{9}$$

Using the fact that $\sigma_u = \sigma_y$ when $\varepsilon = \varepsilon_{\max}$, it follows that

$$\varepsilon_r = \varepsilon_{\max} - \varepsilon_y. \tag{10}$$

Thus, the dependence of the contact load during unloading on the displacement has the form

$$P_u = \sigma_y s\left[\frac{u - u_{\max}}{(H^* - h_i)\varepsilon_y} + 1\right]. \tag{11}$$

3.2 Load-Unload Behavior of the Fractal Surface. First, consider the loading process. When the rigid half-space reaches the nth stage of asperities, the asperities above the nth stage are compressed. The strain of the ith stage of asperities can be obtained by replacing u in Eq. (4) with h_n as

$$\varepsilon_i = \frac{h_n - h_i}{H^* - h_i}. \tag{12}$$

It can be shown that $\varepsilon_i > \varepsilon_j$, for $i > j > n$. Therefore, when some stages of asperities deform plastically, we can find a critical stage, the n_c th stage, such that the asperities above the critical stage deform plastically while those below the critical stage deform elastically. Then the contact load P_n can be expressed as

$$P_n = \sum_{i=n+1}^{n_c} E\varepsilon_i s_i + \sum_{i=n_c+1}^{\infty} \sigma_y s_i, \tag{13}$$

where s_i denotes the contact area of the ith stage of asperities. The first term on the right-hand side of Eq. (13) represents the contact force due to elastic deformation, while the second term due to plastic deformation. By using Eq. (12), the elastic contact force can be expressed as

$$\sum_{i=n+1}^{n_c} E\varepsilon_i s_i = \sum_{i=n+1}^{i=n_c} Es_i \frac{h_n - h_i}{H^* - h_n} = \frac{E}{H^*} \sum_{i=n+1}^{i=n_c} s_i \times \frac{h_n - h_i}{\left(1 - \dfrac{h_i}{H^*}\right)}.$$

Assuming that $h_i \ll H^*$ and neglecting the higher-order terms, the above equation reduces to

$$\sum_{i=n+1}^{n_c} E\varepsilon_i s_i \approx \frac{E}{H^*} \sum_{i=n+1}^{n_c} s_i (h_n - h_i) \tag{14}$$

Substituting Eq. (14) in Eq. (13) yields the contact force as

$$P_n = \frac{E}{H^*} \sum_{i=n+1}^{n_c} s_i (h_n - h_i) + \sigma_y \sum_{i=n_c+1}^{\infty} s_i. \tag{15}$$

This equation contains two different forms of series as Σs_i and $\Sigma h_i s_i$. From the definition of Cantor set and using Eqs. (1) and (2), these two series can be expressed as

$$\sum_{i=n_1}^{n_2} s_i = \sum_{i=n_1}^{n_2} (l_i - l_{i+1}) = l_{n_1} - l_{n_2+1}, \tag{16}$$

$$\sum_{i=n_1}^{n_2} h_i s_i = h_0 l_0 \left(1 - \frac{1}{f_x}\right)\left[\frac{\beta^{n_1} - \beta^{n_2+1}}{1 - \beta}\right], \tag{17}$$

where

$$\beta = 1/(f_x f_z). \tag{18}$$

By using these relations and choosing suitable upper and lower limits for each series, Eq. (15) can be rewritten as

$$\frac{P_n}{P_Y} = \frac{h_0}{\varepsilon_y H^*}\left\{\left(\frac{1}{f_z}\right)^n\left[\left(\frac{1}{f_x}\right)^{n+1} - \left(\frac{1}{f_x}\right)^{n_c+1}\right] - \left(1 - \frac{1}{f_x}\right)\left(\frac{\beta^{n+1} - \beta^{n_c+1}}{1 - \beta}\right)\right\} + \left(\frac{1}{f_x}\right)^{n_c+1}, \tag{19}$$

where

$$P_Y = \sigma_y l_0. \tag{20}$$

The total contact force for purely elastic deformation can be obtained by letting $n_c \to \infty$ in Eq. (19) and the result is

$$\frac{P_n}{P_Y} = \frac{h_0}{\varepsilon_y H^*}\left[\left(\frac{1}{f_z}\right)^n\left(\frac{1}{f_x}\right)^{n+1} - \left(1 - \frac{1}{f_x}\right)\left(\frac{\beta^{n+1}}{1 - \beta}\right)\right]. \tag{21}$$

Then, we proceed to study the unloading behavior of the fractal surface. Let $u_{\max}$ denote the maximum displacement of the rigid half-space, and $\bar{n}_c$ the corresponding critical stage. That is to say, when $u = u_{\max}$, asperities above the $\bar{n}_c$ th stage have plastic contact while those below the $\bar{n}_c$ th stage have elastic contact. For the elastically deformed asperities, the load-displacement curve in the unloading process coincides with that in the loading process. On the other hand, the load-displacement relationship of the plastically deformed asperities during unloading is described by Eq. (11). When the rigid half-space is withdrawn to a stage below the critical stage, say the nth stage, the total contact load can be expressed as

$$P_u = \sum_{i=n+1}^{\bar{n}_c} Es_i \frac{u - h_i}{H^* - h_i} + \sum_{i=n_c+1}^{\infty} Es_i \left(\frac{u - u_{\max}}{H^* - h_i} + \varepsilon_y\right). \tag{22}$$

For stages above the critical stage, due to the plastic deformation, the separation between the top of each stage and the reference plane when the load is removed is different from the original separation. Let $\bar{h}_i$ denote the separation of the top of the ith stage and the reference plane at the end of the unloading process. When the rigid plane is withdrawn to the nth stage that is above the critical stage, the total contact load can be expressed as

$$P_u = \sum_{i=n+1}^{\infty} Es_i \left(\frac{u - u_{\max}}{H^* - h_i} + \varepsilon_y\right), \quad u = \bar{h}_n < h_{nc}. \tag{23}$$

Following the same procedure for analyzing the loading behavior, we obtain the total contact force during unloading as

$$\frac{P_u}{P_Y} = \begin{cases} \dfrac{u}{\varepsilon_y H^*}\left(\dfrac{1}{f_x^{n+1}} - \dfrac{1}{f_x^{\bar{n}_c+1}}\right) - \dfrac{h_0(f_x - 1)}{\varepsilon_y H^* f_x}\left(\dfrac{\beta^{n+1} - \beta^{\bar{n}_c+1}}{1 - \beta}\right) + \dfrac{1}{\varepsilon_y f_x^{\bar{n}_c+1}}\left(\dfrac{u - u_{\max}}{H^*} + \varepsilon_y\right) & u = h_n,\ n \le \bar{n}_c \\ \dfrac{1}{\varepsilon_y f_x^{n+1}}\left(\dfrac{u - u_{\max}}{H^*} + \varepsilon_y\right) & u = \bar{h}_n,\ \bar{n}_c < n. \end{cases} \tag{24}$$

3.3 Asymptotic Analysis. In this section, we proceed to derive the asymptotic load-displacement expression. The difference between the heights of protrusions of the ith and $(i+1)$th stages diminishes as $i \to \infty$. Whence, the displacement can be treated as a continuous variable in the range $n \gg 1$. From the definition of Cantor set and the expression $u = h_n$, we obtain

$$n = -\frac{\log(u/h_0)}{\log(f_z)} \tag{25}$$

and

$$\left(\frac{1}{f_z}\right)^n = \frac{u}{h_0}. \tag{26}$$

Subsequently, it can be shown that for $n \gg 1$,

$$\left(\frac{1}{f_x}\right)^n = \left(\frac{u}{h_0}\right)^\alpha \quad \text{and} \quad \beta^n = \left(\frac{u}{h_0}\right)^{1+\alpha}, \tag{27}$$

in which

$$\alpha = \frac{\log(f_x)}{\log(f_z)}. \tag{28}$$

Then we need to know the relationship between the critical stage n_c and the displacement of the rigid half-space. When the rigid surface reaches the nth stage of asperities ($u = h_n$), the asperities above the n_cth stage deform plastically while those below the critical stage deform elastically. In other words, $\varepsilon_{n_c} < \varepsilon_y \leqslant \varepsilon_{n_c+1}$. Using Eqs. (2) and (12), we obtain

$$\left(\frac{1}{f_z}\right)^{n_c+1} \leqslant \frac{h_n - H^*\varepsilon_y}{h_0(1-\varepsilon_y)} = \frac{u - H^*\varepsilon_y}{h_0(1-\varepsilon_y)} < \left(\frac{1}{f_z}\right)^{n_c}. \tag{29}$$

Let

$$\chi = \frac{u - H^*\varepsilon_y}{h_0(1-\varepsilon_y)}. \tag{30}$$

Equation (29) can be rewritten as

$$n_c < -\frac{\log(\chi)}{\log(f_z)} \leqslant n_c + 1. \tag{31}$$

As can be seen from Eq. (29), if $u/H^* < \varepsilon_y$, n_c does not exist. This indicates that the deformation is purely elastic. On the other hand, if $u/H^* \gg \varepsilon_y$, $n_c \approx n+1$. This implies that the $(n+1)$th stage yields when the rigid surface reaches the nth stage. Hence, the fractal rough surface almost has purely plastic deformation. For asymptotic analysis define

$$n_c = -\frac{\log(\chi)}{\log(f_z)}. \tag{32}$$

It can be shown that

$$(1/f_x)^{n_c} = \chi^\alpha \quad \text{and} \quad \beta^{n_c} = \chi^{1+\alpha}$$

After substituting the above relations into Eqs. (19) and (21), we obtain the following load-displacement relations for purely elastic deformation and elastic-plastic deformation, respectively. For purely elastic deformation,

$$\frac{P}{P_Y} = \left(\frac{h_0}{\varepsilon_y f_x H^*}\right)\left[1 - \frac{(f_x - 1)\beta}{1-\beta}\right]\left(\frac{u}{h_0}\right)^{1+\alpha}. \tag{33}$$

For elastic-plastic deformation,

$$\frac{P}{P_Y} = \left(\frac{h_0}{\varepsilon_y H^* f_x}\right) \times \left\{\left(\frac{u}{h_0}\right)\left[\left(\frac{u}{h_0}\right)^\alpha - \chi^\alpha\right] - \frac{(f_x - 1)\beta}{1-\beta}\left[\left(\frac{u}{h_0}\right)^{1+\alpha} - \chi^{1+\alpha}\right]\right\} + \frac{\chi^\alpha}{f_x}. \tag{34}$$

By a similar procedure, we proceed to analyze the asymptotical unloading behavior of the fractal surface. Let $u_{\max}$ denote the maximum displacement of the rigid plane, and $\overline{n_c}$ be the corresponding critical stage. From the definition of the critical stage, it can be shown that the distance between the top of the $\overline{n_c}$ th stage and the reference plane is

$$\overline{h_{n_c}} = h_0 \chi_M, \tag{35}$$

where

$$\chi_M = \frac{u_{\max} - \varepsilon_y H^*}{(1-\varepsilon_y)h_0}. \tag{36}$$

The distance between the ∞–th stage and the reference plane due to the plastic deformation after the load is removed is

$$\overline{h_\infty} = u_{\max} - \varepsilon_y H^*. \tag{37}$$

During unloading, when the rigid plane is withdrawn to a position below the critical stage, the deformation of the fractal surface is partially plastic. On the other hand, when the rigid plane is withdrawn to a position above the critical stage, the fractal surface has purely plastic deformation. For these two cases, the load-displacement relationship during unloading can be, respectively, expressed as

$$\frac{P}{P_Y} = \begin{cases} \dfrac{(u/h_0)}{\varepsilon_y f_x (H^*/h_0)}\left[\left(\dfrac{u}{h_0}\right)^\alpha - \chi_M^\alpha\right] - \dfrac{(f_x-1)\beta[(u/h_0)^{1+\alpha} - \chi_M^{1+\alpha}]}{\varepsilon_y (H^*/h_0) f_x (1-\beta)} + \left[\dfrac{(u/h_0) - (u_{\max}/h_0)}{\varepsilon_y H^*/h_0} + 1\right]\dfrac{\chi_M^\alpha}{f_x} & \overline{h_{n_c}} \leqslant u < u_{\max} \\ \dfrac{1}{f_x (H^*/h_0)}\left(\dfrac{u}{\varepsilon_y h_0} - \dfrac{1-\varepsilon_y}{\varepsilon_y}\chi_M\right)^{\alpha+1} & \overline{h_\infty} \leqslant u < \overline{h_{n_c}} \end{cases}. \tag{38}$$

4 Coefficient of Restitution

Consider a rigid body with smooth flat contact surface approaching the stationary fractal surface with an initial velocity v_1. Following contact a short period of deformation takes place until the relative velocity between the two impacting bodies vanishes. At this instant, the fractal surface has maximum deformation, and the initial kinetic energy transforms into strain energy stored in the fractal surface if the energy contributed to the elastic wave propagation is negligible. During the remainder of contact a period of restitution occurs until the contact area reduces to zero. For a given incident velocity v_1, the maximum displacement of the rigid plane $u_{\max}$, at which the relative velocity between two impacting bodies vanishes, can be obtained by

$$\frac{1}{2} m v_1^2 = \int_0^{u_{\max}} P(u)\, du, \tag{39}$$

where m is the mass of the rigid body and P is the contact load during loading as described by Eq. (33) or (34), depending on whether plastic deformation is induced. For purely elastic contact, Eq. (33) should be employed. In this case, all the strain energy

stored during loading will be recovered to kinetic energy. The rebound velocity of the rigid body at the end of the period of restitution is the same as the incident velocity. And the coefficient of restitution is unity. For a plastically deformed fractal surface, plastic deformation occurs during loading and only elastic deformation is involved during unloading, [1]. The strain energy released during unloading transforms into kinetic energy of the rigid body. Therefore the rebound velocity v_2 is obtained by

$$\frac{1}{2}mv_2^2=\int_{-h_\infty}^{u_{\max}}P_u(u)du, \tag{40}$$

where the unloading contact load P_u is described by Eq. (38). The coefficient of restitution is obtained by

$$e=\frac{v_2}{v_1}=\left(\frac{\int_0^{u_{\max}}P(u)du}{\int_{-h_\infty}^{u_{\max}}P_u(u)du}\right)^{1/2}. \tag{41}$$

5 Results and Discussion

First, we verify the asymptotic load-displacement relationship. Figures 4(*a*) and (*b*) show the comparison of the asymptotic (solid) and series (dashed) representations of the load-displacement relationship for various values of fractal parameters.

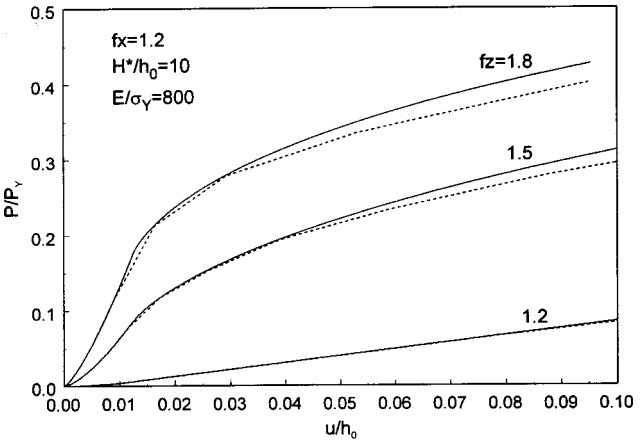

(*a*)

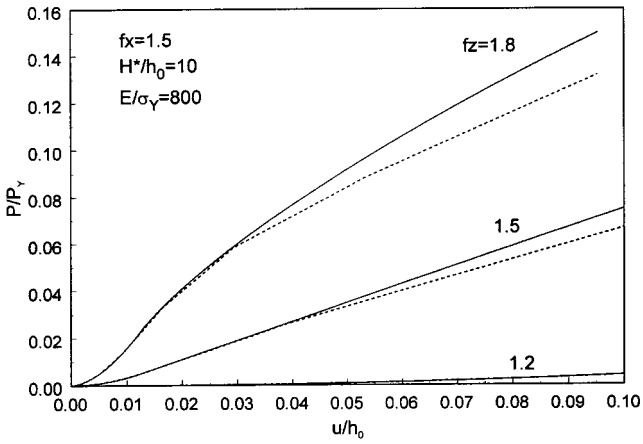

(*b*)

Fig. 4 Comparison of the asymptotic (solid) and series (dashed) results of the load-displacement curves for various values of fractal parameters, (*a*) $f_x=1.2$, (*b*) $f_x=1.5$

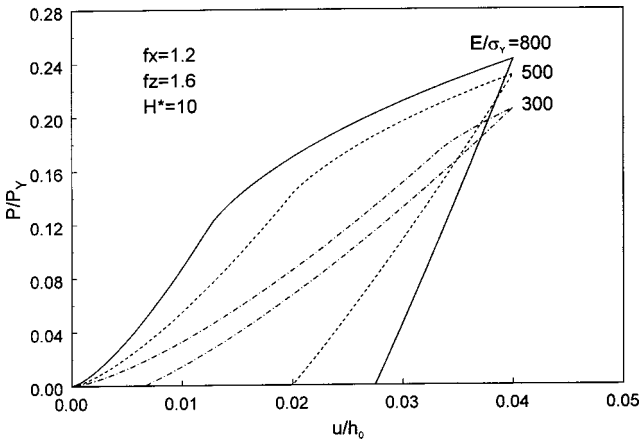

Fig. 5 Load versus displacement as a function of Young's modulus-to-yield stress ratio

As can be seen from the figures, the deviation between the asymptotic and series representations increases with the displacement, as expected. Besides, for a fixed value of f_x, the deviation between the asymptotic and series representations increases with f_z. It is observed that the deviation is less than 10% in the range $u/h_0<0.04$. In the following discussion, we confine the displacement in this range and use the asymptotic representations to study the effects of material properties and fractal parameters on the coefficient of restitution.

Figure 5 shows the load-unload curves at various Young's modulus-to-yield stress ratios. As can be seen from the figure, for a fixed value of displacement, the load increases with the Young's modulus, as expected. The unloading curves exhibit an initially linear response. This is due to the elastic recovery of the fractal surface. Bhattacharya and Nix [26] have shown that materials with a larger Young's modulus-to-yield stress ratio exhibit greater residual depth under a fixed maximum displacement, which is in agreement with the results shown in Fig. 5.

The significance of fractal parameters f_x and f_z on the load-unload curves is shown in Fig. 6. As can be seen from Fig. 6 that, when f_x is held constant, the load required to produce the same displacement increases with f_z. This is due to the fact that a larger f_z indicates a smoother surface. Equations (33) and (34) show that the parameter $\alpha=\log(f_x)/\log(f_z)$ has an import effect on the loading curve. Since α is positive, for purely elastic deformation, the load scales as the displacement to a power greater than one. Therefore, all the loading curves in Fig. 6 are initially convex. As the loading progresses, more and more asperities deform plastically and the last term in Eq. (34) becomes more significant. In this stage, the load scales as the displacement to a power greater than one for $f_x>f_z$, but less than one for $f_x<f_z$. It is observed in Fig. 6 that, as the loading progresses, the loading curve is entirely convex for $\alpha>1$, while changes from convex to concave for $\alpha<1$.

Figure 7 shows the coefficient of restitution versus the dimensionless incident velocity for different values of the Young's modulus-to-yield stress ratio. The dimensionless incident velocity V^* is defined as $V^*=\sqrt{mv^2/(2l_0Eh_0)}$. The coefficient of restitution is equal to unity when the incident velocity is lower than the critical velocity at which onset of plastic deformation occurs. The critical velocity decreases with the increasing Young's modulus-to-yield stress ratio. Once the velocity exceeds the critical velocity, the coefficient of restitution is less than one because some energy is dissipated in plastic deformation. The area enclosed by the load-unload curve and the horizontal axis represents the energy lost in plastic deformation. As shown in Fig. 5, this area increases with the Young's modulus-to-yield stress ratio for a fixed value of maximum displacement. This is due to that most of

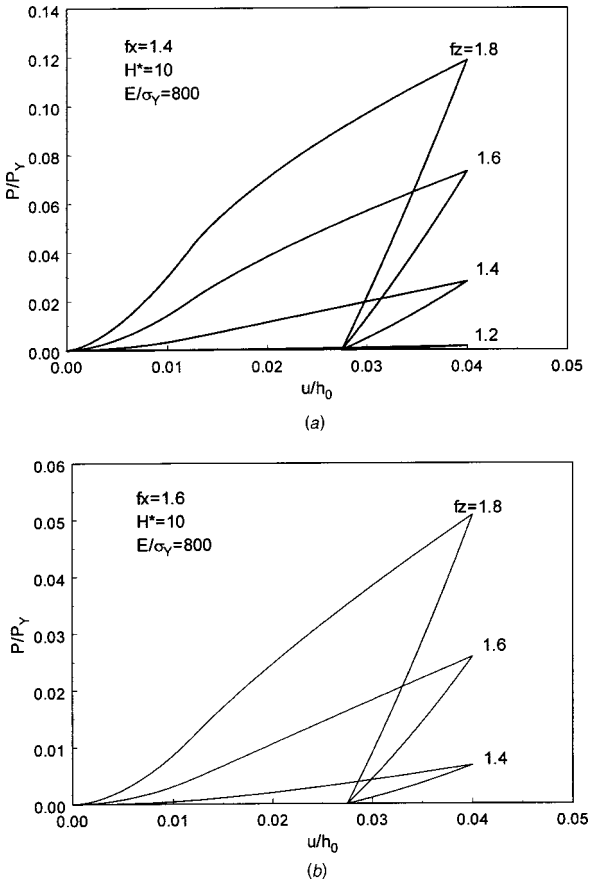

Fig. 6 Load-displacement curves for different values of fractal parameters, (*a*) $f_x=1.4$, (*b*) $f_x=1.8$

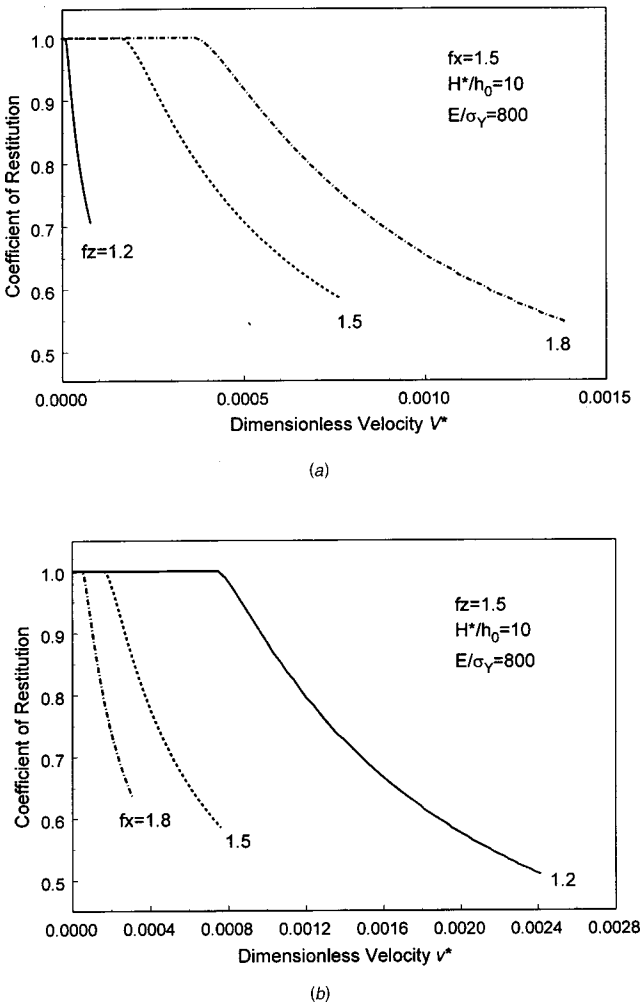

Fig. 8 Coefficient of restitution versus incident velocity for different values of fractal parameters, (*a*) $f_x=1.5$, (*b*) $f_z=1.5$

the asperities are deformed plastically when the Young's modulus to yield stress ratio is large. Figure 7 confirms that the coefficient of restitution decreases as the ratio of Young's modulus-to-yield stress is increased.

The effect of the fractal parameters on the coefficient of restitution is shown in Fig. 8. Figure 8(*a*) shows the coefficient of restitution versus the incident velocity for various values of f_z while f_x is held constant. The critical velocity increases with f_z. Once the incident velocity exceeds the critical velocity, the coefficient of restitution decreases rapidly with the incident velocity. As incident velocity increases, the coefficient of restitution becomes less sensitive to velocity. A similar trend can be seen from Fig. 8(*b*) that the coefficient of restitution decreases with increasing f_x.

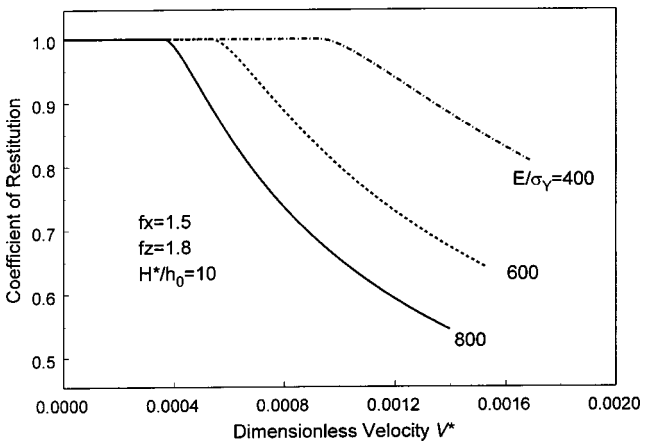

Fig. 7 Coefficient of restitution versus incident velocity as a function of Young's modulus-to-yield stress ratio

6 Conclusion

We studied the effect of surface roughness on the coefficient of restitution. We proposed an elastic-perfectly plastic contact model for a fractal surface in contact with a rigid smooth half-space. The fractal surface was constructed based on the Cantor set. Asymptotic analysis was performed to derive a continuous load-displacement relation. The result shows that the compliance relation depends strongly on the fractal parameters that characterize the surface topography. Based on the load-displacement relation, we investigated the significance of fractal parameters as well as material properties and incident velocity on the coefficient of restitution. It is found that materials with high Young's modulus-to-yield stress ratio have smaller coefficient of restitution. Upon the point the incident velocity exceeds the critical velocity, the coefficient of restitution drops fast with the incident velocity. The sensitivity of the coefficient of restitution to the incident velocity decreases as the incident velocity increases. The coefficient of restitution decreases with increasing fractal dimension.

References

[1] Tabor, D., 1951, *The Hardness of Metals*, Oxford University Press, London.
[2] Goldsmith, W., 1960, *Impact*, Arnold, London.
[3] Johnson, K. L., 1985, *Contact Mechanics*, Cambridge University Press, Cambridge, UK.
[4] Ling, F. F., 1958, ''On Asperity Distributions of Metallic Surface,'' J. Appl. Phys., **29**, pp. 1168–1174.
[5] Nayak, P. R., 1971, ''Random Process Model of Rough Surfaces,'' ASME J. Tribol., **93**, pp. 398–407.
[6] Greenwood, J. A., and Williamson, J. B. P., 1966, ''The Contact of Nominally Flat Surfaces,'' Proc. R. Soc. London, Ser. A, **A295**, pp. 300–319.
[7] Whitehouse, D. J., and Archard, J. F., 1970, ''The Properties of Random Surfaces of Significance in Their Contact,'' Proc. R. Soc. London, Ser. A, **A316**, pp. 97–121.
[8] Bush, A. W., Gibson, R. D., and Thomas, T. R., 1975, ''The Elastic Contact of a Rough Surface,'' Wear, **35**, pp. 87–111.
[9] Yamada, K., Takeda, N., Kagami, J., and Naoi, T., 1978, ''Mechanisms of Elastic Contact and Friction Between Rough Surfaces,'' Wear, **48**, pp. 15–34.
[10] Bhushan, B., 1984, ''Analysis of the Real Area of Contact Between a Polymeric Magnetic Medium and a Rigid Surface,'' ASME J. Tribol., **106**, pp. 26–34.
[11] McCool, J. I., 1986, ''Comparison of Models for the Contact of Rough Surfaces,'' Wear, **107**, pp. 37–60.
[12] Chang, W. R., Etsion, I., and Body, D. B., 1987, ''An Elastic-Plastic Model for the Contact of Rough Surfaces,'' ASME J. Tribol., **109**, pp. 257–263.
[13] Chang, W.-R., and Ling, F. F., 1992, ''Normal Impact Model of Rough Surfaces,'' ASME J. Tribol., **114**, pp. 439–447.
[14] Sayles, R. S., and Thomas, T. R., 1979, ''Measurements of the Statistical Microgeometry of Engineering Surfaces,'' ASME J. Lubr. Technol., **101**, pp. 409–418.
[15] Greenwood, J. A., 1984, ''A Unified Theory of Surface Roughness,'' Proc. R. Soc. London, Ser. A, **A393**, pp. 133–157.
[16] Ling, F. F., 1989, ''The Possible Role of Fractal Geometry in Tribology,'' Tribol. Trans., **32**, pp. 497–505.
[17] Majumdar, A., and Bhushan, B., 1990, ''Role of Fractal Geometry in Roughness Characterization and Contact Mechanics of Surfaces,'' ASME J. Tribol., **112**, pp. 205–216.
[18] Mandelbrot, B. B., 1983, *The Fractal Geometry of Nature*, Freeman, New York.
[19] Kaplan, T., and Gray, L. J., 1985, ''Effect of Disorder on a Fractal Model for the AC Response of a Rough Interface,'' Phys. Rev. B, **32**, pp. 7360–7366.
[20] Church, E. L., 1988, ''Fractal Surface Finish,'' Appl. Opt., **27**, pp. 1518–1526.
[21] Majumdar, A., and Bhushan, B., 1991, ''Fractal Model of Elastic-Plastic Contact Between Rough Surfaces,'' ASME J. Tribol., **113**, pp. 1–11.
[22] Wang, S., and Komvopoulos, K., 1994, ''A Fractal Theory of the Interfacial Temperature Distribution in the Slow Sliding Regime: Part I—Elastic Contact and Heat Transfer Analysis,'' ASME J. Tribol., **116**, pp. 812–823.
[23] Borodich, F. M., and Mosolov, A. B., 1992, ''Fractal Roughness in Contact Problems,'' J. Appl. Math. Mech., **56**, pp. 681–690.
[24] Warren, T. L., Majumdar, A., and Krajcinovic, D., 1996, ''A Fractal Model for the Rigid-Perfectly Plastic Contact of Rough Surfaces,'' ASME J. Appl. Mech., **63**, pp. 47–54.
[25] Cook, R. D., and Young, W. C., 1985, *Advanced Mechanics of Materials*, Macmillan, New York.
[26] Bhattacharya, A. K., and Nix, W. D., 1988, ''Finite Element Simulation of Indentation Experiments,'' Int. J. Solids Struct., **24**, pp. 881–891.

J. C. Mollendorf
Professor

J. D. Felske
Professor

S. Samimy
Graduate Student

Department of Mechanical and Aerospace Engineering,
School of Engineering,
Center for Research and Education in Special Environments,
State University of New York at Buffalo,
Buffalo, NY 14214-3078

D. R. Pendergast
Professor Department of Physiology,
School of Medicine,
Center for Research and Education in Special Environments,
State University of New York at Buffalo,
Buffalo, NY 14214-3078

A Fluid/Solid Model for Predicting Slender Body Deflection in a Moving Fluid

An analytical solution is presented for the steady-periodic shape variation of a thin elastic beam subject to fluid mechanic forces and driven by the motion imposed on its ends. The general solution is applicable to such problems as swim fins and aerodynamic flutter, with the proper choice of boundary conditions. The general results are exemplified here by using specific boundary conditions that mimic the motion of swim fins. The calculated instantaneous shape, position, slopes, and lateral velocities of the fin are compared with corresponding measurements taken from underwater video of fins worn by divers swimming at a controlled speed. The analysis revealed new swim technique parameters that characterize the heel slope and its phase with respect to the heel motion. The calculated power, thrust, and Froude efficiency are presented in terms of these parameters.
[DOI: 10.1115/1.1554416]

1 Introduction

Lighthill [1] used the ''slender-body'' approximation of Munk [2] to work out the inviscid flow and corresponding instantaneous lift per unit length, power, thrust, and Froude efficiency for a slender fish (or swimming mammal) in terms of a specified time-dependent surface shape. The results were presented in terms of a virtual mass per unit length and time averages of functions depending on the slope and normal velocity component of the trailing (or free) edge of the surface. Since the time-dependent surface shape was not known a priori, Lighthill [1] suggested various oscillatory surface motions. In another study at about the same time, Wu [3] imposed oscillatory surface motions for a two-dimensional flat fish. For many applications, however, the shape is a result of the fluid motion and vice versa. That is, the fluid-solid interaction problem is of the moving boundary type.

The presently reported work does not assume a time-dependent surface shape, but rather calculates it by incorporating Lighthill's [1] relationship between the fluid mechanic force and the surface shape into the equation defining the elastic deflection of a Euler-Bernoulli beam.

2 Analysis

Force/Deflection. Take x to be in the direction of the uniform freestream velocity relative to the swimmer, U, (Fig. 1). The local fluid mechanic lift force per unit length, $L(x,t)=\partial F_z/\partial x$, is related to the local, instantaneous surface shape, $h(x,t)$, by the following equation (Lighthill [1])

$$L(x,t)=-(\rho A)\left(\frac{\partial}{\partial t}+U\frac{\partial}{\partial x}\right)^2 h(x,t) \tag{1}$$

where ρ is the freestream fluid density and (ρA) is the virtual mass, per unit length, of a cylinder circumscribing the cross section of the surface, and (ρA) is taken here to be constant.

The dynamic deflection of a thin elastic beam, having density, ρ_b, cross-sectional area, A_b, elastic modulus, E, and moment of inertia, I, is governed by the following equation:

$$(\rho_b A_b)\frac{\partial^2 h(x,t)}{\partial t^2}=F(x,t)-(EI)\frac{\partial^4 h(x,t)}{\partial x^4} \tag{2}$$

where $F(x,t)$ is the instantaneous beam loading (force per unit length).

In our problem, the beam inertia is taken to be much less than the inertia of the virtual mass of fluid $[(\rho_b A_b)\ll(\rho A)]$; then, using Eqs. (1) and (2) where $F(x,t)=L(x,t)$,

$$(EI)\frac{\partial^4 h(x,t)}{\partial x^4}+(\rho A)\left(\frac{\partial}{\partial t}+U\frac{\partial}{\partial x}\right)^2 h(x,t)=0. \tag{3}$$

This gives the quasi-static deflection of the beam under dynamic loading that depends on time-varying inertia forces in the surrounding fluid. Forced motion of the boundary at $x=0$ drives the motion of the surface. In the present study, this forcing is considered to be periodic. Hence, a steady-periodic solution was sought of the form $h(x,t)=\mathrm{Re}\{\hat{h}(x,t)\}$, where $\hat{h}(x,t)=\hat{h}_0(x)e^{i\omega t}$, and ''Re'' indicates ''real part,'' ''$\wedge$'' indicates complex variable, and ω is the frequency of the imposed motion.

The steady-periodic solution of Eq. (3) for the (complex) fin shape is

$$\hat{h}(x,t)=e^{i(\omega t+\delta x)}[\hat{C}_1\cos(\varphi x)+\hat{C}_2\sin(\varphi x)] + e^{i(\omega t-\delta x)}[\hat{C}_3\cosh(\gamma x)+\hat{C}_4\sinh(\gamma x)] \tag{4}$$

where the $\hat{C}_j$ are constants to be determined by the boundary conditions, and

$$\delta\equiv U/(2\sigma) \tag{5}$$

$$\gamma\equiv U\sqrt{\beta-1}/(2\sigma) \tag{6}$$

$$\varphi\equiv U\sqrt{\beta+1}/(2\sigma) \tag{7}$$

Contributed by the Applied Mechanics Division of THE AMERICAN SOCIETY OF MECHANICAL ENGINEERS for publication in the ASME JOURNAL OF APPLIED MECHANICS. Manuscript received by the ASME Applied Mechanics Division, January 29, 2001; final revision, October 16, 2002. Associate Editor: D. A. Siginer. Discussion on the paper should be addressed to the Editor, Prof. Robert M. McMeeking, Department of Mechanical and Environmental Engineering, University of California–Santa Barbara, Santa Barbara, CA 93106-5070, and will be accepted until four months after final publication of the paper itself in the ASME JOURNAL OF APPLIED MECHANICS.

 Copyright © 2003 by ASME

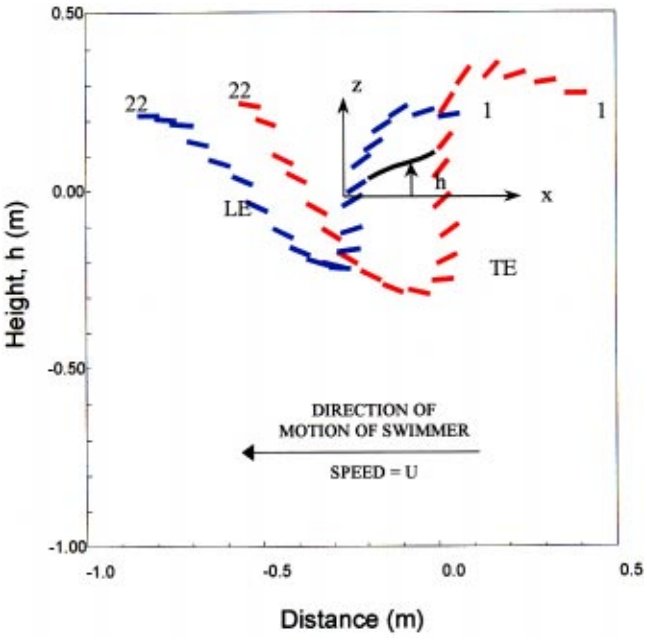

Fig. 1 "Fin signature" showing the measured local, instantaneous slopes of the "leading edge" (LE) and "free end" (trailing edge (TE)). The numbers, 1–22, indicate LE and TE segments at 1/15 second increments. The fin shape is sketched in for segment number 7. Note that $x=0$ is fixed to the LE and $x=l$ is at the TE.

where

$$\sigma \equiv \sqrt{(EI)/(\rho A)} \quad \text{and} \quad \beta \equiv 4\omega\sigma/U^2.$$

Equation (4) indicates the presence of two waves traveling in the beam at the same wave speed, $2\omega\sigma/U$, but in opposite directions.

Boundary Conditions—Swim Fin. The experimentally obtained "fin signature" from Samimy [4], shown as Fig. 1, was used for guidance in determining the boundary conditions to exemplify the mathematical model as it applies to underwater fin swimming. This "fin signature" (Fig. 1) shows a "trace" of the leading and trailing edges (LE and TE) of the fin taken from a video of underwater fin swimming.

For a given human subject, the effectiveness of a fin varies and there is interplay between the fin type and the swimming technique to achieve performance goals, (Pendergast [5]). For example, there is an inverse relationship between kick depth and kick frequency that varies with fin geometry and fin stiffness (Pendergast [5]).

The fin leading edge ($x=0$) is taken to be at the beginning of the flexible part of the fin, near the toe of the swimmer, downstream of the rigid "foot" of the fin. The trailing edge ($x=l$) is at the free end of the flexible region. It is over this portion of the fin (i.e., $0 \leqslant x \leqslant l$) that Samimy [4] studied its elastic behavior. It is then natural to specify the peak to peak amplitude of the kick, $2h_0$, and the kick frequency, $f=\omega/(2\pi)$. Further, an analysis of video of underwater fin swimming (and as will be shown in later figures) Samimy [4] shows that the motion of the leading edge is approximately harmonic, i.e.,

$$\hat{h}(0,t) = h_0 e^{i\omega t}. \tag{8}$$

Similarly, the analysis shows that the slope of the leading edge is also approximately harmonic at the same frequency with amplitude, h_{x0}, but shifted in phase by α, i.e.,

$$\hat{h}_x(0,t) = h_{x0} e^{i(\omega t-\alpha)}. \tag{9}$$

This amounts to a representation of swimming technique in terms of an angular location, α, called the *leading edge coordination angle*, at which the magnitude of the *leading edge slope* is maximum, h_{x0}.

Vanishing shear and moment at the free end (trailing edge) of the fin, $x=l$, provide the remaining two boundary conditions:

$$\hat{h}_{xx}(l,t) = 0 \tag{10}$$

$$\hat{h}_{xxx}(l,t) = 0. \tag{11}$$

Then, using Eqs. (8)–(11), the constants of integration, $\hat{C}_j$, are obtained from the solution of the following linear system:

$$\begin{bmatrix} 1 & 0 & 1 & 0 \\ i\delta & \varphi & -i\delta & \gamma \\ \hat{\pi}_1 & \hat{\pi}_2 & \hat{\pi}_3 & \hat{\pi}_4 \\ \hat{\tau}_1 & \hat{\tau}_2 & \hat{\tau}_3 & \hat{\tau}_4 \end{bmatrix} \times \begin{bmatrix} \hat{C}_1 \\ \hat{C}_2 \\ \hat{C}_3 \\ \hat{C}_4 \end{bmatrix} = \begin{bmatrix} h_0 \\ h_{x0} e^{-i\alpha} \\ 0 \\ 0 \end{bmatrix} \tag{12}$$

where

$$\hat{\pi}_1 \equiv e^{+i\delta l}[-(\varphi^2+\delta^2)\cos(\varphi l) - i(2\delta\varphi)\sin(\varphi l)] \tag{13a}$$

$$\hat{\pi}_2 \equiv e^{+i\delta l}[-(\varphi^2+\delta^2)\sin(\varphi l) + i(2\delta\varphi)\cos(\varphi l)] \tag{13b}$$

$$\hat{\pi}_3 \equiv e^{-i\delta l}[+(\gamma^2-\delta^2)\cosh(\gamma l) - i(2\delta\gamma)\sinh(\gamma l)] \tag{13c}$$

$$\hat{\pi}_4 \equiv e^{-i\delta l}[+(\gamma^2-\delta^2)\sinh(\gamma l) - i(2\delta\gamma)\cosh(\gamma l)] \tag{13d}$$

and

$$\hat{\tau}_1 \equiv e^{+i\delta l}[+(\varphi^3+3\delta^2\varphi)\sin(\varphi l) - i(3\delta\varphi^2+\delta^3)\cos(\varphi l)] \tag{14a}$$

$$\hat{\tau}_2 \equiv e^{+i\delta l}[-(\varphi^3+3\delta^2\varphi)\cos(\varphi l) - i(3\delta\varphi^2+\delta^3)\sin(\varphi l)] \tag{14b}$$

$$\hat{\tau}_3 \equiv e^{-i\delta l}[+(\gamma^3-3\delta^2\gamma)\sinh(\gamma l) - i(3\delta\gamma^2-\delta^3)\cosh(\gamma l)] \tag{14c}$$

$$\hat{\tau}_4 \equiv e^{-i\delta l}[+(\gamma^3-3\delta^2\gamma)\cosh(\gamma l) - i(3\delta\gamma^2-\delta^3)\sinh(\gamma l)]. \tag{14d}$$

The power, $\overline{P}$, thrust, $\overline{T}$, and Froude efficiency, $\overline{\eta}_F$, averaged over one cycle of time period, $t_p=1/f$, follow from Lighthill's analysis, [1]:

$$\overline{P} = -\left(\frac{1}{t_p}\right)\int_{t=0}^{t_p}\int_{x=0}^{l}\frac{\partial h}{\partial t}L(x,t)\,dx\,dt \tag{15a}$$

$$\overline{P} = (\rho A)U\left(\frac{1}{t_p}\right)\int_{t=0}^{t_p}\left[\frac{\partial h}{\partial t}\left(\frac{\partial h}{\partial t}+U\frac{\partial h}{\partial x}\right)\right]_{x=0}^{l} dt \tag{15b}$$

$$\overline{T} = \overline{P}/U - [(\rho A)/2]\left(\frac{1}{t_p}\right)\int_{t=0}^{t_p}\int_{x=0}^{l}\left(\frac{\partial h}{\partial t}+U\frac{\partial h}{\partial x}\right)^2 dx\,dt \tag{16a}$$

$$\overline{T} = [(\rho A)/2]\left(\frac{1}{t_p}\right)\int_{t=0}^{t_p}\left[\left\{\left(\frac{\partial h}{\partial t}\right)^2 - U^2\left(\frac{\partial h}{\partial x}\right)^2\right\}\right]_{x=0}^{l} dt \tag{16b}$$

$$\overline{\eta}_F \equiv \overline{T}U/\overline{P}. \tag{17}$$

3 Results

The results can be conveniently presented in nondimensional form by choosing the characteristic lengths for x and $h(x,t)$ to be l and h_0, respectively, and the characteristic time for t to be ω^{-1}. Equations (3) and (8)–(11) then become

$$(e^2)\hat{H}_{XXXX} + \left(S\frac{\partial}{\partial\tau}+\frac{\partial}{\partial X}\right)^2\hat{H} = 0 \tag{18}$$

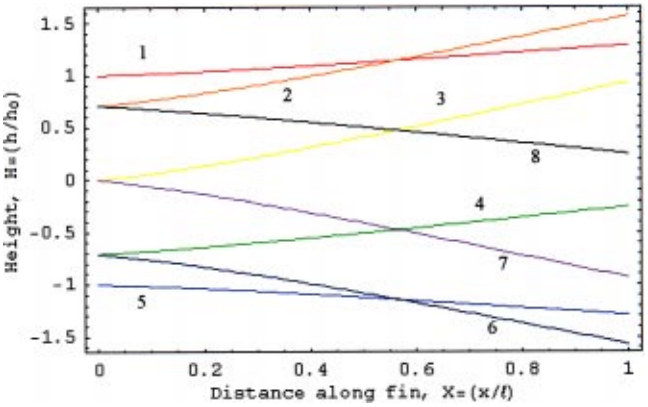

Fig. 2 Calculated fin shapes, $H(X,\tau)$, as a function of X during the kick cycle. Numbers denote increasing multiples of time, τ, in $\pi/4$ increments.

$$\hat{H}(0,\tau)=e^{i\tau} \tag{19}$$

$$\hat{H}_X(0,\tau)=\kappa e^{i(\tau-\alpha)} \tag{20}$$

$$\hat{H}_{XX}(1,\tau)=0 \tag{21}$$

$$\hat{H}_{XXX}(1,\tau)=0. \tag{22}$$

The resulting nondimensional groups are the Strouhal number, S, an elasticity number, e, the maximum leading edge slope, κ, and the angular location of the maximum leading edge slope, α, in radians:

$$S\equiv\omega l/U \tag{23}$$

$$e\equiv\sigma/(lU)=\sqrt{(EI)/(\rho A)}/(lU) \tag{24}$$

$$\kappa\equiv h_{x0}l/h_0 \tag{25}$$

where

$$\hat{H}\equiv\hat{h}/h_0,\quad X\equiv x/l \quad\text{and}\quad \tau\equiv\omega t.$$

Consequently, the nondimensional, instantaneous fin shape, $\mathrm{Re}\{\hat{H}\}$, average power, $\overline{P}/P_c$, average thrust, $\overline{T}/T_c$, and average Froude efficiency, $\overline{\eta}_F$, will be functions of S, e, κ, and α, where $P_c\equiv h_0^2\omega^2U(\rho A)$ and $T_c\equiv P_c/(2U)$. It is noted that the elasticity number, e, represents the ratio of an "elastic" velocity, σ/l, to the freestream velocity, U.

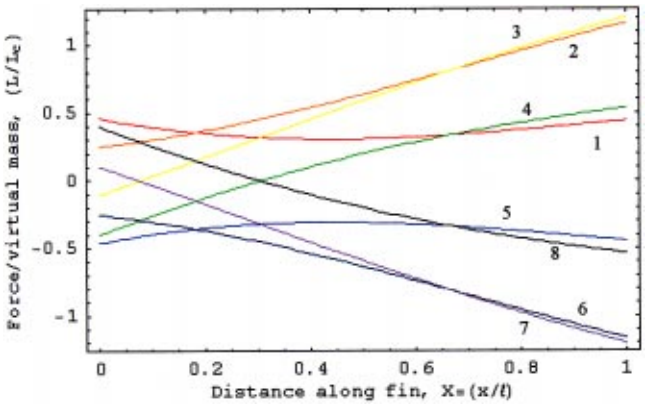

Fig. 3 Calculated lift distribution, $L(X,\tau)/L_c$, as a function of X during the kick cycle. Numbers denote increasing multiples of time, τ, in $\pi/4$ increments, where $L_c\equiv h_0U^2(\rho A)/l^2$.

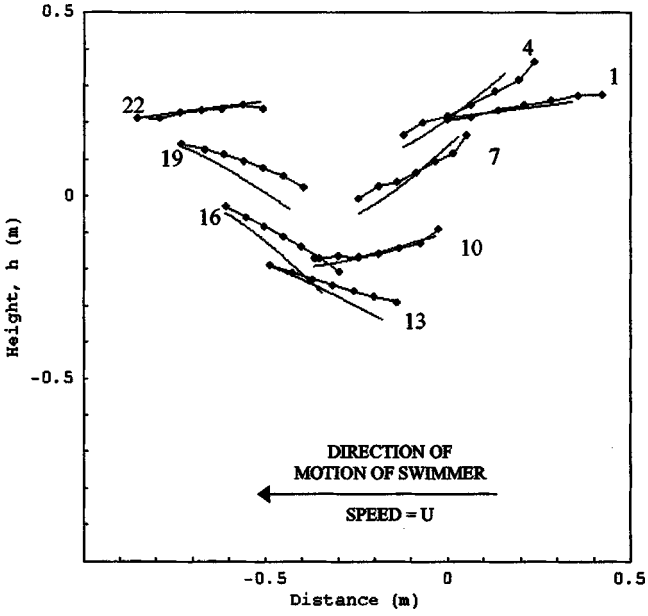

Fig. 4 Fin signature computed for the experimental conditions of Fig. 1. The time interval between each fin trace is 1/5 second. The symbols (connected with lines) are measurements from Samimy [4]. The numbers correspond to those in Fig. 1.

Typical calculated fin shapes and lift distributions are shown in Figs. 2 and 3, for the conditions of Fig. 1, namely: $S=2.52$, $e=1.38$, $\kappa=0.93$, and $\alpha=1.34$ radians.

A calculated (dimensional) fin signature is shown as the line segments in Fig. 4. The symbols (connected with lines) are measurements from Samimy [4]. It can be seen that the fin shapes and positions are in generally good agreement with the measurements. The characteristic lengths for these data are $l=0.342$ m and $h_0=0.213$ m.

Figures 5, 6, and 7 show the time variations of the corresponding instantaneous locations of the leading edge ($x=0$) and trailing edge ($x=l$), their slopes and their vertical velocities, as calculated from the solution of Eq. (3). The symbols are measurements from Samimy [4]. It can be seen that the calculated theoretical results are in generally good agreement with the measurements.

The calculated variations of time-average power, thrust, and Froude efficiency with the swimming technique parameters, κ and α, are shown in Figs. 8, 9, and 10. The data points correspond to

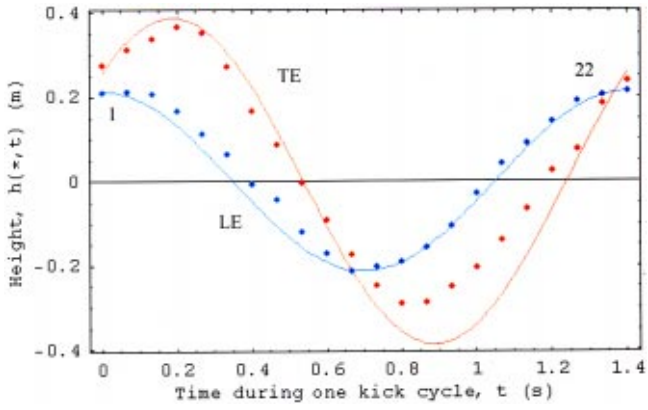

Fig. 5 Time variation of the position of the fin leading edge, $h(0,t)$, (LE) and trailing edge, $h(l,t)$, (TE) for the experimental conditions corresponding to Fig. 1. The symbols are measurements from Samimy [4].

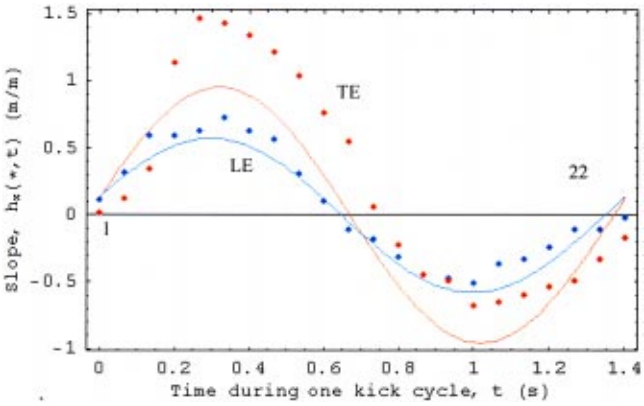

Fig. 6 Time variation of the slope of the fin leading edge, $h_x(0,t)$, (LE) and trailing edge, $h_x(l,t)$, (TE) for the experimental conditions corresponding to Fig. 1. The symbols are measurements from Samimy [4].

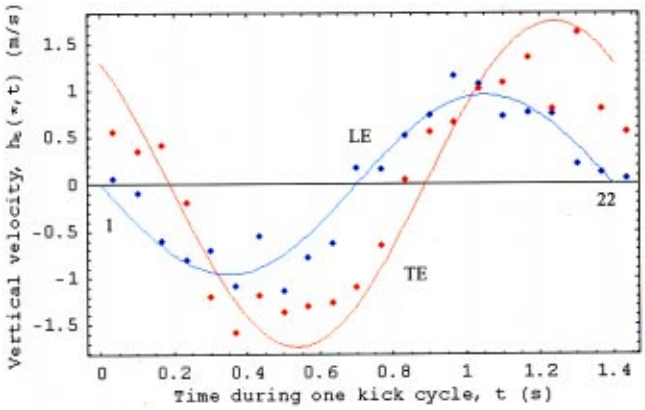

Fig. 7 Time variation of the vertical velocity of the fin leading edge, $h_t(0,t)$, (LE) and trailing edge, $h_t(l,t)$, (TE) for the experimental conditions corresponding to Fig. 1. The symbols are measurements from Samimy [4].

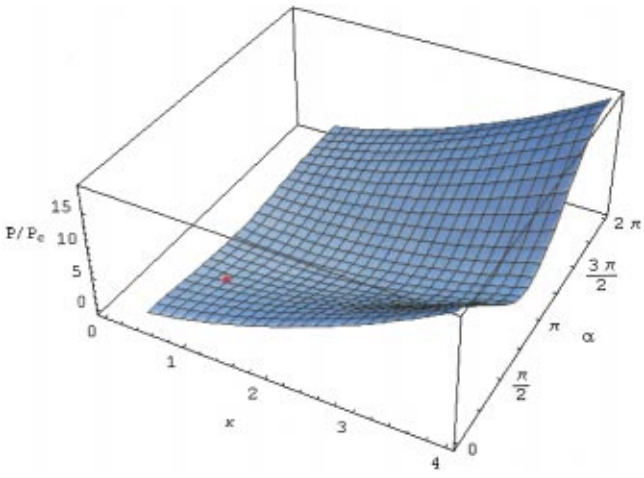

Fig. 8 Variation of the non-dimensional power, $\bar{P}/P_c$, with nondimensional maximum leading edge slope, κ, and leading edge coordination (phase) angle, α. The data point corresponds to the experimental conditions of Fig. 1.

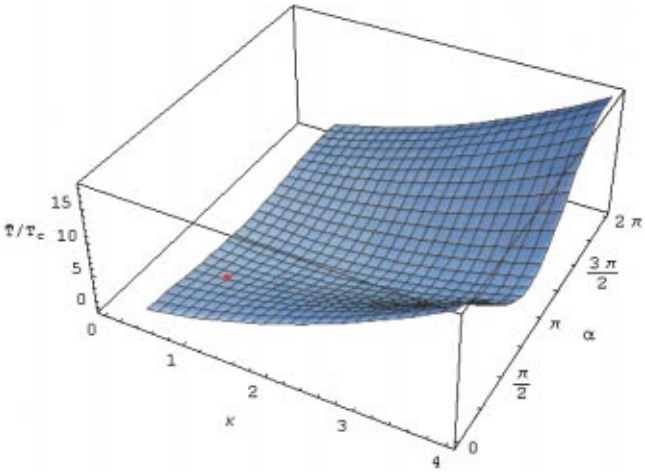

Fig. 9 Variation of the nondimensional thrust, $\bar{T}/T_c$, with nondimensional maximum leading edge slope, κ, and leading edge coordination (phase) angle, α. The data point corresponds to the experimental conditions of Fig. 1.

the experimental conditions of Fig. 1. The behavior suggested by Fig. 10 is striking. It suggests that the swimming technique, as defined in terms of the phase lag, α, of the maximum leading edge slope, κ, can have a dramatic effect on the Froude efficiency, $\bar{\eta}_F$. Indeed, the efficiency shows a precipitous dropoff (to negative $\bar{\eta}_F$) as $\alpha \rightarrow \pi$. Note that negative $\bar{\eta}_F$ implies negative thrust.

4 Conclusions

An analytical solution was obtained for a fluid-solid interaction problem of the moving-boundary type. By using an established approximation for the fluid mechanics, and forcing the motion with a periodic input at the edge of the solid, a closed-form solution was derived for the surface shape as a function of time. Fluid forces, power, thrust, and Froude efficiency were also determined. This solution extends previous work in which the surface shape

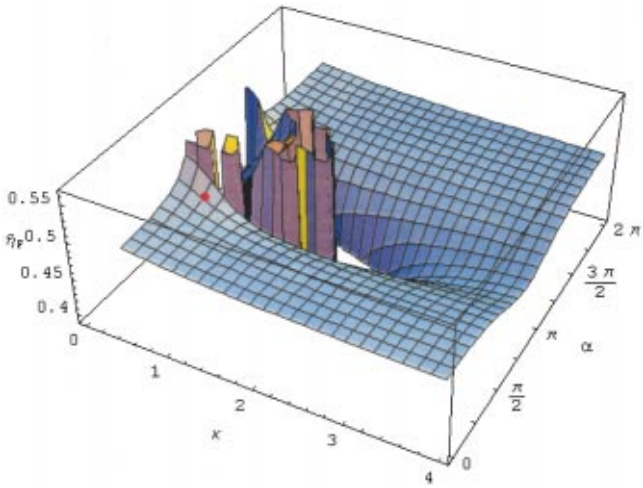

Fig. 10 Variation of the Froude efficiency, $\bar{\eta}_F$, with nondimensional maximum leading edge slope, κ, and leading edge coordination (phase) angle, α. The data point corresponds to the experimental conditions of Fig. 1.

behavior and/or waveform was prescribed. The presently reported solution reveals a prediction of the local, instantaneous shape of an elastic surface in a fluid stream subjected to a prescribed motion at the edge of the solid. It is given in terms of this motion, the freestream velocity and the elastic properties and cross section of the surface. This first application of the theory to underwater fin swimming shows encouraging agreement with experimental data. New swim technique parameters arose naturally from the analysis that characterizes the heel slope and its phase with respect to the heel motion. It is expected that the presently reported results will be useful in guiding both the design optimization of swim fins and the analysis of experimental measurements of underwater and/or surface swimmers. The incorporation of other boundary conditions will permit the analysis of other surface/fluid interactive motions, such as problems in aeroelasticity involving flutter.

Acknowledgments

The authors gratefully acknowledge support for this research from the United States Navy, NAVSEA, Navy Experimental Diving Unit, contract N6133199C0028.

References

[1] Lighthill, M. J., 1960, ''Note on the Swimming of Slender Fish,'' J. Fluid Mech., **9**, pp. 305–317.
[2] Munk, M. M., 1923, ''The Aerodynamic Forces on Airship Hulls,'' NACA Report No. 184, pp. 453–468.
[3] Wu, T. Y.-T., 1960, ''Swimming of a Waving Plate,'' J. Fluid Mech., **10**, pp. 321–344.
[4] Samimy, S., 2002, ''Theoretical and Experimental Analysis of Underwater Fin Swimming,'' Master's Project, State University of New York at Buffalo, Buffalo, NY, July 11.
[5] Pendergast, D. R., 1996, ''Energetics of Underwater Fin Swimming,'' Med. Sci. Sports Exercise, **pp.** 573–580.

S. I. Bakhtiyarov
Research Professor

R. A. Overfelt
Professor

Mechanical Engineering Department,
202 Ross Hall,
Auburn University,
Auburn, AL 36849-5341

A. J. Meir
Professor

P. G. Schmidt
Professor

Department of Mathematics,
218 Parker Hall,
Auburn University,
Auburn, AL 36849-5310

Experimental Measurements of Velocity, Potential, and Temperature Distributions in Liquid Aluminum During Electromagnetic Stirring

An experimental technique has been developed to measure both axial and transverse velocities and temperature distribution in molten aluminum. Couette flow of liquid aluminum, lead, tin, and low melting alloy in cylindrical container was chosen for calibration of the experimental technique and the magnetic probe. Velocity and temperature profiles for liquid aluminum rotating in cylindrical container at different angular velocities are obtained for two different values of the depth. We determined that the velocity values increase with magnetic induction. [DOI: 10.1115/1.1558082]

1 Introduction

Due to its many advantages centrifugal casting is widely used in pipe production. The centrifugal force influences the segregation properties and structure of metals. Several modifications of the centrifugal casting have been developed. One of the most effective modifications to centrifugal casting is electromagnetic stirring. In this method, a rotational magnetic field induces eddy currents in molten metal. The Lorentz (electromagnetic) force results from the interaction between the magnetic field and eddy currents. This force combined with the centrifugal force results in the internal motion of the liquid metal, which significantly reconstructs the cast structure. To develop mathematical models and hydrodynamic computer codes to predict fluid velocity and temperature distributions in molten metals, it is substantive to create an experimental database for electromagnetic stirring process with different metals and alloys.

Spitzer et al. [1] presented a mathematical model to predict the three-dimensional flow field in rotational electromagnetic stirring of round strands. The Navier-Stokes equations, the Maxwell equations and the continuity equation have been solved simultaneously to compute the flow field in the liquid core of the strand. The one-dimensional computations were compared with experimental data obtained for mercury, and a satisfactory agreement has been found. An experimental water model was used to validate the predicted secondary velocity components of the three-dimensional flow. The results demonstrates that in electromagnetic stirring of steel strands, the secondary flow is very significant.

The effects of external magnetic field and water cooling have been experimentally studied by Zhang et al. [2]. It has been shown that the macrostructure of cast Al-Si alloy can be refined by application of electromagnetic stirring or water cooling. The better refinement was achieved by superimposing both of these effects. Due to fluid flow and rapid cooling, silicon solidified as bulbous dendrites near the mould wall.

Contributed by the Applied Mechanics Division of THE AMERICAN SOCIETY OF MECHANICAL ENGINEERS for publication in the ASME JOURNAL OF APPLIED MECHANICS. Manuscript received by the ASME Applied Mechanics Division, Dec. 11, 2001; final revision, Sept. 23, 2002. Associate Editor: D. A. Siginer. Discussion on the paper should be addressed to the Editor, Prof. Robert M. McMeeking, Department of Mechanical and Environmental Engineering, University of California–Santa Barbara, Santa Barbara, CA 93106-5070, and will be accepted until four months after final publication of the paper itself in the ASME JOURNAL OF APPLIED MECHANICS.

To obtain the semisolid Al-7wt%Si alloy, Lim et al. [3] used electromagnetic rotation with an induction motor and observed the size and the distribution state of the primary solid particle, the degree of sphericity, and the fraction of primary solid. Observations of the microstructures of the alloy, which was semisolidified by magnetic stirring, showed that the size of the primary solid particle and its standard deviation increases with the specific solid fraction. The size of the primary solid particle increased from 98 μm to 118 μm as solid fraction increased from 0.2 to 0.5. The degree of sphericity increased with solid fraction.

Griffiths and McCartney [4,5] studied the flow control during solidification using electromagnetic field and the resulting structure. Series of Al-Si alloys of different compositions and Al alloy 7150 were solidified under conditions of controlled heat flow and electromagnetic stirring to examine how the CET was affected by bulk liquid flows, of varying velocity. The results of the study show that the electromagnetic stirring of Al-Si alloys is associated with the rapid removal of bulk liquid superheat and an enhancement in the columnar-equiaxed transition. Increasing stirring current at a constant composition promoted the columnar-equiaxed transition. Authors conclude that large equiaxed zones are associated with high velocity flows and originate from fragments of the dendritic solidification front. Electromagnetic stirring during solidification of an Al alloy 7150 encouraged the formation of equiaxed grains and enhanced the columnar-equiaxed transition. The extent of the equiaxed region increased with the intensity of stirring. The grain refining effect was accompanied by increased macrosegregation due to displacement of the solute enriched interdendritic liquid by the electromagnetically driven bulk liquid.

Currey and Pickles [6] constructed a laboratory-scale electromagnetic stirrer, which was tested on two Al-Si alloys. The results demonstrate that electromagnetic stirring reduced the amount of silicon segregation in the hypereutectic alloy, while in the hypoeutecticalloy stirring promoted dendrite fragmentation. Authors conclude that electromagnetic stirring affects the solidification process by the stirring action and reduces the axial porosity.

Cho et al. [7] devised and experimentally tested a special electromagnetic stirrer which can produce local pulsating flows and vortex flow in molten metals. They investigated the influence of frequency, current and the waveform of current on the flow structure and heat transfer in the liquid In-Ga-Sn metal pool. Authors found that the double frequency mode resulted in more effective

 Copyright © 2003 by ASME

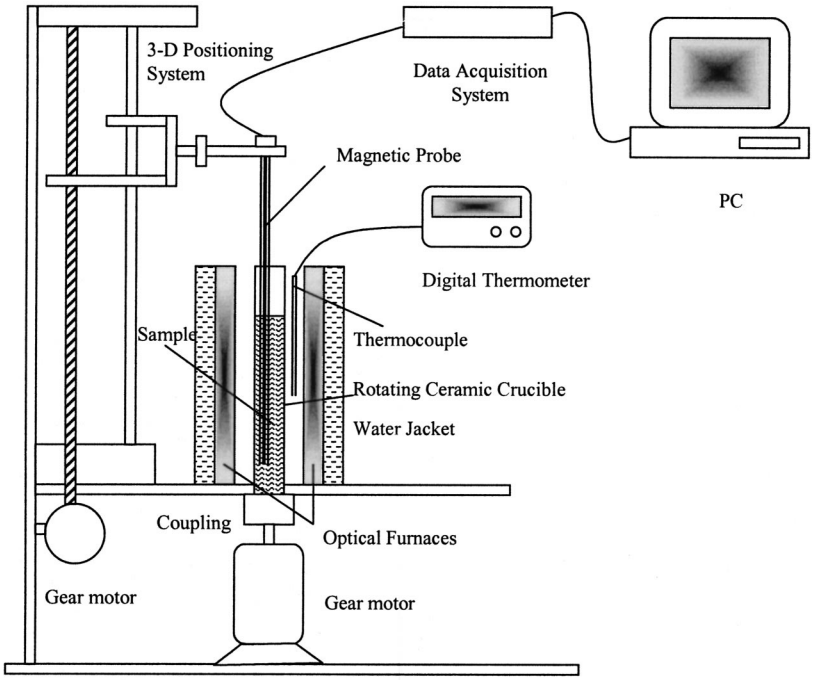

Fig. 1 Experimental apparatus used for local velocity and temperature measurements in molten metals and alloys

heat transfer process compared to the single-frequency mode without incurring a decrease in the averaged flow velocity level.

As seen from the studies reviewed above, there exists a need for techniques to measure simultaneously the temperature and local velocity components in molten metals and alloys. Laser Doppler anemometry, interferometry, stroboscopic visualization, and other most accurate conventional methods for velocity measurements are not applicable in molten metals due to their opacity. The sensors such as the Pitot-Prandtl tubes, [8], are also ineffective due to metal solidification within the manometric tubes. Hot wire sensors can't be employed because of the high thermal conductivity of liquid metals and their high temperature. Therefore, permanent-magnet potential probes have been developed for velocity measurement in these media.

Ricou and Vives [9] developed an incorporated permanent-magnet potential probe of cylindrical shape for local velocity and mass transfer measurement in molten metals. In the absence of an external magnetic field this probe allowed to measure the local velocities within the range 0–10 m/s with a sensitivity of 1 mm/s. The technique was applicable at temperatures as high as 720°C.

Gelfgat et al. [10] experimentally investigated a liquid metal flow induced by a rotating magnetic field in a cylindrical container using a conductive probe with a local magnetic field. Authors obtained azimuthal velocity profiles under various field strengths. A new flow regime with counterrotating fluid was observed when magnetic field of high frequency was applied. The fluid core was found to rotate with negative velocity.

A rare-earth permanent magnet probe was used by Tokunaga et al. [11] to study structure of turbulence in a vertical He-Wood's metal bubbling jet formed in a cylindrical vessel. Two pairs of coupled electrodes were installed at 90 deg intervals around a magnet. The probe enabled measurement of the radial and axial velocity components simultaneously. However, the output voltages of the probe were very low and had to be amplified in two-stages to be processed with an A/D converter.

Weissenfluh [12] developed a similar permanent-magnet probe for local velocity, temperature, and turbulent heat flux measurements in liquid metals. Theoretical expressions have been derived to estimate probe sensitivity to the velocity, temperature, and electricity effects. Various probe constructions have been used in the experiments. It is shown that the probe signal is proportional to average velocity near the permanent-magnet velocity probe. The calibration coefficient as a function of probe construction, velocity distribution, and magnetic field has been determined experimentally. No temperature dependence of the calibration factor has been found in these experiments. The simplified probe equation is formulated as

$$\Delta V = KU - S'_N \Delta T, \tag{1}$$

where U is the spatial average of a velocity component; K and S'_N are factors of proportionality to be determined experimentally; ΔV is an electrical potential drop; ΔT is a temperature difference.

The objective of the present paper is to describe the technique to measure velocity, potential, and temperature distribution in molten metals during electromagnetic stirring and to present preliminary results for the liquid aluminum.

2 Experimental Apparatus and Procedure

A schematic diagram of the experimental apparatus to measure local velocity and temperature in molten metals and alloys during electromagnetic stirring is illustrated in Fig. 1. A computer-controlled DC gear-motor has been used to provide a constant rotational speed to metal sample. The motor allows making measurements at constant speeds from 0 to 250 RPM in 5 RPM increments. A digital stroboscope/tachometer has been used to calibrate the angular speed of the motor with 0.1 RPM resolution.

The metal sample was placed inside a flat-bottomed cylindrical, extruded, high-purity alumina crucible. The crucible was attached to the drive shaft of a gear-motor through a specially designed coupling system to provide concentricity. The alumina crucible (25 mm inside diameter and 152 mm long) filled with alloy samples up to 100 mm high, have been exposed to magnetic field and heating. During each set of experiments it was important to keep the sample high constant. For each sample, the mass was determined according to the required sample volume and density.

As test samples we used pure lead (99.9999% purity), tin (99.999% purity), aluminum (99.9% purity), and a low-melting

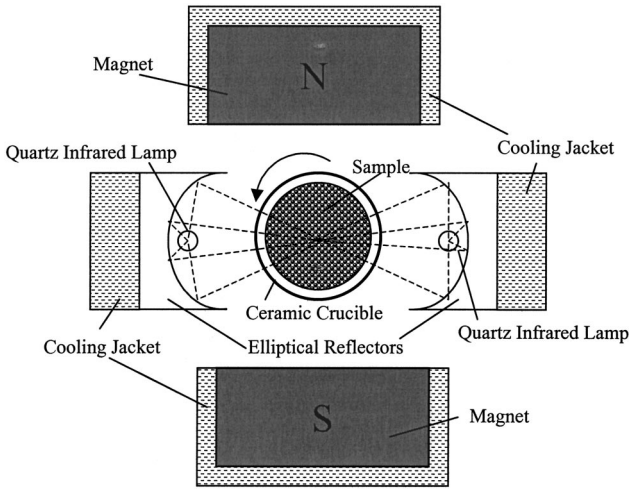

Fig. 2 Diagram of sample-magnetic field-optical furnace arrangement and heating energy focus action

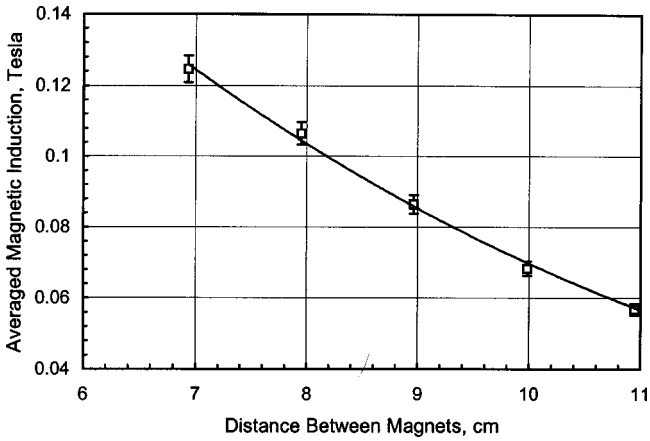

Fig. 4 Variation of measured average magnetic induction with distance between magnets

alloy LMA-158. The melting temperature of this alloy is 70°C, hardness is 12 Brinell, thermal expansion is 0.27%, density is 9.46 g/cm^3, and shear viscosity is 2.05 mPa-s at the melting point. This alloy can be melted in hot water and can be recovered and tested over again.

The motor-driven three-dimensional positioning system has been designed and fabricated to provide a high accuracy positioning to the crucible with the sample, heating elements, magnets, and permanent-magnet potential probe. A gear motor with a maximum speed of 500 rpm was used in the positioning system to provide low-speed variations (0.1%).

Quartz infrared line heating elements, housed in elliptical cast aluminum frames, were used as a furnace in the experiments. The heated length of the chamber is 167 mm. The elliptical reflectors provide concentrated infrared energy to the test specimen. High-density infrared energy is produced by tubular, high-temperature quartz lamps (Q2000T4/CL) with tungsten wire filament emitters. The lamps supply energy (2 kW each) in the infrared region and are housed in an array of elliptical reflectors (Fig. 2). Copper tube connections are provided for inlet and outlet flow of coolant (water) to cool lamp reflector bodies. Tap water at 15°C and 600 kPa was supplied to cool the unit.

The magnetic field was generated by two neodymium permanent magnets. An MG-4D gaussmeter (Walker Scientific Inc.) operating on the Hall-effect principle was used to measure the magnetic field strength. It provided DC and AC field readings from ± 0.1 gauss to ± 2 Tesla with 0.1% resolution. By changing the distance between the magnets we could obtain a magnetic field of desirable strength. It was significant to obtain a magnetic field with uniformly distributed induction. Mapping performed by the MG-4D gaussmeter revealed that the magnetic induction varies in both vertical and horizontal directions. Contour lines for the magnetic induction at different distances between the magnets are shown in Fig. 3. As seen from this figure, the magnetic induction over the test sample varies $\pm 10\%$ in the vertical direction and $\pm 7\%$ in the horizontal direction compared to its average value. Figure 4 shows the variation of the magnetic induction with the distance between the magnets. Neither the coupling system nor the alumina crucible had perceptible disturbing effects upon the applied magnetic field.

The work principle of permanent magnet probes used in previous studies, [9,12], was based on the Faraday's law. An electric conductor moving through a magnetic field induces an electromotive force normal to the magnetic field and the direction of motion. This electromotive force generates an electric field proportional to the magnetic field intensity and to the velocity of the

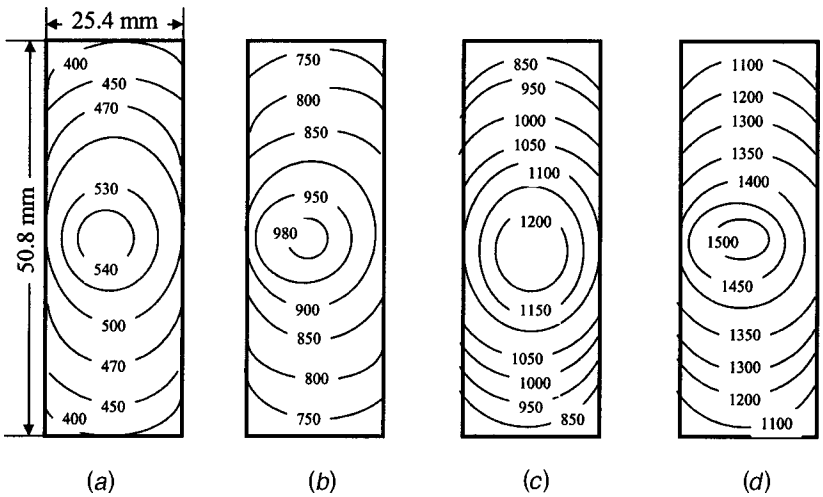

Fig. 3 Contour lines for magnetic induction (in 10^4 T) measured at different distances between magnets: (*a*) 12 cm; (*b*) 9 cm; (*c*) 8 cm; (*d*) 7 cm

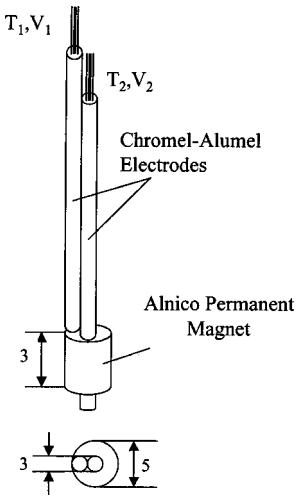

Fig. 5 Schematic diagram of constructed permanent magnet probe (all dimensions are in millimeters)

conductor. The disadvantage of this method is an influence of the probe on the hydrodynamic flow structure during measurements. However, miniaturization and proper design of the probe can reduce these influences and allow the precise measuring of both components of velocity.

The permanent magnet probe shown in Fig. 5 basically made up of a hollow cylindrical permanent magnet and two pairs of electrodes situated at the opposite ends of the magnet. *Sintered Alnico 8H* (main constituents–aluminum, nickel, and cobalt) was used as a permanent magnet. This magnetic material has a 5.25 energy product and high-temperature stability, coercivity, and demagnetization resistance. Its fine grain structure results in high uniform flux distribution and mechanical strength. It was suited to our applications, which required short magnetic length and high-speed motion. At temperatures as high as 700°C these magnets retain half of their magnetization property. Specifications of the permanent magnet are given in Table 1. The two electrodes of two open-ended chromel-alumel thermocouples were used to measure the electric potentials induced by the velocity of liquid metal. The electrodes were housed inside a round, double bore, extruded Alumina tubing.

Table 1 Magnetic and material characteristics of *Sintered Alnico 8H*

Maximum energy product (Bd Hd)	5.25
Residual induction (Br.-Gauss)	7250
Coercive force (Hc-Oersteds)	1975
Intrinsic coercive force (Hc-Oersteds)	2125
Saturation magnetizing force (Hc-Oersteds)	6000
Recoil permeability	3.2
Density (g/cm^3)	7.02
Curie temperature (°C)	850
Hardness-Rockwell	Rc44

The potential difference over the probe tip consists of contributions from the temperature difference between the two electrodes and from several surface integrals around and within the probe. Weissenfluh [12] suggests that the measured temperature difference between the two sensing points is damped by the inertia of the thermocouples and high-frequency temperature oscillations possibly do not affect the surface integrals. In our experiments, calibrating the probes has eliminated the temperature effects. Couette flow of test samples in the liquid state has been chosen in calibration experiments for the following reasons:

1. the velocity profile does not depend on viscosity of the test sample;
2. the velocity is not a function of pressure drop which could create additional difficulties for probe calibration;
3. the shear rates and Reynolds numbers can be controlled easily;
4. calibration tests can be performed with a small amount of test sample which is important to keep constant temperature all over the liquid sample.

From the results and conclusions of the previous investigators, [9,10,12], it becomes obvious that theoretically it is not possible to predict the potential difference between the two sensing electrodes of the probe as a function of the flow velocity. Therefore it is necessary to evaluate the calibration factors experimentally. A schematic diagram of the experimental apparatus for the permanent magnet probe calibration is shown in Fig. 6. A computer-controlled Brookfield rheometer Model DV-III was used to pro-

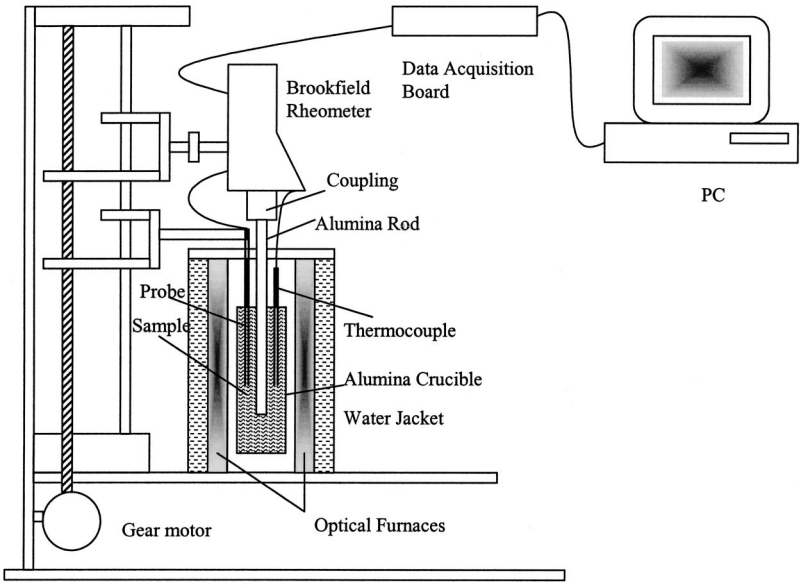

Fig. 6 Experimental apparatus used for velocity probe calibration at Couette flow

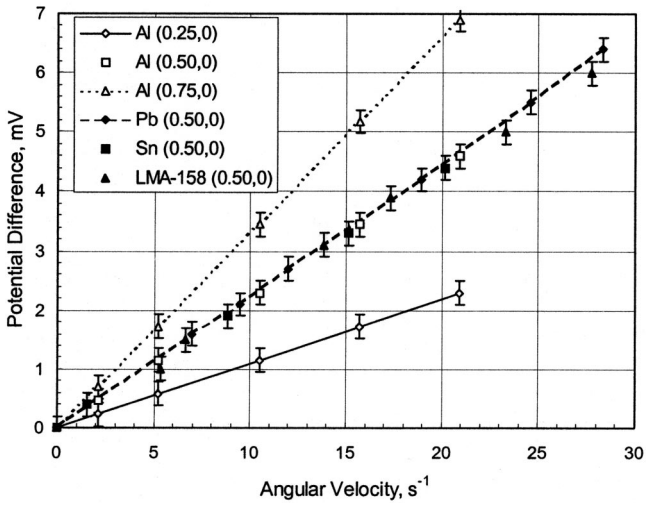

Fig. 7 Response of the probe as a function of angular velocity for liquid aluminum, lead, tin, and low melting alloy LMA-158 (tip of the probe is located in $\xi = y/(R_2 - R_1)$ and $\zeta = 2z/L$)

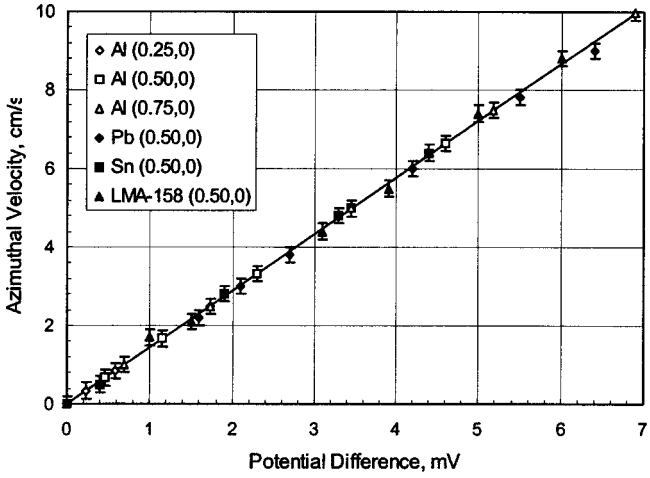

Fig. 8 Calibration of magnet probe for liquid aluminum, lead, tin, and low melting alloy LMA-158

vide a constant rotational speed to inner cylinder from 0 to 250 rpm in 0.1 rpm increments. A 12.7-mm diameter alumina rod was attached to the spindle of the rheometer through a specially designed coupling system to provide concentricity to the rotating rod. The probe was calibrated while the crucible rotated at constant speed. Using the traverse device, the probe could be moved in radial and vertical directions. The alumina crucible of 54-mm inside diameter and 305 mm long with the test sample of certain amount has been exposed to heating. A quad elliptical heating chamber housed in an octagonal cast aluminum frame was used in calibration tests. During calibration tests, it was essential to maintain the sample height constant. For each metal sample the mass was determined according to the required sample volume and density. To eliminate the temperature effects, the potential difference measured at the stationary liquid sample was subtracted from the potential differences obtained during the Couette flow. Figure 7 shows the potential difference as a function of angular velocity for liquid aluminum at different positions of the magnetic probe. The relationship between the potential difference due to the motion relative to the probe tip and the azimuthal component of the velocity in an annular space between the rotational rod and stationary crucible for liquid aluminum (99.9% purity), lead, tin, and low melting alloy is shown in Fig. 8. According to the regression analysis, these experimental data can best be described by the linear relationship

$$\Delta\varphi = av, \tag{2}$$

where $\Delta\varphi$ is a potential difference; v is a local flow velocity; and a is a constant coefficient. With the Pearson product moment correlation coefficient $R = 0.99$ the value of this coefficient for the given probe is $a = 0.692$ mV s/cm.

The calibration results also have been verified by comparing these data with the velocity predictions for Couette flow. The velocity distribution for Couette flow is given by

$$v = \frac{Uy}{R_2 - R_1} + \frac{(R_2 - R_1)^2}{2\mu}\left(\frac{\partial p}{\partial x}\right)\left[\left(\frac{y}{R_2 - R_1}\right)^2 - \left(\frac{y}{R_2 - R_1}\right)\right], \tag{3}$$

where R_1 and R_2 are the radii of the inside and outside cylinders, respectively; U is a velocity at the surface of the rotational cylinder; and μ is viscosity of the liquid. For zero pressure gradient $(\partial p/\partial x = 0)$, the velocity varies linearly with y as

$$v = \frac{Uy}{R_2 - R_1}, \tag{4}$$

where the origin of coordinate y (in the radial direction) was taken at the stationary outer cylinder. Analytical predictions using Eq. (4) are shown in Fig. 9 together with experimental data for liquid aluminum. As we can see, a normalized azimuthal velocity variation across the gap is linear for the aluminum sample and there is good agreement between the experimental results and predictions.

3 Results and Discussion

The effect of the induced magnetic field is characterized by the magnetic Reynolds number defined as

$$\mathrm{Re}_m = \omega\sigma_e\mu_0 R_1^2, \tag{5}$$

where μ_0 is a magnetic permeability, ω is an angular velocity of fluid rotation, σ_e is electrical conductivity, and R_1 is the radius of the sample. It represents the ratio of the induced field to the field of the magnetic probe. Figure 10 shows the variation of the magnetic Reynolds number with the angular velocity for the test samples. As seen from the figure, $\mathrm{Re}_m \ll 1$, which means that

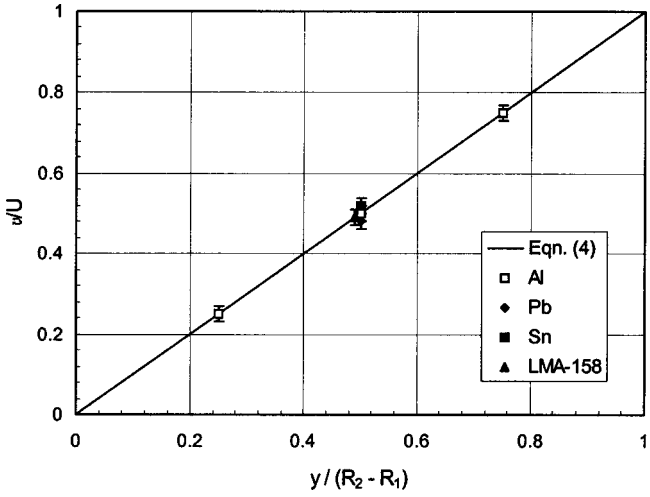

Fig. 9 Normalized velocity profile in the annular space between the cylinders

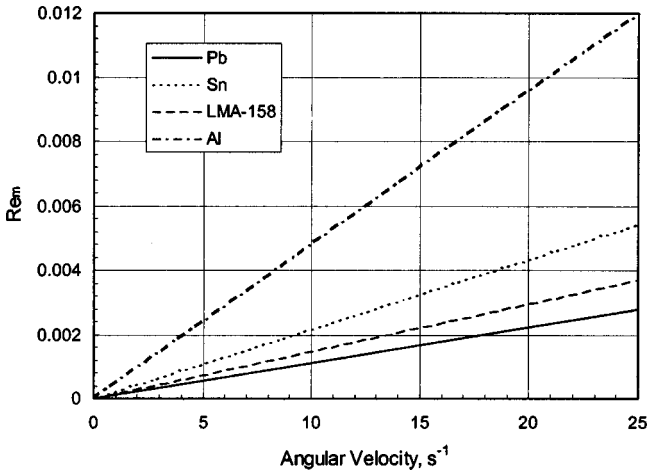

Fig. 10 Variation of the magnetic Reynolds number with the angular velocity for pure liquid lead, tin, aluminum and LMA-158 alloy samples

1. laminar flow regime has been observed in our experiments,
2. the influence of the induced magnetic field can be neglected, and
3. the induction of an electric field by fluctuations of the magnetic field can be disregarded in comparison with the electromagnetic force.

The flow regime of the melt flow in a rotating cylindrical container is determined by the hydraulic Reynolds number, which represents the ratio of inertia forces to viscous forces, and is defined by the formula

$$\mathrm{Re}=\frac{\omega R^2 \rho}{\mu}, \tag{6}$$

where μ and ρ are shear viscosity and density of the liquid metal, respectively, and ω is an angular velocity of fluid rotation. The variation of the Reynolds number with angular velocity for lead, tin, and aluminum is shown in Fig. 11. As seen from this figure, the flow regime in containers for all samples are turbulent, except for molten aluminum at low velocities ($\omega<13\ \mathrm{s}^{-1}$).

Another interesting criterion is the Ekman number, which defines the order of the vertical velocity component in rotational flows. The Ekman number is the ratio of viscous forces to coriolis forces:

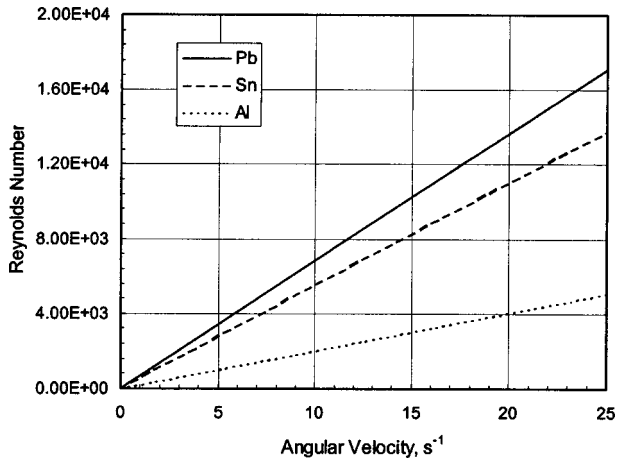

Fig. 11 Variation of hydraulic Reynolds number with the angular velocity for pure liquid lead, tin, and aluminum samples

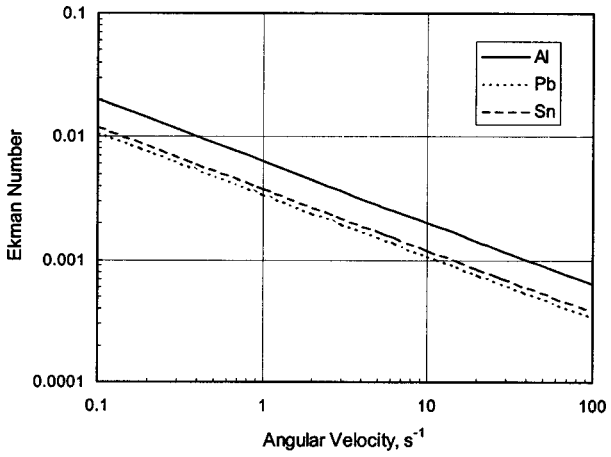

Fig. 12 Variation of Ekman number with the angular velocity for pure liquid lead, tin, and aluminum samples ($L=10$ cm)

$$E=\sqrt{\frac{\mu}{2\rho\omega L^2}}. \tag{7}$$

Figure 12 shows the variation of the Ekman number with the angular velocity of fluid rotation. As seen from this figure, $E<1$ over the angular velocity range used in our experiments. Hence, according to Gelfgat et al. [10], the velocity in the fluid core does not depend on z.

Figure 13 represents the positions of the magnetic probe inside the molten metal. Seven points in radial and two points in vertical directions were chosen inside the liquid metal sample to measure azimuthal velocity.

The measured potential differences at two different values of the depth of the melt are shown in Fig. 14. As seen from this figure, at the same radial positions the potential differences are higher at $2z/L=0.25$ than the potential differences measured at the mid-height of the melt.

Using the calibration results described above and the measured values of the potential differences we can determine the velocity

$\Psi = r/R$	$\psi = 2z/L$
0	0
0.1	0.25
0.2	
0.3	
0.4	
0.5	
0.6	

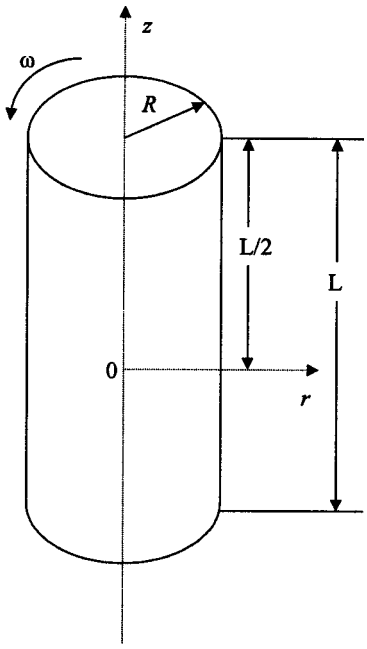

Fig. 13 Positions of magnetic probe inside the liquid metal sample

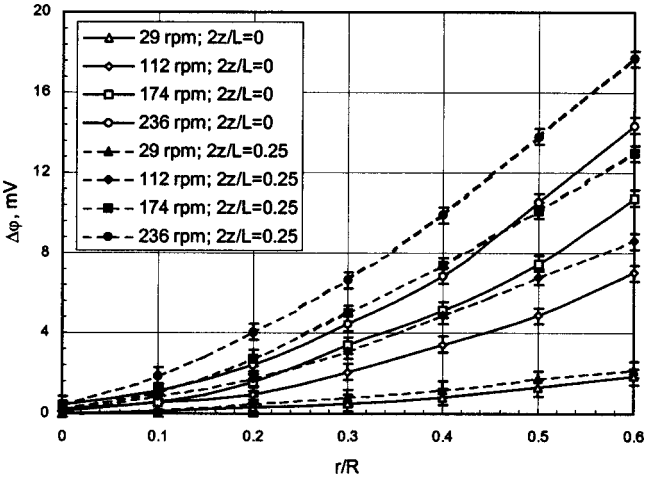

Fig. 14 Measured potential differences for liquid aluminum rotating in cylindrical container at different angular velocities ($B=0$)

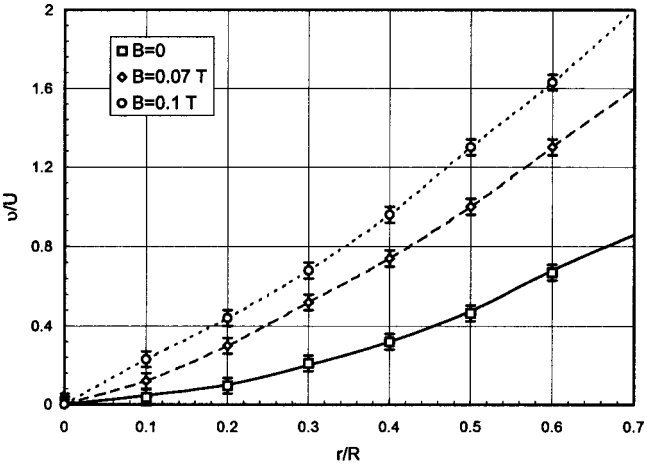

Fig. 16 Measured normalized velocity profiles for liquid aluminum rotating in cylindrical container at different inductions of magnetic field ($\omega=18.23\ s^{-1}$)

profiles in liquid metal. It is possible to eliminate the dependence of velocity profile on angular velocity of the rotation by normalizing the local velocity (v) relative to the velocity at the wall (U). Measured and normalized velocity profiles for liquid aluminum rotating in cylindrical container at different angular velocities are presented in Fig. 15. The velocity profiles obtained for two different values of the depth of the liquid show that the velocity in the rotating core ($r/R<0.1$) does not vary significantly with depth. However, away from the core ($r/R>0.1$) the azimuthal velocity at $2z/L=0.25$ is higher compared to the azimuthal velocity at mid-height of the melt. This phenomenon is related to the "centrifuging" effect. The fluid which rotate with the boundary layer is thrown outwards by centrifugal forces and is replaced by fluid flowing towards the boundary layer in the axial direction. The predictions of the normalized velocity profiles for liquid aluminum determined using an approximate theoretical model for solid body are also shown in Fig. 15. As seen from this figure, there is some difference between the theoretical predictions and experimental data. This can be explained with both the errors in the measurements and the assumptions made in the theory. Unfortunately, the probe size did not allow to make measurements near the container wall. Further modifications in the magnetic probe are needed to measure the velocity profile and velocity fluctuations in a boundary layer near the wall.

Variation of measured normalized velocity profiles for liquid aluminum rotating in cylindrical container with magnetic field induction (at rotating speed $\omega=18.23\ s^{-1}$) is presented in Fig. 16. As seen from the figure, the velocity values increase with magnetic induction. Figure 17 represents the variation of normalized azimuthal velocity with magnetic induction. These results are in good qualitative agreement with numerical simulations and experimental data reported by previous researchers, [1,10]. Gelfgat et al. [10] observed the counterrotation of liquid metal caused by hydrodynamic instabilities near the extreme points of the velocity profiles. As shown in Figs. 15–17, in our experiments we could not observe any counter rotation. We would assume that B_z component is negligibly small at positions where velocity was measured.

Following the procedure used by Weissenfluh [12] we measured the temperature profile in an aluminum melt. To exclude the dependence of temperature profile on wall heat flux, we normalized the local temperature difference ΔT relative to the temperature difference between the container wall and center ΔT_w. Here

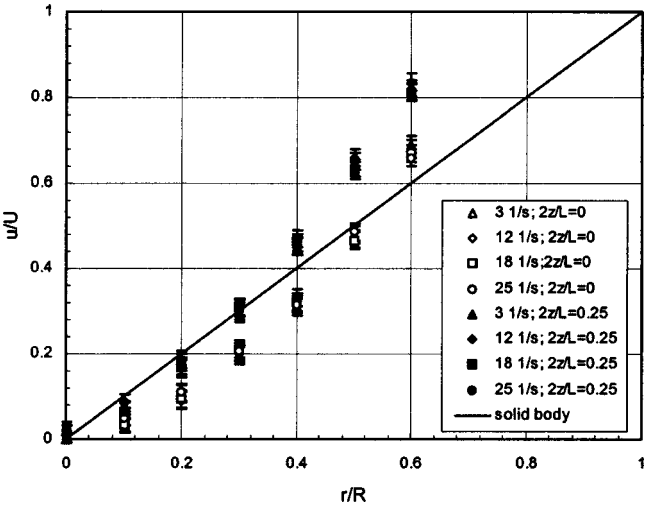

Fig. 15 Measured and theoretical (for solid body) normalized velocity profiles for liquid aluminum rotating in cylindrical container at different angular velocities ($B=0$)

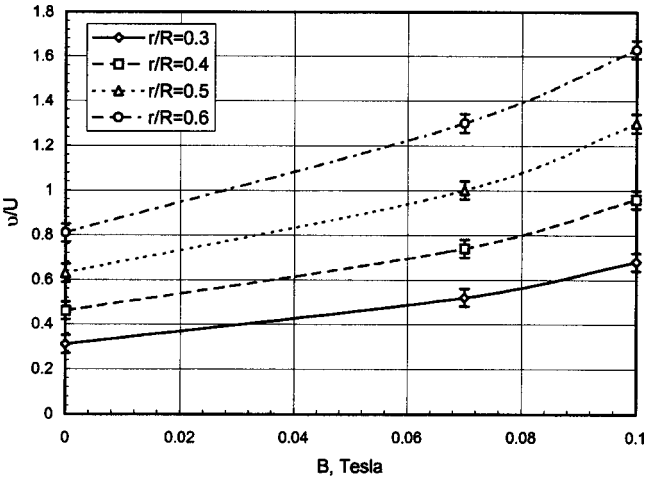

Fig. 17 Variation of azimuthal velocity with magnetic induction for liquid aluminum rotating in cylindrical container at different distances from axis of rotation ($\omega=18.23\ s^{-1}$)

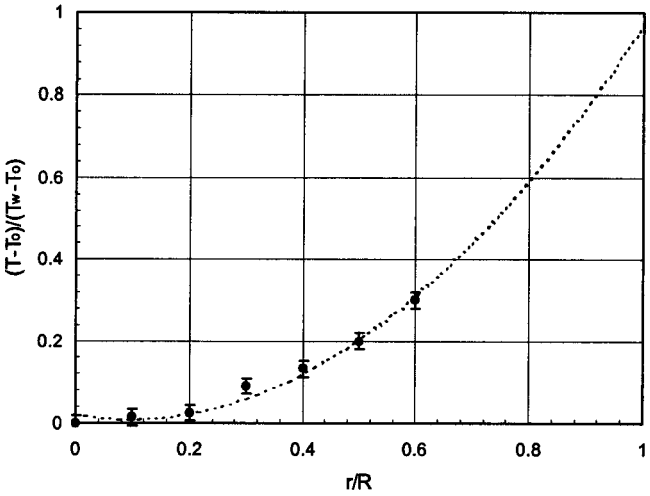

Fig. 18 Normalized temperature profiles in rotating melt of aluminum (ω=18.23 s^{-1}, B=0, z=0)

$$\Delta T = T - T_o \quad \text{and} \quad \Delta T_w = T_w - T_o, \tag{8}$$

T=local temperature, T_o=temperature in the center, and T_w=temperature on the container wall.

The normalized temperature profile in molten aluminum at angular velocity ω=18.23 s^{-1} is presented in Fig. 18. Using a regression analysis the normalized temperature profile can be expressed by the polynomial of power two

$$\frac{T - T_o}{T_w - T_o} = a\left(\frac{r}{R}\right)^2 + b\left(\frac{r}{R}\right) + c, \tag{9}$$

where a, b, and c are coefficients of the polynomial and they are functions of thermophysical properties of melt and angular velocity of container. For molten aluminum at ω=18.23 s^{-1}, a =1.1763, b=−0.2257, and c=0.021.

Conclusions

Experiments were conducted to study a liquid metal rotation in a cylindrical container exposed to the external permanent magnetic field. An experimental technique has been developed to measure the local velocity in molten metals. Couette flow of liquid aluminum, lead, tin and low melting alloy in a cylindrical container was chosen for calibration of the experimental technique and the magnetic probe.

Potential differences and velocity profiles for liquid aluminum rotating in a cylindrical container at different angular velocities are obtained for two different values of the depth. It is shown that the velocity in the rotating core ($r/R<0.1$) does not vary significantly with depth. However, away from the core ($r/R>0.1$) the azimuthal velocity at depth $2z/L=0.25$ is higher compared to the azimuthal velocity at mid-height of the melt.

From normalized velocity profiles for liquid aluminum rotating in a cylindrical container at different inductions of magnetic field (at rotating speed ω=18.23 s^{-1}) we determined that the velocity values increase with magnetic induction.

For the molten aluminum sample we measured the temperature profile, which was normalized to eliminate the dependence of the temperature profile on the wall heat flux. The developed technique will allow optimizing the process parameters of electromagnetic stirring.

Acknowledgments

The authors gratefully acknowledge the financial support received from NASA's Space Product Development at Marshall Space Flight Center under Cooperative Agreement No. NCC8-240. We wish to thank former graduate student Sorin Teodorescu for help in performing the experiments and necessary measurements.

References

[1] Spitzer, K.-H., Dubke, M., and Schwerdtfeger, K., 1986, "Rotational Electromagnetic Stirring in Continuous Casting of Round Strands," Metall. Trans. B, **17B**, pp. 119–131.

[2] Zhang, W., Yang, Y., Liu, Q., Zhu, Y., Zhang, Q., and Hu, Z., 1998, "Effects of Electromagnetic Stirring and Water Cooling on Structure and Segregation in Centrifugally Cast Al-Si Eutectic Alloy," Mater. Sci. Technol., **14**, pp. 306–311.

[3] Lim, S. C., Yoon, E. P., and Kim, J. S., 1997, "The Effect of Electromagnetic Stirring on the Microstructure of Al-7 wt% Si Alloy," J. Mater. Sci. Lett., **10**, pp. 104–109.

[4] Griffiths, W. D., and McCartney, D. G., 1996, "The Effect of Electromagnetic Stirring During Solidification on the Structure of Al-Si Alloys," Mater. Sci. Technol., **A216**, pp. 47–60.

[5] Griffiths, W. D., and McCartney, D. G., 1997, "The Effect of Electromagnetic Stirring on Macrostructure and Macrosegregation in the Aluminum Alloy 7150," Mater. Sci. Technol., **A222**, pp. 140–148.

[6] Currey, D. A., and Pickles, C. A., 1988, "Electromagnetic Stirring of Aluminum-Silicon Alloys," J. Mater. Sci., **23**, pp. 3756–3763.

[7] Cho, Y. W., Chung, S. H., Shim, J. D., Dement'ev, S., and Ivanov, S., 1999, "Fluid Flow and Heat Transfer in Molten Metal Stirred by A Circular Inductor," Int. J. Heat Mass Transf., **42**, pp. 1317–1326.

[8] Branover, H., 1978, *Magnetohydrodynamic Flow in Ducts*, John Wiley and Sons, New York.

[9] Ricou, R., and Vives, C., 1982, "Local Velocity and Mass Transfer Measurements in Molten Metals Using an Incorporated Magnet Probe," Int. J. Heat Mass Transf., **25**, pp. 1579–1588.

[10] Gelfgat, Yu. M., Gorbunov, L. A., and Kolevzon, V., 1993, "Liquid Metal Flow in a Finite-Length Cylinder With a Rotating Magnetic Field," Exp. Fluids, **15**, pp. 411–416.

[11] Tokunaga, H., Iguchi, M., and Tatemichi, H., 1999, "Turbulence Structure of Bottom-Blowing Bubbling Jet in a Molten Wood's Metal Bath," Metall. Trans. B, **30B**, pp. 61–66.

[12] Weissenfluh, T., 1985, "Probes for Local Velocity and Temperature Measurements in Liquid Metal Flow," Int. J. Heat Mass Transf., **28**, pp. 1563–1574.

S. Mukherjee
ASME Fellow
Department of Theoretical
and Applied Mechanics,
Cornell University,
Kimball Hall,
Ithaca, NY 14853
e-mail: sm85@cornell.edu

Glaucio H. Paulino[1]
Mem. ASME
Department of Civil
and Environmental Engineering,
University of Illinois at Urbana-Champaign,
Newmark Laboratory,
205 North Mathews Avenue,
Urbana, IL 61801
e-mail: paulino@uiuc.edu

The Elastic-Viscoelastic Correspondence Principle for Functionally Graded Materials, Revisited

*Paulino and Jin [Paulino, G. H., and Jin, Z.-H., 2001, "Correspondence Principle in Viscoelastic Functionally Graded Materials," ASME J. Appl. Mech., **68**, pp. 129–132], have recently shown that the viscoelastic correspondence principle remains valid for a linearly isotropic viscoelastic functionally graded material with separable relaxation (or creep) functions in space and time. This paper revisits this issue by addressing some subtle points regarding this result and examines the reasons behind the success or failure of the correspondence principle for viscoelastic functionally graded materials. For the inseparable class of nonhomogeneous materials, the correspondence principle fails because of an inconsistency between the replacements of the moduli and of their derivatives. A simple but informative one-dimensional example, involving an exponentially graded material, is used to further clarify these reasons.* [DOI: 10.1115/1.1533805]

1 Introduction

The present study is motivated by a recent investigation of Paulino and Jin [1] on the correspondence principle in functionally graded materials (FGMs), as discussed below. Such materials are those in which the composition and volume fraction of the constituents vary gradually, giving a nonuniform microstructure with continuously graded macroproperties. Various thermomechanical problems related to FGMs have been studied, for example, constitutive modeling, [2], thermal stresses, [3], fracture behavior, [4], viscoelastic fracture, [5–7], time-dependent stress analysis, [8], strain gradient effects, [9], plate bending, [10], higher order theory, [11], and so on. Comprehensive reviews on several aspects of FGMs may be found in the article by Hirai [12], the chapter by Paulino et al. [13], and the book by Suresh and Mortensen [14].

One of the primary application areas of FGMs is high-temperature technology. For example, in a ceramic/metal FGM, the ceramic offers thermal barrier effects and protects the metal from corrosion and oxidation while the FGM is toughened and strengthened by the metallic composition. Materials will exhibit creep and stress relaxation behavior at high temperatures. Viscoelasticity offers a reasonable basis for the study of phenomenological behavior of creep and stress relaxation. The correspondence principle is probably the most useful tool in viscoelasticity because the Laplace transform of the viscoelastic solution can be directly obtained from the existing elastic solution. The viscoelastic correspondence principle, unfortunately, does not hold, in general, for FGMs. Paulino and Jin [1], however, have proved that the correspondence principle of viscoelasticity and thermoviscoelasticity is valid for a class of FGMs where the relaxation functions in shear and dilatation, $\mu(\mathbf{x},t)$ and $K(\mathbf{x},t)$, have separable forms, i.e., $\mu(\mathbf{x},t)=\mu(\mathbf{x})g(t)$ and $K(\mathbf{x},t)=K(\mathbf{x})f(t)$, respectively, in which $\mathbf{x}$ denotes Cartesian coordinates, t is time, and $f(t)$ and $g(t)$ are admissible, but otherwise arbitrary functions of time. For convenience of presentation, let this class of viscoelastic materials be called the ''separable class.'' Thus the rest of the materials constitute the so called ''inseparable class.'' Paulino and Jin have applied the correspondence principle to this ''separable class'' of FGMs to study crack problems under antiplane shear, [5,6], and in-plane loading, [7]. Other authors studying crack problems in nonhomogeneous viscoelastic materials have directly solved the governing viscoelastic equations without using the correspondence principle. For example, Schovanec et al. have considered stationary cracks, [15], quasi-static crack propagation, [16], and dynamic crack propagation, [17], in nonhomogeneous viscoelastic media under antiplane shear conditions. Schovanec and Walton have also considered quasi-static propagation of a plane-strain mode I crack in a power-law inhomogeneous linearly viscoelastic body, [18], and calculated the corresponding energy release rate, [19]. Although a ''separable class'' of viscoelastic materials were studied in Refs. [15] to [19], no use of the correspondence principle was made in their work. As a result, the mathematical calculations in these papers become quite complicated and involved.

It is important to mention some older work related to the subject of this paper. Hilton and Clementes [20] and Hashin [21] have considered viscoelastic problems with piecewise constant properties. Their problems are not directly relevant to the case of continuously varying elastic moduli under consideration in the present work. Schapery [22] has, in fact, considered the continuously varying case in which the (spatially variable) elastic moduli also depend on the Laplace transform parameter s. The present work is concerned only with the *usual class of nonhomogeneous elastic materials* in which the moduli are functions only of the spatial coordinates $\mathbf{x}$, not of time or of the Laplace parameter.

The present paper supplements that by Paulino and Jin [1]. It is first shown that the success or failure of the correspondence principle for linear nonhomogeneous viscoelastic materials rests upon the forms of the spatial derivatives of the relaxation functions, since these quantities appear in the equilibrium equations. This discussion is followed by a simple but informative one-dimensional example for which closed-form solutions are obtained for a Maxwell material under tensile loading with (a) a separable and (b) an inseparable relaxation function. Two kinds of boundary conditions, displacement prescribed and mixed, are considered for this example.

[1]To whom correspondence should be addressed.

Contributed by the Applied Mechanics Division of THE AMERICAN SOCIETY OF MECHANICAL ENGINEERS for publication in the ASME JOURNAL OF APPLIED MECHANICS. Manuscript received by the Applied Mechanics Division, Nov. 6, 2001; final revision, June 7, 2002. Associate Editor: M.-J. Pindera. Discussion on the paper should be addressed to the Editor, Prof. Robert M. McMeeking, Chair, Department of Mechanics and Environmental Engineering, University of California–Santa Barbara, Santa Barbara, CA 93106-5070, and will be accepted until four months after final publication in the paper itself in the ASME JOURNAL OF APPLIED MECHANICS.

 Copyright © 2003 by ASME

2 The Viscoelastic Correspondence Principle for Functionally Graded Materials

Some of the governing equations for nonhomogeneous isotropic linearly elastic and viscoelastic materials, under quasi-static deformation, in the physical and Laplace transformed domains, are outlined below. The standard equations for homogeneous viscoelastic materials are available in many references, e.g., Christensen [23].

2.1 Elasticity. The well-known constitutive equation for linear elastic behavior is

$$\sigma_{ij}(\mathbf{x},t)=\lambda(\mathbf{x})\varepsilon_{kk}(\mathbf{x},t)\,\delta_{ij}+2\mu(\mathbf{x})\varepsilon_{ij}(\mathbf{x},t) \tag{1}$$

where σ_{ij} and ε_{ij} are components of the stress and strain tensors, respectively, λ and μ are Lamé parameters and δ_{ij} are components of the Kronecker delta. It is useful to note that $\lambda=K-(2/3)\mu$ where K and μ are the bulk and shear moduli, respectively, of the material.

Taking Laplace transforms (when they exist) defined as $\overline{f}(s)=\int_0^\infty f(t)\exp^{-st}dt$, (1) becomes

$$\overline{\sigma}_{ij}(\mathbf{x},s)=\lambda(\mathbf{x})\overline{\varepsilon}_{kk}(\mathbf{x},s)\,\delta_{ij}+2\mu(\mathbf{x})\overline{\varepsilon}_{ij}(\mathbf{x},s). \tag{2}$$

Applying the equilibrium equation (in the absence of body forces) in the Laplace transform domain to (2), one obtains

$$0=\overline{\sigma}_{ij,j}(\mathbf{x},s)=\lambda(\mathbf{x})\overline{\varepsilon}_{kk,i}(\mathbf{x},s)+2\mu(\mathbf{x})\overline{\varepsilon}_{ij,j}(\mathbf{x},s)+\lambda_{,i}(\mathbf{x})\overline{\varepsilon}_{kk}(\mathbf{x},s)+2\mu_{,j}(\mathbf{x})\overline{\varepsilon}_{ij}(\mathbf{x},s) \tag{3}$$

where $(\cdot)_{,j}=\partial(\cdot)/\partial x_j$.

2.2 Viscoelasticity. This time, the integral form of the constitutive equation, with relaxation functions $\lambda(\mathbf{x},t)$ and $\mu(\mathbf{x},t)$, is

$$\sigma_{ij}(\mathbf{x},t)=\int_0^t\lambda(\mathbf{x},t-\tau)\frac{\partial\varepsilon_{kk}}{\partial\tau}(\mathbf{x},\tau)\,\delta_{ij}d\tau+2\int_0^t\mu(\mathbf{x},t-\tau)\frac{\partial\varepsilon_{ij}}{\partial\tau}(\mathbf{x},\tau)d\tau \tag{4}$$

and its Laplace transform is

$$\overline{\sigma}_{ij}(\mathbf{x},s)=s\overline{\lambda}(\mathbf{x},s)\overline{\varepsilon}_{kk}(\mathbf{x},s)\,\delta_{ij}+2s\overline{\mu}(\mathbf{x},s)\overline{\varepsilon}_{ij}(\mathbf{x},s). \tag{5}$$

Applying the equilibrium equation to (5) results in

$$0=\overline{\sigma}_{ij,j}(\mathbf{x},s)=s\overline{\lambda}(\mathbf{x},s)\overline{\varepsilon}_{kk,i}(\mathbf{x},s)+2s\overline{\mu}(\mathbf{x},s)\overline{\varepsilon}_{ij,j}(\mathbf{x},s)+s\overline{\lambda}_{,i}(\mathbf{x},s)\overline{\varepsilon}_{kk}(\mathbf{x},s)+2s\overline{\mu}_{,j}(\mathbf{x},s)\overline{\varepsilon}_{ij}(\mathbf{x},s). \tag{6}$$

2.3 Range of Validity of the Correspondence Principle *Consider a nonhomogeneous isotropic linear elastic material with shear and bulk moduli $\mu(\mathbf{x})$ and $K(\mathbf{x})$, respectively. Now consider a boundary value problem for a body B with a fixed boundary ∂B composed of this material. Let ∂B_u and ∂B_τ ($\partial B=\partial B_u\cup\partial B_\tau$) be parts of the boundary on which the displacements and tractions, respectively, are prescribed. It is also assumed that ∂B_u and ∂B_τ do not vary in time. The applied boundary displacements and/or tractions are allowed to be (slowly varying) functions of time–therefore, the fields in B—displacement, strain and stress, can also be functions of time. Inertia and body forces are neglected here. In this situation, the usual (quasi-static) viscoelastic correspondence principle remains valid in general in the separable case, i.e., when the (viscoelastic) relaxation functions in shear and in dilatation have the forms $\mu(\mathbf{x},t)=\mu(\mathbf{x})g(t)$, $K(\mathbf{x},t)=K(\mathbf{x})f(t)$, respectively, where f(t) and g(t) are sufficiently well behaved but otherwise arbitrary functions of time. For the inseparable case, the viscoelastic correspondence principle is not valid in general.*

2.4 Success of Correspondence Principle for the "Separable Class". The crucial step is a comparison of Eqs. (3) and (6) and the replacements:

$$\lambda(\mathbf{x})\Rightarrow s\overline{\lambda}(\mathbf{x},s),\quad \mu(\mathbf{x})\Rightarrow s\overline{\mu}(\mathbf{x},s) \tag{7}$$

$$\lambda_{,i}(\mathbf{x})\Rightarrow s\overline{\lambda}_{,i}(\mathbf{x},s),\quad \mu_{,i}(\mathbf{x})\Rightarrow s\overline{\mu}_{,i}(\mathbf{x},s). \tag{8}$$

A sufficient condition for the validity of the correspondence principle is fulfilled by the "separable class" of linear viscoelastic materials where

$$\lambda(\mathbf{x},t)=\lambda(\mathbf{x})h(t),\quad \mu(\mathbf{x},t)=\mu(\mathbf{x})g(t). \tag{9}$$

Now

$$\overline{\lambda}(\mathbf{x},s)=\lambda(\mathbf{x})\overline{h}(s),\quad \overline{\mu}(\mathbf{x},s)=\mu(\mathbf{x})\overline{g}(s) \tag{10}$$

so that

$$\overline{\lambda}_{,i}(\mathbf{x},s)=\lambda_{,i}(\mathbf{x})\overline{h}(s),\quad \overline{\mu}_{,i}(\mathbf{x},s)=\mu_{,i}(\mathbf{x})\overline{g}(s). \tag{11}$$

Therefore, for this "separable class" of materials, Eq. (6) becomes

$$0=s\lambda(\mathbf{x})\overline{h}(s)\overline{\varepsilon}_{kk,i}(\mathbf{x},s)+2s\mu(\mathbf{x})\overline{g}(s)\overline{\varepsilon}_{ij,j}(\mathbf{x},s)+s\lambda_{,i}(\mathbf{x})\overline{h}(s)\overline{\varepsilon}_{kk}(\mathbf{x},s)+2s\mu_{,j}(\mathbf{x})\overline{g}(s)\overline{\varepsilon}_{ij}(\mathbf{x},s). \tag{12}$$

With the replacements (7) and (10) for the relaxation functions, and (8) and (11) for their derivatives, Eqs. (3) and (12) are compatible; therefore, the correspondence principle is valid for this "separable class" of viscoelastic materials.

2.5 Failure of the Correspondence Principle for the "Inseparable Class". It is now observed that the replacements (7), which work for homogeneous problems, do not, in general, work in the inseparable case. The reason for this is that the replacements (8) are, in general, inconsistent, in the sense that the spatial dependence of $\overline{\lambda}_{,i}(\mathbf{x},s)$ and (or) $\overline{\mu}_{,i}(\mathbf{x},s)$ can be quite different from those (that) of $\lambda_{,i}(\mathbf{x})$ and (or) $\mu_{,i}(\mathbf{x})$, respectively. This issue is rather subtle and the failure of the correspondence principle for the inseparable case is demonstrated by means of a simple example in Section 3 of this paper.

3 An Illustrative One-dimensional Example

This section presents a simple one-dimensional example (see Fig. 1), considering exponentially graded properties, to illustrate the various issues regarding the validity or not of the correspondence principle for viscoelastic functionally graded materials (FGMs). Materials with exponential gradation have been widely used in the technical literature—see, for example, Refs. [13,14]. In the present example, closed-form solutions are obtained for a nonhomogeneous Maxwell material under tensile loading with (a) a separable and (b) an inseparable relaxation function. Two types of boundary conditions, displacement prescribed and mixed, are considered here.

3.1 Relaxation Function in Tension. Consider a nonhomogeneous Maxwell material with tensile parameters $E(x)$ and $\eta(x)$ as shown in Fig. 1(*a*). The relaxation function of this material in tension, together with its Laplace transform, are, [23],

$$E(x,t)=E(x)\exp\left[\frac{-E(x)t}{\eta(x)}\right],\quad \overline{E}(x,s)=\frac{E(x)}{s+E(x)/\eta(x)}. \tag{13}$$

Two cases are considered next:

(a) separable: $E(x)=E_0e^{-\alpha x}$, $\eta(x)=\eta_0e^{-\alpha x}$.

(b) inseparable: $E(x)=E_0e^{-\alpha x}$, $\eta(x)=\eta_0$.

In the above, E_0, η_0, and α are material constants. Notice that α has units $[\text{length}]^{-1}$ and thus $1/\alpha$ expresses the length scale of inhomogeneity. Such an additional length scale characterizes an FGM and influences its material behavior.

3.2 Range of Validity of Correspondence Principle

Separable Class. For case (a), which belongs to the "separable class," one has

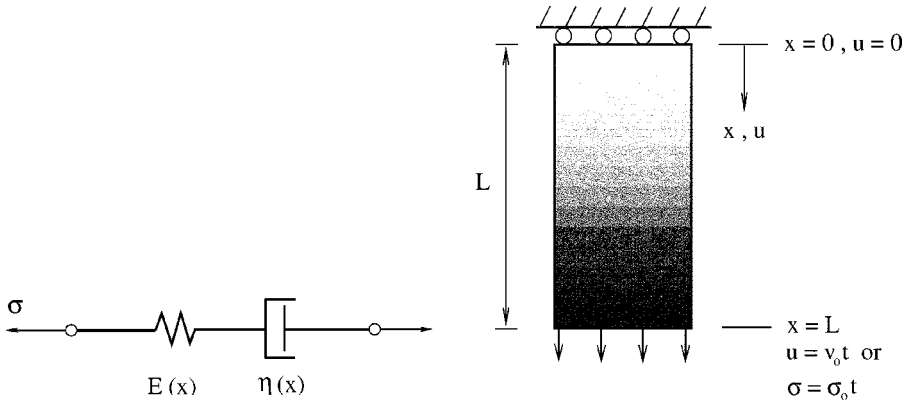

Fig. 1 One-dimensional example; (*a*) nonhomogeneous Maxwell material; (*b*) bar under tensile loading

$$E(x)\Rightarrow s\overline{E}(x,s)=\frac{sE(x)}{s+E_0/\eta_0} \tag{14}$$

$$E'(x)\Rightarrow s\frac{\partial}{\partial x}\overline{E}(x,s)=\frac{sE'(x)}{s+E_0/\eta_0}. \tag{15}$$

In this case, the replacements for $E(x)$ and $E'(x)$ are consistent (see Eqs. (3) and (12)) and the correspondence principle remains valid.

Inseparable class. Now

$$E(x)\Rightarrow s\overline{E}(x,s)=\frac{sE(x)}{s+E(x)/\eta_0}=\frac{sE_0e^{-\alpha x}}{s+(E_0/\eta_0)e^{-\alpha x}}. \tag{16}$$

A consistent replacement for $E'(x)$ should be

$$\frac{sE'(x)}{s+E'(x)/\eta_0}=\frac{-\alpha sE_0e^{-\alpha x}}{s-\alpha(E_0/\eta_0)e^{-\alpha x}}\neq s\frac{\partial}{\partial x}\overline{E}(x,s). \tag{17}$$

This time, the replacements for $E(x)$ and $E'(x)$ are not consistent. As a result, the correspondence principle fails in the inseparable case.

3.3 Tensile Loading on a Maxwell Bar With Displacement Boundary Conditions. A bar, made of Maxwell material, is loaded in tension as shown in Fig. 1(*b*). The lateral surface of the bar is traction free—so that the only nonzero stress is $\sigma_{xx}(x,t)\equiv\sigma(x,t)$. The boundary and initial conditions on the axial displacement $u(x,t)$ are

$$u(0,t)=0,\quad u(L,t)=v_0t;\quad u(x,0)=\varepsilon(x,0)=\sigma(x,0)=0 \tag{18}$$

where v_0 is a constant.

Elastic Solution. Using the usual equations (here $\varepsilon(x,t)$ is the axial strain)

$$\varepsilon(x,t)=\frac{\partial u(x,t)}{\partial x},$$
$$\sigma(x,t)=E(x)\varepsilon(x,t)=E_0e^{-\alpha x}\frac{\partial u(x,t)}{\partial x},\quad \frac{\partial\sigma(x,t)}{\partial x}=0 \tag{19}$$

together with the boundary and initial conditions (18), one gets the solution

$$u(x,t)=v_0t\left[\frac{e^{\alpha x}-1}{e^{\alpha L}-1}\right],\quad \varepsilon(x,t)=\frac{\alpha v_0te^{\alpha x}}{e^{\alpha L}-1},\quad \sigma(x,t)=\frac{\alpha E_0v_0t}{e^{\alpha L}-1}. \tag{20}$$

Note that since the stress must satisfy the equilibrium equation $\partial\sigma/\partial x(x,t)=0$, it must be independent of x.

Case (a) "Separable Class"—Viscoelastic Solution. The viscoelastic solution for this case is obtained easily by applying the correspondence principle. Carrying out the replacement

$$E(x)=E_0e^{-\alpha x}\Rightarrow s\overline{E}(x,s)=\frac{sE(x)}{s+E_0/\eta_0}=\frac{sE_0e^{-\alpha x}}{s+E_0/\eta_0},$$

one gets

$$\overline{\sigma}(x,s)=\frac{\alpha E_0v_0}{s[s+E_0/\eta_0][e^{\alpha L}-1]},$$
$$\sigma(x,t)=\frac{\alpha\eta_0v_0}{[e^{\alpha L}-1]}[1-\exp(-E_0t/\eta_0)]. \tag{21}$$

As expected from the correspondence principle, the solutions for $\varepsilon(x,t)$ and $u(x,t)$ can be easily shown to be the same as the elastic solutions $(20)_2$ and $(20)_1$.

Case (b) "Inseparable Class"—Viscoelastic Solution. It is easy to show that, in this case, an attempt to apply the correspondence principle fails. One gets a stress solution that is a function of x, and, therefore, does not satisfy equilibrium.

The boundary value problem to be solved is defined by the equations (see Fig. 1(*a*))

$$\frac{\partial\sigma}{\partial x}(x,t)=0,\quad \varepsilon(x,t)=\frac{\partial u}{\partial x}(x,t) \tag{22}$$

$$\frac{\partial\sigma}{\partial t}(x,t)+\frac{E(x)}{\eta(x)}\sigma(x,t)=E(x)\frac{\partial\varepsilon}{\partial t}(x,t) \tag{23}$$

together with $E(x)=E_0e^{-\alpha x}$, $\eta(x)=\eta_0$ and the boundary and initial conditions (18).

Taking the Laplace transform of (23), one gets

$$\overline{\sigma}(x,s)=\frac{sE(x)\overline{\varepsilon}(x,s)}{s+E(x)/\eta(x)}=s\overline{E}(x,s)\overline{\varepsilon}(x,s). \tag{24}$$

The stress must satisfy equilibrium $(22)_1$, i.e., it must be independent of x. Therefore, one can write

$$\overline{\sigma}(x,s)=sC(s),\quad \overline{\varepsilon}(x,s)=C(s)/\overline{E}(x,s) \tag{25}$$

where the function $C(s)$ must be obtained from boundary conditions.

Integrating $(25)_2$ with respect to x, and using the boundary conditions in (18), one has

$$\overline{u}(L,s)=\int_0^L\frac{C(s)}{E(x,s)}dx=\frac{v_0}{s^2},\quad C(s)=\frac{v_0}{s^2I(s)} \tag{26}$$

where $I(s)$, with $E(x)=E_0e^{-\alpha x}$, $\eta(x)=\eta_0$, is

$$I(s)=\int_0^L \frac{dx}{E(x,s)}=\frac{s}{\alpha E_0}(e^{\alpha L}-1)+\frac{L}{\eta_0}. \tag{27}$$

From $(25)_1$, $(26)_2$, and (27), one obtains the Laplace transform of the stress, and then the stress as a function of x and t. The result is

$$\overline{\sigma}(x,s)=\frac{v_0}{s\left[\dfrac{s}{\alpha E_0}(e^{\alpha L}-1)+\dfrac{L}{\eta_0}\right]},\quad \sigma(x,t)=\frac{\eta_0 v_0}{L}[1-e^{-bt}] \tag{28}$$

where $b=\alpha L E_0/[\eta_0(e^{\alpha L}-1)]$. With $\sigma(x,t)$ determined, $\varepsilon(x,t)$ is obtained directly from the viscoelastic constitutive Eq. (23). Integrating the resulting expression for $\partial\varepsilon/\partial t(x,t)$ with respect to t, and using the quiescent initial condition $\varepsilon(x,0)=0$, one gets the solution for the strain distribution in the bar. This is

$$\varepsilon(x,t)=\frac{\eta_0 v_0}{LE_0}\left[e^{\alpha x}-\frac{(e^{\alpha L}-1)}{\alpha L}\right][1-e^{-bt}]+\frac{v_0 t}{L}. \tag{29}$$

Note that, in this example, with the elastic strain distribution $\varepsilon(x,t)$ in $(20)_2$ independent of E, $\overline{\varepsilon}(x,s)$ from Eq. (24) *is not* the Laplace transform of the elastic solution $\varepsilon(x,t)$. In other words, contrary to the dictates of the correspondence principle, $\varepsilon(x,t)$ in Eq. (29) is different from the elastic strain solution in Eq. $(20)_2$.

Finally, integrating (29) with respect to x, and using the boundary conditions from (18), leads to the solution for the displacement field in the bar. This is

$$u(x,t)=\frac{\eta_0 v_0}{\alpha LE_0}\left[e^{\alpha x}+\frac{x}{L}(1-e^{\alpha L})-1\right][1-e^{-bt}]+\frac{v_0 xt}{L}. \tag{30}$$

3.4 Tensile Loading on a Maxwell Bar With Mixed Boundary Conditions. That the situation is quite subtle is evident from considering the same example as in Fig. 1(*b*), but this time with the boundary and initial conditions

$$u(0,t)=0,\quad \sigma(L,t)=\sigma_0 t;\quad u(x,0)=\varepsilon(x,0)=\sigma(x,0)=0 \tag{31}$$

where σ_0 is a constant.

Elastic Solution. The elastic solution for this problem is easily obtained. It is

$$\sigma(x,t)=\sigma_0 t,\quad \varepsilon(x,t)=\frac{\sigma_0 te^{\alpha x}}{E_0},\quad u(x,t)=\frac{\sigma_0 te^{\alpha x}}{\alpha E_0}. \tag{32}$$

Case (b) "Inseparable Class"—Viscoelastic Solution. The strategy here is to try the correspondence principle first and then examine the resulting solutions. Applying the correspondence principle, one has

$$\sigma(x,t)=\sigma_0 t,\quad \overline{\varepsilon}(x,s)=\frac{\sigma_0 e^{\alpha x}}{s^2 E_0}+\frac{\sigma_0}{\eta_0 s^3},$$
$$\varepsilon(x,t)=\frac{\sigma_0 te^{\alpha x}}{E_0}+\frac{\sigma_0 t^2}{2\eta_0}. \tag{33}$$

It is easy to show that these solutions satisfy the equilibrium Eqs. $(22)_1$ and the constitutive Eq. (23), together with the boundary and initial conditions (31). Therefore, they are correct. However, the correct solution for the displacement field $u(x,t)$, obtained by integrating $(33)_3$, is

$$u(x,t)=\frac{\sigma_0 te^{\alpha x}}{\alpha E_0}+\frac{\sigma_0 t^2 x}{2\eta_0} \tag{34}$$

whereas the correspondence principle delivers the *wrong solution* $u(x,t)=\varepsilon(x,t)/\alpha$.

4 Concluding Remarks

In a recent paper in this journal, Paulino and Jin [1] have proved that the viscoelastic correspondence principle is valid for a class of functionally graded materials (FGMs) with separable relaxation functions. The present paper revisits this issue and examines the reasons behind the success or failure of the correspondence principle for viscoelastic FGMs. While material nonlinearities, moving boundaries, or moving loads (for example) are well-known reasons for the failure of the viscoelastic correspondence principle, to the best of the authors' knowledge, the reasons for the failure of the principle due to continuously spatially varying material (elastic and viscoelastic) properties have not been discussed before in the literature. Schapery [22] has considered this class of problems, but not for the usual situation in which the elastic material properties depend only on spatial coordinates. Also, it is not clear to the authors of the present paper whether anyone has noticed before that for the inseparable class of nonhomogeneous materials, the viscoelastic correspondence principle fails because of an inconsistency between the replacements of the moduli and of their derivatives (see Eqs. (16)–(17)).

As stated before, the correspondence principle always works for the "separable class" of materials, and does not, in general, for the "inseparable class" of viscoelastic materials. Examples of applications of the correspondence principle to FGM problems in the separable class are available in Refs. [5–7].

Acknowledgments

G. H. Paulino acknowledges the support from NASA-Ames, Engineering for Complex Systems Program, and the NASA-Ames Chief Engineer (Dr. Tina Panontin) through grant NAG 2-1424. He also acknowledges the support from the National Science Foundation (NSF) under grant No. CMS-0115954 (Mechanics & Materials Program) to the University of Illinois at Urbana-Champaign (UIUC).

References

[1] Paulino, G. H., and Jin, Z.-H., 2001, "Correspondence Principle in Viscoelastic Functionally Graded Materials," ASME J. Appl. Mech., **68**, pp. 129–132.
[2] Reiter, T., Dvorak, G. J., and Tvergaard, V., 1997, "Micromechanical Models for Graded Composite Materials," J. Mech. Phys. Solids, **45**, pp. 1281–1302.
[3] Noda, N., 1999, "Thermal Stresses in Functionally Graded Materials," J. Therm. Stresses, **22**, pp. 477–512.
[4] Erdogan, F., 1995, "Fracture Mechanics of Functionally Graded Materials," Composites Eng., **5**, pp. 753–770.
[5] Paulino, G. H., and Jin, Z.-H., 2001, "Viscoelastic Functionally Graded Materials Subjected to Antiplane Shear Fracture," ASME J. Appl. Mech., **68**, pp. 284–293.
[6] Paulino, G. H., and Jin, Z.-H., 2001, "A Crack in a Viscoelastic Functionally Graded Material Layer Embedded Between Two Dissimilar Homogeneous Viscoelastic Layers—Antiplane Shear Analysis," Int. J. Fract., **68**, 283–303.
[7] Jin, Z.-H., and Paulino, G. H., 2002, "A Viscoelastic Functionally Graded Strip Containing a Crack Subjected to In-Plane Loading," Eng. Fract. Mech., **69**, pp. 1769–1790.
[8] Yang, Y. Y., 2000, "Time-Dependent Stress Analysis in Functionally Graded Materials," Int. J. Solids Struct., **37**, pp. 7593–7608.
[9] Paulino, G. H., Chan, Y. S., and Fannjiang, A. C., 2002, "Gradient Elasticity Theory for Mode III Fracture in Functionally Graded Materials—Part I. Crack Perpendicular to the Material Gradation," ASME J. Appl. Mech., in press.
[10] Reddy, J. N., 2000, "Analysis of Functionally Graded Plates," Int. J. Numer. Methods Eng., **47**, pp. 663–684.
[11] Aboudi, J., Pindera, M. J., and Arnold, S. M., 1997, "Microstructural Optimization of Functionally Graded Composites Subjected to a Thermal Gradient via the Coupled Higher-Order Theory," Composites, Part B, **28**, pp. 93–108.
[12] Hirai, T., 1996, "Functionally Gradient Materials," Mater. Sci. Technol., Vol. **17B:** *Processing of Ceramics, Part 2*, R. J. Brook, ed., VCH Verlagsgesellschaft mbH, Weinheim, Germany, pp. 292–341.
[13] Paulino, G. H., Jin, Z.-H., and Dodds, R. H., 2002, "Failure of Functionally Graded Materials," *Comprehensive Structural Integrity*, Vol. 2, B. Karihaloo and W. G. Knauss, eds., Elsevier, New York, Chapter 13.
[14] Suresh, S., and Mortensen, A., 1998, *Fundamentals of Functionally Graded Materials*, Institute of Materials, London.
[15] Alex, R., and Schovanec, L., 1996, "An Anti-Plane Crack in a Nonhomogeneous Viscoelastic Body," Eng. Fract. Mech., **55**, pp. 727–735.
[16] Herrmann, J. M., and Schovanec, L., 1990, "Quasi-Static Mode III Fracture in a Nonhomogeneous Viscoelastic Body," Acta Mech., **85**, pp. 235–249.
[17] Herrmann, J. M., and Schovanec, L., 1994, "Dynamic Steady-State Mode III

Fracture in a Non-Homogeneous Viscoelastic Body,'' Acta Mech., **106**, pp. 41–54.
[18] Schovanec, L., and Walton, J. R., 1987, ''The Quasi-Static Propagation of a Plane Strain Crack in a Power-Law Inhomogeneous Linearly Viscoelastic Body,'' Acta Mech., **67**, pp. 61–77.
[19] Schovanec, L., and Walton, J. R., 1987, ''The Energy Release Rate for a Quasi-Static Mode I Crack in a Nonhomogeneous Linear Viscoelastic Body,'' Eng. Fract. Mech., **28**, pp. 445–454.
[20] Hilton, H. H., and Clements, J. R., 1964, ''Formulation and Evaluation of Approximate Analogies for Transient Temperature Dependent Linear Visco-Elastic Media,'' *Proceedings of the Conference on Thermal Loading and Creep*, Paper 12, pp. 6-17–6-24.
[21] Hashin, Z., 1965, ''Viscoelastic Behavior of Heterogeneous Media,'' ASME J. Appl. Mech., **32**, pp. 630–636.
[22] Schapery, R. A., 1978, ''A Method for Predicting Crack Growth in Nonhomogeneous Viscoelastic Media,'' Int. J. Fract., **14**, pp. 293–309.
[23] Christensen, R. M., 1971, *Theory of Viscoelasticity*, Academic Press, New York.

A. J. Paris[1]
Assistant Professor,
Mem.ASME

G. A. Costello
Professor Emeritus,
Fellow ASME

Theoretical and Applied Mechanics,
University of Illinois at Urbana-Champaign,
Urbana, IL 61801

Bending of Cord Composite Laminate Cylindrical Shells

A theory for the bending of cord composite laminate cylindrical shells is developed. The extension-twist coupling of the cords is taken into account. The general case of a circular cylindrical shell with cord plies at various angles to the shell axis is considered. The differential equations for the displacements are derived. These equations are solved analytically in closed form for a shell subjected to axisymmetric loading and no in-plane tractions. The results of the current study are compared with the commonly used Gough-Tangorra and Akasaka-Hirano solutions. [DOI: 10.1115/1.1544541]

Introduction

A theory for the bending of cord composite laminate cylindrical shells is developed. A cord composite consists of cords embedded in a matrix. Reviews of the cord composites literature are given by Walter [1] and Walter and Patel [2]. Typically, the approach to determine the load-deformation relations for cord composites has been similar to the approach used for conventional composites, [3], and the extension-twist coupling of the cords was ignored. More recently, this coupling has been taken into account in the anaysis of cord composite materials and structures by Paris, Lin, and Costello [4], Kittredge [5], Shield and Costello [6–8], Paris [9], and Paris and Costello [10].

The objective of the current study is to assess the effects of changes in the geometry and/or constituents of a cord composite laminate cylindrical shell on the load-deformation response.

The matrix is assumed to be homogeneous, linear-elastic, and isotropic. The stress-strain relations and the strain-displacement relations in cylindrical coordinates can be found in the book by Love [11].

Costello [12] showed that the cord axial force and twisting moment are linearly proportional to the axial strain and twist of the cord and that the cord bending moment is linearly proportional to the curvature of the cord. Although the axial response of the cords is different in tension than in compression, the bimodular characteristics of the cords will be neglected. The transverse load-carrying capacity of the cords is neglected.

The Kirchhoff-Love hypothesis, [13], is employed. That is, it is assumed that lines straight and normal to the middle surface before deformation remain straight and normal to the middle surface after deformation, that the change in the length of any line normal to the middle surface is negligible, that the shell is thin, and that the strains, displacements, and rotations are small. It is assumed that the cords are perfectly bonded to the matrix and that the volume of the matrix displaced by the cords can be neglected.

The resulting equations for the displacements are solved for axisymmetric loading. The response due to uniformly distributed axisymmetric end loads and uniform internal pressure is found for a semi-infinite cylinder and a finite cylinder. Other solutions are given by Paris [9]. The results of the current study are compared with the commonly used Gough-Tangorra and Akasaka-Hirano solutions [2].

[1]Presently, Visiting Assistant Professor, Mechanical Engineering, Boise State University, Boise, ID 83725, and to whom correspondence should be addressed.

Contributed by the Applied Mechanics Division of THE AMERICAN SOCIETY OF MECHANICAL ENGINEERS for publication in the ASME JOURNAL OF APPLIED MECHANICS. Manuscript received by the Applied Mechanics Division, Apr. 15, 1999; final revision, Aug. 7, 2002. Associate Editor: J. W. Ju. Discussion on the paper should be addressed to the Editor, Prof. Robert M. McMeeking, Chair, Department of Mechanics and Environmental Engineering, University of California–Santa Barbara, Santa Barbara, CA 93106-5070, and will be accepted until four months after final publication in the paper itself in the ASME JOURNAL OF APPLIED MECHANICS.

Formulation

The differential equations for the displacements of a cord composite laminate cylindrical shell are developed. Figure 1 shows a cord composite cylindrical shell with a cord ply off the middle surface at an angle to the shell axis. Figure 2 shows a typical element for the shell. The radius of the middle surface is a; the thickness is h; the cord spacing is b; the distance the cord ply is off the middle surface is z_c; the cord-ply angle is θ; the cylindrical coordinates are x, φ, and z; and the element dimensions in the x and φ directions are Δx and $a\Delta\varphi$, respectively.

Equilibrium Equations. Figure 3 shows a typical element for the shell with (*a*) the tractions and the force resultants and (*b*) the moment resultants. The tractions are p_x, p_φ, and p_z; the force resultants are N_x, $N_{x\varphi}$, $N_{\varphi x}$, N_φ, Q_x, and Q_φ; and the moment resultants are M_x, $M_{x\varphi}$, $M_{\varphi x}$, and M_φ. It is assumed that the force and moment resultants may be represented by a Taylor series. The equilibrium equations for the element may be expressed as

$$\frac{\partial N_x}{\partial x}+\frac{1}{a}\frac{\partial N_{\varphi x}}{\partial\varphi}+p_x=0, \tag{1}$$

$$\frac{\partial N_{x\varphi}}{\partial x}+\frac{1}{a}\frac{\partial N_\varphi}{\partial\varphi}+p_\varphi-\frac{Q_\varphi}{a}=0, \tag{2}$$

$$\frac{\partial Q_x}{\partial x}+\frac{1}{a}\frac{\partial Q_\varphi}{\partial\varphi}+p_z+\frac{N_\varphi}{a}=0, \tag{3}$$

$$\frac{\partial M_{x\varphi}}{\partial x}+\frac{1}{a}\frac{\partial M_\varphi}{\partial\varphi}-Q_\varphi=0, \tag{4}$$

$$\frac{\partial M_x}{\partial x}+\frac{1}{a}\frac{\partial M_{\varphi x}}{\partial\varphi}-Q_x=0, \tag{5}$$

and

$$N_{x\varphi}-N_{\varphi x}+\frac{M_{\varphi x}}{a}=0. \tag{6}$$

Solving Eqs. (4) and (5) for Q_x and Q_φ yields

$$Q_x=\frac{\partial M_x}{\partial x}+\frac{1}{a}\frac{\partial M_{\varphi x}}{\partial\varphi}\quad\text{and}\quad Q_\varphi=\frac{\partial M_{x\varphi}}{\partial x}+\frac{1}{a}\frac{\partial M_\varphi}{\partial\varphi}. \tag{7}$$

Substituting Eqs. (7) into Eqs. (2) and (3) yields

$$\frac{\partial N_{x\varphi}}{\partial x}+\frac{1}{a}\frac{\partial N_\varphi}{\partial\varphi}-\frac{1}{a}\frac{\partial M_{x\varphi}}{\partial x}-\frac{1}{a^2}\frac{\partial M_\varphi}{\partial\varphi}+p_\varphi=0 \tag{8}$$

and

$$\frac{\partial^2 M_x}{\partial x^2}+\frac{1}{a}\frac{\partial^2 M_{x\varphi}}{\partial x\partial\varphi}+\frac{1}{a}\frac{\partial^2 M_{\varphi x}}{\partial x\partial\varphi}+\frac{1}{a^2}\frac{\partial^2 M_\varphi}{\partial\varphi^2}+\frac{N_\varphi}{a}+p_z=0. \tag{9}$$

 Copyright © 2003 by ASME

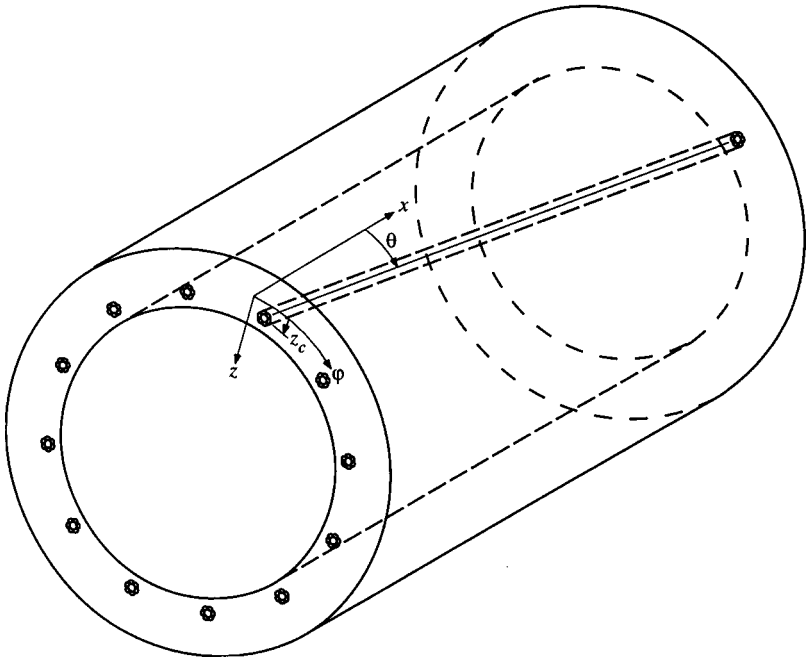

Fig. 1 A cord composite cylindrical shell

Equations (1), (6), (8), and (9) are the equations for the force and moment resultants. There are four equations and eight unknowns, and the problem is statically indeterminate.

Kinematics. Consider a circular cylindrical shell that undergoes a deformation. The displacements of some point A in the x, φ, and z directions are u_A, v_A, and w_A, respectively; and the displacements of the middle surface of the shell in the x, φ, and z directions are u, v, and w, respectively. The Kirchhoff-Love hypothesis yields

$$u_A = u - z\frac{\partial w}{\partial x}, \quad v_A = \left(\frac{a-z}{a}\right)v - \frac{z}{a}\frac{\partial w}{\partial \varphi}, \quad \text{and} \quad w_A = w, \tag{10}$$

where $u = u(x,\varphi)$, $v = v(x,\varphi)$, and $w = w(x,\varphi)$.

Strain-Displacement Relations. The strains are ε_x, ε_φ, and $\gamma_{x\varphi}$, and the strain-displacement relations may be expressed as

$$\varepsilon_x = \frac{\partial u_A}{\partial x}, \quad \varepsilon_\varphi = \frac{1}{r}\left(\frac{\partial v_A}{\partial \varphi} - w_A\right), \quad \text{and} \quad \gamma_{x\varphi} = \frac{1}{r}\frac{\partial u_A}{\partial \varphi} + \frac{\partial v_A}{\partial x}, \tag{11}$$

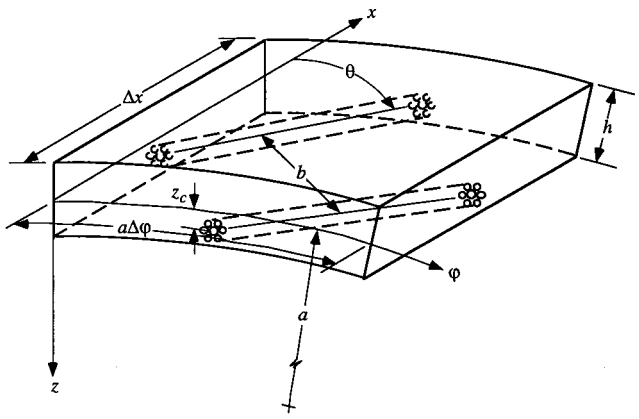

Fig. 2 A typical element for the shell

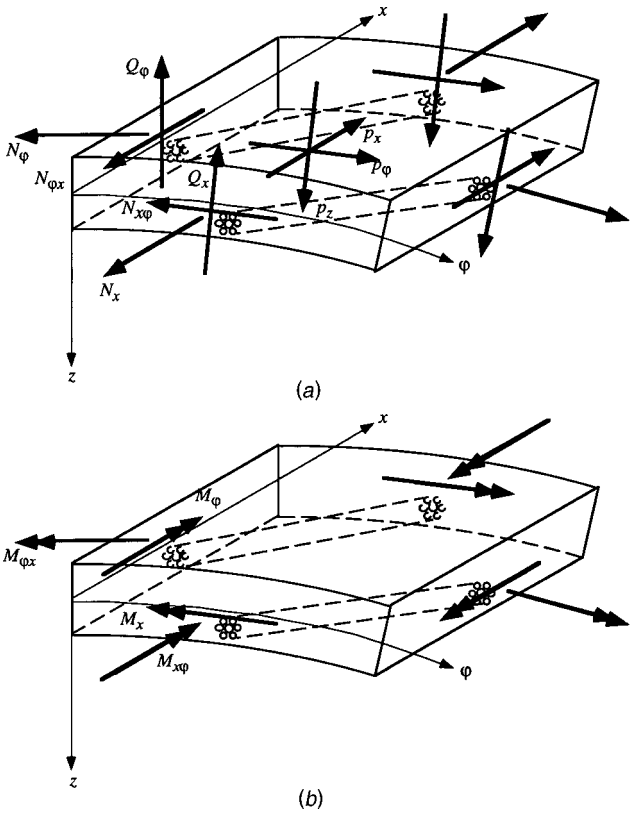

Fig. 3 A typical element for the shell with (*a*) the tractions and the force resultants and (*b*) the moment resultants

where $r=a-z$. The strains of the middle surface are ε_x^o, ε_φ^o, and $\gamma_{x\varphi}^o$, and the curvatures of the middle surface are κ_x, κ_φ, and $\kappa_{x\varphi}$. Equations (10) and (11) yield

$$\begin{Bmatrix}\varepsilon_x\\ \varepsilon_\varphi\\ \gamma_{x\varphi}\end{Bmatrix}=\begin{Bmatrix}\varepsilon_x^o\\ \varepsilon_\varphi^o\\ \gamma_{x\varphi}^o\end{Bmatrix}-z\begin{Bmatrix}\kappa_x\\ \kappa_\varphi\\ 2\kappa_{x\varphi}\end{Bmatrix}, \tag{12}$$

where

$$\varepsilon_x^o=\frac{\partial u}{\partial x},\quad \varepsilon_\varphi^o=\frac{1}{a}\left(\frac{\partial v}{\partial \varphi}-w\right),\quad \gamma_{x\varphi}^o=\frac{1}{a}\frac{\partial u}{\partial \varphi}+\frac{\partial v}{\partial x},$$

$$\kappa_x=\frac{\partial^2 w}{\partial x^2},\quad \kappa_\varphi=\frac{1}{a^2}\left(\frac{\partial^2 w}{\partial \varphi^2}+w\right),$$

and

$$\kappa_{x\varphi}=\frac{1}{a}\left(\frac{\partial^2 w}{\partial x\,\partial \varphi}+\frac{\partial v}{\partial x}\right). \tag{13}$$

Force and Moment Resultants. The force and moment resultants can be expressed as the sum of the force and moment resultants of the matrix and the cords. The stiffness matrices are **A**, **B**, **C**, and **D**, and the components of the stiffness matrices are A_{ij}, B_{ij}, C_{ij}, and D_{ij}. The force and moment resultants may be expressed as

$$\begin{Bmatrix}N_x\\ N_\varphi\\ N_{x\varphi}\\ N_{\varphi x}\end{Bmatrix}=\mathbf{A}\begin{Bmatrix}\varepsilon_x^o\\ \varepsilon_\varphi^o\\ \gamma_{x\varphi}^o\end{Bmatrix}-\mathbf{B}\begin{Bmatrix}\kappa_x\\ \kappa_\varphi\\ 2\kappa_{x\varphi}\end{Bmatrix}$$

and

$$\begin{Bmatrix}M_x\\ M_\varphi\\ M_{x\varphi}\\ M_{\varphi x}\end{Bmatrix}=\mathbf{C}\begin{Bmatrix}\varepsilon_x^o\\ \varepsilon_\varphi^o\\ \gamma_{x\varphi}^o\end{Bmatrix}-\mathbf{D}\begin{Bmatrix}\kappa_x\\ \kappa_\varphi\\ 2\kappa_{x\varphi}\end{Bmatrix}, \tag{14}$$

where

$$\mathbf{A}=\begin{bmatrix}A_{11}&A_{12}&A_{16}\\ A_{21}&A_{22}&A_{26}\\ A_{61}&A_{62}&A_{66}\\ A_{61}^*&A_{62}^*&A_{66}^*\end{bmatrix},\quad \mathbf{B}=\begin{bmatrix}B_{11}&B_{12}&B_{16}\\ B_{21}&B_{22}&B_{26}\\ B_{61}&B_{62}&B_{66}\\ B_{61}^*&B_{62}^*&B_{66}^*\end{bmatrix}, \tag{15}$$

$$\mathbf{C}=\begin{bmatrix}C_{11}&C_{12}&C_{16}\\ C_{21}&C_{22}&C_{26}\\ C_{61}&C_{62}&C_{66}\\ C_{61}^*&C_{62}^*&C_{66}^*\end{bmatrix},\quad \text{and}\quad \mathbf{D}=\begin{bmatrix}D_{11}&D_{12}&D_{16}\\ D_{21}&D_{22}&D_{26}\\ D_{61}&D_{62}&D_{66}\\ D_{61}^*&D_{62}^*&D_{66}^*\end{bmatrix}.$$

Matrix Force and Moment Resultants. The stresses are σ_x, σ_φ, and $\tau_{x\varphi}$, and the stress-strain relations may be expressed as

$$\sigma_x=\frac{E_m}{1-\nu_m^2}(\varepsilon_x+\nu_m\varepsilon_\varphi),\quad \sigma_\varphi=\frac{E_m}{1-\nu_m^2}(\varepsilon_\varphi+\nu_m\varepsilon_x),$$

and

$$\tau_{x\varphi}=\frac{E_m}{2(1+\nu_m)}\gamma_{x\varphi}, \tag{16}$$

where E_m is the modulus of elasticity and ν_m is the Poisson's ratio. The subscripts m and c are used to denote variables related to the matrix and cord, respectively.

The matrix force and moment resultants are found by resolving the stresses acting on the surface of the element of the shell and may be expressed as

$$N_{xm}=\frac{1}{a\Delta\varphi}\int_{-h/2}^{h/2}\sigma_x(a-z)\Delta\varphi dz,\quad N_{\varphi m}=\frac{1}{\Delta x}\int_{-h/2}^{h/2}\sigma_\varphi\Delta x dz,$$

$$N_{x\varphi m}=\frac{1}{a\Delta\varphi}\int_{-h/2}^{h/2}\tau_{x\varphi}(a-z)\Delta\varphi dz,\quad N_{\varphi xm}=\frac{1}{\Delta x}\int_{-h/2}^{h/2}\tau_{x\varphi}\Delta x dz, \tag{17}$$

$$M_{xm}=\frac{1}{a\Delta\varphi}\int_{-h/2}^{h/2}\sigma_x(a-z)\Delta\varphi z dz,\quad M_{\varphi m}=\frac{1}{\Delta x}\int_{-h/2}^{h/2}\sigma_\varphi\Delta x z dz,$$

$$M_{x\varphi m}=\frac{1}{a\Delta\varphi}\int_{-h/2}^{h/2}\tau_{x\varphi}(a-z)\Delta\varphi z dz,$$

and

$$M_{\varphi xm}=\frac{1}{\Delta x}\int_{-h/2}^{h/2}\tau_{x\varphi}\Delta x z dz.$$

The change in these integrals due to the cross-sectional area of the cords is neglected. Equations (12) and (14)–(17) yield the nonzero components of the stiffness matrices:

$$A_{11m}=A_{22m}=C,\quad A_{12m}=A_{21m}=\nu_m C,\quad A_{66m}=\frac{C(1-\nu_m)}{2},$$

$$A_{66m}^*=\frac{C(1-\nu_m)}{2}+\frac{D(1-\nu_m)}{2a^2},\quad B_{11m}=-\frac{D}{a},\quad B_{22m}=\frac{D}{a}, \tag{18}$$

$$B_{66m}=-\frac{D(1-\nu_m)}{2a},\quad B_{66m}^*=C_{66m}^*=\frac{D(1-\nu_m)}{2a},$$

$$C_{11m}=-\frac{D}{a},$$

$$C_{12m}=-\frac{D\nu_m}{a},\quad D_{11m}=D_{22m}=D,\quad D_{12m}=D_{21m}=\nu_m D,$$

$$\text{and}\quad D_{66m}=D_{66m}^*=\frac{D(1-\nu_m)}{2},$$

where C and D are the extensional and flexural rigidity, respectively, of the matrix:

$$C=\frac{E_m h}{1-\nu_m^2}\quad\text{and}\quad D=\frac{E_m h^3}{12(1-\nu_m^2)}. \tag{19}$$

Simplified Equations. A simplified equation is achieved by choosing the appropriate scaling for the coordinates and the displacements, substituting the coordinates and displacements in terms of the scaled coordinates and displacements into the equation, factoring the appropriate constant, and neglecting terms with a small remaining factor. The coordinates in terms of the scaled coordinates are chosen to be

$$x=X\sqrt{ha},\quad a\varphi=\Phi\sqrt{ha},\quad\text{and}\quad z=Z, \tag{20}$$

where X, Φ, and Z are the scaled coordinates. The displacements in terms of the scaled displacements are chosen to be

$$u=U\sqrt{\frac{h}{a}},\quad v=V\sqrt{\frac{h}{a}},\quad\text{and}\quad w=W, \tag{21}$$

where U, V, and W are the scaled displacements. The coordinates in terms of the scaled coordinates and the displacements in terms of the scaled displacements given by Eqs. (20) and (21) were used by Donnell [14]. In some cases it is necessary to expand an equation in a Taylor series before applying the simplification method outlined above.

Applying the simplification method to the strain-displacement relations, Eqs. (12) and (13), yields

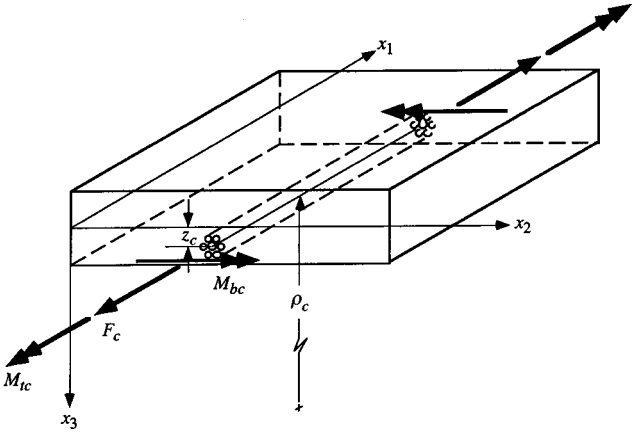

Fig. 4 An element with the cord axial force, twisting moment, and bending moment

$$\varepsilon_x^o=\frac{\partial u}{\partial x},\quad \varepsilon_\varphi^o=\frac{1}{a}\left(\frac{\partial v}{\partial \varphi}-w\right),\quad \gamma_{x\varphi}^o=\frac{1}{a}\frac{\partial u}{\partial \varphi}+\frac{\partial v}{\partial x},$$

$$\kappa_x=\frac{\partial^2 w}{\partial x^2},\quad \kappa_\varphi=\frac{1}{a^2}\frac{\partial^2 w}{\partial \varphi^2},\quad \text{and}\quad \kappa_{x\varphi}=\frac{1}{a}\frac{\partial^2 w}{\partial x\partial \varphi}. \tag{22}$$

Applying the simplification method to the matrix force and moment resultants, Eqs. (14), (15), (18), and (19), yields

$$\begin{aligned} &A_{11m}=A_{22m}=C,\quad A_{12m}=A_{21m}=\nu_m C,\\ &A_{66m}=A_{66m}^*=\frac{C(1-\nu_m)}{2},\\ &D_{11m}=D_{22m}=D,\quad D_{12m}=D_{21m}=\nu_m D,\\ &D_{66m}=D_{66m}^*=\frac{D(1-\nu_m)}{2}, \end{aligned} \tag{23}$$

and the other components of the stiffness matrices are equal to zero. The strain-displacement relations given by Eqs. (12) and (22) and the force and moment resultants given by Eqs. (14), (15), (19), (22), and (23) are the same as those given by Donnell [14].

Cord Force and Moment Resultants. Figure 4 shows an element with the cord axial force, twisting moment, and bending moment. The element rectangular coordinates and principal axes are x_1, x_2, and x_3. The distance the cord ply is off the middle surface is z_c, and the radius of curvature of the cord ply is ρ_c. The cord axial force F_c, twisting moment M_{tc}, and bending moment M_{bc} may be expressed as

$$\frac{F_c}{A_cE_c}=C_1\varepsilon_c+C_2R_c\tau_c,\quad \frac{M_{tc}}{E_cR_c^3}=C_3\varepsilon_c+C_4R_c\tau_c,$$

$$\text{and}\quad \frac{M_{bc}}{E_cR_c^3}=C_5R_c\kappa_c, \tag{24}$$

where A_c is the metallic cross sectional area, R_c is the outside radius of the cord, E_c is the modulus of elasticity of the material, ε_c is the axial strain, τ_c is the twist per unit length, $\kappa_c=1/\rho_c$ is the curvature, and C_1, C_2, C_3, C_4, and C_5 are constants which can be determined analytically, [12].

The strains are ε_1, ε_2, and γ_{12}, the strains of the middle surface are ε_1^o, ε_2^o, and γ_{12}^o, and the curvatures of the middle surface are κ_1, κ_2, and κ_{12}. The strains may be expressed as

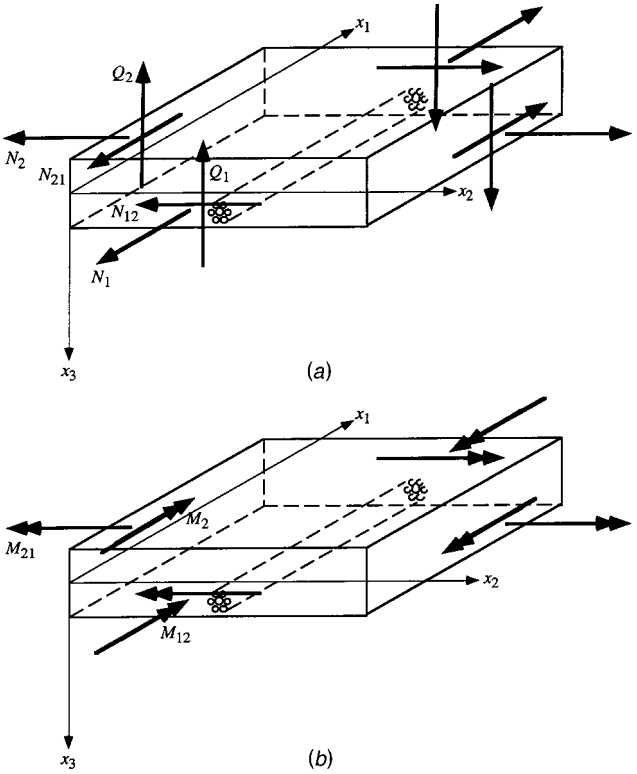

Fig. 5 An element with (*a*) the force resultants and (*b*) the moment resultants

$$\begin{Bmatrix}\varepsilon_1\\ \varepsilon_2\\ \gamma_{12}\end{Bmatrix}=\begin{Bmatrix}\varepsilon_1^o\\ \varepsilon_2^o\\ \gamma_{12}^o\end{Bmatrix}-z\begin{Bmatrix}\kappa_1\\ \kappa_2\\ 2\kappa_{12}\end{Bmatrix}. \tag{25}$$

The cord axial strain ε_c, change in curvature κ_c, and twist per unit length τ_c may be expressed as

$$\varepsilon_c=\varepsilon_1(z=z_c)=\varepsilon_1^o-z_c\kappa_1,\quad \kappa_c=\kappa_1,\quad \text{and}\quad \tau_c=\kappa_{12}. \tag{26}$$

Figure 5 shows an element with (*a*) the tractions and the force resultants, and (*b*) the moment resultants. The force resultants are N_1, N_{12}, N_{21}, N_2, Q_1, and Q_2, and the moment resultants are M_1, M_{12}, M_{21}, and M_2. The axial force, twisting moment, and bending moment in the cord can be divided by the spacing of the cords and resolved into the force and moment resultants. Referring to Figs. 4 and 5, and comparing the force and moment resultants with the cord axial force, twisting moment, and bending moment yields

$$N_{1c}=\frac{F_c}{b},\quad M_{1c}=\frac{F_cz_c-M_{bc}}{b},\quad M_{12c}=-\frac{M_{tc}}{b}, \tag{27}$$

and the other force and moment resultants are equal to zero. Note that by dividing the cord axial force, twisting moment, and bending moment by the spacing of the cords that the cords are smeared out in the x_2 direction but not in the x_3 direction. The position of the cord in the x_3 direction is significant where bending is considered.

The cord force and moment resultants may be expressed in terms of the strains and curvatures of the middle surface. An overbar denotes the principal coordinate system. Equations (24)–(27) yield

$$\begin{Bmatrix} N_{1c} \\ N_{2c} \\ N_{12c} \\ N_{21c} \end{Bmatrix} = \overline{\mathbf{A}}_c \begin{Bmatrix} \varepsilon_1^o \\ \varepsilon_2^o \\ \gamma_{12}^o \end{Bmatrix} - \overline{\mathbf{B}}_c \begin{Bmatrix} \kappa_1 \\ \kappa_2 \\ 2\kappa_{12} \end{Bmatrix} \quad \text{and}$$

$$\begin{Bmatrix} M_{1c} \\ M_{2c} \\ M_{12c} \\ M_{21c} \end{Bmatrix} = \overline{\mathbf{C}}_c \begin{Bmatrix} \varepsilon_1^o \\ \varepsilon_2^o \\ \gamma_{12}^o \end{Bmatrix} - \overline{\mathbf{D}}_c \begin{Bmatrix} \kappa_1 \\ \kappa_2 \\ 2\kappa_{12} \end{Bmatrix}, \tag{28}$$

where the nonzero components of the stiffness matrices are

$$\overline{A}_{11c} = \frac{A_c C_1 E_c}{b}, \quad \overline{B}_{11c} = \overline{C}_{11c} = \frac{A_c C_1 E_c z_c}{b},$$

$$\overline{B}_{16c} = -\frac{A_c C_2 E_c R_c}{2b},$$

$$\overline{C}_{61c} = -\frac{C_3 E_c R_c^3}{b}, \quad \overline{D}_{11c} = \frac{C_5 E_c R_c^4}{b} + \frac{A_c C_1 E_c z_c^2}{b},$$

$$\overline{D}_{16c} = -\frac{A_c C_2 E_c R_c z_c}{2b}, \tag{29}$$

$$\overline{D}_{61c} = -\frac{C_3 E_c R_c^3 z_c}{b}, \quad \text{and} \quad \overline{D}_{66c} = \frac{C_4 E_c R_c^4}{2b}.$$

Figures 6(*a*) and (*b*) show infinitesimal triangular elements of the cord composite with the force and moment resultants acting on them. The element rectangular coordinates are *x*, *y*, and *z*. The only finite dimension is the thickness *h*. The equilibrium equations yield the transformation relations for the force and moment resultants:

$$\begin{Bmatrix} N_x \\ N_y \\ N_{xy} \\ N_{yx} \end{Bmatrix} = \mathbf{S} \begin{Bmatrix} N_1 \\ N_2 \\ N_{12} \\ N_{21} \end{Bmatrix} \quad \text{and} \quad \begin{Bmatrix} M_x \\ M_y \\ M_{xy} \\ M_{yx} \end{Bmatrix} = \mathbf{S} \begin{Bmatrix} M_1 \\ M_2 \\ M_{12} \\ M_{21} \end{Bmatrix}, \tag{30}$$

where the stress resultant transformation matrix **S** is defined as

$$\mathbf{S} = \begin{bmatrix} \cos^2\theta & \sin^2\theta & -\sin\theta\cos\theta & -\sin\theta\cos\theta \\ \sin^2\theta & \cos^2\theta & \sin\theta\cos\theta & \sin\theta\cos\theta \\ \sin\theta\cos\theta & -\sin\theta\cos\theta & \cos^2\theta & -\sin^2\theta \\ \sin\theta\cos\theta & -\sin\theta\cos\theta & -\sin^2\theta & \cos^2\theta \end{bmatrix}. \tag{31}$$

The strain transformation matrix is denoted as **T**. The transformation relations for the strains are

$$\begin{Bmatrix} \varepsilon_1 \\ \varepsilon_2 \\ \dfrac{\gamma_{12}}{2} \end{Bmatrix} = \mathbf{T} \begin{Bmatrix} \varepsilon_x \\ \varepsilon_y \\ \dfrac{\gamma_{xy}}{2} \end{Bmatrix}, \quad \text{where}$$

$$\mathbf{T} = \begin{bmatrix} \cos^2\theta & \sin^2\theta & 2\sin\theta\cos\theta \\ \sin^2\theta & \cos^2\theta & -2\sin\theta\cos\theta \\ -\sin\theta\cos\theta & \sin\theta\cos\theta & \cos^2\theta - \sin^2\theta \end{bmatrix}. \tag{32}$$

Equations (12), (25), and (32) yield

$$\begin{Bmatrix} \varepsilon_1^o \\ \varepsilon_2^o \\ \dfrac{\gamma_{12}^o}{2} \end{Bmatrix} = \mathbf{T} \begin{Bmatrix} \varepsilon_x^o \\ \varepsilon_y^o \\ \dfrac{\gamma_{xy}^o}{2} \end{Bmatrix} \quad \text{and} \quad \begin{Bmatrix} \kappa_1 \\ \kappa_2 \\ \kappa_{12} \end{Bmatrix} = \mathbf{T} \begin{Bmatrix} \kappa_x \\ \kappa_y \\ \kappa_{xy} \end{Bmatrix}. \tag{33}$$

Equations (28), (30), and (33) yield the transformation relations for the stiffness matrices:

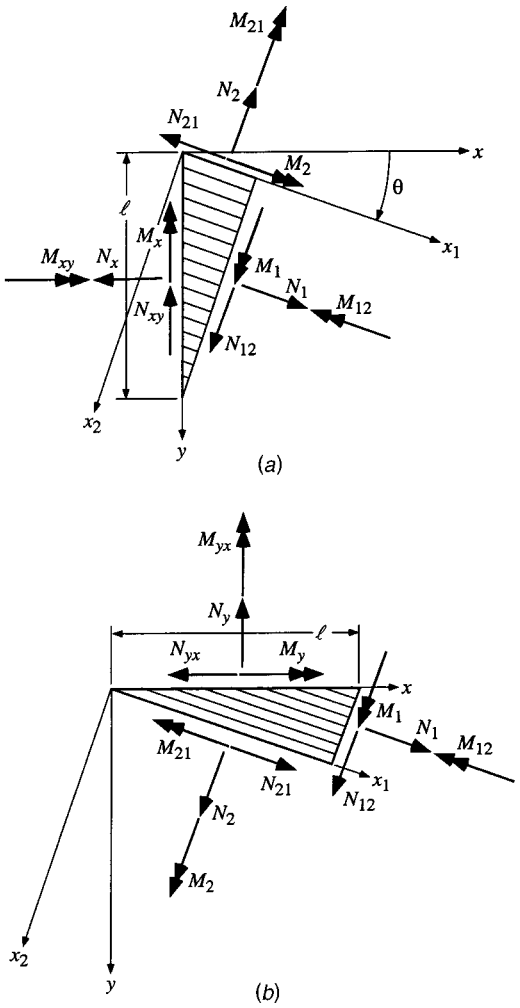

Fig. 6 An infinitesimal triangular element with (*a*) the force resultants and transformed force resultants and (*b*) the moment resultants and transformed moment resultants

$$\mathbf{A}_c = \mathbf{S}\overline{\mathbf{A}}_c\mathbf{R}\mathbf{T}\mathbf{R}^{-1}, \quad \mathbf{B}_c = \mathbf{S}\overline{\mathbf{B}}_c\mathbf{R}\mathbf{T}\mathbf{R}^{-1},$$
$$\mathbf{C}_c = \mathbf{S}\overline{\mathbf{C}}_c\mathbf{R}\mathbf{T}\mathbf{R}^{-1}, \quad \text{and} \quad \mathbf{D}_c = \mathbf{S}\overline{\mathbf{D}}_c\mathbf{R}\mathbf{T}\mathbf{R}^{-1}, \tag{34}$$

where **R** is Reuter's matrix defined as

$$\mathbf{R} = \begin{Bmatrix} 1 & 0 & 0 \\ 0 & 1 & 0 \\ 0 & 0 & 2 \end{Bmatrix}. \tag{35}$$

Stiffnesses. The stiffnesses are the sum of the stiffnesses of the matrix and cords and may be expressed as

$$\mathbf{A} = \mathbf{A}_m + \sum_{k=1}^{N} \mathbf{A}_c^k, \quad \mathbf{B} = \mathbf{B}_m + \sum_{k=1}^{N} \mathbf{B}_c^k,$$
$$\mathbf{C} = \mathbf{C}_m + \sum_{k=1}^{N} \mathbf{C}_c^k, \quad \text{and} \quad \mathbf{D} = \mathbf{D}_m + \sum_{k=1}^{N} \mathbf{D}_c^k, \tag{36}$$

where *k* indicates the *k*th cord ply and *N* is the total number of cord plies.

Differential Equations for the Displacements of the Middle Surface. The differential equations for the displacements of the middle surface of the shell are found. Substituting Eqs. (14), (15), and (22) into Eqs. (1), (8), and (9) yields

$$A_{11}u''+\frac{1}{a}(A_{16}+A_{61}^*)u'^{\bullet}+\frac{A_{66}^*}{a^2}u^{\bullet\bullet}+A_{16}v''+\frac{1}{a}(A_{12}+A_{66}^*)v'^{\bullet}+\frac{A_{62}^*}{a^2}v^{\bullet\bullet}-\frac{A_{12}}{a}w'-\frac{A_{62}^*}{a^2}w^{\bullet}-B_{11}w'''-\frac{1}{a}(2B_{16}+B_{61}^*)w''^{\bullet}-\frac{1}{a^2}(B_{12}+2B_{66}^*)w'^{\bullet\bullet}-\frac{B_{62}^*}{a^3}w^{\bullet\bullet\bullet}+p_x=0, \tag{37}$$

$$\frac{1}{a}(aA_{61}-C_{61})u''+\frac{1}{a^2}(aA_{21}+aA_{66}-C_{21}-C_{26})u'^{\bullet}+\frac{1}{a^3}(aA_{26}-C_{26})u^{\bullet\bullet}+\frac{1}{a}(aA_{66}-C_{66})v''+\frac{1}{a^2}(aA_{62}+aA_{26}-C_{62}+C_{26})v'^{\bullet}+\frac{1}{a^3}(aA_{22}-C_{22})v^{\bullet\bullet}-\frac{1}{a^2}(aA_{62}-C_{62})w'-\frac{1}{a^3}(aA_{22}-C_{22})w^{\bullet}-\frac{1}{a}(aB_{61}-D_{61})w'''-\frac{1}{a^2}(aB_{21}+2aB_{66}-D_{21}-2D_{66})w''^{\bullet}-\frac{1}{a^3}(aB_{62}+2aB_{26}-D_{62}-2D_{26})w'^{\bullet\bullet}-\frac{1}{a^4}(aB_{22}-D_{22})w^{\bullet\bullet\bullet}+p_{\varphi}=0, \tag{38}$$

and

$$\frac{A_{21}}{a}u'+\frac{A_{26}}{a^2}u^{\bullet}+C_{11}u'''+\frac{1}{a}(C_{16}+C_{61}+C_{61}^*)u''^{\bullet}+\frac{1}{a^2}(C_{21}+C_{66}+C_{66}^*)u'^{\bullet\bullet}+\frac{C_{26}}{a^3}u^{\bullet\bullet\bullet}+\frac{A_{26}}{a}v'+\frac{A_{22}}{a^2}v^{\bullet}+C_{16}v'''+\frac{1}{a}(C_{12}+C_{66}+C_{66}^*)v''^{\bullet}+\frac{1}{a^2}(C_{26}+C_{62}+C_{62}^*)v'^{\bullet\bullet}+\frac{C_{22}}{a^3}v^{\bullet\bullet\bullet}-\frac{A_{22}}{a^2}w-\frac{1}{a}(B_{21}+C_{12})w''-\frac{1}{a^2}(2B_{26}+C_{62}+C_{62}^*)w'^{\bullet}-\frac{1}{a^3}(B_{22}+C_{22})w^{\bullet\bullet}-D_{11}w''''-\frac{1}{a^2}(D_{12}+D_{21}+2D_{66}+2D_{66}^*)w''^{\bullet\bullet}-\frac{1}{a}(2D_{16}+D_{61}+D_{61}^*)w'''^{\bullet}-\frac{1}{a^3}(2D_{26}+D_{62}+D_{62}^*)w'^{\bullet\bullet\bullet}-\frac{D_{22}}{a^4}w^{\bullet\bullet\bullet\bullet}+p_z=0, \tag{39}$$

where

$$(\ )'=\frac{\partial(\ )}{\partial x}\quad\text{and}\quad(\ )^{\bullet}=\frac{\partial(\ )}{\partial\varphi}. \tag{40}$$

Equations (37)–(39) are three linear, coupled, nonhomogeneous, partial differential equations with constant coefficients for the three displacements u, v, and w. The coupling is due in part to the extension-twist coupling of the cords.

Results

Axisymmetric Loading. Closed-form solutions are found for a shell subjected to axisymmetric loading and no in-plane tractions. First, a general solution for the displacements is developed. Then, solutions for a semi-infinite cylinder and a finite cylinder loaded by a uniform transverse traction and by end loads are developed.

The shell is subjected to axisymmetric loading and no in-plane tractions. Therefore,

$$p_x=0,\quad p_{\varphi}=0,\quad\text{and}\quad p_z=p_z(x). \tag{41}$$

Since the loads are functions of x only, the displacements of the middle surface will also be functions of x only and may be expressed as

$$u=u(x),\quad v=v(x),\quad\text{and}\quad w=w(x). \tag{42}$$

Note that although the loading is axisymmetric, the displacement v is not assumed to be zero. Since the loads and the displacements are functions of x only, all derivatives with respect to φ are zero.

General Solution. Solving Eqs. (37) and (38) for u'' and v'' and integrating once with respect to x yields

$$u'=\frac{1}{A_{11}(aA_{66}-C_{66})-A_{16}(aA_{61}-C_{61})}\left\{\frac{1}{a}[A_{12}(aA_{66}-C_{66})-A_{16}(aA_{62}-C_{62})]w+[(aA_{66}-C_{66})B_{11}-A_{16}(aB_{61}-D_{61})]w''\right\}+B_1 \tag{43}$$

and

$$v'=\frac{1}{A_{11}(aA_{66}-C_{66})-A_{16}(aA_{61}-C_{61})}\left\{\frac{1}{a}[A_{11}(aA_{62}-C_{62})-A_{12}(aA_{61}-C_{61})]w+[A_{11}(aB_{61}-D_{61})-(aA_{61}-C_{61})B_{11}]w''\right\}+B_2, \tag{44}$$

where B_1 and B_2 are constants of integration to be determined.

Substituting Eqs. (43) and (44) into Eq. (39) yields

$$A_1w''''+(A_2+A_3)w''+A_4w=p, \tag{45}$$

where the constant coefficients A_1, A_2, A_3, and A_4 and the forcing p are defined as

$$A_1=D_{11}-\frac{1}{A_{11}(aA_{66}-C_{66})-A_{16}(aA_{61}-C_{61})}\{C_{11}[(aA_{66}-C_{66})B_{11}-A_{16}(aB_{61}-D_{61})]+C_{16}[A_{11}(aB_{61}-D_{61})-(aA_{61}-C_{61})B_{11}]\},$$

$$A_2=\frac{C_{12}}{a}-\frac{1}{a[A_{11}(aA_{66}-C_{66})-A_{16}(aA_{61}-C_{61})]}\{C_{11}[A_{12}(aA_{66}-C_{66})-A_{16}(aA_{62}-C_{62})]+C_{16}[A_{11}(aA_{62}-C_{62})-A_{12}(aA_{61}-C_{61})]\},$$

$$A_3=\frac{B_{21}}{a}-\frac{1}{a[A_{11}(aA_{66}-C_{66})-A_{16}(aA_{61}-C_{61})]}\{A_{21}[(aA_{66}-C_{66})B_{11}-A_{16}(aB_{61}-D_{61})]+A_{26}[A_{11}(aB_{61}-D_{61})-(aA_{61}-C_{61})B_{11}]\}, \tag{46}$$

$$A_4=\frac{A_{22}}{a^2}-\frac{1}{a^2[A_{11}(aA_{66}-C_{66})-A_{16}(aA_{61}-C_{61})]}\{A_{21}[A_{12}(aA_{66}-C_{66})-A_{16}(aA_{62}-C_{62})]+A_{26}[A_{11}(aA_{62}-C_{62})-A_{12}(aA_{61}-C_{61})]\},$$

and

$$p=\frac{1}{a}(A_{21}B_1+A_{26}B_2)+p_z. \tag{47}$$

Equation (45) has the solution

$$w = e^{-\beta x}[B_3 \cos(\alpha x) + B_4 \sin(\alpha x)] + e^{\beta x}[B_5 \cos(\alpha x) + B_6 \sin(\alpha x)] + w_p(x), \tag{48}$$

where the constants α and β are define as

$$\alpha = \left[\frac{1}{2}\left(\frac{A_4}{A_1}\right)^{1/2} + \frac{(A_2+A_3)}{4A_1}\right]^{1/2} \quad \text{and}$$

$$\beta = \left[\frac{1}{2}\left(\frac{A_4}{A_1}\right)^{1/2} - \frac{(A_2+A_3)}{4A_1}\right]^{1/2}, \tag{49}$$

B_3, B_4, B_5, and B_6 are constants of integration to be determined, and $w_p(x)$ is the particular solution that depends on the transverse loading $p_z(x)$. An alternate form of Eq. (48) is

$$w = D_1 \cosh(\beta x)\cos(\alpha x) + D_2 \cosh(\beta x)\sin(\alpha x) + D_3 \sinh(\beta x)\cos(\alpha x) + D_4 \sinh(\beta x)\sin(\alpha x) + w_p(x), \tag{50}$$

where D_1, D_2, D_3, and D_4 are constants of integration to be determined. The particular problem will determine which form of the solution is most convenient.

Consider the loads that may be applied to the end of a cylindrical shell. The force and moment resultants acting on the end of the cylindrical shell are N_x, $N_{x\varphi}$, Q_x, M_x, and $M_{x\varphi}$. These are the traction boundary conditions. Now consider the net moment of these force and moment resultants about the centerline of the cylindrical shell. The sum of the moments about the centerline over the length $\Delta s = a\Delta\varphi$ is

$$\Sigma M_{CL} = M_{x\varphi}\Delta s - a(N_{x\varphi}\Delta s). \tag{51}$$

The force resultant $N_{x\varphi}$ and moment resultant $M_{x\varphi}$ can be resolved into an equivalent shear force resultant T_x acting on the end of the cylindrical shell. Dividing both sides of Eq. (51) by $a\Delta s$ yields

$$T_x = \frac{\Sigma M_{CL}}{a\Delta s} = \frac{M_{x\varphi}}{a} - N_{x\varphi}. \tag{52}$$

When the transverse traction is $p_z = p_o + p_1 x$, where p_o and p_1 are constants, the particular solution w_p of Eq. (45) is

$$w_p = \frac{1}{A_4}\left[\frac{1}{a}(A_{21}B_1 + A_{26}B_2) + p_o + p_1 x\right]. \tag{53}$$

Semi-Infinite Cylinder With End Loads. Consider a semi-infinite cylinder with a constant transverse traction and end loads. The boundary conditions at $x=0$ are $N_x = N$, $M_x = M$, $Q_x = Q$, and $T_x = T$; and the transverse traction is $p_z = p_o$, where N, M, Q, T, and p_o are constants. It is most convenient to use the form of the solution for w given by Eq. (48). The displacement w is bounded in x, and therefore B_5 and B_6 must be zero. The particular solution w_p is given by Eq. (53), where $p_1 = 0$.

Applying the boundary conditions $N_x = N$ and $T_x = T$ at $x=0$ to Eqs. (14), (15), (22), (43), (44), and (52), and solving for the constants of integration B_1 and B_2 yields

$$B_1 = \frac{(aA_{66} - C_{66})N + aA_{16}T}{A_{11}(aA_{66} - C_{66}) - A_{16}(aA_{61} - C_{61})}$$

and

$$B_2 = \frac{-(aA_{61} - C_{61})N - aA_{11}T}{A_{11}(aA_{66} - C_{66}) - A_{16}(aA_{61} - C_{61})}. \tag{54}$$

Applying the boundary conditions $M_x = M$ and $Q_x = Q$ at $x = 0$ to Eqs. (14), (15), (22), (43), (44), (48), (49), and (53), and solving for the constants of integration B_3 and B_4 yields

$$B_3 = \frac{-A_9(M - A_7) + A_6 Q}{A_6 A_8 - A_5 A_9} \quad \text{and} \quad B_4 = \frac{A_8(M - A_7) - A_5 Q}{A_6 A_8 - A_5 A_9}, \tag{55}$$

where the constants A_5, A_6, A_7, A_8, and A_9 are defined as

$$A_5 = A_1(\alpha^2 - \beta^2) - A_2, \quad A_6 = 2\alpha\beta A_1,$$
$$A_7 = -\frac{A_2}{A_4}\left[\frac{1}{a}(A_{21}B_1 + A_{26}B_2) + p_o\right] + C_{11}B_1 + C_{16}B_2,$$
$$A_8 = \beta[A_1(3\alpha^2 - \beta^2) - A_2], \tag{56}$$

and

$$A_9 = \alpha[A_1(3\beta^2 - \alpha^2) + A_2].$$

The constants of integration B_1, B_2, B_3, B_4, B_5, and B_6 have been determined in terms of the loads, and therefore u', v', and w have been determined in terms of the loads. The displacements u and v can easily be found by integrating the equations for u' and v', respectively, once with respect to x. The two new constants of integration represent rigid-body displacements and may be set equal to zero.

Finite Cylinder With End Loads. Consider a finite cylinder of length $2L$ with end loads and the transverse traction $p_z = p_o$, where p_o is a constant. The boundary conditions are $N_x = N$, $M_x = M$, and $T_x = T$ at $x = \pm L$, $Q_x = Q$ at $x = -L$, and $Q_x = -Q$ at $x = L$.

It is most convenient to use the form of the solution for w given by Eq. (50). The transverse traction $p_z = p_o$, and $p_1 = 0$ in Eq. (53). The cylinder is symmetric about the φz-plane, and therefore the transverse displacement w must also be symmetric, and the constants of integration D_2 and D_3 must be zero.

Applying the boundary conditions $N_x = N$ and $T_x = T$ at $x = \pm L$ to Eqs. (14), (15), (22), (43), (44), and (52), and solving for the constants of integration B_1 and B_2 yields Eqs. (54), the same as for a semi-infinite cylinder.

Applying the boundary conditions $Q_x = -Q$ and $M_x = M$ at $x = L$ to Eqs. (14), (15), (22), (43), (44), (49), (50), and (53), and solving for constants of integration D_1 and D_4 yields

$$D_1 = \frac{-A_9(M - A_7) - A_6 Q}{A_6 A_8 - A_5 A_9} \quad \text{and} \quad D_4 = \frac{A_8(M - A_7) + A_5 Q}{A_6 A_8 - A_5 A_9}, \tag{57}$$

where

$$A_5 = [(\alpha^2 - \beta^2)A_1 - A_2]\cos(\alpha L)\cosh(\beta L) + 2\alpha A_1 \beta \sin(\alpha L)\sinh(\beta L),$$
$$A_6 = -2\alpha A_1 \beta \cos(\alpha L)\cosh(\beta L) + [(\alpha^2 - \beta^2)A_1 - A_2]\sin(\alpha L)\sinh(\beta L),$$
$$A_7 = -\frac{A_2}{A_4}\left[\frac{1}{a}(A_{21}B_1 + A_{26}B_2) + p_o\right] + C_{11}B_1 + C_{16}B_2,$$
$$A_8 = \alpha[(3\beta^2 - \alpha^2)A_1 + A_2]\cosh(\beta L)\sin(\alpha L) + \beta[(3\alpha^2 - \beta^2)A_1 - A_2]\cos(\alpha L)\sinh(\beta L), \tag{58}$$

and

$$A_9 = \beta[(3\alpha^2 - \beta^2)A_1 - A_2]\cosh(\beta L)\sin(\alpha L) - \alpha[(3\beta^2 - \alpha^2)A_1 + A_2]\cos(\alpha L)\sinh(\beta L).$$

The constants of integration B_1, B_2, D_1, D_2, D_3, and D_4 have been determined in terms of the loads, and therefore u', v', and w have been determined in terms of the loads. The displacements u and v can easily be found by integrating the equations for u' and v', respectively, once with respect to x. The two new constants of integration represent rigid-body displacements and may be set equal to zero.

The current solution is compared with the commonly used approximate G–T and A–H solutions. Each shell considered has a single cord ply on the middle surface. First, the results for an axially loaded semi-infinite shell are examined. Second, the re-

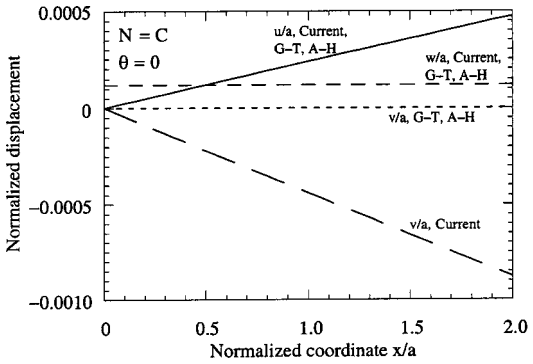

Fig. 7 Normalized displacements u/a, v/a, w/a versus normalized coordinate x/a

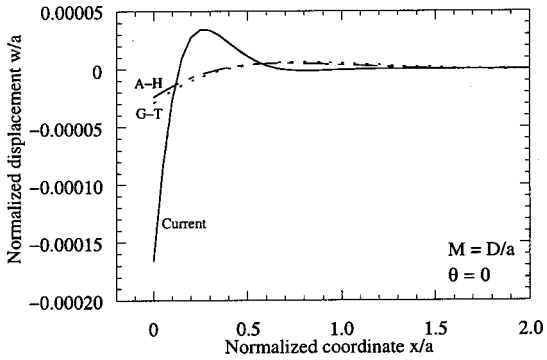

Fig. 8 Normalized displacement w/a versus normalized coordinate x/a

sults for a semi-infinite shell loaded by an edge moment are examined. Third, the results for an axially loaded finite shell are examined.

The G–T equations for the in-plane material properties are

$$E_1=E_cV_c+E_m(1-V_c),$$

$$E_2=\frac{4E_m(1-V_c)[E_cV_c+E_m(1-V_c)]}{3E_cV_c+4E_m(1-V_c)},\quad G_{12}=G_m(1-V_c),$$

$$\nu_{12}=0.5,\quad \text{and}\quad \nu_{21}=\nu_{12}\frac{E_2}{E_1}, \tag{59}$$

where E is the tensile modulus; G is the shear modulus; ν is the Poisson's ratio; and subscripts 1 and 2 indicate the in-plane material properties parallel and perpendicular to the cord direction, respectively. The A–H equations for the in-plane material properties are

$$E_1=E_cV_c,\quad E_2=\frac{4E_m}{3},\quad G_{12}=G_m,\quad \nu_{12}=0.5,\quad \text{and}$$

$$\nu_{21}=0. \tag{60}$$

The G–T and A–H equations and the solution given by Paris [9] are used to find the force and moment resultants and deformations of the shell.

The cord volume fraction V_c is

$$V_c=\frac{A_c}{bh}. \tag{61}$$

The properties of the constituents, the geometry of the semi-infinite cylindrical shell, and the geometry of the finite cylindrical shell are:

Steel cord:	$R_c=0.430$ mm	$A_c=0.440$ mm^2	
	$E_c=200$ GPa		
	$C_1=0.967$	$C_2=0.0828$	$C_3=0.187$
	$C_4=0.0723$	$C_5=0.0638$	
Rubber matrix:	$E_m=10$ MPa	$\nu_m=0.5$	
Shell:	$a=0.318$ m	$h=4R_c=1.71$ mm	$V_c=0.3$
Finite cylinder:	$2L=2a=0.635$ m		

The details of the cord material and geometry can be found in Paris and Costello [10].

Consider a semi-infinite shell with the cords parallel to the shell axis subjected to an axial load $N=C$. Figure 7 shows the normalized displacements u/a, v/a, and w/a versus the normalized coordinate x/a. The curves for u/a are indistinguishable for the current, G–T, and A–H solutions. For the G–T and A–H solutions, v/a is zero. However, for the current solution, u/a and v/a are of the same order of magnitude. The magnitude of v/a is almost twice the magnitude of u/a. The sign of v/a is dependent upon the lay of the cords: here the cords are right lay and the sign of v/a is negative; if the cords were left lay, the sign of v/a would be positive. The curves for w/a are indistinguishable for the current, G–T, and A–H solutions. The shell has significant extension-twist coupling due to the extension-twist coupling of the cords.

Consider a semi-infinite shell with the cords parallel to the shell axis subjected to an edge moment $M=D/a$. Figure 8 shows the normalized displacement w/a versus normalized coordinate x/a. The curve for the current solution is dramatically different from the curves for the G–T and A–H solutions. The curves for w/a for the G–T and A–H solutions are very close. At the end of the shell, where x/a is zero, w/a for the current solution is one order of magnitude greater than those for the G–T and A–H solutions. A larger displacement indicates a smaller bending stiffness. The bending stiffness for the G–T and A–H solutions is larger than the bending stiffness for the current solution since the G–T and A–H solutions smear out the cords over the thickness of the shell and the current solution does not. The value of w/a decays exponentially and has nearly vanished when $x/a>1$ for the current solution and when $x/a>2$ for the G–T and A–H solutions. Figure 9 shows the normalized moment resultant M_x/M versus the normalized coordinate x/a. Again, the curve for the current solution is dramatically different from the curves for the G–T and A–H solutions. The curves for the G–T and A–H solutions are very close. The value of M_x/M decays exponentially and has nearly vanished when $x/a>1$ for the current solution and when x/a

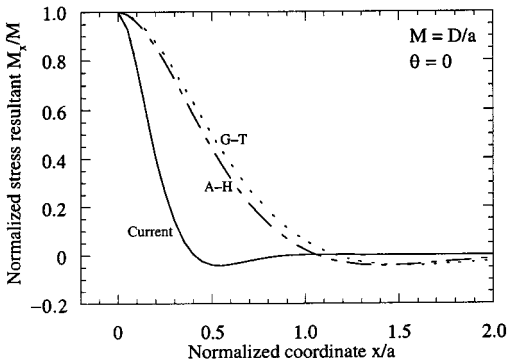

Fig. 9 Normalized moment resultant M_x/M versus normalized coordinate x/a

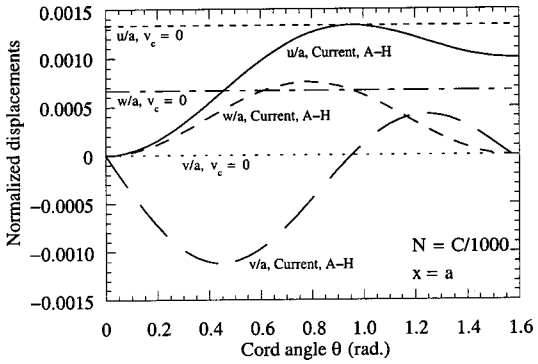

Fig. 11 Normalized displacements u/a, v/a, w/a versus cord angle θ

>2 for the G–T and A–H solutions. The values of w/a and M_x/M decay much more rapidly for the current solution than for the G–T and A–H solutions.

Consider a finite shell subjected to an axial load $N=C$. The cords are parallel to the shell axis. This is an intermediate length shell based upon the analysis of a semi-infinite shell with an edge moment above. Figure 10 shows the normalized displacements u/a, v/a, and w/a versus the normalized coordinate x/a. These results for an axially loaded finite cylinder are similar to those for a semi-infinite cylinder given above, and the discussion is the same as the discussion given above for a semi-infinite shell with the cords parallel to the shell axis subjected to an axial load $N=C$.

Paris and Costello [10] presented an analysis of cord composite cylindrical shells with the cords parallel to the shell axis. The results for the current solution with the cords parallel to the shell axis are indistinguishable from those results.

Consider a finite shell with the cords at an angle to the shell axis subjected to an axial load $N=C/1000$. Figure 11 shows the normalized displacements u/a, v/a, and w/a versus the cord angle θ for the current and A–H solutions. The value of θ varies from zero to $\pi/2$. For the cord composite shell, V_c is 0.3. The results for a pure rubber shell are given for comparison; a pure rubber shell has no cords, and V_c is zero. The curves for u/a, v/a, and w/a for the current and A–H solutions are indistinguishable. The normalized displacement v/a is zero when V_c is zero. As θ increases from 0 to $\pi/2$, u/a and w/a first increase and then decrease. When θ is greater than about 0.667 and less than about 0.956, w/a is larger when the cord volume fraction V_c is 0.3 than when V_c is zero. As θ increases from 0 to $\pi/2$, v/a is at first negative and then positive. These trends are caused by the Poisson's effect of the matrix. For small cord angles the axial strain of the cords is positive and the cords are in tension; for large angles the axial strain of the cords is negative and the cords are in compression; and for some angle in between, the axial strain and force in the cords are zero. When θ is approximately 0.956, the displacements when the cord volume fraction V_c is 0.3 are equal to the displacements when V_c is zero, and the extension-twist coupling of the axially loaded shell vanishes. At this angle, the axial strain of the cords is zero and the cords are neither in tension nor compression. A similar phenomenon has been observed for an axially loaded unidirectional cord-reinforced rubber sheet, [1]. The shell has significant extension-twist coupling due to the cords.

Figures 12, 13, and 14 show the normalized displacements u/a, v/a, and w/a, respectively, versus the cord angle θ for the current, G–T, and A–H solutions. The curves for the current and A–H solutions are indistinguishable, while the G–T solution is dramatically different. All solutions neglect both the transverse and shear stiffnesses of the cords. In addition, the current and A–H solutions neglect any change in the stiffnesses of the matrix

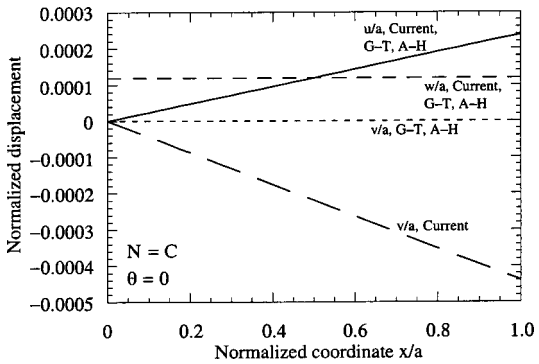

Fig. 10 Normalized displacements u/a, v/a, w/a versus normalized coordinate x/a

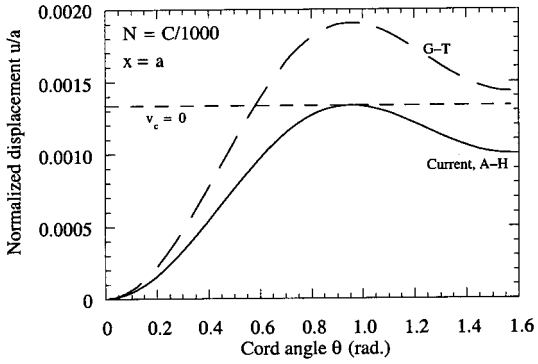

Fig. 12 Normalized displacement u/a versus cord angle θ

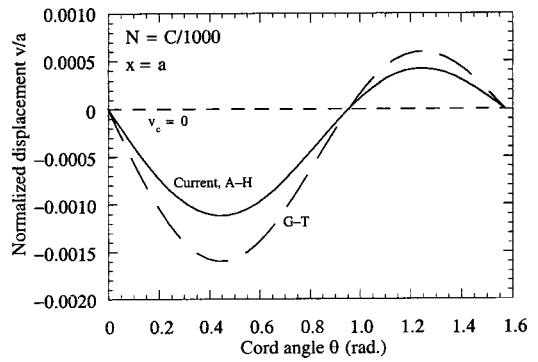

Fig. 13 Normalized displacement v/a versus cord angle θ

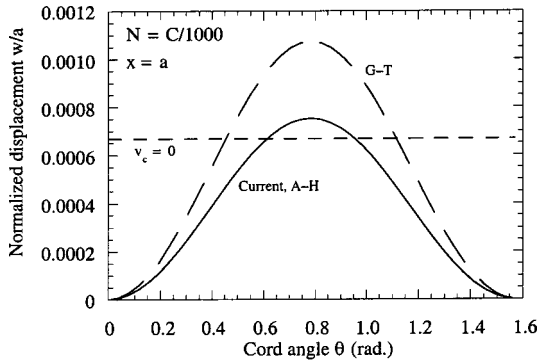

Fig. 14 Normalized displacement *w*/*a* versus cord angle *θ*

due to the volume of matrix material displaced by the cords. The G–T solution, however, accounts for the changes in the volume of the matrix material displaced by the cords, but does not include the transverse or shear stiffnesses of the cords. Thus, the stiffnesses are much smaller and the displacements are much greater for the G–T solution compared with the current and A–H solutions.

Summary and Conclusions

An analytical method for determining the load-deformation behavior of cord composite cylindrical shells was developed. The differential equations for the displacements were found for a shell with cord plies at various angles to the shell axis. The equations were solved analytically in closed form for a shell with axisymmetric loading and no in-plane tractions. The response due to uniformly distributed axisymmetric end loads and uniform internal pressure was found for a semi-infinite cylinder and a finite cylinder.

The results of the current study were compared with the commonly used Gough-Tangorra and Akasaka-Hirano equations. In some cases, the response predicted by the current, G–T, and A–H solutions were indistinguishable. In other cases, the current, G–T, and A–H solutions predicted significantly different responses. The differences in the predicted responses can be attributed to the assumptions and approximations made in developing the current, G–T, and A–H solutions.

Acknowledgments

The authors would like to thank Amit Prakash, Carol K. Shield, and Zhibin Zhang for many conversations regarding the mechanics of cords and cord composite materials, Dmitri L. Vainchtein for discussions on mathematics, James W. Phillips and Sarah E. Zeller for comments and suggestions regarding this manuscript, and the Goodyear Tire and Rubber Company and the University of Illinois at Urbana-Champaign for supporting this work.

References

[1] Walter, J. D., 1978, "Cord-Rubber Tire Composites: Theory and Applications," Rubber Chem. Technol., **51**, pp. 524–576.
[2] Walter, J. D., and Patel, H. P., 1979, "Approximate Expressions for the Elastic Constants of Cord-Rubber Laminates," Rubber Chem. Technol., **52**, pp. 710–724.
[3] Jones, R. M., 1998, *Mechanics of Composite Materials*, 2nd Ed., Taylor and Francis, Philadelphia, PA.
[4] Paris, A. J., Lin, C. C., and Costello, G. A., 1992, "Simple Cord Composites," J. Eng. Mech. Div., **118**, pp. 1939–1948.
[5] Kittredge, C. A., 1991, Static Response of Cord Composite Plates, doctoral thesis, Department of Theoretical and Applied Mechanics, University of Illinois at Urbana-Champaign, Urbana, IL.
[6] Shield, C. K., and Costello, G. A., 1994, "The Effect of Wire Rope Mechanics on the Mechanical Response of Cord Composite Laminates: An Elasticity Approach," ASME J. Appl. Mech., **61**, pp. 1–8.
[7] Shield, C. K., and Costello, G. A., 1994, "The Effect of Wire Rope Mechanics on the Mechanical Response of Cord Composite Laminates: An Energy Approach," ASME J. Appl. Mech., **61**, pp. 9–15.
[8] Shield, C. K., and Costello, G. A., 1994, "Bending of Cord Composite Plates," J. Eng. Mech. Div., **120**, pp. 876–892.
[9] Paris, A. J., 1997, Cord-Reinforced Cylindrical Shells, doctoral thesis, Department of Theoretical and Applied Mechanics, University of Illinois at Urbana-Champaign, Urbana, IL.
[10] Paris, A. J., and Costello, G. A., 2000, "Bending of Cord Composite Cylindrical Shells," ASME J. Appl. Mech., **67**, pp. 117–127.
[11] Love, A. E. H., 1934, *A Treatise on the Mathematical Theory of Elasticity*, 4th Ed., Cambridge University Press, New York.
[12] Costello, G. A., 1997, *Theory of Wire Rope*, 2nd Ed., Springer-Verlag, New York.
[13] Flügge, W., 1966, *Stresses in Shells*, Springer-Verlag, New York.
[14] Donnell, L. H., 1933, "Stability of Thin-Walled Tubes Under Torsion," National Advisory Committee for Aeronautics, Report No. 479.

Zeroth-Order Shear Deformation Theory for Laminated Composite Plates

M. C. Ray
Mechanical Engineering Department,
Indian Institute of Technology,
Kharagpur 721302, India

In this paper a zeroth-order shear deformation theory has been derived for static and dynamic analysis of laminated composite plates. The responses obtained by the theory for symmetric and antisymmetric laminates are compared with the existing solutions. The comparison firmly establishes that this new shear deformation theory can be used for both thick and thin laminated composite plates with high accuracy. [DOI: 10.1115/1.1558077]

1 Introduction

The use of composite materials has been significantly increased during the past decades because of their large strength to weight and stiffness to weight ratios, high thermal stability, excellent resistance to environmental and corrosion attack, and high fatigue strength. An excellent feature of composite materials is that these materials can concurrently be designed while designing the structures. A great deal of researches, [1–7], has been carried out towards the development of various theories for analyzing the laminated composite structures. These theories can broadly be divided into two categories, namely, equivalent single-layer theory (ESL) and layer-wise theories. Among the ESL theories, the classical laminated plate theory (CLPT), [1], is the simplest one and is applicable to thin laminates only. This theory cannot predict accurate results for thick laminates as it does not allow to consider transverse shear deformations. Examples of ESL theories accounting for transverse shear deformations are the first-order shear deformation theory (FSDT), [2], and the higher-order shear deformation theories (HSDT), [3–6]. Although HSDT predicts a more accurate response than the FSDT for both highly thick to thin laminates, the analysis using HSDT involves more computational effort than using the FSDT. However, FSDT requires the use of appropriate shear correction factor for accurate representation of transverse shear deformations. The layerwise theories predict highly accurate responses at the ply level where material discontinuities take place but the complexities involved often restrains one from using these theories.

Recently, a zeroth-order shear deformation theory (ZSDT) has been derived by Shimpi [8], which predicts accurate results for both thick and thin isotropic plates. The theory has the number of advantages over the CLPT and FSDT. For example, it satisfies zero transverse shear stresses on the top and bottom surfaces of the plates, does not require a shear correction factor and avoids shear locking. However, the theory has not yet been extended for the analysis of laminated composite structures. In this paper, an endeavor has been made to develop a zeroth-order shear deformation theory for laminated composite plates.

2 Zeroth-Order Shear Deformation Theory (ZSDT)

Consider a rectangular laminated plate made of N number of orthotropic layers as shown in Fig. 1. The length, width, and thickness of the plate are denoted by a, b, and h, respectively. The midplane of the plate is considered as the reference plane. The origin of the laminate coordinate system (x,y,z) is located on the reference plane $(z=0)$ in such a way that $x=0$, a and $y=0$, b indicate the boundaries of the plates. The thickness coordinates z of the top and bottom surfaces of any (kth) layer are denoted by h_{k+1} and h_k, respectively. The fibers of the kth layer are oriented at an angle θ_k to the x-axis. The transverse displacement w is assumed to be constant through the thickness. The derivation of the theory first aims at satisfying the transverse shear stresses, σ_{xz} and σ_{yz} to be zero at the top and bottom surfaces of the plate while giving rise to parabolic variation of σ_{xz} and σ_{yz} across the thickness. In order to satisfy this condition, the in-plane displacements, u and v at any point (x,y,z) of the laminate in the x and y-directions, may be expressed to describe the kinematics of deformation as follows:

$$u(x,y,z,t)=u_0(x,y,t)-z\frac{\partial w(x,y,t)}{\partial x}+\frac{1}{\lambda_x}\left[\frac{3}{2}\left(\frac{z}{h}\right)-2\left(\frac{z}{h}\right)^3\right]Q_x(x,y,t) \tag{1}$$

$$v(x,y,z,t)=v_0(x,y,t)-z\frac{\partial w(x,y,t)}{\partial y}+\frac{1}{\lambda_y}\left[\frac{3}{2}\left(\frac{z}{h}\right)-2\left(\frac{z}{h}\right)^3\right]Q_y(x,y,t) \tag{2}$$

where, u_0 and v_0 are the displacements at any point $(x,y,0)$ on the reference plane in the x and y-directions, respectively, Q_x and Q_y are the transverse shear stress resultants with λ_x and λ_y being the unknown constants. Evaluation of these constants results in a new displacement theory. The constants λ_x and λ_y can be determined by considering the definitions of the transverse shear stress resultants Q_x and Q_y. For laminated structures these are defined as

$$Q_x=\sum_{k=1}^{N}\int_{h_k}^{h_{k+1}}\sigma_{xz}^k dz \quad \text{and} \quad Q_y=\sum_{k=1}^{N}\int_{h_k}^{h_{k+1}}\sigma_{yz}^k dz. \tag{3}$$

The linear constitutive relations for kth orthotropic layer is given by

$$\begin{Bmatrix}\sigma_x\\ \sigma_y\\ \sigma_{xy}\\ \sigma_{xz}\\ \sigma_{yz}\end{Bmatrix}^k=\begin{bmatrix}C_{11}^k & C_{12}^k & C_{16}^k & 0 & 0\\ C_{12}^k & C_{22}^k & C_{26}^k & 0 & 0\\ C_{16}^k & C_{26}^k & C_{66}^k & 0 & 0\\ 0 & 0 & 0 & C_{55}^k & C_{45}^k\\ 0 & 0 & 0 & C_{45}^k & C_{44}^k\end{bmatrix}\begin{Bmatrix}\varepsilon_x\\ \varepsilon_y\\ \varepsilon_{xy}\\ \varepsilon_{xz}\\ \varepsilon_{yz}\end{Bmatrix}^k \tag{4}$$

in which σ_x, σ_y are the normal stresses in the x and y-directions, respectively, σ_{xy} is the inplane shear stress, and C_{ij}^k denotes the

Contributed by the Applied Mechanics Division of THE AMERICAN SOCIETY OF MECHANICAL ENGINEERS for publication in the ASME JOURNAL OF APPLIED MECHANICS. Manuscript received by the ASME Applied Mechanics Division, Apr. 21, 2002; final revision, Aug. 28, 2002. Associate Editor: M.-J. Pindera. Discussion on the paper should be addressed to the Editor, Prof. Robert M. McMeeking, Department of Mechanical and Environmental Engineering University of California–Santa Barbara, Santa Barbara, CA 93106-5070, and will be accepted until four months after final publication of the paper itself in the ASME JOURNAL OF APPLIED MECHANICS.

 Copyright © 2003 by ASME

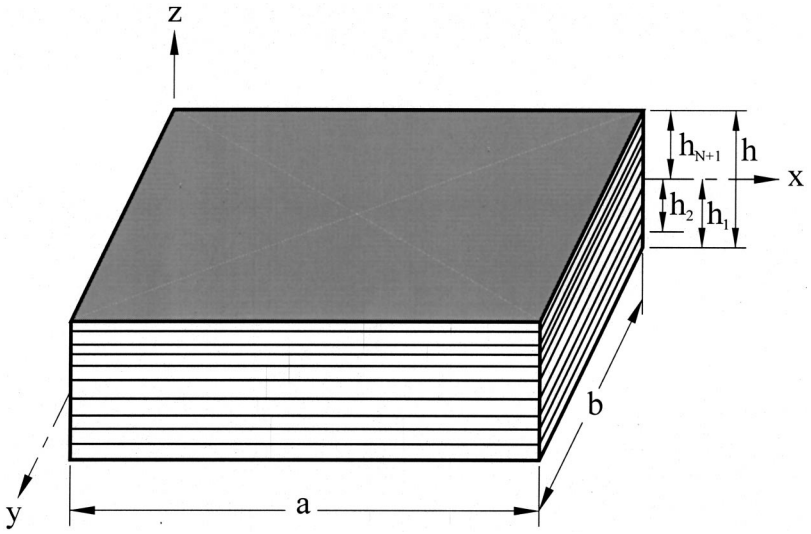

Fig. 1 Laminate configuration

elastic constants with respect to the laminate coordinate system. In the strain vector ε_x, ε_y are the normal strains, ε_{xy} is the inplane strain, and ε_{xz}, ε_{yz} are the transverse shear strains.

Using Eqs. (1)–(2) and the linear strain-displacement relations for infinitesimal strains, [9], the expressions for ε_{xz}, ε_{yz} are obtained as

$$\varepsilon_{xz}=\frac{1}{\lambda_x}\left(\frac{3}{2h}-\frac{6z^2}{h^3}\right)Q_x \quad \text{and} \quad \varepsilon_{yz}=\frac{1}{\lambda_y}\left(\frac{3}{2h}-\frac{6z^2}{h^3}\right)Q_y. \tag{5}$$

It may be noted from the expressions for the in-plane displacements that the effect of transverse shear deformations has been incorporated in the in-plane displacements through the use of transverse shear stress resultants. Hence, the expressions for transverse shear strains given by Eq. (5) do not explicitly contain the rotational displacements due to the transverse shear deformations. Thus the present theory may be called as a zeroth-order shear deformation theory for laminated structures. It can be observed from (5) that the transverse shear strains are zero at the top ($z=h/2$) and bottom ($z=-h/2$) surfaces of the plate thus satisfying the traction free conditions for σ_{xz} and σ_{yz}. In this regard, it may be mentioned here that the high-order shear deformation theory (HSDT) developed by Reddy [6] also satisfies the zero transverse shear stress conditions on the top and bottom surfaces of the plate. But the Reddy's theory, [6], uses high-order rotations to account for the effect of transverse shear deformations whereas the present theory uses transverse shear stress resultants to account for the same. Finally, using (5) in the constitutive relations for σ_{xz}, σ_{yz} and then substituting the resulting relations in (3), λ_x and λ_y can be determined for symmetric and antisymmetric cross-ply and antisymmetric angle-ply laminates as follows:

$$\lambda_x=\sum_{k=1}^{N} C_{55}^k\left[\frac{3}{2h}(h_{k+1}-h_k)-\frac{2}{h^3}(h_{k+1}^3-h_k^3)\right]$$

and

$$\lambda_y=\sum_{k=1}^{N} C_{44}^k\left[\frac{3}{2h}(h_{k+1}-h_k)-\frac{2}{h^3}(h_{k+1}^3-h_k^3)\right]. \tag{6}$$

From Eq. (6) it can be observed that the constants λ_x and λ_y depend on the material properties and thickness parameters of each layer. Evaluating these constants one can proceed for the formulation of the static and dynamic behavior of laminated plates and shells. The next section is concerned with this formulation.

3 Analysis of Laminated Plates Using the Zeroth-Order Shear Deformation Theory (ZSDT)

In this section, the formulation for the analysis of laminated plates using the zeroth-order shear deformation theory derived in the previous section has been presented. Using the displacement field for ZSDT given by Eqs. (1)–(2), the expressions for the normal and in-plane shear strains can be written as

$$\begin{aligned}
\varepsilon_x&=\frac{\partial u_0}{\partial x}-z\frac{\partial^2 w}{\partial x^2}+\frac{1}{\lambda_x}\left[\frac{3}{2}\left(\frac{z}{h}\right)-2\left(\frac{z}{h}\right)^3\right]\frac{\partial Q_x}{\partial x},\\
\varepsilon_y&=\frac{\partial u_0}{\partial x}-z\frac{\partial^2 w}{\partial y^2}+\frac{1}{\lambda_y}\left[\frac{3}{2}\left(\frac{z}{h}\right)-2\left(\frac{z}{h}\right)^3\right]\frac{\partial Q_y}{\partial y},\\
\varepsilon_{xy}&=\frac{\partial u_0}{\partial y}+\frac{\partial v_0}{\partial x}-2z\frac{\partial^2 w}{\partial x\partial y}\\
&\quad+\left[\frac{3}{2}\left(\frac{z}{h}\right)-2\left(\frac{z}{h}\right)^2\right]\left(\frac{1}{\lambda_x}\frac{\partial Q_x}{\partial y}+\frac{1}{\lambda_y}\frac{\partial Q_y}{\partial x}\right).
\end{aligned} \tag{7}$$

The total potential energy U of the plate is given by

$$U=\frac{1}{2}\int_0^a\int_0^b\left(\sum_{k=1}^{N}\int_{h_k}^{h_{k+1}}(\sigma_x\varepsilon_x+\sigma_y\varepsilon_y+\sigma_{xy}\varepsilon_{xy}+\sigma_{xz}\varepsilon_{xz}+\sigma_{yz}\varepsilon_{yz})dz-pw\right)dxdy \tag{8}$$

in which $p(x,y)$ is the externally applied distributed load acting along the z-direction. The kinetic energy T of the plate can be expressed as

$$T=\frac{1}{2}\sum_{k=1}^{N}\int_{h_k}^{h_{k+1}}\int_0^a\int_0^b\rho^k(\dot{u}^2+\dot{v}^2+\dot{w}^2)dxdydz. \tag{9}$$

Substituting Eqs. (8) and (9) into Hamilton's variational principle

$$\delta\int_{t_1}^{t_2}(T-U)dt=0, \tag{10}$$

the following governing equations are obtained:

$$\frac{\partial N_x}{\partial x}+\frac{\partial N_{xy}}{\partial y}=I_0\ddot{u}_0-I_1\frac{\partial\ddot{w}}{\partial x}+\frac{I_8}{\lambda_x}\ddot{Q}_x \tag{11}$$

$$\frac{8\partial N_{xy}}{\partial x}+\frac{\partial N_y}{\partial y}=I_0\ddot{v}_0-I_1\frac{\partial\ddot{w}}{\partial y}+\frac{I_8}{\lambda_y}\ddot{Q}_y \tag{12}$$

$$\frac{\partial^2 M_x}{\partial x^2}+2\frac{\partial^2 M_{xy}}{\partial x\partial y}+\frac{\partial^2 M_y}{\partial y^2}+p = I_0\ddot{w}_0-I_1\left(\frac{\partial\ddot{u}_0}{\partial x}+\frac{\partial\ddot{v}_0}{\partial y}\right)-I_2\left(\frac{\partial^2\ddot{w}}{\partial x^2}+\frac{\partial^2\ddot{w}}{\partial y^2}\right)+I_9\left(\frac{1}{\lambda_x}\frac{\partial\ddot{Q}_x}{\partial x}+\frac{1}{\lambda_y}\frac{\partial\ddot{Q}_y}{\partial y}\right) \tag{13}$$

$$\frac{\partial}{\partial x}\left(M_x-\frac{4}{3h^2}P_x\right)+\frac{\partial}{\partial y}\left(M_{xy}-\frac{4}{3h^2}P_{xy}\right)-\left(Q_x-\frac{4}{h^2}R_x\right) = \frac{I_7}{\lambda_x^2}\ddot{Q}_x+\frac{I_8}{\lambda_x}\ddot{u}_0-\frac{I_9}{\lambda_x}\frac{\partial\ddot{w}}{\partial x} \tag{14}$$

$$\frac{\partial}{\partial x}\left(M_{xy}-\frac{4}{3h^2}P_{xy}\right)+\frac{\partial}{\partial y}\left(M_y-\frac{4}{3h^2}P_y\right)-\left(Q_y-\frac{4}{h^2}R_y\right) = \frac{I_7}{\lambda_y^2}\ddot{Q}_y+\frac{I_8}{\lambda_y}\ddot{v}_0-\frac{I_9}{\lambda_y}\frac{\partial\ddot{w}}{\partial y}. \tag{15}$$

In Eqs. (11)–(15), the various stress resultants (N_x, N_y, N_{xy}, R_x, and R_y) and moment resultants (M_x, M_y, M_{xy}, P_x, P_y, and P_{xy}) are given by

$$(N_x,M_x,P_x)=\sum_{k=1}^{N}\int_{h_k}^{h_{k+1}}\sigma_x^k(1,z,z^2)dz,$$

$$(N_y,M_y,P_y)=\sum_{k=1}^{N}\int_{h_k}^{h_{k+1}}\sigma_y^k(1,z,z^2)dz,$$

$$(N_{xy},M_{xy},P_{xy})=\sum_{k=1}^{N}\int_{h_k}^{h_{k+1}}\sigma_{xy}^k(1,z,z^2)dz$$

and

$$(R_x,R_y)=\sum_{k=1}^{N}\int_{h_k}^{h_{k+1}}z^2(\sigma_{xz}^k,\sigma_{xz}^k)dz. \tag{16}$$

The various mass parameters appearing in (11)–(15) are defined as

$$(I_0,I_1,I_2,I_3,I_4,I_6)=\sum_{k=1}^{N}\int_{h_k}^{h_{k+1}}\rho^k(1,z,z^2,z^3,z^4,z^6)dz, \tag{17}$$

$$I_7=\frac{9}{4h^2}I_2-\frac{6}{h^4}I_4+\frac{6}{h^6}I_6,\quad I_8=\frac{3}{2h}I_1-\frac{2}{h^3}I_3 \quad \text{and}$$

$$I_9=\frac{3}{2h}I_2-\frac{2}{h^3}I_4.$$

The study is concerned with obtaining the Navier solutions using the ZSDT developed here. Accordingly, two types (ss1 and ss2) of simply supported boundary conditions admitting the Navier solutions have been extracted from the variational principle. The ss1 type boundary conditions at $x=0$ and a are

$$v_0=0,\quad w=0,\quad \frac{\partial w}{\partial y}=0,\quad N_x=0,\quad M_x=0,\quad P_x=0,\quad Q_x=0,$$

and those at $y=0$ and b are

$$u_0=0,\quad w=0,\quad \frac{\partial w}{\partial x}=0,\quad N_y=0,\quad M_y=0,\quad P_y=0,\quad Q_y=0. \tag{18}$$

The ss2 type boundary conditions at $x=0$ and a are

$$u_0=0,\quad w=0,\quad \frac{\partial w}{\partial y}=0,\quad N_{xy}=0,\quad M_x=0,\quad P_x=0,\quad Q_x=0,$$

and those at $y=0$ and b are

$$v_0=0,\quad w=0,\quad \frac{\partial w}{\partial x}=0,\quad N_y=0,\quad M_y=0,\quad P_y=0,\quad Q_y=0. \tag{19}$$

In order to obtain the Navier solutions, symmetric and antisymmetric cross-ply laminates and antisymmetric angle-ply laminates are considered. The Navier method admits ss1 type boundary conditions for symmetric and antisymmetric cross-ply laminates. For antisymmetric angle-ply laminates ss2 type boundary conditions must be considered for employing the Navier method. The variables u_0, v_0, w, Q_x, Q_y can be written in terms of eigenfunctions satisfying the ss1 type boundary conditions (18) as follows:

$$\begin{aligned}
u_0&=\sum_{m=1}^{\infty}\sum_{n=1}^{\infty}U_{mn}(t)\cos\frac{m\pi x}{a}\sin\frac{n\pi y}{b},\\
v_0&=\sum_{m=1}^{\infty}\sum_{n=1}^{\infty}V_{mn}(t)\sin\frac{m\pi x}{a}\cos\frac{n\pi y}{b},\\
w&=\sum_{m=1}^{\infty}\sum_{n=1}^{\infty}W_{mn}(t)\sin\frac{m\pi x}{a}\sin\frac{n\pi y}{b},\\
Q_x&=\sum_{m=1}^{\infty}\sum_{n=1}^{\infty}Q_{xmn}(t)\cos\frac{m\pi x}{a}\sin\frac{n\pi y}{b},\\
Q_y&=\sum_{m=1}^{\infty}\sum_{n=1}^{\infty}Q_{ymn}(t)\sin\frac{m\pi x}{a}\cos\frac{n\pi y}{b}
\end{aligned} \tag{20}$$

in which m and n indicate the mode number. For ss2 type boundary conditions (19) the variables u_0, v_0 are to be considered differently as

$$\begin{aligned}
u_0&=\sum_{m=1}^{\infty}\sum_{n=1}^{\infty}U_{mn}(t)\sin\frac{m\pi x}{a}\cos\frac{n\pi y}{b},\\
v_0&=\sum_{m=1}^{\infty}\sum_{n=1}^{\infty}V_{mn}(t)\cos\frac{m\pi x}{a}\sin\frac{n\pi y}{b}.
\end{aligned} \tag{21}$$

In the same manner, the load function can also be expressed in the double Fourier series form as

$$p=\sum_{m=1}^{\infty}\sum_{n=1}^{\infty}P_{mn}(t)\sin\frac{m\pi x}{a}\sin\frac{n\pi y}{b} \tag{22}$$

where

$$P_{mn}(t)=\frac{4}{ab}\int_0^a\int_0^b p(x,y)\sin\frac{m\pi x}{a}\sin\frac{n\pi y}{b}dxdy.$$

Using Eq. (20) or (21), (16) and (17), the governing equilibrium Eqs. (11)–(15) are to be written in terms of the unknown coefficients U_{mn}, V_{mn}, W_{mn}, Q_{xmn}, and Q_{ymn} to obtain the Navier solutions for the laminated plates considered. It may also be observed from (6) that the values of λ_x and λ_y will be of the order of the elastic coefficients C_{55} and C_{44}. Hence the coefficients of inertia associated with $\partial\ddot{w}/\partial x$, $\partial\ddot{w}/\partial y$, $\ddot{Q}_x$, $\ddot{Q}_y$, $\partial\ddot{Q}_x/\partial x$ and $\partial\ddot{Q}_y/\partial y$ turn out to be negligibly small. Also, for symmetric and antisymmetric laminates I_1 and I_8 are zero. Thus the resulting governing equations can be expressed in the matrix form as

$$\begin{Bmatrix} I_0\ddot{U}_{mn} \\ I_0\ddot{V}_{mn} \\ I_5\ddot{W}_{mn} \\ 0 \\ 0 \end{Bmatrix} + \begin{bmatrix} K_{11} & K_{12} & K_{13} & K_{14} & K_{15} \\ K_{12} & K_{22} & K_{23} & K_{24} & K_{25} \\ K_{13} & K_{23} & K_{33} & K_{34} & K_{35} \\ K_{41} & K_{42} & K_{43} & K_{44} & K_{45} \\ K_{51} & K_{52} & K_{53} & K_{54} & K_{55} \end{bmatrix} \begin{bmatrix} U_{mn} \\ V_{mn} \\ W_{mn} \\ Q_{xmn} \\ Q_{ymn} \end{bmatrix} = \begin{Bmatrix} 0 \\ 0 \\ p_{mn} \\ 0 \\ 0 \end{Bmatrix}. \tag{23}$$

In which the elements of matrices will differ from one type of laminate to the other. In case of antisymmetric angle-ply laminates these are obtained as

$$K_{11}=(A_{11}\alpha^2+A_{66}\beta^2),\quad K_{12}=\alpha\beta(A_{12}+A_{66}),$$

$$K_{13}=-(3B_{16}\alpha^2\beta+B_{26}\beta^3),\quad K_{14}=\frac{2\alpha\beta}{\lambda_x}\left(\frac{3}{2h}B_{16}-\frac{2}{h^3}E_{16}\right),$$

$$K_{15}=\frac{1}{\lambda_y}\left[\left(\frac{3}{2h}B_{16}-\frac{2}{h^3}E_{16}\right)\alpha^2+\left(\frac{3}{2h}B_{26}-\frac{2}{h^3}E_{26}\right)\beta^2\right],$$

$$K_{22}=(A_{22}\beta^2+A_{66}\alpha^2),\quad K_{23}=-(3B_{26}\alpha\beta^2+B_{16}\alpha^3),$$

$$K_{24}=\frac{\lambda_y}{\lambda_x}K_{15},$$

$$K_{25}=\frac{2\alpha\beta}{\lambda_y}\left(\frac{3}{2h}B_{26}-\frac{2}{h^3}E_{26}\right),$$

$$K_{33}=D_{11}\alpha^4+2(D_{12}+2D_{66})\alpha^2\beta^2+D_{22}\beta^4,$$

$$K_{34}=-\frac{1}{\lambda_x}\left[\left(\frac{3}{2h}D_{11}-\frac{2}{h^3}F_{11}\right)\alpha^3+\left\{\left(\frac{3}{2h}D_{12}-\frac{2}{h^3}F_{12}\right)+\left(\frac{3}{2h}D_{66}-\frac{2}{h^3}F_{66}\right)\right\}\alpha\beta^2\right],$$

$$K_{35}=-\frac{1}{\lambda_y}\left[\left(\frac{3}{2h}D_{22}-\frac{2}{h^3}F_{22}\right)\alpha^3+\left\{\left(\frac{3}{2h}D_{12}-\frac{2}{h^3}F_{12}\right)+\left(\frac{3}{2h}D_{66}-\frac{2}{h^3}F_{66}\right)\right\}\alpha\beta^2\right],$$

$$K_{41}=\frac{2h\lambda_x}{3}K_{14},\quad K_{42}=\frac{2h\lambda_y}{3}K_{24},\quad K_{43}=\frac{2h\lambda_x}{3}K_{34},$$

$$K_{44}=\left[\frac{1}{\lambda_x}\left\{\left(\frac{3}{2h}D_{11}-\frac{4}{h^3}F_{11}+\frac{8}{3h^5}H_{11}\right)\alpha^2+\left(\frac{3}{2h}D_{66}-\frac{4}{h^3}F_{66}+\frac{8}{3h^5}H_{66}\right)\beta^2-\frac{6}{h^3}D_{55}+\frac{24}{h^5}F_{55}\right\}+1\right],$$

$$K_{45}=\frac{1}{\lambda_y}\left[\frac{3}{2h}(D_{12}+D_{66})-\frac{4}{h^3}(F_{12}+F_{66})+\frac{8}{3h^5}(H_{12}+H_{66})\right]\alpha\beta,$$

$$K_{51}=K_{42},\quad K_{52}=\frac{2h\lambda_y}{3}K_{25},\quad K_{53}=\frac{2h\lambda_y}{3}K_{35},\quad K_{54}=\frac{\lambda_y}{\lambda_x}K_{45},$$

$$K_{55}=\left[\frac{1}{\lambda_y}\left\{\left(\frac{3}{2h}D_{22}-\frac{4}{h^3}F_{22}+\frac{8}{3h^5}H_{22}\right)\beta^2+\left(\frac{3}{2h}D_{66}-\frac{4}{h^3}F_{66}+\frac{8}{3h^5}H_{66}\right)\alpha^2-\frac{6}{h^3}D_{44}+\frac{24}{h^5}F_{44}\right\}+1\right],$$

$$I_5=I_2(\alpha^2+\beta^2),\quad \alpha=\frac{m\pi}{a},\quad \beta=\frac{n\pi}{b}.$$

The stiffness parameters appearing in K_{ij} $(i,j=1,2,\ldots,5)$ are defined as

$$(A_{ij},B_{ij},D_{ij},E_{ij},F_{ij},H_{ij})=\sum_{k=1}^{N}\int_{h_k}^{h_{k+1}}C_{ij}^k(1,z,z^2,z^3,z^4,z^6)dz\quad(i,j=1,2,6). \tag{24}$$

Setting the inertia terms in Eq. (23) to zero, the solutions for static analysis can be obtained. For dynamic analysis, the mechanical load is set to zero and the periodic solutions of the unknown coefficients are assumed as

$$\begin{gathered} U_{mn}(t)=\overline{U}_{mn}e^{i\omega_{mn}t},\quad V_{mn}(t)=\overline{V}_{mn}e^{i\omega_{mn}t}, \\ W_{mn}(t)=\overline{W}_{mn}e^{i\omega_{mn}t}, \\ Q_{xmn}(t)=\overline{Q}_{xmn}e^{i\omega_{mn}t},\quad Q_{ymn}(t)=\overline{Q}_{ymn}e^{i\omega_{mn}t}, \end{gathered} \tag{25}$$

where $i=\sqrt{-1}$, ω_{mn} is the frequency of natural vibration associated with the mode (m,n) and $\overline{U}_{mn}$, $\overline{V}_{mn}$, $\overline{W}_{mn}$, $\overline{Q}_{xmn}$, and $\overline{Q}_{ymn}$ are the unknown amplitudes of vibration. In the absence of externally applied mechanical load, substitution of (25) into (23), leads to the following eigenvalue problem:

$$\left(\begin{bmatrix} \alpha_{11} & \alpha_{12} & \alpha_{13} \\ \alpha_{21} & \alpha_{22} & \alpha_{23} \\ \alpha_{31} & \alpha_{32} & \alpha_{33} \end{bmatrix} - \omega_{mn}^2 \begin{bmatrix} I_0 & 0 & 0 \\ 0 & I_0 & 0 \\ 0 & 0 & I_5 \end{bmatrix}\right) \begin{Bmatrix} \overline{U}_{mn} \\ \overline{V}_{mn} \\ \overline{W}_{mn} \end{Bmatrix} = \begin{Bmatrix} 0 \\ 0 \\ 0 \end{Bmatrix}. \tag{26}$$

The various coefficients appearing in Eq. (26) are given by

$$\alpha_{11}=K_{11}+q_{x1}K_{14}+q_{y1}K_{15},\quad \alpha_{12}=K_{12}+q_{x2}K_{14}+q_{y2}K_{15},$$

$$\alpha_{13}=K_{13}+q_{x3}K_{14}+q_{y3}K_{15},\quad \alpha_{21}=K_{12}+q_{x1}K_{24}+q_{y1}K_{25},$$

$$\alpha_{22}=K_{22}+q_{x2}K_{24}+q_{y2}K_{25},\quad \alpha_{23}=K_{23}+q_{x3}K_{24}+q_{y3}K_{25},$$

$$\alpha_{31}=K_{13}+q_{x1}K_{34}+q_{y1}K_{35},\quad \alpha_{32}=K_{23}+q_{x2}K_{34}+q_{y2}K_{35},$$

$$\alpha_{33}=K_{33}+q_{x3}K_{34}+q_{y3}K_{35},$$

in which

$$q_{xi}=\frac{K_{5i}K_{45}-K_{4i}K_{55}}{K_{44}K_{45}-K_{54}K_{45}},\quad q_{yi}=\frac{K_{5i}K_{44}-K_{4i}K_{54}}{K_{54}K_{45}-K_{44}K_{55}},\quad (i=1,2,3).$$

The eigenvalue problem given by Eq. (26) yields the natural frequency of the laminates associated with a particular mode (m,n).

4 Results and Discussion

Numerical results for both static and dynamic analysis using the zeroth-order shear deformation theory (ZSDT) developed here are evaluated for symmetric and antisymmetric cross-ply laminates and antisymmetric angle-ply laminates. Two materials are considered for evaluating the numerical results as follows:

Material 1: $E_L=172.9$ GPa, $E_T=E_L/25$, $G_{LT}=0.5E_T$, $G_{TT}=0.2E_T$, $\nu_{LT}=\nu_{TT}=0.25$

Material 2: $E_T=210$ GPa, $E_T=E_L/40$, $G_{LT}=0.6E_T$, $G_{TT}=0.5E_T$, $\nu_{LT}=\nu_{TT}=0.25$

where E_L and E_T are the longitudinal and transverse elastic modulus, G_{LT}, G_{LT} are the shear moduli, ν_{LT} is the major Poisson's ratio, and ν_{TT} is the minor Poisson's ratio with L and T signifying the directions parallel and perpendicular to the fiber direction, respectively.

4.1 Results for Static Analysis. For static analysis the plates are subjected to a sinusoidally distributed transverse load and is given by

Table 1 Center deflection and in-plane stresses of square cross-ply (0°/90°/0°) plates (Material 1)

a/h	Source	$\bar{w}\times 10^2$	$\bar{\sigma}_x$	$\bar{\sigma}_y$	$\bar{\sigma}_{xy}$
	ZSDT	1.922	0.735	0.528	0.050
4	FSDT	1.776	0.437	0.477	0.037
	ELS	1.920	0.755	0.534	0.051
	ZSDT	0.712	0.571	0.270	0.028
10	FSDT	0.669	0.513	0.254	0.025
	ELS	0.700	0.590	0.288	0.028
	ZSDT	0.511	0.547	0.205	0.023
20	FSDT	0.491	0.532	0.199	0.022
	ELS	0.520	0.552	0.210	0.023
	ZSDT	0.434	0.540	0.181	0.021
100	FSDT	0.434	0.538	0.180	0.021
	ELS	0.436	0.552	0.181	0.021

$$p(x,y)=q\sin\frac{\pi x}{a}\sin\frac{\pi y}{b} \tag{27}$$

in which q is the amplitude of the load. Accordingly, using $m=n=1$ and neglecting inertia of motion, Eq. (23) can be solved for evaluating the unknown coefficients U_{mn}, V_{mn}, W_{mn}, Q_{xmn}, and Q_{ymn}. Then using Eqs. (1), (2), (4), and (7), the center deflection and maximum stresses are computed. The following nondimensional parameters are used for reporting the results

$$\bar{w}=\frac{E_T h^3}{a^4 q}w(a/2,b/2,0),\quad \bar{\sigma}_x=\frac{h^2}{b^2 q}\sigma_x(a/2,b/2,\pm h/2),$$
$$\bar{\sigma}_y=\frac{h^2}{b^2 q}\sigma_y(a/2,b/2,\pm h/6),\quad \bar{\sigma}_{xy}=\frac{h^2}{b^2 q}\sigma_{xy}(0,0,\pm h/2). \tag{28}$$

Table 1 contains the nondimensionalized center deflection and maximum in-plane stresses for symmetric cross-ply (0°/90°/0°) square plates predicted with the ZSDT derived here. The table also contains the results obtained by a three-dimensional elasticity solution (ELS), [9], and the first-order shear deformation theory (FSDT), [10]. It may be observed from this table that the results obtained by the present zeroth-order shear deformation theory are in excellent agreement with the elasticity solutions. When compared with the elasticity solutions (ELS), ZSDT predicts more accurate results than the FSDT for both thick and thin laminates. The through thickness behavior of the plates are also examined with the ZSDT. Figures 2–4 illustrate the distribution of in-plane stresses across the thickness of a thick ($a/h=4$) simply supported (ss1) symmetric cross-ply (0°/90°/0°) square plate. Since the normal stresses are nonlinear across the thickness, it indicates that the ZSDT can predict warping of the cross section. Table 2 contains the numerical results for center deflection of antisymmetric cross-ply square plates of two and six orthotropic layers. The table also shows the prediction obtained with a HSDT, [6], and FSDT, [10]. It can be observed from this table, that the predictions by the ZSDT differ negligibly from that by the FSDT for both thick and thin antisymmetric cross-ply square plates. The center deflections of two and six layer antisymmetric simply supported (ss2) angle-ply $(\theta/-\theta/\ldots)$ square plates subjected to the sinusoidal loading have been predicted by the ZSDT for different fiber orientations (θ) and are presented in Table 3. The predictions for the same by the HSDT, [6], and FSDT, [10], are also given in Table 3 for the purpose of comparison. It can be observed that the ZSDT also predicts the deflection for antisymmetric angle-ply square plates with high accuracy.

4.2 Results for Dynamic Analysis. The accuracy of the present ZSDT is also investigated through free-vibration analysis of laminated composite plates. A nondimensional frequency parameter has been used for presenting the results as follows:

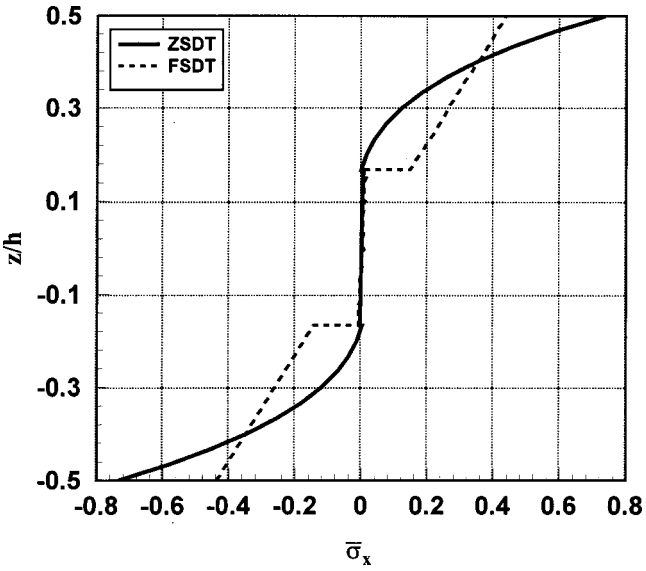

Fig. 2 Variation of in-plane normal stress σ_x across the thickness (Material 1)

$$\bar{\omega}_{mn}=\omega_{mn}\frac{a^2}{h}\sqrt{\frac{\rho}{E_T}}. \tag{29}$$

Table 4 contains the nondimensionalized fundamental frequencies $\bar{\omega}_{mn}$ of a simply supported (ss1) cross-ply laminated (0°/90°/90°/0°) square plate. The table also presents the results obtained by a HSDT, [11], and a closed-form solution, [12]. It may be observed from this table that the fundamental frequencies obtained using ZSDT are in excellent agreement with those obtained by the HSDT and closed-form solutions for $a/h\geq 10$. In case of very thick plate ($a/h=4$), the ZSDT slightly underestimates the predictions depicting further effect of transverse shear deformations. Table 5 displays the frequencies for higher modes of symmetric cross-ply (0°/90°/0°) square plates. In this case results are compared with those obtained by the FSDT, [10]. The comparison indicates that the ZSDT underpredicts the frequencies indicating the pronounced effect of transverse shear deformations on the

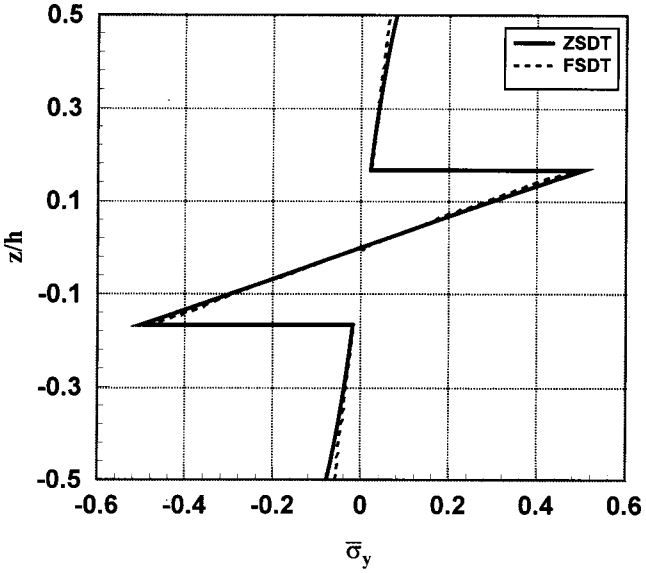

Fig. 3 Variation of in-plane normal stress σ_y across the thickness (Material 1)

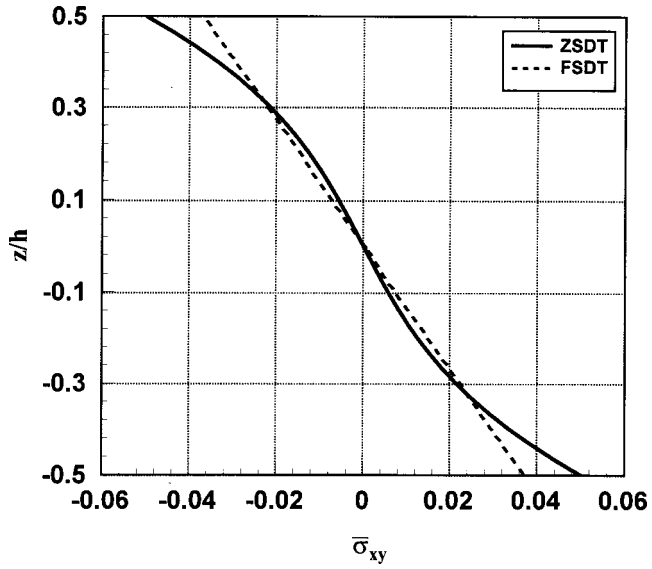

Fig. 4 Variation of in-plane shear stress σ_{xy} across the thickness (Material 1)

higher modes of vibration for thick plates. The fundamental natural frequencies of simply supported antisymmetric cross-ply square plates of two and eight orthotropic layers have been predicted by the ZSDT for thick and thin plates and different modulus ratios (E_1/E_2). These are presented in Table 6 and compared with the predictions by the FSDT, [10]. The results can be observed to be in very good agreement with that by the FSDT, [10]. Table 7 displays the fundamental natural frequencies of simply supported (ss2) antisymmetric angle-ply ($\theta/-\theta/\ldots$) square plates predicted by the present ZSDT, HSDT, [10], and FSDT, [10], for different fiber orientations and number of layers. Without exception, the results are found to be in excellent agreement. But when compared with the HSDT, [10], it may be noticed that the ZSDT is able to predict more pronounced effects of transverse shear deformations as it underestimates the results for very thick plates ($a/h=4$).

Table 2 Deflection of simply supported (ss1) antisymmetric square cross-ply laminated plate (Material 1)

		a/h			
N	Theory	4	10	20	100
	ZSDT	2.001	1.216	1.102	1.065
2	HSDT	1.998	1.216	1.102	1.065
	FSDT	2.149	1.237	1.107	1.065
	ZSDT	1.541	0.638	0.506	0.463
6	HSDT	1.541	0.638	0.506	0.463
	FSDT	1.547	0.635	0.505	0.463

Table 3 Center deflection of simply supported antisymmetric (ss2) angle-ply ($\theta/-\theta/\ldots$) laminated plate (Material 2)

		$\theta=5°$		$\theta=30°$		$\theta=45°$	
a/h	Theory	$N=2$	$N=6$	$N=2$	$N=6$	$N=2$	$N=6$
4	ZSDT	1.258	1.226	1.078	0.884	1.018	0.837
	HSDT	1.263	1.228	1.084	0.885	1.020	0.837
	FSDT	1.316	1.265	1.215	0.899	1.157	0.853
10	ZSDT	0.481	0.445	0.591	0.300	0.557	0.274
	HSDT	0.485	0.448	0.592	0.301	0.558	0.274
	FSDT	0.488	0.449	0.610	0.299	0.577	0.273
20	ZSDT	0.356	0.320	0.516	0.212	0.490	0.190
	HSDT	0.358	0.321	0.518	0.213	0.489	0.191
	FSDT	0.359	0.321	0.522	0.212	0.494	0.190
100	ZSDT	0.316	0.279	0.494	0.184	0.467	0.163
	HSDT	0.316	0.279	0.494	0.184	0.467	0.163
	FSDT	0.316	0.279	0.494	0.184	0.467	0.163

Table 4 Fundamental frequency of symmetric (0°/90°/90°/0°) square laminated plate (Material 2)

a/h	4	10	20	100
ZSDT	8.966	15.061	17.641	18.835
HSDT	9.261	15.090	17.630	18.830
Closed form solution	9.497	15.123	17.662	18.835

Conclusions

In this paper, a zeroth-order shear deformation theory for laminated composite plates have been derived. The following main points can be outlined from the investigations carried out in this paper.

Table 5 Natural frequencies for higher modes of cross-ply (0°/90°/0°) square plates (Material 1)

			a/h	
m	n	Theory	10	100
1	2	ZSDT	18.332	22.810
		FSDT	18.729	22.817
1	3	ZSDT	30.189	40.150
		FSDT	30.932	40.153
2	1	ZSDT	28.875	56.075
		FSDT	30.991	56.210
2	2	ZSDT	32.270	60.076
		FSDT	34.434	60.211
1	4	ZSDT	44.037	66.363
		FSDT	45.923	66.364
2	3	ZSDT	40.077	70.638
		FSDT	42.585	70.764

Table 6 Fundamental natural frequencies of simply supported antisymmetric (0°/90°/ . . .) cross-ply square plate (Material 1)

		$E_L/E_T=10$		$E_L/E_T=25$		$E_L/E_T=40$	
a/h	Theory	$N=2$	$N=8$	$N=2$	$N=8$	$N=2$	$N=8$
10	ZSDT	7.466	9.423	8.925	12.565	10.133	14.473
	FSDT	7.454	9.450	8.900	12.628	10.027	14.562
20	ZSDT	7.807	10.098	9.495	14.229	10.871	17.148
	FSDT	7.802	10.102	9.474	14.241	10.840	17.169
100	ZSDT	7.926	10.344	9.688	14.912	11.152	18.364
	FSDT	7.926	10.344	9.687	14.912	11.150	18.365

Table 7 Fundamental natural frequencies of simply supported antisymmetric (ss2) angle-ply ($\theta/-\theta/\ldots$) square plate (Material 2)

		$\theta=5$		$\theta=30$		$\theta=45$	
a/h	Theory	$N=2$	$N=6$	$N=2$	$N=6$	$N=2$	$N=6$
4	ZSDT	8.495	8.618	9.136	10.126	9.414	10.408
	HSDT	8.715	8.859	9.446	10.577	9.759	10.895
	FSDT	8.531	8.737	8.917	10.502	9.161	10.805
10	ZSDT	14.226	14.841	12.871	18.126	13.259	18.953
	HSDT	14.230	14.848	12.873	18.170	13.263	19.025
	FSDT	14.179	14.840	12.681	18.226	13.044	19.025
20	ZSDT	16.657	17.618	13.847	21.650	14.233	22.867
	HSDT	16.656	17.619	13.849	21.648	14.246	22.877
	FSDT	16.641	17.622	13.790	21.679	14.179	22.913
100	ZSDT	17.781	18.935	14.223	23.295	14.621	24.740
	HSDT	17.780	18.935	14.223	23.295	14.621	24.739
	FSDT	17.780	18.935	14.220	23.297	14.618	24.741

1. ZSDT can predict highly accurate results for both thick and thin laminated composite plates. For very thick plates ZSDT underestimates the results with close accuracy thus indicating the further effect of transverse shear deformations.

2. ZSDT incorporates the effect of transverse shear deformations through the direct use of the transverse shear stress resultants Q_x and Q_y.

3. As compared to FSDT, ZSDT does not require shear correction factors.

4. Although FSDT can produce acceptable responses for both thick and thin laminated composite plates, it does not satisfy the zero transverse shear stress condition on the top and bottom surfaces of the plates. But ZSDT satisfies this condition.

5. ZSDT is free from shear locking as its form approaches that of CLPT when applied to a thin plate.

Based on the above points it may be concluded that the present zeroth-order shear deformation theory appears to be a new addition to the equivalent single-layer shear deformation theories.

References

[1] Whitney, J. M., and Leissa, A. W., 1969, ''Analysis of Heterogeneous Anisotropic Plates,'' ASME J. Appl. Mech., **36**, pp. 261–266.

[2] Whitney, J. M., 1969, ''The Effect of Transverse Shear Deformation in the Bending of Laminated Plates,'' J. Compos. Mater., **3**, pp. 534–547.

[3] Lo, K. H., Christensen, R. M., and Wu, E. M., 1977, ''A High-Order Theory of Plate Deformation, Part 2: Laminated Plates,'' ASME J. Appl. Mech., **44**, pp. 669–676.

[4] Krishna Murthy, A. V., 1977, ''Higher Order Theory for Vibration of Thick Plates,'' AIAA J., **15**, pp. 1823–1824.

[5] Murthy, M. V. V., 1981, ''An Improved Transverse Shear Deformation Theory for Laminated Anisotropic Plates,'' NASA technical Paper 1903, pp. 1–37.

[6] Reddy, J. N., 1984, ''A Simple Higher-Order Theory for Laminated Composite Plates,'' ASME J. Appl. Mech., **51**, pp. 745–752.

[7] Reddy, J. N., 1990, ''A Review of Refined Theories of Laminated Composite plates,'' Shock Vib. Dig., **22**, pp. 3–17.

[8] Shimpi, R. C., 1998, ''Zeroth Order Shear Deformation Theory for Plates,'' AIAA J., **37**, pp. 524–526.

[9] Pagano, N. J., 1970, ''Exact Solutions for Rectangular Bi-directional Composites and Sandwich Plates,'' J. Compos. Mater., **4**, pp. 20–34.

[10] Reddy, J. N., 1997, *Mechanics of Laminated Composite Plates Theory and Analysis*, CRC Press, Boca Raton, FL.

[11] Mallikarjuna and Kant, T., 1989, ''Free Vibration of Symmetrically Laminated Plates Using a Higher Order Theory With Finite Element Technique,'' Int. J. Numer. Methods Eng., **28**, pp. 1875–1889.

[12] Noor, A. K., 1972, ''Free Vibration of Multi-Layered Composite Plates,'' AIAA J., **11**, pp. 1038–1039.

Refined First-Order Shear Deformation Theory Models for Composite Laminates

F. Auricchio
Dipartimento di Meccanica Strutturale,
Università di Pavia,
Via Ferrata 1,
27100 Pavia, Italy
e-mail: auricchio@unipv.it

E. Sacco
Dipartimento di Meccanica, Stuutture, A. & T.,
Università di Cassino,
Via Di Biasio 43,
03043 Cassino, Italy
e-mail: sacco@unicas.it

In the present work, new mixed variational formulations for a first-order shear deformation laminate theory are proposed. The out-of-plane stresses are considered as primary variables of the problem. In particular, the shear stress profile is represented either by independent piecewise quadratic functions in the thickness or by satisfying the three-dimensional equilibrium equations written in terms of midplane strains and curvatures. The developed formulations are characterized by several advantages: They do not require the use of shear correction factors as well as the out-of-plane shear stresses can be derived without post-processing procedures. Some numerical applications are presented in order to verify the effectiveness of the proposed formulations. In particular, analytical solutions obtained using the developed models are compared with the exact three-dimensional solution, with other classical laminate analytical solutions and with finite element results. Finally, we note that the proposed formulations may represent a rational base for the development of effective finite elements for composite laminates.
[DOI: 10.1115/1.1572901]

1 Introduction

The modeling of composite laminated structures is one of the most active research fields of the last decades, since accurate stress analyses are required to design structural parts of mechanical, naval, aeronautical, and aerospace, as well as civil constructions.

In fact, composite laminates present an anisotropic response, with extension-bending coupling and non-negligible shear deformations in the thickness. Furthermore, to prevent the development of the delamination, which strongly limit the performances of composites, [1], an accurate evaluation of the interlaminar out-of-plane stresses (i.e., the shear stress and the normal stress in the thickness direction at the interface between two adjacent laminae) is required.

Actually, several laminate models are available in the literature, [2]. In particular, two different approaches may be distinguished in the laminate modeling, which lead to two classes of laminate theories: the equivalent single-layer theories (ESLTs) and the layerwise theories (LWTs).

The ESLTs represent the direct extension of plate theories to laminates, so that the laminate is reduced to a single-layer plate with equivalent anisotropic material properties. In fact, the classical laminate theory (CLT), [3,4], is an extension of the classical plate theory based on Kirchhoff-Love assumptions, i.e., it neglects the shear deformation in the thickness of the laminate. The first-order shear deformation theory (FSDT) is an extension of the Reissner, [5], and Mindlin, [6], plate models to the case of laminated anisotropic plates. The FSDT presented in Refs. [7,8] allows the determination of satisfactory solutions for a wide class of laminate problems. In particular, accurate results are obtained if proper values of the shear correction factors are adopted. Unfortunately, the exact values of the shear correction factors are known a priori only for very simple cases, [9]. To overcome this difficulty, two different approaches can be found in literature. The first approach consists in the development of iterative predictor-corrector techniques, as proposed by Noor and co-workers, [10–12]. Numerical procedures, developed within the finite element method, were proposed in Refs. [13,14], where new effective laminate elements were presented. The second approach is based on the refinement of the FSDT model, e.g., see Refs. [15,16]. Within this context, Rolfes and Rohwer [17] and Rolfes [18] proposed an improved composite finite element based on FSDT, which does not need the computation of the shear correction factors. They computed the transverse shear stresses from equilibrium equations and they were able to determine a priori the shear profile introducing suitable simplifications, i.e., neglecting the presence of membrane forces and assuming two simultaneous cylindrical bending modes.

Several higher-order shear deformation theories were developed in the literature, [19,20], within the ESLTs; they consider higher-order terms of the thickness coordinate in the representation form of the displacements.

The LWTs are obtained assuming independent shear deformation within each laminate layer, [21–25], so that the displacement field is continuous in the thickness, while the transverse shear strain can be discontinuous along the out-of-plane coordinate. The unknown functions for the LWTs depend on the number of layers in the laminate. A layerwise finite element formulation, which can be implemented in FEA commercial codes, was proposed in Ref. [26]; therein, Barbero discretized each layer in displacement-based three-dimensional elements with two-dimensional kinematic constraints.

The zig-zag theories are deduced from the LWT enforcing the continuity of the out-of-plane shear stresses; thus, the number of unknowns in the zig-zag theories do not depend on the number of layers, [27–30]. In particular, Carrera [30] developed multilayer and zig-zag theories in the framework of the Reissner mixed variational theorem.

Among the several laminate theories, the FSDT appears simple and efficient for many structural problems. In fact, as emphasized above, FSDT is able to predict the response of laminates with satisfactory approximations for most structural problems. On the other hand, finite element commercial codes, mainly based on displacement formulations, requires as input data the values of the shear correction factors. Moreover, the displacement formulations

Contributed by the Applied Mechanics Division of THE AMERICAN SOCIETY OF MECHANICAL ENGINEERS for publication in the ASME JOURNAL OF APPLIED MECHANICS. Manuscript received by the ASME Applied Mechanics Division, March 3, 2002; final revision, October 4, 2002. Associate Editor: M.-J. Pindera. Discussion on the paper should be addressed to the Editor, Prof. Robert M. McMeeking, Department of Mechanical and Environmental Engineering University of California–Santa Barbara, Santa Barbara, CA 93106-5070, and will be accepted until four months after final publication of the paper itself in the ASME JOURNAL OF APPLIED MECHANICS.

 Copyright © 2003 by ASME

of plates and laminate theories are able to recover satisfactory values for the in-plane stresses, while out-of-plane shear and normal stresses are obtained after manipulations of the in-plane results by post-processing the solution, [13,14,31,32]. Post-processing techniques are generally simple and often efficient. Within finite element formulation the use of these techniques is not always straightforward. In fact, the determination of the shear stresses from equilibrium equations requires the computation of the in-plane stress (resultant axial forces and bending moments) derivatives. This can be accomplished developing mixed formulations, or displacement-based laminate finite elements characterized by high-degree polynomial interpolation functions, [13]. The stress derivatives can be also computed performing regularization of the extensional and flexural strain, [14]. The so-called extended two-dimensional method presented by Rolfes et al. [32] does not requires the computation of the stress derivatives; in fact, the assumption of neglecting the membrane forces and of considering the presence of two simultaneous cylindrical bending simplify the laminate equations, so that the bending moment derivatives are equal to the resultant shear stresses.

Furthermore, it can be emphasized that the FSDT allows to determine satisfactory values for the in-plane and out-of-plane stresses. Thus, once the most stressed zones of the laminate are determined using the FSDT, layerwise or zig-zig theories can be adopted in these zone to investigate on the possible delamination and failure.

Aim of the present paper is the development of suitable and viable laminate models based on the equivalent single layer theory. In particular, refined FSDT models, based on new partial mixed formulations, are developed, without introducing any simplification on the laminate problem.

The following features characterize the proposed approach:

- It does not need shear correction factors.
- It does not need to post-process the in-plane solution to get out-of-plane shear stresses.
- It may represent the basis for the development of new and efficient laminate finite elements.

The proposed approach is based on a variational formulation that considers the out-of-plane shear stresses as primarily variables of the problem. A new approach is proposed; in fact, the shear stress profile introduced in the partial mixed functional is obtained considering new independent variables or it is deduced from the three-dimensional local equilibrium equations. In fact, the explicit expression of the shear stresses is obtained by integrating the first two equilibrium equations with respect to the thickness direction. Thus, the shear stresses are expressed as functions of the in-plane stresses, which can be written as functions either of the in-plane strains or of the displacement and rotation fields. Hence, several formulations are obtained. In order to assess the performances of the proposed models, analytical solutions are determined for the proposed models. It can be emphasized that analytical solutions are available only for special cases; in fact, simply supported rectangular cross-ply and angle-ply laminates are considered within the paper. The solutions computed for the proposed models are compared with the exact three-dimensional solution, [33], with other classical laminate analytical solutions, [2], and with finite element results, [13].

In the following the subscript comma indicates the partial derivative $f_{,\alpha}=\partial f/\partial x_\alpha$ and $f_{,z}=\partial f/\partial z$.

2 First-Order Shear Deformation Theory (FSDT) Laminate Model

A laminate plate Ω refers to a flat body, with constant thickness h:

$$\Omega=\left\{(x_1,x_2,z)\in\mathcal{R}^3/z\in\left(-\frac{h}{2},\frac{h}{2}\right),(x_1,x_2)\in\mathcal{A}\subset\mathcal{R}^2\right\} \quad (1)$$

where the plane $z=0$ identifies the midplane $\mathcal{A}$ of the undeformed plate. The laminate is made of n layers and the typical kth layer lies between the thickness coordinates $z=z_k$ and $z=z_{k+1}$, such that $z_1=-h/2$ and $z_{n+1}=h/2$.

The first-order shear deformation theory can be obtained introducing suitable assumptions on both the strain and the stress fields defined in the three-dimensional continuous body Ω, as emphasized in [34] for the case of homogeneous plates. In fact, the FSDT for laminated plates is based on the following well-known assumptions, [35]:

1. The through-the-thickness transverse normal stress is nil, i.e., $\sigma_{zz}=0$.
2. Straight lines perpendicular to the midplane cannot be stretched, i.e., $\varepsilon_{zz}=0$.
3. Straight lines perpendicular to the midplane remain straight after deformation, i.e., $\varepsilon_{1z,z}=\varepsilon_{2z,z}=0$.

Displacement Field. The kinematics is restrained to satisfy the following conditions:

$$\varepsilon_{zz}=0 \quad \varepsilon_{1z,z}=\varepsilon_{2z,z}=0 \quad (2)$$

which leads to the classical representation form for the displacement field:

$$\mathbf{s}(x_1,x_2,z)=\mathbf{u}(x_1,x_2)+z\boldsymbol{\varphi}(x_1,x_2)$$
$$s_z(x_1,x_2,z)=w(x_1,x_2) \quad (3)$$

where

$$\mathbf{s}=\begin{Bmatrix}s_1\\s_2\end{Bmatrix} \quad \mathbf{u}=\begin{Bmatrix}u_1\\u_2\end{Bmatrix} \quad \boldsymbol{\varphi}=\begin{Bmatrix}\varphi_1\\\varphi_2\end{Bmatrix} \quad (4)$$

with $\mathbf{u}$ and $\boldsymbol{\varphi}$ the vectors of the midplane membrane displacements and rotations, respectively.

Strain Field. Denoting by ε_{ij} the typical component of the strain tensor, the in-plane strain vector $\boldsymbol{\varepsilon}=\{\varepsilon_{11}\ \varepsilon_{22}\ 2\varepsilon_{12}\}^T$, associated to the displacement representation (3), is written as

$$\boldsymbol{\varepsilon}=\mathbf{e}+z\boldsymbol{\kappa} \quad (5)$$

where the membrane strain vector $\mathbf{e}$ and the curvature strain vector $\boldsymbol{\kappa}$ are given by

$$\mathbf{e}=\mathbf{L}\mathbf{u} \quad \boldsymbol{\kappa}=\mathbf{L}\boldsymbol{\varphi} \quad \mathbf{L}=\begin{bmatrix}\dfrac{\partial}{\partial x_1} & 0\\ 0 & \dfrac{\partial}{\partial x_2}\\ \dfrac{\partial}{\partial x_2} & \dfrac{\partial}{\partial x_1}\end{bmatrix}. \quad (6)$$

The in-plane strain vector $\boldsymbol{\varepsilon}$ is a linear function of the thickness coordinate z.

The out-of-plane strain field vector $\boldsymbol{\gamma}=\{2\varepsilon_{1z}\ 2\varepsilon_{2z}\}^T$ is obtained as

$$\boldsymbol{\gamma}=\nabla w+\boldsymbol{\varphi} \quad (7)$$

where the symbol ∇ indicates the gradient operator.

Stress Field. The in-plane stresses within each lamina of the composite laminate are computed using the constitutive relationships. In particular, it is assumed that the body Ω is obtained assembling in a staking sequence orthotropic layers, with $z=0$ representing a plane of material symmetry. Thus, denoting by σ_{ij} the typical component of the stress tensor, the in-plane stress vector $\boldsymbol{\sigma}^k=\{\sigma_{11}^k\ \sigma_{22}^k\ \sigma_{12}^k\}^T$ for the kth lamina is given by

$$\boldsymbol{\sigma}^k=\mathbf{C}^k\boldsymbol{\varepsilon}=\mathbf{C}^k(\mathbf{e}+z\boldsymbol{\kappa}) \quad (8)$$

where $\mathbf{C}^k$ is the so-called reduced in-plane constitutive elastic matrix associated to the kth lamina. Note that $\mathbf{C}^k$ is derived from

the three-dimensional constitutive matrix, enforcing the condition 1, i.e., $\sigma_{zz}=0$, [34]. Since each lamina of the laminate presents different elastic properties, the in-plane stress vector $\boldsymbol{\sigma}$ is a discontinuous piecewise linear function of the coordinate z.

The out-of-plane shear stress vector $\boldsymbol{\theta}^k=\{\theta^k_{1z}\ \theta^k_{2z}\}^T$ can be evaluated through constitutive equation as

$$\boldsymbol{\theta}^k=\mathbf{Q}^k\gamma \tag{9}$$

where $Q^k_{\alpha\beta}=\chi_{\alpha\beta}\tilde{Q}^k_{\alpha\beta}$ with $\alpha,\beta=1,2$. Note that $\tilde{Q}^k_{\alpha\beta}$ are the components of the shear elastic matrix of the kth lamina and $\chi_{\alpha\beta}$ are the shear correction factors. As it is well known, the transverse shear stress vector computed by formula (9) is absolutely unsatisfactory; in fact, formula (9) leads to a transverse shear stress field which is not equilibrated at the interfaces of adjacent laminae and it does not satisfy the boundary conditions on the top and on the bottom of the laminate.

A satisfactory field for the out-of-plane shear stress vector $\boldsymbol{\tau}=\{\tau^k_{1z}\ \tau^k_{2z}\}^T$ can be recovered using the equilibrium equations; in the following no body forces and no tangential surface forces on the top and bottom of the laminate are considered; thus, the equilibrium equations give

$$\boldsymbol{\tau}=-\int_{-h/2}^{z}\mathbf{L}^T\boldsymbol{\sigma}d\varsigma, \tag{10}$$

i.e., in components

$$\tau_{\alpha z}=-\int_{-h/2}^{z}(\sigma_{\alpha 1,1}+\sigma_{\alpha 2,2})d\varsigma \quad \text{with} \quad \alpha=1,2. \tag{11}$$

Note that, according to formula (11), it implicitly results $\boldsymbol{\tau}(-h/2)=\mathbf{0}$; the further boundary condition $\boldsymbol{\tau}(h/2)=\mathbf{0}$ has also to be satisfied.

Once the shear stresses in the laminate thickness are determined, the transverse normal stress, which is very important for the delamination failure, can be determined adopting a post-processing method, i.e., by integrating with respect to z the third equilibrium equation:

$$\sigma_{zz}=-\int_{-h/2}^{z}(\tau_{1z,1}+\tau_{2z,2})d\varsigma. \tag{12}$$

It can be emphasized that the in-plane strain components (5) are linear functions of the z thickness coordinate, so that the in-plane stresses (8) are piecewise linear functions of z. As a consequence, the transverse shear stresses computed by the equilibrium Eq. (10) are piecewise quadratic functions. Since the piecewise quadratic shear stress profiles computed by Eq. (10) are widely recognized as the best transverse shear stresses evaluation, within the FSDT model, it can be assumed as basis for the model construction the condition that the through-the-thickness shear stresses $\sigma_{\alpha z}$ are continuous piecewise quadratic functions of the z-coordinate.

A classical problem arising in conjunction with the use of the FSDT is the determination of the shear factors χ_{11}, χ_{22}, and χ_{12} appearing in the matrix $\mathbf{Q}^k$ of Eq. (9). Denoting by $\mathcal{E}^\tau$ and $\mathcal{E}^\theta$ the complementary shear energies in the thickness obtained considering the $\boldsymbol{\tau}$ and $\boldsymbol{\theta}$ shear profiles, respectively, characterized by the same resultant shear stress, the shear correction factors are determined enforcing $\mathcal{E}^\tau=\mathcal{E}^\theta$. The exact values of χ_{11}, χ_{22}, and χ_{12} can be evaluated analytically only for special cases. In particular, Whitney [9] derived an analytical formula of the shear correction factor for the case of cross-ply laminates in cylindrical bending. For a more general case, it is possible to evaluate the shear correction factors developing an iterative procedure. This can be based on the determination of the displacement solution, of in-plane stresses computation via constitutive equations, of the equilibrated shear stresses, of the complementary shear energies and, finally, of new shear correction factors which are adopted to compute a new solution, and so on, [13].

3 Variational Formulation

A mixed functional for the three-dimensional laminate-like body Ω is now considered:

$$H(\mathbf{u},w,\boldsymbol{\varphi},\mathbf{e},\boldsymbol{\kappa},\boldsymbol{\gamma},\boldsymbol{\sigma},\boldsymbol{\tau})=H^{mb}(\mathbf{u},\boldsymbol{\varphi},\mathbf{e},\boldsymbol{\kappa},\boldsymbol{\sigma})+H^s(w,\boldsymbol{\varphi},\boldsymbol{\gamma},\boldsymbol{\tau})-\Pi_{\text{ext}} \tag{13}$$

where H^{mb} is a Hu-Washizu functional accounting for the membrane-bending terms, H^s is a Prange-Hellinger-Reissner functional accounting for the transverse shear terms and Π_{ext} accounts for the boundary conditions and loading forces.

In particular, the membrane-bending functional H^{mb} and the transverse shear functional H^s are written as

$$H^{mb}(\mathbf{u},\boldsymbol{\varphi},\mathbf{e},\boldsymbol{\kappa},\boldsymbol{\sigma})=\frac{1}{2}\int_\Omega(\mathbf{e}+z\mathbf{k})^T\mathbf{C}(\mathbf{e}+z\boldsymbol{\kappa})dv + \int_\Omega[(\mathbf{L}\mathbf{u}-\mathbf{e})+z(\mathbf{L}\boldsymbol{\varphi}-\boldsymbol{\kappa})]^T\boldsymbol{\sigma}dv \tag{14}$$

$$H^s(w,\boldsymbol{\varphi},\boldsymbol{\tau})=\int_\Omega(\nabla w+\boldsymbol{\varphi})^T\boldsymbol{\tau}dv-\frac{1}{2}\int_\Omega\boldsymbol{\tau}^T\mathbf{T}\boldsymbol{\tau}dv \tag{15}$$

where $\mathbf{T}^k=(\mathbf{Q}^k)^{-1}$ is the shear compliance matrix of the kth layer.

Performing the integration along the thickness coordinate, the membrane-bending mixed functional (14) takes the form

$$\tilde{H}^{mb}(\mathbf{u},\boldsymbol{\varphi},\mathbf{e},\boldsymbol{\kappa},\mathbf{N},\mathbf{M})=\frac{1}{2}\int_{\mathcal{A}}(\mathbf{e}^T\mathbf{A}\mathbf{e}+2\mathbf{e}^T\mathbf{B}\boldsymbol{\kappa}+\boldsymbol{\kappa}^T\mathbf{D}\boldsymbol{\kappa})dA + \int_{\mathcal{A}}\{[(\mathbf{L}\mathbf{u})-\mathbf{e}]^T\mathbf{N}+[(\mathbf{L}\boldsymbol{\varphi})-\boldsymbol{\kappa}]^T\mathbf{M}\}dA. \tag{16}$$

The matrices $\mathbf{A}$, B, and $\mathbf{D}$ represent the membrane, the membrane-bending coupling and the bending elastic stiffness matrices of a n layer laminate, respectively, defined by equations

$$\mathbf{A}=\sum_{k=1}^{n}\mathbf{C}^k(z_{k+1}-z_k) \tag{17}$$

$$\mathbf{B}=\frac{1}{2}\sum_{k=1}^{n}\mathbf{C}^k(z^2_{k+1}-z^2_k) \tag{18}$$

$$\mathbf{D}=\frac{1}{3}\sum_{k=1}^{n}\mathbf{C}^k(z^3_{k+1}-z^3_k). \tag{19}$$

Moreover, the resultant membrane force and bending moment vectors, $\mathbf{N}$ and $\mathbf{M}$, are defined as

$$\mathbf{N}=\int_{-h/2}^{h/2}\boldsymbol{\sigma}dz \quad \mathbf{M}=\int_{-h/2}^{h/2}z\boldsymbol{\sigma}dz. \tag{20}$$

Because of the constitutive Eqs. (8), taking into account the definitions (17), (18), and (19), it results:

$$\mathbf{N}=\mathbf{A}\mathbf{e}+\mathbf{B}\boldsymbol{\kappa} \quad \mathbf{M}=\mathbf{B}\mathbf{e}+\mathbf{D}\boldsymbol{\kappa}. \tag{21}$$

Hence, the mixed functional (13) for the laminate can be written in terms of the introduced resultant forces and bending moments as

$$\tilde{H}(\mathbf{u},w,\boldsymbol{\varphi},\mathbf{e},\boldsymbol{\kappa},\boldsymbol{\gamma},\mathbf{N},\mathbf{M},\boldsymbol{\tau})=\tilde{H}^{mb}(\mathbf{u},\boldsymbol{\varphi},\mathbf{e},\boldsymbol{\kappa},\mathbf{N},\mathbf{M}) + H^s(w,\boldsymbol{\varphi},\boldsymbol{\gamma},\boldsymbol{\tau})-\Pi_{\text{ext}}. \tag{22}$$

A full displacement formulation of the membrane-bending functional $\tilde{H}^{mb}$ is recovered, implicitly satisfying the resultant constitutive laws (21) and the compatibility Eqs. (6):

$$\mathcal{E}^{mb}(\mathbf{u},\boldsymbol{\varphi})=\frac{1}{2}\int_{\mathcal{A}}[(\mathbf{Lu})^T\mathbf{ALu}+2(\mathbf{Lu})^T\mathbf{BL}\boldsymbol{\varphi}+(\mathbf{L}\boldsymbol{\varphi})^T\mathbf{DL}\boldsymbol{\varphi}]dA. \tag{23}$$

It can be emphasized that different laminate models can be recovered depending on the expression considered for the through-the-thickness shear stress. In particular, two classes of models are herein considered:

- The shear stress profile are approximated introducing independent variables.
- The shear stress profile are written as function of the midplane strains and curvatures using the equilibrium Eqs. (10).

In the following, four variational formulations of the laminate problem are derived, considering different representation forms of the out-of-plane shear stress vector.

4 Independent Approximation of the Shear Stresses

The first refined model, denoted in the following as RM1, is derived considering independent approximations of the shear stresses. In fact, the shear stress profile is represented as a continuous piecewise quadratic function in the thickness, satisfying the boundary conditions. Hence, within the kth layer, it is assumed

$$\boldsymbol{\tau}^k=\mathbf{t}_o^k\frac{z_{k+1}-z}{z_{k+1}-z_k}+\mathbf{t}_o^{k+1}\frac{z-z_k}{z_{k+1}-z_k}-\mathbf{t}^k(z_{k+1}-z)(z-z_k) \tag{24}$$

with $\mathbf{t}_o^1=\mathbf{t}_o^{n+1}=\mathbf{0}$. In the formula (24) $\mathbf{t}_o^k$ represents the shear stress vector at the interface between the layers $k-1$ and k, while $\mathbf{t}^k$ gives the curvature profile of the shear stress in kth layer.

Introducing the representation formula (24) in the transverse shear energy (15), it applies

$$\begin{aligned}\tilde{H}^s=&-\frac{1}{2}\int_{\mathcal{A}}\sum_{k=1}^{n}\left[(\mathbf{R}^k\mathbf{t}_o^k)^T\mathbf{t}_o^k+(\mathbf{R}^k\mathbf{t}_o^{k+1})^T\mathbf{t}_o^k-(\tilde{\mathbf{R}}^k\mathbf{t}^k)^T\mathbf{t}_o^k\right]dA\\&+-\frac{1}{2}\int_{\mathcal{A}}\sum_{k=1}^{n}\left[(\mathbf{R}^k\mathbf{t}_o^{k+1})^T\mathbf{t}_o^{k+1}-(\tilde{\mathbf{R}}^k\mathbf{t}^k)^T\mathbf{t}_o^{k+1}\right]dA\\&+-\frac{1}{2}\int_{\mathcal{A}}\sum_{k=1}^{n}[(\hat{\mathbf{R}}^k\mathbf{t}^k)^T\mathbf{t}^k]dA+\int_{\mathcal{A}}(\nabla w\\&+\boldsymbol{\varphi})^T\sum_{k=1}^{n}\frac{z_{k+1}-z_k}{2}\left(\mathbf{t}_o^k+\mathbf{t}_o^{k+1}-\mathbf{t}^k\frac{(z_{k+1}-z_k)^2}{3}\right)dA\end{aligned} \tag{25}$$

where

$$\mathbf{R}^k=\frac{z_{k+1}-z_k}{3}\mathbf{T}^k\quad\tilde{\mathbf{R}}^k=\frac{(z_{k+1}-z_k)^3}{6}\mathbf{T}^k\quad\hat{\mathbf{R}}^k=\frac{(z_{k+1}-z_k)^5}{30}\mathbf{T}^k. \tag{26}$$

Finally, the mixed functional (22) takes the form

$$\begin{aligned}&\hat{H}(\mathbf{u},w,\boldsymbol{\varphi},\mathbf{e},\boldsymbol{\kappa},\mathbf{N},\mathbf{M},\mathbf{t}_o^2,..,\mathbf{t}_o^n,\mathbf{t}^1,..,\mathbf{t}^n)\\&\quad=\tilde{H}^{mb}(\mathbf{u},\boldsymbol{\varphi},\mathbf{e},\boldsymbol{\kappa},\mathbf{N},\mathbf{M})+\hat{H}^s(w,\boldsymbol{\varphi},\mathbf{t}_o^2,..,\mathbf{t}_o^n,\mathbf{t}^1,..,\mathbf{t}^n)-\Pi_{\text{ext}}.\end{aligned} \tag{27}$$

The number of the unknowns in the FSDT refined model RM1 depends on the number of layers. Since the transverse shear stress profile does not depend on the in-plane stresses, the membrane and bending terms can be written adopting a full displacement approach functional, substituting $\tilde{H}^{mb}$ with $\mathcal{E}^{mb}$ in Eq. (27).

The presented approach leads to serious drawbacks. In fact, the stationary condition of the mixed functional (22) with respect to the shear stress τ gives

$$0=\partial_\tau H^s(w,\boldsymbol{\varphi},\boldsymbol{\tau})=\int_\Omega(\nabla w+\boldsymbol{\varphi})^T\delta\boldsymbol{\tau}dv-\frac{1}{2}\int_\Omega\boldsymbol{\tau}^T\mathbf{T}\delta\boldsymbol{\tau}dv \tag{28}$$

i.e., $\mathbf{T}^k\boldsymbol{\tau}^k=\nabla w+\boldsymbol{\varphi}$; thus, Eq. (28) represents the complementary constitutive equation written in variational form. Because of the displacement representation form (3) for the FSDT, the second term of Eq. (28) is constant in the thickness, so that the shear stress vector τ is enforced to be piecewise constant in the thickness. When the stress τ is represented by formula (24), the variational Eq. (28) enforces the constitutive law in approximated form; enlarging the space of the shear parameters $\mathbf{t}_o^2,..,\mathbf{t}_o^n,\mathbf{t}^1,..,\mathbf{t}^n$, i.e., increasing the number of independent parameters defining the stress $\boldsymbol{\tau}$ given by formula (24), the constitutive Eq. (28) tends to be enforced in a stronger manner, so that the shear stress profile tends to become piecewise constant in the laminate thickness.

5 Equilibrated Shear Stress

5.1 Shear Stress Computation. The out-of-plane shear stress $\boldsymbol{\tau}$, computed using the equilibrium Eqs. (10), is a continuous piecewise quadratic function of the thickness coordinate; thus, the transverse shear stress $\boldsymbol{\tau}^k$ at the kth lamina is given by

$$\boldsymbol{\tau}^k(z)=-\int_{z_k}^{z}\mathbf{L}^T\boldsymbol{\sigma}^k d\varsigma+\boldsymbol{\tau}_o^k \tag{29}$$

where $\boldsymbol{\tau}_o^k$ is the stress evaluated at $z=z_k$:

$$\boldsymbol{\tau}_o^k=-\int_{-h/2}^{z_k}\mathbf{L}^T\boldsymbol{\sigma}d\varsigma. \tag{30}$$

Substituting the expression (8) into the formula (30) gives

$$\boldsymbol{\tau}_o^k=-\int_{-h/2}^{z_k}\mathbf{L}^T\mathbf{C}(\mathbf{e}+\varsigma\boldsymbol{\kappa})d\varsigma=-\mathbf{L}^T(\hat{\mathbf{A}}^k\mathbf{e}+\hat{\mathbf{B}}^k\boldsymbol{\kappa}) \tag{31}$$

with

$$\hat{\mathbf{A}}^k=\sum_{i=1}^{k-1}\mathbf{C}^i(z_{i+1}-z_i)\quad\hat{\mathbf{B}}^k=\frac{1}{2}\sum_{i=1}^{k-1}\mathbf{C}^i(z_{i+1}^2-z_i^2). \tag{32}$$

Then, taking into account expressions (8) and (31) and performing the integration in the thickness, the out-of-plane shear stress $\boldsymbol{\tau}^k$ (29) becomes

$$\begin{aligned}\boldsymbol{\tau}^k(z)&=-\mathbf{L}^T\left[(z-z_k)\mathbf{C}^k\mathbf{e}+\frac{1}{2}(z^2-z_k^2)\mathbf{C}^k\boldsymbol{\kappa}\right]-\mathbf{L}^T(\hat{\mathbf{A}}^k\mathbf{e}+\hat{\mathbf{B}}^k\boldsymbol{\kappa})\\&=-\mathbf{L}^T(\mathbf{A}^k(z)\mathbf{e}+\mathbf{B}^k(z)\boldsymbol{\kappa})\end{aligned} \tag{33}$$

where

$$\begin{aligned}\mathbf{A}^k(z)&=(z-z_k)\mathbf{C}^k+\hat{\mathbf{A}}^k\\\mathbf{B}^k(z)&=\frac{1}{2}(z^2-z_k^2)\mathbf{C}^k+\hat{\mathbf{B}}^k.\end{aligned} \tag{34}$$

Moreover, in order to satisfy the boundary condition $\boldsymbol{\tau}(h/2)=\mathbf{0}$ exactly, the formula (33) is enhanced by adding a linear term which is zero at $z=-h/2$:

$$\boldsymbol{\tau}^k(z)=-\mathbf{L}^T(\mathbf{A}^k(z)\mathbf{e}+\mathbf{B}^k(z)\boldsymbol{\kappa})+\mathbf{a}\left(z+\frac{1}{2}h\right). \tag{35}$$

The vector $\mathbf{a}$ is evaluated enforcing the boundary condition:

$$\mathbf{0}=\boldsymbol{\tau}^n(h/2)=-\mathbf{L}^T(\mathbf{Ae}+\mathbf{B}\boldsymbol{\kappa})+\mathbf{a}h \tag{36}$$

where $\mathbf{A}^n(h/2)=\mathbf{A}$ and $\mathbf{B}^n(h/2)=\mathbf{B}$ are the membrane and membrane-bending coupling elastic matrices of the laminate defined by Eqs. (17) and (18), respectively. Solving Eq. (36) with respect to the vector $\mathbf{a}$, we obtain

$$\mathbf{a}=\frac{1}{h}\mathbf{L}^T(\mathbf{A}\mathbf{e}+\mathbf{B}\boldsymbol{\kappa}). \tag{37}$$

Substituting expression (37) into formula (35), the out-of-plane shear stress $\boldsymbol{\tau}^k$ takes the form

$$\boldsymbol{\tau}^k(z)=-\mathbf{L}^T\left\{\left[\mathbf{A}^k(z)-\frac{1}{h}\left(z+\frac{1}{2}h\right)\mathbf{A}\right]\mathbf{e}+\left[\mathbf{B}^k(z)-\frac{1}{h}\left(z+\frac{1}{2}h\right)\mathbf{B}\right]\boldsymbol{\kappa}\right\}. \tag{38}$$

A suitable form for the expression of the out-of-plane shear stress $\boldsymbol{\tau}^k$, useful for the next developments, is proposed. In fact, the formula (38) can be rewritten in the following equivalent form:

$$\boldsymbol{\tau}^k(z)=-\mathbf{L}^T[(\mathbf{A}^{k(0)}+z\mathbf{A}^{k(1)})\mathbf{e}+(\mathbf{B}^{k(0)}+z\mathbf{B}^{k(1)}+z^2\mathbf{B}^{k(2)})\boldsymbol{\kappa}] \tag{39}$$

where

$$\mathbf{A}^{k(0)}=\hat{\mathbf{A}}^k-z_k\mathbf{C}^k-\frac{1}{2}\mathbf{A}\quad \mathbf{A}^{k(1)}=\mathbf{C}^k-\frac{1}{h}\mathbf{A} \tag{40}$$

$$\mathbf{B}^{k(0)}=\hat{\mathbf{B}}^k-\frac{1}{2}z_k^2\mathbf{C}^k-\frac{1}{2}\mathbf{B}\quad \mathbf{B}^{k(1)}=-\frac{1}{h}\mathbf{B}\quad \mathbf{B}^{k(2)}=\frac{1}{2}\mathbf{C}^k. \tag{41}$$

Next, several refined FSDT laminate formulations, based on the use of equilibrated shear stresses, are derived.

5.2 Refined Model RM2. The FSDT refined model RM2 is deduced substituting the expression (39) of the transverse shear stress vector $\boldsymbol{\tau}$, obtained from the three-dimensional equilibrium equations, into the mixed shear functional $\tilde{H}^s$ defined in (15). Thus,

$$\begin{aligned}\overline{\tilde{H}}^s=&\int_{\mathcal{A}}\sum_{k=1}^{n}\left\{\frac{1}{2}\mathbf{T}^k\mathbf{L}^T\mathbf{X}^{k(0)}\mathbf{e}+\mathbf{T}^k\mathbf{L}^T\mathbf{Y}^{k(0)}\boldsymbol{\kappa}\right\}^T\mathbf{L}^T\mathbf{A}^{k(0)}\mathbf{e}dA+\int_{\mathcal{A}}\sum_{k=1}^{n}\left\{\frac{1}{2}\mathbf{T}^k\mathbf{L}^T\mathbf{X}^{k(1)}\mathbf{e}+\mathbf{T}^k\mathbf{L}^T\mathbf{Y}^{k(1)}\boldsymbol{\kappa}\right\}^T\mathbf{L}^T\mathbf{A}^{k(1)}\mathbf{e}dA\\&+\frac{1}{2}\int_{\mathcal{A}}\sum_{k=1}^{n}[\mathbf{T}^k\mathbf{L}^T\mathbf{Y}^{k(0)}\boldsymbol{\kappa}]^T\mathbf{L}^T\mathbf{B}^{k(0)}\boldsymbol{\kappa}dA+\frac{1}{2}\int_{\mathcal{A}}\sum_{k=1}^{n}[\mathbf{T}^k\mathbf{L}^T\mathbf{Y}^{k(1)}\boldsymbol{\kappa}]^T\mathbf{L}^T\mathbf{B}^{k(1)}\boldsymbol{\kappa}dA+\frac{1}{2}\int_{\mathcal{A}}\sum_{k=1}^{n}[\mathbf{T}^k\mathbf{L}^T\mathbf{Y}^{k(2)}\boldsymbol{\kappa}]^T\mathbf{L}^T\mathbf{B}^{k(2)}\boldsymbol{\kappa}dA\\&+\int_{\mathcal{A}}(\nabla w+\boldsymbol{\varphi})^T\sum_{k=1}^{n}(\mathbf{L}^T\mathbf{X}^{k(0)}\mathbf{e}+\mathbf{L}^T\mathbf{Y}^{k(0)}\boldsymbol{\kappa})dA\end{aligned} \tag{42}$$

where

$$\mathbf{X}^{k(0)}=-\left[(z_{k+1}-z_k)\mathbf{A}^{k(0)}+\frac{1}{2}(z_{k+1}^2-z_k^2)\mathbf{A}^{k(1)}\right] \tag{43}$$

$$\mathbf{X}^{k(1)}=-\left[\frac{1}{2}(z_{k+1}^2-z_k^2)\mathbf{A}^{k(0)}+\frac{1}{3}(z_{k+1}^3-z_k^3)\mathbf{A}^{k(1)}\right]$$

$$\begin{aligned}\mathbf{Y}^{k(0)}=&-\left[(z_{k+1}-z_k)\mathbf{B}^{k(0)}+\frac{1}{2}(z_{k+1}^2-z_k^2)\mathbf{B}^{k(1)}\right.\\&\left.+\frac{1}{3}(z_{k+1}^3-z_k^3)\mathbf{B}^{k(2)}\right]\end{aligned} \tag{44}$$

$$\begin{aligned}\mathbf{Y}^{k(1)}=&-\left[\frac{1}{2}(z_{k+1}^2-z_k^2)\mathbf{B}^{k(0)}+\frac{1}{3}(z_{k+1}^3-z_k^3)\mathbf{B}^{k(1)}\right.\\&\left.+\frac{1}{4}(z_{k+1}^4-z_k^4)\mathbf{B}^{k(2)}\right]\end{aligned}$$

$$\begin{aligned}\mathbf{Y}^{k(2)}=&-\left[\frac{1}{3}(z_{k+1}^3-z_k^3)\mathbf{B}^{k(0)}+\frac{1}{4}(z_{k+1}^4-z_k^4)\mathbf{B}^{k(1)}\right.\\&\left.+\frac{1}{5}(z_{k+1}^5-z_k^5)\mathbf{B}^{k(2)}\right].\end{aligned}$$

The mixed functional (22) for the model RM2 takes the form

$$\overline{\tilde{H}}(\mathbf{u},w,\boldsymbol{\varphi},\mathbf{e},\boldsymbol{\kappa},\mathbf{N},\mathbf{M})=\tilde{H}^{mb}(\mathbf{u},\boldsymbol{\varphi},\mathbf{e},\boldsymbol{\kappa},\mathbf{N},\mathbf{M})+\overline{\tilde{H}}^s(w,\boldsymbol{\varphi},\mathbf{e},\boldsymbol{\kappa})-\Pi_{\text{ext}}. \tag{45}$$

The number of the unknowns in the FSDT refined RM2 model does not depend on the number of layers; this fact represents an advantageous feature of the proposed RM2 formulation with respect to the RM1 model.

5.3 Refined Model RM3. A possible disadvantage of the refined model RM2 is represented by the large number of unknown functions with respect to the classical full displacement formulation. In fact, functional (45) depends on five displacement parameters $(u_1,u_2,w,\varphi_1,\varphi_2)$, on six midplane strains and curvatures $(e_{11},e_{22},e_{12},\kappa_{11},\kappa_{22},\kappa_{12})$ on six axial and bending resultants $(N_{11},N_{22},N_{12},M_{11},M_{22},M_{12})$.

As matter of fact, in the membrane-bending Hu-Washizu functional $\tilde{H}^{mb}$, defined by Eq. (16), the resultant stress vectors $\mathbf{N}$ and $\mathbf{M}$ can be regarded as the Lagrange multipliers of the constraints corresponding to the compatibility Eqs. (6). The FSDT refined model RM3 is obtained implicitly satisfying the compatibility Eqs. (6) in the membrane-bending Hu-Washizu functional (16); thus, the full displacement membrane-bending functional (23) is obtained. Moreover, the penalty approach is adopted to enforce the constraint (6) in the mixed functional (42); in fact, a penalty term is added into the governing functional, which results in

$$\tilde{\mathcal{E}}(\mathbf{u},w,\boldsymbol{\varphi},\mathbf{e},\boldsymbol{\kappa})=\mathcal{E}^{mb}(\mathbf{u},\boldsymbol{\varphi})+\overline{\tilde{H}}^s(w,\boldsymbol{\varphi},\mathbf{e},\boldsymbol{\kappa})+\Lambda(\mathbf{u},\boldsymbol{\varphi},\mathbf{e},\boldsymbol{\kappa})-\Pi_{\text{ext}} \tag{46}$$

where the penalty term Λ is defined by

$$\Lambda=\frac{1}{2\eta}\int_{\mathcal{A}}[(\mathbf{L}\mathbf{u}-\mathbf{e})^T(\mathbf{L}\mathbf{u}-\mathbf{e})+(\mathbf{L}\boldsymbol{\varphi}-\boldsymbol{\kappa})^T(\mathbf{L}\boldsymbol{\varphi}-\boldsymbol{\kappa})]dA \tag{47}$$

with η the penalty parameter.

According the penalty method, the resultant stresses are deduced as

$$\mathbf{N}=\frac{1}{\eta}(\mathbf{Lu}-\mathbf{e}) \quad \mathbf{M}=\frac{1}{\eta}(\mathbf{L}\boldsymbol{\varphi}-\boldsymbol{\kappa}) \tag{48}$$

5.4 Refined Model RM4. The refined model RM4 is based on the full displacement-based variational formulation. In fact, it is obtained enforcing the strain displacement Eqs. (6) in the shear functional (42). Thus, the functional $\bar{H}^s$-becomes

$$\begin{aligned}\tilde{H}^s=&\int_{\mathcal{A}}\sum_{k=1}^{n}\left\{\frac{1}{2}[\mathbf{T}^k\mathbf{L}^T\mathbf{X}^{k(0)}\mathbf{Lu}]^T+[\mathbf{T}^k\mathbf{L}^T\mathbf{Y}^{k(0)}\mathbf{L}\boldsymbol{\varphi}]^T\right\}\mathbf{L}^T\mathbf{A}^{k(0)}\mathbf{Lu}dA+\int_{\mathcal{A}}\sum_{k=1}^{n}\left\{\frac{1}{2}[\mathbf{T}^k\mathbf{L}^T\mathbf{X}^{k(1)}\mathbf{Lu}]^T+[\mathbf{T}^k\mathbf{L}^T\mathbf{Y}^{k(1)}\mathbf{L}\boldsymbol{\varphi}]^T\right\}\mathbf{L}^T\mathbf{A}^{k(1)}\mathbf{Lu}dA\\&+\frac{1}{2}\int_{\mathcal{A}}\sum_{k=1}^{n}[\mathbf{T}^k\mathbf{L}^T\mathbf{Y}^{k(0)}\mathbf{L}\boldsymbol{\varphi}]^T\mathbf{L}^T\mathbf{B}^{k(0)}\mathbf{L}\boldsymbol{\varphi}dA+\frac{1}{2}\int_{\mathcal{A}}\sum_{k=1}^{n}[\mathbf{T}^k\mathbf{L}^T\mathbf{Y}^{k(1)}\mathbf{L}\boldsymbol{\varphi}]^T\mathbf{L}^T\mathbf{B}^{k(1)}\mathbf{L}\boldsymbol{\varphi}dA\\&+\frac{1}{2}\int_{\mathcal{A}}\sum_{k=1}^{n}[\mathbf{T}^k\mathbf{L}^T\mathbf{Y}^{k(2)}\mathbf{L}\boldsymbol{\varphi}]^T\mathbf{L}^T\mathbf{B}^{k(2)}\mathbf{L}\boldsymbol{\varphi}dA+\int_{\mathcal{A}}(\nabla w+\boldsymbol{\varphi})^T\sum_{k=1}^{n}(\mathbf{L}^T\mathbf{X}^{k(0)}\mathbf{Lu}+\mathbf{L}^T\mathbf{Y}^{k(0)}\mathbf{L}\boldsymbol{\varphi})dA.\end{aligned} \tag{49}$$

Hence, the full displacement functional governing the laminate problem is

$$\tilde{\bar{\mathcal{E}}}(\mathbf{u},w,\boldsymbol{\varphi})=\mathcal{E}^{mb}(\mathbf{u},\boldsymbol{\varphi})+\tilde{H}^s(w,\mathbf{u},\boldsymbol{\varphi})-\Pi_{\text{ext}}. \tag{50}$$

The recovered potential energy functional (50) appears very appealing since it presents only five unknown functions, i.e., u_1, u_2, w, φ_1, and φ_2. On the other hand, second-order derivatives of the in-plane displacement and the rotation vectors, i.e., $\mathbf{u}$ and $\boldsymbol{\varphi}$, appear in the functional $\tilde{\bar{\mathcal{E}}}$. From a numerical point of view, the presence of the second-order derivatives of the unknown functions in the governing functional could represent a drawback. In fact, in the perspective of developing suitable finite laminate elements based on refined FSDT theories, a greater continuity of the interpolation functions is required.

6 Numerical Applications

With the aim of verifying the accuracy of the proposed FSDT refined models, some numerical calculations are developed. Results are carried out for homogeneous plates as well as for composite laminates. In particular, square plates, characterized by the in-plane dimension a and subjected to transversal sinusoidal loading, are considered. The laminates have the side to thickness ratio $\rho=h/a=0.10$. The following elastic properties are introduced in the computations:

$$\frac{E_L}{E_T}=25, \quad \nu_{LT}=0.25, \quad \frac{G_{LT}}{E_T}=0.5, \quad \frac{G_{TT}}{E_T}=0.2 \tag{51}$$

which correspond to a strongly orthotropic graphite-epoxy material. The subscripts $_L$ and $_T$ indicate the longitudinal and transversal principal material directions.

6.1 Cylindrical Bending. Initially, homogeneous and cross-ply laminated plates in cylindrical bending, subjected to the sinusoidal load $p=p_0\sin(\alpha x)$ with $\alpha=\pi/a$, are studied. In particular, antisymmetric [0/90] and symmetric [0/90/0] laminates are considered. In Table 1, the results obtained using the refined models are put in comparison with the exact three-dimensional analytical solution (3D_AS) obtained by Pagano [33] and with those recovered through the classical Mindlin-Reissner theory (FSDT). In particular, FSDT solutions are obtained considering the shear corrector factor χ equal to $\chi_0=5/6$ and the exact value of shear corrector factor proposed by Whitney χ_W, [8]. Results are reported in terms of the dimensionless maximum displacement $w_{\max}$ defined as

$$w_{\max}=100\frac{E_T w_C}{p_0 h\rho^4} \tag{52}$$

where w_C represents the transversal displacement occuring in the center of the laminate, i.e. $w_C=w(a/2,a/2)$.

It is apparent the effectiveness of the refined models RM2, RM3, and RM4. In fact, RM2, RM3, and RM4 results are in perfect agreement with the FSDTχ_W and 3D_AS solutions; in other words, the RM2, RM3, and RM4 approaches are able to recover the FSDTχ_W model without the use of the shear correction factors. Moreover, the RM1 appears satisfactory for the homogeneous plate and for the antisymmetric [0/90] laminate, while it is absolutely unsatisfactory when the symmetric [0/90/0] laminate is considered.

In Fig. 1 the dimensionless shear stress profile τ_{1z}/p_0 for the homogeneous plate in cylindrical bending is reported. The results obtained by the four proposed refined models, i.e., RM1, RM2, RM3, and RM4, are compared with the shear stress derived by the analytical three-dimensional solution. It can be noted the perfect agreement between all the computed solutions with the exact three-dimensional solution.

Then, the homogeneous plate in cylindrical bending is studied considering fictitious staking sequences of one layer [0], three equal layers [0/0/0] and ten equal layers [0/0/0/0/0/0/0/0/0/0]. Results in terms of dimensionless shear stress profile τ_{1z}/p_0 in the plate thickness are reported in Fig. 2. It can be noted that the RM2, RM3 and RM4 proposed models lead all to the same solution in perfect agreement with the exact three-dimensional solution. On the contrary, the RM1 model gives different solutions depending on the number of layers considered for the fictitious staking sequence. In particular, for $n=10$ the shear stress is almost constant in the core of the plate. In fact, increasing the number of layers, i.e., increasing the number of independent functions approximating the shear stresses, the constitutive Eq. (9) tends to be enforced. Thus, enlarging the space of the shear parameters $\mathbf{t}_o^2,..,\mathbf{t}_o^n,\mathbf{t}^1,..,\mathbf{t}^n$ the shear stress profile tends to become constant for the homogeneous plate.

Table 1 Dimensionless maximum displacement $w_{\max}$ defined by formula (52) for homogeneous plate and for [0/90] and [0/90/0] composite laminates in cylindrical bending

$w_{\max}$	Homogeneous	[0/90]	[0/90/0]
FSDTχ_0	0.7347060	2.9662221	0.8136198
FSDTχ_W	0.7347060	2.9713422	0.9443031
RM1	0.7347060	2.9482925	0.7902380
RM2	0.7347060	2.9722354	0.9443031
RM3	0.7347060	2.9722354	0.9443031
RM4	0.7347033	2.9721543	0.9443031
3D_AS	0.7316710	2.9502480	0.9306170

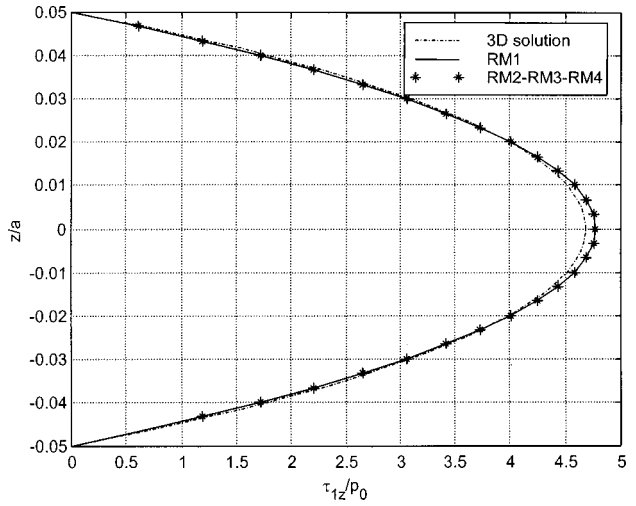

Fig. 1 Dimensionless shear stress τ_{1z}/p_0 at $x_1=0$ for homogeneous plate in cylindrical bending; comparison between the different solutions

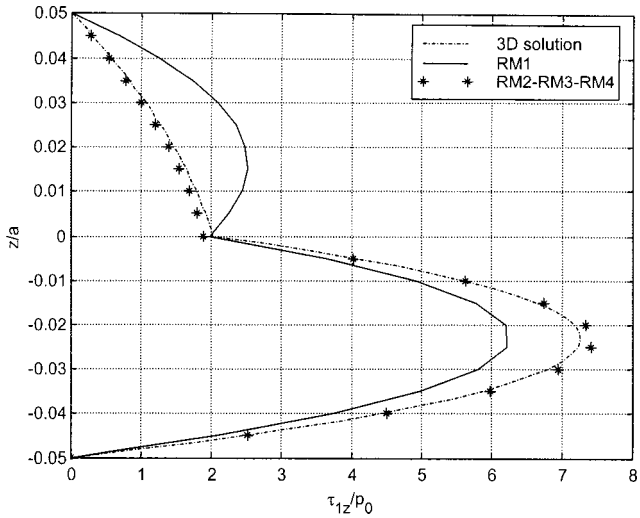

Fig. 3 Dimensionless shear stress τ_{1z}/p_0 at $x_1=0$ for the [0/90] laminate in cylindrical bending; comparison between the different solutions

In Figs. 3 and 4 the dimensionless shear stresses τ_{1z}/p_0 are plotted for the [0/90] and [0/90/0] laminates, respectively. Again it can be noted the good agreement between the solutions obtained using the RM2, RM3, and RM4 models and the three-dimensional analytical solution. On the contrary, the RM1 model, based on the assumption of independent approximation of the shear stresses, leads to unsatisfactory solution, since the profile appears absolutely inadequate.

6.2 Simply Supported Laminates

Cross-Ply Laminates. Cross-ply laminates subjected to the sinusoidal load $p=p_0\sin(\alpha x)\sin(\alpha y)$ with $\alpha=\pi/a$, are considered. The following SS1 boundary conditions are adopted:

$$u_2=w=\varphi_2=0 \quad N_{11}=M_{11}=0 \quad \text{at } x_1=0 \quad \text{and} \quad x_1=a$$

$$u_1=w=\varphi_1=0 \quad N_{22}=M_{22}=0 \quad \text{at } x_2=0 \quad \text{and} \quad x_2=a.$$

Results are computed for homogeneous plate and for [0/90] and [0/90/0] laminates.

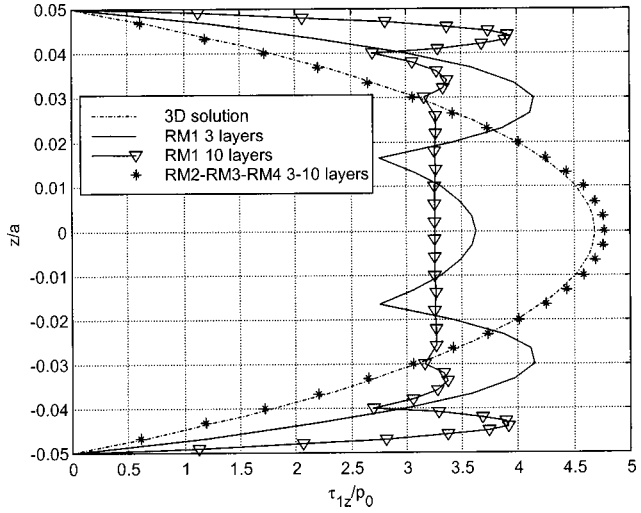

Fig. 2 Dimensionless shear stress τ_{1z}/p_0 at $x_1=0$ for homogeneous plate in cylindrical bending; comparison between the different solutions computed considering one, three, and ten equal layers

In Table 2 the dimensionless maximum displacement $w_{\max}$ defined by formula (52) is reported; in particular, results are obtained, considering

- the classical FSDT analytical solution with $\chi=\chi_0=5/6$,
- the finite element solution (FEMχ_0) with $\chi=\chi_0$,

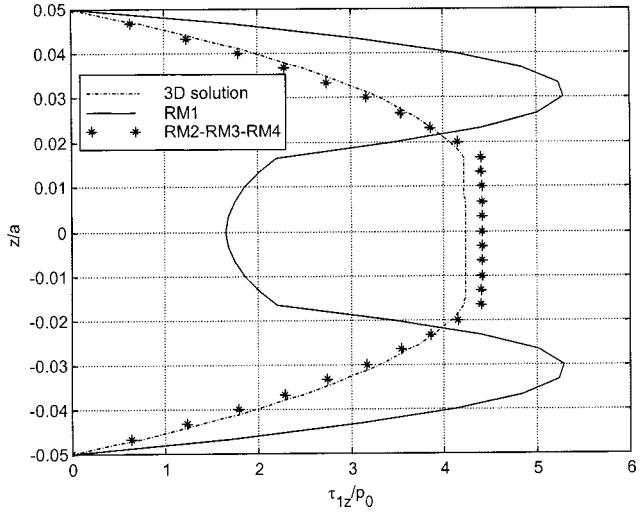

Fig. 4 Dimensionless shear stress τ_{1z}/p_0 at $x_1=0$ for the [0/90] laminate in cylindrical bending; comparison between the different solutions

Table 2 Dimensionless maximum displacement $w_{\max}$ defined by formula (52) for homogeneous plate and for [0/90] and [0/90/0] cross-ply laminates

$w_{\max}$	Homogeneous	[0/90]	[0/90/0]
FSDTχ_0	0.6382997	1.237270	0.669302
FEMχ_0	0.63834	1.2373	0.66930
FEMχ	0.63834	1.2319	0.76377
RM1	0.6382997	-	-
RM2	0.6382997	1.231817	0.763779
RM3	0.6382997	1.231817	0.763779
RM4	0.6382997	1.231817	0.763779
3D	0.6338085	1.224799	0.751425

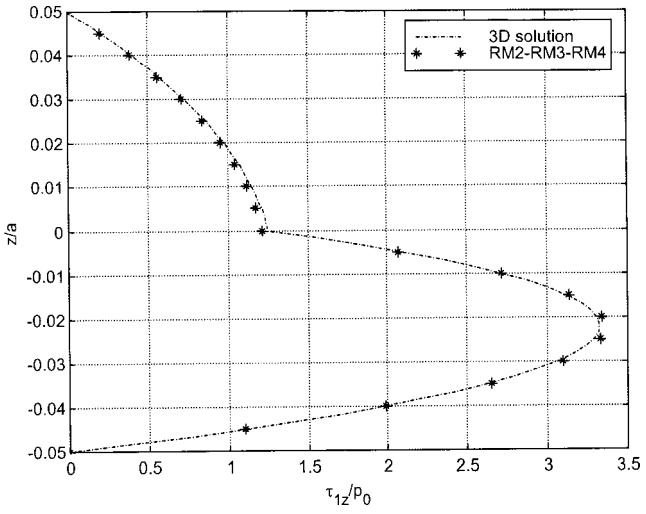

Fig. 5 Dimensionless shear stress τ_{1z}/p_0 for the [0/90] laminate computed at $x_1=0$, $x_2=a/2$; comparison with the three-dimensional analytical solution

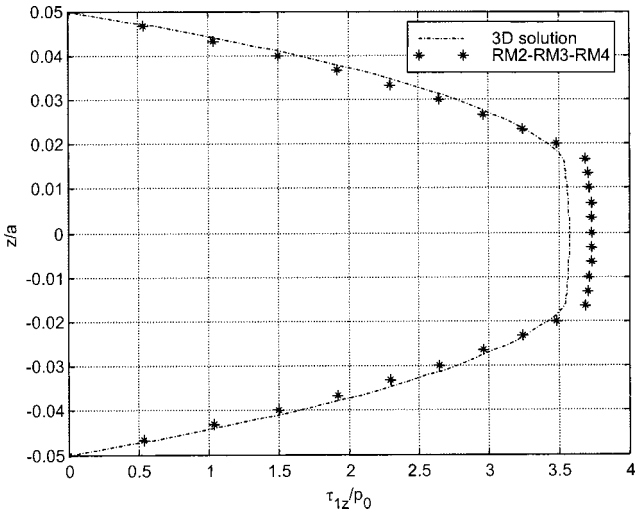

Fig. 7 Dimensionless shear stress τ_{1z}/p_0 for the [0/90/0] laminate computed at $x_1=0$, $x_2=a/2$; comparison with the three-dimensional analytical solution

- the finite element solution (FEMχ) with exact value of the shear correction factor computed by the iterative procedure proposed in [13],
- the RM1 analytical solution only for the homogeneous plate,
- the RM2, RM3, and RM4 analytical solutions, and
- the exact three-dimensional solution 3D-AS.

In Figs. 5 and 6 the dimensionless shear stress profiles τ_{1z}/p_0 and τ_{2z}/p_0 for the [0/90] laminate are plotted, respectively. Analogously, in Figs. 7 and 8 the shear stress profiles are plotted for the [0/90/0] laminate. It can be noted that the proposed models are able to approximate very accurately the exact three-dimensional solution for both the considered laminations.

Finally, in Fig. 9 the dimensionless displacement $w_{\max}$ defined by formula (52), computed for the [0/90/0] lamination, is plotted versus the ratio $\rho=h/a$. In particular, the RM3 solution is compared with three dimensions with the FSDTχ_0, with the FSDTχ and with the classical laminate theory (CLT) solutions. It can be emphasized the good accordance between the RM3 and the analytical three-dimensional solutions for a wide range of the ratio ρ.

Angle-Ply Laminate. The antisymmetric [−45/45] angle-ply laminate subjected to the sinusoidal load $p=p_0\sin(\alpha x)\sin(\alpha y)$ with $\alpha=\pi/a$, is considered. The following SS2 boundary conditions are adopted:

$$u_1=w=\varphi_2=0 \quad N_{12}=M_{11}=0 \quad \text{at } x_1=0 \quad \text{and} \quad x_1=a$$

$$u_2=w=\varphi_1=0 \quad N_{12}=M_{22}=0 \quad \text{at } x_2=0 \quad \text{and} \quad x_2=a.$$

In Table 3 the dimensionless maximum displacement $w_{\max}$ defined by formula (52) is reported; in particular, results are obtained, considering

- the classical FSDT analytical solution with $\chi=\chi_0$ and
- the RM2, RM3, and RM4 analytical solutions.

It can be noted that the RM2, RM3, and RM4 models give all the same results which differ from the FSDT solution obtained adopting the shear correction factor $\chi=5/6$. Finally, in Fig. 10 the shear stress profile τ_{1z}/p_0 for the angle-ply laminate is plotted.

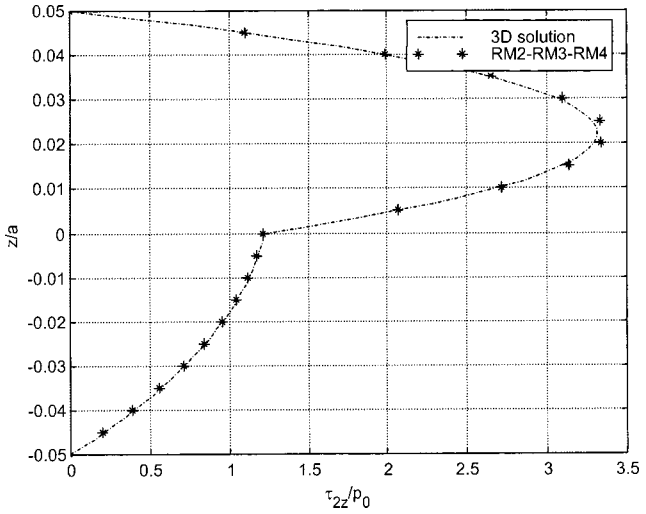

Fig. 6 Dimensionless shear stress τ_{2z}/p_0 for the [0/90] laminate computed at $x_1=a/2$, $x_2=0$; comparison with the three-dimensional analytical solution

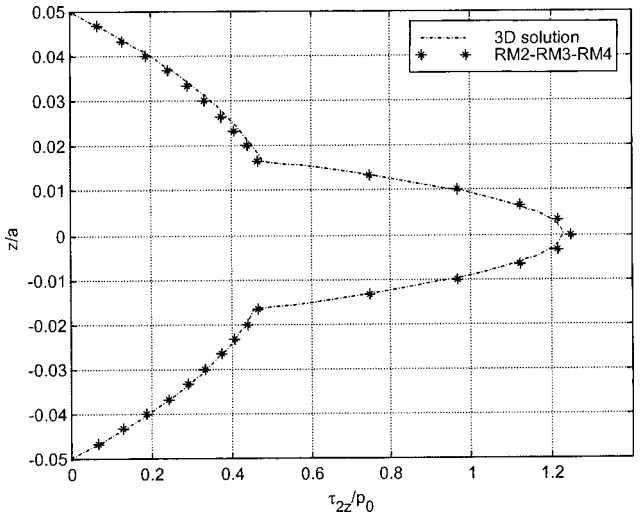

Fig. 8 Dimensionless shear stress τ_{2z}/p_0 for the [0/90/0] laminate computed at $x_1=a/2$, $x_2=0$; comparison with the three-dimensional analytical solution

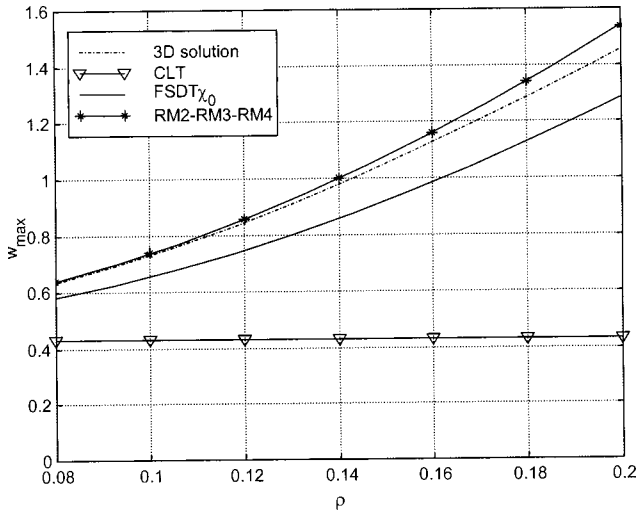

Fig. 9 Dimensionless displacement w_{max} versus the thickness to side ratio

7 Conclusions

Refined laminate models are presented. They are derived considering mixed variational formulations of the laminate problem, introducing suitable representation forms of the shear stresses in the plate thickness. It is obtained that independent approximations of the shear stresses can lead to unsatisfactory models, which are not able to recover the correct profiles of the stresses.

The proposed RM2, RM3, and RM4 models, obtained representing the transverse shear stress profile by using the three-dimensional equations, are very satisfactory; in fact, the solutions obtained by these models are in very good accordance with the three-dimensional analytical solution.

The RM2 approach appears the more suitable in view to develop effective laminate finite elements. In fact, the RM3 model needs the use of a penalty parameter, which is not always simple to set; on the other hand, the RM4 requires the use of smoother approximation functions in the finite element formulation, since second-order derivatives appear in the governing functional.

The proposed model does not suffer of any limitation about the number of layers defining the stacking sequence and of the ply angles; more complex situations can be investigated, including quasi-isotropic laminates. More complex cases can be studied developing suitable finite elements based on the proposed formulations. In fact, the presented mixed principles, in particular the RM2 model, are the bases for the development of new and performing finite elements. One of the major problems in developing mixed laminate finite elements, is the definition of the approximation functions used for the midplane strains and curvatures in order to verify the stability requirement, related to the LBB condition. Finally, full displacement finite elements can be recovered from the refined model RM2 performing static condensation of strain and stress variables.

Table 3 Dimensionless maximum displacement w_{max} defined by formula (52) for the [−45/45] angle-ply composite laminate

Model	FSDTχ_0	RM2	RM3	RM4
w_{max}	0.8828107	0.8929168	0.8929168	0.8929168

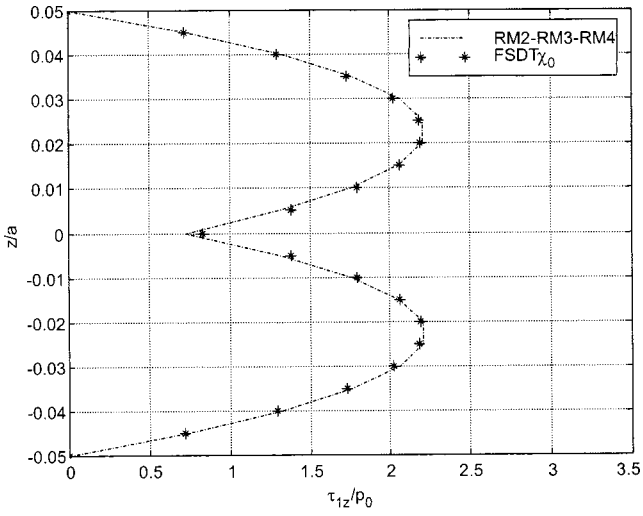

Fig. 10 Dimensionless shear stress τ_{1z}/p_0 for the [−45/45] laminate computed at $x_1=0$, $x_2=a/2$; comparison with first-order shear deformation theory ($\chi=5/6$) analytical solution

References

[1] Ochoa, O. O., and Reddy, J. N., 1992, *Finite Element Analysis of Composite Laminates*, Kluwer, Dordrecht, The Netherlands.

[2] Reddy, J. N., 1997, *Mechanics of Laminated Composite Plates, Theory and Analysis*, CRC Press, Boca Raton, FL.

[3] Reissner, E., and Stavsky, Y., 1961, "Bending and Stretching of Certain Types of Heterogeneous Aeolotropic Elastic Plates," ASME J. Appl. Mech., **28**, pp. 402–412.

[4] Ambartsumyan, S. A., 1970, *Theory of Anisotropic Plates*, Technomic, Lancaster, PA.

[5] Reissner, E., 1945, "The Effect of Transverse Shear Deformation on the Bending of Elastic Plates," ASME J. Appl. Mech., **12**, pp. 69–77.

[6] Mindlin, R. D., 1951, "Influence of Rotatory Inertia and Shear on Flexural Motions of Isotropic, Elastic Plates," ASME J. Appl. Mech., **38**, pp. 31–38.

[7] Yang, P. C., Norris, C. H., and Stavsky, Y., 1996, "Elastic Wave Propagation in Heterogeneous Plates," Int. J. Solids Struct., **2**, pp. 665–684.

[8] Whitney, J. M., and Pagano, N. J., 1970, "Shear Deformation in Heterogeneous Anisotropic Plates," ASME J. Appl. Mech., **37**, pp. 1031–1036.

[9] Whitney, J. M., 1973, "Shear Correction Factors for Orthotropic Laminates Under Static Load," ASME J. Appl. Mech., **40**, pp. 302–304.

[10] Noor, A. K., and Burton, W. S., 1990, "Assessment of Computational Models for Multilayered Anisotropic Plates," Comput. Struct., **14**, pp. 233–265.

[11] Noor, A. K., Burton, W. S., and Peters, J. M., 1990, "Predictor-Corrector Procedures for Stress and Free Vibration Analyses of Multilayered Composite Plates and Shells," Comput. Methods Appl. Mech. Eng., **82**, pp. 341–363.

[12] Noor, A. K., Burton, W. S., and Bert, C. W., 1996, "Computational Model for Sandwich Panels and Shells," Appl. Mech. Rev., **49**, pp. 155–199.

[13] Auricchio, F., and Sacco, E., 1999, "A Mixed-Enhanced Finite Element for the Analysis of Laminated Composite Plates," Int. J. Numer. Methods Eng., **44**, pp. 1481–1504.

[14] Alfano, G., Auricchio, F., Rosati, L., and Sacco, E., 2001, "MITC Finite Elements for Laminated Composite Plates," Int. J. Numer. Methods Eng., **50**, pp. 707–738.

[15] Pai, P. F., 1995, "A New Look at the Shear Correction Factors and Warping Functions of Anisotropic Laminates," Int. J. Solids Struct., **32**, pp. 2295–2313.

[16] Yunquin, Q., and Knight, N. F. Jr., 1996, "A Refined First-Order Shear-Deformation Theory and Its Justification by Plane-Strain Bending Problem of Laminated Plates," Int. J. Solids Struct., **33**, pp. 49–64.

[17] Rolfes, R., and Rohwer, K., 1997, "Improved Transverse Shear Stresses in Composite Finite Element Based on First Order Shear Deformation Theory," Int. J. Numer. Methods Eng., **40**, pp. 51–60.

[18] Rolfes, R., 1998, "Evaluation of Transverse Thermal Stresses in Composite Plates Based on First Order Shear Deformation Theory," Comput. Methods Appl. Mech. Eng., **167**, pp. 355–368.

[19] Lo, K. H., Christensen, R. M., and Wu, E. M., 1978, "A High-Order Theory of Plate Deformation. Part II: Laminated Plates," ASME J. Appl. Mech., **44**, pp. 669–676.

[20] Reddy, J. N., 1984, "A Simple High-Order Theory for Laminated Composite Plates," ASME J. Appl. Mech., **51**, pp. 745–752.

[21] Seide, P., 1980, "An Improved Approximate Theory for Bending of Laminated Plates," Mech. Today, **5**, pp. 451–466.

[22] Reddy, J. N., 1987, "A Generalization of Two-Dimensional Theories of Laminated Plates," Commun. Appl. Numer. Methods **3**, pp. 173–180.

[23] Reddy, J. N., 1990, "On Refined Theories of Composite Laminates," Meccanica, **25**, pp. 230–238.

[24] Reddy, J. N., Barbero, E. J., and Teply, J. L., 1990, "An Accurate Determination of Stresses in Thick Laminates Using a Generalized Plate Theory," Int. J. Numer. Methods Eng., **29**, pp. 1–14.

[25] Bisegna, P., and Sacco, E., 1997, "A Layer-Wise Laminate Theory Rationally Deduced From Three-Dimensional Elasticity," ASME J. Appl. Mech., **64**, pp. 538–544.

[26] Barbero, E. J., 1992, "3-D Finite Element for Laminated Composites With 2-D

Kinematic Constraints,'' Comput. Struct., **45**, pp. 263–271.
[27] Di Sciuva, M., and Icardi, U., 1993, ''Discrete-Layer Models for Multilayered Shells Accounting for Interlayer Continuity,'' Meccanica, **28**, pp. 281–291.
[28] Carrera, E., 1999, ''Multilayered Shell Theories Accounting for a Layer-Wise Mixed Description. Part I. Governing Equations. Part II. Numerical Evaluations,'' AIAA J., **37**, pp. 1117–1124.
[29] Aitharaju, V. R., and Averill, R. C., 2000, ''C^0 Zig-Zag Kinematic Displacement Models for the Analysis of Laminated Composites,'' Mech. Compos. Mat. Struct., **6**, pp. 31–56.
[30] Carrera, E., 2001, ''Developments, Ideas, and Evaluations Based Upon Reissner's Mixed Variational Theorem in the Modeling of Multilayered Plates and Shells,'' Appl. Mech. Rev., **54**, pp. 301–328.
[31] Maenghyo, Cho, and Min-Ho, Kim, 1996, ''A Postprocess Method Using a Displacement Field of Higher-Order Shell Theory,'' Compos. Struct., **34**, pp. 185–196.
[32] Rolfes, R., Rohwer, K., and Ballerstaedt, M., 1998, ''Efficient Linear Transverse Normal Stress Analysis of Layered Composite Plates,'' Compos. Struct. , **68**, pp. 643–652.
[33] Pagano, N. J., 1970, ''Exact Solutions for Rectangular Bidirectional Composites and Sandwich Plates,'' J. Compos. Mater., **4**, pp. 20–34.
[34] Bisegna, P., and Sacco, E., 1997, ''A Rational Deduction of Plate Theories From the Three-Dimensional Linear Elasticity,'' Z. Angew. Math. Mech., **77**, pp. 349–366.
[35] Auricchio, F., and Sacco, E., 1999, ''Partial-Mixed Formulation and Refined Models for the Analysis of Composite Laminates Within a FSDT,'' Compos. Struct., **46**, pp. 103–113.

C.-H. Lin

M.-H. R. Jen[1]
e-mail: jmhr@mail.nsysu.edu.tw

Department of Mechanical and Electro-Mechanical Engineering,
National Sun Yat-Sen University,
Kaohsiung, Taiwan 80424, Republic of China

Analysis of Laminated Anisotropic Cylindrical Shell by Chebyshev Collocation Method

The governing equations of a laminated anisotropic cylindrical shell problem are a system of partial differential equations. The boundary conditions will complicate the problem. Thus, it is hard to handle the governing equations in the form of functions of independent variables. Herein, Chebyshev collocation method is proposed to achieve the exact solution theoretically of such a difficult problem. Finally, two examples with numerical results are presented. The preciseness and efficiency of the proposed Chebyshev collocation method for laminated anisotropic shell problem are highlighted. [DOI: 10.1115/1.1574059]

Introduction

Shells have been widely applied to many engineering structural elements, e.g., pressure vessels, submarine hulls, ship hulls, and fuselages of airplanes, etc. From the survey of literature, plenty of research is published in the field of shell problems. However, as for the work in this paper, the specified references on thin shells are merely pointed out. Kraus [1] derived the governing equations of isotropic thin shell problems. Ambartsumyan [2] developed the theory and dealt with the problems about some anisotropic shell problems. Flügge [3] presented the solutions for laminated anisotropic shells. He assumed the solutions as doubly infinite trigonometric series which must satisfy the boundary conditions. Then, substituting the solutions back to the governing equations, the unknown coefficients could be resolved. The solutions obtained by the method proposed by Flügge are functions of two independent variables which are much more applicable than any other methods. In spite of the abovementioned advantages, the method will be blocked in the cases of the complicated material properties and boundary conditions. Chaudhuri [4] proposed a method to generate the exact solutions for arbitrarily laminated anisotropic cylindrical shell. Nevertheless, the method proposed by Chaudhuri was limited to the field of tube, and it did not work for the part of cylindrical shell. All the theories mentioned above are based on Kirchhoff-Love's [5] hypotheses. To overcome the disadvantages as discussed in the literature, Chebyshev collocation methods, [6–8], associated with boundary conditions are used to achieve a more general form of the laminated anisotropic cylindrical shell problem.

Chebyshev Polynominals

The Chebyhsev polynominal is named after the Russian mathematician P. F. Chebyshev (1821-1994). Chebyshev polynomials are known as a kind of orthogonal polynomials that can be applied to numerical analysis. For solving systems of partial differential equations in this paper, some basic formulas are listed as follows.

The nth-order Chebyshev polynomial, [9], is expressed as

$$T_n(x)=\cos(n\theta),\quad x=\cos(\theta),\quad -1\leqslant x\leqslant 1, \tag{1}$$

where n is a non-negative integer. By the trigonometric relation, there exists

$$\cos((n+1)\theta)+\cos((n-1)\theta)=2\cos(n\theta), \tag{2}$$

and the recurrence equations can be generated as

$$T_{n+1}(x)=2xT_n(x)-T_{n-1}(x),\quad T_0(x)=1,\quad T_1(x)=x. \tag{3}$$

From Eq. (3) the first few Chebyshev polynomials are represented as

$$\begin{aligned}
T_2(x)&=2x^2-1\\
T_3(x)&=4x^3-3x\\
T_4(x)&=8x^4-8x^2+1\\
T_5(x)&=16x^5-20x^3+5x\\
&\cdots\cdots\cdots\\
T_n(x)&=\frac{1}{2}\left\{(2x)^n-\left[2\binom{n-1}{1}-\binom{n-2}{1}\right](2x)^{n-2}\right.\\
&\left.+\left[2\binom{n-2}{2}-\binom{n-3}{2}\right](2x)^{n-4}-\cdots\right\},\quad n\geqslant 1,\\
&\text{where } \binom{n-1}{1}=\frac{(n-1)!}{(n-1-1)!1!},\\
\binom{n-2}{1}&=\frac{(n-2)!}{(n-2-1)!1!},\quad \binom{n-2}{2}=\frac{(n-2)!}{(n-2-2)!2!},\ \text{etc.}
\end{aligned} \tag{4}$$

Alternatively, x^n can be expressed in Chebyshev polynomials as

$$x^n=\frac{1}{2^{n-1}}\left[T_n(x)+\binom{n}{1}T_{n-2}(x)+\binom{n}{2}T_{n-4}(x)+\cdots\right]. \tag{5}$$

Thus, the expansion for $x^mT_n(x)$ is

$$x^mT_n(x)=\frac{1}{2^m}\sum_{i=0}^{m}\binom{m}{i}T_{n-m+2i}(x). \tag{6}$$

Using the weighting function $(1-x^2)^{-1/2}$, the orthogonality condition of Chebyshev polynomials can be presented as

$$\int_{-1}^{1}(1-x^2)^{-1/2}T_m(x)T_n(x)dx=\begin{cases}0, & m\neq n\\ \dfrac{\pi}{2}, & m=n\neq 0\\ \pi, & m=n=0\end{cases}. \tag{7}$$

Now, $f(x)$ defined by the Chebyshev series for $-1\leqslant x\leqslant 1$ is given by

[1]To whom correspondence should be addressed.

Contributed by the Applied Mechanics Division of THE AMERICAN SOCIETY OF MECHANICAL ENGINEERS for publication in the ASME JOURNAL OF APPLIED MECHANICS. Manuscript received by the ASME Applied Mechanics Division, September 7, 2000; final revision, June 5, 2001. Associate Editor: M. Ortiz. Discussion on the paper should be addressed to the Editor, Prof. Robert M. McMeeking, Department of Mechanical and Environmental Engineering University of California–Santa Barbara, Santa Barbara, CA 93106-5070, and will be accepted until four months after final publication of the paper itself in the ASME JOURNAL OF APPLIED MECHANICS.

 Copyright © 2003 by ASME

$$f(x)=\frac{1}{2}a_0T_0(x)+\sum_{n=1}^{\infty}a_nT_n(x), \tag{8}$$

where

$$a_n=\frac{2}{\pi}\int_{-1}^{1}(1-x)^{-1/2}f(x)T_n(x)dx. \tag{9}$$

In the appreciation of Chebyshev polynomials in the most engineering problems, any range $a\leqslant y\leqslant b$ can be transformed into the Chebyshev polynomials' range $-1\leqslant x\leqslant 1$. The independent variable x in Eqs. (1)–(9) can be replaced by

$$x=\frac{2}{b-a}y+\frac{-b-a}{b-a}. \tag{10}$$

Formulation for Laminated Anisotropic Cylindrical Shell

The strain-displacement relations and equilibrium equations of shell problems can be obtained by the method cited in Ref. [1]. Please refer to [1] for further details of implementation. For simplicity, only the final results are listed.

First of all, the position vector equation of the parametric curves of surface can be represented as

$$\mathbf{r}(\alpha_1,\alpha_2)=f_1(\alpha_1,\alpha_2)\mathbf{i}+f_2(\alpha_1,\alpha_2)\mathbf{j}+f_3(\alpha_1,\alpha_2)\mathbf{k}, \tag{11}$$

where f_1, f_2, and f_3 are continuous and single-valued functions of two variable parameters α_1 and α_2. The position vectors of curvilinear coordinates are represented in Fig. 1. The differential change $d\mathbf{r}$ in the vector $\mathbf{r}$ is

$$d\mathbf{r}=\mathbf{r}_{,1}d\alpha_1+\mathbf{r}_{,2}d\alpha_2, \tag{12}$$

where $\mathbf{r}_{,i}=\partial\mathbf{r}/\partial\alpha_i$, $i=1,2$. Taking the scalar product of $d\vec{\mathbf{r}}$ with itself gives the square of magnitude of the differential change $d\mathbf{r}$ as

$$(ds)^2=d\mathbf{r}\cdot d\mathbf{r}=\breve{E}(d\alpha_1)^2+2\breve{F}\,d\alpha_1d\alpha_2+\breve{G}(d\alpha_2)^2, \tag{13}$$

where

$$\begin{aligned}\breve{E}&=\mathbf{r}_{,1}\cdot\mathbf{r}_{,1},\\ \breve{F}&=\mathbf{r}_{,1}\cdot\mathbf{r}_{,2},\\ \breve{G}&=\mathbf{r}_{,2}\cdot\mathbf{r}_{,2}.\end{aligned} \tag{14}$$

In Eqn. (13), $\breve{E}$, $\breve{F}$, and $\breve{G}$ are called the first fundamental magnitudes. If the parametric curves form an orthogonal net, then $\breve{F}=0$ and Eq. (13) becomes

$$(ds)^2=A_1^2(d\alpha_1)^2+A_2^2(d\alpha_2)^2, \tag{15}$$

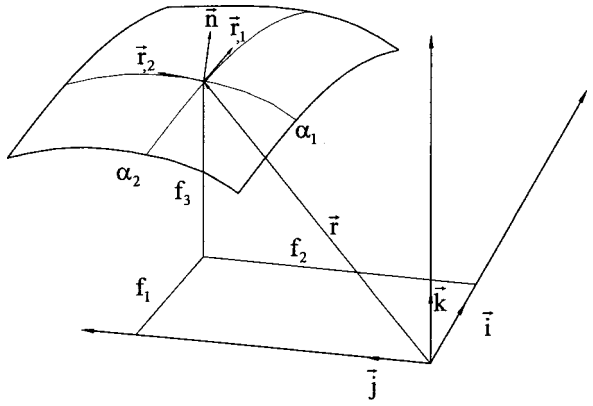

Fig. 1 Position vectors of a surface

where A_1 and A_2 are Lamé parameters and expressed as

$$\begin{aligned}A_1&=\sqrt{\breve{E}},\\ A_2&=\sqrt{\breve{G}}.\end{aligned} \tag{16}$$

The unit normal vector is given as

$$\mathbf{n}(\alpha_1,\alpha_2)=\frac{\mathbf{r}_{,1}\times\mathbf{r}_{,2}}{|\mathbf{r}_{,1}\times\mathbf{r}_{,2}|}. \tag{17}$$

And, the normal curvature is

$$K_n=\frac{d\mathbf{r}\cdot d\mathbf{n}}{d\mathbf{r}\cdot d\mathbf{r}}. \tag{18}$$

Similarly, the differential change vector $d\mathbf{n}$ can be expressed as

$$d\mathbf{n}=\mathbf{n}_{,1}d\alpha_1+\mathbf{n}_{,2}d\alpha_2. \tag{19}$$

Substitute Eqs. (12) and (19) into Eq. (18), it generates the normal curvature

$$K_n=\frac{\breve{L}(d\alpha_1)^2+2\breve{M}(d\alpha_1d\alpha_2)+\breve{N}(d\alpha_2)^2}{\breve{E}(d\alpha_1)^2+2\breve{F}(d\alpha_1d\alpha_2)+\breve{G}(d\alpha_2)^2}, \tag{20}$$

where

$$\begin{aligned}\breve{L}&=\mathbf{r}_{,1}\cdot\mathbf{n}_{,1},\\ 2\breve{M}&=(\mathbf{r}_{,1}\cdot\mathbf{n}_{,2}+\mathbf{r}_{,2}\cdot\mathbf{n}_{,1}),\\ \breve{N}&=\mathbf{r}_{,2}\cdot\mathbf{n}_{,2}.\end{aligned} \tag{21}$$

In Eq. (21), L, M, and N are called the second fundamenta magnitudes.

If $d\alpha_2=0$ and $d\alpha_1=0$, Eq. (20) becomes

$$\begin{aligned}K_1&=\frac{1}{R_1}=\frac{\breve{L}}{\breve{E}},\\ K_2&=\frac{1}{R_2}=\frac{\breve{N}}{\breve{G}},\end{aligned} \tag{22}$$

where R_1 and R_2 are the radii in the directions of α_1 and α_2, respectively.

According to Kirchhoff-Love's first approximation to the theory of thin elastic shells, [1], there are four postulates as follows: (a) the shell is thin, (b) the deflections of the shell are small, (c) the transverse normal stress is negligible, and (d) normals to the reference surface of the shell remain normal to it and undergo no change in length during deformation. Therefore, the strain-displacement relations in a thin elastic shell, [1], are given by

$$\begin{aligned}\varepsilon_1&=\varepsilon_1^0+z\kappa_1,\\ \varepsilon_2&=\varepsilon_2^0+z\kappa_2,\\ \gamma_{12}&=\gamma_{12}^0+z\kappa_{12},\end{aligned} \tag{23}$$

where

$$\begin{aligned}\varepsilon_1^0&=\frac{1}{A_1}\frac{\partial u_1}{\partial\alpha_1}+\frac{u_2}{A_1A_2}\frac{\partial A_1}{\partial\alpha_2}+\frac{w}{R_1},\\ \varepsilon_2^0&=\frac{1}{A_2}\frac{\partial u_2}{\partial\alpha_2}+\frac{u_1}{A_1A_2}\frac{\partial A_2}{\partial\alpha_1}+\frac{w}{R_2},\\ \gamma_{12}^0&=\frac{A_2}{A_1}\frac{\partial}{\partial\alpha_1}\left(\frac{u_2}{A_2}\right)+\frac{A_1}{A_2}\frac{\partial}{\partial\alpha_2}\left(\frac{u_1}{A_1}\right),\\ \kappa_1&=\frac{1}{A_1}\frac{\partial\beta_1}{\partial\alpha_1}+\frac{\beta_2}{A_1A_2}\frac{\partial A_1}{\partial\alpha_2},\\ \kappa_2&=\frac{1}{A_2}\frac{\partial\beta_2}{\partial\alpha_2}+\frac{\beta_1}{A_1A_2}\frac{\partial A_2}{\partial\alpha_1},\\ \kappa_{12}&=\frac{A_2}{A_1}\frac{\partial}{\partial\alpha_1}\left(\frac{\beta_2}{A_2}\right)+\frac{A_1}{A_2}\frac{\partial}{\partial\alpha_2}\left(\frac{\beta_1}{A_1}\right).\end{aligned} \tag{24}$$

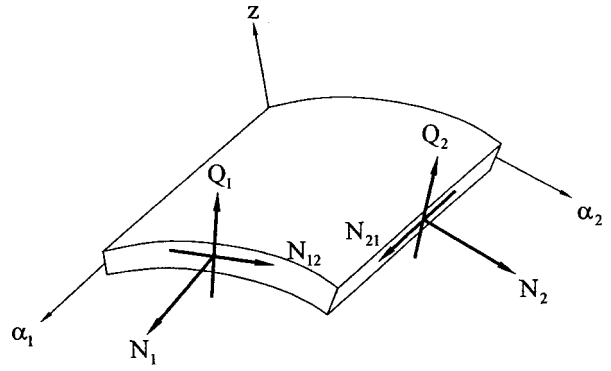

Fig. 2 Nomenclature for stress resultants and shear stress resultants

The quantities of β_1 and β_2 in Eq. (24) are the rotations tangential to the reference surface oriented along the parametric lines α_1 and α_2. They are

$$\beta_1=\frac{u_1}{R_1}-\frac{1}{A_1}\frac{\partial w}{\partial \alpha_1},$$
$$\beta_2=\frac{u_2}{R_2}-\frac{1}{A_2}\frac{\partial w}{\partial \alpha_2}. \tag{25}$$

The following equilibrium equations are derived by Hamilton's principle, [1], some terms in the equations are omitted for the consideration in static case.

$$\frac{\partial(N_1A_2)}{\partial\alpha_1}+\frac{\partial(N_{21}A_1)}{\partial\alpha_2}+N_{12}\frac{\partial A_1}{\partial\alpha_2}-N_2\frac{\partial A_2}{\partial\alpha_1}+A_1A_2\frac{Q_1}{R_1}=0,$$
$$\frac{\partial(N_{12}A_2)}{\partial\alpha_1}+\frac{\partial(N_1A_1)}{\partial\alpha_2}+N_{21}\frac{\partial A_2}{\partial\alpha_1}-N_1\frac{\partial A_1}{\partial\alpha_2}+A_1A_2\frac{Q_2}{R_2}=0,$$
$$\frac{\partial(Q_1A_2)}{\partial\alpha_1}+\frac{\partial(Q_2A_1)}{\partial\alpha_2}-\left(\frac{N_1}{R_1}+\frac{N_2}{R_2}\right)A_1A_2-q_nA_1A_2=0, \tag{26}$$
$$\frac{\partial(M_1A_2)}{\partial\alpha_1}+\frac{\partial(M_{21}A_1)}{\partial\alpha_2}+M_{12}\frac{\partial A_1}{\partial\alpha_2}-M_2\frac{\partial A_2}{\partial\alpha_1}-Q_1A_1A_2=0,$$
$$\frac{\partial(M_{12}A_2)}{\partial\alpha_1}+\frac{\partial(M_2A_1)}{\partial\alpha_2}+M_{21}\frac{\partial A_2}{\partial\alpha_1}-M_1\frac{\partial A_1}{\partial\alpha_2}-Q_2A_1A_2=0.$$

In Eq. (26) the positive directions of N_1, N_2, N_{12}, N_{21}, Q_1, and Q_2 are defined as shown in Fig. 2. Meanwhile, the positive directions of M_1, M_2, M_{12} and M_{21} are defined in Fig. 3. Due to symmetry of stress tensor, i.e., $\tau_{12}=\tau_{21}$, and the characteristics of "thin" shell, $N_{12}=N_{21}$ and $M_{12}=M_{21}$ are provided in Eq. (26).

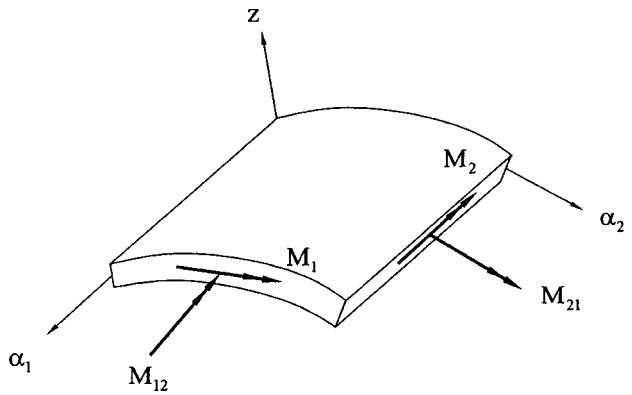

Fig. 3 Nomenclature for moment resultants

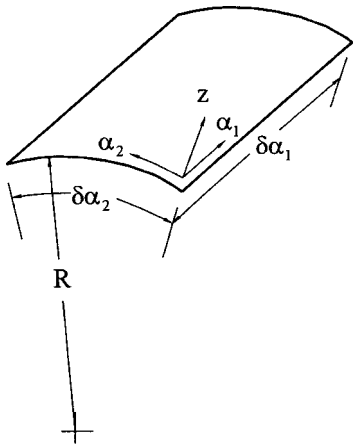

Fig. 4 Contour of the cylindrical shell

The natural boundary conditions are as follows.
Along the edge of constant α_1:

$$N_1=\overline{N}_1,\ \text{or}\ u_1=\overline{u}_1,$$
$$T_{12}=\overline{T}_{12},\ \text{or}\ u_2=\overline{u}_2,$$
$$V_1=\overline{V}_1,\ \text{or}\ w=\overline{w}, \tag{27a}$$
$$M_1=\overline{M}_1,\ \text{or}\ \beta_1=\overline{\beta}_1.$$

Along the edge of constant α_2:

$$N_2=\overline{N}_2,\ \text{or}\ u_2=\overline{u}_2,$$
$$T_{21}=\overline{T}_{21},\ \text{or}\ u_1=\overline{u}_1,$$
$$V_2=\overline{V}_2,\ \text{or}\ w=\overline{w}, \tag{27b}$$
$$M_2=\overline{M}_2,\ \text{or}\ \beta_2=\overline{\beta}_2,$$

where

$$T_{nt}=N_{nt}+\frac{M_{nt}}{R_t},$$
$$V_n=Q_n+\frac{1}{A_t}\frac{\partial M_{nt}}{\partial\alpha_t},\quad n,\ t=1,\ 2. \tag{28}$$

The symbols n and t denote normal and tangential directions on a designated boundary edge.

Now let the position vector of a cylindrical shell problem be

$$\mathbf{r}(\alpha_1,\alpha_2)=\alpha_1\mathbf{i}+R\sin(\alpha_2)\mathbf{j}+R\cos(\alpha_2)\mathbf{k}, \tag{29}$$

where the definitions of α_1, α_2, and R are represented in Fig. 4.

Substituting Eq. (29) into Eqs. (14)–(22) and manipulating the results provides

$$A_1=1,\quad A_2=R,\quad R_1=\infty,\quad R_2=R. \tag{30}$$

Substituting Eq. (30) into Eqs. (25) and (24) to yield

$$\beta_1=-w_{,1},\quad \beta_2=\frac{u_2}{R}-\frac{1}{R}w_{,2}, \tag{31}$$

and

$$\varepsilon_1^0=u_{1,1},\quad \varepsilon_2^0=\frac{1}{R}u_{2,2}+\frac{w}{R},\quad \gamma_{12}^0=u_{2,1}+\frac{1}{R}u_{1,2},$$
$$\kappa_1=-w_{,11},\quad \kappa_2=\frac{1}{R^2}u_{2,2}-\frac{1}{R^2}w_{,22},\quad \kappa_{12}=\frac{1}{R}u_{2,1}-\frac{2}{R}w_{,12}. \tag{32}$$

Again, substituting Eq. (30) into the last two equations of Eq. (26), and after rearrangement, we have

$$Q_1 = M_{1,1} + \frac{1}{R} M_{12,2},$$
$$Q_2 = M_{12,1} + \frac{1}{R} M_{2,2}. \tag{33}$$

The substitution of Eqs. (30), (33) into the first three equations of Eq. (26) yields the simplified equilibrium equations

$$N_{1,1} + \frac{1}{R} N_{12,2} = 0,$$
$$N_{12,1} + \frac{1}{R} N_{2,2} + \frac{1}{R}\left(M_{12,1} + \frac{1}{R} M_{2,2} \right) = 0, \tag{34}$$
$$M_{1,11} + \frac{2}{R} M_{12,12} + \frac{1}{R^2} M_{2,22} - \frac{N_2}{R} = q_n.$$

Finally, substituting Eqs. (30), (33) into Eq. (28) gives

$$T_{12} = N_{12}, \quad T_{21} = N_{21},$$
$$V_1 = M_{1,1} + \frac{2}{R} M_{12,2}, \quad V_1 = M_{2,2} + \frac{2}{R} M_{12,1}. \tag{35}$$

The stress-strain relations for the kth layer [10,11] in a laminated anisotropic cylindrical shell are expressed as

$$\begin{Bmatrix} \sigma_1 \\ \sigma_2 \\ \tau_{12} \end{Bmatrix}_k = \begin{bmatrix} \bar{Q}_{11} & \bar{Q}_{12} & \bar{Q}_{16} \\ \bar{Q}_{12} & \bar{Q}_{22} & \bar{Q}_{26} \\ \bar{Q}_{16} & \bar{Q}_{26} & \bar{Q}_{66} \end{bmatrix}_k \left\{ \begin{Bmatrix} \varepsilon_1^0 \\ \varepsilon_2^0 \\ \gamma_{12}^0 \end{Bmatrix} + z \begin{Bmatrix} \kappa_1 \\ \kappa_2 \\ \kappa_{12} \end{Bmatrix} \right\}, \tag{36}$$

where

$$\begin{aligned}
\bar{Q}_{11} &= Q_{11}\cos^4\theta + 2(Q_{12}+2Q_{66})\sin^2\theta\cos^2\theta + Q_{22}\sin^4\theta, \\
\bar{Q}_{12} &= (Q_{11}+Q_{22}-4Q_{66})\sin^2\theta\cos^2\theta + Q_{12}(\sin^4\theta+\cos^4\theta), \\
\bar{Q}_{22} &= Q_{11}\sin^4\theta + 2(Q_{12}+2Q_{66})\sin^2\theta\cos^2\theta + Q_{22}\cos^4\theta, \\
\bar{Q}_{16} &= (Q_{11}-Q_{12}-2Q_{66})\sin\theta\cos^3\theta \\
&\quad + (Q_{12}-Q_{22}+2Q_{66})\sin^3\theta\cos\theta, \\
\bar{Q}_{26} &= (Q_{11}-Q_{12}-2Q_{66})\sin^3\theta\cos\theta \\
&\quad + (Q_{12}-Q_{22}+2Q_{66})\sin\theta\cos^3\theta, \\
\bar{Q}_{66} &= (Q_{11}+Q_{22}-2Q_{12}-2Q_{66})\sin^2\theta\cos^2\theta \\
&\quad + Q_{66}(\sin^4\theta+\cos^4\theta).
\end{aligned} \tag{37}$$

In Eq. (37), θ is the angle of ply orientation (the more precise definition about θ is described in Ref. [10]) and

$$Q_{11} = \frac{E_1}{1-\nu_{12}\nu_{21}},$$
$$Q_{12} = Q_{21} = \frac{\nu_{12}E_1}{1-\nu_{12}\nu_{21}} = \frac{\nu_{21}E_2}{1-\nu_{12}\nu_{21}}, \tag{38}$$
$$Q_{22} = \frac{E_2}{1-\nu_{12}\nu_{21}},$$
$$Q_{66} = G_{12}.$$

The stress and moment resultants are defined as

$$\begin{Bmatrix} N_1 \\ N_2 \\ N_{12} \end{Bmatrix} = \sum_{k=1}^{N} \int_{z_{k-1}}^{z_k} \begin{Bmatrix} \sigma_1 \\ \sigma_2 \\ \tau_{12} \end{Bmatrix}_k dz \tag{39}$$

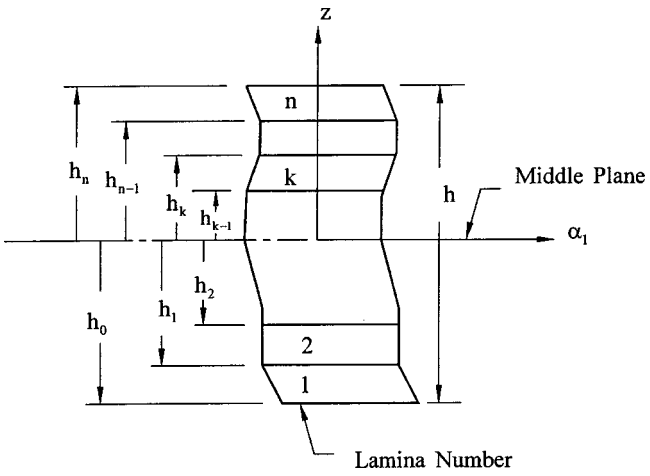

Fig. 5 Geometry of multilayered laminate

and

$$\begin{Bmatrix} M_1 \\ M_2 \\ M_{12} \end{Bmatrix} = \sum_{k=1}^{N} \int_{z_{k-1}}^{z_k} \begin{Bmatrix} \sigma_1 \\ \sigma_2 \\ \tau_{12} \end{Bmatrix}_k z dz \tag{40}$$

where z_k and z_{k-1} are described in Fig. 5.

Substituting Eq. (36) into Eqs. (39) and (40), respectively, and rearranging the results, the stress and moment resultants can be expressed as

$$\begin{Bmatrix} N_1 \\ N_2 \\ N_{12} \\ M_1 \\ M_2 \\ M_{12} \end{Bmatrix} = \begin{bmatrix} A_{11} & A_{12} & A_{16} & B_{11} & B_{12} & B_{16} \\ A_{12} & A_{22} & A_{26} & B_{12} & B_{22} & B_{26} \\ A_{16} & A_{26} & A_{66} & B_{16} & B_{26} & B_{66} \\ B_{11} & B_{12} & B_{16} & D_{11} & D_{12} & D_{16} \\ B_{12} & B_{22} & B_{26} & D_{12} & D_{22} & D_{26} \\ B_{16} & B_{26} & B_{66} & D_{16} & D_{26} & D_{66} \end{bmatrix} \begin{Bmatrix} \varepsilon_1^0 \\ \varepsilon_2^0 \\ \gamma_{12}^0 \\ \kappa_1 \\ \kappa_2 \\ \kappa_{12} \end{Bmatrix}, \tag{41}$$

where

$$A_{ij} = \sum_{k=1}^{N} (\bar{Q}_{ij})_k (z_k - z_{k-1}),$$
$$B_{ij} = \frac{1}{2}\sum_{k=1}^{N} (\bar{Q}_{ij})_k (z_k^2 - z_{k-1}^2), \tag{42}$$
$$D_{ij} = \frac{1}{3}\sum_{k=1}^{N} (\bar{Q}_{ij})_k (z_k^3 - z_{k-1}^3),$$
$$i, \ j = 1, \ 2, \ 6.$$

Finally, substituting Eq. (32) into Eq. (41), it generates six equations. For convenience, the results are abbreviated as

$$\begin{aligned}
N_1 &= A_{11}u_{1,1} + A_{12}\left(\frac{1}{R}u_{2,2} + \frac{w}{R}\right) + \cdots + B_{16}\left(\frac{1}{R}u_{2,1} - \frac{2}{R}w_{,12}\right), \\
N_2 &= A_{12}u_{1,1} + A_{22}\left(\frac{1}{R}u_{2,2} + \frac{w}{R}\right) + \cdots + B_{26}\left(\frac{1}{R}u_{2,1} - \frac{2}{R}w_{,12}\right), \\
N_{12} &= A_{16}u_{1,1} + A_{26}\left(\frac{1}{R}u_{2,2} + \frac{w}{R}\right) + \cdots + B_{66}\left(\frac{1}{R}u_{2,1} - \frac{2}{R}w_{,12}\right), \\
M_1 &= B_{11}u_{1,1} + B_{12}\left(\frac{1}{R}u_{2,2} + \frac{w}{R}\right) + \cdots + D_{16}\left(\frac{1}{R}u_{2,1} - \frac{2}{R}w_{,12}\right),
\end{aligned} \tag{43}$$

$$M_2=B_{12}u_{1,1}+B_{22}\left(\frac{1}{R}u_{2,2}+\frac{w}{R}\right)+\cdots+D_{26}\left(\frac{1}{R}u_{2,1}-\frac{2}{R}w_{,12}\right),$$

$$M_{12}=B_{16}u_{1,1}+B_{26}\left(\frac{1}{R}u_{2,2}+\frac{w}{R}\right)+\cdots+D_{66}\left(\frac{1}{R}u_{2,1}-\frac{2}{R}w_{,12}\right).$$

Moreover, the substitution of Eq. (43) into Eq. (34) yields

$$\begin{aligned}
&(A_{11}u_{1,11}+\cdots)+\frac{1}{R}(A_{16}u_{1,12}+\cdots)=0,\\
&(A_{16}u_{1,11}+\cdots)+\frac{1}{R}(A_{12}u_{1,12}+\cdots)\\
&\quad+\frac{1}{R}\left[(B_{16}u_{1,11}+\cdots)+\frac{1}{R}(B_{12}u_{1,12}+\cdots)\right]=0,\\
&(B_{11}u_{1,111}+\cdots)+\frac{2}{R}(B_{16}u_{1,112}+\cdots)\\
&\quad+\frac{1}{R^2}(B_{12}u_{1,122}+\cdots)-\frac{1}{R}(A_{12}u_{1,1}+\cdots)=q_n.
\end{aligned}\tag{44}$$

To solve the system of partial differential equations of Eq. (44), the Chebyshev collocation method is used as discussed in the next section.

Chebyshev Collocation Method

Consider a rectangular plate with the dimensions $[X_1,X_2]\times[Y_1,Y_2]$ and it implies that $X_1\leqslant\alpha_1\leqslant X_2$ and $Y_1\leqslant\alpha_2\leqslant Y_2$. First of all, separate the equilibrium Eqs. (44) and boundary conditions (27*a*), (27*b*) into three groups as follows:

Group 1: Eq. (44.1) and

$$N_1=\overline{N}_1,\ \text{or}\ u_1=\overline{u}_1,\ (\text{on the edge of constant}\ \alpha_1)\tag{45a}$$

$$T_{21}=\overline{T}_{21},\ \text{or}\ u_1=\overline{u}_1,\ (\text{on the edge of constant}\ \alpha_2).\tag{45b}$$

Group 2: Eq. (44.2) and

$$T_{12}=\overline{T}_{12},\ \text{or}\ u_2=\overline{u}_2,\ (\text{on the edge of constant}\ \alpha_1)\tag{46a}$$

$$N_2=\overline{N}_2,\ \text{or}\ u_2=\overline{u}_2,\ (\text{on the edge of constant}\ \alpha_2).\tag{46b}$$

Group 3: Eq. (44.3) and

$$\begin{aligned}&V_1=\overline{V}_1,\ \text{or}\ w=\overline{w},\\ &M_1=\overline{M}_1,\ \text{or}\ \beta_1=\overline{\beta}_1\end{aligned}\quad(\text{on the edge of constant}\ \alpha_1),\tag{47a}$$

$$\begin{aligned}&V_2=\overline{V}_2,\ \text{or}\ w=\overline{w},\\ &M_2=\overline{M}_2,\ \text{or}\ \beta_2=\overline{\beta}_2\end{aligned}\quad(\text{on the edge of constant}\ \alpha_2).\tag{47b}$$

Let the solutions to the system of partial differential equations be

$$\begin{aligned}
u_1(\alpha_1,\alpha_2)&=\sum_{m=0}^{M}\sum_{n=0}^{N}a_{mn}\hat{T}_m(\alpha_1)\tilde{T}_n(\alpha_2),\\
u_2(\alpha_1,\alpha_2)&=\sum_{m=0}^{M}\sum_{n=0}^{N}b_{mn}\hat{T}_m(\alpha_1)\tilde{T}_n(\alpha_2),\\
w(\alpha_1,\alpha_2)&=\sum_{m=0}^{M}\sum_{n=0}^{N}c_{mn}\hat{T}_m(\alpha_1)\tilde{T}_n(\alpha_2),
\end{aligned}\tag{48}$$

where

$$\begin{aligned}
\hat{T}_m(\alpha_1)&=T_m\left(\frac{1}{X_2-X_1}(2\alpha_1-X_2-X_1)\right),\\
\tilde{T}_n(\alpha_2)&=T_n\left(\frac{1}{Y_2-Y_1}(2\alpha_2-Y_2-Y_1)\right).
\end{aligned}\tag{49}$$

Equation (49) can be derived by linear transformation in order to satisfy that the variables in Chebyshev polynomials within the interval $[-1,1]$.

Let the Chebyshev-extrema points, [12], (i.e., also named Gauss-Lobatto points) be

$$\begin{aligned}
\hat{\alpha}_i&=\frac{X_2+X_1}{2}-\frac{X_2-X_1}{2}\cos\left(\frac{\pi i}{M}\right),\ i=0,\ 1,\cdots,\ M,\\
\tilde{\alpha}_j&=\frac{Y_2+Y_1}{2}-\frac{Y_2-Y_1}{2}\cos\left(\frac{\pi j}{N}\right),\ j=0,\ 1,\cdots,\ N.
\end{aligned}\tag{50}$$

For example, if a plate is subjected to the transverse load q_n with four edges simply supported, the boundary conditions are

$$\text{Group 1:}\ \begin{cases}u_1=0.(\alpha_1=\text{const.})\\ u_1=0.(\alpha_2=\text{const.})\end{cases}\tag{51a}$$

$$\text{Group 2:}\ \begin{cases}u_2=0.(\alpha_1=\text{const.})\\ u_2=0.(\alpha_2=\text{const.})\end{cases}\tag{51b}$$

$$\text{Group 3:}\ \begin{cases}w=0,\ M_1=0.(\alpha_1=\text{const.})\\ w=0,\ M_2=0.(\alpha_2=\text{const.})\end{cases}.\tag{51c}$$

By the collocation method, [13], the substitution of Eq. (48) into Eq. (44) and Eqs. (51*a*,*b*,*c*) yields

$$\begin{aligned}
\text{Group 1:}\ &\sum_{m=0}^{M}\sum_{n=0}^{N}\{a_{mn}[A_{11}\hat{T}_m^{(2)}(\hat{\alpha}_i)\tilde{T}_n(\tilde{\alpha}_j)+\cdots]\\
&+b_{mn}[A_{12}\hat{T}_m^{(1)}(\hat{\alpha}_i)\tilde{T}_n^{(1)}(\tilde{\alpha}_j)+\cdots]\\
&+\cdots-2c_{mn}[B_{16}\hat{T}_m^{(2)}(\hat{\alpha}_i)\tilde{T}_n^{(1)}(\tilde{\alpha}_j)+\cdots]\}=0,\\
&i=1,2,\cdots,M-1,\ j=1,2,\cdots,N-1
\end{aligned}\tag{52a}$$

$$u_1(X_1,\tilde{\alpha}_j)=\sum_{m=0}^{M}\sum_{n=0}^{N}a_{mn}\hat{T}_m(X_1)\tilde{T}_n(\tilde{\alpha}_j)=0,\quad j=0,1,\cdots,N\tag{52b}$$

$$u_1(X_2,\tilde{\alpha}_j)=\sum_{m=0}^{M}\sum_{n=0}^{N}a_{mn}\hat{T}_m(X_2)\tilde{T}_n(\tilde{\alpha}_j)=0,\quad j=0,1,\cdots,N\tag{52c}$$

$$u_1(\hat{\alpha}_i,Y_1)=\sum_{m=0}^{M}\sum_{n=0}^{N}a_{mn}\hat{T}_m(\hat{\alpha}_i)\tilde{T}_n(Y_1)=0,\ i=1,\cdots,M-1\tag{52d}$$

$$u_1(\hat{\alpha}_i,Y_2)=\sum_{m=0}^{M}\sum_{n=0}^{N}a_{mn}\hat{T}_m(\hat{\alpha}_i)\tilde{T}_n(Y_2)=0,\ i=1,\cdots,M-1\tag{52e}$$

$$\begin{aligned}
\text{Group 2:}\ &\sum_{m=0}^{M}\sum_{n=0}^{N}\{a_{mn}[A_{16}\hat{T}_m^{(2)}(\hat{\alpha}_i)\tilde{T}_n(\tilde{\alpha}_j)+\cdots]\\
&+b_{mn}[A_{26}\hat{T}_m^{(1)}(\hat{\alpha}_i)\tilde{T}_n^{(1)}(\tilde{\alpha}_j)+\cdots]\\
&+\cdots-2c_{mn}[B_{66}\hat{T}_m^{(2)}(\hat{\alpha}_i)\tilde{T}_n^{(1)}(\tilde{\alpha}_j)+\cdots]\}=0,\\
&i=1,2,\cdots,M-1,\ j=1,2,\cdots,N-1
\end{aligned}\tag{53a}$$

$$u_2(X_1,\tilde{\alpha}_j)=\sum_{m=0}^{M}\sum_{n=0}^{N} b_{mn}\hat{T}_m(X_1)\tilde{T}_n(\tilde{\alpha}_j)=0,\ \ j=0,1,\cdots,N \tag{53b}$$

$$u_2(X_2,\tilde{\alpha}_j)=\sum_{m=0}^{M}\sum_{n=0}^{N} b_{mn}\hat{T}_m(X_2)\tilde{T}_n(\tilde{\alpha}_j)=0,\ \ j=0,1,\cdots,N \tag{53c}$$

$$u_2(\hat{\alpha}_i,Y_1)=\sum_{m=0}^{M}\sum_{n=0}^{N} b_{mn}\hat{T}_m(\hat{\alpha}_i)\tilde{T}_n(Y_1)=0,\ \ i=1,\cdots,M-1 \tag{53d}$$

$$u_2(\hat{\alpha}_i,Y_2)=\sum_{m=0}^{M}\sum_{n=0}^{N} b_{mn}\hat{T}_m(\hat{\alpha}_i)\tilde{T}_n(Y_2)=0,\ \ i=1,\cdots,M-1 \tag{53e}$$

$$\text{Group 3:}\ \sum_{m=0}^{M}\sum_{n=0}^{N}\{a_{mn}[B_{11}\hat{T}_m^{(3)}(\hat{\alpha}_i)\tilde{T}_n(\tilde{\alpha}_j)+\cdots]+b_{mn}[B_{12}\hat{T}_m^{(2)}(\hat{\alpha}_i)\tilde{T}_n^{(1)}(\tilde{\alpha}_j)+\cdots]+\cdots-2c_{mn}[D_{16}\hat{T}_m^{(3)}(\hat{\alpha}_i)\tilde{T}_n^{(1)}(\tilde{\alpha}_j)+\cdots]\}=q_n,$$
$$i=2,3,\cdots,M-2,\ \ j=2,3,\cdots,N-2 \tag{54a}$$

$$w(X_1,\tilde{\alpha}_j)=\sum_{m=0}^{M}\sum_{n=0}^{N} c_{mn}\hat{T}_m(X_1)\tilde{T}_n(\tilde{\alpha}_j)=0,\ \ j=0,1,\cdots,N \tag{54b}$$

$$w(X_2,\tilde{\alpha}_j)=\sum_{m=0}^{M}\sum_{n=0}^{N} c_{mn}\hat{T}_m(X_2)\tilde{T}_n(\tilde{\alpha}_j)=0,\ \ j=0,1,\cdots,N \tag{54c}$$

$$w(\hat{\alpha}_i,Y_1)=\sum_{m=0}^{M}\sum_{n=0}^{N} c_{mn}\hat{T}_m(\hat{\alpha}_i)\tilde{T}_n(Y_1)=0,\ \ i=1,\cdots,M-1 \tag{54d}$$

$$u_1(\hat{\alpha}_i,Y_2)=\sum_{m=0}^{M}\sum_{n=0}^{N} c_{mn}\hat{T}_m(\hat{\alpha}_i)\tilde{T}_n(Y_2)=0,\ \ i=1,\cdots,M-1 \tag{54e}$$

$$M_1(X_1,\tilde{\alpha}_j)=\sum_{m=0}^{M}\sum_{n=0}^{N}\{a_{mn}[B_{11}\hat{T}_m^{(1)}(X_1)\tilde{T}_n(\tilde{\alpha}_j)+\cdots]+b_{mn}[B_{12}\hat{T}_m(X_1)\tilde{T}_n^{(1)}(\tilde{\alpha}_j)+\cdots]+\cdots-2c_{mn}[D_{16}\hat{T}_m^{(1)}(X_1)\tilde{T}_n^{(1)}(\tilde{\alpha}_j)+\cdots]\}=0,$$
$$j=1,2,\cdots,N-1 \tag{54f}$$

$$M_1(X_2,\tilde{\alpha}_j)=\sum_{m=0}^{M}\sum_{n=0}^{N}\{a_{mn}[B_{11}\hat{T}_m^{(1)}(X_2)\tilde{T}_n(\tilde{\alpha}_j)+\cdots]+b_{mn}[B_{12}\hat{T}_m(X_2)\tilde{T}_n^{(1)}(\tilde{\alpha}_j)+\cdots]+\cdots-2c_{mn}[D_{16}\hat{T}_m^{(1)}(X_2)\tilde{T}_n^{(1)}(\tilde{\alpha}_j)+\cdots]\}=0,$$
$$j=1,2,\cdots,N-1 \tag{54g}$$

$$M_2(\hat{\alpha}_i,Y_1)=\sum_{m=0}^{M}\sum_{n=0}^{N}\{a_{mn}[B_{12}\hat{T}_m^{(1)}(\hat{\alpha}_i)\tilde{T}_n(Y_1)+\cdots]+b_{mn}[B_{22}\hat{T}_m(\hat{\alpha}_i)\tilde{T}_n^{(1)}(Y_1)+\cdots]+\cdots-2c_{mn}[D_{26}\hat{T}_m^{(1)}(\hat{\alpha}_i)\tilde{T}_n^{(1)}(Y_1)+\cdots]\}=0,$$
$$i=2,3\cdots,N-2 \tag{54h}$$

$$M_2(\hat{\alpha}_i,Y_2)=\sum_{m=0}^{M}\sum_{n=0}^{N}\{a_{mn}[B_{12}\hat{T}_m^{(1)}(\hat{\alpha}_i)\tilde{T}_m(Y_2)+\cdots]+b_{mn}[B_{22}\hat{T}_m(\hat{\alpha}_i)\tilde{T}_n^{(1)}(Y_2)+\cdots]+\cdots-2c_{mn}[D_{26}\hat{T}_m^{(1)}(\hat{\alpha}_i)\tilde{T}_n^{(1)}(Y_2)+\cdots]\}=0,$$
$$i=2,3\cdots,N-2. \tag{54i}$$

Both of the numbers of the total equations in three groups and all the unknown constants (a_{mn}, b_{mn}, c_{mn}) are $3(M+1)(N+1)$. Through this, the unique solution of the unknown constants (a_{mn}, b_{mn}, c_{mn}) can be received. Other problems with any different boundary conditions can be solved similarly via the method mentioned above.

Examples

Case 1:

Consider a four-layered cross-ply laminated clamped composite cylindrical shell which is subjected to a uniformly distributed load $q_n=1000$ Pa. The contour of the cylindrical shell is represented in Fig. 4.

Material: graphite/epoxy T300/5208.

Mechanical properties of a lamina with unidirectional fibers:

$$E_1=181\ \text{GPa},\ \ E_2=10.3\ \text{GPa},$$
$$G_{12}=7.17\ \text{GPa},\ \ \nu_{12}=0.28. \tag{55}$$

Thickness of each layer: 0.125 mm.

Stacking sequence: [0/90/90/0].

Dimension: $[0,4]\text{m}\times[0,\pi/6]$radian, i.e., $0\leqslant\alpha_1\leqslant 4$ and $0\leqslant\alpha_2\leqslant\pi/6$.

Radius of the cylindrical shell: $R=5$ m.

For clamped edges, the boundary conditions are as follows:

For $\alpha_1=0$ and $\alpha_1=4$:

$$u_1=u_2=w=\beta_1=0. \tag{56}$$

For $\alpha_2=0$ and $\alpha_2=\pi/6$:

$$u_2=u_1=w=\beta_2=0. \tag{57}$$

Solution procedure:

1. By Eq. (42), A_{ij}, B_{ij}, and D_{ij} (i, $j=1$, 2, 6) can be calculated, and then substitute the results into Eq. (44).
2. Substitute Eq. (48) into Eq. (44) with boundary conditions (56) and (57).
3. Separate these equations into three groups as previously described.
4. After the manipulation by Chebyshev collocation method as mentioned above, the unknown constants a_{mn}, b_{mn}, and c_{mn} in Eq. (48) can be obtained.
5. Substitute a_{mn}, b_{mn}, and c_{mn} into Eq. (48) to receive u_1, u_2, and w.
6. Substitute u_1, u_2, and w into Eq. (43) to obtain the stress and moment resultants.

For $M=N=12$ in Eq. (48), all the results of u_1, u_2, w, N_1, N_2, N_{12}, M_1, M_2, and M_{12} are depicted in Figs. 6–14, respectively.

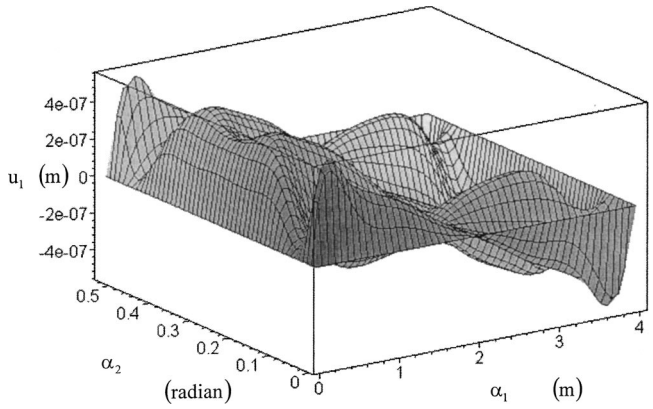

Fig. 6 Displacement of u_1 in Case 1

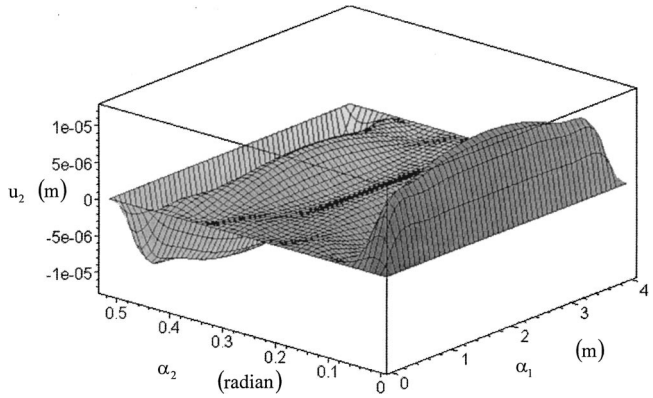

Fig. 7 Displacement of u_2 in Case 1

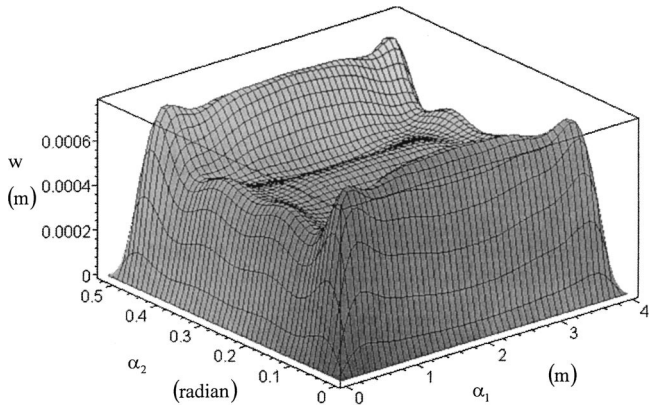

Fig. 8 Displacement of w in Case 1

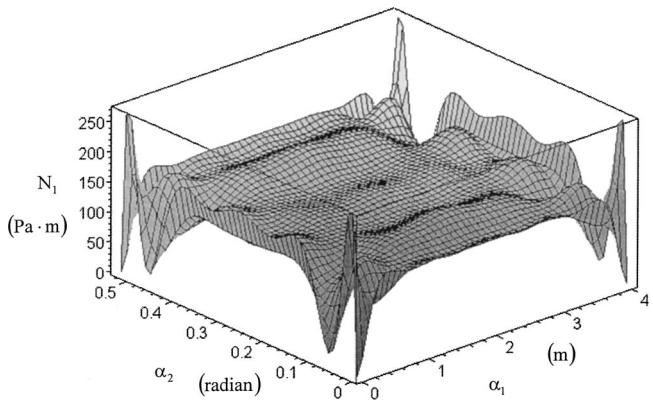

Fig. 9 Stress resultant N_1 in Case 1

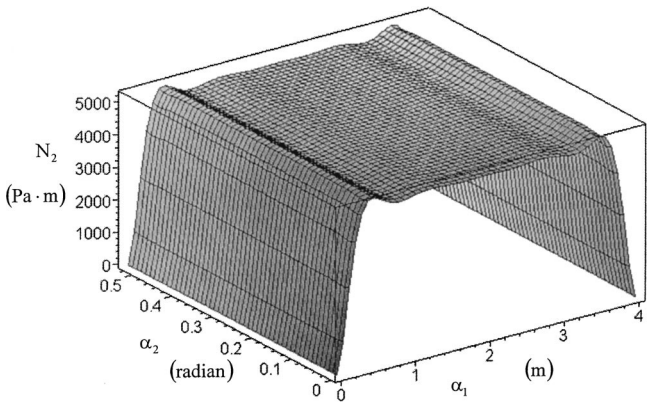

Fig. 10 Stress resultant N_2 in Case 1

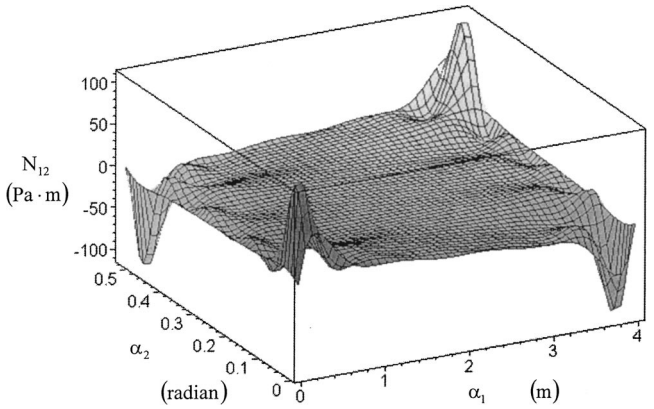

Fig. 11 Stress resultant N_{12} in Case 1

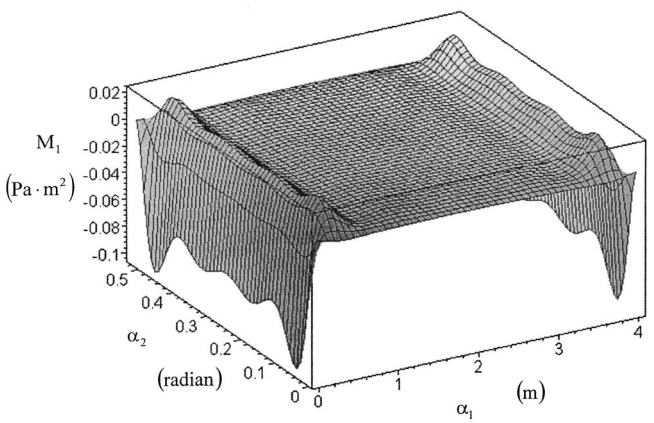

Fig. 12 Moment resultant M_1 in Case 1

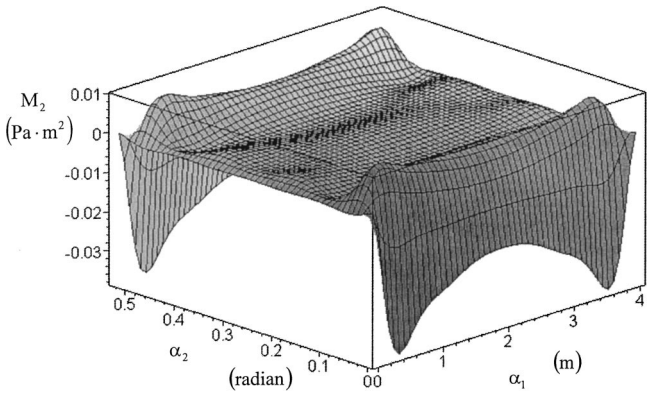

Fig. 13 Moment resultant M_2 in Case 1

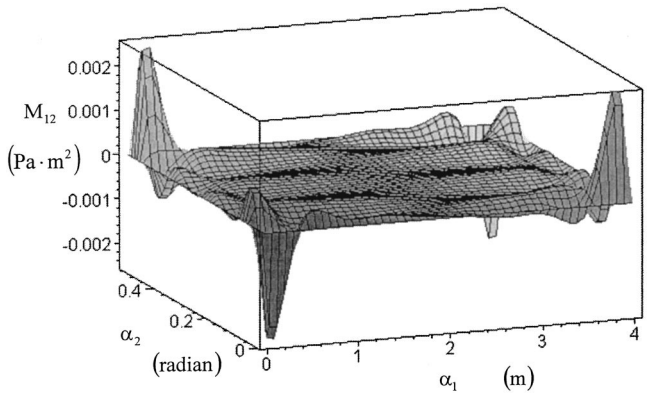

Fig. 14 Moment resultant M_{12} in Case 1

The numerical results of u_1, u_2, w, N_1, and N_2 are listed in Tables 1–5 for reference. At the same time, the results by finite element method incorporated with NASTRAN software are demonstrated to validate the correctness of the method of Chebyshev polynomials. A 32×16 (32 for α_1-direction, 16 for α_2-direction) mesh is adopted for the finite element method in this case. However, the results of N_{12}, M_1, M_2, and M_{12} are approaching to zero in the interior region of the cylindrical shell. Although some maximal values occur near the corners or edges of the cylindrical shell, they are omitted herein.

The results (M and N in Eq. (48) are greater than 12) are extremely close to those in column (C_12_12). Thus the only results in columns (C_8_8), (C_10_10), and (C_12_12) are presented in this case.

Let $\Delta\alpha_2$ be the range of α_2. Provided $R\Delta\alpha_2$=constant, the magnitude of R must be decreased by increasing the magnitude of $\Delta\alpha_2$. This causes the displacement w decreasing when the radius R is decreased. For convenience, the middle point of the shell is specified as the sample location in each interval of α_2, and take $\alpha_2=\pi/12$ for each interval. The phenomenon of the center-point displacement w versus the change of curvature is plotted in Fig. 15.

Case 2:

Consider a four-layered cross-ply laminated composite cylindrical shell which is subjected to a uniformly distributed load $q_n=1000$ Pa. The cylindrical shell is clamped on the edges $\alpha_1=0,\alpha_1=4$ and simply supported on the edges $\alpha_2=0,\alpha_2=\pi/6$.

The mechanical properties, thickness of each layer, and the dimensions are the same as those in Case 1.

For clamped edges, the boundary conditions are as follows:

For $\alpha_1=0,4$:

$$u_1=u_2w=\beta_1=0. \tag{58}$$

For simply supported edges, the boundary conditions are as follows:

For $\alpha_2=0,\pi/6$:

$$u_1=u_2=V_2=M_2=0. \tag{59}$$

Table 1 The displacement of u_1 in Case 1

Tc(**) u_1 (unit: m) Po(*)	C_8_8(I)	C_10_10(II)	C_12_12(III)	Na(IV)
(1, π/48)	3.71799E-7 (−901)	1.71899E-7 (−470)	−4.94760E-8 (6.56)	−4.64279E-8
(1, 2π/48)	4.12555E-8 (−119)	1.63615E-7 (−177)	−2.23942E-7 (4.78)	−2.13726E-7
(1, 3π/48)	4.70309E-7 (168)	3.48953E-7 (98)	1.88485E-7 (7.21)	1.75810E-7
(1, 4π/48)	8.29816E-7 (2105)	4.11935E-7 (995)	3.91099E-8 (3.96)	3.76202E-8
(1, 5π/48)	4.70309E-7 (168)	3.48953E-7 (98)	1.88485E-7 (7.21)	1.75810E-7
(1, 6π/48)	4.12555E-8 (−119)	1.63615E-7 (−177)	−2.23942E-7 (4.78)	−2.13726E-7
(1, 7π/48)	3.71799E-7 (−901)	1.71899E-7 (−470)	−4.94760E-8 (6.56)	−4.64279E-8
(2, π/48)	0	0	0	0
(2, 2π/48)	0	0	0	0
(2, 3π/48)	0	0	0	0
(2, 4 π /48)	0	0	0	0
(2, 5π/48)	0	0	0	0
(2, 6π/48)	0	0	0	0
(2, 7π/48)	0	0	0	0
(3, π/48)	−3.71799E-7 (−901)	−1.71899E-7 (−470)	4.94760E-8 (6.56)	4.64279E-8
(3, 2π/48)	−4.12555E-8 (−119)	−1.63615E-7 (−177)	2.23942E-7 (4.78)	2.13726E-7
(3, 3π/48)	−4.70309E-7 (168)	−3.48953E-7 (98)	−1.88485E-7 (7.21)	−1.75810E-7
(3, 4π/48)	−8.29816E-7 (2105)	−4.11935E-7 (995)	−3.91099E-8 (3.96)	−3.76202E-8
(3, 5π/48)	−4.70309E-7 (168)	−3.48953E-7 (98)	−1.88485E-7 (7.21)	−1.75810E-7
(3, 6π/48)	−4.12555E-8 (−119)	−1.63615E-7 (−177)	2.23942E-7 (4.78)	2.13726E-7
(3, 7π/48)	−3.71799E-7 (−901)	−1.71899E-7 (−470)	4.94760E-8 (6.56)	4.64279E-8

Notes: Po(*): position (α_1,α_2).

Tc(**): type of collocation points.

(I): Chebyshev collocation method ($M=N=8$ in Eq. (48)). The values in the parentheses of the C_8_8 column indicate the errors compared with the results of NASTRAN. The errors are calculated by the formula (C_8_8)−Na/Na×100%.

(II): Chebyshev collocation method ($M=N=10$ in Eq. (48)). The errors are calculated by the formula (C_10_10)−Na/Na ×100% and expressed in parentheses.

(III): Chebyshev collocation method ($M=N=12$ in Eq. (48)). The errors are calculated by the formula (C_12_12)−Na/Na ×100% and listed in parentheses.

(IV): Numerical solutions obtained by the finite element method and NASTRAN software and designated by Na.

Table 2 The displacement of u_2 in Case 1

Tc(**) u_2 (unit: m) Po(*)	C_8_8(I)	C_10_10(II)	C_12_12(III)	Na(IV)
(1, π/48)	1.99395E-5 (136)	9.44063E-6 (12)	8.16273E-6 (−3.58)	8.46580E-6
(1, 2π/48)	5.25849E-6 (−475)	−2.65204E-6 (89)	−1.29907E-6 (−7.48)	−1.40410E-6
(1, 3π/48)	−6.98802E-6 (2762)	3.81387*E*-7 (−256)	−2.29287E-7 (−6.09)	−2.44156E-7
(1, 4π/48)	0	0	0	0
(1, 5π/48)	6.98802E-6 (2762)	−3.81387E-7 (−256)	2.29287E-7 (−6.09)	2.44156E-7
(1, 6π/48)	−5.25849E-6 (−475)	2.65204E-6 (89)	1.29907E-6 (−7.48)	1.40410E-6
(1, 7 π/48)	−1.99395E-5 (136)	−9.44063E-6 (12)	−8.16273E-6 (−3.58)	−8.46580E-6
(2, π/48)	1.91868E-5 (82)	9.96128E-6 (−5)	1.00206E-5 (−4.71)	1.05160E-5
(2, 2π/48)	4.71305E-6 (−334)	−2.49949E-6 (24)	−1.86362E-6 (−7.65)	−2.01800E-6
(2, 3π/48)	−7.17021E-6 (1470)	−2.45568E-7 (−46)	−4.29606E-7 (−5.92)	−4.56640E-7
(2, 4π/48)	0	0	0	0
(2, 5π/48)	7.17021E-6 (1470)	2.45568E-7 (−46)	4.29606E-7 (−5.92)	4.56640E-7
(2, 6 π/48)	−4.71305E-6 (−334)	2.49949E-6 (24)	1.86362E-6 (−7.65)	2.01800E-6
(2, 7π/48)	−1.91868E-5 (82)	−9.96128E-6 (−5)	−1.00206E-5 (−4.71)	−1.05160E-5
(3, π/48)	1.99395E-5 (136)	9.44063E-6 (12)	8.16273E-6 (−3.58)	8.46580E-6
(3, 2π/48)	5.25849E-6 (−475)	−2.65204E-6 (89)	−1.29907E-6 (−7.48)	−1.40410E-6
(3, 3π/48)	−6.98802E-6 (2762)	3.81387E-7 (−256)	−2.29287E-7 (−6.09)	−2.44156E-7
(3, 4π/48)	0	0	0	0
(3, 5 π/48)	6.98802E-6 (2762)	−3.81387E-7 (−256)	2.29287E-7 (−6.09)	2.44156E-7
(3, 6π/48)	−5.25849E-6 (−475)	2.65204E-6 (89)	1.29907E-6 (−7.48)	1.40410E-6
(3, 7π/48)	−1.99395E-5 (136)	−9.44063E-6 (12)	−8.16273E-6 (−3.58)	−8.46580E-6

The solution procedure is similar to that in Case 1.

For $M=N=12$ in Eq. (48), all the results of u_1, u_2, w, N_1, N_2, N_{12}, M_1, M_2, and M_{12} in the case are depicted in Figs. 16–24, respectively. Comparing the results ($M=N=12$ in Eq. (48)) with those obtained by NASTRAN (the mesh is same as in Case 1), all the errors of the results are very small. For space saving, numerical result lists are omitted.

Similarly, as the final description in Case 2, the trend of center-point deflection versus the change of curvature is plotted in Fig. 25.

Table 3 The displacement of w in Case 1

Tc(**) w (unit: m) Po(*)	C_8_8(I)	C_10_10(II)	C_12_12(III)	Na(IV)
(1, π/48)	5.62959E-4 (−24)	7.31787E-4 (−1.21)	7.34624E-4 (−0.83)	7.40790E-4
(1, 2π/48)	8.45028E-4 (54)	5.60092E-4 (2.18)	5.27200E-4 (−3.82)	5.48130E-4
(1, 3π/48)	5.67917E-4 (15)	4.55912E-4 (−7.53)	4.88377E-4 (−0.95)	4.93070E-4
(1, 4π/48)	3.61999E-4 (−32)	5.63981E-4 (5.81)	5.35111E-4 (0.39)	5.33010E-4
(1, 5π/48)	5.67917E-4 (15)	4.55912E-4 (−7.53)	4.88377E-4 (−0.95)	4.93070E-4
(1, 6π/48)	8.45028E-4 (54)	5.60092E-4 (2.18)	5.27200E-4 (−3.82)	5.48130E-4
(1, 7π/48)	5.62959E-4 (−24)	7.31787E-4 (−1.21)	7.34624E-4 (−0.83)	7.40790E-4
(2, π/48)	5.45022E-4 (−25)	7.44034E-4 (1.82)	7.31242E-4 (−0.07)	7.30720E-4
(2, 2π/48)	8.17424E-4 (38)	5.67869E-4 (−4.01)	5.81378E-4 (−1.73)	5.91590E-4
(2, 3π/48)	5.42535E-4 (17)	4.57548E-4 (−1.53)	4.63682E-4 (−0.21)	4.64650E-4
(2, 4π/48)	3.38754E-4 (−38)	5.63529E-4 (2.78)	5.53511E-4 (0.95)	5.48290E-4
(2, 5π/48)	5.42535E-4 (17)	4.57548E-4 (−1.53)	4.63682E-4 (−0.21)	4.64650E-4
(2, 6π/48)	8.17424E-4 (38)	5.67869E-4 (−4.01)	5.81378E-4 (−1.73)	5.91590E-4
(2, 7π/48)	5.45022E-4 (−25)	7.44034E-4 (1.82)	7.31242E-4 (−0.07)	7.30720E-4
(3, π/48)	5.62959E-4 (−24)	7.31787E-4 (−1.21)	7.34624E-4 (−0.83)	7.40790E-4
(3, 2π/48)	8.45028E-4 (54)	5.60092E-4 (2.18)	5.27200E-4 (−3.82)	5.48130E-4
(3, 3π/48)	5.67917E-4 (15)	4.55912E-4 (−7.53)	4.88377E-4 (−0.95)	4.93070E-4
(3, 4π/48)	3.61999E-4 (−32)	5.63981E-4 (5.81)	5.35111E-4 (0.39)	5.33010E-4
(3, 5π/48)	5.67917E-4 (15)	4.55912E-4 (−7.53)	4.88377E-4 (−0.95)	4.93070E-4
(3, 6π/48)	8.45028E-4 (54)	5.60092E-4 (2.18)	5.27200E-4 (−3.82)	5.48130E-4
(3, 7π/48)	5.62959E-4 (−24)	7.31787E-4 (−1.21)	7.34624E-4 (−0.83)	7.40790E-4

Table 4 The stress resultant of N_1 in Case 1

N_1 Tc(**) (unit: Pa·m) Po(*)	C_8_8(I)	C_10_10(II)	C_12_12(III)	Na(IV)
(1, π/48)	126.780 (−13)	143.158 (−1.81)	145.375 (−0.29)	145.798
(1, 2π/48)	162.593 (6.47)	135.476 (−11.3)	144.597 (−5.32)	152.716
(1, 3π/48)	130.567 (−11)	126.974 (−13.4)	137.399 (−6.34)	146.703
(1, 4π/48)	105.455 (−28.4)	133.906 (−9.10)	142.990 (−2.93)	147.320
(1, 5π/48)	130.567 (−11)	126.974 (−13.4)	137.399 (−6.34)	146.703
(1, 6π/48)	162.593 (6.47)	135.476 (−11.3)	144.597 (−5.32)	152.716
(1, 7π/48)	126.780 (−13)	143.158 (−1.81)	145.375 (−0.29)	145.798
(2, π/48)	141.717 (−1.55)	141.235 (−1.89)	150.120 (4.29)	143.951
(2, 2π/48)	144.233 (−15.3)	141.715 (−16.7)	160.306 (−5.81)	170.209
(2, 3π/48)	132.355 (−7.54)	130.859 (−8.58)	134.798 (−5.83)	143.148
(2, 4π/48)	121.953 (−17.5)	125.636 (−15.0)	144.721 (−2.09)	147.813
(2, 5π/48)	132.355 (−7.54)	130.859 (−8.58)	134.798 (−5.83)	143.148
(2, 6π/48)	144.233 (−15.3)	141.715 (−16.7)	160.306 (−5.81)	170.209
(2, 7π/48)	141.717 (−1.55)	141.235 (−1.89)	150.120 (4.29)	143.951
(3, π/48)	126.780 (−13)	143.158 (−1.81)	145.375 (−0.29)	145.798
(3, 2π/48)	162.593 (6.47)	135.476 (−11.3)	144.597 (−5.32)	152.716
(3, 3π/48)	130.567 (−11)	126.974 (−13.4)	137.399 (−6.34)	146.703
(3, 4π/48)	105.455 (−28.4)	133.906 (−9.10)	142.990 (−2.93)	147.320
(3, 5π/48)	130.567 (−11)	126.974 (−13.4)	137.399 (−6.34)	146.703
(3, 6π/48)	162.593 (6.47)	135.476 (−11.3)	144.597 (−5.32)	152.716
(3, 7π/48)	126.780 (−13)	143.158 (−1.81)	145.375 (−0.29)	145.798

Discussion

Through the features of Chebyshev collocation method as stated, the method can be used to solve the problems of laminated anisotropic shells with complicated boundary conditions. The solutions to most problems in this field of laminated anisotropic shells can be obtained by the proposed method; however, there are two groups of problems which still can not be accomplished. They are (a) the problem of a shell subjected to concentrated loading, and (b) the problem of thick laminated anisotropic shells. In group (a), it is hard to handle if the position of the concentrated loading is not located at one of the collocation points. However, that may be overcome by selecting larger values of M and N, e.g., M and

Table 5 The stress resultant of N_2 in Case 1

N_2 Tc(**) (unit: Pa·m) Po(*)	C_8_8(I)	C_10_10(II)	C_12_12(III)	Na(IV)
(1, π/48)	5189.97 (3.87)	4943.26 (−1.06)	4962.83 (−0.67)	4996.41
(1, 2π/48)	162.59 (−96.7)	135.48 (−97.3)	4964.71 (−0.70)	4999.89
(1, 3π/48)	5203.38 (4.09)	4944.36 (−1.10)	4964.21 (−0.70)	4999.16
(1, 4π/48)	105.46 (−97.9)	133.91 (−97.3)	4964.26 (−0.70)	4999.18
(1, 5π/48)	5203.38 (4.09)	4944.36 (−1.10)	4964.21 (−0.70)	4999.16
(1, 6π/48)	162.59 (−96.7)	135.48 (−97.3)	4964.71 (−0.70)	4999.89
(1, 7π/48)	5189.97 (3.87)	4943.26 (−1.06)	4962.83 (−0.67)	4996.41
(2, π/48)	4998.47 (0.02)	4999.01 (0.03)	4998.89 (0.02)	4997.68
(2, 2π/48)	144.23 (−97.1)	141.72 (−97.2)	5000.37 (0.02)	4999.48
(2, 3π/48)	4999.95 (0.01)	5000.08 (0.01)	5000.04 (0.01)	4999.53
(2, 4π/48)	121.95 (−97.6)	125.64 (−97.5)	4999.73 (0.01)	4999.19
(2, 5π/48)	4999.95 (0.0)	5000.08 (0.01)	5000.04 (0.01)	4999.53
(2, 6π/48)	144.23 (−97)	141.72 (−97.2)	5000.37 (0.02)	4999.48
(2, 7π/48)	4998.47 (0.02)	4999.01 (0.03)	4998.89 (0.02)	4997.68
(3, π/48)	5189.97 (3.87)	4943.26 (−1.06)	4962.83 (−0.67)	4996.41
(3, 2π/48)	162.59 (−96.7)	135.48 (−97.3)	4964.71 (−0.70)	4999.89
(3, 3π/48)	5203.38 (4.09)	4944.36 (−1.10)	4964.21 (−0.70)	4999.16
(3, 4π/48)	105.46 (−97.9)	133.91 (−97.3)	4964.26 (−0.70)	4999.18
(3, 5π/48)	5203.38 (4.09)	4944.36 (−1.10)	4964.21 (−0.70)	4999.16
(3, 6π/48)	162.59 (−96.7)	135.48 (−97.3)	4964.71 (−0.70)	4999.89
(3, 7π/48)	5189.97 (3.87)	4943.26 (−1.06)	4962.83 (−0.67)	4996.41

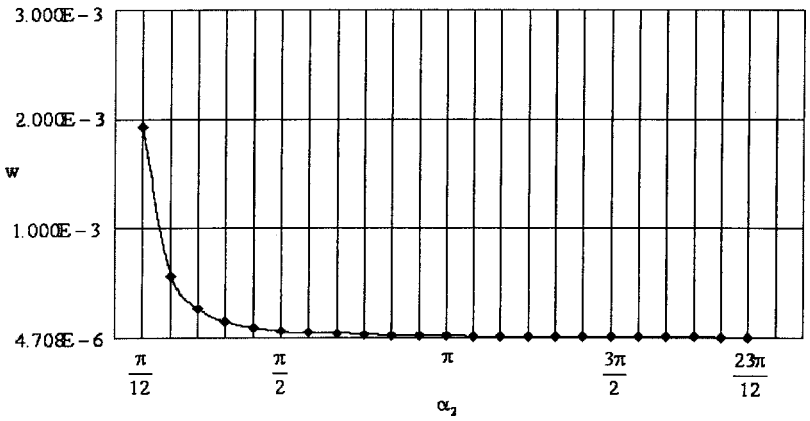

Fig. 15 The centerpoint deflection versus the change of shell curvature in Case 1

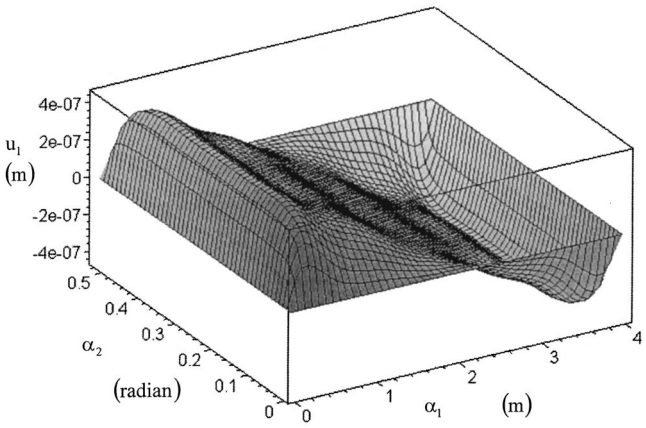

Fig. 16 Displacement of u_1 in Case 2

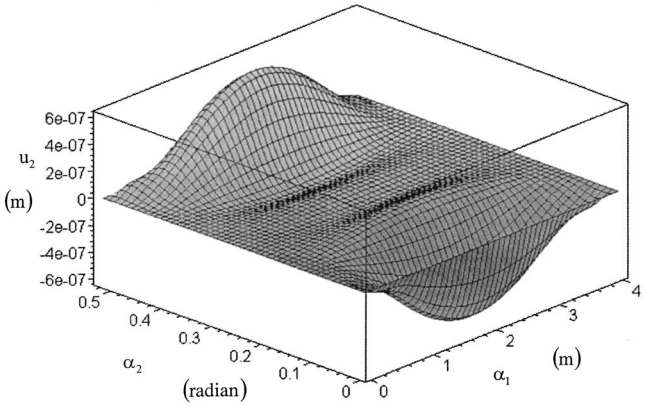

Fig. 17 Displacement of u_2 in Case 2

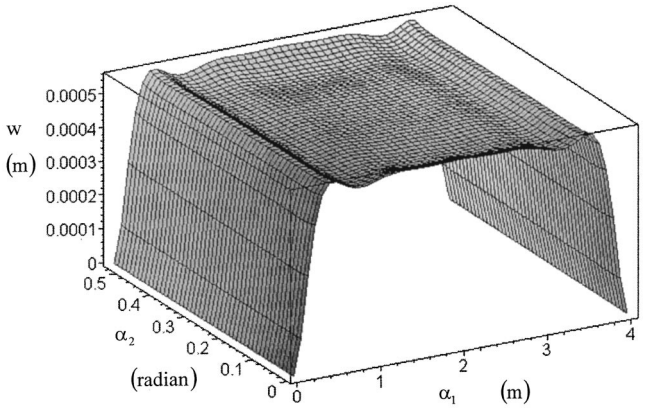

Fig. 18 Displacement of w in Case 2

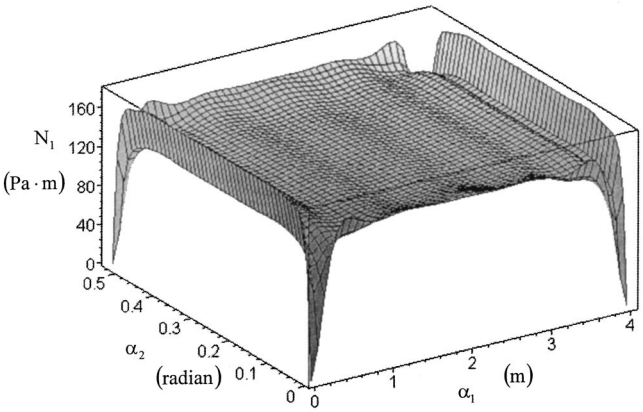

Fig. 19 Stress resultant N_1 in Case 2

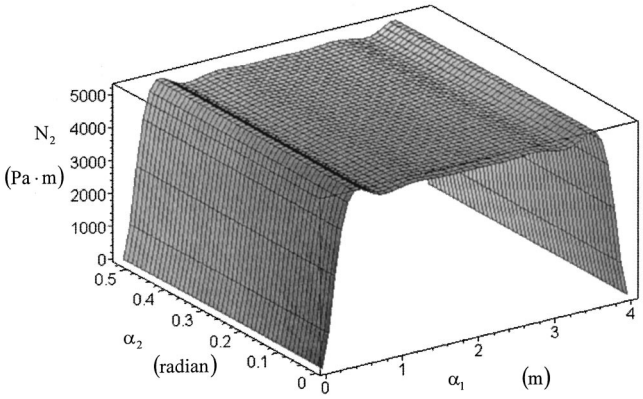

Fig. 20 Stress resultant N_2 in Case 2

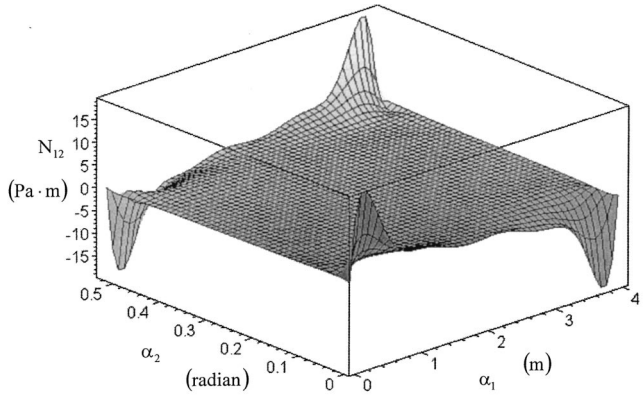

Fig. 21 Stress resultant N_{12} in Case 2

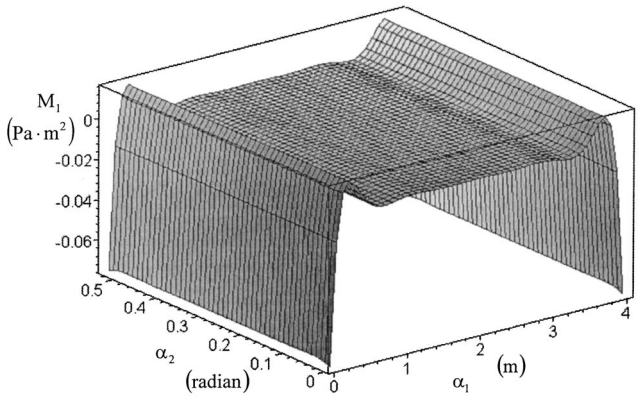

Fig. 22 Moment resultant M_1 in Case 2

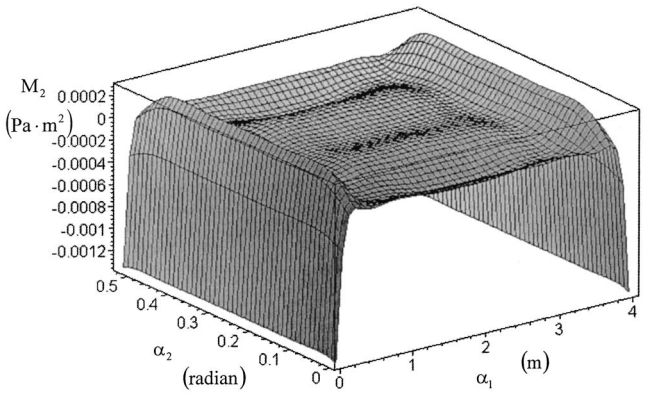

Fig. 23 Moment resultant M_2 in Case 2

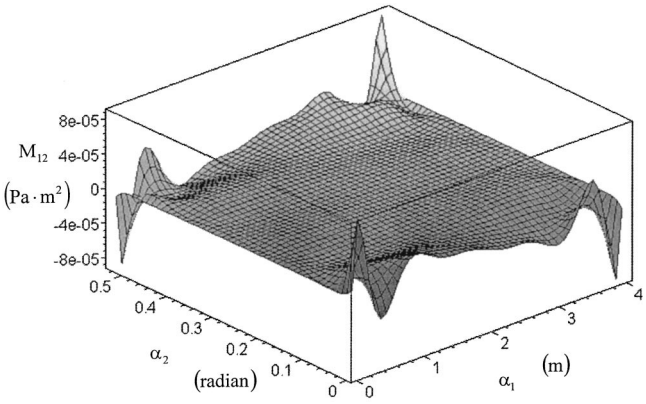

Fig. 24 Moment resultant M_{12} in Case 2

N are 12 in two cases, for example. The larger values M and N make every collocation point close to the adjacent collocation points. That will match the position of concentrated loading asymptotically. In group (b), the effects of σ_z, τ_{1z}, and τ_{2z} (z is the direction of the normal to the middle surface) are neglected owing to the thin shell theory, nevertheless the terms of σ_z, τ_{1z}, and τ_{2z} (interlaminar stresses) should be considered in thick laminated anisotropic shells. On the other hand, it is possible that the Chebyshev collocation method can be used to handle the nonlinear problems. As for the nonlinear problems the efforts should be put to solve a system of nonlinear partial differential equations. Please refer to Refs. [14], [15]. Some methods, like the Picard iteration, are possibly useful for solving the nonlinear problems.

From the section of examples, compare the solutions of the Chebyshev collocation method to those by the finite element method and NASTRAN software in Cases 1 and 2. NASTRAN is a precise and reliable finite element analysis software that has been widely used in many fields, such as science, physics, and engineering. In the two cases, the solutions of NASTRAN software are listed in comparison with the results in columns (C_8_8), (C_10_10), and (C_12_12) of the Chebyshev collocation method. It is found that most of the values of error in columns (C_8_8) and (C_10_10) are much greater than those in column (C_12_12). The result of the Chebyshev collocation method in column (C_12_12) are very close to that by NASTRAN software. That implies the Chebyshev collocation method is a correct and acceptable one. As for the curvature effect on deflection, it is obviously observed that the higher the curvature, the larger the deflection in both cases. That strongly hints that the original curvature of a thin shell will affect the deflection significantly.

Conclusion

The Chebyshev collocation method is proposed herein to tentatively solve most of the problems of laminated anisotropic thin shells with any boundary conditions due to any type of loading, except the concentrated load. The method possesses two merits: (a) it is more efficient and applicable than traditional methods, e.g., the Fourier series method, to handle the problems of complicated material properties and boundary conditions, and (b) the analytical results of the method are a group of functions that is more useful than those of finite difference and finite element methods. The numerical results in comparison with those by NASTRAN software prove that the proposed method is satisfactorily acceptable. To the extension, the problems of any type of loading and complex geometry are the further research objective.

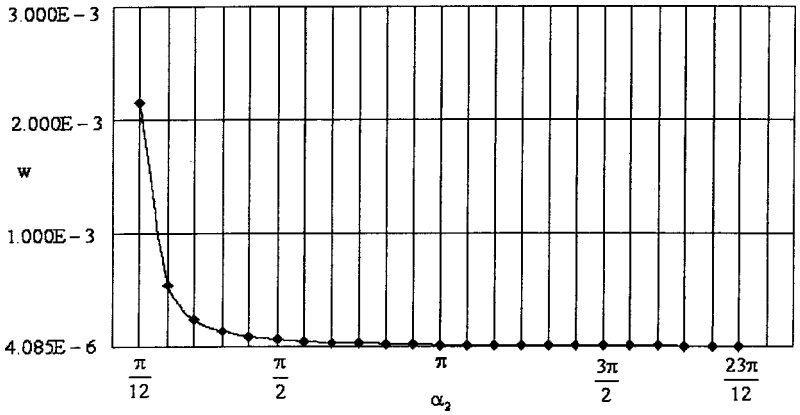

Fig. 25 The centerpoint deflection versus the change of shell curvature in Case 2

Nomenclature

$A_{11}, A_{12}, \cdots, A_{66}$ = extensional stiffness
A_1, A_2 = Lamé parameter
a_{mn}, b_{mn}, c_{mn} = coefficients of Chebyshev series
$B_{11}, B_{12}, \cdots, B_{66}$ = coupling stiffness
$D_{11}, D_{12}, \cdots, D_{66}$ = bending stiffness
$E_1, E_2, G_{12}, \nu_{12}$ = mechanical properties of a lamina with unidirectional fibers
$\breve{E}, \breve{F}, \breve{G}$ = first fundamental magnitudes of shell theory
f_1, f_2, f_3 = functions of curvilinear coordinates
K_n = normal curvature
$\breve{L}, \breve{M}, \breve{N}$ = second fundamental magnitudes of shell theory
$\mathbf{n}$ = unit normal vector
N_1, N_2, N_{12} = stress resultants
M_1, M_2, M_{12} = moment resultants
Q_1, Q_2 = shear stress resultants in α_1 and α_2-directions
$Q_{11}, Q_{12}, \cdots, Q_{66}$ = reduced stiffness in natural coordinate system
$\overline{Q}_{11}, \overline{Q}_{12}, \cdots, \overline{Q}_{66}$ = reduced stiffness in arbitrary coordinate system
$\mathbf{r}$ = position vector
R = radius of a cylindrical shell
R_1, R_2 = radii in α_1 and α_2-directions
T_{12}, T_{21}, V_1, V_2 = Kirchoff's effective shear stress resultants
$T_n(x)$ = the nth-order Chebyshev polynominal
$\hat{T}_m(\alpha_1)$, $\tilde{T}_n(\alpha_2)$ = modified Chebyshev polynomials in specified intervals
u_1, u_2, w = displacements in α_1, α_2 and normal to the surface directions
α_1, α_2, z = curvilinear coordinates of the surface
β_1, β_2 = rotations tangential to the reference surface
$\varepsilon_1^0, \varepsilon_2^0, \gamma_{12}^0$ = strains at the laminate geometry midplane
$\kappa_1, \kappa_2, \kappa_{12}$ = curvatures of the laminate

References

[1] Kraus, H., 1972, *Thin Elastic Shells: An Introduction to the Theoretical Foundations and the Analysis of Their Static and Dynamic Behavior*, John Wiley and Sons, New York.
[2] Ambartsumyan, S. A., 1961, *Theory of Anisotropic Shells*, Moscow, English translation, NASA-TT-F118, 1964.
[3] Flügge, W., 1996, *Stress in Shells*, Springer, Berlin, pp. 1851–1858.
[4] Chaudhuri, R. A., 1986, "Arbitrarily Laminated, Anisotropic Cylindrical Shell Under Internal Pressure," AIAA J., **24**(11), pp. 1851–1858.
[5] Love, A. E. H., 1944, *A Treatise on the Mathematical Theory of Elasticity*, Dover, New York.
[6] Kjellmert, B., 1997, "A Chebyshev Collocation Multidomain Method to Solve the Reissner-Mindlin Equations for the Transient Response of an Anisotropic Plate Subjected to Impact," Int. J. Numer. Methods Eng., **40**, pp. 3689–3702.
[7] Lu, Y. Y., 1995, "A Chebyshev Collocation Method for Computing the Eigenvalues of the Laplacian," Int. J. Numer. Methods Eng., **38**, pp. 231–243.
[8] Wright, K., 1963–1964, "Chebyshev Collocation Methods for Ordinary Differential Equations," Comput. J., **6**, pp. 358–365.
[9] Fox, L., and Parker, I. B., 1968, *Chebyshev Polynomials in Numerical Analysis*, Oxford University Press, Oxford UK.
[10] Jones, R. M., 1975, *Mechanics of Composite Materials*, Scripta Mathematica, New York.
[11] Tsai, S. W., and Hahn, H. T., 1980, *Introduction to Composite Materials*, Technomic, Lancaster, PA.
[12] Boyd, J. P., 1989, *Chebyshev and Fourier Spectral Methods*, Springer-Verlag, New York.
[13] Karageorghis, A., 1991, "A Note on the Satisfaction of the Boundary Conditions for Chebyshev Collocation Methods in Rectangular Domains," J. Sci. Comput., **6**(1), pp. 21–26.
[14] Clenshaw, C. W., and Norton, H. J., 1963–1964, "The Solution of Nonlinear Ordinary Differential Equations in Chebyshev Series," Comput. J.,, **6**, pp. 88–92.
[15] Norton, H. J., 1964, "The Iterative Solution of Non-Linear Ordinary Differential Equations on Chebyshev Series," Comput. J., **7**, pp. 76–85.

C. N. Duong
e-mail: cong.n.duong@boeing.com

J. Yu

The Boeing Company,
2401 E. Wardlow Road,
MC C078-0209,
Long Beach, CA 90807-5309

Analysis of a Plate Containing a Polygon-Shaped Inclusion With a Uniform Eigencurvature

An infinite isotropic plate containing a polygon-shaped inclusion with a uniform eigencurvature is analyzed. An algorithmic closed-form solution of the curvature is derived for both interior and exterior points of the polygon. [DOI: 10.1115/1.1572898]

1 Introduction

A problem of an infinite isotropic plate with an embedded inhomogeneity or external reinforcement under thermomechanical loading is of practical interest since it has been found in many engineering applications. A particular example in aerospace application is a bonded composite repair over a cracked metallic structure. A repair method using composite patches to reinforce the cracked structure has been shown to be very promising owing to the light weight, high stiffness and strength of the composite. The inhomogeneous plate under thermo- mechanical loads will induce both bending and in-plane deformations, [1]. This problem can be solved more conveniently by the equivalent inclusion method, in which the stresses and strain induced by an inhomogeneity occupied region Ω will be approximated by those induced by the eigenstrains and eigencurvatures in the same region of the homogeneous material when these eigenstrains and eigencurvatures are selected appropriately, [1]. Closed-form solutions for inclusion problems with eigenstrains and eigencurvatures are, therefore, also of practical interests. While most existing works on inclusion problems concern with a plane or three dimensional solid containing eigenstrains [see the book by Mura [2] for the comprehensive reviews], only few deals with a plate containing eigencurvatures. Beoms [3] was the first one to consider the problem of a plate containing an elliptical inclusion with a uniform eigencurvature. The approach employed by Beoms [3] will be extended here to include the analysis of a polygon-shaped inclusion with a uniform eigencurvature. The curvature and corresponding resultant moment are obtained by performing the integrations according to the Rodin's algorithmic solution procedure, [4], for a two-dimensional planar inclusion with uniform eigenstrains. Another algorithmic solution to the uniform eigenstrain problem also develops closed-form solutions that are used in a computational approach to describe elastic fields in a polygon-shaped inclusion, [5]. However, the computational approach taken by Rodin is particularly attractive because it is simple and robust.

2 Formulation

Consider a deformation of an infinite isotropic plate containing a polygonal subregion Ω in which a uniform eigencurvature κ_{ij}^* is prescribed. Following Beom [3], the curvature $\kappa_{ij}(\mathbf{x})$ and the eigencurvature κ_{ij}^* are related by an Eshelby-type tensor S_{ijkl} such that

$$\kappa_{ij}(\mathbf{x}) = S_{ijkl}(\mathbf{x})\kappa_{kl}^* \tag{1}$$

where

$$S_{ijkl}(\mathbf{x}) = -\left[\int_\Omega \tilde{M}_{kl}(\xi,\mathbf{x})dA\right]_{,ij}, \tag{2}$$

$$\tilde{M}_{kl}(\xi,\mathbf{x}) = -\frac{1}{4\pi}\left[(1+\nu)\ln\rho\,\delta_{kl} + (1-\nu)\frac{(\xi_k - x_k)(\xi_l - x_l)}{\rho^2}\right],$$

$$\rho = |\xi - \mathbf{x}|, \tag{3}$$

δ_{ij} is the Kronecker delta, ν is the Poisson ratio, and the subscript comma denotes a partial differentiation with respect to in-plane coordinates.

Introducing integrals H and H_{kl} defined, respectively, by

$$H(x) = \int_\Omega \ln\rho\, dA$$

$$H_{kl}(x) = \int_\Omega \frac{(\xi_k - x_k)(\xi_l - x_l)}{\rho^2} dA, \tag{4}$$

then $S_{ijkl}(\mathbf{x})$ in Eq. (2) can be rewritten as

$$S_{ijkl}(\mathbf{x}) = \frac{1}{4\pi}[(1+\nu)H_{,ij}\delta_{kl} + (1-\nu)H_{kl,ij}]. \tag{5}$$

An algorithm to evaluate S_{ijkl} as prescribed by Eq. (5) for an arbitrarily polygonal region will be delineated in the next section. Once S_{ijkl} and κ_{ij} are determined, respectively, from Eqs. (5) and (1), the resultant moment is then computed from the curvature as [3],

$$M_{ij} = \begin{cases} D_{ijkl}(\kappa_{kl} - \kappa_{kl}^*) & \text{inside } \Omega \\ D_{ijkl}\kappa_{kl} & \text{outside } \Omega \end{cases} \tag{6}$$

where D_{ijkl} is the bending stiffness tensor and it is defined in [6].

3 Algorithm

S_{ijkl} is evaluated by using Rodin's algorithm [4]. This algorithm will be briefly summarized here. The reader should refer to [4] for more details. Rodin's algorithm is implemented in three stages. First, the inclusion domain Ω is decomposed into a set of triangular elements in such a way that $\mathbf{x}$, the point where the solution is evaluated is a common vertex of all the elements. Second, H, H_{kl}, and thus S_{ijkl} are calculated for each element in its element coordinate system and transform the components of S_{ijkl} to global coordinates. Third, S_{ijkl} is assembled from the elemental contributions. Using Rodin's terminology, [4], the triangular elements which make up of the domain Ω are called duplexes and they are referred to as simplexes for the case of right triangles. Since a duplex can be formed from two simplexes and

Contributed by the Applied Mechanics Division of THE AMERICAN SOCIETY OF MECHANICAL ENGINEERS for publication in the ASME JOURNAL OF APPLIED MECHANICS. Manuscript received by the ASME Applied Mechanics Division, July 3, 2000; final revision, Aug. 19, 2002. Associate Editor: B. M. Moran. Discussion on the paper should be addressed to the Editor, Prof. Robert M. McMeeking, Department of Mechanical and Environmental Engineering University of California–Santa Barbara, Santa Barbara, CA 93106-5070, and will be accepted until four months after final publication of the paper itself in the ASME JOURNAL OF APPLIED MECHANICS.

 Copyright © 2003 by ASME

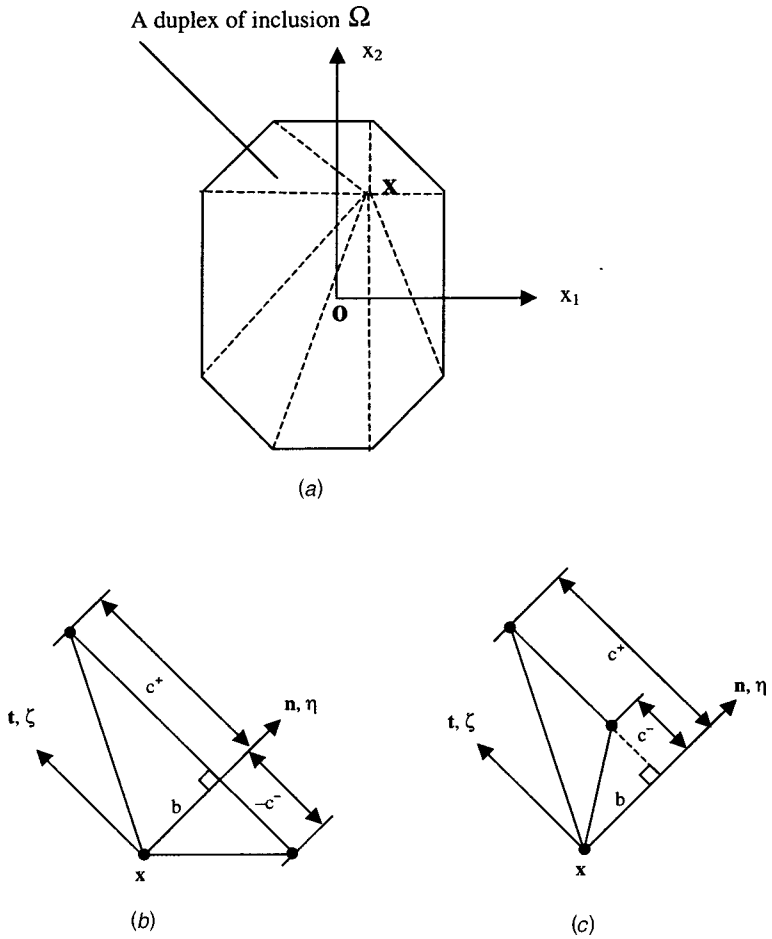

Fig. 1 Two-dimensional construction of duplexes used in Rodin's algorithm, [4]. Part (*a*) shows the global structure and coordinate systems. Parts (*b*) and (*c*) show typical duplexes, with vertices shown as filled circles. In the (η,ζ) coordinate system, for duplex (*b*) add the simplex with vertices (0,0), (b,c^-), (b,0) to the simplex with vertices (0,0), (b,0), (b,c^+), while for duplex (*c*) subtract the simplex with vertices (0,0), (b,0), (b,c^-) from the simplex with vertices (0,0), (b,0), (b,c^+).

the computation for the latter is more efficient than that for the former, the elemental tensor S_{ijkl} will be derived here for a simplex in its element coordinate system.

Referring to Fig. 1, let us define the element coordinate system as follows. It has the origin at **x**, basis vector (**n**,**t**) where **n** is an unit vector outward normal to the edge and **t** is the tangent vector, and the corresponding coordinates (η, ζ). In these coordinates, the positions of vertices are represented by the pairs (b, c^+) and (b, c^-). For a convex polygon, b is positive when **x** is an interior point of Ω and becomes negative for otherwise. For a simplex with one of the vertices defined by (b,c), H and H_{kl} in Eq. (4) can be rewritten as

$$H(\mathbf{x})=\frac{1}{2}\int_0^b\int_0^{c\eta/b}\ln(\eta^2+\zeta^2)\,d\zeta\,d\eta,$$

$$H_{\zeta\zeta}(\mathbf{x})=\int_0^b\int_0^{c\eta/b}\frac{\zeta^2}{\eta^2+\zeta^2}\,d\zeta\,d\eta,$$

$$H_{\zeta\eta}(\mathbf{x})=H_{\eta\zeta}(\mathbf{x})=\int_0^b\int_0^{c\eta/b}\frac{\zeta\eta}{\eta^2+\zeta^2}\,d\zeta\,d\eta, \tag{7}$$

$$H_{\eta\eta}(\mathbf{x})=\int_0^b\int_0^{c\eta/b}\frac{\eta^2}{\eta^2+\zeta^2}\,d\zeta\,d\eta,$$

which, upon integration, will yield the following results:

$$H(b,c)=-\frac{b}{4}\left[3c-2b\,\tan^{-1}\left(\frac{c}{b}\right)-c\ln(b^2+c^2)\right],$$

$$H_{\zeta\zeta}(b,c)=\frac{b^2}{2}\left[\frac{c}{b}-\tan^{-1}\left(\frac{c}{b}\right)\right],$$

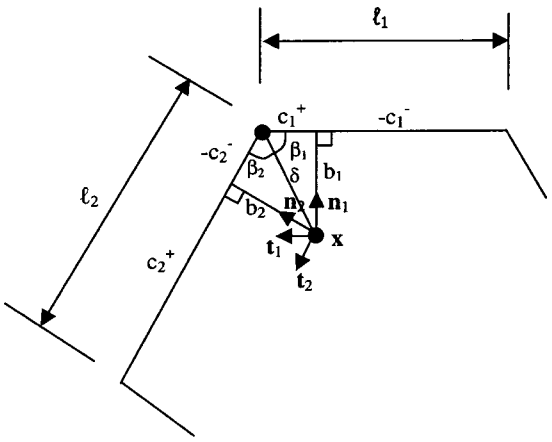

Fig. 2 Geometrical parameters of the duplexes for evaluating the asymptotic form of the vertex singularity, [4]

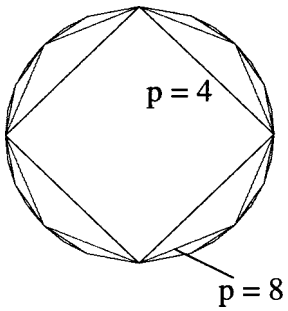

Fig. 3 Regular polygon-shaped inclusions

$$H_{\zeta\eta}(b,c)=H_{\eta\zeta}(b,c)=\frac{b^2}{4}[\ln(b^2+c^2)-\ln b^2],$$
$$H_{\eta\eta}(b,c)=\frac{b^2}{2}\tan^{-1}\left(\frac{c}{b}\right). \tag{8}$$

To obtain the tensor S_{ijkl} in the global coordinate system, H and H_{kl} must be differentiate with respect to $\mathbf{x}$ as prescribed in (5). However, it is more convenient to obtain S_{ijkl} in the element coordinate system since (i) $b=b(\mathbf{x})$, $c=c(\mathbf{x})$ and (ii) in the latter coordinates $\partial b/\partial\eta=\partial c/\partial\zeta=-1$ and $\partial b/\partial\zeta=\partial c/\partial\eta=0$. It can be shown that by using Voigt's convention, S_{ijkl} in the element coordinate system is represented by a 3×3 matrix as

$$S_{11}=S_{\eta\eta\eta\eta}=\frac{1}{4\pi}\left[2\alpha-\frac{(2-\nu)}{2}\sin 2\alpha+\frac{(1-\nu)}{8}\sin 4\alpha\right]$$

$$S_{12}=S_{\eta\eta\zeta\zeta}=\frac{1}{4\pi}\left[2\nu\alpha+\frac{(1-2\nu)}{2}\sin 2\alpha-\frac{(1-\nu)}{8}\sin 4\alpha\right]$$

$$S_{13}=S_{\eta\eta\eta\zeta}=\frac{(\nu-1)}{32\pi}[5-6\cos 2\alpha+\cos 4\alpha-4\log(\sec^2\alpha)]$$

$$S_{21}=S_{\zeta\zeta\eta\eta}=\frac{1}{16\pi}[2\nu-(1-\nu)\cos 2\alpha]\sin 2\alpha$$

$$S_{22}=S_{\zeta\zeta\zeta\zeta}=\frac{1}{16\pi}[2+(1-\nu)\cos 2\alpha]\sin 2\alpha$$

$$S_{23}=S_{\zeta\zeta\eta\zeta}=\frac{1}{8\pi}[(1-\nu)\cos^2\alpha\cos 2\alpha]$$

$$S_{31}=S_{\eta\zeta\eta\eta}=\frac{1}{32\pi}[3(\nu-1)+4\cos 2\alpha-(1-\nu)\cos 4\alpha$$
$$+2(1+\nu)\log(\sec^2\alpha)$$

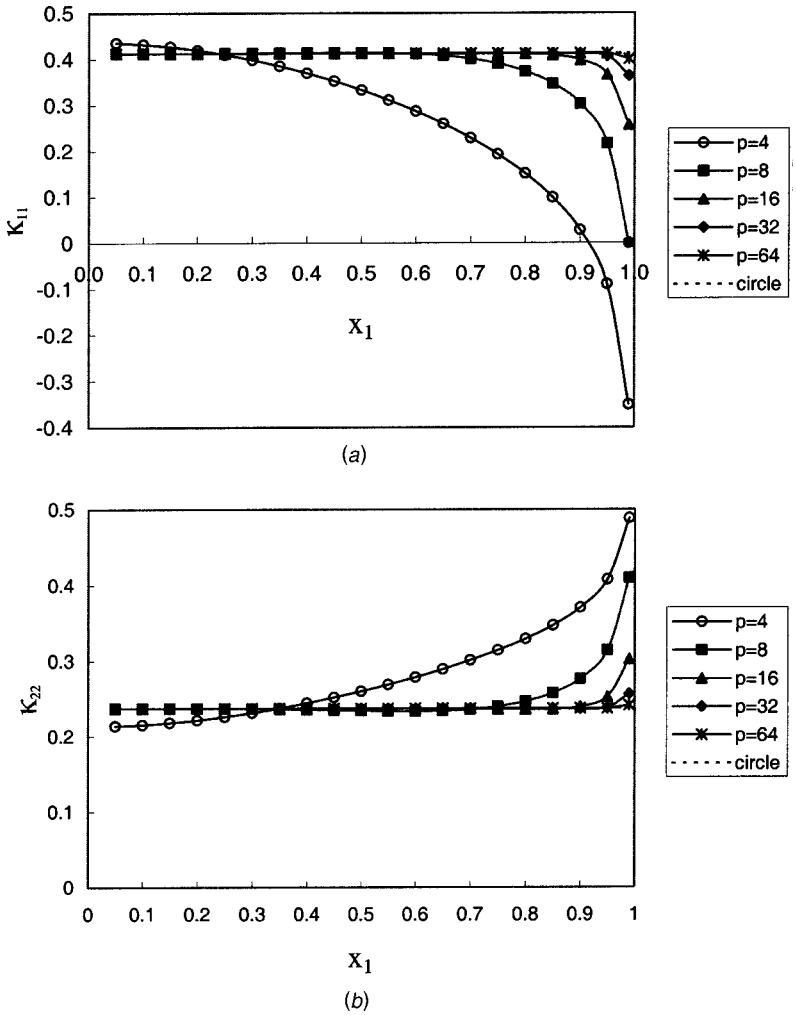

Fig. 4 Curvatures κ_{11} and κ_{22} in regular polygon-shaped inclusions along the x_1-axis for an eigencurvature $\kappa^*_{ij}=(1, 0, 0)$. (*a*) κ_{11}, (*b*) κ_{22}

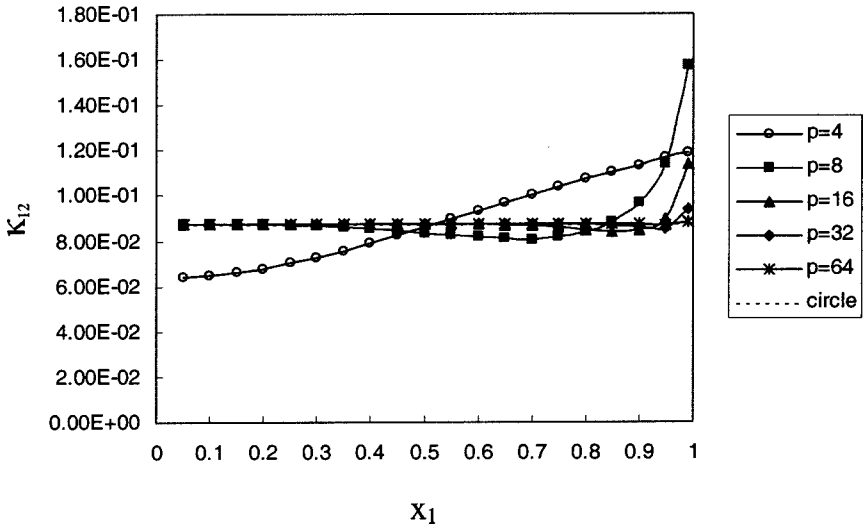

Fig. 5 Curvatures κ_{12} in regular polygon-shaped inclusions along x_1-axis for an eigencurvature $\kappa^*_{ij}=(0, 0, 1)$

$$S_{32}=S_{\eta\zeta\zeta\xi}=\frac{1}{32\pi}[(1-\nu)+4\nu\cos 2\alpha+(1-\nu)\cos 4\alpha$$
$$+2(1+\nu)\log(\sec^2\alpha)$$
$$S_{33}=S_{\eta\zeta\eta\zeta}=\frac{1}{4\pi}[(1-\nu)\cos\alpha\sin^3\alpha]$$
$$\alpha=\tan^{-1}\left(\frac{c}{b}\right). \tag{9}$$

Similar to the strain solution obtained earlier by Rodin [4] for a ''planar'' inclusion with a uniform eigenstrain, the present curvature solution has a logarithmic singularity near the vertex and it is not constant inside subregion Ω. This vertex singularity can be addressed in a similar manner as in [4]. By assigning the subscripts 1 and 2 to the edges that form the vertex (see Fig. 2) and denoting lengths of these edges by ℓ_1 and ℓ_2, from Fig. 2, the following relations hold for a point $\mathbf{x}$ close to the vertex:

$$b_1=\delta\sin\beta_1, \quad c_1^+=\delta\cos\beta_1, \quad c_1^-=-\ell_1+\delta\cos\beta_1\approx-\ell_1,$$
$$b_2=\delta\sin\beta_2, \quad c_2^+=\ell_2-\delta\cos\beta_2\approx\ell_2, \quad c_2^-=-\delta\cos\beta_2,$$

where δ is the distance from $\mathbf{x}$ to the vertex and it approaches 0. By evaluating S_{ijkl} at $\mathbf{x}$ [via Eq. (9)] using the above expressions for b and c, and discarding all nonsingular terms, S_{ijkl} takes the following asymptotic form:

$$\mathbf{S}\approx\frac{1}{16\pi}(\mathbf{M}_1-\mathbf{M}_2)\ln\frac{\ell}{\delta},$$

where ℓ is a representative edge length, tensors $\mathbf{M}_1$ and $\mathbf{M}_2$ are represented by the same matrix in the basis $(\mathbf{n}_1, \mathbf{t}_1)$ and $(\mathbf{n}_2, \mathbf{t}_2)$ and that matrix is defined by

$$\mathbf{M}=\begin{bmatrix} 0 & 0 & 2(1-\nu) \\ 0 & 0 & 0 \\ 1+\nu & 1+\nu & 0 \end{bmatrix}.$$

4 Numerical Examples

Numerical examples of the curvature given by Eq. (1) are shown in this section. κ_{ij} are computed for a family of regular polygons inscribed into a unit circle centered at the origin O of the coordinate system as shown in Fig. 3. The Poisson ratio of the plate is assumed to be 0.3 throughout the computation. The vertices of the polygon in polar coordinates are prescribed by

$$r_k=1 \quad \text{and} \quad \theta_k=2\pi\frac{(k-1)}{p}; \quad k=1,2,\ldots,p,$$

where p is the number of sides of the polygon. Computational results of κ_{11} and κ_{22} along the x_1-axis for $\kappa^*_{ij}=(1,0,0)$ and for various values of p are plotted in Figs. 4(*a*) and Fig. 4(*b*), respectively. It should be noted that κ_{12} are equal to 0 in this case. The result from Beom [3] for a circular inclusion is also included in the figure for comparison. Similarly, the results of κ_{12} along the x_1-axis for $\kappa^*_{ij}=(0,0,1)$ are plotted in Fig. 5 while κ_{11} and κ_{22} are determined to be zero. In Figs. 4 and 5, κ_{11}, κ_{22} and κ_{12} are evaluated along the x_1 axis using twenty points at equal spaces over the half-polygonal domain and these points correspond to those chosen on the plots. From Figs. 4 and 5, the curvature distributions are not uniform inside the inclusion but approach to the Beom's solutions with the increasing number of sides.

5 Conclusions

An infinite isotropic plate with a uniform eigencurvature in a polygon-shaped inclusion is analyzed. The method employed is simple and robust. An algorithmic closed-form solution of the curvature is obtained. This solution can be used as one of the basic solutions for obtaining the elastic fields in an isotropic plate containing a general shaped inhomogeneity. The solution of the latter problem is of practical interest because it finds a wide range of applications including analyses and designs of adhesively bonded repairs with an octagonal patch in aging aircraft, [7,8].

References

[1] Beom, H. G., and Earmme, Y. Y., 1999, ''The Elastic Field of an Elliptic Cylindrical Inclusion in a Laminate with Multiple Isotropic Layers,'' ASME J. Appl. Mech., **66**, pp. 165–171.
[2] Mura, T., 1987, *Mechanics of Defects in Solids*, Martinus Nijhoff, Dordrecht.
[3] Beom, H. G., 1998, ''Analysis of a Plate Containing an Elliptic Inclusions With Eigencurvatures,'' Arch. Appl. Mech., **68**, pp. 422–432.
[4] Rodin, G. J., 1996, ''Eshelby's Inclusion Problem for Polygons and Polyhedra,'' J. Mech. Phys. Solids, **44**, pp. 1977–1995.
[5] Nozaki, H., and Taya, M., 1997, ''Elastic Fields in a Polygon-Shaped Inclusion with Uniform Eigenstrains,'' ASME J. Appl. Mech., **64**, pp. 495–501.
[6] Jones, R. M., 1975, *Mechanics of Composite Materials*, McGraw-Hill, New York.
[7] Duong, C. N., Wang, J. J., and Yu, J., 2000, ''An Approximate Algorithmic Solution for the Elastic Fields in Bonded Patched Sheets,'' Int. J. Solids Struct., **38**, pp. 4685–4699.
[8] Duong, C. N., and Yu, J., 2003, ''Thermal Stresses in a One-Sided Bonded Repair by a Plate Inclusion Model,'' J. Thermal Stresses, **26**, pp. 457–466.

S. S. Kulkarni
Graduate Student,
e-mail: ssk18@cornell.edu

S. Mukherjee[1]
Professor,
Fellow ASME
e-mail: sm85@cornell.edu

Department of Theoretical and Applied Mechanics,
Cornell University,
Ithaca, NY 14853

M. D. Grigoriu
Professor,
Department of Environmental and Civil Engineering,
Cornell University,
Ithaca, NY 14853
e-mail: mdg12@cornell.edu

Local Solutions in Potential Theory and Linear Elasticity Using Monte Carlo Methods

A numerical method called the boundary walk method is described in this paper. The boundary walk method is a local method in the sense that it directly gives the solution at the point of interest. It is based on a global integral representation of the unknown solution in the form of potentials, followed by evaluating the integrals in the resulting series solutions using Monte Carlo simulation. The boundary walk method has been applied to solve interior problems in potential theory with either Dirichlet or Neumann boundary conditions. It has also been applied to solve interior problems in linear elasticity with either displacement or traction boundary conditions. Weakly singular integral formulations in linear elasticity, to which the boundary walk method has been applied, are also derived. Finally, numerical results, which are computed by applying the boundary walk method to solve some two-dimensional problems over convex domains in potential theory and linear elasticity, are presented. These solutions are compared with the known analytical solutions (when available) or with solutions from the standard boundary element method. [DOI: 10.1115/1.1558074]

1 Introduction

The commonly used numerical methods in physics and engineering can be roughly categorized as global or local methods. Global methods are those which provide the solution over the entire domain of the problem. The finite element method and the boundary element method are the two most commonly used global methods in practice. The main disadvantage of global methods is that they are indirect. The solution first needs to be computed over the entire domain of the problem and then the solution at the points of interest needs to be interpolated. This makes the global methods, in general, inefficient if solutions at only a few points are desired. Another disadvantage associated with a global method is the need to discretize the domain (e.g., finite element method) or the surface of the domain (e.g., boundary element method). Meshing is a burdensome task and the conversion of the domain/surface to elements in the finite element method/boundary element method is often computationally intensive. Also, the discretization involved may lead to inexact problem geometry and inaccurate implementation of the boundary conditions.

Local methods are those which give the solution at the point of interest directly and generally do not need any discretization of the domain/surface. Such methods have several advantages over the global methods. For example, they are inherently parallel and hence much less programming effort is required to parallelize the code when compared with either the finite element method or the boundary element method. These methods are especially well suited to boundary value problems where critical regions, such as points in the domain where a function of interest attains its maximum or minimum value, are well known. In such cases there is no need to obtain the solution in the entire domain since it is only required at a few points (see, e.g., Arsenjev [1]). Some local methods based on Brownian motion simulation (see Kim [2]) are efficient for homogenization problems for materials with heterogeneous or random material properties. But the main disadvantage of the local methods is their rather limited applicability (at present) to solve engineering problems when compared to methods like the finite element method or the boundary element method. Increasing the versatility of local methods is a matter of continuing research.

The present paper illustrates the application of a local method, called the boundary walk method, to solve problems in potential theory and linear elasticity on two-dimensional convex domains. Numerical examples are presented in the form of some simple examples on convex domains.

The local method described in this paper is called a boundary walk method since it simulates a random walk on the boundary of the domain. It is based on a global integral representation of the solution in a form of a potential. The solution of the integral equation of the corresponding density is sought in the form of a power series. The individual terms in the series are then evaluated using Monte Carlo integration. This avoids any meshing and leads to an accurate implementation of the problem geometry and boundary conditions. It also avoids the ''curse of dimensionality'' associated with classical quadrature schemes (see Evans [3]). A detailed description of the boundary walk method can be found in Sabelfeld [4] and [5]. Hoffman [6] has also described the boundary walk method to solve Laplace's equation with Dirichlet boundary conditions. A similar method is also used in practice to study neutron and other particle transport problems in physics (see Kalos [7]).

Another local method based on an integral representation, called the walk on sphere method, is presented in Sabelfeld [4] for solution of the Laplace, Poisson, Helmholtz, and biharmonic equations. A similar method, called the floating random walk, has been applied by Haji-Sheikh [8] to obtain solutions of equations for steady and transient heat conduction. Sabelfeld [9] has also expanded the walk on sphere method for systems of elliptic equations with constant coefficients. A brief decription and application of the walk on sphere method also appears in Arsenjev [1]. The walk on sphere method is based on a local integral representation of the solution as opposed to the boundary walk method. The main disadvantage of the walk on sphere method (see Hoffman [6]) is the need to use very small random steps near the boundary.

[1]To whom correspondence should be addressed.

Contributed by the Applied Mechanics Division of THE AMERICAN SOCIETY OF MECHANICAL ENGINEERS for publication in the ASME JOURNAL OF APPLIED MECHANICS. Manuscript received by the ASME Applied Mechanics Division, Nov. 30, 2001; final revision, Aug. 20, 2002. Associate Editor: D. A. Kouris. Discussion on the paper should be addressed to the Editor, Prof. Robert M. McMeeking, Department of Mechanical and Environmental Engineering University of California–Santa Barbara, Santa Barbara, CA 93106-5070, and will be accepted until four months after final publication of the paper itself in the ASME JOURNAL OF APPLIED MECHANICS.

 Copyright © 2003 by ASME

Also the determination of the closest boundary position, which is needed at every step, is nontrivial for complex domains.

Another local method called the random walk method (see Chati [10]) is also used to numerically solve a class of second order partial differential equations. It is based on the properties of diffusion processes, Itô calculus and Monte Carlo simulation and details can be found in Øksendal [11].

One of the main contributions of the current paper is that it demonstrates the application of the boundary walk method to solve problems in potential theory with either Dirichlet or Neumann boundary conditions and linear elasticity with either displacement or traction boundary conditions. The Dirichlet problem for Laplace's equation is included for completeness even though it has been previously solved by Hoffman [6]. The present paper also presents weakly singular formulations for displacement prescribed and traction prescribed problems in linear elasticity, for two-dimensional simply connected domains that are suitable for use with the boundary walk method. The use of a weakly singular formulation simplifies the solution procedure considerably as explained later. The weakly singular formulation for the displacement problem is based on the double layer potential of the second kind as described in Kupradze [12]. The weakly singular formulation for the traction problem is based on the one given in Mikhailov [13] and the fact that stresses everywhere in a body, for traction prescribed problems, are independent of material constants.

The remainder of the paper is organized as follows. Section 2 presents the theoretical background of the boundary walk method. Section 3 describes the procedure to obtain local solutions of the Laplace's equation subjected to either Dirichlet or Neumann boundary conditions. Section 4 describes the solutions to the Navier's equation subjected to either displacement or traction boundary conditions using weakly singular formulations. Section 5 presents numerical results obtained by applying the boundary walk method to solve some test problems. Finally, some concluding remarks appear in Section 6.

Although attempts to numerically solve elasticity problems by the boundary walk method exist in the literature (e.g., Shia [14]), to the best of the author's knowledge, the present work represents the first careful attempt at solving a certain class of elasticity problems by the boundary walk method. In particular, appropriate integral representations are chosen for solving the displacement prescribed and traction prescribed boundary value problems.

2 Theoretical Background

This section is divided into three parts. The first part describes the class of problems which can be solved using the boundary walk method and the basic procedure followed in obtaining the required solution. The second part defines the estimators used to evaluate the multidimensional integrals occurring in the solution. The third part describes the densities used in generating the random variables which are used in the estimators.

2.1 Solution of an Integral Equation. The boundary walk method is mainly concerned with evaluating integrals of the type

$$I_{x_0}=\mathcal{R}\mu(x_0)=\int_\Gamma R(x_0,y)\mu(y)dS(y) \quad x_0\in D \tag{1}$$

where

$$\mu(y)=\lambda\int_\Gamma K(y,y')\mu(y')dS(y')+f(y) \quad y\in\Gamma\equiv\partial D. \tag{2}$$

Here $D\subset R^n$, $\lambda\in R$ and I_{x_0} denotes the value of the integral functional $I(x)$ at the point x_0. For potential problems, $R(x,y)$, $K(x,y)$, $\mu(y)$, $f(y)$, and $I(x)$ are scalar valued functions. For problems in linear elasticity, $R(x,y)$ and $K(x,y)$ are matrix valued functions while $\mu(y)$, $f(y)$, and $I(x)$ are vector valued functions.

First, Eq. (2) is solved by assuming that $\mu(y)$ can be represented as a uniformly convergent series of the form

$$\mu(y)=\mu_0(y)+\lambda\mu_1(y)+\lambda^2\mu_2(y)+\ldots. \tag{3}$$

Substituting Eq. (3) into Eq. (2) and equating equal powers of λ, one obtains

$$\begin{aligned}\mu_0(y)&=f(y)\\ \mu_1(y)&=\mathcal{K}^1\mu_0(y)\\ \mu_2(y)&=\mathcal{K}^2\mu_0(y)\\ &\vdots\\ \mu_k(y)&=\mathcal{K}^k\mu_0(y).\end{aligned} \tag{4}$$

Here

$$\begin{aligned}&\mathcal{K}^0\mu_0(y)=\mu_0(y)=f(y)\\ &\mathcal{K}^1\mu_0(y)=\mathcal{K}[\mathcal{K}^0\mu_0](y)=\int_\Gamma K(y,y_1)f(y_1)dS(y_1)\\ &\mathcal{K}^2\mu_0(y)=\mathcal{K}[\mathcal{K}^1\mu_0](y)=\int_\Gamma\int_\Gamma K(y,y_1)K(y_1,y_2)f(y_2)dS(y_2)dS(y_1)\\ &\vdots\\ &\mathcal{K}^k\mu_0(y)=\mathcal{K}[\mathcal{K}^{k-1}\mu_0](y)=\underbrace{\int_\Gamma\ldots\int_\Gamma}_{k\text{ times}}K(y,y_1)\ldots K(y_{k-1},y_k)f(y_k)dS(y_k)\ldots dS(y_1).\end{aligned}$$

To obtain I_{x_0} in Eq. (1), the series (3) is first multiplied by $R(x_0,y)$ and then integrated termwise over Γ. This is justified since the series is assumed to be uniformly convergent. The final expression for I_{x_0} is then given by

$$I_{x_0}=\sum_{n=0}^{\infty}\lambda^n\mathcal{R}\mathcal{K}^n f(y). \tag{5}$$

2.2 Monte Carlo Integration. Monte Carlo integration is used to evaluate the individual terms in Eq. (5). Monte Carlo integration converts the calculation of an integral to an equivalent expected value problem. The basic idea of the Monte Carlo method used to evaluate integrals is briefly explained next.

Consider the evaluation of an integral

$$I=\int_a^b\phi(x)dx=\int_a^b p(x)\frac{\phi(x)}{p(x)}dx. \tag{6}$$

Suppose $p(x)$ is non-negative, $\int_a^b p(x)dx=1$ and

$$p(x)>0 \quad \text{if} \quad \phi(x)\neq 0.$$

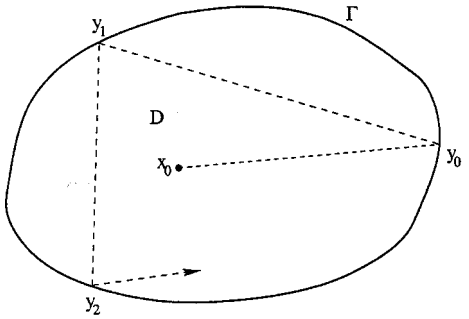

Fig. 1 Boundary walk method

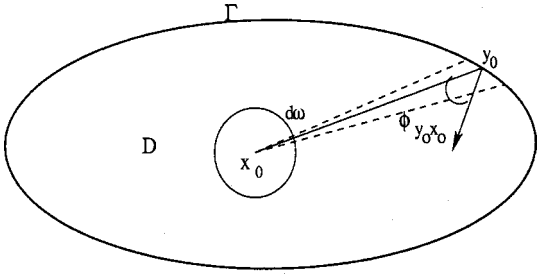

Fig. 2 Initial distribution

Hence p is a density function and

$$I=E\left[\frac{\phi(x)}{p(x)}\right]$$

where $E(\cdot)$ is the expectation operator. Based on the samples $x_1, \ldots, x_N$ from p, the estimator of Eq. (6) is then given by

$$\hat{I}=\frac{1}{N}\sum_{i=1}^{N}\frac{\phi(x_i)}{p(x_i)}.$$

The Monte Carlo method used in the present paper (see Rubinstein [15]) is an extension of this idea to evaluate multidimensional integrals. The reason behind using this particular method is that it efficiently exploits the iterative nature of the individual terms in the series solution. (Please refer to Fig. 1.) Let $Y=\{y_0,y_1,\ldots y_n,\ldots\}$ be a Markov chain with $\{y_i\in\Gamma, i=0\ldots n\}$, where y_0 is distributed in Γ with initial density $p_0(y_0)$ and the next points are determined from the transition density $p(y_{i-1},y_i)$. Hence $p_0(y_0)dS(y_0)$ is the probability of going from the given point x_0, to a neighborhood $dS(y_0)$ of the point y_0. Similarly $p(y_{i-1},y_i)dS(y_i)$ is the probability of going from point y_{i-1} to a neighborhood $dS(y_i)$ of the point y_i given point y_{i-1}. The choice of $p_0(y_0)$ and $p(y_{i-1},y_i)$ can be arbitrary but they need to satisfy the following constraints:

$$p_0(y_0)>0 \quad \text{if } R(x_0,y_0)\neq 0$$

$$p(y_{i-1},y_i)>0 \quad \text{if } K(y_{i-1},y_i)\neq 0.$$

Then

$$E[\zeta_k]=\int_\Gamma R(x_0,y_0)K^k f(y_0)dS(y_0)$$

where the random variable

$$\zeta_k=\frac{R(x_0,y_0)}{p_0(y_0)}W_k f(y_k) \tag{7}$$

has density $p_0(y_0)p(y_0,y_1)\ldots p(y_{k-1},y_k)$ and

$$W_k=W_{k-1}\frac{K(y_{k-1},y_k)}{p(y_{k-1},y_k)}, \quad W_0\equiv 1.$$

The random variable defined in Eq. (7) is used to construct a direct estimator given by

$$\hat{I}=\frac{1}{N}\sum_{i=1}^{N}\zeta_k^i \tag{8}$$

where ζ_k^i is the ith sample used to evaluate the kth term in the series.

Similarly,

$$E[\zeta_k^*]=\int_\Gamma R(x_0,y_0)K^k f(y_0)dS(y_0)$$

where the random variable

$$\zeta_k^*=R(x_0,y_k)W_k^*\frac{f(y_0)}{p_0(y_0)} \tag{9}$$

has density $p_0(y_0)p(y_0,y_1)\ldots p(y_{k-1},y_k)$ and

$$W_k^*=\frac{K(y_k,y_{k-1})}{p(y_{k-1},y_k)}W_{k-1}^*, \quad W_0^*\equiv 1.$$

The random variable defined in Eq. (9) is used to construct an adjoint estimator given by

$$\hat{I}=\frac{1}{N}\sum_{i=1}^{N}\zeta_k^{*i} \tag{10}$$

where ζ_k^{*i} is the ith sample used to evaluate the kth term in the series.

The random variables ζ_k and ζ_k^* are scalars for potential problems and vectors for two and three-dimensional problems in linear elasticity.

2.3 Densities. As mentioned earlier, the initial density and the transition density can be chosen arbitrarily as long as the relevant constraints are satisfied. The procedure described earlier to estimate the integrals is identical to a standard variance reduction technique called importance sampling discussed in the literature. It is a well-known fact (see Rubinstein [15]) that any positive function that has a shape similar to the integrand and that can be normalized, integrated and then inverted may yield a density that reduces the variance of the estimator. Hence, a judicious use of the density helps in reducing the variance of the estimator.

In the present paper, the initial density for all problems (potential and linear elasticity) is chosen to be $R(x,y)$, the kernel in Eq. (11). The transition density is chosen to be $|K(x,y)|$, where $K(x,y)$ is the kernel in Eq. (12). These particular choices of these densities are motivated by their physical interpretation and by the fact that they cancel out the weak singularities present in the integrand. These densities chosen are also known to be the optimal densities for potential problems.

The physical interpretation of $R(x,y)$ with $(x\in D,\ y\in\Gamma)$ for convex domains is explained next. (Please refer to Fig. 2.) The first point on the boundary, y_0, is chosen by shooting a ray from the point x_0 in a direction which is uniformly distributed in the interval $[0,2\pi]$, and by finding its point of intersection with the boundary. Since only convex bodies are considered, the ray will intersect the boundary at only one point, say y_0. Then the probability of going from the point x_0 to a neighborhood, $dS(y_0)$, of the point y_0, is given by $p_0(y_0)dS(y_0)=d\omega/(2\pi)$. Here $d\omega$ is the angle subtended by $dS(y_0)$ on a unit circle centered at x_0 and is given by $\cos(\phi_{y_0,x_0})dS(y_0)/r$. (It is analogous to the solid angle subtended at a point by a surface in a three-dimensional problem.) Hence

$$p_0(y_0)dS(y_0)=\frac{d\omega}{2\pi}=\frac{\cos(\phi_{y_0,x_0})dS(y_0)}{2\pi r}=R(x_0,y_0)dS(y_0).$$

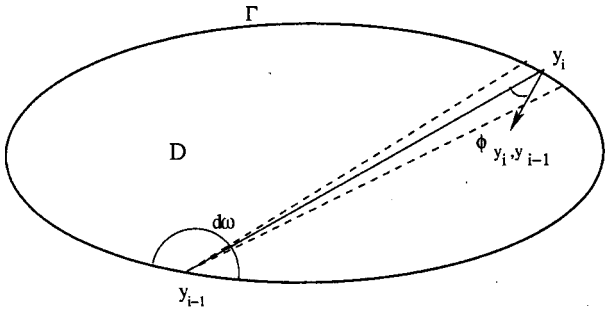

Fig. 3 Intermediate distribution

Therefore

$$p_0(y_0)=R(x_0,y_0).$$

The transition density $|K(x,y)|$ with $(x,y\in\Gamma)$, can be interpreted similarly. (Please refer to Fig. 3.) It can be shown that

$$p(y_{i-1},y_i)dS(y_i)=\frac{d\omega}{\pi}=\frac{\cos(\phi_{y_i,y_{i-1}})dS(y_i)}{\pi r}$$
$$=|K(y_{i-1},y_i)|dS(y_i).$$

Hence

$$p(y_{i-1},y_i)=|K(y_{i-1},y_i)|.$$

Using the above densities, the integrals occurring in Eq. (5) are estimated by using the direct estimator (see Eq. (8)) or the adjoint estimator (see Eq. (10)).

Boundary integral formulations for problems in potential theory and linear elasticity, which are suitable for the application of the boundary walk method, are presented next. The reader is referred to, e.g., Jaswon [16] for a general discussion of indirect boundary integral formulations in potential theory and elasticity.

3 Potential Theory

A formulation for the solution of a Dirichlet problem using a double layer potential (see Günter [17]), and for the solution of a Neumann problem using a single layer potential (see Günter [17]) are presented. The choice of the formulations (i.e., single or double layer) is dictated by the general form of Eqs. (1) and (2).

3.1 Interior Dirichlet Problem. The interior Dirichlet problem in potential theory is concerned with the solution of

$$\Delta u(x)=0,\quad x\in D$$

subject to

$$u(y)=g(y),\quad y\in\Gamma$$

at a point $x_0\in D$. The solution can be written in the form of a double layer potential

$$u(x_0)=\frac{1}{2\pi}\int_\Gamma\frac{\partial}{\partial n_y}\log|y-x_0|\mu(y)dS(y)$$
$$=\frac{1}{2\pi}\int_\Gamma\frac{\cos(\phi_{y,x_0})}{r}\mu(y)dS(y)\qquad(11)$$

where $\mu(y)$ satisfies the integral equation

$$\mu(y)=-\frac{1}{\pi}\int_\Gamma\frac{\cos(\phi_{y',y})\mu(y')}{r}dS(y')+2g(y).\qquad(12)$$

Here $\phi_{y',y}$ denotes the angle between the inward normal at point y' and the ray from point y' to y. It can now be observed that the boundary walk method can be applied to obtain $u(x_0)$ with

$$R(x_0,y)=\cos(\phi_{y,x_0})/(2\pi r),$$

$$K(y,y')=-\cos(\phi_{y',y})/(\pi r),\quad f(y)=2g(y)\quad\text{and}\quad\lambda=1.$$

One point to note is that the series (3) needs to be modified because $\lambda=-1$ is a pole of the resolvent of the kernel (see Günter [17]). This implies that the radius of convergence of the series is strictly less than 1 and hence would diverge when evaluated at $\lambda=1$. It is modified by the method of pole elimination which consist of first multiplying both sides of the series (3) by $(\lambda+1)$, then collecting the coefficients with equal powers of λ. The modified series is then multiplied by $R(x_0,y_0)$ and integrated termwise. $u(x_0)$ is obtained by evaluating the series at $\lambda=1$ and is given by

$$u(x_0)=\frac{1}{2}\mathcal{R}f(y)+\frac{1}{2}\sum_{n=1}^{\infty}\mathcal{R}(\mathcal{K}^{n-1}f(y)+\mathcal{K}^nf(y)).\qquad(13)$$

The individual terms in Eq. (13) are evaluated using the direct estimator given in Section 2.2 and the densities given in Section 2.3.

3.2 Interior Neumann Problem. The interior Neumann problem in potential theory is concerned with the solution of

$$\Delta u(x)=0,\quad x\in D$$

subject to

$$\frac{\partial u(y)}{\partial n}=g(y),\quad y\in\Gamma$$

and

$$\int_\Gamma g(y)dS(y)=0$$

at a point $x_0\in D$. The solution can be written in the form of a single layer potential

$$u(x_0)=\frac{1}{2\pi}\int_\Gamma\log|y-x_0|\mu(y)dS(y)\qquad(14)$$

where $\mu(y)$ satisfies the integral equation

$$\mu(y)=\frac{1}{\pi}\int_\Gamma\frac{\cos(\phi_{y,y'})\mu(y')}{r}dS(y')-2g(y).\qquad(15)$$

The boundary walk method is now applied to obtain the solution at $u(x_0)$ with

$$R(x_0,y)=\log|y-x_0|/(2\pi),\quad K(y,y')=-\cos(\phi_{y,y'})/(\pi r),$$
$$f(y)=-2g(y)\quad\text{and}\quad\lambda=-1.$$

It is interesting to note that the series (3) does not need any modification for the interior Neunmann problem and can be directly evaluated at $\lambda=-1$. This is because the solvability condition needs to be satisfied for the solution to exist and the satisfaction of the solvability condition leads to the cancellation of the pole of the resolvent (see Günter [17]). As a result, the radius of convergence of the series is strictly greater than 1 and hence it does not diverge when evaluated at $\lambda=-1$. $u(x_0)$ is therefore given by

$$u_{x_0}=\sum_{n=0}^{\infty}(-1)^n\mathcal{R}\mathcal{K}^nf(y).\qquad(16)$$

The individual terms in Eq. (16) are evaluated using the adjoint estimator given in Section 2.2 and the densities given in Section 2.3.

4 Linear Elasticity

It can be easily observed that the usual boundary integral formulation given by Rizzo [18]

$$u_i(x_0)=\int_\Gamma U_{ij}(x_0,y)t_j(y)dS(y)$$
$$-\int_\Gamma T_{ij}(x_0,y)u_j(y)dS(y) \quad x_0\in D$$
$$u_i(y)=\int_\Gamma 2U_{ij}(y,z)t_j(z)dS(z)$$
$$-\int_\Gamma 2T_{ij}(y,z)u_j(z)dS(z) \quad y,z\in\Gamma \tag{17}$$

is not suitable for the application of the boundary walk method. Here $U_{ij}(x,y)$ (see Eq. (25)) and $T_{ij}(x,y)$ (see Eq. (26)) are the usual kernels found in the boundary element method literature. Another important point to note is that the above formulation is strongly singular. The difficulty in using a strongly singular formulation with the densities defined earlier is that the estimators (see Eq. (8) and Eq. (10)) have infinite variance. One way to overcome this problem is to define different estimators (see Sabelfeld [4]). But this is a computationally expensive task. Another possible way is to use different densities while preserving the earlier definition of the estimators. But then one loses the advantage of working with densities that are very easy to sample from, and at the same time have a simple physical interpretation. To overcome the problems associated with using a strongly singular formulation, a weakly singular formulation is used for displacement prescribed and traction prescribed problems. These formulations are weakly singular if the boundary Γ is assumed to be satisfy the following condition:

$$|\cos(\phi_{y',y})|<C|y-y'|^\lambda, \quad y',y\in\Gamma, \quad C=\text{constant}, \quad 0<\lambda\leqslant 1$$

where $\phi_{y',y}$ is the angle between the inward normal at point y' and a ray from point y' to point y. The derivation of these weakly singular formulations is presented next.

4.1 Displacement Prescribed Problem. The derivation of the weakly singular formulation presented here for two-dimensional problems is based on a similar derivation for three-dimensional problems given in Kupradze [12]. The derivation of the usual $T_{ij}(x,y)$ kernel found in the Rizzo [18] formulation is also given simultaneously for the purpose of comparison.

The displacement field in a linear isotropic elastic solid in the absence of body forces is governed by the Navier equation,

$$\mu\Delta\mathbf{u}+(\lambda+\mu)\nabla(\nabla\cdot\mathbf{u})=\mathbf{0}, \tag{18}$$

where μ and λ are the Lamè constants. The standard stress tensor is given by

$$\mathbf{S}=\mu(\nabla\mathbf{u}+\nabla\mathbf{u}^T)+\lambda(\nabla\cdot\mathbf{u})\mathbf{I}. \tag{19}$$

Equation (18) can also be written as

$$\mu\Delta\mathbf{u}+(\alpha+\beta)\nabla(\nabla\cdot\mathbf{u})=\mathbf{0} \tag{20}$$

where α and β are constants and $(\alpha+\beta)=(\lambda+\mu)$. Equation (20) leads to an introduction of a pseudo-stress tensor which is given by

$$\mathbf{S}^P=\mu\nabla\mathbf{u}+\alpha\nabla\mathbf{u}^T+\beta(\nabla\cdot\mathbf{u})\mathbf{I}. \tag{21}$$

In the case when $\alpha=\mu$ and $\beta=\lambda$, the pseudo-stress tensor is identical to the standard stress tensor. Multiplying the standard stress tensor $\mathbf{S}$ and the pseudo-stress tensor $\mathbf{S}^P$ by the normal $\mathbf{n}$ on the boundary gives the standard traction $\mathbf{t}$ and the pseudo-traction $\mathbf{t}^P$ i.e.,

$$\mathbf{t}(\mathbf{u})=\mathbf{S}\mathbf{n}, \quad \mathbf{t}^P(\mathbf{u})=\mathbf{S}^P\mathbf{n}.$$

Here,

$$\mathbf{t}(\ )=2\mu\frac{\partial}{\partial\mathbf{n}}(\ )+\lambda\mathbf{n}\nabla\cdot(\ )+\mu(\mathbf{n}\times\nabla\times(\ )) \tag{22}$$

and

$$\mathbf{t}^P(\ )=(\alpha+\mu)\frac{\partial}{\partial\mathbf{n}}(\ )+\beta\mathbf{n}\nabla\cdot(\ )+\alpha(\mathbf{n}\times\nabla\times(\ )). \tag{23}$$

Now the columns $\mathbf{g}^j(xy)$, $j=1,2$ of the Kelvin matrix

$$\mathbf{U}=[\mathbf{g}^1\mathbf{g}^2] \tag{24}$$

with elements

$$U_{ij}(x,y)=(\mathbf{g}^j)_i=C\left((3-4\nu)\delta_{ij}\log r-\frac{\partial r}{\partial y_i}\frac{\partial r}{\partial y_j}\right) \tag{25}$$

where

$$C=-\frac{1}{8\pi\mu(1-\nu)}$$

are fundamental solutions of Eq. (18). The transpose of the matrix which results from the application of $\mathbf{t}$ to the columns of $\mathbf{U}$ with respect to point y gives the usual $\mathbf{T}$ matrix with elements

$$T_{ij}(x,y)=-\frac{1}{4\pi(1-\nu)r}\left[\frac{\partial r}{\partial n_y}\left((1-2\nu)\delta_{ij}+2\frac{\partial r}{\partial y_i}\frac{\partial r}{\partial y_j}\right)\right.$$
$$\left.-(1-2\nu)\left(\frac{\partial r}{\partial y_i}n_j(y)-\frac{\partial r}{\partial y_j}n_i(y)\right)\right]. \tag{26}$$

As seen from above, the matrix $\mathbf{T}$ is strongly singular.

To obtain a weakly singular matrix, consider the action of the pseudo-traction operator on the columns of (24) with respect to point y.

Now,

$$\left(\frac{\partial\mathbf{g}^j(x,y)}{\partial\mathbf{n}(y)}\right)_i=C\left[\frac{1}{r}\frac{\partial r}{\partial n_y}\left((3-4\nu)\delta_{ij}+2\frac{\partial r}{\partial y_i}\frac{\partial r}{\partial y_j}\right)\right.$$
$$\left.-\frac{1}{r}\left(\frac{\partial r}{\partial y_j}n_i(y)+\frac{\partial r}{\partial y_i}n_j(y)\right)\right] \tag{27}$$

Similarly,

$$(\mathbf{n}(y)\nabla\cdot(\mathbf{g}^j))_i=2C(1-2\nu)\frac{1}{r}\frac{\partial r}{\partial y_j}n_i(y). \tag{28}$$

Also,

$$(\mathbf{n}(y)\times\nabla\times(\mathbf{g}^j))_i=4C(1-\nu)\left(\frac{1}{r}\frac{\partial r}{\partial y_i}n_j(y)-\frac{1}{r}\frac{\partial r}{\partial n_y}\delta_{ij}\right). \tag{29}$$

Therefore,

$$T^P_{ij}(x,y)=(\mathbf{t}^P(\mathbf{g}^j))_i$$
$$=\frac{1}{r}\frac{\partial r}{\partial n_y}\left[\left(C(3-4\nu)\delta_{ij}+2C\frac{\partial r}{\partial y_i}\frac{\partial r}{\partial y_j}\right)\right.$$
$$\left.\times(\alpha+\mu)-4C(1-\nu)\alpha\delta_{ij}\right]-\frac{1}{r}\frac{\partial r}{\partial y_j}n_i(y)(C(\alpha+\mu)$$
$$-2C(1-2\nu)\beta)-\frac{1}{r}\frac{\partial r}{\partial y_i}n_j(y)(C(\alpha+\mu)$$
$$-4C(1-\nu)\alpha). \tag{30}$$

It is observed from Eq. (30) that a weakly singular matrix can be obtained from the matrix $\mathbf{T}^P$ by choosing

$$\alpha=\frac{\mu}{3-4\nu} \tag{31}$$

$$\beta=\frac{2\mu(1-\nu)}{(3-4\nu)(1-2\nu)}.$$

The transpose of the weakly singular matrix obtained for the above values of α and β is denoted by $\mathbf{T}^*$. The elements of $\mathbf{T}^*$ are given by

$$T^*_{ij}(x,y)=-\frac{1}{\pi(3-4\nu)}\frac{1}{r}\frac{\partial r}{\partial n_y}\left[(1-2\nu)\delta_{ij}+\frac{\partial r}{\partial y_i}\frac{\partial r}{\partial y_j}\right]. \tag{32}$$

It is also observed that by choosing $\alpha=\mu$ and $\beta=\lambda$ in the matrix $\mathbf{T}^P$, we get the transpose of matrix $\mathbf{T}$ as expected.

It can be shown that the columns of $\mathbf{T}^*$ satisfy Eq. (18) and hence it is used to form the double-layer potential of the second kind (see Kupradze [12]). Using the above potential, the solution to the interior displacement problem can be written as

$$u_i(x_0)=-\int_\Gamma T^*_{ij}(x_0,y)\mu_j(y)dS(y) \tag{33}$$

where $\mu_i(y)$ satisfies the following integral equation:

$$\mu_i(y)=\int_\Gamma 2T^*_{ij}(y,y')\mu_j(y')dS(y')+2g_i(y) \tag{34}$$

and g_i is the prescribed displacement.

It can now be observed that the boundary walk method can be applied to obtain $\mathbf{u}(x_0)$ with

$$\mathbf{R}(x_0,y)=-\mathbf{T}^*(x_0,y),\quad \mathbf{K}(y,y')=2\mathbf{T}^*(y,y'),$$
$$\mathbf{f}(y)=2\mathbf{g}(y)\quad \text{and}\quad \lambda=1.$$

Here $\mathbf{u}(x)$ and $\mathbf{g}(y)$ are vector functions and $\mathbf{R}(x,y)$ and $\mathbf{T}(x,y)$ are matrix valued functions. $\lambda=-1$ is pole of the resolvent of the kernel (see Kupradze [12]) and therefore a similar modification to the one proposed for the Dirichlet problem (for Laplace's equation) is needed here. Finally, $\mathbf{u}(x_0)$ is given by

$$\mathbf{u}(x_0)=\frac{1}{2}\mathcal{R}f(y)+\frac{1}{2}\sum_{n=1}^{\infty}\mathcal{R}(\mathcal{K}^{n-1}f(y)+\mathcal{K}^nf(y)). \tag{35}$$

The individual terms in Eq. (35) are then estimated using the direct estimator defined earlier.

4.2 Traction Prescribed Problem. The approach presented in the previous section to obtain a weakly singular integral equation is not suitable for the traction prescribed problem because the pseudo-traction has no physical meaning. A rigorous approach, based on using a two-dimensional analog of the Weil potential, is presented in Mikhailov [13] to derive weakly singular integral equations for traction prescribed problems. It is also explicitly pointed out that the stresses obtained for a linearized Stokes system (incompressible material) using a hydrodynamic potential of a simple layer, the stresses obtained for an elastic material with $\nu=1/2$ using a single layer potential, and the stresses obtained using the analog of the Weil potential for an elastic material, all are identical. A simpler approach, based on the above observation, and the fact that *the stresses everywhere in a body with prescribed tractions on the boundary are independent of the material constants*, is used here to derive the weakly singular integral equation. The derivation of the weakly singular formulation for an interior traction prescribed problem is presented next.

The displacement at a point x_0 in a body with prescribed tractions on the boundary can be represented in a form of a single layer potential:

$$u_i(x_0)=\int_\Gamma U_{ji}(y,x_0)f_j(y)dS(y). \tag{36}$$

The corresponding stresses are given by

$$\sigma_{il}(x_0)=\int_\Gamma S_{ilj}(y,x_0)f_j(y)dS(y) \tag{37}$$

where $f_i(y)$ satisfies the following integral equation:

$$f_i(y)=-\int_\Gamma 2S_{ilj}(y',y)n_l(y)f_j(y')dS(y')+2t_i(y) \tag{38}$$

and t_i are the prescribed tractions. Here

$$S_{ilj}(y,x_0)=\frac{1}{4\pi(1-\nu)r}\left[\left(2\frac{\partial r}{\partial y_i}\frac{\partial r}{\partial y_l}\frac{\partial r}{\partial y_j}+(1-2\nu)\delta_{ij}\frac{\partial r}{\partial y_l}\right)-(1-2\nu)\left(\delta_{il}\frac{\partial r}{\partial y_j}-\delta_{lj}\frac{\partial r}{\partial y_i}\right)\right]. \tag{39}$$

It is seen that the kernel in Eq. (38) is strongly singular. By making use of the previously mentioned observation in Mikhailov [13], and the fact that for a traction prescribed problem the stresses are independent of the material constants ν and μ, ν can be set to 1/2 in Eq. (39). This simplifies the equation to

$$S_{ilj}(y,x_0)=\frac{1}{\pi}\frac{1}{r}\frac{\partial r}{\partial y_i}\frac{\partial r}{\partial y_l}\frac{\partial r}{\partial y_j}. \tag{40}$$

Using Eq. (40), Eq. (38) can be written as

$$f_i(y)=-\int_\Gamma 2K^*_{ij}(y',y)f_j(y')dS(y')+2t_i(y) \tag{41}$$

where

$$K^*_{ij}(y',y)=\frac{1}{\pi}\frac{1}{r}\frac{\partial r}{\partial y'_i}\frac{\partial r}{\partial y'_j}\frac{\partial r}{\partial y'_l}n_l(y). \tag{42}$$

It is now observed that the kernel in Eq. (41) is weakly singular. This solution is identical to the one given in Mikhailov [13]. It is interesting to point out that the observation of the fact that the stress in an elastic body subjected to traction boundary conditions is independent of material parameters, leads to a very simple derivation of Eq. (40).

Equation (37), along with Eq. (41), with the kernel given in Eq. (42), can now solved for $\sigma(x_0)$ with the boundary walk method with

$$\mathbf{R}(x_0,y)=\mathbf{S}(x_0,y),\quad \mathbf{K}(y,y')=2\mathbf{K}^*(y',y),$$
$$\mathbf{f}(y)=2\mathbf{t}(y)\quad \text{and}\quad \lambda=-1.$$

Here $\mathbf{u}(x)$ and $\mathbf{g}(y)$ are vector functions and $\mathbf{R}(x,y)$ and $\mathbf{T}(x,y)$ are matrix valued functions. Also the components of stress are represented in a form of a vector $\boldsymbol{\sigma}$. Now $\lambda=1$ is a pole of the resolvent of the kernel while the satisfaction of the solvability condition leads to the cancellation of the pole at $\lambda=-1$ (see Mikhailov [13]). Hence, a modification similar to the one for the displacement prescribed problem is required and $\boldsymbol{\sigma}(x_0)$ is finally given by

$$\sigma(x_0)=\frac{1}{2}\mathcal{R}f(y)+\frac{1}{2}\sum_{n=1}^{\infty}\mathcal{R}(\mathcal{K}^nf(y)-\mathcal{K}^{n-1}f(y))(-1)^n. \tag{43}$$

The individual terms in Eq. (43) are then estimated using the adjoint estimator defined earlier.

5 Numerical Results

The boundary walk method is used herein to solve some problems in potential theory and linear elasticity and the calculated results are compared with the exact results in most cases. The effect of the geometry of the problem on the accuracy of the computed results is studied. A point to note is that even though integral equation formulations for both potential theory and elasticity has been given for bodies with smooth boundaries, the same

Table 1 Solution of a Dirichlet problem on an ellipse with $a=1$, $b=2$ at $\theta=\pi/4$

r	k	Computed Value	Std. Dev	Exact Value	% Error
0.2	4	1.09213	0.01602	1.10614	1.267
0.4	5	1.14196	0.01997	1.12019	1.811
0.6	4	0.98904	0.01543	1.01045	2.119
0.8	6	0.73811	0.02265	0.74902	1.457

Monte Carlo simulation parameters: $N=100{,}000$, $n=7$, $s=0.005$, $\epsilon=0.005$

Table 2 Solution of a Dirichlet problem on an ellipse with $a=1$, $b=5$ at $\theta=\pi/4$

r	k	Computed Value	Std. Dev	Exact Value	% Error
0.2	4	0.88768	0.01282	0.87573	1.365
0.4	5	0.21791	0.01529	0.20692	5.311
0.6	5	−0.79405	0.01488	−0.79959	0.692
0.8	6	−1.67908	0.01795	−1.67502	0.242

Monte Carlo simulation parameters: $N=200{,}000$, $n=7$, $s=0.005$, $\epsilon=0.005$

equations have been used to solve problems having nonsmooth boundaries (e.g., a wedge). An attempt has been made to justify it using the following arguments given in Parton [19].

The nature of the solution of both potential theory and linear elasticity, in the neighborhood of a corner, has been well studied. Therefore, it seems justifiable to extend formally the equations derived for smooth boundaries to solve problems with nonsmooth boundaries with proper control based on the known information about the properties of the solution.

A more rigorous approach, which involves modifying the governing integral equations, is described in detail in Atkinson [20].

Remark. There are two important issues to consider while computing the result using a series expansion in which individual terms are calculated using Monte Carlo integration:

(a) the number of the terms in a series, n.

(b) the number of samples to evaluate the individual terms, N.

A naive approach is adopted in the present paper in deciding the two parameters, and is as follows. The various modifications to the original series which were explained earlier guaranty that the modified series converges uniformly. Therefore, a fixed number of terms of the modified series, say n, are calculated using a fixed N. The number of samples is chosen so that the standard deviation s, of each term, is less than a predefined number. The first k terms are considered if

$$|S_{k+1}-S_k|\leq\epsilon$$

where S_k denotes the partial sum of the first k terms and ϵ is again a predefined number. The pair (s,ϵ) will henceforth be referred to as the tolerance. The numerical results which are computed for a given value of a tolerance are presented next.

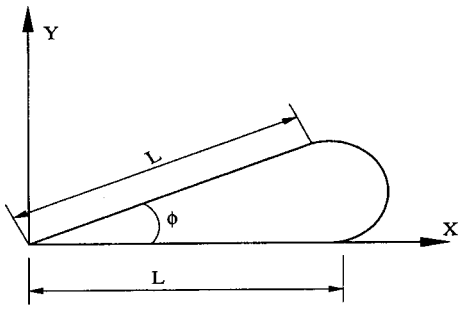

Fig. 4 Pie-shaped region for the Dirichlet problem

5.1 Potential Theory

5.1.1 Dirichlet Problems. The boundary walk method is used to solve Dirichlet problems on ellipses with $b/a=2$ and $b/a=5$, and also on a pie shaped region. For the ellipse problems, the following exact solution is assumed:

$$u(x,y)=\exp(x)\cos(y).$$

This solution is prescribed on the boundary of each ellipse. The results at

$$x=r(a\cos(\theta))$$

$$y=r(b\sin(\theta))$$

for the ellipse with $b/a=2$ are presented in Table 1. *This particular form of describing the point of interest is followed throughout the paper whenever problems on ellipses are solved.*

It is seen that the number of terms required to compute the result (within a prescribed tolerance) depends on the location of the point of interest. It is also seen that an increase in the number of terms included leads to increases in the standard deviation of the computed answer. The results for the ellipse with $b/a=5$ are presented in Table 2.

As seen from Table 2, the increase in the b/a ratio leads to an increase in the number of samples needed to achieve the desired upper bound for the standard deviation in each individual term. It also observed that a larger number of terms in the series need to be considered with the increase in the b/a ratio. The increase in the number of samples can be explained by the fact that choosing a direction which is uniformly distributed leads to a nonuniform distribution of points on the boundaries of bodies having elongated shapes. As a result more samples are needed to achieve the required tolerance. It is also well known that the standard boundary element method requires a finer discretization for solving a problem on an ellipse with an aspect ratio 5 compared with an aspect ratio of 2.

The Dirichlet problem is also solved for the pie shaped region shown in Fig. 4 with $\phi=3/10\pi$ and $L=1$ (see Atkinson [20]). The two sides meeting at the origin are both straight line segments of length L, and the remaining portion of the boundary is an arc of a circle which is tangent to the two straight edges. The following

Table 3 Solution of a Dirichlet problem on a pie with $\phi=3/10\pi$ and $L=1$

	ϕ_0	ϕ_1	ϕ_2	ϕ_3	ϕ_4	ϕ_5	ϕ_6
Computed Mean	0.63317	−0.57639	0.04940	−0.01862	0.00441	0.00158	0.00113
Std. Dev	0.00281	0.00438	0.00483	0.00487	0.00488	0.00489	0.00488

Monte Carlo simulation parameters: $N=250{,}000$, $s=0.005$, $\epsilon=0.005$

Table 4 Solution of a Dirichlet problem on a pie with $\phi=3/10\pi$ and $L=1$

	ϕ_0	ϕ_1	ϕ_2	ϕ_3	ϕ_4	ϕ_5	ϕ_6
Computed Mean	0.63504	−0.57424	0.04732	−0.01840	0.00349	−0.00148	−0.00015
Std. Dev	0.00141	0.00219	0.00242	0.00244	0.00244	0.00244	0.00244

Monte Carlo simulation parameters: $N=1{,}000{,}000$, $s=0.003$, $\epsilon=0.003$

solution, which is harmonic in the domain, and has boundary values that are smoothly differentiable on the boundary, except at a corner, is assumed here:

$$u(r,\theta)=r^{10/3}\sin\left(\frac{10}{3}\theta\right).$$

Again, this solution is prescribed on the boundary of the pie-shaped region. The reason for choosing this particular solution is that it has been proved by Wasow [21] that in the vicinity of corner point, the solution to the Dirichlet problem satisfies

$$u(x,y)=\begin{cases} O(r^{\alpha}) & \alpha\neq m, \quad \text{a positive integer} \\ O(r^{\alpha}\log(r)) & \alpha=m, \quad \text{an integer} \end{cases}$$

for $0\leqslant r\leqslant\epsilon$, for some $\epsilon>0$, and point (x,y) inside the domain. Results for the problem with $\phi=3/10\pi$ and $L=1$ at

$$x=r\cos(\theta)$$

$$y=r\sin(\theta)$$

for $r=0.5$ and $\theta=3/20\pi$ are presented in Table 3.

Here $\phi_0,\ldots,\phi_6$ are the first seven terms in the series given by Eq. (13). It is observed from Table 3 that the series indeed converges for the pie shaped region which has a nonsmooth boundary. The desired solution is obtained by considering the first four terms and is given by 0.08756 with a standard deviation of 0.01685. The exact answer is 0.09921. To increase the accuracy and decrease the standard deviation, the values of both s and ϵ were changed to 0.003. To achieve this tolerance, the number of samples was increased from 250,000 to 1,000,000. The results for $N=1{,}000{,}000$ are shown in Table 4.

This time, the result is computed by considering the first five terms in the series and is given by 0.090069 with a standard deviation of 0.01090. This result is slightly better than the previous one. This does indicate that the results are expected to converge with increase in the number of samples. This particular example illustrates one particular shortcoming of the boundary walk method. As is generally true for other numerical methods, the boundary walk method is not useful for estimating quantities whose absolute values are close to zero in magnitude, without using a considerable number of sample points. This observation was also verified by solving the Dirichlet problem on an ellipse with $b/a=2$ with the exact solution

$$u(x,y)=\exp(x)\cos(y)-1$$

for points close to the origin.

Table 5 Solution of a Neumann problem on an ellipse with $a=1$, $b=2$ at $\theta=\pi/4$

r	k	Computed Value	Std. Dev	Exact Value	% Error
0.2	5	1.10627	0.01336	1.10614	0.011
0.4	5	1.11961	0.01458	1.12019	0.052
0.6	5	1.00616	0.01778	1.01045	0.425
0.8	7	0.74907	0.03006	0.74902	0.007

Monte Carlo simulation parameters: $N=400{,}000$, $n=8$, $s=0.005$, $\epsilon=0.005$

5.1.2 Neumann Problems. The boundary walk method is used to solve the Neumann problem on an ellipse with $b/a=2$ and $b/a=5$. Since the results are unique upto an additive constant, the gradient of the field variable in the x-direction is calculated. Another approach would be to fix the field variable at one interior point in the domain, apply the Kelvin transformation, and solve the resulting exterior Dirichlet problem (see Atkinson [20]). This will be tried in the future.

The following exact solution is assumed:

$$u(x,y)=\exp(x)\cos(y)$$

Table 6 Solution of a Neumann problem on an ellipse with $a=1$, $b=5$ at $\theta=\pi/4$

r	k	Computed Value	Std. Dev	Exact Value	% Error
0.2	7	0.88654	0.02460	0.87573	1.234
0.4	7	0.20776	0.02471	0.20692	0.406
0.6	7	−0.80706	0.03232	−0.79959	0.934
0.8	7	−1.67133	0.05128	−1.67502	0.220

Monte Carlo simulation parameters: $N=1{,}000{,}000$, $n=10$, $s=0.01$, $\epsilon=0.01$

Table 7 Solution of a displacement problem on an ellipse with $a=1$, $b=2$ at $\theta=\pi/4$

r		k	Computed Value	Std. Dev	Exact Value	% Error
0.2	u	7	0.03588	0.00416	0.03807	5.752
	v	8	0.08169	0.00560	0.07615	7.275
0.4	u	7	0.07195	0.00413	0.07615	5.510
	v	8	0.15751	0.00558	0.15230	3.420
0.6	u	10	0.11349	0.00704	0.11422	0.391
	v	9	0.23477	0.00658	0.22845	2.766
0.8	u	10	0.15128	0.00694	0.15230	0.670
	v	9	0.31048	0.00653	0.30460	1.930

Monte Carlo simulation parameters: $N=1{,}200{,}000$, $n=12$, $s=0.0010$, $\epsilon=0.0015$

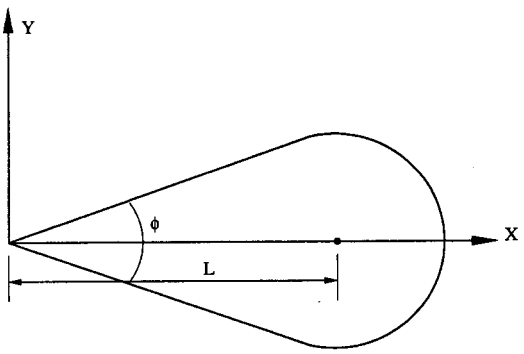

Fig. 5 Wedge-shaped region for the displacement problem

Table 8 Solution of a displacement problem on a wedge with $\phi=\pi/4$ and $L=1$

	ϕ_0	ϕ_1	ϕ_2	ϕ_3	ϕ_4	ϕ_5
Computed Mean (u)	0.15906	−0.02256	0.00333	−0.00260	−0.00088	0.00024
Std. Dev	0.00028	0.00037	0.00038	0.00041	0.00044	0.00048
Computed Mean (v)	−0.00016	0.00004	0.00011	0.00018	−0.00040	−0.00018
Std. Dev	0.00015	0.00026	0.00029	0.00034	0.00038	0.00042

Monte Carlo simulation parameters: $N=200{,}000$, $n=8$, $s=0.0010$, $\epsilon=0.0010$

and the corresponding Neumann boundary conditions are imposed on the boundary of the body. Results for the ellipse $b/a=2$ are presented in the Table 5.

As seen from Table 5, the number of samples needed to attain the required tolerance is more than for the corresponding Dirichlet problem with the same geometry. The number of terms needed to compute the solution is also more. Both of these effects could be attributed to the fact that the boundary conditions for this Neumann problem are more complicated.

The results for the Neumann problem for an ellipse with $b/a=5$ with the same exact solution are presented in Table 6.

As seen from Table 6, the number of samples needed to achieve the required tolerance, which was relaxed in this case, is about two and half times the number required with $b/a=2$. This can again be attributed to the elongated shape of the ellipse with $b/a=5$ which leads to nonuniform sampling from the boundary.

5.2 Linear Elasticity

5.2.1 Displacement Problems. The boundary walk method is used to solve displacement prescribed problems on a thin ellipse and on a wedge. For both these problems, displacement boundary conditions corresponding to unit normal boundary traction are applied. The Poisson's ratio, ν, is assumed to be 0.3 and the shear modulus, μ, is assumed to be 1.0. The exact solution assuming $u(0,0)=0$ and $v(0,0)=0$ is given by

$$u=\frac{(1-\nu)}{2\mu(1+\nu)}x$$

$$v=\frac{(1-\nu)}{2\mu(1+\nu)}y.$$

The results on an ellipse with $b/a=2$ are presented in Table 7.

It is seen from Table 7 that more terms are needed as the point of interest approaches the boundary. It also confirms the previous observation that the boundary walk method is not quite accurate in estimating quantities whose absolute magnitude is "small."

The boundary walk method is also used to solve the displacement problem on a wedge shaped region. The purpose of this problem is to demonstrate the applicability of the derived equations to solve problems on domains-with non-smooth boundaries. The wedge is as shown in Fig. 5.

The two sides meeting at the origin are straight line segments with included angle ϕ and are tangent to the circle with center $(L,0)$. Displacements corresponding to unit normal tractions are applied on the boundary. Results of the problem with $\phi=\pi/4$ and $L=1$ at

$$x=r\cos(\theta)$$

$$y=r\sin(\theta)$$

for $r=0.5$ and $\theta=0$, are presented next in Table 8.

Here $\phi_0,\ldots,\phi_5$ are the first six terms in series (35). According to the tolerance criteria, the first four terms are taken to compute the displacement in the x-direction. The computed displacement is 0.13724 with a standard deviation of 0.00144. This compares well with the actual result which is 0.13462. To calculate the displacement in the y-direction, only the first term is taken. The exact answer is of course 0.0.

5.2.2 Traction Problems. The boundary walk method is used to solve a traction problem on an ellipse. Unit normal traction is applied on portions S_1 and S_2 of the boundary where $S_1=\{x,y:\pi/4\leq\theta\leq 3/4\pi,x,y\in\Gamma\}$ and $S_2=\{x,y:5/4\pi\leq\theta\leq 7/4\pi,x,y\in\Gamma\}$. (Please refer to Fig. 6.)

The solutions obtained using the boundary walk method (BWM) are compared with those obtained using the standard boundary element method (BEM) with linear continuous elements. The results on an ellipse with $b/a=2$ are presented in Table 9. It is seen that the results are quite accurate. Note that the largest stresses (in absolute magnitude) are estimated well in all the four points under consideration while a large difference be-

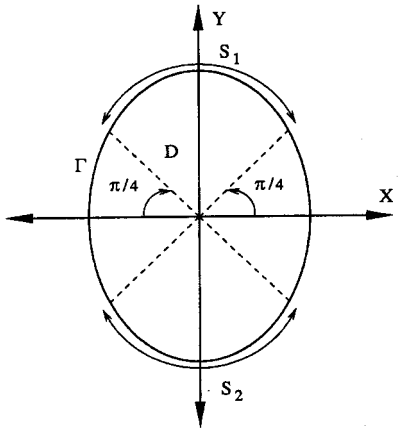

Fig. 6 Problem definition for the traction prescribed problem

Table 9 Solution of a traction problem on an ellipse with $a=1$, $b=2$ at $\theta=\pi/4$

r		k	Computed (BWM)	Std. Dev	Computed (BEM)	% Difference
0.2	σ_{xx}	4	−0.12643	0.00383	−0.12207	3.572
	σ_{yy}	4	0.84200	0.00479	0.84320	0.142
	σ_{xy}	2	−0.01762	0.00083	−0.01651	6.723
0.4	σ_{xx}	4	−0.09576	0.00421	−0.08726	9.741
	σ_{yy}	4	0.85596	0.00522	0.85403	0.226
	σ_{xy}	3	−0.05833	0.00185	−0.06000	2.783
0.6	σ_{xx}	5	−0.02090	0.00816	−0.02379	12.148
	σ_{yy}	5	0.86272	0.00974	0.85299	1.141
	σ_{xy}	3	−0.10674	0.00209	−0.11000	2.964
0.8	σ_{xx}	5	0.07039	0.01155	0.05424	29.775
	σ_{yy}	5	0.85088	0.01370	0.83576	1.809
	σ_{xy}	3	−0.13214	0.00267	−0.13829	4.447

Monte Carlo simulation parameters: $N=1{,}200{,}000$, $n=7$, $s=0.0050$, $\epsilon=0.0050$

tween the boundary element method and boundary walk method results is observed when estimating the smallest stress (in absolute magnitude). For example, the percentage difference between σ_{xx} computed at $r=0.8$ using the boundary element method and the boundary walk method is around 30%. But this stress is of the order of 10% of the maximum stress (σ_{yy}). Inaccurate estimation of minor stress components can occur from other numerical methods as well, but is of little practical concern as long as the major components are obtained accurately.

Remarks.

- The computational time (wall clock) for solving the above problems (potential theory and linear elasticity) is of the order of few minutes on a machine with a Pentium 3 processor (650 Mhz) and having 256 Mb of RAM.
- Large sample sizes are required for several examples in this paper in order to estimate ''small'' quantities with the prescribed tolerance.

6 Concluding Remarks

A local method called the boundary walk method has been described and applied to solve two-dimensional problems in potential theory and linear elasticity. The method is local in the sense that the solution at a point of interest is obtained directly. The necessary integral representations needed to apply the boundary walk method are also presented. Simple problems are solved using the boundary walk method to show the feasibility the method. The numerical results are in reasonable agreement with the exact solutions. To further develop this method and improve its efficiency and accuracy, the following issues will be investigated in the near future:

(a) Develop the method to solve problems with mixed boundary conditions.
(b) Apply the method to solve problems in multiply connected domains.
(c) Get accurate error estimates which depend on the number of terms considered in the series and the number of samples used to compute the integrals.
(d) Develop more efficient ways of carrying out Monte Carlo integration.

The versatility of the boundary walk method in its current state, is definitely not comparable to common numerical methods like the finite element method or the boundary element method. But addressing some or all of these issues mentioned above will help in improving its range of applicability.

Acknowledgments

This research has been supported by NSF Grant CMS-9912524 to Cornell University. The computing for this research was carried out using the resources of the Cornell Theory Center, which receives funding from Cornell University, New York State, the National Center for Research Resources at the National Institutes of Health, the National Science Foundation, the Defense Department Modernization program, the United States Department of Agriculture, and corporate partners.

References

[1] Arsenjev, D. G., Ivanov, V. M., and Kul'chitsky, O. Y., 1999, *Adaptive Methods of Computational Mathematics and Mechanics, Stochastic Varient*, World Scientific, Singapore.
[2] Kim, C. I., and Torquato, S., 1989, ''Determination of the Effective Conductivity of Heterogeneous Media by Brownian Motion Simulation,'' J. Appl. Phys., **68**, 3892–3903.
[3] Evans, M., and Swartz, T., 2000, *Approximating Integrals via Monte Carlo and Deterministic Methods*, Oxford University Press, Oxford, UK.
[4] Sabelfeld, K. K., 1991, *Monte Carlo Methods in Boundary Value Problems*, Springer-Verlag, Berlin.
[5] Sabelfeld, K. K., and Simonov, N. A., 1994, *Random Walks on Boundary for Solving PDEs*, VSP, Utrecht, The Netherlands.
[6] Hoffman, T. J., and Banks, N. E., 1974, ''Monte Carlo Solution to the Dirichlet Problem With the Double Layer Potential Density,'' Trans. Am. Nucl. Soc., **18**, pp. 136–137.
[7] Kalos, H. K., and Whitlock, A. P., 1986, *Monte Carlo Methods*, John Wiley and Sons, New York.
[8] Haj-Sheikh, A., and Sparrow, E. M., 1966, ''The Floating Random Walk and Its Applications to Monte Carlo Solutions of Heat Transfer,'' SIAM (Soc. Ind. Appl. Math.) J. Appl. Math., **14**, pp. 370–389.
[9] Sabelfeld, K. K., and Talay, D., 1995, ''Integral Formulation of the Boundary Value Problems and the Method of the Random Walk on the Spheres,'' Monte Carlo Meth. Appl., **1**, pp. 1–34.
[10] Chati, K. C., Grigoriu, M. D., Kulkarni, S. S., and Mukherjee, Subrata, 2001, ''Random Walk Method for the Two- and Three-dimensional Laplace, Poisson and Helmholt'z Equations,'' Int. J. Numer. Methods Eng., **51** , pp. 1133–1156.
[11] Øksendal, B., 1992, *Stochastic Differential Equations*, Springer, New York.
[12] Kupradze, V. D., 1965, *Potential Methods in the Theory of Elasticity*, Israel Program for Scientific Translations, Jerusalem.
[13] Mikhailov, S. E., 1989, ''Spectral Properties and Solution Methods for Some Integral Equations of Elasticity for Plane Non-Simply-Connected Bodies with Corner Points Under Forces Specified on the Boundary,'' Mech. Solids, **24**, pp. 53–63.
[14] Shia, D., and Hui, C., 2000, ''A Monte Carlo Solution Method for Linear Elasticity,'' Int. J. Solids Struct., **37**, pp. 6085–6105.
[15] Rubinstein, R. Y., 1981, *Simulation and the Monte Carlo Method*, John Wiley and Sons, New York.
[16] Jaswon, M. A., and Symm, G. T., 1977, *Integral Equation Methods in Potential Theory and Elastostatics*, Academic Press, New York.
[17] Günter, N. M., 1967, *Potential Theory*, Frederick Ungar, New York.
[18] Rizzo, F. J., 1967, ''An Integral Equation Approach to Boundary Value Problems of Classical Elastostatics,'' Q. J. Mech. Appl. Math., **25**, pp. 83–95.
[19] Parton, V. Z., and Perlin, P. I., 1982, *Integral Equations in Elasticity*, Mir, Moscow.
[20] Atkinson, K. E., 1997, *The Numerical Solution of Integral Equations of the Second Kind*, Cambridge University Press, Cambridge, UK.
[21] Wasow, W., 1957, ''Asymptotic Development of the Solution of Dirichlet's Problem at Analytic Corner,'' Duke Math. J., **24**, pp. 47–56.

On the Eshelby's Inclusion Problem for Ellipsoids With Nonuniform Dilatational Gaussian and Exponential Eigenstrains

P. Sharma[1]
General Electric Corporate R&D,
Niskayuna, NY 12309

R. Sharma
Massachusetts Institute of Technology,
Cambridge, MA 02139

This work investigates the three-dimensional elastic state of inclusions in which the prescribed stress-free transformation strains or eigenstrains are spatially nonuniform and distributed either in a Gaussian, or an exponential manner. The prescribed eigenstrain distributions are taken to be dilatational. Typical research in the micromechanics of inclusions and inhomogeneities has dealt, by and large, with spatially uniform eigenstrains and, to some limited degree, with polynomial distributions. Solutions to Eshelby's inclusion problem, where eigenstrains are Gaussian and exponential in nature, do not exist. Such eigenstrain distributions arise naturally due to highly localized point-source type heating (typical in electronic chips), due to compositional differences, and those due to diffusion related mechanisms among others. The current paper provides such a solution for ellipsoidal shaped inclusions located in an infinite isotropic elastic matrix. It is shown, similar to the much-discussed uniform eigenstrain problem, that the elastic state is completely determined in closed form save for some simple one-dimensional integrals that are evaluated trivially using numerical quadrature. For the specialized case of a spherical shape, solutions in terms of known functions are derived and numerical results are presented. The elastic state both within and outside the inclusion is investigated. For the specific case of a sphere, the elastic strain energies are given in terms of simple formulas. Some applications of the current work in various areas such as electronics, micromechanics of composites, and material science are also discussed. [DOI: 10.1115/1.1558078]

1 Introduction

Since the celebrated work of Eshelby [1–3] on the elastic state of inclusions and inhomogeneities, extensive work on this subject has appeared in various forms. Following Mura [4], we define an inclusion to be a bounded volume located in a material with identical material properties but containing a finite stress-free transformation strain (or eigenstrain) within its domain. The value of the eigenstrain is null outside the inclusion domain. An inhomogeneity is defined as a bounded volume with material properties different than those of the surrounding material or matrix. Various examples of naturally occurring eigenstrains are those due to thermal expansion, lattice parameter mismatch, inelastic deformation, swelling strain, compositional differences, magnetomechanical, or electromechanical strains, etc.

The following monographs have provided comprehensive reviews of the micromechanics of inclusions and related problems: Mura [4], Nemat-Nasser and Hori [5], and Markov and Preziosi [6]. Some other collections of work include: Weng et al. [7] and Bilby et al. [8]. The review articles by Mura et al. [9] and Mura [10] also provide a good overview along with some more recent references. In view of the existence of these detailed reviews, an elaborate survey of eigenstrain or inclusion problems is redundant. However, to establish context, some limited and relevant literature is discussed below.

A somewhat limited amount of analytical work on nonuniform eigenstrains has focused on polynomial distributions. Sendeckyj [11] first considered the problem of polynomial distributions of eigenstrains. His work was extended by Moschovidis [12] and Moschovidis and Mura [13]. In particular, polynomial distributions of eigenstrains were found to be useful in dealing with the elastic interactions between inhomogeneities, [13–14], and more recently by Shodja and Sarvestani [15] to tackle the coated inhomogeneity problem. Rodin and Hwang [16] provide an excellent discussion on the use of polynomial distributions of eigenstrains in the solution of interaction problems of inhomogeneities. Polynomial eigenstrains in anisotropic materials were investigated by Asaro and Barnett [17] and Mura and Kinoshita [18].

Apart from the aforementioned works, several other contributors have extended Eshelby's original work on inclusions and inhomogeneities. Furuhashi et al. [19], Ru and Schiavone [20], and Zhong and Meguid [21], among others have considered slipping inclusions where the matrix-inclusion bonding is imperfect. Of particular technological interests are coated inclusions, which have been studied by Walpole [22] who presents a simple approximate model for infinitesimally thin coatings. His work is extended and refined by others such as Weng et al. [23], Cherkaoui et al. [24], and others. Ru [25] has focused on providing solution for inclusions of arbitrary shape. Solutions to inclusion problems have also been extended to piezoelectric medium; e.g., Taya [26], Ru [27], Deng and Meguid [28], and Mikata [29] are some recent references. Chiu [30] provided the solution to the problem of a parallelepiped inclusion containing uniform eigenstrains, while recently Nozaki and Taya [31] have solved the more general problem of a polyhedral inclusion with uniform eigenstrains. Other contributions abound in this active area of research which both relevance and brevity considerations preclude us from citing.

Presently, no semianalytical or analytical solutions to the nonuniform eigenstrain problem exist (where the distribution is not of polynomial nature). The polynomial distribution (as evidenced by expressions provided by Moschovidis [12] and noted by Rodin and Hwang [16]) is extremely tedious to implement even for a

[1]To whom correspondence should be addressed. e-mail: sharma@crd.ge.com

Contributed by the Applied Mechanics Division of THE AMERICAN SOCIETY OF MECHANICAL ENGINEERS for publication in the ASME JOURNAL OF APPLIED MECHANICS. Manuscript received by the ASME Applied Mechanics Division, Jan. 15, 2002; final revision, Sept. 27, 2002. Associate Editor: H. Gao. Discussion on the paper should be addressed to the Editor, Prof. Robert M. McMeeking, Department of Mechanical and Environmental Engineering University of California–Santa Barbara, Santa Barbara, CA 93106-5070, and will be accepted until four months after final publication of the paper itself in the ASME JOURNAL OF APPLIED MECHANICS.

 Copyright © 2003 by ASME

second degree polynomial and thus, practically speaking, provides only a limited departure from the uniformly eigenstrained inclusion problem. On the other hand, several problems in the physics and mechanics of materials naturally give rise to eigenstrain distributions which are Gaussian and exponential in nature. The one-dimensional equivalent of these distributions can be expressed parametrically (in terms of a varying parameter t and constant ρ) as

$$\text{Gaussian:} \quad \rho e^{-t^2} \tag{1a}$$

$$\text{Exponential:} \quad \rho e^{-t} \tag{1b}$$

In this article, we endeavor to provide both the interior and exterior solution to the elastic state of ellipsoidal inclusions with prescribed Gaussian or exponential dilatational eigenstrains, where the parameter t in Equations (1a–b) represents an arbitrary distance within the ellipsoidal inclusion with respect to the centroid of the inclusion domain.

The solution is reduced to a point where only a trivial numerical evaluation of a one-dimensional integral is required for the general ellipsoid (much like the case for the classic uniform eigenstrain problem where numerical evaluation of elliptic integrals is required). However, for the specialized case of a sphere, a completely closed-form solution (expressible in terms of known mathematical functions) is derived and numerical results are presented for the physically meaningful dilatational case. The elastic strain energy of the spherical inclusion is evaluated and reduced to simple formulas involving one-dimensional integrals.

Several applications are foreseen for this work:

1. Electronic chips, in particular various kinds of FETs (e.g., MESFETs), are characterized by extremely localized point-source type transient heating. Thus, temperature at some source point (of power generation) is a maximum and falls of very rapidly in all directions. Such a nonuniform temperature distribution leads to thermal eigenstrains distributed in a Gaussian or exponential fashion. The localized mechanical deformation of electronic structures can have a significant influence on the electronic properties. A recent paper by Johnson and Freund [32] is a useful reference on the effect of mechanical strain on the electronic properties of semiconducting materials. Knowledge of the elastic state by itself is also desirable to assess propensity of the electronic structure to mechanical damage.
2. Eigenstrains can often arise due to diffusion of materials, compositional changes, etc. Such eigenstrains obey the diffusion differential equation often leading to Gaussian or in some cases exponential distributions.
3. Applications are also envisaged in transient problems where the final eigenstrain is uniform, but the transient state is nonuniform and can be approximated by exponential eigenstrain distributions.
4. Both the exponential and Gaussian distributions are very versatile in the sense that by introducing the controlling constant k in the exponents (see Section 2, Eqs. (5a–d), one can tailor these distributions to mimic a variety of nonuniform distributions. Needless to say, several mathematical functions can be expressed as linear combination of the exponential function and thus the solution to the exponentially distributed eigenstrain automatically provides a solution to a whole class of eigenstrain distributions.

In Section 2, Eshelby's formalism is revisited and briefly reviewed. The central problem is formulated. The solution for the general ellipsoid is discussed in Section 3 while a specialized closed-form derivation is made for a spherical inclusion in Section 4. Numerical results for the spherical inclusion are also presented and discussed. A short note on the calculation of the elastic stain energy of a spherical inclusion with Gaussian/exponential eigenstrain is provided in Section 5, followed by closing remarks in Section 6.

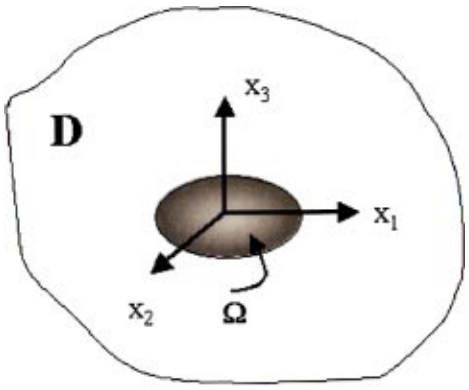

Fig. 1 An inclusion Ω confined in an infinite linear elastic medium *D*. The origin of the coordinate system is at the center of the inclusion.

2 Problem Formulation

In this section only a concise description of Eshelby's formalism is given and thereafter the problem central to this paper is formulated. Both boldfaced and index notation will be used.

Consider an infinite linear elastic material, D, defined by the fourth-order elasticity tensor $\mathbf{C}$, containing an inclusion (Ω) with a prescribed eigenstrain $\boldsymbol{\varepsilon}^*$, not necessarily uniform (Fig. 1). Eshelby showed that the constrained strain or final strain could be expressed in integral form as follows, [1,2,4]:

$$\varepsilon^c_{ij}(\mathbf{x}) = -\frac{1}{2}\int_\Omega C_{klmn}\varepsilon^*_{mn}(\mathbf{x})[G_{ik,lj}(\mathbf{x},\mathbf{x}') + G_{jk,li}(\mathbf{x},\mathbf{x}')]d\mathbf{x}' \tag{2}$$

Here, $G_{ij}(\mathbf{x},\mathbf{x}')$ is the fundamental solution to the Kelvin's problem of a point load in an infinite solid. It is given by (for isotropic materials):

$$G_{ij}(\mathbf{x},\mathbf{x}') = \frac{1}{16\pi\mu(1-\nu)|\mathbf{x}-\mathbf{x}'|} \times\left[(3-4\nu)\delta_{ij} + \frac{(x_i-x_i')(x_j-x_j')}{|\mathbf{x}-\mathbf{x}'|^2}\right] \tag{3}$$

Here, μ is the shear modulus, ν is the Poisson's ratio and δ_{ij} is the Kronecker's delta. For uniform eigenstrains in ellipsoids, the resulting constrained strain (Eq. (2)) is also uniform and can be related to the eigenstrain via the famous Eshelby tensor:

$$\varepsilon^c_{ij} = S_{ijkl}(\nu, a_i/a_j)\varepsilon^*_{ij}. \tag{4}$$

Equation (4) was one of the most important results of Eshelby's original work, [1]. Eshelby's tensor is only a function of the matrix Poisson's ratio and the ellipsoidal aspect ratios (a_i/a_j). The various components of Eshelby's tensor are well documented by Mura [4] for the general ellipsoid, for various specific subsets of the ellipsoid (i.e., elliptic cylinder, flat ellipsoid, etc.), as well as other shapes such as the parallelepiped.

Having established appropriate context, we formulate our problem as follows: Consider an ellipsoidal inclusion, Ω, perfectly bonded to the infinite matrix (D) in which it is located (Fig. 1). Then we seek the constrained strain and hence the complete stress state, both inside and outside the inclusion domain, given the following eigenstrain distributions:

$$\text{Ellipsoidal Domain} \quad \left\{\Omega: \frac{x_p x_p}{a_p} \leqslant 1\right\}$$

$$\text{Gaussian:} \quad \varepsilon^*_{ij}(\mathbf{x}) = \varepsilon^0_{ij} e^{-k^2(x_p x_p/a_p^2)} \quad \mathbf{x}\in\Omega \tag{5a}$$

$$= 0 \quad \mathbf{x}\notin\Omega \tag{5b}$$

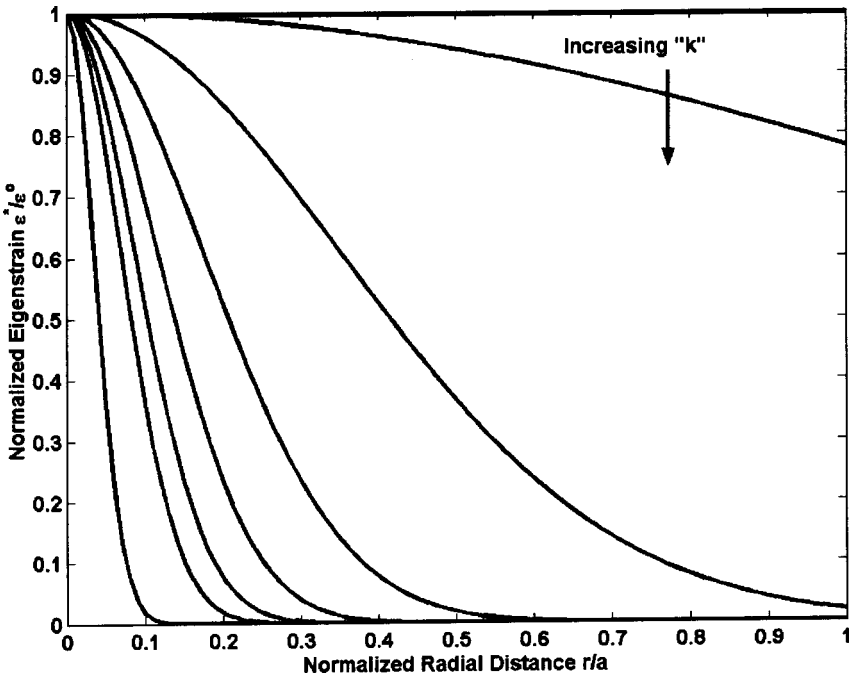

Fig. 2 Parametric variation of Gaussian eigenstrains as a function of *k* along a radial axis of a spherical inclusion

$$\text{Exponential:}\quad \varepsilon^*_{ij}(\mathbf{x})=\varepsilon^0_{ij}e^{-(k\sqrt{x_p x_p/a_P^2})} \quad \mathbf{x}\in\Omega \tag{5c}$$

$$=0 \quad \mathbf{x}\notin\Omega \tag{5d}$$

We will consider only the case of dilatational eigenstrains, i.e., $\varepsilon^*_{ij}=\varepsilon^0\delta_{ij}$. Here, a_i, are the semiaxes of the ellipsoid and conventional summation rules apply unless otherwise noted. A repeated index in uppercase is not summed but takes on the same value as it lowercase counterpart. To clarify the notation, the exponent in the Gaussian distribution is written explicitly as: $x_1^2/a_1^2+x_2^2/a_2^2+x_3^2/a_3^2$. In the specific case of a sphere, both distributions depend only on the radial distance from the center of the inclusion. ε^0, is simply a normalizing space-independent strain tensor. The parameter, k, not present in the earlier definition (Eqs. (1*a*,*b*) has been introduced to generalize the distributions further. As an illustration the spatial variation of the Gaussian distribution along the x_1-axis of the sphere is shown in Fig. 2 (although, in the highly symmeterized case of a sphere, the distribution is identical along all diametrical directions). The reader will note that as $k\to 0$, we approach the uniform eigenstrain problem. This fact should serve as a check on our results.

3 General Solution for Ellipsoids With Dilatational Eigenstrains

In this section, the general solution for ellipsoids is presented for the case when the eigenstrains are dilatational. Most frequently, the naturally occurring and physically meaningful eigenstrains (such as those due to thermal, diffusional, or compositional gradients, etc.) are dilatational in nature.

Using Eq. (3) in Eq. (2) one can obtain the final solution as, [1],

$$\varepsilon^c_{ij}(\mathbf{x})=\frac{1}{8\pi(1-v)}[\Psi_{kl,klij}-2v\Phi_{kk,ij}-2(1-v)(\Phi_{ik,kj}+\Phi_{jk,ki})]. \tag{6}$$

Here, ψ and Φ are biharmonic and harmonic potentials of the ellipsoid. They are given as

$$\Psi_{ij}(\mathbf{x})=\int_\Omega |\mathbf{x}-\mathbf{x}'|\varepsilon^*_{ij}(\mathbf{x}')d\mathbf{x}' \tag{7}$$

$$\Phi_{ij}(\mathbf{x})=\int_\Omega \frac{1}{|\mathbf{x}-\mathbf{x}'|}\varepsilon^*_{ij}(\mathbf{x}')d\mathbf{x}'. \tag{8}$$

Generally, an assumption of uniformity of the eigenstrain, $\boldsymbol{\varepsilon}^*$, is made, [4], and is taken outside the integrals in Eqs. (7), (8), thus reducing the problem of finding the elastic state of the inclusion to the evaluation of harmonic and biharmonic potentials of the inclusion shape. For the ellipsoidal inclusion with uniform eigenstrains, the final result is embodied in Eq. (4).

For the dilatational case (where the tensor $\boldsymbol{\varepsilon}^0$ in Eqs. (5*a*,*b*) is replaced by $\varepsilon^0\delta_{ij}$), we can modify Eq. (6) to be written as

$$\varepsilon^c_{ij}(\mathbf{x})=-\frac{1+v}{4\pi(1-v)}\varepsilon^0\Phi_{,ij}. \tag{9}$$

This follows directly from the general relations between the harmonic and biharmonic potentials, [33–35],

$$\begin{aligned}\Psi_{ij,kk}(\mathbf{x})&=2\Phi_{ij}(\mathbf{x})\\ \Psi_{ij,kkll}(\mathbf{x})&=2\Phi_{ij,ll}(\mathbf{x})=-8\pi\varepsilon^*_{ij}(\mathbf{x})\\ &\quad \text{for}\ \ \mathbf{x}\in\Omega\\ &=0\ \ \text{for}\ \mathbf{x}\notin\Omega.\end{aligned} \tag{10}$$

The yet unknown harmonic potential term (in Eq. (8)) can be written explicitly as

$$\text{Gaussian:}\quad \Phi_{,ij}(\mathbf{x})=\frac{\partial}{\partial x_i}\frac{\partial}{\partial x_j}\int_\Omega\int_\Omega\int_\Omega \frac{e^{-k^2(x'_m x'_m/a_M^2)}}{|\mathbf{x}-\mathbf{x}'|}d\mathbf{x}' \tag{11a}$$

$$\text{Exponential:}\quad \Phi_{,ij}(\mathbf{x})=\frac{\partial}{\partial x_j}\frac{\partial}{\partial x_j}\int_\Omega\int_\Omega\int_\Omega \frac{e^{-k\sqrt{(x'_m x'_m/a_M^2)}}}{|\mathbf{x}-\mathbf{x}'|}d\mathbf{x}'. \tag{11b}$$

At this point we appeal to a generalized theorem proven by Chandrasekhar [35] and presented in a slightly different form by Neutsch [36] to reduce Eqs. (11*a*,*b*) to simpler integrals. Details of the theorem, its application to our case and the detailed derivation are recorded in Appendix A. But first, the differentiation is carried out within the integral itself (Appendix A). Upon reduction of the integrals, the final results obtained are (Appendix A)

$$\text{Gaussian:}\quad \Phi_{,ij}(\mathbf{x}) = 2\pi a_1 a_2 a_3 [(2k^2 G_1) x_i x_j - G_2 \delta_{ij}] \tag{12a}$$

$$\text{Exponential:}\quad \Phi_{,ij}(\mathbf{x}) = 2\pi a_1 a_2 a_3 [(kE_1) x_i x_j - E_2 \delta_{ij}]. \tag{12b}$$

Here, $\{G_1, G_2\}$ and $\{E_1, E_2\}$ will be called the G and the E integrals, respectively, and are expressed as

$$G_1 = \int_\lambda^\infty \left(\frac{1}{a_M^2+s}\right) \frac{e^{-k^2(x_m x_m/a_M^2)}}{\sqrt{(a_1^2+s)(a_2^2+s)(a_3^2+s)}}\, ds \tag{13a}$$

$$G_2 = \int_\lambda^\infty \left(\frac{1}{a_M^2+s}\right) \frac{e^{-k^2(x_m x_m/a_M^2)}}{\sqrt{(a_1^2+s)(a_2^2+s)(a_3^2+s)}}\, ds \tag{13b}$$

$$E_1 = \int_\lambda^\infty \frac{k}{\sqrt{\dfrac{x_m x_m}{a_M^2}}} \left(\frac{1}{a_M^2+s}\right)^2 \frac{e^{-k\sqrt{x_m x_m/a_M^2}}}{\sqrt{(a_1^2+s)(a_2^2+s)(a_3^2+s)}}\, ds \tag{13c}$$

$$E_2 = \int_\lambda^\infty \left(\frac{1}{a_M^2+s}\right) \frac{e^{-k\sqrt{x_m x_m/a_M^2}}}{\sqrt{(a_1^2+s)(a_2^2+s)(a_3^2+s)}}\, ds. \tag{13d}$$

The factor λ is ubiquitous in ellipsoid potential-related problems (e.g., [31]) and is defined as

$$\lambda = 0 \qquad \mathbf{x} \in \Omega \tag{14a}$$

$$\left\{ \lambda > 0 \,\middle|\, 1 - \frac{x_i x_i}{a_i^2+\lambda} = 0 \right\} \qquad \mathbf{x} \notin \Omega. \tag{14b}$$

We note in passing that a consequence of Eq. (12*a*,*b*) is the presence of a deviatoric component in the second derivative of the harmonic potential. Therefore, even a purely dilating inclusion will experience (as intuitive) constrained shear strains in certain directions; an effect not seen in the solution to uniformly dilating inclusion problem, [1].

Obviously, the solution to this fairly complicated problem is now simply reduced to the evaluation of the one-dimensional E and G integrals. This is similar to the classic uniform eigenstrain problem where the final solution is reduced to the evaluation of certain elliptic integrals. For the general ellipsoid, the E and G integrals and λ have to be evaluated numerically, although, their simple form makes it trivial (especially in typical mathematical packages such as MATHEMATICA and MATLAB). For the specific case of a sphere, further reduction is possible and is tackled in the next section. It should be noted that the E and G integrals depend on λ and hence, Eqs. (12)–(14) compactly represent the solution to the elastic state both in the interior and the exterior of the ellipsoidal inclusion.

4 Closed-Form Solution for a Sphere

In this section, our results are specialized for the spherical shape, which permits simple closed-form expressions in terms of known mathematical functions. Further details are in Appendix B, but the final results are quoted as follows:

$\mathbf{x} \in \Omega$:

$$G_1 = \frac{\gamma(5/2, k^2 r^2/a^2)}{k^5 r^5}, \tag{15a}$$

$$G_2 = \frac{\gamma(3/2, k^2 r^2/a^2)}{k^3 r^3}, \tag{15b}$$

$$E_1 = \frac{2\,\gamma(4, kr/a)}{k^4 r^5}, \tag{15c}$$

$$E_2 = \frac{2\,\gamma(3, kr/a)}{k^3 r^3}, \tag{15d}$$

$\mathbf{x} \notin \Omega$:

$$G_1 = \frac{\gamma(5/2, k^2)}{k^5 r^5}, \tag{15e}$$

$$G_2 = \frac{\gamma(3/2, k^2)}{k^3 r^3}, \tag{15f}$$

$$E_1 = \frac{2\,\gamma(4, k)}{k^4 r^5}, \tag{15g}$$

$$E_2 = \frac{2\,\gamma(3, k)}{k^3 r^3} \tag{15h}$$

The function, $\gamma(n,x)$ is the incomplete gamma function of x of order n. At a very quick glance, it may erroneously appear that the interior E and G integrals are singular at the origin; however, a closer look will indicate that as $r \to 0$, these integrals steadily approach a constant value (as will be indicated in the numerical results, Figs. 3–6).

The stress-field due to the inclusion is given by

$$\begin{aligned} \sigma_{ij}(\mathbf{x}) &= C_{ijkl}[\varepsilon_{ij}^c(\mathbf{x}) - \varepsilon_{ij}^*(\mathbf{x})], \quad \mathbf{x} \in \Omega \\ & C_{ijkl}\varepsilon_{ij}^c(\mathbf{x}), \quad \mathbf{x} \notin \Omega \end{aligned} \tag{16}$$

As an illustration, numerical results for the stress components along the x_1-axis are presented in Fig. 3 for the Gaussian distribution ($k=1$). In what follows the Poisson ratio for the matrix is taken to be $\nu=0.3$. The stresses have been normalized with respect to the product of matrix Young's modulus, E, and the magnitude of the dilatational eigenstrain, ε^0. Unlike the classical case of uniform eigenstrain problem, the interior stress state is nonuniform. As expected, there is a discontinuity in the normal stress components across the inclusion-matrix interface, adequately captured by our solution since exterior solutions is explicitly included. Along the x_1-axis, the shear stresses are zero. Also, outside the inclusion, the stress components asymptotically decay, thus satisfying the zero traction boundary conditions at infinity for the inclusion problem.

Figure 4 plots the variation of the stress components along the line $x_1 = x_2$, $x_3 = 0$. In this instance, there is a nonzero shear stress σ_{12}, which vanishes at the center of the inclusion (due to the spherical symmetry of the eigenstrain distribution) and at infinity. Note that the continuity of σ_{12} across the inclusion boundary is a consequence of the dilatational nature of the prescribed eigenstrains; an eigenstrain distribution with a deviatoric component will cause a jump in the shear stresses at the inclusion boundary.

In the limit of $k \to 0$ (corresponding to a homogeneous distribution of eigenstrain in the inclusion), the results in Figs. 3 and 4 collapse into a single curve (Fig. 5), and we recover Eshelby's classical solution to the inclusion problem for a sphere. This constitutes a useful validation of our results. We further explore the asymptotic limit of our solution in Fig. 6, where the stress component σ_{11} for various values of k is shown. For small values of k the eigenstrain is nearly uniform and the classical uniform eigenstrain solution is recovered. This is rather interesting since our expressions (in terms of the incomplete gamma function) are of completely different form than those derived by Eshelby [1] and Mura [4]. Nevertheless, our expressions are equivalent to those presented by Eshelby-Mura for the uniform eigenstrain case (as

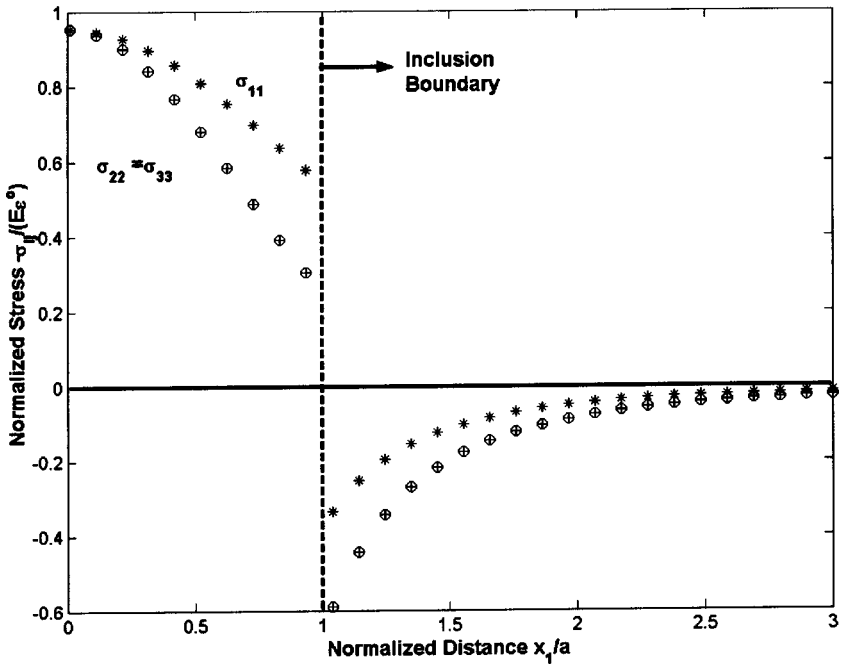

Fig. 3 Nonzero components of the stress tensor along the x_1-axis of a spherical inclusion loaded with dilatational Gaussian eigenstrains ($k=1$)

$k\rightarrow 0$). Thus, in addition to solving the nonuniform Gaussian/exponential eigenstrain problem, we have also recovered a novel form of a pre-existing classical solution.

5 Elastic Strain Energy of a Sphere With Gaussian/Exponential Eigenstrains

For the general case of an ellipsoidal inclusion, evaluation of the elastic strain energy can only proceed numerically, although, the reduction of the overall problem to simple one-dimensional integrals (Eqs. (13*a–d*)) makes such a calculation simple. However, for the case of a spherical inclusion, fairly simple expressions can be derived and are presented in this section.

The elastic strain energy can be written as

$$W=\frac{1}{2}\int_D\int\int\int \sigma_{ij}(\mathbf{x})[\varepsilon^c_{ij}(\mathbf{x})-\varepsilon^*_{ij}(\mathbf{x})]dD. \qquad (17)$$

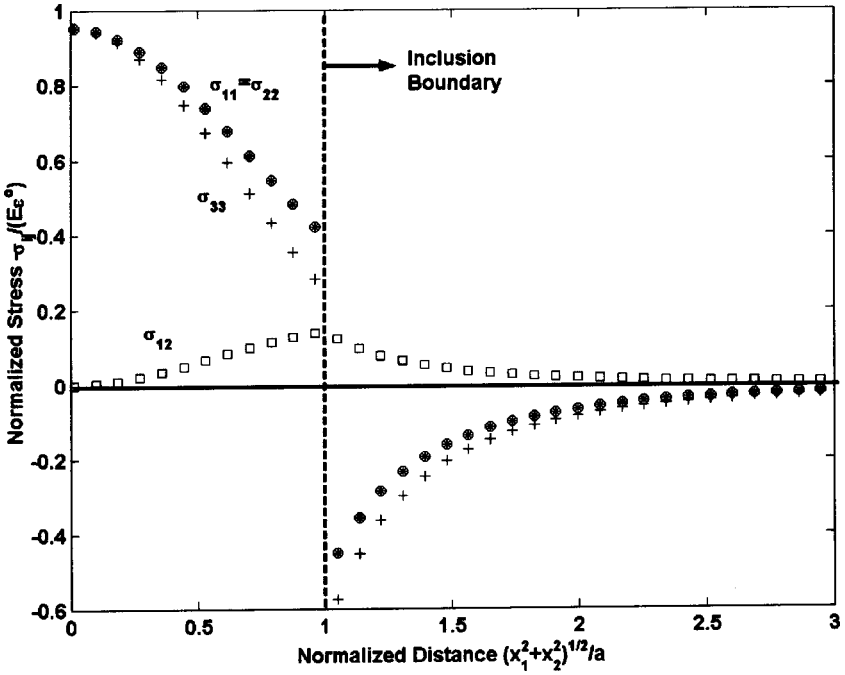

Fig. 4 Nonzero components of the stress tensor along the line defined by $x_1=x_2$, $x_3=0$ of a spherical inclusion loaded with dilatational Gaussian eigenstrains ($k=1$)

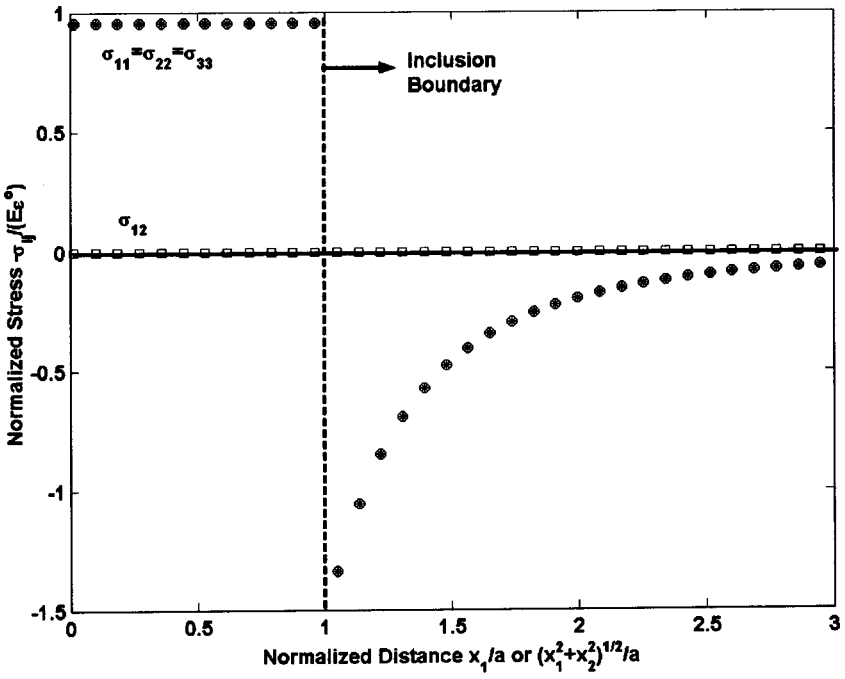

Fig. 5 Components of the stress tensor along the x_1-axis or a line defined by $x_1=x_2$, $x_3=0$ of a spherical inclusion loaded with either dilatational Gaussian eigenstrains or dilatational exponential eigenstrains in the limit of $k\to 0$ (Eshelby's classical solution)

Integrating by parts, incorporating the equilibrium conditions, and setting the tractions zero at the boundary of the body D, Eq. (17) can be reduced to

$$W=-\frac{1}{2}\int\int\int_{\Omega}\sigma_{ij}(\mathbf{x})\varepsilon^{*}_{ij}(\mathbf{x})d\Omega. \tag{18}$$

After some tedious algebra we can write the final expressions as

$$\text{Gaussian:}\quad W^{g}=3K\varepsilon^{0}[W^{g}_{1}-3\varepsilon^{0}W^{g}_{2}] \tag{19a}$$

$$\text{Exponential:}\quad W^{e}=3K\varepsilon^{0}[W^{e}_{1}-3\varepsilon^{0}W^{e}_{2}] \tag{19b}$$

Here, K is the bulk modulus and the "W quantities" are expressed as

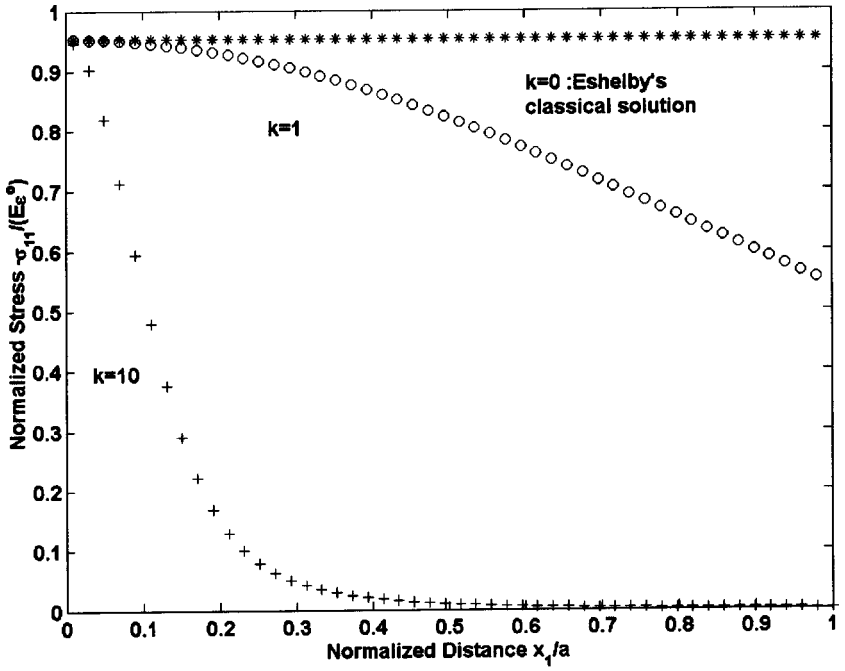

Fig. 6 Interior solution for σ_{11} along the x_1-axis of a spherical inclusion, as a function of k, due to Gaussian eigenstrains

$$W_1^g = -\frac{2\pi(1+\nu)}{3(1-\nu)}\varepsilon^0\left(\frac{a}{kr}\right)^3 \times\left\{\int_0^a\left[2\gamma\left(\frac{5}{2},\frac{k^2r^2}{a^2}\right)-3\gamma\left(\frac{3}{2},\frac{k^2r^2}{a^2}\right)\right]e^{-k^2r^2/a^2}dr\right\} \tag{20a}$$

$$W_2^g = \frac{\pi a^3\gamma(3/2,2k^2)}{k^3\sqrt{2}} \tag{20b}$$

$$W_1^e = -\frac{4\pi(1+\nu)}{3(1-\nu)}\varepsilon^0\left(\frac{a}{kr}\right)^3 \times\left\{\int_0^a\left[\gamma\left(4,\frac{kr}{a}\right)-3\gamma\left(3,\frac{kr}{a}\right)\right]e^{-kr/a}dr\right\} \tag{20c}$$

$$W_2^e = \frac{\pi a^3\gamma(3,2k)}{2k^3}. \tag{20d}$$

6 Closing Remarks

In the present work, the elastic state of inclusions undergoing dilatational nonuniform Gaussian and exponential eigenstrains was solved. Interior and exterior elastic solutions for the general ellipsoid were reduced to simple one-dimensional integrals analogous to the classical uniform eigenstrain problem. Specific closed-form solutions to the elastic state were presented for a spherical inclusion together with an expression for the elastic strain energy. To the best of the authors' knowledge, such solutions appear for the first time.

The present work directly allows the solution to several practical problems, namely, nonuniform heating, diffusion related and transient problems where the transient distributions are nonuniform, etc. Further, using the controlling parameter, k, a variety of nonuniformity can be introduced. In the limit, $k\to 0$, the classical uniform eigenstrain solution is recovered.

Within the boundaries of the posed problem, our solution is exact, however, the present work has two main restrictive features: (i) The eigenstrains are of dilatational nature. Insofar as inclusion problems are concerned (as opposed to inhomogeneity problems), there are several sources of eigenstrains that are predominantly dilatational (e.g., thermal strains, swelling strains, etc.). However, future work is anticipated where this restriction is removed. Such an effort will entail the calculation of the biharomic potential over an ellipsoidal volume for given nonuniform eigenstrains. (ii) We considered two main types of spatial distributions: Gaussian and exponential. In both cases, the spatial variation is based solely upon the absolute distance from the center (i.e., there is no angular variation). Again, for many naturally occurring eigenstrains, such a restriction does not seem to be unreasonable.

Appendix A

Derivation of Eqs. (12*a*,*b*) and (13*a*,*b*). The Newtonian harmonic potential of a mass with density, ρ is simply

$$\Phi(\mathbf{x}) = \int_\Omega \frac{\rho(\mathbf{x}')}{|\mathbf{x}-\mathbf{x}'|}d\mathbf{x}'. \tag{21}$$

For homogeneous ellipsoids, Eq. (21) reduces to the classical uniform harmonic potential and was used by Eshelby [1] in his celebrated work. The harmonic potential for uniform density is well documented by several monographs on the potential theory (e.g., [33,36,37]). For nonuniform distributions, a particularly elegant result is that derived by Dyson [35]: If the density of the ellipsoid is given by

$$\rho(\mathbf{x}) = \frac{m}{a_1a_2a_3}\left(1-\frac{x_ix_i}{a_I^2}\right)^{m-1} f\left(\frac{x_1}{a_1},\frac{x_2}{a_2},\frac{x_3}{a_3}\right), \quad m>0, \tag{22}$$

the Newtonian potential then is expressed as

$$\Phi(\mathbf{x}) = \int_\lambda^\infty\left(1-\frac{x_ix_i}{a_I^2+s}\right)^m\sum_{n=0}^\infty\frac{s^n\left(1-\frac{x_ix_i}{a_I^2+s}\right)^n}{2^{2n}n!(n+m)!/m!} \times\left\{\frac{a_I^2+s}{a_I^2}\frac{\partial}{\partial x_i}\frac{\partial}{\partial x_i}\right\}^n f\left(\frac{a_1x_1}{a_1^2+s},\frac{a_2x_2}{a_2^2+s},\frac{a_3x_3}{a_3^2+s}\right)\frac{ds}{\Delta} \tag{23}$$

$$\Delta = \frac{1}{\sqrt{(a_1^2+s)(a_2^2+s)(a_3^2+s)}}.$$

For the specialized case where the density depends only on the absolute distance from the centroid of the ellipsoid, it can be shown using either Chandarsekhar [33] or Neutsch [34] that Eq. (23) reduces to

$$\Phi(\mathbf{x}) = \pi a_1a_2a_3\int_\lambda^\infty\left[\frac{\int_{x_ix_i/(a_i^2+s)}^\infty\rho\left(t=\frac{x_ix_i}{a_I^2}\right)dt}{\Delta}\right]ds. \tag{24}$$

The interior integral in Eq. (24) is straightforward to evaluate for the Gaussian and exponential distributions. Simple twice-differentiation within the integral sign leads directly to Eqs. (12*a*–*b*) and (13*a*–*d*).

Appendix B

Derivation of Eqs. (15*a*–*h*). Using, $a_1=a_2=a_3=a$, the E and G integrals can be expressed as

$$G_1 = \int_\lambda^\infty\frac{e^{-k^2r^2/(a^2+s)}}{(a^2+s)^{7/2}}ds, \tag{25a}$$

$$G_2 = \int_\lambda^\infty\frac{e^{-k^2r^2/(a^2+s)}}{(a^2+s)^{5/2}}ds \tag{25b}$$

$$E_1 = \int_\lambda^\infty\frac{1}{r}\frac{e^{-kr/\sqrt{a^2+s}}}{(a^2+s)^3}ds, \tag{25c}$$

$$E_2 = \int_\lambda^\infty\frac{e^{-kr/\sqrt{a^2+s}}}{(a^2+s)^{5/2}}ds. \tag{25d}$$

Here r is the radial distance from the center of the sphere, i.e., x_ix_i. Using Gradshteyn et al. [38] and the fact that for a sphere, the cubic equation in Eq. (14*b*) yields, $\lambda=r^2-a^2$ in the exterior, one can easily recover Eqs. (15*a*–*h*).

References

[1] Eshelby, J. D., 1957, "The Determination of the Elastic Field of an Ellipsoidal Inclusion and Related Problems," Proc. R. Soc. London, Ser. A, **A241**, pp. 376–396.

[2] Eshelby, J. D., 1959, "The Elastic Field Outside an Ellipsoidal Inclusion," Proc. R. Soc. London, Ser. A, **A252**, pp. 561–569.

[3] Eshelby, J. D., 1961, "Elastic Inclusions and Inhomogeneities," *Progress in Solid Mechanics* 2, I. N. Sneddon and R. Hill, eds., North Holland, Amsterdam, pp. 89–140.

[4] Mura, T., 1987, *Micromechanics of Defects in Solids*, Martinus Nijhoff, Hague, The Netherlands.

[5] Nemat-Nasser, S., and Hori, M., 1999, *Micromechanics: Overall Properties of Heterogeneous Solids*, Elsevier, New York.

[6] Markov, K., and Preziosi, L., 2000, *Heterogeneous Media: Micromechanics Modeling Methods and Simulations*, Birkhauser Verlag, Switzerland.

[7] Weng, G. J., Taya, M., and Abe, H., eds., 1990, *Micromechanics and Inhomogeneity: The Toshio Mura Anniversary Volume*, Springer-Verlag, New York.

[8] Bilby, B. A., Miller, K. J., and Willis, J. R., 1984, *IUTAM/IFC/ICM Symposium on Fundamentals of Deformation and Fracture*, Sheffield, England, Apr.

2–5, Eshelby Memorial Symposium, Cambridge University Press, Cambridge, UK.
[9] Mura, T., Shodja, H. M., and Hirose, Y., 1996, ''Inclusion Problems,'' Appl. Mech. Rev., **49**(10), Part 2, pp. S118–S127.
[10] Mura, T., 2000, ''Some New Problems in the Micromechanics,'' Mater. Sci. Eng., A, **A285**(1–2), pp. 224–228.
[11] Sendeckyj, G. P., 1967, ''Ellipsoidal Inhomogeneity Problem,'' Ph.D. dissertation, Northwestern University, Evanston, IL.
[12] Moschovidis, Z. A., 1975, ''Two Ellipsoidal Inhomogeneities and Related Problems Treated by the Equivalent Inclusion Method'', Ph.D. thesis, Northwestern University, Illinois.
[13] Moschovidis, Z. A., and Mura, T., 1975, ''Two-Ellipsoidal Inhomogeneities by the Equivalent Inclusion Method,'' ASME J. Appl. Mech., **42**, pp. 847–852.
[14] Johnson, W. C., Earmme, Y. Y., and Lee, J. K., 1980, ''Approximation of the Strain Field Associated With an Inhomogeneous Precipitate I: Theory,'' ASME J. Appl. Mech., **47**, pp. 775–780.
[15] Shodja, H. M., and Sarvestani, A. S., 2001, ''Elastic Fields in Double Inhomogeneity by the Equivalent Inclusion Method,'' ASME J. Appl. Mech., **68**, pp. 3–10.
[16] Rodin, G. J., and Hwang, Yuh-Long, 1991, ''On the Problem of Linear Elasticity for an Infinite Region Containing a Finite Number of Nonintersecting Spherical Inhomogeneities,'' Int. J. Solids Struct., **27(2)**, pp. 145–159.
[17] Asaro, R. J., and Barnett, D. M., 1975, ''The Non-uniform Transformation Strain Problem for an Anisotropic Ellipsoidal Inclusion,'' J. Mech. Phys. Solids, **23**, pp. 77–83.
[18] Mura, T., and Kinoshita, N., 1978, ''The Polynomial Eigenstrain Problem or an Anisotropic Ellipsoidal Inclusion,'' Phys. Status Solidi A, **48**, pp. 447–450.
[19] Furuhashi, R., Huang, J. H., and Mura, T., 1992, ''Sliding Inclusions and Inhomogeneities with Frictional Interfaces,'' ASME J. Appl. Mech., **59**, pp. 783–788.
[20] Ru, C. Q., and Schiavone, P., 1997, ''A Circular Inclusion With Circumferentially Inhomogeneous Interface in Antiplane Shear,'' Proc. R. Soc. London, Ser. A, **453**, pp. 2551–2572.
[21] Zhong, Z., and Meguid, S. A., 1996, ''On the Eigenstrain Problem of a Spherical Inclusion With an Imperfectly Bonded Interface,'' ASME J. Appl. Mech., **63**, pp 877–883.
[22] Walpole, L. J., 1978, ''Coated Inclusion in an Elastic Medium,'' Proc. Cambridge Philos. Soc., **83**, pp. 495–506.
[23] Luo, H. A., and Weng, G. J., 1989, ''On Eshelby's S-Tensor in Three Phase Cylindrically Concentric Solid,'' Mech. Mater., **8**(2–3), pp. 77–88.
[24] Cherkaoui, M., Sabar, H., and Berveiller, M., 1994, ''Micromechanical Approach of the Coated Inclusion Problem and Applications to Composite Problems,'' J. Eng. Mater. Technol., **116**(3), pp. 274–278.
[25] Ru, C. Q., 1999, ''Analytic Solution for Eshelby's Problem of an Inclusion of Arbitrary Shape in a Plane or Half-plane,'' Trans. ASME, J. Appl. Mech., **66**, pp. 315–322.
[26] Taya, M., 1999, ''Micromechanics Modeling of Smart Composites,'' Composites, Part A **30A(4)**, pp. 531–536.
[27] Ru, C. Q., 2000, ''Eshelby's Problem for Two-Dimensional Piezoelectric Inclusions of Arbitrary Shape,'' Proc. R. Soc. London, Ser. A, **456(1997)**, pp. 1051–1068.
[28] Deng, W., and Meguid, S. A., 1999, ''Closed Form Solutions for Partially Debonded Circular Inclusion in Piezoelectric Materials,'' Acta Mech., **137**(3–4), pp. 167–181.
[29] Mikata, Y., 2001, ''Explicit Determination of Piezoelectric Eshelby Tensors for a Spheroidal Inclusion,'' Int. J. Solids Struct., **38**(40–41), pp. 7045–7063.
[30] Chiu, Y. P., 1977, ''On the Stress Field due to Initial Strains in Cuboid Surrounded by an Infinite Elastic Space,'' ASME J. Appl. Mech., **44**, pp. 587–590.
[31] Nozaki, H., and Taya, M., 2001, ''Elastic Fields in a Polyhedral Inclusion With Uniform Eigenstrains and Related Problems,'' ASME J. Appl. Mech., **68**, pp. 441–452.
[32] Johnson, H. T., and Freund, L. B., 2001, ''The Influence of Strain on Confined Electronic States in Semiconductor Quantum Structures,'' Int. J. Solids Struct., **38**, pp. 1045–1062.
[33] Chandrasekhar, S., 1969, *Ellipsoidal Figures of Equilibrium*, Dover, New York.
[34] Neutsch, W., 1979, ''On the Gravitational Energy of Ellipsoidal Bodies and Some Related Functions,'' Astron. Astrophys., **72**(3), pp. 339–347.
[35] Dyson, F. W., 1891, ''The Potentials of Ellipsoids with Variable Density,'' Quart. J. Pure Appl. Math., **XXV**, pp. 259–288.
[36] Kellogg, O. D., 1953, *Foundation of Potential Theory*, Dover, New York.
[37] MacMillan, W. D., 1958, *The Theory of the Potential*, Dover, New York.
[38] Gradshteyn, I. S., Ryzhik, I. M., and Jeffrey, A., 1994, *Table of Integrals, Series, and Products*, Academic Press, San Diego, CA.

The Stress Response of Radially Polarized Rotating Piezoelectric Cylinders

D. Galic
Graduate Student
e-mail: galic@uclink.berkeley.edu

C. O. Horgan
e-mail: coh8p@virginia.edu
Fellow ASME

Structural and Solid Mechanics Program,
Department of Civil Engineering,
University of Virginia,
Charlottesville, VA 22904

Recent advances in smart structures technology have lead to a resurgence of interest in piezoelectricity, and in particular, in the solution of fundamental boundary value problems. In this paper, we develop an analytic solution to the axisymmetric problem of an infinitely long, radially polarized, radially orthotropic piezoelectric hollow circular cylinder rotating about its axis at constant angular velocity. The cylinder is subjected to uniform internal pressure, or a constant potential difference between its inner and outer surfaces, or both. An analytic solution to the governing equilibrium equations (a coupled system of second-order ordinary differential equations) is obtained. On application of the boundary conditions, the problem is reduced to solving a system of linear algebraic equations. The stress distribution in the tube is obtained numerically for a specific piezoceramic of technological interest, namely PZT-4. For the special problem of a uniformly rotating solid cylinder with traction-free surface and zero applied electric charge, explicit closed-form solutions are obtained. It is shown that for certain piezoelectric solids, stress singularities at the origin can occur analogous to those occurring in the purely mechanical problem for radially orthotropic elastic materials. [DOI: 10.1115/1.1572900]

1 Introduction

In recent years there has been a resurgence of interest in piezoelectricity, motivated by advances in smart structures technology. Classic reference works on the subject include those of Tiersten [1], Berlincourt [2], Berlincourt et al. [3], and Jaffe et al. [4]. While [1] is primarily concerned with waves and oscillations, this book also contains a concise summary of the basic equations of static and dynamic linear piezoelectricity. The piezoelectric phenomenon has been exploited for decades. Classic piezoelectric devices include microphones and record players. More recent applications have focussed on improving existing devices and transforming them into ''smart structures.'' For example, piezoelectric *actuators* can be used to modify the shape of an airfoil, thereby reducing transverse vortices, [5], or to maintain proper tension with overhead electrical wires on a locomotive pantograph, [6]. In addition to being used as actuators, which respond to changes in an electric field by producing mechanical strain, they can also be used as *sensors*, which respond to a mechanical strain by producing an electrical signal. One notable civil engineering application of piezoelectric sensors is in structural health monitoring, [7]. A change in the level of strain will produce an electric charge and trigger sensors in the structure.

Piezoelectric polycrystalline materials are manufactured through a process of poling, which involves heating to high temperatures under the influence of an electric field [8]. As a result, dipoles are reoriented, and point roughly in the poling direction, although their precise arrangement is still somewhat random. Upon application of a voltage, electric forces cause the dipoles to straighten out in the direction of their general inclination, which causes mechanical strain. Anisotropy is essential for the phenomenon to occur.

We are concerned in this paper with special classes of piezoelectric materials, namely radially polarized materials. One of the early papers to explore a radially polarized cylindrical medium was that of Adelman, Stavsky, and Segal [9]. Like many of their predecessors, the authors of [9] were interested in the dynamic problem. Some of the issues raised in [9] were further explored in the book by Parton and Kudryavtsev [10]. Recent papers which treat some static analyses of radially polarized media include [11–14]. All of these papers use infinite series solutions for the governing equations. The present authors have developed an alternate solution technique for such problems in [15].

Horgan and Baxter [16] formulated an analytic solution technique for the mechanical problem of an infinitely long, hollow circular cylinder composed of a cylindrically anisotropic homogeneous linearly elastic material and rotating about its axis at constant angular velocity. In the present paper, we consider piezoelectric analogs of the problems investigated in [16]. We consider a rotating hollow circular cylinder composed of a radially polarized cylindrically anisotropic piezoelectric material, e.g., PZT-4 or $BaTiO_3$, and subjected to internal pressure, together with a potential difference induced by electrodes attached to the inner and outer surfaces of the cylinder. An analytic solution technique is developed for the electromechanical problem, where stresses are produced by the combined effects of rotation internal pressure and voltage difference.

In Section 2, we give a brief summary of the basic constitutive equations for linear piezoelectric solids. In Section 3, these equations are specialized to cylindrical polar coordinates and the axisymmetric problem described above is formulated. The governing equilibrium equations in polar form are shown to reduce to a coupled system of second-order differential equations for the radial displacement and electric potential field. These differential equations are solved analytically, and on applying three different sets of boundary conditions an analytic solution method for boundary value problems is developed. In Section 4, the stress distributions in the cylinder are discussed in detail for the piezoceramic PZT-4. In Section 5, we consider the special problem of a rotating *solid* cylinder with traction-free surface and zero applied electric charge. For this problem, explicit closed-form solutions are obtained. It is shown that stress singularities at the origin can

Contributed by the Applied Mechanics Division of THE AMERICAN SOCIETY OF MECHANICAL ENGINEERS for publication in the ASME JOURNAL OF APPLIED MECHANICS. Manuscript received by the ASME Applied Mechanics Division, May 5, 2002; final revision, November 8, 2002. Associate Editor: L. T. Wheeler. Discussion on the paper should be addressed to the Editor, Prof. Robert M. McMeeking, Department of Mechanical and Environmental Engineering, University of California–Santa Barbara, Santa Barbara, CA 93106-5070, and will be accepted until four months after final publication of the paper itself in the ASME JOURNAL OF APPLIED MECHANICS.

 Copyright © 2003 by ASME

occur for certain piezoelectric materials analogous to those occurring in the purely mechanical problem for radially orthotropic elastic materials.

2 Basic Constitutive Equations

The governing constitutive equations (see, e.g., [1,2]) for a homogeneous anisotropic piezoelectric solid can be written as

$$\varepsilon_i = s_{ij}\sigma_j + d_{mi}E_m, \tag{1}$$

$$D_m = d_{mi}\sigma_i + \epsilon^T_{mk}E_k, \tag{2}$$

where the well-known single suffix notation is used for stress and strain, i.e., i,j run from 1:6, m,k run from 1:3, and the usual summation convention is used. In the above, ε_i and σ_j are the mechanical strain and stress, respectively, s_{ij} are the elastic compliances, D_m is the electric displacement vector (also referred to as the charge density) and E_k the electric field. The d_{mi} are the piezoelectric moduli, in units of Coulombs/Newton (C/N), which relate the electrical and mechanical effects. The ϵ^T_{mk} denote the dielectric permittivity constants at constant stress, in units of Farads/meter (F/m). An alternate, inverted form of the governing equations (see, e.g., [2]) is

$$\sigma_i = c_{ij}\varepsilon_j - e_{mi}E_m, \tag{3}$$

$$D_m = e_{mi}\varepsilon_i + \epsilon^S_{mk}E_k. \tag{4}$$

The d_{mi} have been replaced by e_{mi}, which are also piezoelectric moduli, whose units are C/m^2, and the elastic compliances s_{ij} have been replaced by elastic stiffnesses c_{ij}. The ϵ^S_{mk} denote the dielectric permittivity constants at constant strain. Their units are the same as those of ϵ^T_{mk} but their values are different. We also note that E_m can be written in terms of the electric potential ϕ as

$$\mathbf{E} = -\nabla\phi. \tag{5}$$

In this paper, we will specialize our general analysis to the piezoceramic PZT-4 (a lead zirconium titanate), which is widely used in smart materials and structures technology (see, e.g., [7,8]).

3 Rotating Hollow Circular Cylinder

We consider a hollow circular cylinder $a \leqslant r \leqslant b$ subjected to axisymmetric mechanical and electrical loading on its lateral surface (see Fig. 1).

The detailed boundary conditions will be given below. The cylinder is rotating about its axis at constant angular velocity ω and is assumed to be sufficiently long so that end effects need not be considered. In cylindrical polar coordinates (see, e.g., [10]), the governing equations, in the absence of body forces, for the axisymmetric stress and electric displacement fields are

$$\frac{d\sigma_{rr}}{dr} + \frac{1}{r}(\sigma_{rr} - \sigma_{\theta\theta}) + \rho_d\omega^2 r = 0, \tag{6}$$

$$\frac{dD_r}{dr} + \frac{1}{r}D_r = 0, \tag{7}$$

where D_r is the radial component of the electric displacement vector and ρ_d is the constant material density.

The constitutive Eqs. (3), (4) for the piezoelectric material when specialized to cylindrically orthotropic materials, polarized in the radial direction, may be written as (see, e.g., [10])

$$\begin{aligned} \sigma_{rr} &= c_{33}\varepsilon_r + c_{13}\varepsilon_\theta - e_{33}E_r, \\ \sigma_{\theta\theta} &= c_{13}\varepsilon_r + c_{11}\varepsilon_\theta - e_{31}E_r, \\ D_r &= e_{31}\varepsilon_\theta + e_{33}\varepsilon_r + \epsilon_{33}E_r. \end{aligned} \tag{8}$$

Since

$$\varepsilon_r = \frac{du_r}{dr}, \quad \varepsilon_\theta = \frac{u_r}{r}, \tag{9}$$

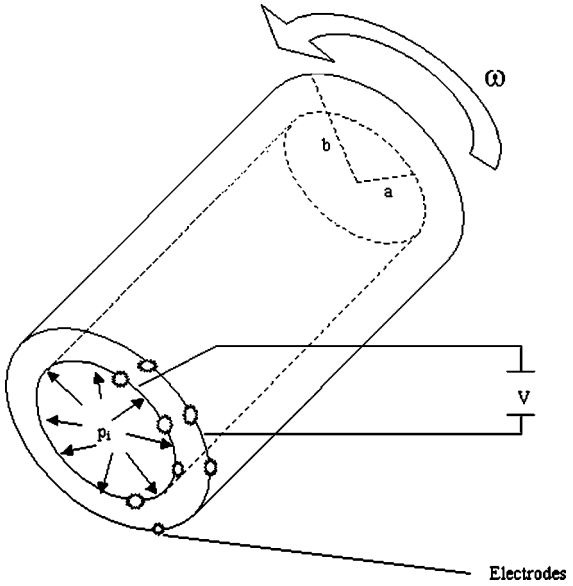

Fig. 1 Hollow circular cylinder subject to uniform internal pressure p_i and applied voltage V, rotating with constant velocity ω

and

$$E_r = -\frac{d\phi}{dr}, \tag{10}$$

where $u_r(r)$ is the radial displacement and $\phi = \phi(r)$ is the electric potential, we write (8) as

$$\sigma_{rr} = c_{33}\frac{du_r}{dr} + c_{13}\frac{u_r}{r} + e_{33}\frac{d\phi}{dr}, \tag{11}$$

$$\sigma_{\theta\theta} = c_{13}\frac{du_r}{dr} + c_{11}\frac{u_r}{r} + e_{31}\frac{d\phi}{dr}, \tag{12}$$

$$D_r = e_{31}\frac{u_r}{r} + e_{33}\frac{du_r}{dr} - \epsilon_{33}\frac{d\phi}{dr}. \tag{13}$$

The elastic constants are c_{33}, c_{13}, c_{11}, the piezoelectric constants are e_{33}, e_{31}, and ϵ_{33} is the dielectric permittivity at constant strain (the superscript S has been dropped). A discussion of the mechanical anisotropy arising in consideration of cylindrically orthotropic elastic materials may be found in [16]. Such anisotropy arises, for example, in carbon fibers during the manufacture of composites and in the casting of metals.

When (11)–(13) are used in (6), (7), we obtain

$$r^2 c_{33}\frac{d^2u}{dr^2} + r c_{33}\frac{du}{dr} - c_{11}u + r^2 e_{33}\frac{d^2\phi}{dr^2} + r(e_{33} - e_{31})\frac{d\phi}{dr} + \rho_d\omega^3 r^3 = 0 \tag{14}$$

and

$$r^2 e_{33}\frac{d^2u}{dr^2} + r(e_{33} + e_{31})\frac{du}{dr} - r^2\epsilon_{33}\frac{d^2\phi}{dr^2} - r\epsilon_{33}\frac{d\phi}{dr} = 0, \tag{15}$$

respectively, where the subscript on u has been dropped for simplicity. Equations (14), (15) constitute a coupled system of linear second-order ordinary differential equations for u and ϕ. It is useful to nondimensionalize the equations. This may be accomplished by dividing (14) by c_{33} and (15) by e_{33}. Then, if we set

$$\frac{c_{11}}{c_{33}} = \alpha, \tag{16}$$

$$\frac{e_{31}}{e_{33}} = \beta, \tag{17}$$

$$\frac{c_{33}\epsilon_{33}}{e_{33}^2} = \gamma, \tag{18}$$

and define a new potential function as

$$\Phi = \frac{e_{33}}{c_{33}}\phi, \tag{19}$$

we may write (14), (15) as

$$r^2\frac{d^2u}{dr^2} + r\frac{du}{dr} - \alpha u + r^2\frac{d^2\Phi}{dr^2} + r(1-\beta)\frac{d\Phi}{dr} + \rho_d\frac{\omega^2 r^3}{c_{33}} = 0, \tag{20}$$

$$r^2\frac{d^2u}{dr^2} + r(1+\beta)\frac{du}{dr} - r^2\gamma\frac{d^2\Phi}{dr^2} - r\gamma\frac{d\Phi}{dr} = 0. \tag{21}$$

The constants α, β, γ are dimensionless parameters. While α depends only on the elastic constants and β on the piezoelectric constants, the parameter γ involves all three of the radial elastic, piezoelectric, and dielectric permittivity constants and thus provides a measure of the degree of piezoelectric coupling. As shown in Horgan and Baxter [16], the constant α can also be written as

$$\alpha = \frac{\overline{E}_\theta}{\overline{E}_r}, \tag{22}$$

where $\overline{E}_\theta, \overline{E}_r$ denote the Young's moduli in the azimuthal and radial directions, respectively. When $\alpha > 1$, an elastic material is *circumferentially orthotropic* and when $\alpha < 1$, the material is *radially orthotropic*. In piezoelectric materials, other factors contribute to the nature of the orthotropy.

We also nondimensionalize the independent variable. For the hollow cylinder of concern with $a \leqslant r \leqslant b$, we set

$$\rho = \frac{r}{a}, \tag{23}$$

and

$$\eta = \frac{b}{a}, \tag{24}$$

so that $1 \leqslant \rho \leqslant \eta$. On reevaluating all derivatives using the chain rule, we rewrite (14), (15) as

$$\rho^2\frac{d^2u}{d\rho^2} + \rho\frac{du}{d\rho} - \alpha u + \rho^2\frac{d^2\Phi}{d\rho^2} + \rho(1-\beta)\frac{d\Phi}{d\rho} + \frac{\rho_d\omega^2}{c_{33}}a^3\rho^3 = 0, \tag{25}$$

$$\rho^2\frac{d^2u}{d\rho^2} + \rho(1+\beta)\frac{du}{d\rho} - \gamma\rho^2\frac{d^2\Phi}{d\rho^2} - \gamma\rho\frac{d\Phi}{d\rho} = 0, \tag{26}$$

where $u = u(\rho)$, $\Phi = \Phi(\rho)$.

It is convenient to define a new dimensionless constant as

$$\Omega = \frac{\rho_d\omega^2 a^2}{c_{33}}, \tag{27}$$

which allows us to rewrite (25) as

$$\rho^2\frac{d^2u}{d\rho^2} + \rho\frac{du}{d\rho} - \alpha u + \rho^2\frac{d^2\Phi}{d\rho^2} + \rho(1-\beta)\frac{d\Phi}{d\rho} + \Omega a\rho^3 = 0. \tag{28}$$

We use the change of variables $\rho = e^t$ to rewrite (28), (26) as a system with constant coefficients. The final coupled system of ordinary differential equations becomes

$$u'' - \alpha u + \Phi'' - \beta\Phi' = -\Omega a e^{3t}, \tag{29}$$

$$u'' + \beta u' - \gamma\Phi'' = 0, \tag{30}$$

where the prime denotes differentiation with respect to t.

On writing (29), (30) in differential operator form, one can readily uncouple this system into a single fourth-order equation for u or Φ. In this way, one can obtain the solution pair

$$u(t) = \frac{(\beta\omega_1 - \omega_1^2)}{(\omega_1^2 - \alpha)}Ae^{\omega_1 t} + \frac{(\beta\omega_2 - \omega_2^2)}{(\omega_2^2 - \alpha)}Be^{\omega_2 t} - \frac{\beta}{\alpha}C + aK_2e^{3t}, \tag{31}$$

$$\Phi(t) = Ae^{\omega_1 t} + Be^{\omega_2 t} + Ct + D + aK_1e^{3t}, \tag{32}$$

where

$$\omega_{1,2} = \pm\sqrt{\frac{\beta^2 + \alpha\gamma}{1+\gamma}}. \tag{33}$$

The constants K_1, K_2 are given by

$$K_1 = \frac{\Omega(1 + \frac{1}{3}\beta)}{(\beta^2 + \alpha\gamma - 9 - 9\gamma)}, \quad K_2 = \frac{\gamma\Omega}{(\beta^2 + \alpha\gamma - 9 - 9\gamma)}, \tag{34}$$

where it is assumed that $\beta^2 + \alpha\gamma - 9 - 9\gamma \neq 0$ and A, B, C, D are arbitrary constants. From (33) we have

$$\omega_1^2 - \alpha = \omega_2^2 - \alpha = \frac{\beta^2 - \alpha}{1+\gamma} \tag{35}$$

and it is assumed that $\beta^2 \neq \alpha$.

Since $t = \ln\rho$, we have thus established that the solution pair of Eqs. (25), (26) can be written as

$$u = \frac{(\beta\omega_1 - \omega_1^2)}{(\omega_1^2 - \alpha)}A\rho^{\omega_1} + \frac{(\beta\omega_2 - \omega_2^2)}{(\omega_2^2 - \alpha)}B\rho^{\omega_2} - \frac{\beta}{\alpha}C + aK_2\rho^3, \tag{36}$$

$$\Phi = A\rho^{\omega_1} + B\rho^{\omega_2} + C\ln\rho + D + aK_1\rho^3. \tag{37}$$

We also require expressions for the nondimensionalized stresses, which we obtain from (11), (12), and (19). Thus

$$\frac{\sigma_{rr}a}{c_{33}} = \frac{du}{d\rho} + \delta\frac{u}{\rho} + \frac{d\Phi}{d\rho}, \tag{38}$$

$$\frac{\sigma_{\theta\theta}a}{c_{33}} = \delta\frac{du}{d\rho} + \alpha\frac{u}{\rho} + \beta\frac{d\Phi}{d\rho}, \tag{39}$$

where the new dimensionless parameter δ is given by

$$\delta = \frac{c_{13}}{c_{33}}. \tag{40}$$

Note that δ depends only on the *elastic* constants.

On substituting the expressions for u and Φ from (36), (37) into (38), (39), we get

$$\frac{\sigma_{rr}}{c_{33}} = A\left[\rho^{\omega_1 - 1}\left(\frac{\beta\omega_1^2 + \delta\beta\omega_1 - \delta\omega_1^2 - \alpha\omega_1}{\omega_1^2 - \alpha}\right)\right]\frac{1}{a} + B\left[\rho^{\omega_2 - 1}\left(\frac{\beta\omega_2^2 + \delta\beta\omega_2 - \delta\omega_2^2 - \alpha\omega_2}{\omega_2^2 - \alpha}\right)\right]\frac{1}{a} + C\left[\rho^{-1}\left(1 - \frac{\delta\beta}{\alpha}\right)\right]\frac{1}{a} + \rho^2(3K_2 + \delta K_2 + 3K_1), \tag{41}$$

$$\frac{\sigma_{\theta\theta}}{c_{33}} = A\left[\rho^{\omega_1 - 1}\left(\frac{\delta\beta\omega_1^2 - \delta\omega_1^3 - \alpha\omega_1^2 + \beta\omega_1^3}{\omega_1^2 - \alpha}\right)\right]\frac{1}{a} + B\left[\rho^{\omega_2 - 1}\left(\frac{\delta\beta\omega_2^2 - \delta\omega_2^3 - \alpha\omega_2^2 + \beta\omega_2^3}{\omega_2^2 - \alpha}\right)\right]\frac{1}{a} \tag{42}$$

$$+ \rho^2(3\delta K_2 + \alpha K_2 + 3\beta K_1). \tag{43}$$

It is convenient to define a new dimensionless potential Φ_1 as

$$\Phi_1=\frac{\Phi}{a}, \tag{44}$$

and so (37) can be written as

$$\Phi_1=A(\rho^{\omega_1})\frac{1}{a}+B(\rho^{\omega_2})\frac{1}{a}+C(\ln\rho)\frac{1}{a}+D\frac{1}{a}+K_1\rho^3. \tag{45}$$

We will examine three sets of boundary conditions, referred to henceforth as Cases 1, 2, and 3. In Case 1 the cylinder is subjected to a uniform internal pressure, zero electric potential difference across the cylindrical annulus, and free mechanical boundary conditions on the outer surface. Thus the rotating tube can be viewed as acting as a *sensor* in this case. In Case 2, we impose free mechanical boundary conditions on both internal and external surfaces. However, there is a uniform potential difference prescribed across the annulus. Physically, such a state could be achieved by placing electrodes on the inner and outer surfaces of the cylinder, [10]. In this case, the rotating tube acts as an *actuator*. For convenience, we will take the potential on the outer surface to be zero, and the potential on the inner surface to be a nonzero constant. Case 3 is the combined loading case, a superposition of Cases 1 and 2. The boundary conditions for each case can be written as follows:

$$\text{Case 1: } \frac{\sigma_{rr}}{c_{33}}(1)=-p_i,\ \ \frac{\sigma_{rr}}{c_{33}}(\eta)=0,\ \ \Phi_1(1)=0,\ \ \Phi_1(\eta)=0, \tag{46}$$

$$\text{Case 2: } \frac{\sigma_{rr}}{c_{33}}(1)=0,\ \ \frac{\sigma_{rr}}{c_{33}}(\eta)=0,\ \ \Phi_1(1)=\overline{\phi},\ \ \Phi_1(\eta)=0, \tag{47}$$

$$\text{Case 3: } \frac{\sigma_{rr}}{c_{33}}(1)=-p_i,\ \frac{\sigma_{rr}}{c_{33}}(\eta)=0,\ \ \Phi_1(1)=\overline{\phi},\ \ \Phi_1(\eta)=0, \tag{48}$$

where the constants p_i and $\overline{\phi}$ are the prescribed dimensionless pressure and potential, respectively. It is convenient to normalize by taking $p_i=1$, $\overline{\phi}=1$, and so the boundary conditions (46)–(48) will henceforth be written as

$$\text{Case 1: } \frac{\sigma_{rr}}{c_{33}}(1)=-1,\ \ \frac{\sigma_{rr}}{c_{33}}(\eta)=0,\ \ \Phi_1(1)=0,\ \ \Phi_1(\eta)=0, \tag{49}$$

$$\text{Case 2: } \frac{\sigma_{rr}}{c_{33}}(1)=0,\ \ \frac{\sigma_{rr}}{c_{33}}(\eta)=0,\ \ \Phi_1(1)=1,\ \ \Phi_1(\eta)=0, \tag{50}$$

$$\text{Case 3: } \frac{\sigma_{rr}}{c_{33}}(1)=-1,\ \ \frac{\sigma_{rr}}{c_{33}}(\eta)=0,\ \ \Phi_1(1)=1,\ \ \Phi_1(\eta)=0. \tag{51}$$

Equations (41) and (45) can each be used to rewrite the boundary conditions, one pair at the inner surface of the cylinder and one at the outer surface. For each of the Cases 1, 2, or 3, the system of linear algebraic equations for the constants A,B,C,D can be written in the form

$$\mathbf{M}\mathbf{a}_n=\mathbf{b}_n(n=1,2,3) \tag{52}$$

where the 4×4 coefficient matrix $\mathbf{M}$ is defined in terms of column vectors

$$\mathbf{M}=[\mathbf{m}_1\ \ \mathbf{m}_2\ \ \mathbf{m}_3\ \ \mathbf{m}_4], \tag{53}$$

where

$$\mathbf{m}_1=\begin{Bmatrix} \dfrac{\beta\omega_1^2+\delta\beta\omega_1-\delta\omega_1^2-\alpha\omega_1}{\omega_1^2-\alpha} \\ \eta^{\omega_1-1}\left(\dfrac{\beta\omega_1^2+\delta\beta\omega_1-\delta\omega_1^2-\alpha\omega_1}{\omega_1^2-\alpha}\right) \\ 1 \\ \eta^{\omega_1} \end{Bmatrix}, \tag{54}$$

$$\mathbf{m}_2=\begin{Bmatrix} \dfrac{\beta\omega_2^2+\delta\beta\omega_2-\delta\omega_2^2-\alpha\omega_2}{\omega_2^2-\alpha} \\ \eta^{\omega_2-1}\left(\dfrac{\beta\omega_2^2+\delta\beta\omega_2-\delta\omega_2^2-\alpha\omega_2}{\omega_2^2-\alpha}\right) \\ 1 \\ \eta^{\omega_2} \end{Bmatrix}, \tag{55}$$

$$\mathbf{m}_3=\begin{Bmatrix} 1-\dfrac{\delta\beta}{\alpha} \\ \eta^{-1}\left(1-\dfrac{\delta\beta}{\alpha}\right) \\ 0 \\ \ln\eta \end{Bmatrix}, \tag{56}$$

$$\mathbf{m}_4=\begin{Bmatrix} 0 \\ 0 \\ 1 \\ 1 \end{Bmatrix}. \tag{57}$$

Each set of boundary conditions determines the form of the column vector $\mathbf{b}$ on the right side in (52). Thus $\mathbf{b}_1$, $\mathbf{b}_2$, and $\mathbf{b}_3$ correspond to Cases 1, 2, and 3, respectively:

$$\mathbf{b}_1=\begin{Bmatrix} -1-3K_2-\delta K_2-3K_1 \\ (-3K_2-\delta K_2-3K_1)\eta^2 \\ -K_1 \\ -K_1\eta^3 \end{Bmatrix}, \tag{58}$$

$$\mathbf{b}_2=\begin{Bmatrix} -3K_2-\delta K_2-3K_1 \\ (-3K_2-\delta K_2-3K_1)\eta^2 \\ 1-K_1 \\ -K_1\eta^3 \end{Bmatrix}, \tag{59}$$

$$\mathbf{b}_3=\begin{Bmatrix} -1-3K_2-\delta K_2-3K_1 \\ (-3K_2-\delta K_2-3K_1)\eta^2 \\ 1-K_1 \\ -K_1\eta^3 \end{Bmatrix}, \tag{60}$$

where we recall from (34), (27) that

$$K_1=\frac{\Omega(1+\frac{1}{3}\beta)}{(\beta^2+\alpha\gamma-9-9\gamma)}, \tag{61}$$

$$K_2=\frac{\gamma\Omega}{(\beta^2+\alpha\gamma-9-9\gamma)}, \tag{62}$$

$$\Omega=\frac{\rho_d\omega^2a^2}{c_{33}}. \tag{63}$$

The unknown constants A,B,C,D can be found using Cramer's Rule and so

$$A=\frac{|\mathbf{M}_{1n}|}{|\mathbf{M}|},\ \ B=\frac{|\mathbf{M}_{2n}|}{|\mathbf{M}|},\ \ C=\frac{|\mathbf{M}_{3n}|}{|\mathbf{M}|},\ \ D=\frac{|\mathbf{M}_{4n}|}{|\mathbf{M}|}, \tag{64}$$

where

$$\mathbf{M}_{1n}=[\mathbf{b}_n\ \ \mathbf{m}_2\ \ \mathbf{m}_3\ \ \mathbf{m}_4], \tag{65}$$

Table 1 Material constants for PZT-4

PZT-4	
c_{33}	115×10^9 Pa
c_{11}	139×10^9 Pa
c_{13}	74.3×10^9 Pa
e_{31}	-5.20 C/m^2
e_{33}	15.1 C/m^2
ϵ_{33}	5.62×10^{-9} F/m

$$\mathbf{M}_{2n}=[\mathbf{m}_1\ \ \mathbf{b}_n\ \ \mathbf{m}_3\ \ \mathbf{m}_4], \tag{66}$$

$$\mathbf{M}_{3n}=[\mathbf{m}_1\ \ \mathbf{m}_2\ \ \mathbf{b}_n\ \ \mathbf{m}_4], \tag{67}$$

$$\mathbf{M}_{2n}=[\mathbf{m}_1\ \ \mathbf{m}_2\ \ \mathbf{m}_3\ \ \mathbf{b}_n]. \tag{68}$$

We remark that on formally setting $\omega=0$ in the preceding (so that $K_1=0, K_2=0$), we recover results for the analogous static problems. See Galic and Horgan [15] for a detailed discussion of the static problem. Because of the algebraic complexity of the problem, further analytic expressions for the constants A,B,C,D will not be sought. Rather, we will provide numerical results for each of the Cases 1, 2, and 3, for the piezoceramic PZT-4.

4 Results for the Piezoceramic PZT-4

We present our numerical results in the form of plots of the stresses and potential throughout the cylinder. The piezoelectric material PZT-4 has been selected because of its technological importance. The moduli for PZT-4 are given in Table 1 (values taken from [2,3]; see [17] for a convenient table). On recalling the definitions of the dimensionless parameters $\alpha, \beta, \gamma, \delta$ from (16)–(18), (40), respectively, we obtain Table 2.

Table 2 Dimensionless parameters

PZT-4	
α	1.21
β	-0.34
γ	2.83
δ	0.65

The plots in Figs. 2–4 depict results for each of the three cases of boundary conditions (49)–(51), as well as for three different aspect ratios, $\eta=1.3,2,4$. All quantities are plotted versus dimensionless radius ρ defined in (23). Since $1\leqslant\rho\leqslant\eta$, the plot for a given aspect ratio will terminate at that value of η. We observe from (63) that the rotational term Ω depends on the density of the solid ρ_d, the inner radius a, the prescribed angular velocity ω, and the elastic constant c_{33}. The rotational term Ω has been normalized to $\Omega=1$ in Figs. 2 through 6.

Radial stress plots for Case 1 boundary conditions are shown in the middle subfigure of Fig. 2. The graph for each aspect ratio begins at $\sigma_{rr}/c_{33}=-1$, then attains an internal maximum and has value zero at the outer boundary. The graphs for $\eta=1.3$ and $\eta=2$ are nearly identical. In both cases, the internal maximum has a value close to zero, so that the difference between end values is approximately equal to the difference between the absolute maxima and minima of the graph. For $\eta=4$, however, the difference between absolute maxima and minima is five times greater than the difference between end values. For large aspect ratios, the effect of rotation dominates whereas for small aspect ratios, the predominant effect is that of the internal pressure.

The hoop stresses, shown in the bottom subfigure, are all monotonically decreasing. Again, the graphs for $\eta=1.3$ and $\eta=2$ are virtually identical. As the aspect ratio η increases to $\eta=4$, there is a greater absolute difference between end values than for the lower aspect ratios. The effect of rotation on the tubes with higher aspect ratios is likewise apparent in the potential distributions, shown in the upper subfigure of Fig. 2. Plots for $\eta=1.3$ and $\eta=2$ exhibit a single internal potential minimum. The graph for $\eta=4$ has a double concavity, exhibiting both an internal minimum and maximum before returning to its prescribed value of $\Phi_1=0$ at the outer boundary.

Case 2, shown in Fig. 3, is more interesting. From the lower bottom subfigure, we see that the $\eta=1.3$ hoop stress has changed

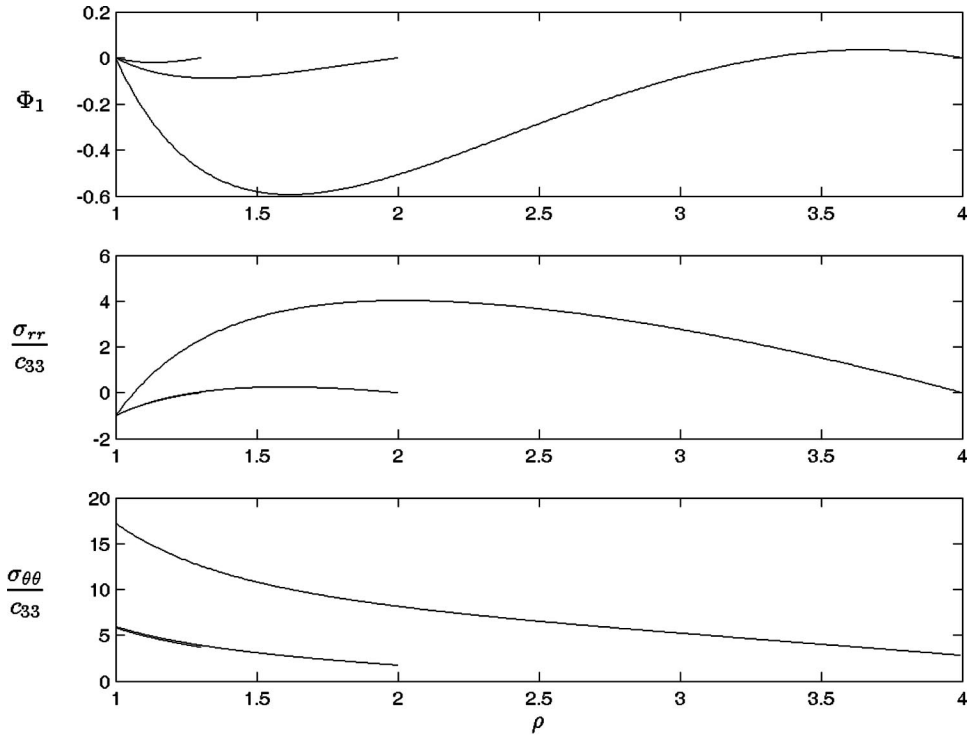

Fig. 2 Rotating hollow PZT-4 cylinder: $\Omega=1$. Case 1: plots for stresses and potential for $\eta=1.3, 2, 4$ ($\eta=b/a$).

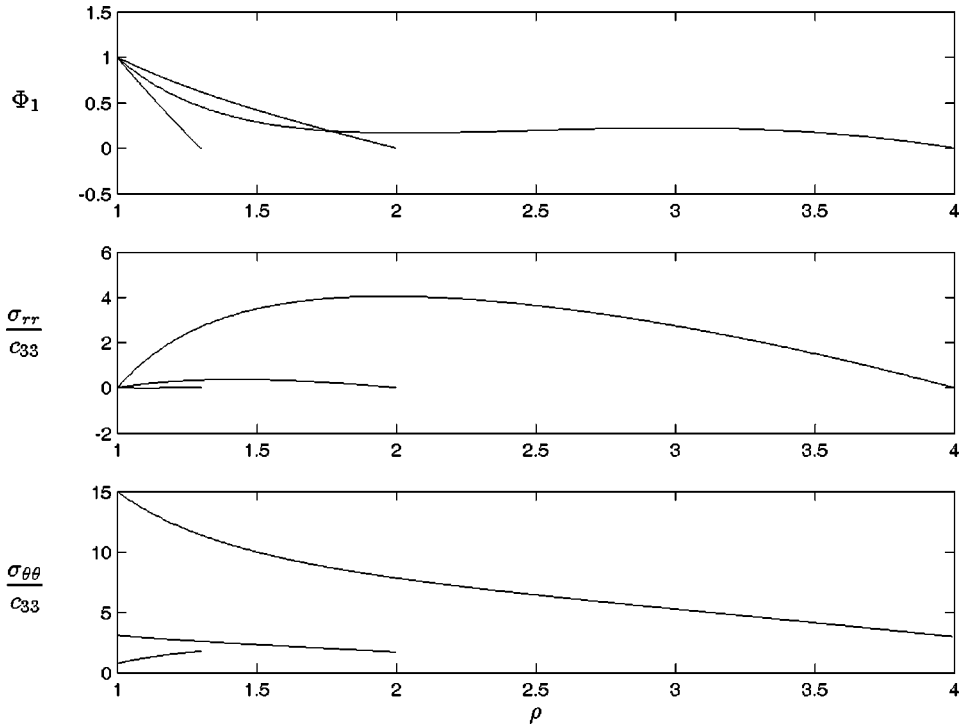

Fig. 3 Rotating hollow PZT-4 cylinder: $\Omega=1$. Case 2: plots for stresses and potential for $\eta=1.3, 2, 4$ ($\eta=b/a$).

concavity and is now *increasing* from the inner to the outer boundary. The remaining two hoop stresses are still decreasing. This has interesting consequences, which will be further discussed below. The radial stress response, both in shape and magnitude, is virtually unchanged from that in Fig. 2. The electric potentials are shown in the upper subfigure of Fig. 3. For $\eta=1.3$ and $\eta=2$, the potentials decrease almost linearly from their prescribed value of 1 at the inner radius to zero at the outer radius. Careful examination reveals the $\eta=2$ potential to be slightly concave up. This trend is more apparent in the $\eta=4$ graph, where the potential has

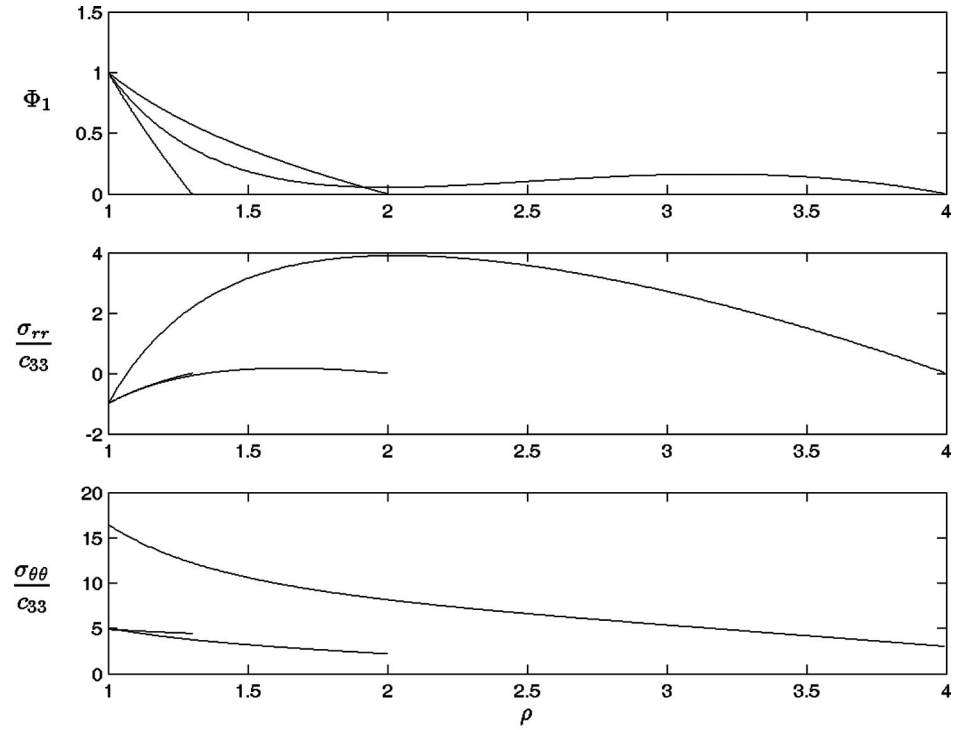

Fig. 4 Rotating hollow PZT-4 cylinder: $\Omega=1$. Case 3: plots for stresses and potential for $\eta=1.3, 2, 4$ ($\eta=b/a$).

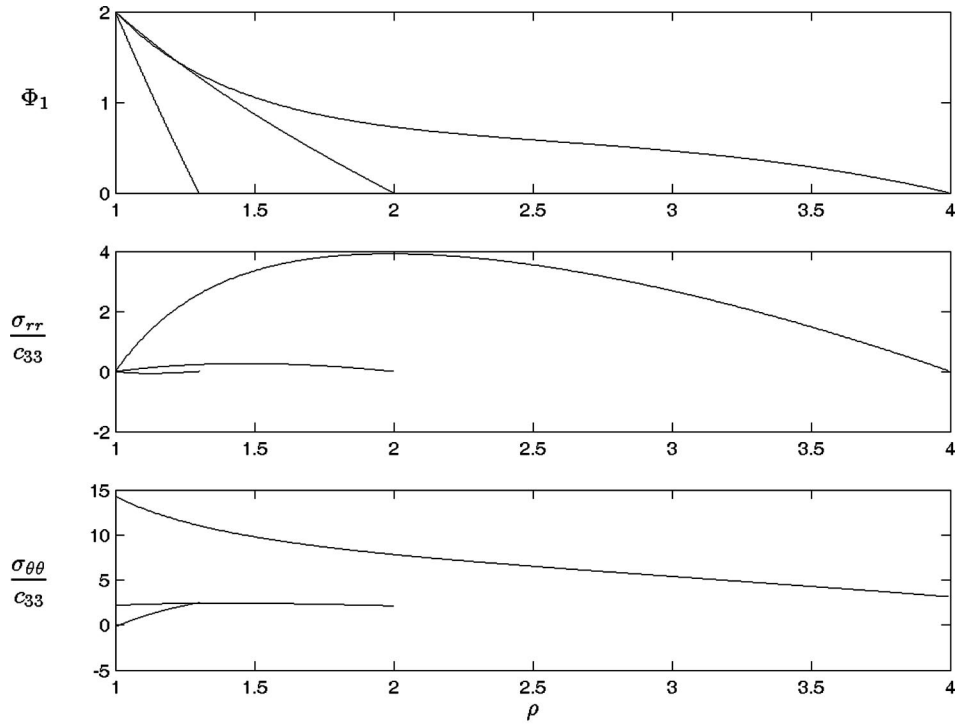

Fig. 5 Rotating hollow PZT-4 cylinder: $\Omega=1$. Modified Case 2 ($\Phi_1(0)=2$): plots for stresses and potential for $\eta=1.3, 2, 4$ ($\eta=b/a$).

the double concavity already seen in Fig. 2. As the aspect ratio increases, the stress and electric response is increasingly influenced by the rotation, rather than by the specific boundary conditions applied,

Case 3 (Fig. 4) is a superposition of Cases 1 and 2. The plots of the potential (upper subfigure) resemble those of Case 2, since the values occurring in Case 2 dominate those of Case 1. The hoop stresses (lower subfigure) are monotonically decreasing as in Fig. 2. The radial stress response is again similar to that of Figs. 2 and 3.

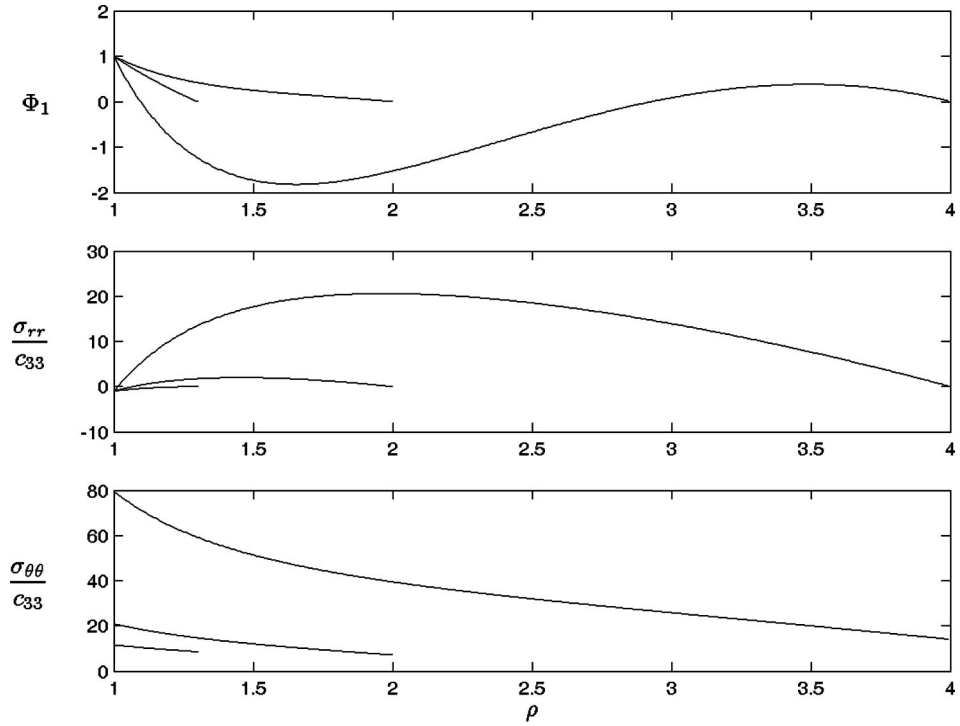

Fig. 6 Rotating hollow PZT-4 cylinder: $\Omega=5$. Case 3: plots for stresses and potential for $\eta=1.3, 2, 4$ ($\eta=b/a$).

Recall that in the lower subfigure of Fig. 3, for $\eta=1.3$ the hoop stress is increasing whereas for $\eta=2$ the hoop stress is decreasing. This suggests that by slightly modifying the boundary conditions, we could obtain a *virtually uniform hoop stress* for some aspect ratio. Such uniformity of the hoop stress was demonstrated in [15] for the static problem. In fact, on setting $\Phi_1(0)=2$ and plotting these modified Case 2 boundary conditions, we can achieve a nearly uniform hoop stress distribution for aspect ratio $\eta=2$. This is shown in the lower subfigure of Fig. 5. The technological consequences of a uniform hoop stress are interesting, because orthotropic elastic cylinders fail at a critical hoop stress. Here we have shown that a suitably applied electric field can "neutralize" a pre-existing mechanical hoop stress distribution.

In Fig. 6, we show Case 3 plots for a higher rotational speed, namely $\Omega=5$. On comparing with Fig. 4, we see that the double concavity in the plot for the potential for $\eta=4$ has become even more pronounced. The radial and hoop stresses have similar shapes to those in Fig. 4, but their values have increased. Further increase of the rotational speed beyond $\Omega=5$ leads to graphs similar to those in Fig. 6.

5 Rotating Solid Cylinder

We now examine the problem of a rotating *solid* piezoelectric cylinder of radius b. We will see that in this case, explicit closed-form analytic solutions can be obtained. We nondimensionalize the radial coordinate as

$$\rho=\frac{r}{b}, \tag{69}$$

so that

$$0\leqslant\rho\leqslant 1. \tag{70}$$

It can be easily shown that the analysis of Section 3 carries over on formally replacing a by b. Thus, the solutions for the stresses and potential are

$$\begin{aligned}\frac{\sigma_{rr}}{c_{33}}=&A\left[\rho^{\omega_1-1}\left(\frac{\beta\omega_1^2+\delta\beta\omega_1-\delta\omega_1^2-\alpha\omega_1}{\omega_1^2-\alpha}\right)\right]\frac{1}{b}\\&+B\left[\rho^{\omega_2-1}\left(\frac{\beta\omega_2^2+\delta\beta\omega_2-\delta\omega_2^2-\alpha\omega_2}{\omega_2^2-\alpha}\right)\right]\frac{1}{b}\\&+C\left[\rho^{-1}\left(1-\frac{\delta\beta}{\alpha}\right)\right]\frac{1}{b}+\rho^2(3K_2+\delta K_2+3K_1),\end{aligned} \tag{71}$$

$$\begin{aligned}\frac{\sigma_{\theta\theta}}{c_{33}}=&A\left[\rho^{\omega_1-1}\left(\frac{\delta\beta\omega_1^2-\delta\omega_1^3-\alpha\omega_1^2+\beta\omega_1^3}{\omega_1^2-\alpha}\right)\right]\frac{1}{b}\\&+B\left[\rho^{\omega_2-1}\left(\frac{\delta\beta\omega_2^2-\delta\omega_2^3-\alpha\omega_2^2+\beta\omega_2^3}{\omega_2^2-\alpha}\right)\right]\frac{1}{b}\\&+\rho^2(3\,\delta K_2+\alpha K_2+3\beta K_1),\end{aligned} \tag{72}$$

and

$$\Phi_1=A(\rho^{\omega_1})\frac{1}{b}+B(\rho^{\omega_2})\frac{1}{b}+C(\ln\rho)\frac{1}{b}+D\frac{1}{b}+K_1\rho^3, \tag{73}$$

respectively. Likewise, the displacement is

$$u(\rho)=\frac{(\beta\omega_1-\omega_1^2)}{(\omega_1^2-\alpha)}A\rho^{\omega_1}+\frac{(\beta\omega_2-\omega_2^2)}{(\omega_2^2-\alpha)}B\rho^{\omega_2}-\frac{\beta}{\alpha}C+bK_2\rho^3. \tag{74}$$

In the preceding, K_1 and K_2 are given by (61) and (62), respectively, with

$$\Omega=\rho_d\frac{\omega^2b^2}{c_{33}}. \tag{75}$$

The constants $A-D$ are arbitrary and will be determined from the boundary conditions.

Since we are concerned with a solid cylinder, the displacement and electric field at the origin must be finite. Thus, the constants B and C must be set equal to zero. The solutions for the stresses and potential then reduce to

$$\begin{aligned}\frac{\sigma_{rr}}{c_{33}}=&A\left[\rho^{\omega_1-1}\left(\frac{\beta\omega_1^2+\delta\beta\omega_1-\delta\omega_1^2-\alpha\omega_1}{\omega_1^2-\alpha}\right)\right]\frac{1}{b}\\&+\rho^2(3K_2+\delta K_2+3K_1),\end{aligned} \tag{76}$$

$$\begin{aligned}\frac{\sigma_{\theta\theta}}{c_{33}}=&A\left[\rho^{\omega_1-1}\left(\frac{\delta\beta\omega_1^2-\delta\omega_1^3-\alpha\omega_1^2+\beta\omega_1^3}{\omega_1^2-\alpha}\right)\right]\frac{1}{b}\\&+\rho^2(3\,\delta K_2+\alpha K_2+3\beta K_1),\end{aligned} \tag{77}$$

and

$$\Phi_1=A(\rho^{\omega_1})\frac{1}{b}+D\frac{1}{b}+K_1\rho^3, \tag{78}$$

respectively. We suppose that the lateral boundary is traction-free and that the electric potential is zero there, hence

$$\frac{\sigma_{rr}}{c_{33}}(1)=0, \tag{79}$$

$$\Phi_1(1)=0. \tag{80}$$

On using (76) in (79) we obtain

$$A=\frac{-b(3K_2+\delta K_2+3K_1)}{\left(\frac{\beta\omega_1^2+\delta\beta\omega_1-\delta\omega_1^2-\alpha\omega_1}{\omega_1^2-\alpha}\right)}. \tag{81}$$

On inserting (81) into (78) and using (80), we find that

$$D=\frac{b(3K_2+\delta K_2+3K_1)}{\left(\frac{\beta\omega_1^2+\delta\beta\omega_1-\delta\omega_1^2-\alpha\omega_1}{\omega_1^2-\alpha}\right)}-bK_1. \tag{82}$$

Thus the solutions (76)–(78) for the stresses and electric potential can be written

$$\frac{\sigma_{rr}}{c_{33}}=k_1(-\rho^{\omega_1-1}+\rho^2), \tag{83}$$

$$\frac{\sigma_{\theta\theta}}{c_{33}}=k_4\left(\frac{-k_1k_3}{k_4k_2}\rho^{\omega_1-1}+\rho^2\right), \tag{84}$$

$$\Phi_1=-\frac{k_1}{k_2}\rho^{\omega_1}+K_1\rho^3+\left(\frac{k_1}{k_2}-K_1\right), \tag{85}$$

where

$$k_1=\left[\frac{(3+\delta)\gamma+3+\beta}{\beta^2+\alpha\gamma-9-9\gamma}\right]\Omega, \tag{86}$$

$$k_2=\frac{\beta\omega_1^2+\delta\beta\omega_1-\delta\omega_1^2-\alpha\omega_1}{\omega_1^2-\alpha}, \tag{87}$$

$$k_3=\omega_1k_2, \tag{88}$$

$$k_4=\left[\frac{(3\,\delta+\alpha)\gamma+(3+\beta)\beta}{\beta^2+\alpha\gamma-9-9\gamma}\right]\Omega. \tag{89}$$

Thus, for a solid piezoelectric cylinder, the solutions (83)–(85) are in explicit closed form.

Before discussing our results for the piezoelectric problem, we turn to its purely mechanical analog. The stresses for the case of an infinitely long rotating solid linearly elastic cylinder can be obtained by formally discarding the electric terms in (28), solving the differential equation for u, and employing boundedness con-

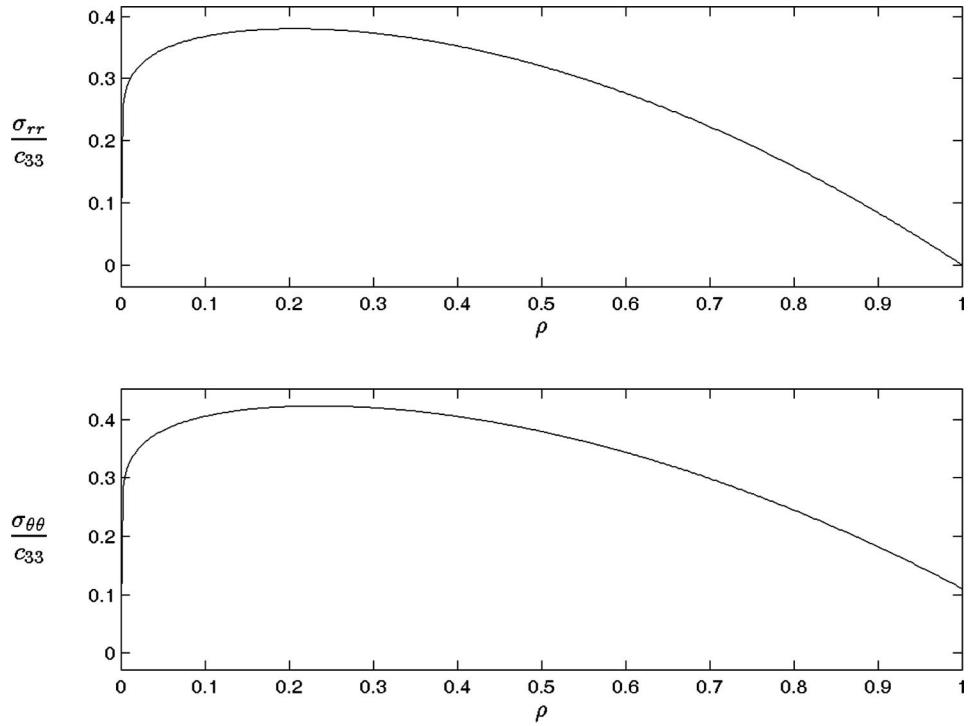

Fig. 7 Stress plots for rotating solid circumferentially orthotropic elastic cylinder of radius *b* ($\Omega=5$). The elastic constants are identical to those of PZT-4.

ditions at the origin. Expressions for u are then substituted into the stress-displacement relations, i.e., (38) and (39) without the Φ terms. On applying the boundary condition (79), one obtains

$$\frac{\sigma_{rr}}{c_{33}}=\frac{(3+\delta)\Omega}{9-\alpha}[\rho^{\sqrt{\alpha}-1}-\rho^2], \tag{90}$$

$$\frac{\sigma_{\theta\theta}}{c_{33}}=\frac{\Omega}{9-\alpha}[(3+\delta)\rho^{\sqrt{\alpha}-1}-(3\delta+\alpha)\rho^2]. \tag{91}$$

Aside from differences in notation, Eqs. (90) and (91) are similar to Eqs. (38) and (39) of Horgan and Baxter [16], obtained for a rotating elastic orthotropic disk in plane stress. As mentioned earlier, α can be written as

$$\alpha=\frac{\overline{E}_\theta}{\overline{E}_r}, \tag{92}$$

and we recall from (75) that

$$\Omega=\rho_d\frac{\omega^2 b^2}{c_{33}}. \tag{93}$$

When $\alpha>1$, the elastic material is *circumferentially orthotropic*, while if $\alpha<1$, the material is *radially orthotropic*, [16]. For an elastic material whose mechanical properties are identical to the mechanical properties of PZT-4, we have seen in Table 2 of Section 4 that $\alpha=1.21$ and $\delta=0.65$. The stresses (90) and (91) for such a material are plotted in Fig. 7, and these graphs are similar to Figs. 6 and 7 of [16]. Both the radial and hoop stresses tend to zero at the origin, as is shown in [16] for *any* circumferentially orthotropic material. This can be seen directly from (90), (91) as $\rho\to 0$. On the other hand, for radially orthotropic materials ($\alpha<1$), it can be seen from (90), (91) that there are stress singularities at the origin, [16]. We recall from [16] that the stress response in the *isotropic* case ($\alpha=1$) is quite different.

The purely mechanical material for which the stresses are plotted in Fig. 7 has a value of α identical to that of PZT-4, i.e., $\alpha=1.21$. Thus, one might expect that PZT-4 would behave like a circumferentially orthotropic elastic material. However, the stress plots for PZT-4 in Fig. 8 are quite different from those in Fig. 7. As we see in the lower two subfigures of Fig. 8, the stresses for PZT-4 tend to *infinity* at the origin. As pointed out above, stress singularities at the center of a rotating elastic solid cylinder are characteristic of a *radially orthotropic* elastic material, that is, of a material for which $\alpha<1$. In Fig. 8 we see these singularities occurring in a piezoelectric material for which $\alpha>1$. This apparent paradox can be explained on returning to Eqs. (83) and (84). We note that each of these equations contains a ρ^{ω_1-1} term, where we recall from (33) that

$$\omega_1=\sqrt{\frac{\beta^2+\alpha\gamma}{1+\gamma}}. \tag{94}$$

Thus for $\omega_1<1$, stress singularities occur as one approaches the origin while for $\omega_1>1$, the stresses are zero at the origin. On using (94), these conditions may be written directly in terms of the parameters α, β, γ defined in (16)–(18). Thus stress singularities occur at the origin if

$$\gamma(\alpha-1)<1-\beta^2 \tag{95}$$

while the stresses are zero at the origin if the sign in (95) is reversed.

For PZT-4, it can be verified on using Table 2 that ω_1 has a value of 0.96. Thus for PZT-4, $\omega_1<1$ so that (95) is satisfied and one obtains the stress singularities shown in Fig. 8. Thus, for a rotating solid piezoelectric cylinder, it is not the purely elastic parameter α, but rather ω_1 (a combination of electrical and mechanical parameters) which determines the full nature of the orthotropy. In this sense, PZT-4 in fact behaves like a radially orthotropic elastic material.

In Fig. 7 for the purely elastic cylinder, both the radial and hoop stresses have an *interior* maximum. The maximum hoop stress occurs approximately at $\rho=0.25$ and has a value of $\sigma_{\theta\theta}/c_{33}\approx 0.42$. For the piezoelectric cylinder with results shown in Fig. 8,

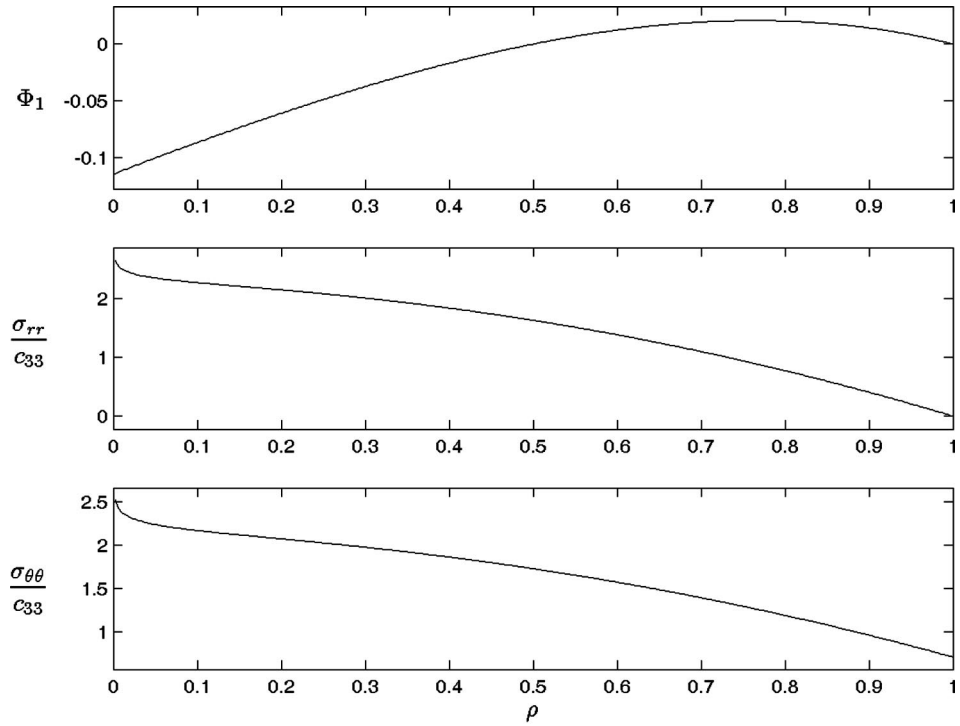

Fig. 8 Rotating solid PZT-4 cylinder of radius b ($\Omega=5$): plots for the stresses and potential versus $\rho=r/b$

we see that even before the hoop stress tends to infinity as one approaches the origin, it attains values in excess of $\sigma_{\theta\theta}/c_{33}=2$. This may be attributed to the rotation induced piezoelectric effect. Rotation induces both stresses and electric potential, and the induced electric potential further increases the stresses.

6 Concluding Remarks

It should be noted that the virtual uniformity of the hoop stresses discussed in Section 4 for the hollow cylinder has been demonstrated for the specific piezoceramic PZT-4. It would be of interest to explore this phenomenon analytically for general piezoceramics but we shall not pursue this here. The technological implications of the above are significant. For example, it shows that an existing mechanical hoop stress distribution can be neutralized by a suitably applied electric field.

The special case of a rotating solid piezoelectric cylinder, free of traction and applied voltage on its surface was seen to be amenable to a full analytic solution. In this case, explicit closed-form solutions were obtained. It was shown that stress singularities at the origin can occur for certain piezoelectric materials, analogous to those occurring in the purely mechanical problem for radially orthotropic materials.

Finally, we note that here attention has been focussed on radially polarized piezoelectric cylinders. The axisymmetric problem for axially polarized piezoelectric tubes, exhibiting transverse isotropy, has also been considered in the literature (see, e.g., [10]). This problem is particularly simple since there is a complete uncoupling of mechanical and electrical effects in this case.

Acknowledgment

D. G. would like to thank the ARCS Foundation and the Virginia Space Grant Consortium for their support of his graduate education. The research of C. O. H. was supported by NASA under grant number NCC-1-02019 and by NSF under grant DMS 02-1750.

References

[1] Tiersten, H. F., 1969, *Linear Piezoelectric Plate Vibrations*, Plenum Press, New York.
[2] Berlincourt, D. A., 1971, ''Piezoelectric Crystals and Ceramics,'' *Ultrasonic Transducer Materials*, O. E. Mattiat, ed., Plenum Press, New York, pp. 63–124.
[3] Berlincourt, D. A., Curran, D. R., and Jaffe, H., 1964, ''Piezoelectric and Piezomagnetic Materials and Their Function in Transducers,'' *Physical Acoustics: Principles and Methods*, W. P. Mason, ed., Academic Press, New York, pp. 169–270.
[4] Jaffe, B., Cook, Jr., W. R., and Jaffe, H., 1971, *Piezoelectric Ceramics*, Academic Press, London.
[5] Destuynder, P., 1999, ''A Few Remarks on the Controllability of an Aeroacoustic Model Using Piezo-Devices,'' *Smart Structures*, J. Holnicki-Szulc and J. Rodellar, eds., Kluwer Academic Publishers, Dordrecht, pp. 53–62.
[6] Jiang, H. W., Schmid, F., Brand, W., and Tomlinson, G. R., 1999, ''Controlling Pantograph Dynamics Using Smart Technology,'' *Smart Structures*, J. Holnicki-Szulc and J. Rodellar, eds., Kluwer, Dordrecht, pp. 125–132.
[7] Kawiecki, G., 1999, ''Piezogenerated Elastic Waves for Structural Health Monitoring,'' *Smart Structures*, J. Holnicki-Szulc and J. Rodellar, eds., Kluwer, Dordrecht, pp. 133–142.
[8] Gandhi, M. V., and Thompson, B. S., 1992 *Smart Materials and Structures*, Chapman and Hall, London.
[9] Adelman, N. T., Stavsky, Y., and Segal, E., 1975, ''Axisymmetric Vibrations of Radially Polarized Piezoelectric Ceramic Cylinders,'' J. Sound Vib., **38**, pp. 245–254.
[10] Parton, V. Z., and Kudryavtsev, B. A., 1988, *Electromagnetoelasticity: Piezoelectrics and Electrically Conductive Solids*, Gordon and Breach Science Publishers, New York, (translated by E. G. Strel'chenko).
[11] Heyliger, P., 1997, ''A Note on the Static Behavior of Simply Supported Piezoelectric Cylinders,'' Int. J. Solids Struct., **34**, pp. 3781–3794.
[12] Heyliger, P., and Wu, Y.-C., 1999, ''Electric Fields in Layered Piezoelectric Spheres,'' Int. J. Eng. Sci., **37**, pp. 143–161.
[13] Chen, W.-Q., 1999, ''Problems of Radially Polarized Piezoelectric Bodies,'' Int. J. Solids Struct., **36**, pp. 4317–4332.
[14] Chen, C., Shen, Y., and Liang, X., 1999, ''Three Dimensional Analysis of Piezoelectric Circular Cylindrical Shell of Finite Length,'' Acta Mech., **134**, pp. 235–249.
[15] Galic, D. and Horgan, C. O., 2002, ''Internally Pressurized Radially Polarized Piezoelectric Cylinders,'' J. Elast., **66**, pp. 257–272.
[16] Horgan, C. O., and Baxter, S. C., 1996, ''Effects of Curvilinear Anisotropy on Radially Symmetric Stresses in Anisotropic Linearly Elastic Solids,'' J. Elast., **42**, pp. 31–48.
[17] Dunn, M. L., and Taya, M., 1994, ''Electroelastic Field Concentrations In and Around Inhomogeneities in Piezoelectric Solids,'' ASME J. Appl. Mech., **61**, pp. 474–475.

H. J. Ding[1]
Department of Civil Engineering,
Zhejiang University,
Hangzhou 310027,
Peoples' Republic of China
e-mail: hjding@mail.hz.zj.cn

H. M. Wang
Department of Mechanics,
Zhejiang University,
Hangzhou 310027,
Peoples' Republic of China

W. Q. Chen
Department of Civil Engineering,
Zhejiang University,
Hangzhou 310027,
Peoples' Republic of China

Transient Responses in a Piezoelectric Spherically Isotropic Hollow Sphere for Symmetric Problems

By virtue of the separation of variables technique, the spherically symmetric electroelastic dynamic problem of a spherically isotropic hollow sphere is transformed to an integral equation about a function with respect to time, which can be solved successfully by means of the interpolation method. Then the solution of displacements, stresses, electric displacements, and electric potential are obtained. The present method is suitable for a piezoelectric hollow sphere with an arbitrary thickness subjected to spherically symmetric electric potential and radial mechanical loads, that both can be arbitrary functions about the time variable, at the internal and external surfaces. [DOI: 10.1115/1.1554415]

1 Introduction

The dynamic problems of hollow spheres and spherical shells have been studied for many years. For elastic materials, based on the momentless thin shell theory, Huth and Cole [1] studied the stress waves in a spherical shell produced by dynamic loads. The dynamic responses in a thin spherical shell subjected to an axisymmetric pressure loading were considered by Baker et al. [2]. Using the method of characteristics, Chou and Koenig [3] and Rose et al. [4] studied the dynamic responses of cylindrical and spherical shells. By means of the finite Hankel transform and Laplace transform, Cinelli [5] obtained the theoretical solutions of dynamic problems of cylindrical and spherical shells. Pao and Ceranoglu [6] completed the transient responses in a thick-walled spherical shell by the ray theory. While for piezoelectric materials, Loza and Shul'ga [7,8] studied the axisymmetric free and forced vibrations of piezoceramic hollow spheres. Shul'ga [9–11] discussed the radial and three-dimensional free vibrations of piezoceramic hollow spheres. Heyliger and Wu [12] investigated the spherically symmetric free vibration with the radial electric displacement zero on the boundary. Cai et al. [13] obtained the natural frequencies of a piezoceramic hollow sphere submerged in a compressible fluid. Chen et al. [14] studied the three-dimensional free vibration of a fluid-filled piezoelectric hollow sphere. Borisyuk and Kirichok [15] analyzed the spherically symmetric steady-state responses in a piezoceramic hollow sphere submerged in a compressible fluid. Li et al. [16] solved the spherically symmetric steady-state responses in a laminated spherical shell consisting of piezoelectric and elastic layers. Comparing with the nonpiezoelectric case, it is more difficult to obtain the dynamic analytical solution because of the special coupling effect between mechanical deformation and electrical field in piezoelectric materials. At present, most works on dynamic behaviors of piezoelectric hollow spheres are concerned with problems of free vibration and steady-state response while the transient responses, although they are very important practically, have not been studied to the author's knowledge.

In this paper, the separation of variables technique is applied to solve transient responses of the spherically symmetric problem of piezoelectric hollow spheres subjected to dynamic loads. First, a new dependent variable is introduced to rewrite the governing equation, the mechanical boundary conditions as well as the initial conditions. Second, a special function is introduced to transform the inhomogeneous mechanical boundary conditions into the homogeneous ones. Third, by virtue of the orthogonal expansion technique, along with the initial conditions as well as electrical boundary conditions, the integral equation about a function with respect to time is derived, which can be solved by means of the interpolation method. The displacements, stresses, electric displacements, and electric potential are finally obtained. The present method is suitable for a hollow sphere with an arbitrary thickness subjected to arbitrary mechanical and electrical loads. Numerical examples are considered and comparison of responses between a piezoelectric sphere and the purely elastic sphere is made.

2 Basic Equations

To study the hollow sphere, it is convenient to use the spherical coordinate system (r,θ,φ) with the origin identical to the center of the sphere. For the spherically symmetric problem, we have $u_\theta = u_\varphi = 0$, $u_r = u_r(r,t)$ and $\Phi = \Phi(r,t)$, where $u_i\ (i = r,\theta,\varphi)$ and Φ are components of displacement and electric potential, respectively. In this case, the strain-displacement relations are simplified as

$$\gamma_{rr} = \frac{\partial u_r}{\partial r}, \quad \gamma_{\theta\theta} = \gamma_{\varphi\varphi} = \frac{u_r}{r}, \tag{1}$$

where γ_{ij} are the strain components. The constitutive relations of spherically isotropic, radially polarized piezoelectric media also read as

$$\begin{aligned} \sigma_{\theta\theta} &= (c_{11}+c_{12})\gamma_{\theta\theta} + c_{13}\gamma_{rr} + e_{31}\frac{\partial\Phi}{\partial r}, \\ \sigma_{rr} &= 2c_{13}\gamma_{\theta\theta} + c_{33}\gamma_{rr} + e_{33}\frac{\partial\Phi}{\partial r}, \\ D_r &= 2e_{31}\gamma_{\theta\theta} + e_{33}\gamma_{rr} - \varepsilon_{33}\frac{\partial\Phi}{\partial r}, \end{aligned} \tag{2}$$

[1]To whom correspondence should be addressed.

Contributed by the Applied Mechanics Division of THE AMERICAN SOCIETY OF MECHANICAL ENGINEERS for publication in the ASME JOURNAL OF APPLIED MECHANICS. Manuscript received by the ASME Applied Mechanics Division, Jan. 30, 2002; final revision, Sept. 15, 2002. Associate Editor: A. K. Mal. Discussion on the paper should be addressed to the Editor, Prof. Robert M. McMeeking, Department of Mechanical and Environmental Engineering University of California–Santa Barbara, Santa Barbara, CA 93106-5070, and will be accepted until four months after final publication of the paper itself in the ASME JOURNAL OF APPLIED MECHANICS.

 Copyright © 2003 by ASME

where c_{ij}, e_{ij}, and ε_{ij} are elastic, piezoelectric, and dielectric constants, respectively, and σ_{ij} and D_r are the components of stress and the radial electric displacement, respectively. The equation of motion is

$$\frac{\partial \sigma_{rr}}{\partial r}+2\,\frac{\sigma_{rr}-\sigma_{\theta\theta}}{r}=\rho\,\frac{\partial^2 u_r}{\partial t^2}, \tag{3}$$

where ρ is the mass density. In absence of free charge density, the charge equation of electrostatics is

$$\frac{1}{r^2}\,\frac{\partial}{\partial r}(r^2 D_r)=0. \tag{4}$$

For the analysis, the following nondimensional quantities are introduced:

$$c_1=\frac{c_{11}}{c_{33}},\quad c_2=\frac{c_{12}}{c_{33}},\quad c_3=\frac{c_{13}}{c_{33}},\quad e_1=\frac{e_{31}}{\sqrt{c_{33}\varepsilon_{33}}},\quad e_3=\frac{e_{33}}{\sqrt{c_{33}\varepsilon_{33}}},$$

$$\sigma_i=\frac{\sigma_{ii}}{c_{33}}(i=r,\theta,\varphi),\quad \phi=\sqrt{\frac{\varepsilon_{33}}{c_{33}}}\,\frac{\Phi}{b},\quad D=\frac{D_r}{\sqrt{c_{33}\varepsilon_{33}}}, \tag{5}$$

$$u=\frac{u_r}{b},\quad \xi=\frac{r}{b},\quad s=\frac{a}{b},\quad c_v=\sqrt{\frac{c_{33}}{\rho}},\quad \tau=\frac{c_v}{b}t,$$

where a and b are the inner and outer radii of the hollow sphere, respectively. Then by virtue of Eq. (5), Eqs. (1)–(4) can be rewritten as follows:

$$\gamma_{rr}=\frac{\partial u}{\partial \xi},\quad \gamma_{\theta\theta}=\gamma_{\varphi\varphi}=\frac{u}{\xi}. \tag{6}$$

$$\sigma_\theta=(c_1+c_2)\,\frac{u}{\xi}+c_3\frac{\partial u}{\partial \xi}+e_1\frac{\partial \phi}{\partial \xi},$$

$$\sigma_r=2c_3\frac{u}{\xi}+\frac{\partial u}{\partial \xi}+e_3\frac{\partial \phi}{\partial \xi}, \tag{7}$$

$$D=2e_1\frac{u}{\xi}+e_3\frac{\partial u}{\partial \xi}-\frac{\partial \phi}{\partial \xi}.$$

$$\frac{\partial \sigma_r}{\partial \xi}+2\,\frac{\sigma_r-\sigma_\theta}{\xi}=\frac{\partial^2 u}{\partial \tau^2}. \tag{8}$$

$$\frac{1}{\xi^2}\,\frac{\partial}{\partial \xi}(\xi^2 D)=0. \tag{9}$$

The boundary conditions are

$$\sigma_r(s,\tau)=p_a(\tau),\quad \sigma_r(1,\tau)=p_b(\tau), \tag{10a}$$

$$\phi(s,\tau)=\phi_a(\tau),\quad \phi(1,\tau)=\phi_b(\tau), \tag{10b}$$

where $p_a(\tau)$ and $p_b(\tau)$ are the known dimensionless pressures acting on the internal and external surfaces of the sphere, respectively, and $\phi_a(\tau)$ and $\phi_b(\tau)$ are the known dimensionless electric potentials imposed on the internal and external surfaces, respectively.

The initial conditions are expressed as

$$\tau=0:\quad u(\xi,0)=u_0(\xi),\quad \dot{u}(\xi,0)=v_0(\xi), \tag{11}$$

where a dot over a quantity denotes its partial derivative with respect to time.

3 Analysis

First, we rewrite the third equation in Eq. (7) as

$$\frac{\partial \phi}{\partial \xi}=2e_1\frac{u}{\xi}+e_3\frac{\partial u}{\partial \xi}-D. \tag{12}$$

Then substituting the above equation into the first two equations in Eq. (7), gives

$$\sigma_\theta=(c_1^D+c_2^D)\,\frac{u}{\xi}+c_3^D\frac{\partial u}{\partial \xi}-e_1 D,$$

$$\sigma_r=2c_3^D\frac{u}{\xi}+c_0^D\frac{\partial u}{\partial \xi}-e_3 D, \tag{13}$$

where

$$c_1^D=c_1+e_1^2,\quad c_2^D=c_2+e_1^2,\quad c_3^D=c_3+e_1e_3,\quad c_0^D=1+e_3^2. \tag{14}$$

The solution of Eq. (9) is

$$D(\xi,\tau)=\frac{1}{\xi^2}\,d(\tau) \tag{15}$$

where $d(\tau)$ is an unknown function with respect to the dimensionless time τ. Substituting Eq. (13) into Eq. (8) and utilizing Eq. (15) gives

$$\frac{\partial^2 u}{\partial \xi^2}+\frac{2}{\xi}\,\frac{\partial u}{\partial \xi}-\frac{\mu_1^2}{\xi^2}u=\frac{1}{c_L^2}\,\frac{\partial^2 u}{\partial \tau^2}-2\,\frac{e_1}{c_0^D}\,\frac{1}{\xi^3}\,d(\tau), \tag{16}$$

where

$$\mu_1=\sqrt{2\,\frac{c_1^D+c_2^D-c_3^D}{c_0^D}},\quad c_L=\sqrt{c_0^D}. \tag{17}$$

Utilizing the second equation in Eqs. (13) and (15), we can rewrite Eq. (10*a*) as

$$\xi=s:\quad c_0^D\frac{\partial u}{\partial \xi}+2c_3^D\frac{u}{\xi}=p_a(\tau)+\frac{e_3}{s^2}\,d(\tau),$$

$$\xi=1:\quad c_0^D\frac{\partial u}{\partial \xi}+2c_3^D\frac{u}{\xi}=p_b(\tau)+e_3 d(\tau). \tag{18}$$

Secondly, a new dependent variable $w(\xi,\tau)$ is introduced:

$$u(\xi,\tau)=\xi^{-1/2}w(\xi,\tau). \tag{19}$$

Then Eqs. (16), (18), and (11) become

$$\frac{\partial^2 w}{\partial \xi^2}+\frac{1}{\xi}\,\frac{\partial w}{\partial \xi}-\frac{\mu^2}{\xi^2}w=\frac{1}{c_L^2}\,\frac{\partial^2 w}{\partial \tau^2}+X(\xi)d(\tau), \tag{20}$$

$$\xi=s:\quad \frac{\partial w}{\partial \xi}+h\,\frac{w}{\xi}=p_1(\tau),$$

$$\xi=1:\quad \frac{\partial w}{\partial \xi}+h\,\frac{w}{\xi}=p_2(\tau), \tag{21}$$

$$w(\xi,0)=u_1(\xi),\quad \dot{w}(\xi,0)=v_1(\xi), \tag{22}$$

where

$$h=2\,\frac{c_3^D}{c_0^D}-\frac{1}{2},\quad \mu=\sqrt{\mu_1^2+\frac{1}{4}},\quad X(\xi)=-2\,\frac{e_1}{c_0^D}\,\frac{1}{\xi^{5/2}},$$

$$p_1(\tau)=\frac{s^{1/2}}{c_0^D}\left[p_a(\tau)+\frac{e_3}{s^2}d(\tau)\right],\quad p_2(\tau)=\frac{1}{c_0^D}[p_b(\tau)+e_3 d(\tau)], \tag{23}$$

$$u_1(\xi)=\xi^{1/2}u_0(\xi),\quad v_1(\xi)=\xi^{1/2}v_0(\xi).$$

Third, in order to transform the inhomogeneous mechanical boundary conditions into the homogeneous ones, we assume

$$w(\xi,\tau)=w_1(\xi,\tau)+w_2(\xi,\tau), \tag{24}$$

where $w_2(\xi,\tau)$ satisfies the inhomogeneous mechanical boundary conditions and can be taken as

$$w_2(\xi,\tau)=A_0(\xi-s)^m p_2(\tau)+B_0(\xi-1)^m p_1(\tau), \tag{25}$$

in which

$$A_0=\frac{1}{m(1-s)^{m-1}+h(1-s)^m},$$

$$B_0=\frac{1}{m(s-1)^{m-1}+h(s-1)^m/s}, \tag{26}$$

and m is an integer no less than 2, which should satisfy

$$[m(1-s)^{m-1}+h(1-s)^m][m(s-1)^{m-1}+h(s-1)^m/s]\neq 0. \tag{27}$$

Substituting $p_1(\tau)$ and $p_2(\tau)$ in Eq. (23) into Eq. (25) gives

$$w_2(\xi,\tau)=f_1(\xi)p_a(\tau)+f_2(\xi)p_b(\tau)+f_3(\xi)d(\tau), \tag{28}$$

where

$$f_1(\xi)=s^{1/2}\frac{B_0}{c_0^D}(\xi-1)^m, \quad f_2(\xi)=\frac{A_0}{c_0^D}(\xi-s)^m,$$

$$f_3(\xi)=e_3\left[\frac{1}{s^2}f_1(\xi)+f_2(\xi)\right]. \tag{29}$$

Substituting Eq. (24) into Eqs. (20)–(22) yields

$$\frac{\partial^2 w_1(\xi,\tau)}{\partial\xi^2}+\frac{1}{\xi}\frac{\partial w_1(\xi,\tau)}{\partial\xi}-\frac{\mu^2}{\xi^2}w_1(\xi,\tau)=\frac{1}{c_L^2}\frac{\partial^2 w_1(\xi,\tau)}{\partial\tau^2}+g(\xi,\tau), \tag{30}$$

$$\frac{\partial w_1(\xi,\tau)}{\partial\xi}+h\frac{w_1(\xi,\tau)}{\xi}=0, \quad (\xi=s \text{ and } 1), \tag{31}$$

$$w_1(\xi,0)=u_2(\xi)-f_3(\xi)d(0), \quad \dot{w}_1(\xi,0)=v_2(\xi)-f_3(\xi)\dot{d}(0), \tag{32}$$

where

$$g(\xi,\tau)=g_1(\xi,\tau)+g_2(\xi)d(\tau)+g_3(\xi)\ddot{d}(\tau), \tag{33a}$$

$$u_2(\xi)=u_1(\xi)-f_1(\xi)p_a(0)-f_2(\xi)p_b(0),$$
$$v_2(\xi)=v_1(\xi)-f_1(\xi)\dot{p}_a(0)-f_2(\xi)\dot{p}_b(0) \tag{33b}$$

and

$$g_1(\xi,\tau)=f_4(\xi)p_a(\tau)+f_5(\xi)p_b(\tau)+[f_1(\xi)\ddot{p}_a(\tau)+f_2(\xi)\ddot{p}_b(\tau)]/c_L^2,$$

$$g_2(\xi)=\frac{\mu^2}{\xi^2}f_3(\xi)-\frac{1}{\xi}\frac{df_3(\xi)}{d\xi}-\frac{d^2f_3(\xi)}{d\xi^2}+X(\xi),$$

$$g_3(\xi)=\frac{f_3(\xi)}{c_L^2},$$

$$f_4(\xi)=\frac{\mu^2}{\xi^2}f_1(\xi)-\frac{1}{\xi}\frac{df_1(\xi)}{d\xi}-\frac{d^2f_1(\xi)}{d\xi^2}, \tag{34}$$

$$f_5(\xi)=\frac{\mu^2}{\xi^2}f_2(\xi)-\frac{1}{\xi}\frac{df_2(\xi)}{d\xi}-\frac{d^2f_2(\xi)}{d\xi^2}.$$

Using the separation of variables technology, the solution of Eq. (30) can be assumed as

$$w_1(\xi,\tau)=\sum_i R_i(\xi)F_i(\tau), \tag{35}$$

where $F_i(\tau)$ is an undetermined function and $R_i(\xi)$ is given as follows:

$$R_i(\xi)=J_\mu(k_i\xi)Y(\mu,k_i,s)-Y_\mu(k_i\xi)J(\mu,k_i,s), \tag{36}$$

in which $J_\mu(k_i\xi)$ and $Y_\mu(k_i\xi)$ are Bessel functions of the first and second kinds of order μ. The eigenvalues k_i, arranged in an ascending order, are a series of positive roots of the following equation:

$$J(\mu,k_i,s)Y(\mu,k_i,1)-J(\mu,k_i,1)Y(\mu,k_i,s)=0, \tag{37}$$

where

$$J(\mu,k_i,\xi)=\frac{dJ_\mu(k_i\xi)}{d\xi}+h\frac{J_\mu(k_i\xi)}{\xi},$$

$$Y(\mu,k_i,\xi)=\frac{dY_\mu(k_i\xi)}{d\xi}+h\frac{Y_\mu(k_i\xi)}{\xi}. \tag{38}$$

It can be shown that $w_1(\xi,\tau)$ given in Eq. (35) satisfies the homogeneous mechanical boundary conditions in Eq. (31). Substituting Eq. (35) into Eq. (30) gives

$$-c_L^2\sum_i k_i^2F_i(\tau)R_i(\xi)=\sum_i R_i(\xi)\frac{d^2F_i(\tau)}{d\tau^2}+c_L^2g(\xi,\tau). \tag{39}$$

By virtue of the orthogonal properties of Bessel functions, it is easy to verify that $R_i(\xi)$ has the following properties:

$$\int_s^1 \xi R_i(\xi)R_j(\xi)d\xi=N_i\delta_{ij}, \tag{40}$$

where δ_{ij} is the Kronecker delta, and

$$N_i=\frac{1}{2k_i^2}\left\{\left[\frac{dR_i(1)}{d\xi}\right]^2-s^2\left[\frac{dR_i(s)}{d\xi}\right]^2+k_i^2[R_i^2(1)-s^2R_i^2(s)]-\mu^2[R_i^2(1)-R_i^2(s)]\right\}, \tag{41}$$

in which $dR_i(s)/d\xi=dR_i(\xi)/d\xi|_{\xi=s}$ and $dR_i(1)/d\xi=dR_i(\xi)/d\xi|_{\xi=1}$. Utilizing Eq. (40), we can derive the following equation from Eq. (39):

$$\frac{d^2F_i(\tau)}{d\tau^2}+\omega_i^2F_i(\tau)=q_i(\tau), \tag{42}$$

where

$$q_i(\tau)=q_{1i}(\tau)+h_{1i}d(\tau)+h_{2i}\ddot{d}(\tau),$$

$$\omega_i=k_ic_L, \quad q_{1i}(\tau)=-\frac{c_L^2}{N_i}\int_s^1 \xi g_1(\xi,\tau)R_i(\xi)d\xi, \tag{43}$$

$$h_{1i}=-\frac{c_L^2}{N_i}\int_s^1 \xi g_2(\xi)R_i(\xi)d\xi, \quad h_{2i}=-\frac{c_L^2}{N_i}\int_s^1 \xi g_3(\xi)R_i(\xi)d\xi.$$

The solution of Eq. (42) is

$$F_i(\tau)=H_{1i}\cos\omega_i\tau+\frac{H_{2i}}{\omega_i}\sin\omega_i\tau+\frac{1}{\omega_i}\int_0^\tau q_i(p)\sin\omega_i(\tau-p)dp. \tag{44a}$$

We can derive the following equation from Eq. (44*a*)

$$\dot{F}_i(\tau)=-\omega_iH_{1i}\sin\omega_i\tau+H_{2i}\cos\omega_i\tau+\int_0^\tau q_i(p)\cos\omega_i(\tau-p)dp, \tag{44b}$$

where H_{1i} and H_{2i} are unknown constants. Using Eq. (35), Eq. (32), and utilizing Eq. (40), gives

$$H_{1i}=I_{1i}+I_{2i}d(0), \quad H_{2i}=I_{3i}+I_{2i}\dot{d}(0), \tag{45}$$

where

$$I_{1i}=\frac{1}{N_i}\int_s^1 \xi u_2(\xi)R_i(\xi)d\xi, \quad I_{2i}=\frac{-1}{N_i}\int_s^1 \xi f_3(\xi)R_i(\xi)d\xi,$$

$$I_{3i}=\frac{1}{N_i}\int_s^1 \xi v_2(\xi)R_i(\xi)d\xi. \tag{46}$$

Noticing that $q_i(\tau)$ in Eq. (44) includes $\ddot{d}(\tau)$, we use the integration-by-parts formula and obtain

$$\int_0^\tau \ddot{d}(p)\sin\omega_i(\tau-p)dp$$

$$=-\dot{d}(0)\sin\omega_i\tau-d(0)\omega_i\cos\omega_i\tau+\omega_i d(\tau)$$

$$-\omega_i^2\int_0^\tau d(p)\sin\omega_i(\tau-p)dp. \tag{47}$$

Substituting the first equation in Eq. (43) into Eq. (44*a*) and utilizing Eq. (47), gives

$$F_i(\tau)=F_{1i}(\tau)+h_{2i}d(\tau)+\left(\frac{h_{1i}}{\omega_i}-h_{2i}\omega_i\right)\int_0^\tau d(p)\sin\omega_i(\tau-p)dp, \tag{48}$$

where

$$F_{1i}(\tau)=H_{1i}\cos\omega_i\tau+\frac{H_{2i}}{\omega_i}\sin\omega_i\tau+\frac{1}{\omega_i}\int_0^\tau q_{1i}(p)\sin\omega_i(\tau-p)dp$$

$$-\frac{h_{2i}}{\omega_i}[\dot{d}(0)\sin\omega_i\tau+d(0)\omega_i\cos\omega_i\tau]. \tag{49}$$

In the following, we will determine $d(\tau)$ from the electric boundary conditions. Substituting Eq. (15) into Eq. (12), gives

$$\frac{\partial\phi}{\partial\xi}=2e_1\frac{u}{\xi}+e_3\frac{\partial u}{\partial\xi}-\frac{1}{\xi^2}d(\tau). \tag{50}$$

Then substituting Eq. (24) into Eq. (19), and utilizing Eqs. (28) and (35), we obtain

$$u(\xi,\tau)=\xi^{-1/2}\left[\sum_i R_i(\xi)F_i(\tau)+f_1(\xi)p_a(\tau)+f_2(\xi)p_b(\tau)\right.$$

$$\left.+f_3(\xi)d(\tau)\right]. \tag{51}$$

Integrating Eq. (50) and utilizing Eq. (51), derives

$$\phi(\xi,\tau)=\phi_1(\xi)p_a(\tau)+\phi_2(\xi)p_b(\tau)+\phi_3(\xi)d(\tau)$$

$$+\sum_i \phi_{4i}(\xi)F_i(\tau)+\phi_a(\tau), \tag{52}$$

where

$$\phi_1(\xi)=2e_1\int_s^\xi \xi^{-3/2}f_1(\xi)d\xi+e_3[\xi^{-1/2}f_1(\xi)-s^{-1/2}f_1(s)],$$

$$\phi_2(\xi)=2e_1\int_s^\xi \xi^{-3/2}f_2(\xi)d\xi+e_3[\xi^{-1/2}f_2(\xi)-s^{-1/2}f_2(s)],$$

$$\phi_3(\xi)=2e_1\int_s^\xi \xi^{-3/2}f_3(\xi)d\xi+e_3[\xi^{-1/2}f_3(\xi)-s^{-1/2}f_3(s)]+\frac{1}{\xi}-\frac{1}{s}, \tag{53}$$

$$\phi_{4i}(\xi)=2e_1\int_s^\xi \xi^{-3/2}R_i(\xi)d\xi+e_3[\xi^{-1/2}R_i(\xi))-s^{-1/2}R_i(s)].$$

If $\xi=1$, Eq. (52) reads as

$$\phi_b(\tau)=\phi_1(1)p_a(\tau)+\phi_2(1)p_b(\tau)+\phi_3(1)d(\tau)$$

$$+\sum_i \phi_{4i}(1)F_i(\tau)+\phi_a(\tau). \tag{54}$$

Then

$$\dot{\phi}_b(\tau)=\phi_1(1)\dot{p}_a(\tau)+\phi_2(1)\dot{p}_b(\tau)+\phi_3(1)\dot{d}(\tau)$$

$$+\sum_i \phi_{4i}(1)\dot{F}_i(\tau)+\dot{\phi}_a(\tau). \tag{55}$$

If $\tau=0$, we can determine $d(0)$ and $\dot{d}(0)$ from Eqs. (54) and (55) by virtue of Eqs. (44) and (45):

$$d(0)=\frac{\phi_b(0)-\phi_a(0)-\phi_1(1)p_a(0)-\phi_2(1)p_b(0)-\Sigma_i\phi_{4i}(1)I_{1i}}{\phi_3(1)+\Sigma_i\phi_{4i}(1)I_{2i}}, \tag{56}$$

$$\dot{d}(0)=\frac{\dot{\phi}_b(0)-\dot{\phi}_a(0)-\phi_1(1)\dot{p}_a(0)-\phi_2(1)\dot{p}_b(0)-\Sigma_i\phi_{4i}(1)I_{3i}}{\phi_3(1)+\Sigma_i\phi_{4i}(1)I_{2i}}.$$

Substituting $d(0)$ and $\dot{d}(0)$ into Eqs. (45) and (49), then H_{1i} and H_{2i} become known and $F_{1i}(\tau)$ is a known function. Substituting Eq. (48) into Eq. (54) derives

$$\psi(\tau)=E_1d(\tau)+\sum_i E_{2i}\int_0^\tau d(p)\sin\omega_i(\tau-p)dp, \tag{57}$$

where

$$\psi(\tau)=\phi_b(\tau)-\phi_a(\tau)-\phi_1(1)p_a(\tau)-\phi_2(1)p_b(\tau)$$

$$-\sum_i \phi_{4i}(1)F_{1i}(\tau), \tag{58}$$

$$E_1=\phi_3(1)+\sum_i \phi_{4i}(1)h_{2i}, \quad E_{2i}=\phi_{4i}(1)\left(\frac{h_{1i}}{\omega_i}-h_{2i}\omega_i\right).$$

It is noted that Eq. (57) is a Volterra integral equation of the second kind, which is sure to have a unique solution, [17]. For some cases, the analytical solutions can be obtained. While for the general case, numerical methods are needed. In this paper, we will construct the recursive formula by making use of a linear interpolation function approximation of $d(\tau)$. Practically, the numerical result can be obtained efficiently by the present method. In order to show the method, we first divide the time interval $[0,\tau_n]$ into n subintervals, with discrete time points $\tau_0=0$, τ_1, $\tau_2,\ldots\tau_n$. Then the interpolation function at the interval $[\tau_{j-1},\tau_j]$ is

$$d(\tau)=\zeta_j(\tau)d(\tau_{j-1})+\eta_j(\tau)d(\tau_j) \quad (j=1,2,\ldots,n), \tag{59}$$

where

$$\zeta_j(\tau)=\frac{\tau-\tau_j}{\tau_{j-1}-\tau_j}, \quad \eta_j(\tau)=\frac{\tau-\tau_{j-1}}{\tau_j-\tau_{j-1}}, \quad (j=1,2,\ldots,n). \tag{60}$$

Substituting Eq. (59) into Eq. (57), gives

$$\psi(\tau_j)=E_1d(\tau_j)+\sum_i E_{2i}\sum_{k=1}^{j}[L_{ijk}d(\tau_{k-1})+M_{ijk}d(\tau_k)] \tag{61}$$

where

$$L_{ijk}=\int_{\tau_{k-1}}^{\tau_k}\zeta_k(p)\sin\omega_i(\tau_j-p)dp,$$

$$M_{ijk}=\int_{\tau_{k-1}}^{\tau_k}\eta_k(p)\sin\omega_i(\tau_j-p)dp,$$

$$(k=1,2\ldots j, \quad j=1,2\ldots n). \tag{62}$$

Then we can derive the following formula from Eq. (61):

$$d(\tau_j) = \frac{\psi(\tau_j) - \Sigma_i E_{2i} \Sigma_{k=1}^{j-1} [L_{ijk} d(\tau_{k-1}) + M_{ijk} d(\tau_k)] - d(\tau_{j-1}) \Sigma_i E_{2i} L_{ijj}}{E_1 + \Sigma_i E_{2i} M_{ijj}}, \quad (j = 1,2 \ldots n). \tag{63}$$

In Eq. (56), we have obtained $d(0)$, then from which we can obtain $d(\tau_j)$, $(j=1,2,\ldots,n)$ step by step by virtue of Eq. (63). After $d(\tau)$ is obtained, $u(\xi,\tau)$ and $\phi(\xi,\tau)$ also can be determined.

4 Numerical Results and Discussions

We first study the validity of the proposed numerical method for solving the integral equation $\psi(\tau) = E_1 d(\tau) + \Sigma_{i=1}^{m} E_{2i} \int_0^\tau d(p) \sin \omega_i (\tau - p) dp$. Note that if $d(\tau)$ is a polynomial or an exponential function of time τ, the function $\psi(\tau)$ can be obtained explicitly by substituting $d(\tau)$ into the integral equation and performing the integration analytically.

Example 1. In this example, we consider two forms of $d(\tau)$, i.e., $d(\tau) = 100.0 + 50.0\tau + 2.0\tau^2 + 0.1\tau^3$ and $d(\tau) = 100.0 \times e^{-0.2\tau} + 50.0$, for which analytical express of $\psi(\tau)$ can be obtained. For calculation, we take $m=30$, $\omega_i = \{1.4278,\ 7.4792,\ 14.6938,\ 21.9699,\ 29.2605,\ 36.5568,\ 43.8559,\ 51.1566,\ 58.4583,\ 65.7607,\ 73.0635,\ 80.3667,\ 87.6701,\ 94.9737,\ 102.2775,\ 109.5814,\ 116.8854,\ 124.1895,\ 131.4936,\ 138.7978,146.1021,\ 153.4064,\ 160.7107,\ 168.015,\ 175.3194,\ 182.6238,\ 189.9283,\ 197.2327,\ 204.5372,\ 211.8417\}$, $E_1 = -0.691662$, $E_{2i} = \{0.1040,\ 0.60669,\ 0.0093643,\ 0.19733,\ 0.0044263,\ 0.117959,\ 0.00291596,\ 0.0841636,\ 0.0021776,\ 0.0654299,\ 0.0017385,\ 0.05352,\ 0.0014472,\ 0.04528,\ 0.0012396,\ 0.03924,\ 0.0010842,\ 0.03462,\ 0.00096343,\ 0.030976,\ 0.0008669,\ 0.028025,\ 0.00078796,\ 0.025587,\ 0.0007222,\ 0.02354,\ 0.0006666,\ 0.021796,\ 0.00061894,\ 0.020296\}$, and $\psi(\tau)$ is obtained theoretically by substituting the prescribed $d(\tau)$ into the integral equation. The results presented in Tables 1 and 2 are for the polynomial $d(\tau)$, while those in Tables 3 and 4 for the exponential $d(\tau)$. The method using the trapezium rule to solve the integral equation can be found in Ref. [18].

From Tables 1–4, we can find that the present method has a very high accuracy for numerical computation. In the following, we will study the transient response of a piezoelectric hollow sphere using the present method.

Example 2. The transient response of a PZT-4 piezoelectric hollow sphere subjected to a constant pressure suddenly applied on the internal surface is considered. The material constants are $c_{11} = c_{22} = 139.0$ GPa, $c_{12} = 77.8$ GPa, $c_{13} = 74.3$ GPa, $c_{33} = 115.4$ GPa, $e_{31} = -5.2$ C/m^2, $e_{33} = 15.1$ C/m^2, $\varepsilon_{33} = 5.62 \times 10^{-9}$ C^2/(Nm^2). For the sake of comparison, we also consider an elastic hollow sphere with the elastic constants identical to those of the PZT-4 sphere. The boundary conditions are

$$p_a(\tau) = -\sigma_0 H(\tau), \quad p_b(\tau) = 0.0, \qquad \phi_a(\tau) = 0.0, \quad \phi_b(\tau) = 0.0, \tag{64}$$

where σ_0 is a prescribed constant stress, and $H(\tau)$ is the Heaviside function. In the following, we take $\sigma_0 = 1.0$, $s = 0.5$, $m = 2$, and $n = 200$, and the first 40 terms of the series in Eq. (35) for numerical calculations.

Figure 1 shows the responses of σ_r at $\xi = 0.75$ (the middle surface) in the PZT-4 and elastic hollow spheres. From the curves, we can see that the curve of the PZT-4 sphere is different from that of the elastic one.

Figure 2 gives the responses of σ_θ at $\xi = 0.5$ (the internal surface) in the PZT-4 and elastic hollow spheres. For the PZT-4 sphere, we find that the maximum value of the dynamic hoop stress appears at the internal surface, which is tensile. The first peak value appears at the time $\tau = 1.45$ and it is 2.25 times of the applied stress. For the elastic hollow sphere, we have almost the same observations, except that the first peak value is just 1.99 times of the applied stress, which is less than that in the PZT-4 sphere.

Figures 3 and 4 illustrate the responses of dimensionless radial electric displacement D at different locations ($\xi = 0.5$, $\xi = 0.75$ and $\xi = 1.0$) and the distributions of dimensionless electric potential ϕ at the different times ($\tau = 0.1$, $\tau = 0.2$ and $\tau = 0.5$), respectively, in the PZT-4 hollow sphere subjected to a sudden constant pressure on the internal surface. From Fig. 4, we find that the calculated electric potentials both at the internal and external surfaces are

Table 1 Numerical results for step length $\Delta\tau = 0.1$

		The Trapezium Rule		The Present Method	
Time	Theoretical Results	Numerical Results	Relative Error	Numerical Results	Relative Error
0.0	100.0	100.0000	0.000	100.000	0.000
2.0	208.8	193.6295	−7.266E-2	208.8018	8.842E-6
4.0	338.4	322.9652	−4.561E-2	338.4019	5.681E-6
6.0	493.6	470.8311	−4.613E-2	493.6021	4.328E-6
8.0	679.2	650.1156	−4.282E-2	679.2021	3.145E-6
10.0	900.0	862.1855	−4.202E-2	900.0021	2.306E-6

Table 2 Numerical results for step length $\Delta\tau = 0.5$

		The Trapezium Rule		The Present Method	
Time	Theoretical Results	Numerical Results	Relative Error	Numerical Results	Relative Error
0.0	100.0	100.000	0.000	100.000	0.000
10.0	900.0	686.866	−0.237	900.072	7.948E-5
20.0	2700.0	2059.821	−0.237	2700.131	4.856E-5
30.0	6100.0	4612.715	−0.244	6100.163	2.674E-5
40.0	11700.0	8857.273	−0.243	11700.231	1.978E-5
50.0	20100.0	15218.591	−0.243	20100.282	1.380E-5

Table 3 Numerical results for step length $\Delta\tau = 0.1$

		The Trapezium Rule		The Present Method	
Time	Theoretical Results	Numerical Results	Relative Error	Numerical Results	Relative Error
0.0	150.000	150.000	0.000	150.000	0.000
2.0	117.032	101.913	−1.289E-1	117.033	1.050E-5
4.0	94.933	91.641	−3.468E-2	94.933	5.867E-6
6.0	80.119	73.017	−8.865E-2	80.120	6.475E-6
8.0	70.190	71.912	2.454E-2	70.189	−2.609E-6
10.0	63.534	63.653	1.882E-3	63.533	−5.344E-6

Table 4 Numerical results for step length $\Delta\tau = 0.5$

		The Trapezium Rule		The Present Method	
Time	Theoretical Results	Numerical Results	Relative Error	Numerical Results	Relative Error
0.0	150.000	150.000	0.000	150.000	0.000
10.0	63.534	53.110	−0.164	63.536	3.254E-5
20.0	51.832	42.306	−0.184	51.845	2.505E-4
30.0	50.248	31.182	−0.379	50.245	−5.253E-5
40.0	50.036	39.326	−0.214	50.051	3.500E-4
50.0	50.005	37.043	−0.259	50.020	3.028E-4

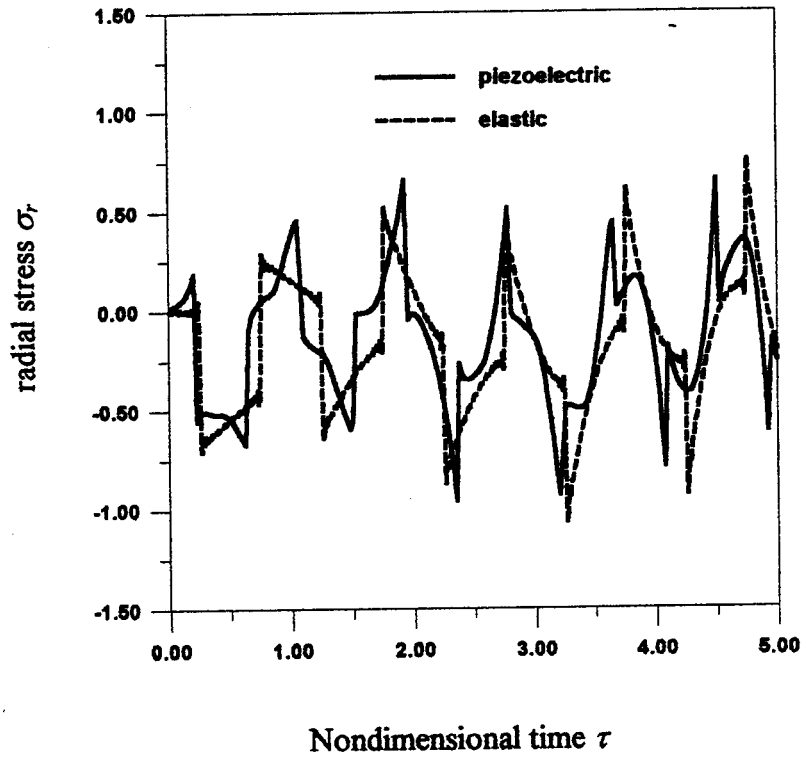

Fig. 1 History of dynamic stress σ_r at ξ=0.75

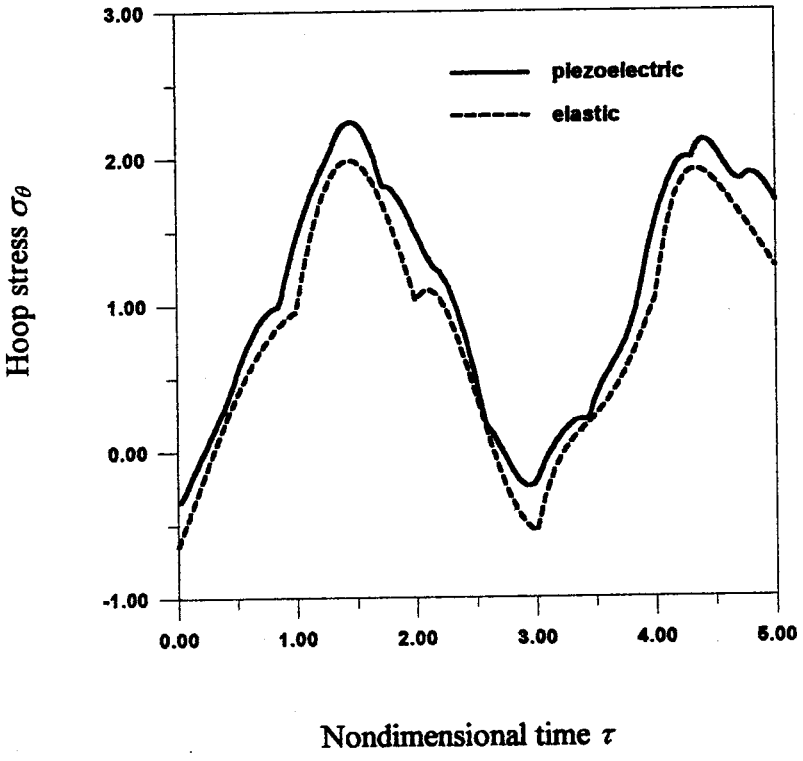

Fig. 2 History of dynamic stress σ_θ at ξ=0.5

zero, which satisfy the prescribed electric boundary conditions. The correctness of the numerical results is thus clarified in this respect.

Example 3. The transient response of a PZT-4 piezoelectric hollow sphere subjected to a constant electric potential suddenly imposed on the external surface is considered here. The material constants are the same as those in Example 2. The boundary conditions become

$$p_a(\tau)=0.0, \quad p_b(\tau)=0.0, \tag{65}$$

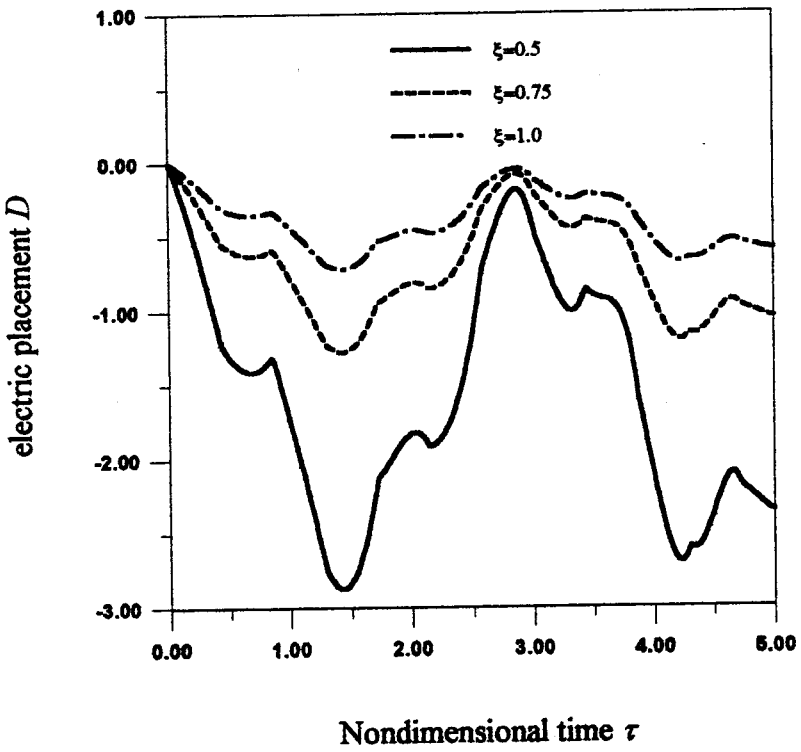

Fig. 3 Histories of dynamic electric displacement *D* at different locations

$$\phi_a(\tau)=0.0, \quad \phi_b(\tau)=\phi_0 H(\tau),$$

where ϕ_0 is the prescribed constant electric potential. For numerical calculations, the same parameters as that in Example 2 are employed, except that $\phi_0=1.0$ is used instead of $\sigma_0=1.0$.

Figures 5 and 6 show the dynamic responses of σ_r and σ_θ in the PZT-4 hollow sphere. From the results, we find that the maximum value of σ_r appears near $\xi=0.75$ (the middle surface), while that of σ_θ appears at $\xi=0.5$ (the internal surface). The first peak

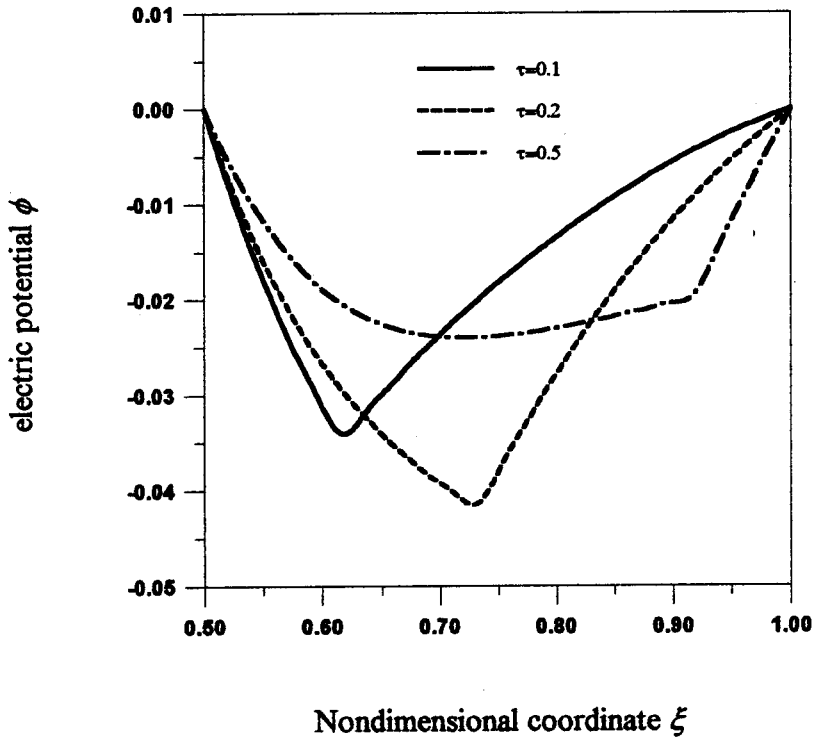

Fig. 4 Distributions of dynamic electric potential ϕ at different times

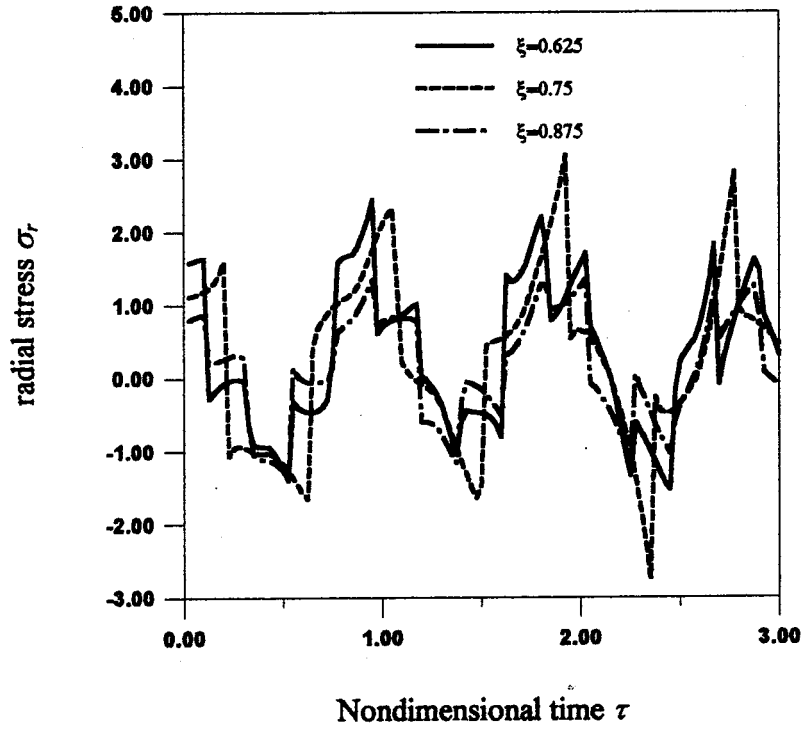

Fig. 5 Histories of dynamic stress σ_r at different locations

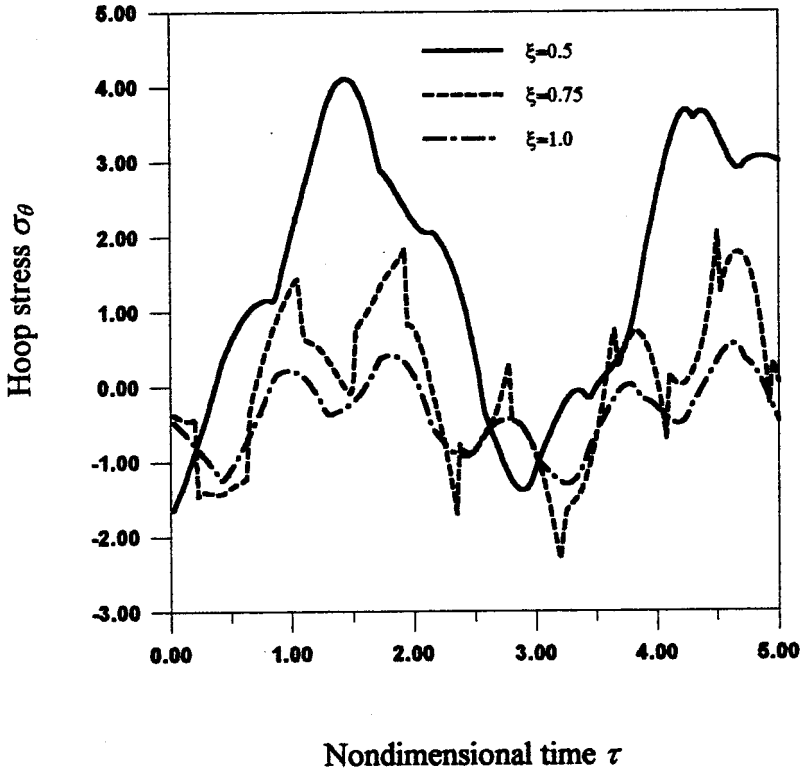

Fig. 6 Histories of dynamic stress σ_θ at different locations

value of σ_θ is 4.11 that appears at $\tau=1.45$. Figures 7 and 8 give the dynamic responses of D and ϕ at different locations ($\xi=0.5$, $\xi=0.75$, and $\xi=1.0$) in the PZT-4 sphere. It is seen that the maximum absolute value of D appears at the internal surface, and the calculated electric potential also satisfies the prescribed electric boundary conditions.

In terms of the numerical results for different terms of the series in Eq. (35), we find that the results vary very slightly between that of 30 terms and 40 terms. So we take the first 40 terms of the series in Eq. (35) for computation involved in Examples 2 and 3.

If the electric boundary conditions in Eq. (10*b*) are expressed by the electric displacement, only one boundary condition will be

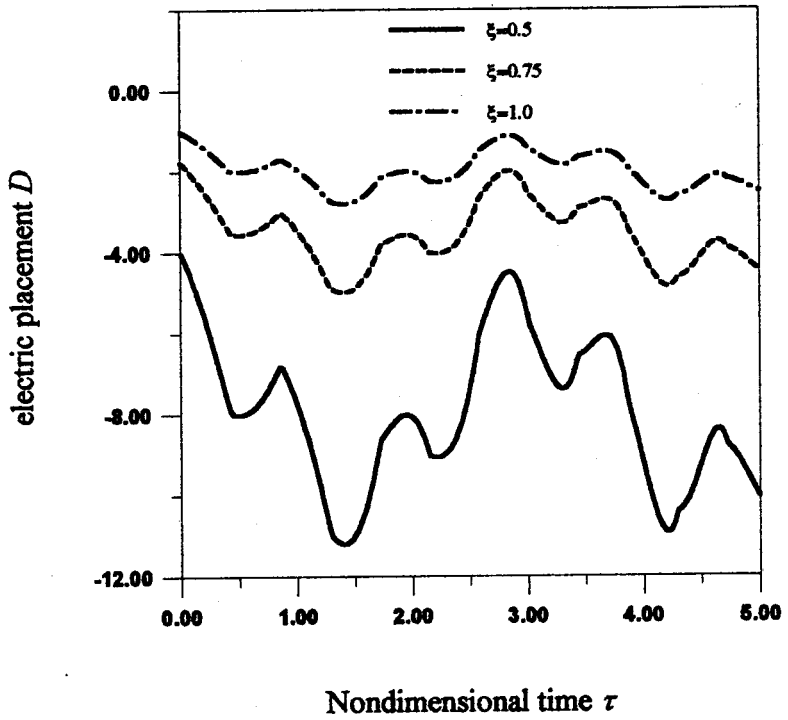

Fig. 7 Histories of dynamic electric displacement *D* at different locations

involved. That is because, if the electric displacement is prescribed on one surface, then the distribution of the electric displacement can be determined immediately from Eq. (15). In this case, from the beginning to Eq. (49), the displacement solution can be determined and the procedure of solving the integral equation can be avoided. The expression for electric potential can also be written as Eq. (52). But if we want to determine $\phi(\xi,\tau)$ completely, one boundary condition related to ϕ must be known. That is, either $\phi_a(\tau)$ or $\phi_b(\tau)$ should be prescribed. The relationship between $\phi_a(\tau)$ and $\phi_b(\tau)$ is given in Eq. (54).

If $\zeta_k(\tau)$ and $\eta_k(\tau)$ are polynomials of τ, the integration in Eq. (62) can be obtained explicitly, which can improve the computing

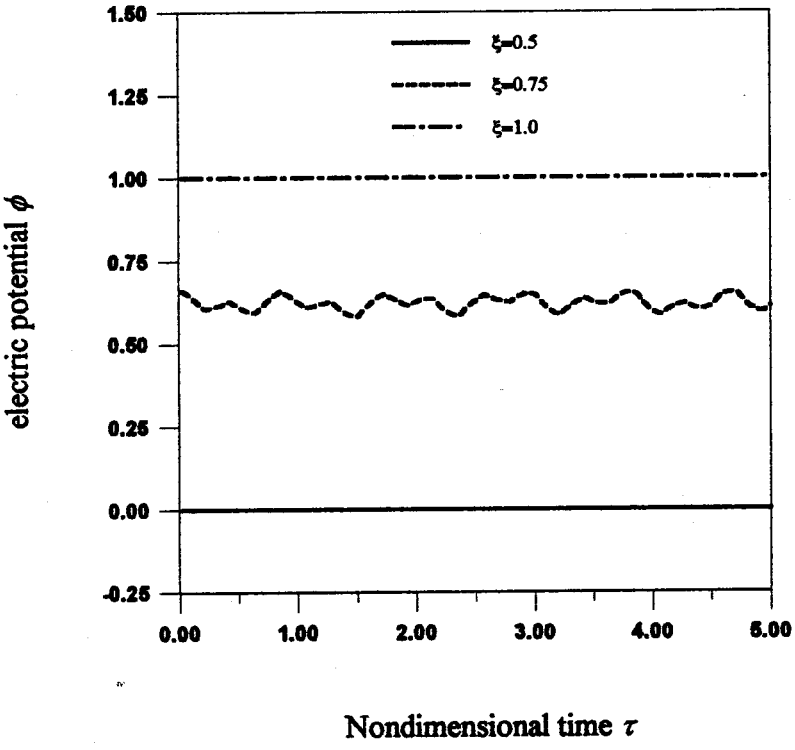

Fig. 8 Histories of dynamic electric potential ϕ at different locations

accuracy. Using linear or high-order interpolation functions to approximate $d(\tau)$, accurate results can be obtained efficiently. It is noted here that the recursive formula is very simple for the linear interpolation function approximation, especially when an equal time-step is adopted. Based on many numerical tests, we find that satisfactory numerical results can be obtained when the time-step $\Delta\tau \leqslant 0.05$.

5 Conclusions

The paper firstly transforms the spherically symmetric elastodynamic problem of a piezoelectric spherically isotropic hollow sphere into a Volterra integral equation of the second kind about a function with respect to time. Then a highly accurate numerical method is particularly proposed and the problem is then completely solved. The work enriches the solution method for dynamic problems in piezoelasticity. It is also very useful for carrying out the active control of structures using piezoelectric materials.

Acknowledgments

The work was supported by the National Natural Science Foundation of China (No. 10172075).

References

[1] Huth, J. H., and Cole, J. D., 1955, ''Elastic-Stress Waves Produced by Pressure Loads on a Spherical Shell,'' ASME J. Appl. Mech., **22**, pp. 473–478.
[2] Baker, W. E., Hu, W. C. L., and Jackson, T. R., 1966, ''Elastic Response of Thin Spherical Shells to Axisymmetric Blast Loading,'' ASME J. Appl. Mech., **33**, pp. 800–806.
[3] Chou, P. C., and Koenig, H. A., 1966, ''A Unified Approach to Cylindrical and Spherical Elastic Waves by Method of Characters,'' ASME J. Appl. Mech., **33**, pp. 159–167.
[4] Rose, J. L., Chou, S. C., and Chou, P. C., 1973, ''Vibration Analysis of Thick-Walled Spheres and Cylinders,'' J. Acoust. Soc. Am., **53**, pp. 771–776.
[5] Cinelli, G., 1966, ''Dynamic Vibrations and Stresses in Elastic Cylinders and Spheres,'' ASME J. Appl. Mech., **33**, pp. 825–830.
[6] Pao, Y. H., and Ceranoglu, A. N., 1978, ''Determination of Transient Responses of a Thick-Walled Spherical Shell by the Ray Theory,'' ASME J. Appl. Mech., **45**, pp. 114–122.
[7] Loza, I. A., and Shul'ga, N. A., 1984, ''Axisymmetric Vibrations of a Hollow Piezoceramic Sphere With Radial Polarization,'' Sov. Appl. Mech., **20**, pp. 113–117.
[8] Loza, I. A., and Shul'ga, N. A., 1990, ''Forced Axisymmetric Vibrations of a Hollow Piezoceramic Sphere With an Electrical Method of Excitation,'' Sov. Appl. Mech., **26**, pp. 818–822.
[9] Shul'ga, N. A., 1986, ''Electroelastic Oscillation of a Piezoceramic Sphere With Radial Polarization,'' Sov. Appl. Mech., **22**, pp. 497–500.
[10] Shul'ga, N. A., 1990, ''Radial Electroelastic Vibrations of a Hollow Piezoceramic Sphere,'' Sov. Appl. Mech., **22**, pp. 731–734.
[11] Shul'ga, N. A., 1993, ''Harmonic Electroelastic Oscillations of Spherical Bodies,'' Sov. Appl. Mech., **29**, pp. 812–817.
[12] Heyliger, P., and Wu, Y. C., 1999, ''Electroelastic Fields in Layered Piezoelectric Spheres,'' Int. J. Eng. Sci., **37**, pp. 143–161.
[13] Cai, J. B., Chen, W. Q., Ye, G. R., and Ding, H. J., 2000, ''Natural Frequencies of Submerged Piezoceramic Hollow Spheres,'' Acta Mech. Sin., **16**, pp. 55–62.
[14] Chen, W. Q., Ding, H. J., and Xu, R. Q., 2001, ''Three Dimensional Free Vibration Analysis of a Fluid-Filled Piezoelectric Hollow Sphere,'' Comput. Struct., **79**, pp. 653–663.
[15] Borisyuk, A. I., and Kirichok, I. F., 1979, ''Steady-State Radial Vibrations of Piezoceramic Spheres in Compressible Fluid,'' Sov. Appl. Mech., **15**, pp. 936–940.
[16] Li, H. Y., Liu, Z. X., and Lin, Q. R., 2000, ''Spherical-Symmetric Steady-State Response of Piezoelectric Spherical Shell Under External Excitation,'' Appl. Math. Mech., **21**, pp. 947–956.
[17] Kress, R., 1989, *Linear Integral Equations (Applied Mathematical Sciences, Volume 82)*, Springer-Verlag, Berlin.
[18] Christopher, T. H., and Baker, M. A., 1977, *The Numerical Treatment of Integral Equations*, Clarendon Press, Oxford, UK.

Journal of Applied Mechanics

Brief Notes

A Brief Note is a short paper that presents a specific solution of technical interest in mechanics but which does not necessarily contain new general methods or results. A Brief Note should not exceed 2500 words *or equivalent* (a typical one-column figure or table is equivalent to 250 words; a one line equation to 30 words). Brief Notes will be subject to the usual review procedures prior to publication. After approval such Notes will be published as soon as possible. The Notes should be submitted to the Editor of the JOURNAL OF APPLIED MECHANICS. Discussions on the Brief Notes should be addressed to the Editorial Department, ASME International, Three Park Avenue, New York, NY 10016-5990, or to the Editor of the JOURNAL OF APPLIED MECHANICS. Discussions on Brief Notes appearing in this issue will be accepted until two months after publication. Readers who need more time to prepare a Discussion should request an extension of the deadline from the Editorial Department.

Elastic Singularity Interacting With Various Types of Interfaces

S. T. Choi

Y. Y. Earmme[1]
e-mail: yyearmme@kaist.ac.kr
Mem. ASME

Department of Mechanical Engineering, ME3013 KAIST, Science Town, Daejeon 305-701, Republic of Korea

The elastic solution for a singularity in an anisotropic trimaterial with perfectly bonded interfaces was obtained in the previous work by Choi and Earmme. The term "trimaterial" denotes an infinite body composed of three dissimilar materials bonded along two parallel interfaces. It is shown in this paper that when the interfaces of an anisotropic trimaterial are one of the following types: (i) perfectly bonded, (ii) rigid, (iii) separated, (iv) separated without slip, and (v) slipping interfaces, the elastic solution for a singularity in the trimaterial has the same form as that for a singularity in a trimaterial with perfectly bonded interfaces, but with the bimaterial matrices properly altered.
[DOI: 10.1115/1.1571858]

1 Introduction

The interface between two monocrystalline materials exists in frequently used structures of microelectronics and optoelectronics. To accommodate the lattice mismatch across the interface, various types of interfaces and interface structures evolve in such a way that the total free energy of the system is at its lowest value, [1]. For example, the defects like dislocations are often formed at the interface to relax the mismatch strain, and the periodic array of those dislocations makes the interface incoherent. However, the elastic field near defects cannot be easily obtained because of the difficulty in satisfying the boundary conditions at the free surfaces and/or various types of interfaces. Recently, Choi and Earmme [2] obtained the solution of a singularity in an anisotropic trimaterial by employing the method of analytic continuation, [3], and Schwarz-Neumann's alternating technique, [4]. In their study, two interfaces are considered as perfectly bonded interfaces. It will be shown in this study that the solution of a singularity in an anisotropic trimaterial with (i) perfectly bonded, (ii) separated, (iii) rigid, (iv) separated without slip, and (v) slipping interfaces can be easily obtained from their solution. To make this presentation concise, the notations in [2] are employed here and the reader is referred to [2] if the more detailed explanation or explicit form is needed for the quantity omitted here for convenience of reduction in length.

2 Solution Procedure and Result

The elastic field of an anisotropic body can be represented in terms of three functions $f_j(z_j)$ $(j=1,2,3)$, each of which is analytic in its argument $z_j = x_1 + \bar{\mu}_j x_2$ for a two-dimensional problem, i.e., with geometry and external loading invariant in the x_3-direction. Here μ_j is the eigenvalue with positive imaginary part of the sextic equation, Eq. (6) of [2]. The convention of summation over a repeated subscript is used, but the index with underlined bar does not imply summation, that is, $A_{ij}f_j(z_j) = A_{i1}f_1(z_1) + A_{i2}f_2(z_2) + A_{i3}f_3(z_3)$ but $f_j(z_j) \neq f_1(z_1) + f_2(z_2) + f_3(z_3)$. If the anisotropic material has the monoclinic symmetry plane with respect to $x_3 = 0$, the in-plane and antiplane deformations are decoupled, [5], which will be separately considered in this paper. The coupled case may be easily treated by the extension of the same procedure as described in this paper, however, we omit it in this brief note.

In-Plane Deformation. Let us consider an anisotropic bimaterial (Fig. 1(*a*)) undergoing inplane deformation. Across the interface, the normal and shear stresses are continuous, that is, $\sigma^a_{2i}(x_1) = \sigma^b_{2i}(x_1)$ $(i=1,2)$, where the superscripts *a* and *b* stand for materials *a* and *b*, respectively. In this study, five types of interfaces are considered, which are classified according to the boundary conditions as follows:

Type 1(perfectly bonded) : $u^a_1(x_1) = u^b_1(x_1), \quad u^a_2(x_1) = u^b_2(x_1),$

Type 2(separated) : $\sigma^b_{21}(x_1) = \sigma^b_{22}(x_1) = 0,$

Type 3(rigid) : $u^b_1(x_1) = u^b_2(x_1) = 0,$

Type 4(separated without slip) : $u^a_1(x_1) = u^b_1(x_1), \sigma^b_{22}(x_1) = 0,$

Type 5(slipping) : $\sigma^b_{21}(x_1) = 0, u^a_2(x_1) = u^b_2(x_1).$

It is noted here that Type 2 interface means the free surface.

[1]To whom correspondence should be addressed.

Contributed by the Applied Mechanics Division of THE AMERICAN SOCIETY OF MECHANICAL ENGINEERS for publication in the ASME JOURNAL OF APPLIED MECHANICS. Manuscript received by the ASME Applied Mechanics Division, April 21, 2002; final revision, November 12, 2002. Associate Editor: J. R. Barber.

 Copyright © 2003 by ASME

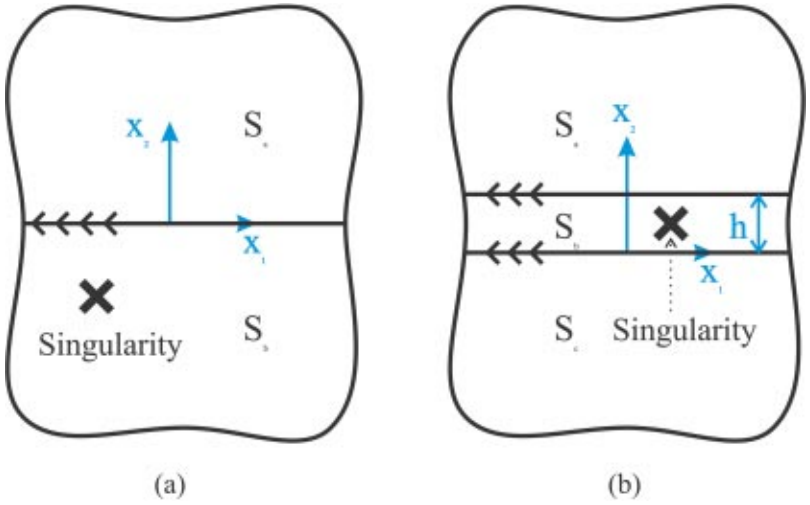

Fig. 1 Singularity in an anisotropic bimaterial (*a*) and trimaterial (*b*)

By applying the method of analytic continuation, Suo [3] expressed the solution for a singularity in an anisotropic bimaterial (Fig. 1(*a*)) with perfectly bonded interface (i.e., Type 1 interface) as follows, [2]:

$$f_i(z_{\underline{i}})=\begin{cases} U_{ij}^{ab} f_j^0(z_{\underline{i}}^a), & \text{in } S_a, \\ \overline{V}_{ij}^{ab}\overline{f}_j^0(z_{\underline{i}}^b)+f_i^0(z_{\underline{i}}^b), & \text{in } S_b, \end{cases} \tag{1}$$

in which $f_j^0(z)$ is the solution for the same singularity in a homogeneous medium, and $\mathbf{U}$ and $\mathbf{V}$ are expressed in terms of material matrices $\mathbf{L}$ and $\mathbf{B}$ as, [2],

$$\mathbf{U}^{ab}=(\mathbf{L}^a)^{-1}(\mathbf{I}+\mathbf{T}^{ab})\mathbf{L}^b, \tag{2}$$

$$\mathbf{V}^{ab}=(\overline{\mathbf{L}}^b)^{-1}\mathbf{T}^{ab}\mathbf{L}^b, \tag{3}$$

$$\mathbf{T}^{ab}=(\mathbf{B}^a+\overline{\mathbf{B}}^b)^{-1}(\mathbf{B}^b-\mathbf{B}^a) \quad \text{(Type 1 interface)}. \tag{4}$$

By employing the similar procedure used by Suo [3] for an anisotropic bimaterial having one of the other types of interface, the solution for a singularity in the anisotropic bimaterial can be obtained, but the details are suppressed here. Interestingly, the solution has the same form as Eq. (1), while only the bimaterial matrix $\mathbf{T}^{ab}$ is altered as follows:

$$\mathbf{T}^{ab}=-\mathbf{I}, \quad \text{(Type 2 interface)} \tag{5}$$

$$\mathbf{T}^{ab}=(\overline{\mathbf{B}}^b)^{-1}\mathbf{B}^b, \quad \text{(Type 3 interface)} \tag{6}$$

$$\mathbf{T}^{ab}=\text{diag}\left(\frac{B_{11}^b-B_{11}^a}{B_{11}^b+B_{11}^a},-1\right), \quad \text{(Type 4 interface)} \tag{7}$$

$$\mathbf{T}^{ab}=\text{diag}\left(-1,\frac{B_{22}^b-B_{22}^a}{B_{22}^b+B_{22}^a}\right), \quad \text{(Type 5 interface)} \tag{8}$$

where diag( ) denotes a diagonal matrix and $\mathbf{I}$ is the identity matrix. We note here that the results obtained from Eqs. (5) and (6) coincide with those of Suo [3]. Also it is remarked here that the matrix $\mathbf{T}^{ab}$ represents the mismatch of elastic constants of two constituent materials and also includes the information about the interface.

Choi and Earmme [2] employed the alternating technique together with the method of analytic continuation to analyze a singularity in a trimaterial with two parallel interfaces (Type 1) as shown in Fig. 1(*b*), resulting in

$$f_i(z_{\underline{i}})=\begin{cases} U_{ij}^{ab}\sum_{n=1}^{\infty} f_j^n(z_{\underline{i}}^a-\mu_{\underline{i}}^a h+\mu_{\underline{j}}^b h), & \text{in } S_a, \\ \sum_{n=1}^{\infty}[f_i^n(z_{\underline{i}}^b)+\overline{V}_{ij}^{ab}\overline{f}_j^n(z_{\underline{i}}^b-\mu_{\underline{i}}^b h+\overline{\mu}_{\underline{j}}^b h)], & \text{in } S_b, \\ U_{ij}^{cb}f_j^0(z_{\underline{i}}^c)+U_{ij}^{cb}\overline{V}_{jk}^{ab}\sum_{n=1}^{\infty}\overline{f}_k^n(z_{\underline{i}}^c-\mu_{\underline{j}}^b h+\overline{\mu}_{\underline{k}}^b h), & \text{in } S_c, \end{cases} \tag{9}$$

in which the recurrence formula for $f_i^n(z)$ is

$$f_i^{n+1}(z)=\begin{cases} f_i^0(z)+\overline{V}_{ij}^{cb}\overline{f}_j^0(z), & \text{if } n=0, \\ \overline{V}_{ij}^{cb}V_{jk}^{ab}f_k^n(z-\overline{\mu}_{\underline{j}}^b h+\mu_{\underline{k}}^b h), & \text{if } n=1,2,3,\ldots. \end{cases} \tag{10}$$

Equation (9) with Eq. (10) is considered as the general solution for a singularity in an anisotropic trimaterial, each interface of which is one of Type 1–5 interfaces. Depending on the type of the interface at $x_2=h$ (and $x_2=0$), all we have to do is to replace the matrix $\mathbf{T}^{ab}$ (and $\mathbf{T}^{cb}$) in Eqs. (9) and (10) by the corresponding matrix given in Eqs. (4)–(8).

Antiplane Deformation. For the antiplane deformation, three types of interfaces are considered as follows:

$$\text{Type 1(perfectly bonded)} : u_3^a(x_1)=u_3^b(x_1),$$

$$\text{Type 2(separated)} : \sigma_{23}^b(x_1)=0,$$

$$\text{Type 3(rigid)} : u_3^b(x_1)=0.$$

Using the same procedure as in in-plane deformation, the general solution for an antiplane singularity regardless of the type of interface is expressed in terms of the solution $f_3^0(z)$ for the same singularity in a homogeneous medium as

$$f_3(z_3)=\begin{cases} (1+T^{ab})f_3^0(z_3^a), & \text{in } S_a, \\ f_3^0(z_3^b)+T^{ab}\overline{f}_3^0(z_3^b), & \text{in } S_b, \end{cases} \tag{11}$$

for an anisotropic bimaterial (Fig. 1(*a*)), [3], and

$$f_3(z_3)=\begin{cases}(1+T^{ab})F(z_3^a-\mu_3^a h+\mu_3^b h), & \text{in } S_a,\\ F(z_3^b)+T^{ab}\overline{F}(z_3^b-2\alpha hi), & \text{in } S_b,\\ (1+T^{cb})[f_3^0(z_3^c)+T^{ab}\overline{F}(z_3^c-2\alpha hi)], & \text{in } S_c,\end{cases} \tag{12}$$

for an anisotropic trimaterial (Fig. 1(*b*)), [2]. Here, $\alpha=\mathrm{Im}(\mu_3^b)$ and

$$F(z)=\sum_{n=0}^{\infty}(T^{cb}T^{ab})^n[f_3^0(z+2\alpha hni)+T^{ab}\overline{f_3^0}(z+2\alpha hni)]. \tag{13}$$

Depending on the type of interface at $x_2=h$ (or $x_2=0$), the constant T^{ab} (or T^{cb}) becomes

$$T^{ab}=\frac{B_{33}^b-B_{33}^a}{B_{33}^b+B_{33}^a}, \quad \text{(Type 1 interface)} \tag{14}$$

$$T^{ab}=-1, \quad \text{(Type 2 interface)} \tag{15}$$

$$T^{ab}=1 \quad \text{(Type 3 interface)}. \tag{16}$$

For line force or screw dislocation at (x_1^0,x_2^0), the homogeneous solution $f_3^0(z)$ is given as

$$f_3^0(z_3)=\frac{q_3}{2\pi}\ln(z_3-s_3), \quad q_3=-\frac{b_3}{2B_{33}}+\frac{p_3}{2}i, \tag{17}$$

where $s_3=x_1^0+\mu_3 x_2^0$. When both interfaces at $x_2=h$ and $x_2=0$ in a trimaterial are rigid interfaces (Type 3) or separated interfaces (Type 2), that is, $T^{ab}=T^{cb}=T=1$ or -1, respectively, using the homogeneous solution (17), the solution given in Eqs. (12) and (13) reduces to a closed form as

$$\begin{aligned}f_3(z_3^b)&=\frac{q_3}{2\pi}\sum_{n=-\infty}^{\infty}\ln(z_3^b-s_3^b+2\alpha hni)\\ &\quad+T\frac{\overline{q}_3}{2\pi}\sum_{n=-\infty}^{\infty}\ln(z_3^b-\overline{s}_3^b+2\alpha hni)\\ &=\frac{q_3}{2\pi}\ln\left\{\sin\left[\frac{\pi i}{2\alpha h}(z_3^b-s_3^b)\right]\right\}\\ &\quad+T\frac{\overline{q}_3}{2\pi}\ln\left\{\sin\left[\frac{\pi i}{2\alpha h}(z_3^b-\overline{s}_3^b)\right]\right\} \quad \text{in } S_b.\end{aligned} \tag{18}$$

By comparing the series solution (the first equality) with the closed-form solution (the second equality) in Eq. (18), it is inferred that the rate of convergence of the series solution depends on the boundary condition at both interfaces through the constant T as well as on the type of singularity through q_3. That is, the solution for line force with $T=1$ (Type 3) is more rapidly convergent than that for line force with $T=-1$ (Type 2). This tendency is reversed for a screw dislocation. It is also inferred from this observation that the rate of convergence of the trimaterial solution given in Eqs. (9) and (10) for in-plane deformation may depend on the boundary condition at both interfaces, the type of singularity, and the direction of singularity (e.g., the direction of Burgers vector), as already mentioned by Choi and Earmme [2].

3 Concluding Remarks

It is shown in this paper that when the interfaces of an anisotropic trimaterial are one of the following types: (i) perfectly bonded, (ii) separated, (iii) rigid, (iv) separated without slip, and (v) slipping interfaces, the elastic solution for a singularity in the trimaterial has the same form as that for a singularity in a trimaterial with perfectly bonded interfaces, but with the bimaterial matrices $\mathbf{T}^{ab}$ and $\mathbf{T}^{cb}$ properly altered. The rate of convergence of the trimaterial solution depends on the bimaterial matrix including the information about the interface and the type of the singularity.

Acknowledgments

Financial support from MOST (the Ministry of Science and Technology, Korea) through Computer Aided Reliability Evaluation (CARE) Laboratory for Electronic Packaging (National Research Laboratory) at KAIST is gratefully acknowledged.

References

[1] Ikuhara, Y., and Pirouz, P., 1998, "High Resolution Transmission Electron Microscopy Studies of Metal/Ceramics Interfaces," Microsc. Res. Tech., **40**, pp. 206–241.

[2] Choi, S. T., and Earmme, Y. Y., 2002, "Elastic Study on Singularities Interacting With Interfaces Using Alternating Technique: Part I. Anisotropic Trimaterial," Int. J. Solids Struct., **39**, pp. 943–957.

[3] Suo, Z., 1990, "Singularities, Interfaces and Cracks in Dissimilar Anisotropic Media," Proc. R. Soc. London, Ser. A, **A427**, pp. 331–358.

[4] Sokolnikoff, I. S., 1956, *Mathematical Theory of Elasticity*, McGraw-Hill, New York, pp. 318–326.

[5] Ting, T. C. T., 1996, *Anisotropic Elasticity: Theory and Applications*, Oxford University Press, New York.

Michell's General Solutions for Torsionless Axisymmetric Problems With Body Forces in Elasticity

Y. C. Lou

M. Z. Wang

Department of Mechanics and Engineering Science, Peking University, Beijing 100871, People's Republic of China

In this note, it is pointed out that simple modified Michell's general solutions may treat the torsionless axisymmetric problems with both axial and radial body forces in elasticity and are more convenient in some cases contrast to Love's solutions.

[DOI: 10.1115/1.1571857]

There are two kinds of general solution for the torsionless axisymmetric problem. One is Love's solution, the other is Michell's solution. Both are complete, [1]. Using Love's solution, Fung [2] obtained the solutions of the problems with body forces f_z. Simmonds [3] solved the problems with both body forces f_z and f_r with a modified form of Love's solution. It will be pointed out in the following discussion that we can also use the modified Michell's general solution to solve the problems with both body forces and for some cases it is more convenient to use Michell's solution.

Referring to circular cylindrical coordinates $\{r,\theta,z\}$, a torsionless axisymmetric displacement field has the form

$$\mathbf{u}=u_r(r,z)\mathbf{e}_r+u_z(r,z)\mathbf{e}_z. \tag{1}$$

Of course, we suppose that the underlying body is a body of revolution, and its half-meridional surface is denoted by G. In this case, the displacement equation of equilibrium for homogeneous, isotropic, linear elasticity with body forces is read as

$$\nabla^2\mathbf{u}+\frac{1}{1-2\nu}\nabla(\nabla\cdot\mathbf{u})=-\frac{1}{\mu}\mathbf{f} \tag{2}$$

Contributed by the Applied Mechanics Division of THE AMERICAN SOCIETY OF MECHANICAL ENGINEERS for publication in the ASME JOURNAL OF APPLIED MECHANICS. Manuscript received by the ASME Applied Mechanics Division, January 30, 2002; final revision, November 11, 2002. Associate Editor: J. R. Barber.

Copyright © 2003 by ASME

where ν is Poisson's ratio, μ is the shear modul, $\mathbf{f}$ is the body force vector, which is given by

$$\mathbf{f}=f_r(r,z)\mathbf{e}_r+f_z(r,z)\mathbf{e}_z. \tag{3}$$

The modified Michell's solution is written as

$$\mathbf{u}=\nabla^2(\mathbf{e}_r M)-\frac{1}{2(1-\nu)}\nabla(\nabla\cdot\mathbf{e}_r M)+\mathbf{e}_r\Phi \tag{4}$$

where M is Michell's potential and Φ exists only when body force f_z is not zero.

Substituting (4) into (2) yields the equations

$$\begin{cases}\left(\nabla^2-\dfrac{1}{r^2}\right)\left(\nabla^2-\dfrac{1}{r^2}\right)M+\nabla^2\Phi+\dfrac{1}{1-2\nu}\dfrac{\partial}{\partial r}\left(\dfrac{\partial\Phi}{\partial r}+\dfrac{\Phi}{r}\right)=-f_r(r,z) & (5a)\\ \dfrac{1}{1-2\nu}\dfrac{\partial}{\partial z}\left(\dfrac{\partial\Phi}{\partial r}+\dfrac{\Phi}{r}\right)=-f_z(r,z). & (5b)\end{cases}$$

Contrast to Love's solution, it is more convenient to use Michell's solution when only body force f_r exists.

From (5*b*), we can get

$$\Phi=-(1-2\nu)r\int_{r_0}^{r}\int_{z_0}^{z}\frac{1}{t}f_z(t,\varsigma)d\varsigma dt. \tag{6}$$

The definite integral in (6) is over the half-meridional surface G. Thus the region G must be both z-convex and r-convex. The case will happen for (2) of Simmonds [3], too. When G is not convex, we have to use two components of Galerkin's vector as Fung's suggestion, [2].

References

[1] Wang, M. Z., 1988, "On the Completeness of Solutions of Boussinesq, Timpe, Love and Michell in Axisymmetric Elasticity," J. Elast., **19**, pp. 85–92.

[2] Fung, Y. Z., 1965, *Foundations of Solid Mechanics*, Prentice-Hall, Englewood Cliffs NJ.

[3] Simmonds, J. G., 2000, "Love's Stress Function for Torsionless Axisymmetric Deformation of Elastically Isotropic Bodies With Body Forces," ASME J. Appl. Mech., **67**, pp. 628–629.

A Note on the Estimation of Nonlinear System Damping

P. J. Torvik

Fellow ASME

Professor Emeritus of Aerospace Engineering and Engineering Mechanics, Air Force Institute of Technology, 1866 Winchester Road, Xenia, OH 45385.

System damping for a single mode in resonance is often estimated from a measurement of the bandwidth of the frequency response function. While the bandwidth is customarily measured between the half-power frequencies, it is also possible to choose any other fraction of the maximum amplitude. If the damping is linear, i.e., if the loss factor is independent of amplitude, the same damping will be found with any such choice. While intuition might suggest that the damping of a nonlinear system would be better estimated from a bandwidth taken closer to the maximum amplitude, this is shown to be false. [DOI: 10.1115/1.1571859]

Contributed by the Applied Mechanics Division of THE AMERICAN SOCIETY OF MECHANICAL ENGINEERS for publication in the ASME JOURNAL OF APPLIED MECHANICS. Manuscript received by the ASME Applied Mechanics Division, March 26, 2002; final revision, December 18, 2002. Associate Editor: N. C. Perkins.

The use of half-power bandwidths (the difference between the two frequencies at 0.707 maximum amplitude) for the extraction of estimates of the loss factor from resonant response curves is discussed in most elementary texts on vibration and has become a staple in the procedures for modal testing, [1]. It is generally understood that the use of this procedure invokes the assumptions that the system acts as a single degree-of-freedom system and that all system elements are linear; in particular, that the damping is linear, i.e., that the loss factor is independent of amplitude.

While it might appear that, when loss factors increase with amplitude, estimates can be improved by taking bandwidths (appropriately compensated) higher on the response curve, i.e., at r-amplitude points, where r is a convenient number in the range $0.707<r<1$. Bandwidths at the half-power and 80% power frequencies are shown on a resonant response curve given as in Fig. 1. It is understood that the degree of experimental error introduced in so doing will increase as the two frequencies to be differenced approach each other. Nonetheless, with data of sufficient quality, it seems intuitively obvious that the use of larger values of r should improve the estimate of damping. It will be shown here that this is false.

Consider a single degree-of-freedom system having the response.

$$\frac{A}{X_{ST}}\approx\sqrt{\frac{1}{(1-f^2)^2+(\eta_0 A^m)^2}} \tag{1}$$

where A is the magnitude of the complex amplitude of the response, $X(t)=A\exp(i\Omega t)$, to an input $F(t)=F_0\exp(i\Omega t)$. In the above, $f=\Omega/\omega_0$, ω_0 is the undamped natural frequency, and $X_{ST}=F_0/K$, K being an effective stiffness. Equation (1) is written for nonlinear structural damping with amplitude dependence modeled by

$$\eta(A)=\eta_0 A^m \tag{2}$$

with $m\geqslant 0$. For the linear system, $m=0$. The response curve in Fig. 1 is for structural damping with $m=1$ and $\eta_0=0.001$. For viscous damping, η_0 may be replaced by $2\xi_0 f$, where ξ is the fraction of critical damping.

After rearranging Eq. (1) into the form

$$f^2=1\pm\sqrt{(X_{ST}/A)^2-(\eta_0 A^m)^2} \tag{3}$$

a relationship between the bandwidth and the damping at the maximum amplitude ($f=1$, or resonance) may be obtained. Clearly, the maximum amplitude A_R occurs when the radical vanishes, or

$$\frac{A_R}{X_{ST}}=\frac{1}{\eta_0 A_R^m}=\frac{1}{\eta(A_R)}. \tag{4}$$

Copyright © 2003 by ASME

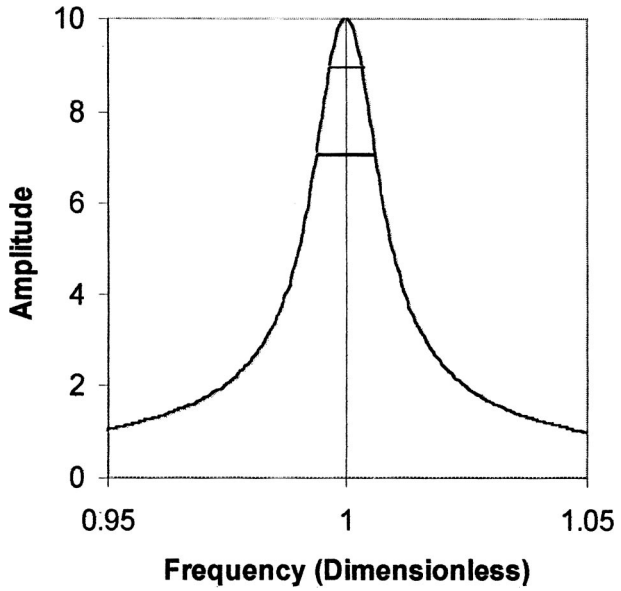

Fig. 1 Frequency response with bandwidths at 50% power and 80% power

Then, if f_1 and f_2 denote the dimensionless frequencies where the amplitude is a fraction, r, of the peak amplitude, Eq. (3) becomes

$$f_{1,2}^2 = 1 \pm \eta(A_R)\sqrt{1/r^2 - r^{2m}}. \tag{5}$$

This bandwidth relationship is most neatly expressed in terms of the difference of squared frequencies, or

$$\eta(A_R) = (f_2^2 - f_1^2)/(2\sqrt{1/r^2 - r^{2m}}). \tag{6}$$

For lightly damped systems, $f_2^2 - f_1^2 \approx 2(f_2 - f_1)$, leading (for $m = 0$) to the familiar result for the half-power bandwidth that $\Delta f = \eta$.

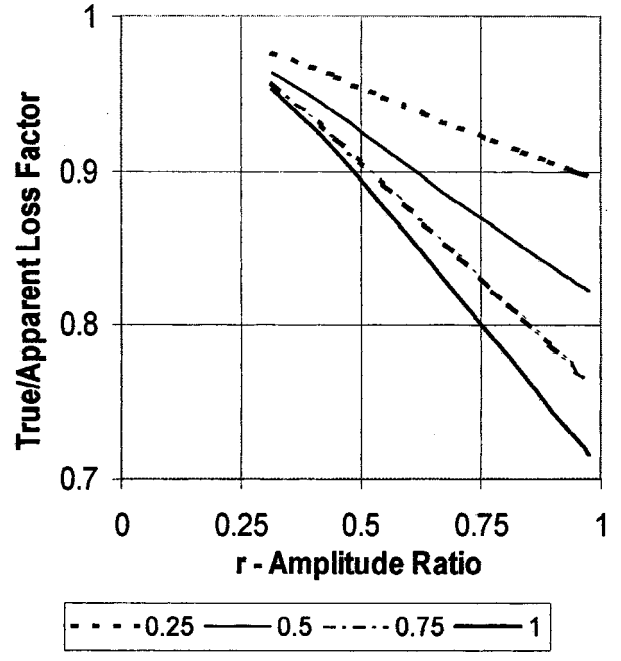

Fig. 2 Estimation of measurement errors introduced by nonlinear damping

For the linear case ($m = 0$), Eq. (6) becomes

$$\eta = (f_2^2 - f_1^2)/(2\sqrt{1/r^2 - 1}), \tag{7}$$

which is the appropriate relationship for estimating loss factors when using other than the half-power points, and is equivalent to other forms, as have been discussed elsewhere, [2]. However, when Eq. (7) is used in the presence of an amplitude-dependent loss factor ($m \neq 0$), it will give only an "apparent" loss factor. The error so introduced may be determined from the ratio of Eqs. (6) and (7), or

$$\eta_{\text{TRUE}} / \eta_{\text{APPARENT}} = \sqrt{1/r^2 - 1}/\sqrt{1/r^2 - r^{2m}}. \tag{8}$$

Values of m in the range of 0 to 1 are of particular interest as it has been observed, [3], that common materials typically dissipate energy according to the form $D = J\sigma^N$, with N falling between 2 and 3 at the values of stress normally allowed in design. As the stored energy is proportional to the square of stress, it follows that the ratio of dissipated to stored energy, and the loss factor for such materials will have amplitude dependence with a power between 0 and 1. The ratio given in Eq. (8) is plotted in Fig. 2 for several such values.

Intuition may lead one to expect that better estimates of the damping corresponding to the peak amplitude should result from observations made closer to that resonant peak. Figure 2 demonstrates that this is not true. Rather, taking observations at larger values of r and using Eq. (7) increases the error when damping increases with amplitude. One should rather take data at lower ratios. For $r = 0.707$ and $m = 1$, the error is of the order of 20%. Not only do the errors increase for larger values of r, but for the structural designer they also become less conservative. An overestimate of damping in the testing of a material or component can lead to an overestimate of the damping of the final system, possibly giving rise to unexpectedly large resonant amplitudes in service. In choosing a lower value of r, one must also exercise caution, as the influence of other modes may be expected to become more significant as the bandwidth is expanded, and measurement noise may be come more significant at the lower signal amplitude. Values of r of 0.707 and 0.577 have been given, [4], as being commonly used.

Once values of loss factor have been obtained over a range of amplitudes by using Eq. (7), the results may be plotted as log loss factor versus log amplitude. If a straight line provides a reasonable "fit," the slope is the appropriate value for the exponent in Eq. (2) and may be used in Eq. (8) to adjust the original results. But, since the necessary correction is smaller for lower values of r, and since the quality of results should improve with the concomitant larger frequency difference (subject to possible influences of other modes and a lower signal/noise ratio), lower values of r are still to be preferred over higher.

References

[1] Ewins, D. J., 1984, *Modal Testing: Theory and Practice*, John Wiley and Sons, New York, p. 188.
[2] Jones, D. I. G., 2001, *Handbook of Viscoelastic Vibration Damping*, John Wiley, Chichester, UK, pp. 16, 208.
[3] Lazan, B. J., 1968, *Damping of Materials and Members in Structural Mechanics*, Pergamon Press, Oxford, UK, p. 135.
[4] Plunkett, R., 1979, "Measurement of Damping," *Structural Damping*, ASME, New York, p. 119.

A Symmetric Boundary Element Method/Finite Element Method Coupling Procedure for Two-Dimensional Elastodynamic Problems

G. Y. Yu
School of Civil and Structural Engineering, Nanyang Technological University, Nanyang Avenue, Singapore 639798
e-mail: cgyyu@ntu.edu.sg

In this paper, a symmetric collocation boundary element method (SCBEM)/finite element method (FEM) coupling procedure is given and applied to a two-dimensional elastodynamic problem. The use of symmetry for the boundary element method not only saves memory storage but also enables the employment of efficient symmetric equation solvers. This is especially important for BEM/FEM coupling procedure. Compared with the symmetric Galerkin boundary element method (SGBEM) where double-space integration should be carried out, SCBEM is easier and faster.
[DOI: 10.1115/1.1571856]

1 Introduction

The traditional collocation boundary element method (TCBEM) has been proven to be useful and robust. However, some unpleasant features hinder its broader applications. The most pertinent is the lack of symmetry for some coefficient matrices, which makes the computer code less efficiency, especially for the boundary element method/finite element method (BEM/FEM) coupling procedure where huge amounts of unknowns often exist in the finite element method domain. Symmetric Galerkin BEM (SGBEM) was first proposed by Sirtori [1] for linear elastic analysis, and then used by many researchers in various applications, [2–4]. One of the main problems for SGBEM is that one has to solve the hypersingular integrals appeared. Although numerous papers have been published to deal with the hypersingular integrals, [5–8], there are still many spaces that need more research works. The double-space integrations can increase the accuracy for SGBEM, but with a cost of computer time.

Through matrix manipulation, symmetric collocation BEM (SCBEM) formulation is derived in this paper. As only one space integration is involved and no hypersingularity appears, the SCBEM/FEM coupling procedure can overcome the defects for SGBEM/FEM while maintain its merits. The accuracy and validity for the symmetric coupling procedure are shown in a classical example.

2 Symmetric Coupling Procedure

The traditional collocation boundary element method (TCBEM) formulation for two-dimensional elastodynamic problems can be written as, [9],

$$\mathbf{H}_D\mathbf{u}^n=\mathbf{G}_D\mathbf{p}^n+\sum_{m=1}^{n-1}\mathbf{G}_D^{mn}\mathbf{p}^m-\sum_{m=1}^{n-1}\mathbf{H}_D^{mn}\mathbf{u}^m \tag{1}$$

Contributed by the Applied Mechanics Division of THE AMERICAN SOCIETY OF MECHANICAL ENGINEERS for publication in the ASME JOURNAL OF APPLIED MECHANICS. Manuscript received by the ASME Applied Mechanics Division, October 7, 2001; final revision, December 17, 2002. Associate Editor: B. M. Moran.

where $\mathbf{u}^m$ and $\mathbf{p}^m$ are, respectively, the displacement and traction vectors at time t_m, $m=1,2,\cdots,n$. Normally, $\mathbf{H}_D=\mathbf{H}_D^{nn}$ and $\mathbf{G}_D=\mathbf{G}_D^{nn}$ are not symmetric. When the asymmetric boundary element method is coupled with the symmetric finite element method the coupling scheme will not be symmetric. Therefore, the following symmetrization procedure is used.

Multiplying Eq. (1) by $\mathbf{G}_D^T$ and $\mathbf{H}_D^T$, respectively, one can get

$$\mathbf{L}_D^{GH}\mathbf{u}^n=\mathbf{L}_D^{GG}\mathbf{p}^n+\sum_{m=1}^{n-1}\mathbf{L}_D^{GGmn}\mathbf{p}^m-\sum_{m=1}^{n-1}\mathbf{L}_D^{GHmn}\mathbf{u}^m \tag{2}$$

$$(\mathbf{L}_D^{GH})^T\mathbf{p}^n=\mathbf{L}_D^{HH}\mathbf{u}^n+\sum_{m=1}^{n-1}\mathbf{L}_D^{HHmn}\mathbf{u}^m-\sum_{m=1}^{n-1}\mathbf{L}_{DT}^{HGmn}\mathbf{p}^m \tag{3}$$

where $\mathbf{L}_D^{GG}=\mathbf{G}_D^T\mathbf{G}_D$, $\mathbf{L}_D^{GH}=\mathbf{G}_D^T\mathbf{H}_D$, $\mathbf{L}_D^{HH}=(\mathbf{H}_D)^T\mathbf{H}_D$, $\mathbf{L}_D^{GGmn}=\mathbf{G}_D^T\mathbf{G}_D^{mn}$, $\mathbf{L}_D^{GHmn}=\mathbf{G}_D^T\mathbf{H}_D^{mn}$, $\mathbf{L}_{DT}^{HGmn}=(\mathbf{H}_D)^T\mathbf{G}_D^{mn}$, $\mathbf{L}_D^{HHmn}=(\mathbf{H}_D)^T\mathbf{H}_D^{mn}$. $\mathbf{L}_D^{GG}$ and $\mathbf{L}_D^{HH}$ are symmetric matrices.

Double nodes cannot be used here if the tractions for both of these two nodes are unknown. For corner points, two nodes with small distance can be used. However, if traction for at least one of the double nodes is known, double nodes can also be used. While a similar way with double nodes can be used to calculate $\mathbf{H}_D$ so as to increase the accuracy.

In order to get the symmetric boundary element method formulation ready to be used in BEM/FEM coupling procedure, the whole boundary for the boundary element method domain should be divided into three parts, Γ_1—where displacements are prescribed, Γ_2—where traction components are prescribed and the boundary element/finite element interface Γ_i. Subscript "1," "2," and "**i**" are used to represent, respectively, the variables on Γ_1, Γ_2, and Γ_i. Applying Eqs. (2) and (3) to Γ_1 and Γ_2, respectively, one gets:

$$\begin{aligned}
&[\mathbf{L}_{D11}^{GH}\quad\mathbf{L}_{D12}^{GH}\quad\mathbf{L}_{D1i}^{GH}]\begin{Bmatrix}\mathbf{u}_1^n\\ \mathbf{u}_2^n\\ \mathbf{u}_i^n\end{Bmatrix}\\
&\quad=[\mathbf{L}_{D11}^{GG}\quad\mathbf{L}_{D12}^{GG}\quad\mathbf{L}_{D1i}^{GG}]\begin{Bmatrix}\mathbf{p}_1^n\\ \mathbf{p}_2^n\\ \mathbf{p}_i^n\end{Bmatrix}\\
&\qquad+\sum_{m=1}^{n-1}[\mathbf{L}_{D11}^{GGmn}\quad\mathbf{L}_{D12}^{GGmn}\quad\mathbf{L}_{D1i}^{GGMn}]\begin{Bmatrix}\mathbf{p}_1^m\\ \mathbf{p}_2^m\\ \mathbf{p}_i^m\end{Bmatrix}\\
&\qquad-\sum_{m=1}^{n-1}[\mathbf{L}_{D11}^{GHmn}\quad\mathbf{L}_{D12}^{GHmn}\quad\mathbf{L}_{D1i}^{GHmn}]\begin{Bmatrix}\mathbf{u}_1^m\\ \mathbf{u}_2^m\\ \mathbf{u}_i^m\end{Bmatrix}
\end{aligned} \tag{4}$$

$$\begin{aligned}
&[(\mathbf{L}_{D12}^{GH})^T\quad(\mathbf{L}_{D22}^{GH})^T\quad(\mathbf{L}_{Di2}^{GH})^T]\begin{Bmatrix}\mathbf{p}_1^n\\ \mathbf{p}_2^n\\ \mathbf{p}_i^n\end{Bmatrix}\\
&\quad=[\mathbf{L}_{D21}^{HH}\quad\mathbf{L}_{D22}^{HH}\quad\mathbf{L}_{D2i}^{HH}]\begin{Bmatrix}\mathbf{u}_1^n\\ \mathbf{u}_2^n\\ \mathbf{u}_i^n\end{Bmatrix}\\
&\qquad+\sum_{m=1}^{n-1}[\mathbf{L}_{D21}^{HHmn}\quad\mathbf{L}_{D22}^{HHmn}\quad\mathbf{L}_{D2i}^{HHmn}]\begin{Bmatrix}\mathbf{u}_1^m\\ \mathbf{u}_2^m\\ \mathbf{u}_i^m\end{Bmatrix}\\
&\qquad-\sum_{m=1}^{n-1}[\mathbf{L}_{DT21}^{HGmn}\quad\mathbf{L}_{DT22}^{HGmn}\quad\mathbf{L}_{DT2i}^{HGmn}]\begin{Bmatrix}\mathbf{P}_1^m\\ \mathbf{p}_2^m\\ \mathbf{p}_i^m\end{Bmatrix}.
\end{aligned} \tag{5}$$

Applying both Eqs. (2) and (3) to Γ_i one gets

 Copyright © 2003 by ASME

$$
\begin{aligned}
&[\mathbf{L}_{Di1}^{GH} \quad \mathbf{L}_{Di2}^{GH} \quad \mathbf{L}_{Dii}^{GH}]\begin{Bmatrix}\mathbf{u}_1^n\\ \mathbf{u}_2^n\\ \mathbf{u}_i^n\end{Bmatrix}\\
&\quad=[\mathbf{L}_{Di1}^{GG} \quad \mathbf{L}_{Di2}^{GG} \quad \mathbf{L}_{Dii}^{GG}]\begin{Bmatrix}\mathbf{p}_1^n\\ \mathbf{p}_2^n\\ \mathbf{p}_i^n\end{Bmatrix}\\
&\qquad+\sum_{m=1}^{n-1}[\mathbf{L}_{Di1}^{GGmn} \quad \mathbf{L}_{Di2}^{GGmn} \quad \mathbf{L}_{Dii}^{GGmn}]\begin{Bmatrix}\mathbf{p}_1^m\\ \mathbf{p}_2^m\\ \mathbf{p}_i^m\end{Bmatrix}\\
&\qquad-\sum_{m=1}^{n-1}[\mathbf{L}_{Di1}^{GHmn} \quad \mathbf{L}_{Di2}^{GHmn} \quad \mathbf{L}_{Dii}^{GHmn}]\begin{Bmatrix}\mathbf{u}_1^m\\ \mathbf{u}_2^m\\ \mathbf{u}_i^m\end{Bmatrix} \qquad (6)
\end{aligned}
$$

$$
\begin{aligned}
&[(\mathbf{L}_{D1i}^{GH})^T \quad (\mathbf{L}_{D2i}^{GH})^T \quad (\mathbf{L}_{Dii}^{GH})^T]\begin{Bmatrix}\mathbf{p}_1^n\\ \mathbf{p}_2^n\\ \mathbf{p}_i^n\end{Bmatrix}\\
&\quad=[\mathbf{L}_{Di1}^{HH} \quad \mathbf{L}_{Di2}^{HH} \quad \mathbf{L}_{Dii}^{HH}]\begin{Bmatrix}\mathbf{u}_1^n\\ \mathbf{u}_2^n\\ \mathbf{u}_i^n\end{Bmatrix}\\
&\qquad+\sum_{m=1}^{n-1}[\mathbf{L}_{Di1}^{HHmn} \quad \mathbf{L}_{Di2}^{HHmn} \quad \mathbf{L}_{Dii}^{HHmn}]\begin{Bmatrix}\mathbf{u}_1^m\\ \mathbf{u}_2^m\\ \mathbf{u}_i^m\end{Bmatrix}\\
&\qquad-\sum_{m=1}^{n-1}[\mathbf{L}_{DTi1}^{HGmn} \quad \mathbf{L}_{DTi2}^{HGmn} \quad \mathbf{L}_{DTii}^{HGmn}]\begin{Bmatrix}\mathbf{p}_1^m\\ \mathbf{p}_2^m\\ \mathbf{p}_i^m\end{Bmatrix}. \qquad (7)
\end{aligned}
$$

Combining Eqs. (4) to (7) and move all unknowns to the left, one can get

$$
\begin{aligned}
&\begin{bmatrix}
-\mathbf{L}_{D11}^{GG} & \mathbf{L}_{D12}^{GH} & -\mathbf{L}_{D1i}^{GG} & \mathbf{L}_{D1i}^{GH}\\
(\mathbf{L}_{D12}^{GH})^T & -\mathbf{L}_{D22}^{HH} & (\mathbf{L}_{Di2}^{GH})^T & -\mathbf{L}_{D2i}^{HH}\\
-\mathbf{L}_{Di1}^{GG} & \mathbf{L}_{Di2}^{GH} & -\mathbf{L}_{Dii}^{GG} & \mathbf{L}_{Dii}^{GH}\\
(\mathbf{L}_{D1i}^{GH})^T & -\mathbf{L}_{Di2}^{HH} & (\mathbf{L}_{Dii}^{GH})^T & -\mathbf{L}_{Dii}^{HH}
\end{bmatrix}\begin{Bmatrix}\mathbf{p}_1^n\\ \mathbf{u}_2^n\\ \mathbf{p}_i^n\\ \mathbf{u}_i^n\end{Bmatrix}\\
&\quad=\begin{bmatrix}
-\mathbf{L}_{D11}^{GH} & \mathbf{L}_{D12}^{GG}\\
\mathbf{L}_{D21}^{HH} & -(\mathbf{L}_{D22}^{GH})^T\\
-\mathbf{L}_{Di1}^{GH} & \mathbf{L}_{Di2}^{GG}\\
\mathbf{L}_{Di1}^{HH} & -(\mathbf{L}_{D2i}^{GH})^T
\end{bmatrix}\begin{Bmatrix}\mathbf{u}_1^n\\ \mathbf{p}_2^n\end{Bmatrix}\\
&\qquad+\sum_{m=1}^{n-1}\begin{bmatrix}
\mathbf{L}_{D11}^{GGmn} & \mathbf{L}_{D12}^{GGmn} & \mathbf{L}_{D1i}^{GGmn}\\
-\mathbf{L}_{DT21}^{HGmn} & -\mathbf{L}_{DT22}^{HGmn} & -\mathbf{L}_{DT2i}^{HGmn}\\
\mathbf{L}_{Di1}^{GGmn} & \mathbf{L}_{Di2}^{GGmn} & \mathbf{L}_{Dii}^{GGmn}\\
-\mathbf{L}_{DTi1}^{HGmn} & -\mathbf{L}_{DTi2}^{HGmn} & -\mathbf{L}_{DTii}^{HGmn}
\end{bmatrix}\begin{Bmatrix}\mathbf{p}_1^m\\ \mathbf{p}_2^m\\ \mathbf{p}_i^m\end{Bmatrix}\\
&\qquad+\sum_{m=1}^{n-1}\begin{bmatrix}
-\mathbf{L}_{D11}^{GHmn} & -\mathbf{L}_{D12}^{GHmn} & -\mathbf{L}_{D1i}^{GHmn}\\
\mathbf{L}_{D21}^{HHmn} & \mathbf{L}_{D22}^{HHmn} & \mathbf{L}_{D2i}^{HHmn}\\
-\mathbf{L}_{Di1}^{GHmn} & -\mathbf{L}_{Di2}^{GHmn} & -\mathbf{L}_{Dii}^{GHmn}\\
\mathbf{L}_{Di1}^{HHmn} & \mathbf{L}_{Di2}^{HHmn} & \mathbf{L}_{Dii}^{HHmn}
\end{bmatrix}\begin{Bmatrix}\mathbf{u}_1^m\\ \mathbf{u}_2^m\\ \mathbf{u}_i^m\end{Bmatrix}. \qquad (8)
\end{aligned}
$$

Equation (8) can be written in a more compact form as

$$\mathbf{A}_{D0}\mathbf{X}^n=\mathbf{Y}^n. \qquad (9)$$

As both $\mathbf{L}_D^{GG}$ and $\mathbf{L}_D^{HH}$ are symmetric matrices, the time domain collocation boundary element method formulation given by (8) or (9) is symmetric.

Equation (8) or (9) is the relationship between distributed traction and displacement, while the finite element method formulation represents the relationship between concentrate nodal load and displacement. Therefore, in order to couple with the finite element method the unknown traction $\mathbf{p}_i^n$ in Eq. (8) should be converted to the equivalent nodal load $\mathbf{R}_i^n$. The same space interpolation function is used for $\mathbf{p}_i^n$ in the boundary element method domain and the corresponding traction $\mathbf{p}_{Fi}^n$ in the finite element method domain on the interface. Subscript "**F**" represents the variables in the finite element method domain, to distinguish it from those variables in the boundary element method domain. Therefore, the equivalent nodal load vector at time t^n on the interface can be written as

$$\mathbf{R}_{Fi}^n=\mathbf{F}\mathbf{p}_{Fi}^n \qquad (10)$$

for the finite element method, and

$$\mathbf{R}_i^n=\mathbf{F}\mathbf{p}_i^n \qquad (11)$$

for the boundary element method.

Using the equilibrium condition $\mathbf{p}_{Fi}^n=-\mathbf{p}_i^n$ one can get

$$\mathbf{p}_i^n=\mathbf{F}^{-1}\mathbf{R}_i^n=-\mathbf{p}_{Fi}^n=\mathbf{F}^{-1}(-\mathbf{R}_{Fi}^n), \qquad (12)$$

Substituting Eq. (12) into Eq. (8), and considering the compatibility condition, $\mathbf{u}_{Fi}^n=\mathbf{u}_i^n$, one can get

$$
\begin{aligned}
&\begin{bmatrix}
-\mathbf{L}_{D11}^{GG} & \mathbf{L}_{D12}^{GH} & -\mathbf{L}_{D1i}^{GG}\mathbf{F}^{-1} & \mathbf{L}_{D1i}^{GH}\\
(\mathbf{L}_{D12}^{GH})^T & -\mathbf{L}_{D22}^{HH} & (\mathbf{L}_{Di2}^{GH})^T\mathbf{F}^{-1} & -\mathbf{L}_{D2i}^{HH}\\
-\mathbf{L}_{Di1}^{GG} & \mathbf{L}_{Di2}^{GH} & -\mathbf{L}_{Dii}^{GG}\mathbf{F}^{-1} & \mathbf{L}_{Dii}^{GH}\\
(\mathbf{L}_{D1i}^{GH})^T & -\mathbf{L}_{Di2}^{HH} & (\mathbf{L}_{Dii}^{GH})^T\mathbf{F}^{-1} & -\mathbf{L}_{Dii}^{HH}
\end{bmatrix}\begin{Bmatrix}\mathbf{p}_1^n\\ \mathbf{u}_2^n\\ -\mathbf{R}_{Fi}^n\\ \mathbf{u}_{Fi}^n\end{Bmatrix}\\
&\quad=\begin{bmatrix}
-\mathbf{L}_{D11}^{GH} & \mathbf{L}_{D12}^{GG}\\
\mathbf{L}_{D21}^{HH} & -(\mathbf{L}_{D22}^{GH})^T\\
-\mathbf{L}_{Di1}^{GH} & \mathbf{L}_{Di2}^{GG}\\
\mathbf{L}_{Di1}^{HH} & -(\mathbf{L}_{D2i}^{GH})^T
\end{bmatrix}\begin{Bmatrix}\mathbf{u}_1^n\\ \mathbf{p}_2^n\end{Bmatrix}\\
&\qquad+\sum_{m=1}^{n-1}\begin{bmatrix}
\mathbf{L}_{D11}^{GGmn} & \mathbf{L}_{D12}^{GGmn} & \mathbf{L}_{D1i}^{GGmn}\\
-\mathbf{L}_{DT21}^{HGmn} & -\mathbf{L}_{DT22}^{HGmn} & -\mathbf{L}_{DT2i}^{HGmn}\\
\mathbf{L}_{Di1}^{GGmn} & \mathbf{L}_{Di2}^{GGmn} & \mathbf{L}_{Dii}^{GGmn}\\
-\mathbf{L}_{DTi1}^{HGmn} & -\mathbf{L}_{DTi2}^{HGmn} & -\mathbf{L}_{DTii}^{HGmn}
\end{bmatrix}\begin{Bmatrix}\mathbf{p}_1^m\\ \mathbf{p}_2^m\\ \mathbf{p}_i^m\end{Bmatrix}\\
&\qquad+\sum_{m=1}^{n-1}\begin{bmatrix}
-\mathbf{L}_{D11}^{GHmn} & -\mathbf{L}_{D12}^{GHmn} & -\mathbf{L}_{D1i}^{GHmn}\\
\mathbf{L}_{D21}^{HHmn} & \mathbf{L}_{D22}^{HHmn} & \mathbf{L}_{D2i}^{HHmn}\\
-\mathbf{L}_{Di1}^{GHmn} & -\mathbf{L}_{Di2}^{GHmn} & -\mathbf{L}_{Dii}^{GHmn}\\
\mathbf{L}_{Di1}^{HHmn} & \mathbf{L}_{Di2}^{HHmn} & \mathbf{L}_{Dii}^{HHmn}
\end{bmatrix}\begin{Bmatrix}\mathbf{u}_1^m\\ \mathbf{u}_2^m\\ \mathbf{u}_i^m\end{Bmatrix}. \qquad (13)
\end{aligned}
$$

In order to convert Eq. (13) into symmetric form, multiplying its third row by $-(\mathbf{F}^{-1})^T$, one can get

$$
\begin{bmatrix}
-\mathbf{L}_{D11}^{GG} & \mathbf{L}_{D12}^{GH} & \mathbf{L}_{D1i}^{GG}\mathbf{F}^{-1} & \mathbf{L}_{D1i}^{GH} \\
(\mathbf{L}_{D12}^{GH})^T & -\mathbf{L}_{D22}^{HH} & -(\mathbf{L}_{Di2}^{GH})^T\mathbf{F}^{-1} & -\mathbf{L}_{D2i}^{HH} \\
(\mathbf{F}^{-1})^T\mathbf{L}_{Di1}^{GG} & -(\mathbf{F}^{-1})^T\mathbf{L}_{Di2}^{GH} & -(\mathbf{F}^{-1})^T\mathbf{L}_{Dii}^{GG}\mathbf{F}^{-1} & -(\mathbf{F}^{-1})^T\mathbf{L}_{Dii}^{GH} \\
(\mathbf{L}_{D1i}^{GH})^T & -\mathbf{L}_{Di2}^{HH} & -(\mathbf{L}_{Dii}^{GH})^T\mathbf{F}^{-1} & -\mathbf{L}_{Dii}^{HH}
\end{bmatrix}
\begin{Bmatrix}
\mathbf{p}_1^n \\ \mathbf{u}_2^n \\ \mathbf{R}_{Fi}^n \\ \mathbf{u}_{Fi}^n
\end{Bmatrix}
$$

$$
=\begin{bmatrix}
-\mathbf{L}_{D11}^{GH} & \mathbf{L}_{D12}^{GG} \\
\mathbf{L}_{D21}^{HH} & -(\mathbf{L}_{D22}^{GH})^T \\
(\mathbf{F}^{-1})^T\mathbf{L}_{Di1}^{GH} & -(\mathbf{F}^{-1})^T\mathbf{L}_{Di2}^{GG} \\
\mathbf{L}_{Di1}^{HH} & -(\mathbf{L}_{D2i}^{GH})^T
\end{bmatrix}
\begin{Bmatrix}
\mathbf{u}_1^n \\ \mathbf{p}_2^n
\end{Bmatrix}
+\sum_{m=1}^{n-1}
\begin{bmatrix}
\mathbf{L}_{D11}^{GGmn} & \mathbf{L}_{D12}^{GGmn} & \mathbf{L}_{D1i}^{GGmn} \\
-\mathbf{L}_{DT21}^{HGmn} & -\mathbf{L}_{DT22}^{HGmn} & -\mathbf{L}_{DT2i}^{HGmn} \\
-(\mathbf{F}^{-1})^T\mathbf{L}_{Di1}^{GGmn} & -(\mathbf{F}^{-1})^T\mathbf{L}_{Di2}^{GGmn} & -(\mathbf{F}^{-1})^T\mathbf{L}_{Dii}^{GGmn} \\
-\mathbf{L}_{DTi1}^{HGmn} & -\mathbf{L}_{DTi2}^{HGmn} & -\mathbf{L}_{DTii}^{HGmn}
\end{bmatrix}
\begin{Bmatrix}
\mathbf{p}_1^m \\ \mathbf{p}_2^m \\ \mathbf{p}_i^m
\end{Bmatrix}
$$

$$
+\sum_{m=1}^{n-1}
\begin{bmatrix}
-\mathbf{L}_{D11}^{GHmn} & -\mathbf{L}_{D12}^{GHmn} & -\mathbf{L}_{D1i}^{GHmn} \\
\mathbf{L}_{D21}^{HHmn} & \mathbf{L}_{D22}^{HHmn} & \mathbf{L}_{D2i}^{HHmn} \\
(\mathbf{F}^{-1})^T\mathbf{L}_{Di1}^{GHmn} & (\mathbf{F}^{-1})^T\mathbf{L}_{Di2}^{GHmn} & (\mathbf{F}^{-1})^T\mathbf{L}_{Dii}^{GHmn} \\
\mathbf{L}_{Di1}^{HHmn} & \mathbf{L}_{Di2}^{HHmn} & \mathbf{L}_{Dii}^{HHmn}
\end{bmatrix}
\begin{Bmatrix}
\mathbf{u}_1^m \\ \mathbf{u}_2^m \\ \mathbf{u}_i^m
\end{Bmatrix} \tag{14}
$$

As all unknowns are on the left-hand side, Eq. (14) is the symmetric boundary element method formulation which can be used directly to couple with the finite element method.

3 Numerical Example

The example depicted in Fig. 1, presented previously by Mansur [9], consists of a one-dimensional rod under a Heaviside-type forcing function, and has been chosen to be analyzed by SCBEM/FEM scheme. The displacements, u_1 and u_2, were assumed to be zero at $x_1=0$, and the tractions were also taken as null at $x_2=0$ and $x_2=b$, for any time t. At $x_1=a$ and $t=0$, a load $p_1=pH(t\text{-}0)$ was suddenly applied and kept constant until the end of the analysis (E is the Young's modulus, Poisson coefficient was considered null). 128 finite elements and 32 boundary elements with the length L_j were used to discretize each half into which the domain was subdivided (see Fig. 1).

Figures 2 show time histories of the displacement component u_1 and the stress component σ_{11} at point $D(a/2,b/2)$ from SCBEM/FEM. The parameter $\beta=c_1\Delta t/L_j$ was kept constant and equal to 0.6 in the analyses. Comparing with the analytical results, one can see that reasonable results can be obtained from the SCBEM/FEM procedure given in this paper for elastodynamic problems.

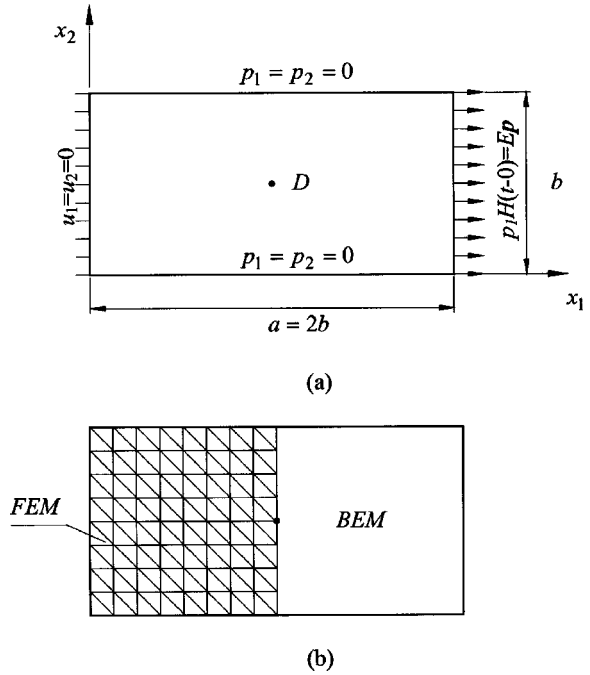

Fig. 1 One-dimensional rod under a Heaviside-type forcing function: topology, load, and discretization

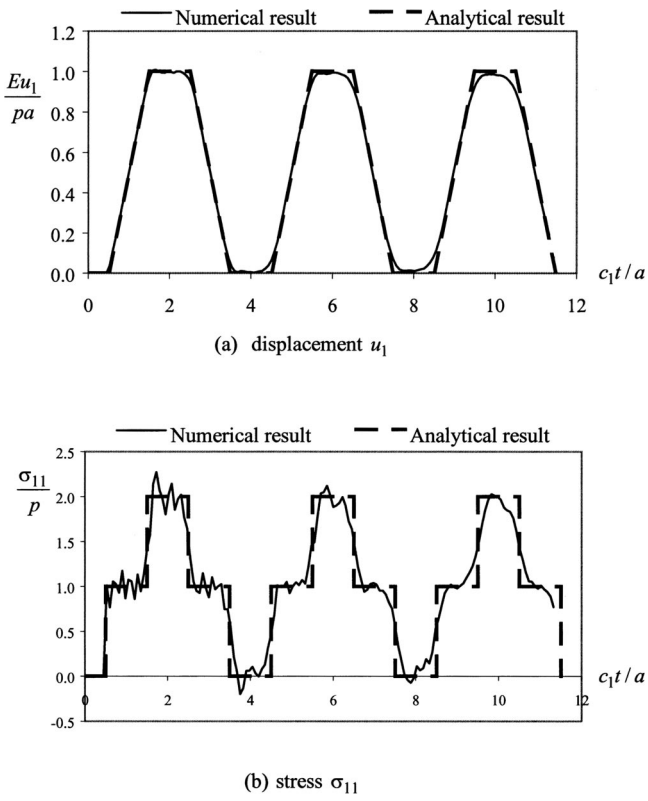

Fig. 2 Time histories for the response at point $D(a/2,b/2)$ from SCBEM/FEM procedure for $\beta=0.6$ and $\theta=1.4$

4 Conclusions

SCBEM/FEM coupling procedure has been given and applied to a two-dimensional elastodynamic problem. Symmetry of coefficient matrix can save up to 50% memory storage, and enable the employment of efficient symmetric computation techniques that

can subsequently save the computer time, especially for the coupling procedure. There is no restriction for the SCBEM/FEM coupling procedure; it can be easily applied to scalar wave problems and three-dimensional problems.

References

[1] Sirtori, S., 1979, ''General Stress Analysis Method by Means of Integral Equations and Boundary Elements,'' Meccanica, **14**, pp. 210–218.
[2] Maier, G., Novati, G., and Sirtori, S., 1990, *On Symmetrization in Boundary Element Elastic-Plastic Analysis: Discretization Methods in Structural Mechanics*, eds. G. Kuhn and H. Mang, Springer-Verlag, Berlin, pp. 191–200.
[3] Bonnet, M., Maier, G., and Polizzotto, C., 1998, ''Symmetric Galerkin Boundary Element Methods,'' Appl. Mech. Rev., **51**(11), pp. 669–704.
[4] Carini, A., Diligent, M., Maranesi, P., and Zanella, M., 1999, ''Analytical Integrations for Two-Dimensional Elastic Analysis by the Symmetric Galerkin Boundary Element Method,'' Computational Mech., Berlin, **23**, pp. 308–323.
[5] Tanaka, M., Sladek, V., and Sladek, J., 1994, ''Regularization Techniques Applied to Boundary Element Methods,'' Appl. Mech. Rev., **47**(10), pp. 457–499.
[6] Gray, L. J., and Martha, L. F., 1990, ''Ingraffea AR. Hypersingular Integrals in Boundary Element Fracture Analysis,'' Int. J. Numer. Methods Eng., **29**, pp. 1135–1158.
[7] Guiggiani, M., 1994, ''Hypersingular Formulation for Boundary Stress Evaluation,'' Eng. Anal. Boundary Elem., **13**, pp. 169–179.
[8] Gallego, R., and Dominguez, J., 1996, ''Hypersingular BEM for Transient Elastodynamics,'' Int. J. Numer. Methods Eng., **39**, pp. 1681–1705.
[9] Mansur, W. J., 1983, ''A Time-Stepping Technique to Solve Wave Propagation Problems Using the Boundary Element Method,'' Ph.D. thesis, University of Southampton, Southampton, UK.

Dynamic Fracture in Brittle Solids at High Rates of Loading

Y.-Q. Zhang
Protective Technology Research Center, School of Civil and Environmental Engineering, Nanyang Technological University, Singapore 639798

H. Hao
Department of Civil and Resource Engineering, University of Western Australia Nedlands, Western Australia 6009

This paper presents a dynamic damage model for predicting fracture and fragmentation of brittle materials subjected to loads with high loading rates. This model is based on the mechanics of microcrack nucleation, growth, and coalescence to formulate the evolution of damage. The damage in the model is assumed to be isotropic and is a function of time and applied stress. The model provides a direct, explicit, and quantitative method to determine the rate-dependent fracture stress and fragment size generated by crack coalescence in the dynamic fragmentation process. It considers the experimental facts that a brittle material does not fail if the applied stress is lower than its static strength and certain time duration is needed for fracture to take place when it is subjected to a stress higher than its static strength. Comparisons between theoretical predictions and test data are made and shown to be in good agreement. [DOI: 10.1115/1.1571854]

1 Introduction

The dynamic fracture and fragmentation of brittle materials has a wide range of physical relevance including, but not limited to, such phenomena as rock comminution, the milling of powders, hard particle impact of ceramic and ceramic composite structures, and the penetration of ceramic armour. When a brittle material is under high-rate deformation, large stresses are generated in a relatively short time. Thus, many cracks are nucleated and they propagate simultaneously in the material, ultimately coalescing and separating the solid into fragments. High-rate loading occurs in a wide range of technologically important applications including such obvious examples as rock blasting, shattering of glass, and armor penetration. When the loading rate is high, the mechanical response of a material is generally different from what it is at a low-loading rate. Such rate dependence is observed for nearly all the brittle materials including rock, ceramics, and glasses, [1].

When a brittle material is subjected to a tensile stress it can support that stress and does not fail unless the value of the stress is larger than its static strength. Furthermore, it will not fail either even though the stress is well above the static strength but the time duration is very short. In dynamic loading, the stress can exceed the material strength, but it may not damage the material if its duration is too short. Dynamic damage is accumulated as a function of time and applied stress. From the viewpoint of microcrack activation and growth, microcracks may be activated by a high stress level and show a tendency for further growth. However, actual growth is possible only when the time duration of the stress is long enough, [2].

It is important to understand the mechanisms of dynamic damage and fragmentation. A lot of theoretical models intended to correlate the features of dynamic fracture and fragmentation have been suggested. Shockey et al. [3] have developed models based on the activation, growth, and coalescence of inherent distributions of fracture-producing flaws, predicting crack and fragment size spectra resulting from blast loading. Grady and Kipp [4] presented a description of dynamic fracture and fragmentation of rock mass with emphasis on the strain-rate dependence of measurable fracture properties. Taylor et al. [5] developed a damage model to simulate stress-wave-induced rock fracture during blasting based on the analysis of cracked systems on a continuum level. In the continuum models, [4,5] it is assumed that microcracks initiate and grow immediately when the strain becomes tensile. Based on energy balance principles, many models which provide a rational basis for prediction of fragment size in a fragmentation event have been developed, [6–8].

In this paper, a constitutive model for the dynamic damage and fragmentation of brittle materials is presented. The damage in the model is assumed to be isotropic and is a function of time and applied stress. The model provides a direct, explicit, and quantitative method to determine the rate-dependent fracture stress and fragment size generated by crack coalescence in the dynamic fragmentation process. It takes account of the experimental facts that a brittle material does not fail if the applied stress is lower than its static strength and certain time duration is needed for fracture to take place when it is subjected to a stress higher than its static strength.

2 Damage

Microscopic crack growth results in stiffness and strength degradation of loaded structures, which is measured by the introduction into the constitutive equations of a damage variable. For isotropic damage, it will be defined as a scalar parameter D. Then in accordance with the strain equivalence principle, the stress-strain relation can be expressed as

$$\sigma = E(1-D)\varepsilon \tag{1}$$

where E is the Young's modulus for the undamaged virgin material, σ is a tensile stress, and ε is a tensile strain.

Grady and Kipp [4] followed Walsh's approximate microstructural theory of the elastic properties of fractured rock, [9], and defined the scalar variable of the damage D in terms of the volume of idealized penny-shaped cracks in the material as

Contributed by the Applied Mechanics Division of THE AMERICAN SOCIETY OF MECHANICAL ENGINEERS for publication in the ASME JOURNAL OF APPLIED MECHANICS. Manuscript received by the ASME Applied Mechanics Division, February 5, 2002, final revision, July 26, 2002. Associate Editor: K. Ravi-Chandar.

Copyright © 2003 by ASME

$$D = NV \tag{2}$$

where N is the number of cracks per unit volume and $V = 4/3\pi r^3$ is the spherical region surrounding the penny-shaped crack of radius r which approximates the stress-relieved volume due to the traction-free boundary of the crack.

As certain time duration is needed for fracture to take place when a brittle material is subjected to a stress higher than its static strength, the evolution of damage can be determined by the number of cracks which activate at the time t as follows:

$$D(t) = \int_{t_c}^{t} \dot{N}(s) V(t-s) ds \tag{3}$$

where t_c is the time duration needed for the tensile strain ε to reach the critical value $\varepsilon_{cr} = \sigma_{st}/E$, in which σ_{st} is the static tensile strength, and the crack density increase

$$\dot{N} = \alpha \langle \varepsilon - \varepsilon_{cr} \rangle^{\beta} \tag{4}$$

which is similar to that defined by Yang et al. [10]. In Eq. (4), the angular bracket $\langle \cdot \rangle$ denotes that the function is defined by $\langle x \rangle = (|x| + x)/2$, and α and β are material parameters.

As for the volume $V(t-s)$, it is determined by a microstructural law for the growth of cracks, which are activated at past time s,

$$V(t-s) = \frac{4}{3}\pi r^3 = \frac{4}{3}\pi c_g^3 (t-s)^3, \tag{5}$$

where c_g is the crack growth velocity and generally $0 < c_g < c_l$ (c_l is the elastic wave speed), [8].

The derivative of Eq. (5) is based on the assumption that as soon as cracks activate, the growth velocity reaches c_g very quickly. Thus substituting Eqs. (4) and (5) into Eq. (3), we have

$$D(t) = \frac{4}{3}\alpha\pi c_g^3 \int_{t_c}^{t} \langle \varepsilon - \varepsilon_{cr} \rangle^{\beta} (t-s)^3 ds. \tag{6}$$

A simple example is the case with a constant strain loading rate, i.e., $\varepsilon(t) = \dot{\varepsilon}_0 t$, where $\dot{\varepsilon}_0$ is a constant strain rate. Substituting this into Eq. (6) gives an expression for damage growth

$$D(t) = \frac{4}{3}\alpha\pi c_g^3 \dot{\varepsilon}_0^{\beta} \int_{t_c}^{t} \langle s - t_c \rangle^{\beta} (t-s)^3 ds = m\dot{\varepsilon}_0^{\beta} (t - t_c)^{\beta+4} \tag{7}$$

where the relation $t_c = \varepsilon_{cr}/\dot{\varepsilon}_0$ is used, and

$$m = \frac{8\pi c_g^3 \alpha}{(\beta+1)(\beta+2)(\beta+3)(\beta+4)}, \tag{8}$$

which is seen to be a constant, depending on the material properties.

3 Fracture Stress and Fragment Size Predictions

If the tensile strain and damage scalar corresponding to the fracture stress σ_F are denoted by ε_F and D_F, respectively, from Eq. (1) we have

$$\sigma_F = (1 - D_F) E \varepsilon_F \tag{9}$$

where $\varepsilon_F = \dot{\varepsilon}_0 t_F$, and t_F is the total time to reach the fracture stress. From Eq. (7),

$$t_F - t_c = \left(\frac{D_F}{m} \right)^{1/(\beta+4)} \dot{\varepsilon}_0^{-\beta/(\beta+4)}. \tag{10}$$

Combining Eqs. (9) and (10), and using the relation $\varepsilon_{cr} = \dot{\varepsilon}_0 t_c$, the fracture stress at a certain strain rate in uniaxial tensile can be obtained as

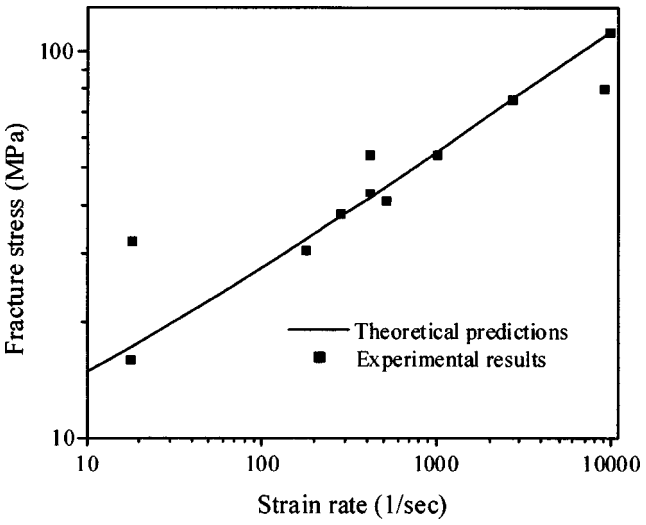

Fig. 1 Fracture stress for different values of applied strain rate

$$\sigma_F = (1 - D_F)\sigma_{st} + E(1 - D_F)\left(\frac{D_F}{m} \right)^{1/(\beta+4)} \dot{\varepsilon}_0^{4/(\beta+4)}. \tag{11}$$

Dependence of the fracture stress on strain rate is provided by the above equation. Since fracture stress for many brittle materials such as rock and concrete depends on the cube root of the strain rate, [7,11], β can be taken as equal to 8. Combining Eqs. (8) and (11),

$$\alpha = \frac{D_F}{n} \dot{\varepsilon}_0^4 \left(\frac{E(1 - D_F)}{\sigma_F - (1 - D_F)\sigma_{st}} \right)^{\beta+4} \tag{12}$$

where

$$n = \frac{8\pi c_g^3}{(\beta+1)(\beta+2)(\beta+3)(\beta+4)}. \tag{13}$$

Fragments are associated with crack initiation, propagation and coalescence, thus it is necessary to know the crack size in order to predict the fragment size. For this reason, the damage defined by Eq. (3) is given in terms of the distribution of crack size

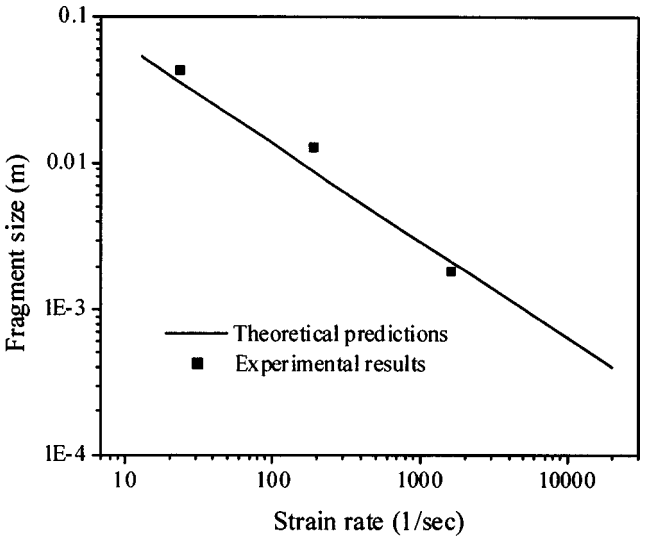

Fig. 2 Dominant fragment size for different values of applied strain rate

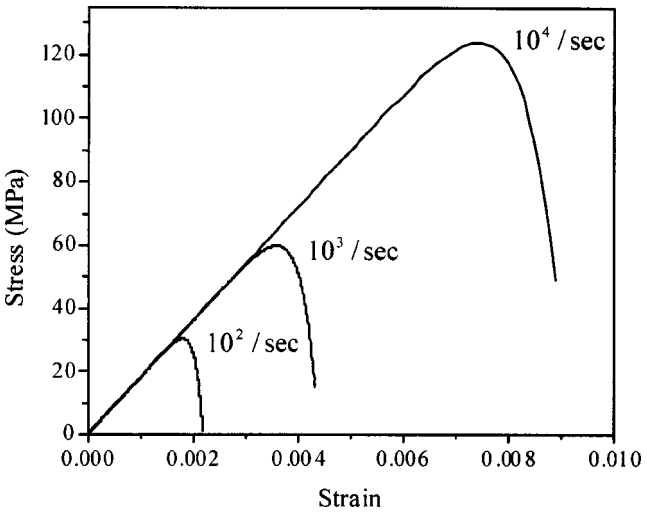

Fig. 3 Stress versus strain over three orders of magnitude of strain rate

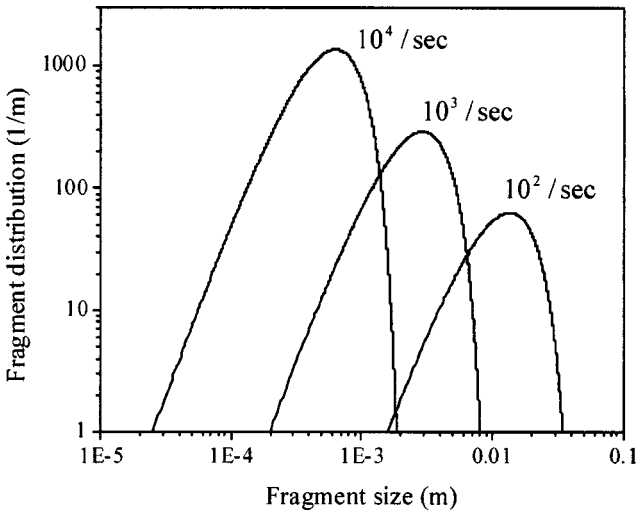

Fig. 4 Fragment distributions corresponding to different constant strain rates

$$D(t)=\int_0^{c_g(t-t_c)}\omega(r,t)dr \tag{14}$$

where

$$\omega(r,t)=\frac{4\pi r^3}{3c_g}\alpha\dot{\varepsilon}_0^{\beta}(t-t_c-r/c_g)^{\beta} \tag{15}$$

is the damage or crack volume fraction distribution.

Fragmentation is defined to occur when the damage

$$D(t_f)=1, \tag{16}$$

which corresponds to fracture coalescence at time t_f. At fracture coalescence it is assumed that the fragment sides are formed by the fracture faces. Noting that the crack radius $r=L/2$ with L being the nominal fragment size, the fragment size distribution can be obtained as follows:

$$F(L)=\frac{1}{2}\omega(L/2,t_f). \tag{17}$$

Combining Eqs. (15) and (17), we have

$$F(L)=\frac{\pi\alpha L^3}{12c_g}\dot{\varepsilon}_0^{\beta}[t_f-t_c-L/(2c_g)]^{\beta}. \tag{18}$$

It is evident that the fragment size distribution is also dependent on the strain rate. To determine the dependence on the strain rate of the dominant fragment size (fragment size corresponding to the largest volume fraction of material), the fragment size distribution $F(L)$ can be maximized with respect to the fragment size L. It is found that the fragment size distribution $F(L)$ has a maximum when

$$L_m=\frac{6c_g}{\beta+3}(t_f-t_c). \tag{19}$$

Combining Eqs. (7) and (16) gives

$$t_f-t_c=m^{-1/(\beta+4)}\dot{\varepsilon}_0^{-\beta/(\beta+4)}. \tag{20}$$

Substituting Eq. (20) into Eq. (19), we have

$$L_m=\frac{6c_g}{\beta+3}m^{-1/(\beta+4)}\dot{\varepsilon}_0^{-\beta/(\beta+4)}. \tag{21}$$

This is the expression for the dependence of dominant fragment size on the strain rate.

4 Application

In this section, the response of oil shale with kerogen content approximately 80 ml/kg subjected to a tensile stress is studied to verify the above theoretical derivations. The representative properties of 80 ml/kg oil shale are: elastic modulus $E=18$ GPa, density $\rho=2.0$ Mg/m^3, and elastic wave speed of $c_l=3.0$ km/s, [4]. In this study, the static tensile strength is assumed to be 5 MPa.

Using the above oil shale properties, the material parameters in the model will be determined for oil shale. The parameter β is taken to be equal to 8 so that the fracture stress is cube root dependent on the loading rate. According to the numerical investigations and some test results of brittle materials under high rate loading, [10,12], the damage value is about 0.22 when the dynamic tensile stress reaches the dynamic failure stress. If the strain rate of quasi-static experiments is assumed to be 10^{-2}/sec and the crack growth velocity c_g is 1300 m/sec as adopted by Grady and Kipp [4], the corresponding value of the parameter α calculated by Eq. (12) is about 8.85×10^{33}/m^{3}sec.

Thus from Eqs. (11) and (21), the fracture stress and the fragment size can be predicted by using the determined parameters. The theoretical predictions are compared with the experimental data provided by Grady and Kipp [4], which is, respectively, shown in Fig. 1 and Fig. 2. As can be seen, the predicted values of the fracture stress and the dominant fragment sizes agree reasonably well with the test data.

Figure 3 shows the stress-strain relation for the oil shale over three orders of magnitude of the strain rate. It can be seen that the peak stress before strain softening increases with the strain rate.

Fragment distributions calculated from Eq. (18) for the three constant strain rates are shown in Fig. 4. Fragment sizes at the highest strain rate of 10^4/sec are very small with a dominant size of about 0.63 mm. On the other hand, at the lowest strain rate of 10^2/sec the dominant fragment size is about 13.6 mm.

5 Conclusions

A model for dynamic damage and fragmentation of brittle materials has been developed. It emphasizes the strain-rate dependence of measurable fracture properties such as the fracture strength and fragment size. The model considers the following experimental facts: (1) a brittle material does not fail if the applied stress is lower than its static strength; (2) when a brittle material is

subjected to a stress higher than its static strength a certain time duration is needed so that the fracture can take place.

This model is essentially based on the mechanics of microcrack nucleation, growth and coalence to formulate the evolution of damage. The model provides a direct, explicit, and quantitative method to determine the rate-dependent fracture strength and fragment size generated by crack coalescence in the dynamic fragmentation process. The theoretical predictions are compared with the experimental data, and it is found that the predicted values of the fracture stress and the dominant fragment sizes agree reasonably well with the test results.

References

[1] Clifton, R. J., 2000, ''Response of Materials Under Dynamic Loading,'' Int. J. Solids Struct., **37**, pp. 105–113.

[2] Li, X. B., Chen, S. R., and Gu, D. S., 1994, ''Dynamic Strength of Rock Under Impulse Loads With Different Stress Waveforms and Durations,'' J. Cent.-South Inst. Mining Metall., **25**(3), pp. 55–67 (in Chinese).

[3] Shockey, D. A., Curran, D. R., Seaman, L., Rosenberg, J. T., and Petersen, C. F., 1974, ''Fragmentation of Rock Under Dynamic Loads,'' Int. J. Rock Mech. Min. Sci., **11**, pp. 303–317.

[4] Grady, D. E., and Kipp, M. E., 1980, ''Continuum Modelling of Explosive Fracture in Oil Shale,'' Int. J. Rock Mech. Min. Sci. Geomech. Abstr., **17**, pp. 147–157.

[5] Taylor, L. M., Chen, E. P., and Kuszmaul, J. S., 1986, ''Micro-crack Induced Damage Accumulation in Brittle Rock Under Dynamic Loading,'' Comput. Methods Appl. Mech. Eng., **55**, pp. 301–320.

[6] Grady, D. E., 1988, ''The Spall Strength of Condensed Matter,'' J. Mech. Phys. Solids, **36**, pp. 353–358.

[7] Liu, L., and Katsabanis, P. D., 1997, ''Development of a Continuum Damage Model for Blasting Analysis,'' Int. J. Rock Mech. Min. Sci., **34**, pp. 217–231.

[8] Miller, O., Freund, L. B., and Needleman, A., 1999, ''Modelling and Simulation of Dynamic Fragmentation in Brittle Materials,'' Int. J. Fract., **96**, pp. 101–125.

[9] Walsh, J. B., 1965, ''The Effect of Cracks on the Compressibility of Rock,'' J. Geophys. Res., **70**, pp. 381–389.

[10] Yang, R., Bawden, W. F., and Katsabanis, P. D., 1996, ''A New Constitutive Model for Blast Damage,'' Int. J. Rock Mech. Min. Sci. Geomech. Abstr., **33**, pp. 245–254.

[11] Kipp, M. E., and Grady, D. E., 1979, ''The Micro Mechanics of Impact Fracture of Rock,'' Int. J. Rock Mech. Min. Sci. Geomech. Abstr., **16**, pp. 293–302.

[12] Grady, D. E., and Kipp, M. E., 1987, ''Dynamic Rock Fragmentation,'' *Fracture Mechanics of Rock*, B. K. Atkinson, ed., Academic Press, London, pp. 429–475.